PULSED ELECTRIC FIELDS IN BIOTECHNOLOGY

EDITED BY: Saša Haberl Meglič, Damijan Miklavčič and Eugene Vorobiev
PUBLISHED IN: Frontiers in Bioengineering and Biotechnology

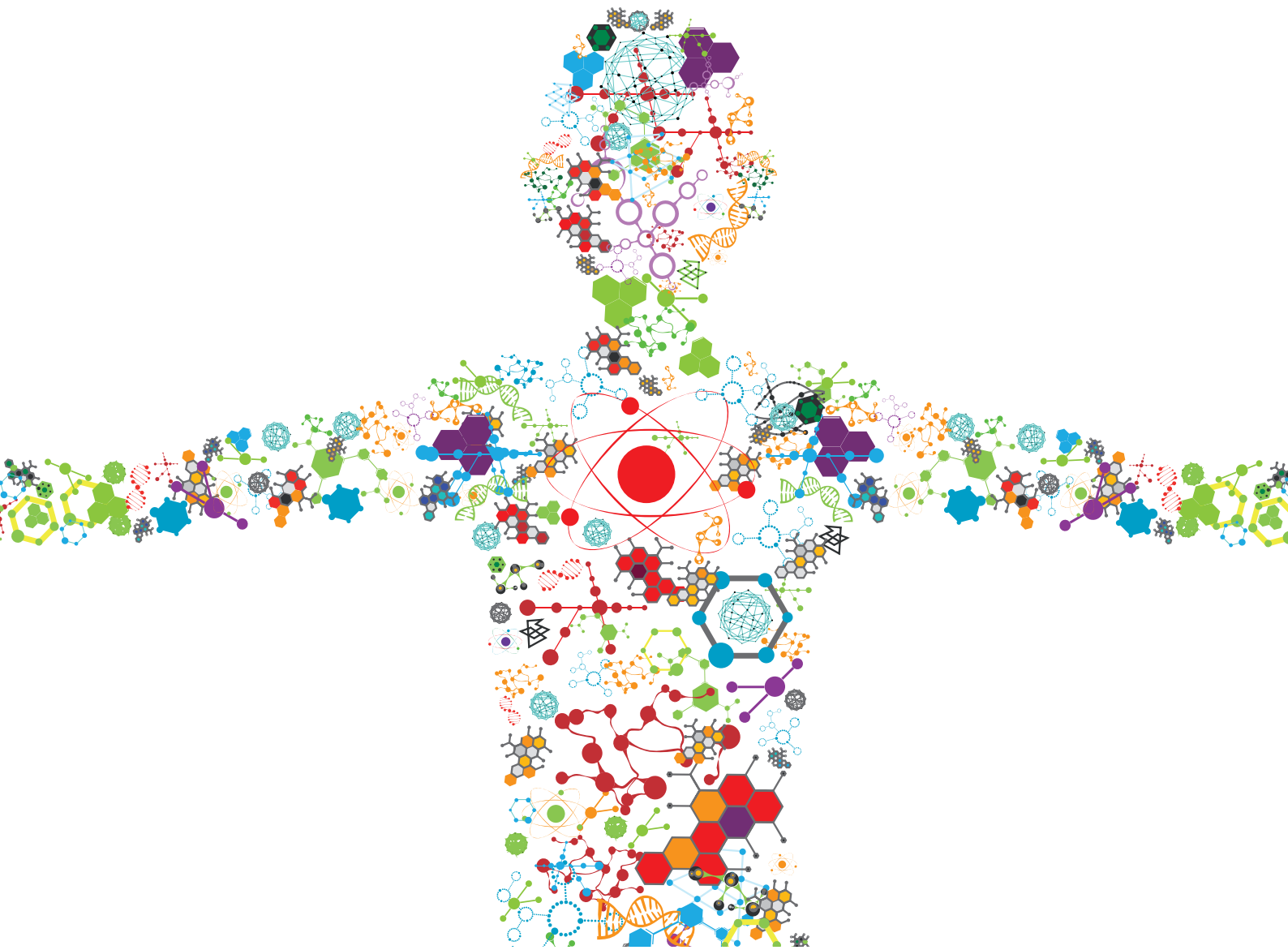

frontiers Research Topics

Frontiers eBook Copyright Statement

The copyright in the text of individual articles in this eBook is the property of their respective authors or their respective institutions or funders. The copyright in graphics and images within each article may be subject to copyright of other parties. In both cases this is subject to a license granted to Frontiers.

The compilation of articles constituting this eBook is the property of Frontiers.

Each article within this eBook, and the eBook itself, are published under the most recent version of the Creative Commons CC-BY licence. The version current at the date of publication of this eBook is CC-BY 4.0. If the CC-BY licence is updated, the licence granted by Frontiers is automatically updated to the new version.

When exercising any right under the CC-BY licence, Frontiers must be attributed as the original publisher of the article or eBook, as applicable.

Authors have the responsibility of ensuring that any graphics or other materials which are the property of others may be included in the CC-BY licence, but this should be checked before relying on the CC-BY licence to reproduce those materials. Any copyright notices relating to those materials must be complied with.

Copyright and source acknowledgement notices may not be removed and must be displayed in any copy, derivative work or partial copy which includes the elements in question.

All copyright, and all rights therein, are protected by national and international copyright laws. The above represents a summary only. For further information please read Frontiers' Conditions for Website Use and Copyright Statement, and the applicable CC-BY licence.

ISSN 1664-8714
ISBN 978-2-88966-936-3
DOI 10.3389/978-2-88966-936-3

About Frontiers

Frontiers is more than just an open-access publisher of scholarly articles: it is a pioneering approach to the world of academia, radically improving the way scholarly research is managed. The grand vision of Frontiers is a world where all people have an equal opportunity to seek, share and generate knowledge. Frontiers provides immediate and permanent online open access to all its publications, but this alone is not enough to realize our grand goals.

Frontiers Journal Series

The Frontiers Journal Series is a multi-tier and interdisciplinary set of open-access, online journals, promising a paradigm shift from the current review, selection and dissemination processes in academic publishing. All Frontiers journals are driven by researchers for researchers; therefore, they constitute a service to the scholarly community. At the same time, the Frontiers Journal Series operates on a revolutionary invention, the tiered publishing system, initially addressing specific communities of scholars, and gradually climbing up to broader public understanding, thus serving the interests of the lay society, too.

Dedication to Quality

Each Frontiers article is a landmark of the highest quality, thanks to genuinely collaborative interactions between authors and review editors, who include some of the world's best academicians. Research must be certified by peers before entering a stream of knowledge that may eventually reach the public - and shape society; therefore, Frontiers only applies the most rigorous and unbiased reviews.
Frontiers revolutionizes research publishing by freely delivering the most outstanding research, evaluated with no bias from both the academic and social point of view. By applying the most advanced information technologies, Frontiers is catapulting scholarly publishing into a new generation.

What are Frontiers Research Topics?

Frontiers Research Topics are very popular trademarks of the Frontiers Journals Series: they are collections of at least ten articles, all centered on a particular subject. With their unique mix of varied contributions from Original Research to Review Articles, Frontiers Research Topics unify the most influential researchers, the latest key findings and historical advances in a hot research area! Find out more on how to host your own Frontiers Research Topic or contribute to one as an author by contacting the Frontiers Editorial Office: frontiersin.org/about/contact

PULSED ELECTRIC FIELDS IN BIOTECHNOLOGY

Topic Editors:
Saša Haberl Meglič, University of Ljubljana, Slovenia
Damijan Miklavčič, University of Ljubljana, Slovenia
Eugene Vorobiev, University of Technology Compiegne, France

Citation: Meglič, S. H., Miklavčič, D., Vorobiev, E., eds. (2021). Pulsed Electric Fields in Biotechnology. Lausanne: Frontiers Media SA. doi: 10.3389/978-2-88966-936-3

Table of Contents

05 ***Editorial: Pulsed Electric Fields in Biotechnology***
Saša Haberl Meglič, Eugene Vorobiev and Damijan Miklavčič

07 ***Kinetic Modeling and Numerical Simulation as Tools to Scale Microalgae Cell Membrane Permeabilization by Means of Pulsed Electric Fields (PEF) From Lab to Pilot Plants***
Justus Knappert, Christopher McHardy and Cornelia Rauh

26 ***Pulsed Electric Field Extraction of α and β-Acids From Pellets of* Humulus lupulus *(Hop)***
George Ntourtoglou, Evangelia Anastasia Tsapou, Fotini Drosou, Eleni Bozinou, Stavros Lalas, Panagiotis Tataridis and Vassilis Dourtoglou

38 ***Development of a Continuous Pulsed Electric Field (PEF) Vortex-Flow Chamber for Improved Treatment Homogeneity Based on Hydrodynamic Optimization***
Felix Schottroff, Justus Knappert, Pauline Eppmann, Anna Krottenthaler, Tobias Horneber, Christopher McHardy, Cornelia Rauh and Henry Jaeger

53 ***Electroporation as a Solvent-Free Green Technique for Non-Destructive Extraction of Proteins and Lipids From* Chlorella vulgaris**
Tina Eleršek, Karel Flisar, Blaž Likozar, Marina Klemenčič, Janvit Golob, Tadej Kotnik and Damijan Miklavčič

62 ***Development of a Multi-Pulse Conductivity Model for Liver Tissue Treated With Pulsed Electric Fields***
Yajun Zhao, Shuang Zheng, Natalie Beitel-White, Hongmei Liu, Chenguo Yao and Rafael V. Davalos

73 ***Proof-of-Concept of Electrical Activation of Liposome Nanocarriers: From Dry to Wet Experiments***
Laura Caramazza, Martina Nardoni, Annalisa De Angelis, Patrizia Paolicelli, Micaela Liberti, Francesca Apollonio and Stefania Petralito

87 ***Enzymatic Processes Triggered by PEF for Astaxanthin Extraction From* Xanthophyllomyces dendrorhous**
Diederich Aguilar-Machado, Carlota Delso, Juan Manuel Martinez, Lourdes Morales-Oyervides, Julio Montañez and Javier Raso

99 ***Pulsed Electric Fields-Assisted Extraction of Valuable Compounds From Arthrospira Platensis: Effect of Pulse Polarity and Mild Heating***
Daniele Carullo, Gianpiero Pataro, Francesco Donsì and Giovanna Ferrari

114 ***Evaluation and Optimization of Protein Extraction From* E. coli *by Electroporation***
Saša Haberl Meglič, Nika Janež, Matjaž Peterka, Karel Flisar, Tadej Kotnik and Damijan Miklavčič

126 ***Confocal Microscopy Improves3D Microdosimetry Applied to Nanoporation ExperimentsTargeting Endoplasmic Reticulum***
Annalisa De Angelis, Agnese Denzi, Caterina Merla, Frank M. Andre, Lluis M. Mir, Francesca Apollonio and Micaela Liberti

135 ***AC Pulsed Field Ablation is Feasible and Safe in Atrial and Ventricular Settings: A Proof-of-Concept Chronic Animal Study***
Guido Caluori, Eva Odehnalova, Tomasz Jadczyk, Martin Pesl, Iveta Pavlova, Lucia Valikova, Steffen Holzinger, Veronika Novotna, Vladimir Rotrekl, Ales Hampl, Michal Crha, Dalibor Cervinka and Zdenek Starek

149 ***Extraction of Proteins and Other Intracellular Bioactive Compounds From Baker's Yeasts by Pulsed Electric Field Treatment***
Valentina Ganeva, Boyana Angelova, Bojidar Galutzov, Vasilij Goltsev and Miroslava Zhiponova

frontiers in Bioengineering and Biotechnology

EDITORIAL
published: 30 April 2021
doi: 10.3389/fbioe.2021.639150

Editorial: Pulsed Electric Fields in Biotechnology

Saša Haberl Meglič[1]*, *Eugene Vorobiev*[2] *and Damijan Miklavčič*[1]

[1] Faculty of Electrical Engineering, University of Ljubljana, Ljubljana, Slovenia, [2] University of Technology Compiegne, Compiègne, France

Keywords: extraction of value compounds, product modification and properties, modeling and numerical simulations, PEF bioprocessing, equipment design in biotechnology, pulsed field ablation

Editorial on the Research Topic

Pulsed Electric Fields in Biotechnology

Almost five decades ago it was shown that the permeability of a vesicular membrane can be increased by exposure to electric pulses. Today we know that when we expose the cell membrane to electric pulses of adequate strength and induced transmembrane voltage surpasses a certain value, the cell membrane becomes permeable. Thus, small or large molecules can be introduced into or extracted from cells. The phenomenon is called electroporation and is today showing remarkable promise in various fields: medicine, biology, and food- and biotechnology.

Especially applications of electric pulses in biotechnology have attracted much attention over recent years. Pulsed electric fields (PEF) in biotechnology are being rapidly developed and used in a wide range of areas: exploitation of microorganisms for producing value compounds, manufacture of biofuels from renewable feedstocks, removal pathogenic microorganisms from various water sources (i.e., hospital wastewaters), and liquid foods where vitamins and the food's color, flavor, or texture is unaffected. Nevertheless, a vast amount of work still needs to be done.

As the population grows, so does the need for a variety of dietary supplements and high-quality value compounds. Therefore, researchers began to look for new ways to obtain these compounds. One possible way is to grow microorganism cells that can produce these for us. Several physical or chemical methods are already established in order to disrupt microorganism cells and collect their content. Nevertheless, the main drawbacks of many chemical methods are the use of expensive chemicals and the necessity of removing them from the final product. Furthermore, on the pharmaceutical production scale, the use of such chemicals is restricted by regulatory bodies. The largest drawback of physical methods is the extensive fragmentation of the microorganism, which requires a costly downstream purification process. Consequently, the cost of value compounds' extraction remains high, providing strong motivation for new extraction tools and procedures. A Research Topic on Pulsed Electric Fields in Biotechnology is therefore aimed at providing a comprehensive update on the extraction of value compounds by means of electroporation from microorganisms. Since electroporation is affecting every cell membrane, assortments of microorganisms are being presented where proteins, carbohydrates, and dyes are being extracted by means of electroporation. The most important advantage when using electroporation compared to other established methods for extraction was found to be the lack of co-extracting impurities (Haberl Meglič et al.; Eleršek et al.; Ganeva et al.). Although extraction by means of electroporation largely avoids total cell disintegration with which the extract is a mix of extracted compounds with debris, the protocol still needs to be optimized in order to obtain a higher yield. Thus, a combination of electroporation with other methods, such as mild heating, could represent a suitable approach for the efficient recovery of value compounds (Carullo et al.). Furthermore, the optimization of solvent media is crucial in order to obtain the wanted compound from the microorganism, and the extraction of the antioxidant can be mediated by enzymatic esterase activity triggered by PEF

OPEN ACCESS

Edited and reviewed by:
Manfred Zinn,
HES-SO Valais-Wallis, Switzerland

***Correspondence:**
Saša Haberl Meglič
sasa.haberl-meglic@fe.uni-lj.si

Specialty section:
This article was submitted to Bioprocess Engineering, a section of the journal Frontiers in Bioengineering and Biotechnology

Received: *08 December 2020*
Accepted: *01 April 2021*
Published: *30 April 2021*

Citation:
Haberl Meglič S, Vorobiev E and Miklavčič D (2021) Editorial: Pulsed Electric Fields in Biotechnology. Front. Bioeng. Biotechnol. 9:639150. doi: 10.3389/fbioe.2021.639150

(Aguilar-Machado et al.). Additionally, more accurate microdosimetric numerical models of cells are needed in order to investigate the electroporation phenomenon and to more precisely set up efficient and controlled electroporation protocol. That can be achieved by building a realistic model of biological cells using optical microscopy images with highlighted cell compartments (De Angelis et al.).

In order to facilitate PEF application on a large scale, the development of continuous treatments has been pursued. A standard PEF continuous treatment system therefore consists of a pulse generator that enables continuous pulse treatment, flow chambers with electrodes, and a fluid-handling system. In order to overcome hurdles in PEF continuous systems such as inhomogeneous treatment conditions, a treatment chamber with more homogeneous flow properties inside is presented (Schottroff et al.). Since there is also a difficulty in comparing data obtained in different chambers or at different scales, kinetic modeling, and numerical simulations of treatment chambers are needed and also presented within this topic (Knappert et al.).

In the food industry, PEF shows great promise especially in the extraction of juice from fruits and vegetables. Namely, standard methods (enzymatic, mechanical, or thermal treatment) can cause a loss in juice quality (loss of vitamins *etc.*) and taste due to heating or enzymatic activity.

Hops are the most complex and costly raw material used in the brewing industry since they give the beer its flavor and also preserve the beverage. Although different brewing technologies are used in order to enhance the extraction of acids from hops, the possibility of using PEF for this purpose was also presented for the first time (Ntourtoglou et al.).

Although the topic mainly focuses on electroporation in biotechnology, also remarkable achievements can be found in medicine. There is an increasing interest in using biocompatible nanotechnologies in medicine, combined with the electric field, which can be used as drug delivery systems. Thus, the likelihood of controlling the release of drugs from liposome vesicles using electric fields is presented. The study's experimental results are supported by simulations in order to reveal the accompanying interactions and to optimize the electroporation protocol (Caramazza et al.). Also, the characterization of conductivity changes induced by electroporation using all treatment pulses is presented in order to simulate the electroporation process more precisely. Such a model is vital for treatment planning in medicine where electroporation is used (Zhao et al.).

A very new technology that will with great certainty completely change cardiac ablation is pulsed-field atrial and ventricular myocardial ablation. Presented herein is a proof-of-concept work with clearly stated claims of feasibility and safety. Nevertheless, further and systematic preclinical quantification both in the atrial and ventricular myocardium is necessary before stepping into the clinical validation of non-inferiority (Caluori et al.).

This Research Topic collected selected contributions from participants of the third World Congress on Electroporation, Pulsed Electric Fields in Biology, Medicine, Food and Environmental Technologies, held in Toulouse, France, on September 3–6, 2019 (https://wc2019.electroporation.net/).

AUTHOR CONTRIBUTIONS

SHM drafted the manuscript. DM and EV critically revised the manuscript. All authors read and approved the submitted manuscript.

Conflict of Interest: The authors declare that the research was conducted in the absence of any commercial or financial relationships that could be construed as a potential conflict of interest.

Copyright © 2021 Haberl Meglič, Vorobiev and Miklavčič. This is an open-access article distributed under the terms of the Creative Commons Attribution License (CC BY). The use, distribution or reproduction in other forums is permitted, provided the original author(s) and the copyright owner(s) are credited and that the original publication in this journal is cited, in accordance with accepted academic practice. No use, distribution or reproduction is permitted which does not comply with these terms.

frontiers in Bioengineering and Biotechnology

ORIGINAL RESEARCH
published: 24 March 2020
doi: 10.3389/fbioe.2020.00209

Kinetic Modeling and Numerical Simulation as Tools to Scale Microalgae Cell Membrane Permeabilization by Means of Pulsed Electric Fields (PEF) From Lab to Pilot Plants

Justus Knappert, Christopher McHardy and Cornelia Rauh*

Department of Food Biotechnology and Food Process Engineering, Technische Universität Berlin, Berlin, Germany

OPEN ACCESS

Edited by:
Saša Haberl Meglič,
University of Ljubljana, Slovenia

Reviewed by:
Daniel Christopher Sweeney,
Oak Ridge National Laboratory (DOE), United States
Changhong Yao,
Sichuan University, China

****Correspondence:***
Justus Knappert
justus.knappert@tu-berlin.de

Specialty section:
This article was submitted to Bioprocess Engineering, a section of the journal Frontiers in Bioengineering and Biotechnology

Received: *23 December 2019*
Accepted: *03 March 2020*
Published: *24 March 2020*

Citation:
Knappert J, McHardy C and Rauh C (2020) Kinetic Modeling and Numerical Simulation as Tools to Scale Microalgae Cell Membrane Permeabilization by Means of Pulsed Electric Fields (PEF) From Lab to Pilot Plants. Front. Bioeng. Biotechnol. 8:209. doi: 10.3389/fbioe.2020.00209

Pulsed Electric Fields (PEF) is a promising technology for the gentle and energy efficient disruption of microalgae cells such as *Chlorella vulgaris*. The technology is based on the exposure of cells to a high voltage electric field, which causes the permeabilization of the cell membrane. Due to the dependency of the effective treatment conditions on the specific design of the treatment chamber, it is difficult to compare data obtained in different chambers or at different scales, e.g., lab or pilot scale. This problem can be overcome by the help of numerical simulation since it enables the accessibility to the local treatment conditions (electric field strength, temperature, flow field) inside a treatment chamber. To date, no kinetic models for the cell membrane permeabilization of microalgae are available what makes it difficult to decide if and in what extent local treatment conditions have an impact on the permeabilization. Therefore, a kinetic model for the perforation of microalgae cells of the species *Chlorella vulgaris* was developed in the present work. The model describes the fraction of perforated cells as a function of the electric field strength, the temperature and the treatment time by using data which were obtained in a milliliter scale batchwise treatment chamber. Thereafter, the model was implemented in a CFD simulation of a pilot-scale continuous treatment chamber with colinear electrode arrangement. The numerical results were compared to experimental measurements of cell permeabilization in a similar continuous treatment chamber. The predicted values and the experimental data agree reasonably well what demonstrates the validity of the proposed model. Therefore, it can be applied to any possible treatment chamber geometry and can be used as a tool for scaling cell permeabilization of microalgae by means of PEF from lab to pilot scale. The present work provides the first contribution showing the applicability of kinetic modeling and numerical simulation for designing PEF processes for the purpose of biorefining microalgae biomass. This can help to develop new processes and to reduce the costs for the development of new treatment chamber designs.

Keywords: Pulsed Electric Fields, numerical simulation, computational fluid dynamics, microalgae, inactivation kinetic, scale- up, cell membrane permeabilization

INTRODUCTION

Microalgae are often considered to have a great potential as a resource for the biotechnology and food industries. Due to the high protein content in some species of up to 70% of the dry weight (Becker, 2007), they are a promising alternative source for high value proteins. These are particular needed in the near future since it is expected that the world population reaches 9.8 billion people in 2050 (United Nations- Department of Economic and Social Affairs, 2017). Besides proteins, microalgae can deliver many other ingredients with health benefits such as polyunsaturated fatty acids (PUFAs), pigments or diverse carbohydrates, what makes them even more interesting for applications in the food industry (Caporgno and Mathys, 2018). But except from some niche products, such as high valuable pigments or whole cells as food additives, microalgae did not reach marked maturity today (Lam et al., 2018). This is attributed to the high cost of production for microalgae biomass and their intracellular metabolites. A major part of the production costs is associated with the downstream processing, which includes all processing steps after the cell cultivation, and which is crucial for the production of valuable metabolites. A key process thereby is the disruption of the cells which enhances or even enables the extractability of almost all intracellular metabolites (Ruiz et al., 2016). Except of water-soluble substances such as some proteins or carbohydrates, the extraction of valuables like pigments or fatty acids requires the use of non-polar solvents. However, many green solvents such as ethanol cannot penetrate the cells and therefore, they do not reach the same yield as other solvents such as chloroform, hexane or butanol (Zbinden et al., 2013), which on the other hand have a negative impact on the environment, health and safety (Capello et al., 2007) and are therefore not approved for applications in the food and beverage industry. Cell disruption is therefore indispensable to enable the use of green solvents such as ethanol and moreover, it is essential for using algae biomass as a raw material within a biorefinery concept.

Because some species are characterized by a small cell size of a few micrometers and a rigid cell wall, the disruption of microalgae cells as *Chlorella* needs a high amount of energy and therefore, the recovery of valuables from microalgae cells becomes very expensive. Today, there are several mechanical techniques available for cell disruption such as bead milling (BM), high pressure homogenization (HPH), ultrasonication (US), microwave treatment (MW) or Pulsed Electric Field (PEF) (Günerken et al., 2015). Even if high pressure homogenization and bead milling are considered to be the most effective techniques for cell disruption, their main disadvantage is the resulting small cell debris and the non-selective release of intracellular components (D'Hondt et al., 2017). A promising alternative is disruption of cells by means of Pulsed Electric Fields (PEF). The technique is based on the exposure of cells to an external pulsating electric field which leads to an uprising transmembrane potential. The formation of hydrophilic pores in the cell membrane is favored if the transmembrane potential exceeds a critical value (Glaser et al., 1988). Consequently, the cell membrane is permeabilized, what leads to the enhancement of mass transfer processes across the cell membrane (Pataro et al., 2017). Because of this mechanism, the attention for applying PEF to improve the extraction of metabolites from microalgae cells increased in the last years. The target molecules contained a large variety of valuables, namely pigments like chlorophyll, lutein or phycocyanin (Grimi et al., 2014; Luengo et al., 2014, 2015; Parniakov et al., 2015; Zocher et al., 2016; Martínez et al., 2017), carbohydrates (Parniakov et al., 2015; Postma et al., 2016; Pataro et al., 2017; Carullo et al., 2018), proteins (Grimi et al., 2014; Aouir et al., 2015; Coustets et al., 2015; Parniakov et al., 2015; Postma et al., 2016; Lam et al., 2017a,b; Nehmé et al., 2017; Pataro et al., 2017), and lipids (Goettel et al., 2013; Zbinden et al., 2013; Silve et al., 2018a,b). All these studies have in common that the work was done at a microliter or milliliter scale and that the achieved results are specific for the used equipment and the respective treatment homogeneity. Because the distribution of an electric field inside PEF treatment chambers strongly depends on the geometry, it is difficult to compare the results of the listed works and furthermore, it is nearly impossible to scale the results to a plant at larger scale.

Until today there is no valid tool to transfer results obtained in PEF plants at laboratory scale to plants at the pilot or even the industrial scale. The strong dependency of the treatment homogeneity, namely the electric field distribution, temperature distribution and the velocity field, on the geometry of the treatment chamber has been shown by many numerical investigations (Toepfl et al., 2007; Gerlach et al., 2008; Jaeger et al., 2009; Rauh et al., 2010; Meneses et al., 2011). For example, Gerlach et al. demonstrated the dependency of the electric field homogeneity on the inner radius of the insulator between the high voltage and the grounding electrodes of a colinear treatment chamber. But even if the electric field, temperature and velocity distributions inside such a chamber are known, a direct evaluation of the impact of local conditions on the overall degree of cell permeabilization is difficult if permeabilization itself is not simulated as well.

In order to evaluate such effects numerically, a model is required which describes the rate of cell permeabilization as a function of the electric field strength, temperature magnitude and exposure time. Such a model can be included in numerical simulations of the PEF process so that the overall degree of cell permeabilization can be evaluated as the summarized effect of the local treatment conditions on the cell population while passing the treatment zone. However, no suitable model for the effect of PEF on microalgae is available so far. This gap shall be closed with the present work. The objective of this study is therefore to derive a kinetic model for the cell permeabilization of the microalgae *Chlorella vulgaris* from data gained in laboratory experiments being conducted on a small cuvette scale with homogeneous treatment conditions. The kinetic model is thereafter implemented in the commercial software Ansys CFX19 as part of a holistic numerical model for the PEF process in order to investigate by numerical simulation the effects of different treatment conditions inside a colinear treatment chamber with a volume flow of up to 15 L h^{-1}. Furthermore, experiments are conducted in a similar setup in order to show that the kinetic model is capable of correctly predicting the overall degree of cell

permeabilization. If this condition is met, it can be a useful tool for designing treatment chambers on the industrial scale on the basis of data from laboratory experiments.

MATERIALS AND METHODS

Microalgae Cultivation

All experiments were performed using *Chlorella vulgaris*, strain number SAG 211-11b, obtained from the algae collection from the University of Göttingen (SAG, Culture Collection of Algae, Göttingen, Germany). The strain was maintained until its usage in Erddekot + Salz + Peptone-medium (ESP-Medium) under continuous illumination of 20 μmol m^{-2} s^{-1} on a shaker (100 rpm). The recipe for the medium is provided by the SAG.

To produce biomass for the experiments, *Chlorella vulgaris* was cultivated autotrophically in a bubble column photobioreactor with a culture volume of 1.5 L (reactor volume 1.65 L). The cultivation was carried out in modified Bolds Basal Medium with threefold nitrogen and Vitamins (3N-BBM + V medium), according to the recipe of the Culture Collection of Algae and Protozoa. The culture was aerated with air enriched with 2.5% CO_2 at a volume flow rate of 800 ml min^{-1}. Artificial illumination was realized with two LED panels (LED-Mg) with a total area of 0.171 m^2. The light intensity was set to 150 μmol m^{-2} s^{-1}, which was measured on a fixed point of reference in the middle of the bubble column reactor right above the liquid level. The whole bubble column was placed in a tempered water bath to control the temperature at 25°C. The cells were harvested semi-continuously every third day via a sampling port. The volume of harvested cell suspension was replaced with autoclaved 3N-BBM + V medium. A preliminary test was carried out to determine the specific growth rate of the culture in order to make sure that it is always in the late exponential growth phase when harvested (data not shown).

To determine the cell density of the culture, a correlation between the biomass dry weight and the extinction at 750 nm was established. The extinction of several diluted cell samples was measured in 1 cm cuvettes by using an UV/VIS-Spectrometer (Lambda 25, Perkin Elmer). The cell dry weight of the same samples was determined by filtering through pre-dried glass microfiber filters (Whatman GF/F, pore size 0.7 μm). After filtering the samples, the filters were washed twice with distilled water to remove salts and then dried for 24 h at 80°C. For each data point, cell dry weight and extinction were measured in triplicate.

PEF Treatment

Sample Preparation

After collecting the cells, the dry biomass concentration for all PEF treatments was adjusted to 1 g L^{-1}. Therefore, the microalgae suspension was concentrated by centrifugation at 5000 g for 10 min before adjusting the cell concentration. After centrifugation, the pellet was resuspended in fresh 3N-BBM + V medium so that the desired cell concentration resulted, which was verified by UV/VIS Spectrometry. The cell suspension was tempered to the specific temperature of the respective experiment in 2 ml tubes (Eppendorf, Germany) on a shaker for a minimum of 15 min. 3N-BBM + V medium served as the treatment media. Its electrical conductivity at 20°C was 1.3 mS cm^{-1}.

PEF Systems and Experimental Design

Pulsed Electric Fields-treatments at cuvette scale were performed in order to derive data for the kinetic modeling. The experiments were conducted in a prototype treatment plant, being designed inhouse. The storage capacity of the plant is 19.5 nF [Ceramite Y5U 6800Z-Kondensatoren (Behlke Electronic GmbH, Kronberg, Germany)]. It is charged by a 20 kV and 80 mA high voltage charging unit. The capacitors are discharged in exponential decay pulses using a thyristor switch (HTS 160-500SCR, Behlke Electronic GmbH, Kronberg, Germany). Voltage and current were directly measured at the treatment chamber by a 75 MHz high voltage probe and a 100 MHz current probe, respectively. The signals were visualized with a 400 MHz digital storage oscilloscope (TDS220-Oszilloskop, Sony Tektronix, Beaverton, United States). Electroporation cuvettes (VWR) with parallel plates and an electrode gap of 4 mm were used for the treatment. Prior to each experiment, the electroporation cuvettes were tempered to the desired treatment temperature in a sand bath for at least 30 min. For temperature control during the experiment, the whole plant was placed below a temperature-controlled incubator hood (Certomat, HK, Sartorius, Germany). The effect of electric field strength, initial treatment temperature and treatment time was investigated. Therefore, the electric field strength was varied in 5 steps, namely 6.5, 9, 13.5, 20, and 27 kV cm^{-1}. The effect of the temperature was investigated on three stages at 20, 30, and 40°C for every level of the applied electric field strength. For all combinations of temperature and electric field strength, the cells were treated with 0, 1, 2, 4, 8, 16, 32, and 64 exponential electric pulses with a time constant of 3.7 $\pm$ 0.63 μs, which measures the time in which the pulse decays to 64% of the peak voltage. The temperature in the electroporation cuvettes was measured directly before and after the treatment with a manual measuring device. The highest measured temperature increase was 8.2°C. All experiments were conducted in duplicate and those with 64 pulses in triplicate.

A second series of experiments was conducted in a treatment plant at pilot scale with a colinear treatment chamber. The assembly of the treatment chamber is the same as the one being investigated in numerical simulations (see **Figure 1**). The inner diameter of the electrodes and the insulators was 6 mm and 4 mm, respectively. The length of the grounding and high voltage electrode was 65 mm and 35 mm, respectively. The length of the insulators was 4 mm. Both, the high voltage and the grounding electrodes are manufactured from stainless steel. A 7 kW modulator (ScandiNova) was used to deliver quasi-rectangular monopolar pulses with a pulse width of 5 μs. An overshoot and ringing of the voltage was observed during the pulse, which is caused by the electrical conductivity of the 3N-BBM + V medium and the related impedance mismatching. Despite this observation, the electrical conductivity of the medium was not changed with regard to the industrial application of PEF in the context of microalgae biorefinery and the respective typical composition of growth media. The *C. vulgaris* cell

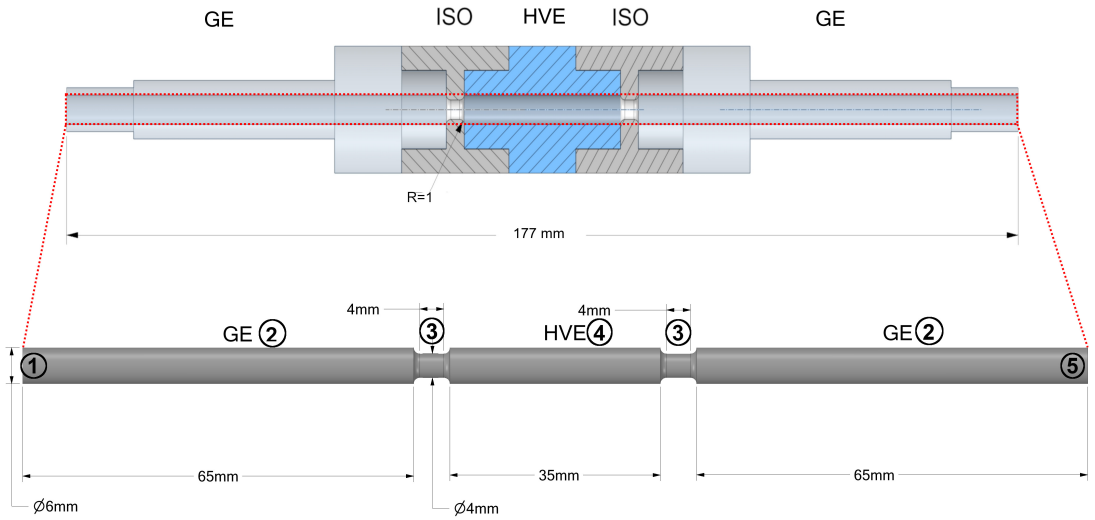

FIGURE 1 | Schematic view of a colinear treatment chamber as it was used for CFD simulations and pilot scale experiments. The dash-dotted line indicates the symmetry of the domain, whereby the outlet is located at the right end of the fluid domain. The numbers indicate the boundaries of the domain for which the boundary conditions are summarized in **Table 2**. GE, Grounding electrode; ISO, Insulator; HVE, High voltage electrode.

suspension was pumped through the entire system by using a micro annular gear pump (HNP Mikrosysteme, Germany, type: mzr 7205). Before entering the treatment chamber, the cell suspension was tempered to the treatment temperature in a heat exchanger. In order to drive the system into a thermal steady-state (no further heating of pipes and electrodes), a saline solution with the same conductivity as the microalgae suspension was treated prior to each experiment with similar conditions. The achievement of steady-state conditions was monitored by measuring the temperature of the liquid before and after the treatment chamber. After reaching constant conditions, a three-way valve was used to switch between the saline solution and the microalgae suspension. The residence time inside the whole plant was determined in a preliminary experiment using food colors (data not shown). In accordance to these measurements, samples of the treated algae were not taken before a time interval of 2 min has been passed after switching from saline solution to algae suspension. For each parameter set two samples were taken within a time interval of at least 30 s. After taking the samples, the valve was switched back to the saline solution, the pulse generator was switched off and the next treatment parameters were set. According to the experimental plan, the liquid volume flow was varied between 100 and 200 ml min^{-1}, the inlet temperature from 30 to 40°C and the applied voltage from 7 to 15 kV, being measured directly at the treatment chamber. To exclude possible effects on the measured degree of cell disruption by preheating or by the pump, a zero sample was taken before switching the pulse modulator on.

Flow Cytometry

The fraction of perforated cells (F_p) in all treated samples was determined by the uptake of the fluorescents dye propidium iodide (PI, concentration c = 1000 mg ml^{-1}; Molecular Probes; Lot No.: 45B5; Exmax/Emmax 492/638). PI is a hydrophilic dye which cannot penetrate through the intact cell membrane. After the PEF treatment, cell suspensions were directly diluted in ice cooled 3N-BBM + V medium and stored on ice until further use. The dilution factor was 1:100 which leads to a dry biomass concentration of around 10 mg L^{-1} or 10^6 cells ml^{-1}, respectively (checked with a hemocytometer). The PI was added 15 ± 2 min after the PEF treatment so that only the irreversibly perforated cells were detected with this staining protocol (Luengo et al., 2014). PI was added to a final concentration of 11 µg ml^{-1}. The samples were shaken in the dark at 23°C and 300 rpm for 15 min. The fluorescent signal was measured with a flow cytometer (BD Accuri C6, Becton Dickinson, United States). The signal was captured on the FL2 emission filter at 585/40 nm. The flow rate was set to 14 µl min^{-1} and 20 µl per sample were measured at a front scatter threshold of 80000 (arbitrary units). A preliminary test was conducted for the distinction between the signal of the perforated and the unperforated cells. Therefore, a mixture of 50% living algae cells and of 50% heat inactivated cells was prepared. Two clearly separable peaks occurred, and each peak contained 50% of the overall measured events, whereby the peak with the stronger fluorescence signal represented the perforated cells. A line of calibration was inserted between these peaks and was saved as a template for further experiments. Each treated sample was stained in duplicates and all stained samples were measured as duplicates.

Numerical Model

Governing Equations

The governing equations are based on the conservation equations for mass, momentum, energy and charge (Wölken et al., 2017; Fiala et al., 2001; Lindgren et al., 2002; Gerlach et al., 2008; Jaeger et al., 2009). Specific assumptions applied in this work are that the presence of cells does not affect the flow of the suspension and

therefore, the cell suspension can be treated as an incompressible single-phase fluid. These assumptions can be justified with the low concentration of cells during the treatment (1 gL^{-1}) and their small size, leading to a low volume fraction, negligible cell-cell interactions and a small value of the Stokes number (Crowe et al., 2011). Then, the conservation equation for mass can be written as

$$\nabla \cdot \boldsymbol{u} = 0 \tag{1}$$

Where u is the fluid velocity vector. It is assumed that no direct effects of the electric field on the flow exist. Therefore, the conservation equation for momentum is given by

$$\frac{\partial \rho \boldsymbol{u}}{\partial t} + \nabla \cdot \left(\rho \boldsymbol{u}\boldsymbol{u}^T\right) = -\nabla p + \nabla \cdot \mu \left(\nabla \boldsymbol{u} + (\nabla \boldsymbol{u})^{\mathrm{T}}\right) + \rho \boldsymbol{g} \tag{2}$$

Wherein t is the time, ρ is the fluid density, p is the pressure, μ the fluid dynamic viscosity and g the vector of gravitational acceleration. Because of the incompressibility of the fluid, its internal energy can be described by the applied thermal energy alone. Therefore, the energy conservation equation becomes

$$c_p \frac{\partial \rho T}{\partial t} + c_p \nabla \cdot (\rho \boldsymbol{u} T) = \nabla \cdot (\lambda \nabla T) + \pi_e \tag{3}$$

wherein c_p is the heat capacity of the fluid, T the total temperature and K the fluids thermal conductivity. The term π_e represents a source term for the internal energy. In the case of PEF, the source term describes the increase of internal energy by Joule heating. The thermal transport only takes place during the duration τ of a pulse so that the source term must be corrected by the effective fraction of time during which the electric field is active, which is given by the product of the pulse duration and the pulse repetition rate f. Thus, the source term in equation (3) becomes

$$\pi_e = \tau f \sigma E^2 \tag{4}$$

Where σ is the electric conductivity of the fluid and E represents the local strength of the electric field. For the computation of the latter, another equation is needed. The electric field strength can be calculated by solving a transport equation for carriers of electric charge. With the assumptions of an electrostatic field, charge conservation and Ohm's law for the electric current, the transport equation reduces to a Laplace equation for the scalar electric potential Φ (Wölken et al., 2017):

$$\nabla \cdot (\sigma \nabla \Phi) = 0 \tag{5}$$

By solving (5), the electric field can be computed from the electric potential with the relation:

$$E = -\nabla \Phi \tag{6}$$

The fraction F_p of permeabilized microalgae cells is a local property of the carrier cell population, which is affected by the action of the treatment and its transport in space. The transport of F_p is coupled to the transport of the cells. As mentioned before, microalgae cells are considered as passive tracers which have no influence on the fluid behavior and do not interact with each other. This is a safe assumption at microorganism concentrations in the order of 10^{14} m^{-3} as being considered here and it implies that the transport of cells by diffusion is not significant. Thus, the transport equation for the activity of passive biological tracers F_p can be expressed as follows (Rauh et al., 2009):

$$\frac{\partial F_p}{\partial t} + \nabla \cdot \left(\boldsymbol{u}\, F_p\right) = \pi_{\mathrm{F_p}} \tag{7}$$

The term $\pi_{\mathrm{F_p}}$ represents a source term for the fraction of perforated cells. It is a function of the electric field strength and the treatment temperature and will be derived in section "Results" from experimental data.

Thermophysical Fluid Properties

The material properties of the fluid depend strongly on the temperature. The temperature dependency of the material properties is therefore considered according to the equations being listed in **Table 1**.

Computational Domain and Grid Generation

The computational domain as depicted in **Figure 1** consists of two grounding electrodes (2), one high voltage electrode (4) and two isolator rings (3). The numbers (1) and (5) indicate the inlet and the outlet of the fluid domain, respectively. The domain was automatically discretized with tetrahedral mesh elements by means of the software Ansys Meshing. The mesh was additionally refined in regions where high gradients of the flow velocity were expected, especially within and after the isolator rings. Also, the region at the wall of the domain was meshed by prism layers since a large gradient of the velocity can be expected here due to the no slip boundary condition. A mesh convergence study with 5 different meshes was performed in which the effect of the mesh element size on F_p and the flow and temperature fields was studied. The final mesh was chosen such that the deviation of all quantities was less than 3% in relation to their value on the finest of all generated meshes.

Boundary Conditions

The applied boundary conditions are summarized in **Table 2**. For the inflow, a parabolic velocity profile was assumed according to expectable laminar flow conditions, which were estimated by means of the Reynolds number. The inlet velocity profile was calculated from the Hagen-Poiseuille equation for a given volumetric flow rate $\dot{V}$. At the walls, the common no-slip condition was assumed, thus the liquid velocity is zero. At the inlet of the chamber, a static temperature T_0 was assumed. Furthermore, adiabatic walls were assumed, thus no heat flux across the walls. This assumption is justified because PEF treatment chambers are usually covered by insulating materials. For the electrostatic model zero-flux boundary conditions at the inlet, outlet and the isolators were assumed. The voltage at the high voltage electrode was set to a static value U_0, while it was set to zero at the grounding. The fraction of perforated cells F_p was set to 0 at the inlet of the chamber and a zero-gradient condition was applied at the outlet.

TABLE 1 | Temperature dependency of the fluid material properties.

Property	Symbol	Equation
Density[1]	ρ $[\mathrm{kg\ m^{-3}}]$	$1000.22 + 1.0205 \cdot 10^{-2} \cdot T_c - 5.8149 \cdot 10^{-3} \cdot T_c^2 + 1.496 \cdot 10^{-5} \cdot T_c^3$
Heat capacity[1]	c_p $[\mathrm{kJ\ kg^{-1}K^{-1}}]$	$4176.2 - 0.0909 \cdot T_c + 5.4731 \cdot 10^{-3} \cdot T_c^2$
Thermal conductivity[1]	κ $[\mathrm{W\ m^{-1}K^{-1}}]$	$0.57109 + 1.7625 \cdot 10^{-3} \cdot T_c - 6.7036 \cdot 10^{-6} \cdot T_c^2$
Dynamic viscosity[1]	μ $[\mathrm{kg\ m^{-1}s^{-1}}]$	$2.414 \cdot 10^{-5} \cdot 10^{\left(\frac{247.8\,[K]}{T_K - 140\,[K]}\right)}$
Electric conductivity[2]	σ $[\mathrm{S\ m^{-1}}]$	$0.889 \cdot 10^{\frac{A}{B}} \cdot \sigma_{ref}$
	A	$1.37023 \cdot (T_c - 20°C) + 8.36 \cdot 10^{-4} \cdot (T_c - 20°C)^2$
	B	$109 + T_c$
	σ_{ref}	$1.2\ \mathrm{mS\ cm^{-1}}$

The subscript C describes the temperature in degree Celsius, the subscript K stands for Kelvin. [1]Wölken et al., 2017; [2]Atkins and de Paula, 2006.

TABLE 2 | Boundary conditions applied in the CFD simulation.

Location	Electrostatic model	Flow model	Thermal model	Transport equation
Inlet (1)	$\nabla\Phi = 0$	$u = 2 \cdot \frac{\dot{V}}{\pi R^2} \cdot \left(1 - \left(\frac{r}{R}\right)^2\right)\ v = 0\ w = 0$	$T = T_0$	$F_p = 0$
Grounding (2)	$U = 0$	$u_{wall} = 0$	$q_{wall} = 0$	$\nabla F_p = 0$
Isolator (3)	$\nabla\Phi = 0$	$u_{wall} = 0$	$q_{wall} = 0$	$\nabla F_p = 0$
High voltage electrode (4)	$U = U_0$	$u_{wall} = 0$	$q_{wall} = 0$	$\nabla F_p = 0$
Outlet (5)	$\nabla\Phi = 0$	$p_{stat} = p_{spec}$	$\nabla T = 0$	$\nabla F_p = 0$

*The respective boundaries are indicated by the numbers in **Figure 1**.*

TABLE 3 | Chosen parameter levels for the CFD parameter study.

	Voltage [kV]	Inlet temperature [K]	Frequency [Hz]	Flow rate [$m^3\ s^{-1}$]
Level 1	7	293	100	1.66e-06
Level 2	11	298	150	2.50e-06
Level 3	15	303	200	3.33e-06

Numerical Parameter Study

The numerical model described in section "Numerical Model" was used to perform a parameter study in order to investigate the effect of different treatment conditions on the degree of cell permeabilization. The specific parameter combinations were chosen by means of the response surface methodology. Flow rate, pulse repetition frequency, voltage and inlet temperature were chosen as explanatory variables and varied on 3 levels, whereby the levels of the voltage, flow rate, temperature and frequency were the same as applied in the second experimental series as described in section "PEF Systems and Experimental Design." The respective levels are summarized in **Table 3**. Pulse duration was set to a fixed value of 5 µs. The degree of cell permeabilization and the temperature increase were chosen as response variables. The design of experiments led to 30 design points in total, whereby the repetitions were neglected because no variance occurs in numerical simulations with similar settings.

RESULTS

Experiments in Electroporation Cuvettes

In order to obtain experimental data for the derivation of a kinetic model for cell perforation, experiments in electroporation cuvettes were conducted. The evolution of the fraction of perforated cells (F_p) with respect to the treatment time, the electric field strength and the treatment temperature is presented in **Figure 2**. It can be seen that only treatments with electric field strength higher than 20 kV $\mathrm{cm^{-1}}$ led to a full perforation of the cell population at all tested treatment temperatures. Furthermore, **Figure 2** shows that the increase of the electric field strength from 20 to 27 kV $\mathrm{cm^{-1}}$ reduced the treatment time being necessary for a complete perforation. For example, at 40°C and 27 kV $\mathrm{cm^{-1}}$, 100% of the cell suspension were permeabilized within a time of $0.48 \cdot 10^{-4}$ s while at 40°C and 20 kV $\mathrm{cm^{-1}}$ twice the time was needed to achieve the same result. Note that the treatment time is the effective time during which the electric field is active.

An important parameter for assessing the electroporation process is the specific energy input w_{spec}. For a batch treatment it can be calculated with the expression

$$w_{spec} = \frac{U_0^2 C n_p}{2m} \tag{8}$$

Here, U_0 is the applied voltage (measured at the treatment chamber), C is the capacitance of the capacitors of the PEF plant, n_p is the number of applied pulses and m is the mass of the treated sample. According to equation (8), a specific energy input of 19.6 kJ $\mathrm{kg^{-1}}$ was needed to perforate 100% of

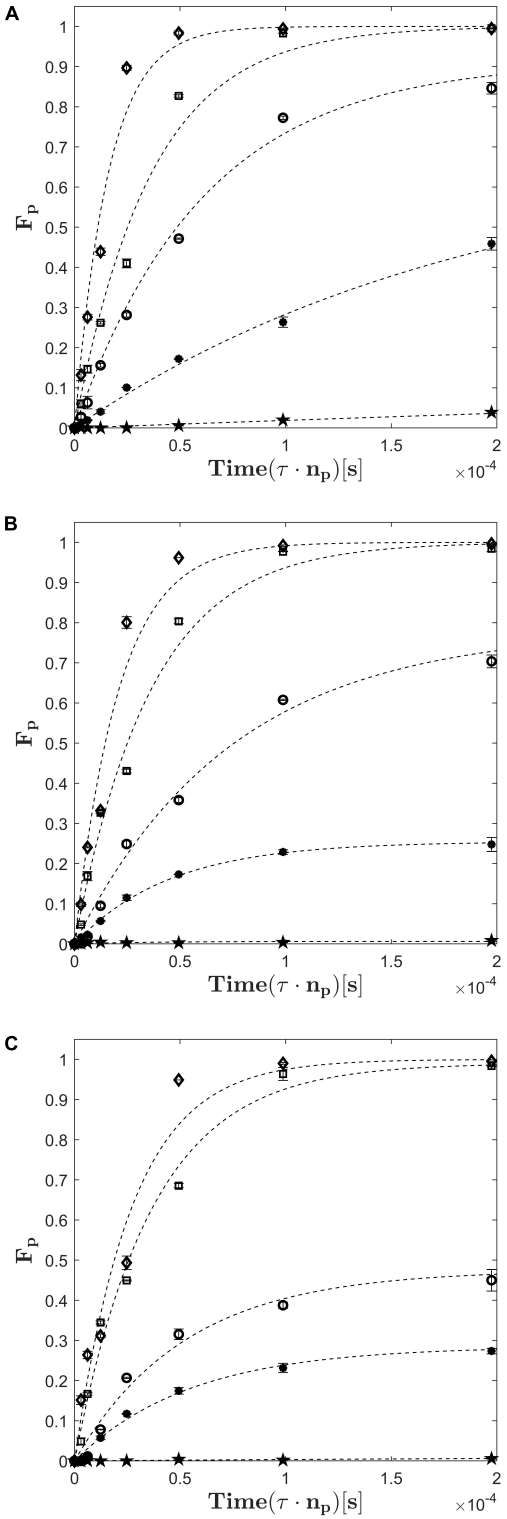

FIGURE 2 | Fraction of perforated cells (F_p) as a function of electric field strength, treatment time and treatment temperature (**A:** 40°C, **B:** 30°C, **C:** 20°C). The electric field strength is indicated by different symbols: 6.5 kV cm^{-1} (stars), 9 kV cm^{-1} (filled circles), 13.5 kV cm^{-1} (empty circles), 20 kV cm^{-1} (squares), 27 kV cm^{-1} (diamonds). Error bars indicate the standard deviation. The dashed lines are best fits obtained with equation (9).

the cells at 40°C and 27 kV cm^{-1}, whereas 23.56 kJ kg^{-1} was necessary at 40°C and 20 kV cm^{-1}. Even if these results might be biased because of the large difference between the applied treatment times, they indicate that the required specific energy input for the complete cell perforation decreases if the electric field strength increases. It seems therefore preferable to operate at high electric field strength in the case of industrial applications. Another result of the experiments is that the lowest applied field strength of 6.5 kV cm^{-1} was not high enough to perforate a considerable amount of *C. vulgaris* cells, see **Figure 2**. Even at the highest treatment temperature of 40°C, only around 4% of the population was perforated after the longest treatment time. **Figure 2** further indicates that the treatment at 13.5 kV cm^{-1} and 9 kV cm^{-1} were insufficient to perforate the complete cell population, independently from temperature. Also, the fraction of perforated cells F_p converges to a maximum value ($F_{p,max}$) for electric field strengths at which no complete perforation was achieved. For example, at 9 kV cm^{-1} and 40°C, the value of $F_{p,max}$ was found to be $F_{p,max} \approx 0.45$.

As it can be seen in **Figure 3**, the maximum fraction of perforated cells $F_{p,max}$ depends not only on the electric field strength but also on the treatment temperature. For example, $F_{p,max}$ increased steadily with temperature at 13.5 kV cm^{-1} ($F_{p,max}$ = 0.45 at 20°C, 0.704 at 30°C and 0.846 at 40°C). At 9 kV cm^{-1}, a similar increase can be observed if the treatment temperature is changed from 30 to 40°C while no significant difference between treatments at 20°C and 30°C was found. If the electric field strength exceeds 13.5 kV cm^{-1}, the value of $F_{p,max}$ becomes independent from the treatment temperature because the entire cell population is electroporated. Regarding

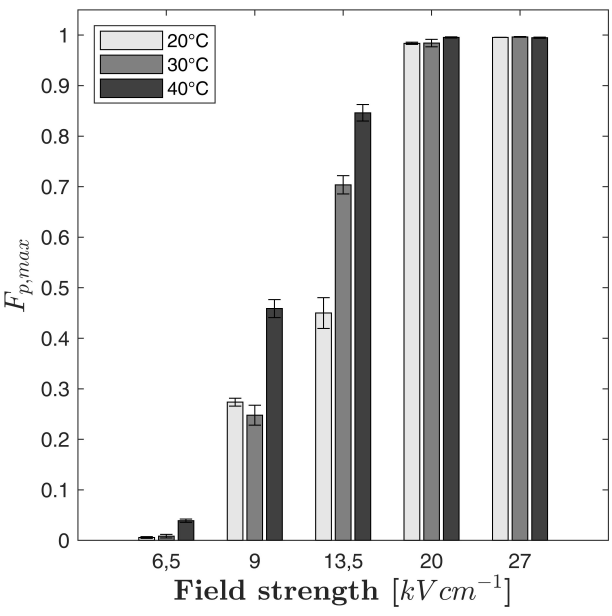

FIGURE 3 | Measured maximum fraction of perforated cells ($F_{p,max}$) with respect to the electric field strength and the treatment temperature. Error bars indicate the standard deviation.

the modeling of the cell disruption kinetics, it is therefore crucial to describe $F_{p,max}$ as a function of the electric field strength and the treatment temperature. However, the temperature plays an important role for the kinetics of cell perforation at all field strengths. As indicated by **Figures 2A–C**, the slope of the fitted curves increases with temperature at a given electric field strength (similar markers). Therefore, not only the parameter $F_{p,max}$ is a function of temperature but also the time constant of the kinetic model.

The experimental results indicate that the cell permeabilization process can be realized at moderate temperature (e.g., 30°C) since a complete perforation of the cell population is achieved at a sufficiently high electric field strength. A further increase of temperature to 40°C only affects the number of required pulses to reach a complete permeabilization, thus the treatment time. This finding might be beneficial for the permeabilization of microalgae because less thermal energy must be spent for pre-heating of the suspension and in addition the risk of damaging thermally sensitive products can be reduced. The adequate description of the cellular permeabilization kinetics is therefore an important step for designing cell disruption processes and optimization of the operation conditions. Particularly, this is the case for PEF in colinear chambers due to the inhomogeneous electric field, velocity and temperature distributions, which lead to wide residence time distributions and local temperature hotspots (Gerlach et al., 2008; Jaeger et al., 2009; Wölken et al., 2017).

Kinetic Model for Cell Perforation

Primary Model Equations

A suitable kinetic model for cell permeabilization must consider the electric field strength, the treatment temperature and the treatment time. The modeling approach applied in this work is based on the work of Saulis and Venslauskas (1993). In their model, the formation of pores in the cell membrane is considered as a Poisson process so that the fraction of non-perforated cells after time t is given by a Poisson distribution. A cell is assumed to be permeabilized if the number of pores exceeds a critical value. In the present study, cells are considered to be permeabilized as soon as the first pore appears because they become accessible for the PI staining. In that case, the Poisson distribution becomes a simple exponential distribution. As discussed above, the kinetic model must include an additional term $F_{p,max}$ describing the upper limit for the fraction of perforated cells as a function of the electric field strength E and the treatment temperature T. With this extension, the kinetic model of Saulis and Venslauskas becomes

$$F_p = F_{p,max}\left(1 - \exp\left(-k_f t\right)\right) \tag{9}$$

Herein k_f is a kinetic parameter for the pore formation and t represents the treatment time. In the case of a batch treatment, it can be expressed as

$$t = n_p \tau$$

where τ represents the pulse duration and n_p the number of pulses, respectively. In the case of a continuous treatment chamber, the pulse repetition rate f and the residence time t_R needs to be taken into account (Raso et al., 2016). Therefore, t can be represented as

$$t = f \tau t_R$$

In order to derive the model parameters k_f and $F_{p,max}$ as a function of the electric field strength and temperature, equation (9) was fitted to the experimental data shown in **Figure 2**. The built-in function *lsqnonlin* of MATLAB2019a was used for the fitting procedure, which minimizes a user-defined error function. For the present problem, the error was defined as the absolute deviation between the model and experimental measurements at constant temperature and electric field strength.

$$\epsilon_{Fp} = \sqrt{\left(F_{p,Sim} - F_{p,Exp}\right)^2} \tag{10}$$

$F_{p,Exp}$ represents the experimental data and $F_{p,Sim}$ the solution of equation (9). The iterated values of k_f and $F_{p,max}$ were determined for all combinations of treatment temperature and electric field strength (R^2 = 0.984), thus leading to a set of 15 values for each parameter. The root mean square error (RMSE) is used as a quality measure for the fitting procedure. The RMSE with dimension of F_p takes values of 0.0352 for 20°C, 0.0345 for 30°C, 0.0342 for 40°C and 0.0346 for the complete data set. The resulting fits are shown by the dashed lines in **Figure 2**. The determined parameters are named $k_{f,exp}$ and $F_{p,max,exp}$ hereafter.

Secondary Model Equations

In order to express the model parameters k_f and $F_{p,max}$ in terms of the electric field strength and the temperature, secondary model equations are needed. Saulis and Venslauskas suggested a function which describes the rate of pore formation k_f by the product of an Arrhenius-type term for the temperature dependency of natural pore formation in the membrane and a second exponential term which accounts for the stabilization of naturally formed pores by the increase of the transmembrane potential. Since the transmembrane potential in an electric field is a function of the location on the cell surface (Krassowska and Filev, 2007), the latter is integrated over the cell membrane surface in order to calculate the overall effect of the electric field on the formation of pores. The proposed model for the rate of pore formation reads

$$k_f = A_c\left[s^{-1}\right]\ \exp\left(-\frac{B_c\,[K]}{T}\right) \times$$

$$\int_{-1}^{1} exp\left[\left(\frac{C_c\left[K\ V^{-1}\right]}{T}\right)\cdot\left(\frac{3}{2}E^2 D_c\,[m]\cdot \text{y-E}_c\,[V]\right)^2\right] dy \tag{11}$$

where A_c, B_c, C_c, D_c, and E_c are constant fitting parameters summarizing different properties of the cell and the surrounding media. The reader is referred to **Appendix A** for their exact meaning. The quantity y is the substituent for $\cos(\phi)$, whereby ϕ is the angle to the cell surface normal. The best fit of equation (11) to the determined primary model parameter $k_{f,exp}$ was

calculated similarly as described above. The error function of the optimization was defined by the expression

$$\epsilon_{k_f} = \sqrt{\left(k_{f,model} - k_{f,exp}\right)^2} \tag{12}$$

where $k_{f,exp}$ stands for the rate constants being determined by the fit of equation (9) to the experimental data and $k_{f,model}$ for the solution of equation (11). **Figure 4A** compares the predicted values for $k_{f,model}$ as calculated by equation (11) with the values of the fitting parameter $k_{f,exp}$ of equation (9). The overall quality of the fit is indicated by the RMSE, which equals $6.428.10^3$ s^{-1}. As it is indicated by the bisector, equation (11) with fitted parameters A_c, B_c, C_c, D_c, and E_c describes the general trends ($R^2 = 0.847$) but fails to provide a detailed description of the rate constants at low to moderate treatment intensities. Even though the model for the rate of pore formation has a strong mechanistic background, its structure is complex and contains a large number of parameters, which entails the risk of overfitting. Moreover, regarding the intended implementation of the kinetic model into a holistic numerical model for the PEF process, equation (11) is inconvenient to solve and additional numerical costs arise through the need of integrating the transmembrane potential over the cell surface.

Therefore, a simplified model equation for the description of the pore formation rate k_f was developed and compared to the results obtained by equation (11). Sadik et al. (2014) showed for mouse fibroblast cells that the viability of the cells decreased linearly with the treatment time and quadratic with the electric field strength. According to these findings, k_f can be expressed as:

$$k_f = A_c \exp\left(-\frac{B_c}{T}\right) E^2 \tau \tag{13}$$

A_c is a fitting parameter which adjusts the influence of the electric energy and the temperature on the pore formation and takes the value $A_c = 3.92.10^7$ V^2 m^{-2} s^{-2} for the present case. Similar to the model of Saulis and Venslauskas (1993), the temperature is taken into account by the Arrhenius model with parameter B_c, which is determined as $B_c = 7.28.10^3$ K^{-1}. The overall quality of the fit is indicated by $R^2 = 0.895$ and the RMSE = $5.687.10^3$ s^{-1}, which is one order of magnitude smaller than the predicted values. As it can be seen from **Figure 4B** and the error measures, equation (13) predicts the values for k_f better than equation (11). Especially the low values of k_f are better described, which is particularly important with regard to the simulation of cell permeabilization under the inhomogeneous conditions in colinear continuous treatment chambers. Because of the higher accuracy and the structural benefits, equation (13) was chosen as a model for the rate constant k_f .

The second parameter which needs to be expressed in terms of electric field strength and temperature is the maximum fraction of perforated cells $F_{p,max}$. In order to obtain a secondary model equation, a two-step procedure is applied. The values being determined by fitting the primary model, equation (9), to the experimental data were fitted isothermally with a Weibull distribution as a function of the electric field strength:

$$F_{p,max} = 1 - \exp\left(-\frac{E}{\lambda_S}\right)^{k_S} \tag{14}$$

The best fit of the parameters λ_S and k_S was obtained by finding the minimum of the error function:

$$\epsilon_{F_p} = \sqrt{\left(F_{p,max,model} - F_{p,max,exp}\right)^2} \tag{15}$$

Thereby, the value of $F_{p,max}$ was restricted to the upper and lower bounds of 0 and 1. The quality of the fit is determined in terms of $R^2 = 0.977$ and the RMSE = 0.057 in units of F_p. In a second step, the fitted parameters λ_S and k_S were expressed in terms of the temperature with an exponential and a linear equation, respectively. The resulting equations read

$$\lambda_S = A_\lambda \exp\left(-B_\lambda T\right) \tag{16}$$

$$k_S = A_k T + B_k \tag{17}$$

with the parameters $A_\lambda = 6.683.10^9$ V m^{-1}, $B_\lambda = 0.0201$ K^{-1} ($R^2 = 0.997$), $A_k = -0.0742$ K^{-1} and $B_k = 26.51$ ($R^2 = 0.997$). The quality of the fits is assessed in terms of the RMSE, which takes values of $4.786.10^4$ and 0.0131 in units of λ_S and k_S, respectively, both being two magnitudes smaller than the predicted values. **Figure 5** depicts the predicted values for $F_{p,max,model}$ versus the values of $F_{p,max,exp}$. As indicated by the bisector, the developed model equation describes the general trends fairly good. At low electric field strength and low treatment temperatures, the model slightly overpredicts $F_{p,max}$. Regarding the application of the model to the simulation of a continuous treatment chamber, this error seems of minor importance because $F_{p,max}$ will probably not be reached during the common short residence times. For example, at 6.5 and 9 kV cm^{-1} 64 pulses were needed to reach $F_{p,max}$. This number of pulses is very high for the case of a continuous treatment since the pulse repetition rate is often limited by the utilized processing equipment. In this study, a maximum of 22 pulses was applied in the colinear treatment chamber at the highest pulse repetition rate and the lowest flow rate, respectively (estimate is based on the mean residence time in the treatment zone). On the other hand, as it can be seen in **Figure 5**, one value is clearly underpredicted by the model. This value belongs to the treatment at 9 kV cm^{-1} and 20°C (compare also **Figure 3**). As described in section "PEF Treatment," the experiments with the longest treatment time were conducted in triplicate and therefore it is unlikely that measurement errors explain the deviation. Instead, it might be caused by an erroneous estimate of $F_{p,max}$ at these conditions. It can be seen from **Figure 2**, that the value of $F_{p,max}$ might be slightly higher for treatments at low intensity since the maximum value was not reached after the longest treatment time. For future research it is therefore recommendable to choose the treatment time long enough for reaching a plateau for F_p at any treatment condition. For that, the control of the temperature during the PEF treatment is of high importance in order to distinguish between

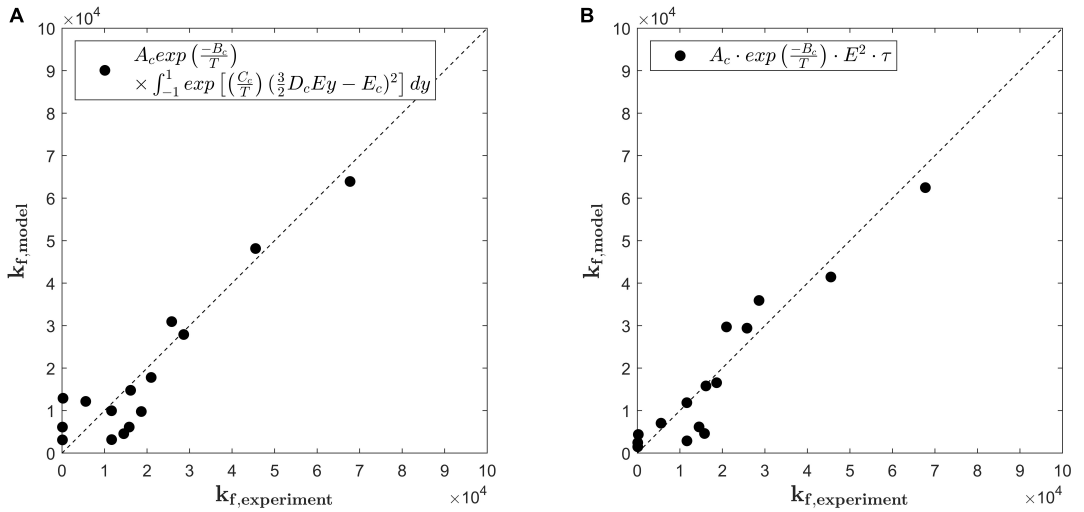

FIGURE 4 | Parity plots for pore formation rate $k_{f,experiment}$ obtained by a primary fit of the experimental data and the pore formation rate $k_{f,model}$ as predicted by equation (11) **(A)** and equation (13) **(B)** with respect to the electric field strength E and total temperature T. The subscripted letter c in the legends indicates modeling constants.

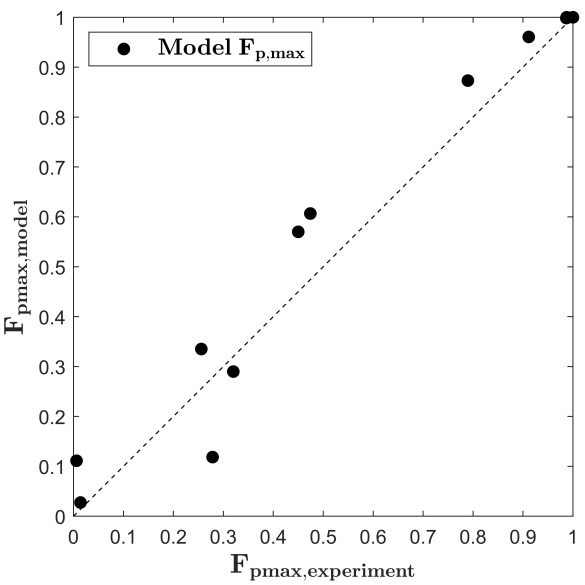

FIGURE 5 | Parity plots for the maximum fraction of perforated cells ($F_{p,max}$) according to equations (14)–(17) and $F_{p,max}$ obtained by the primary fit of the experimental data.

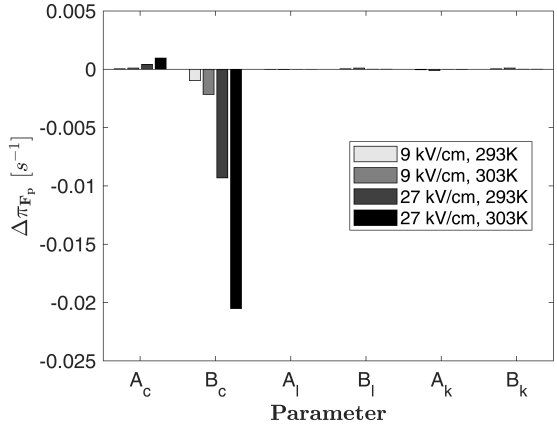

FIGURE 6 | Parameter sensitivity of the source term as given by equation (18) for $F_p = 0$ and different values of the temperature and electric field strength. The quantity $\Delta\pi_{F_p}$ is the change of the source term if one parameter is increased by 1% of its value while all others are kept constant.

PEF and temperature effects. Nevertheless, the aim of the study is to find optimal parameters for the upscaling of the treatment chamber so that treatment conditions leading to low degrees of permeabilization are of minor interest.

Overall Kinetic Model

For the usage of the cell permeabilization kinetics in the process model (see section "Governing Equations"), a rate equation for the perforation of cells must be formulated, which represents the source term π_{F_p} in equation (7). The source term represents the fraction of intact cells being permeabilized per time increment. Therefore, π_{F_p} is given by the time derivative of equation (9), which is

$$\pi_{F_p} = \frac{dF_p}{dt} = k_f \tau f \left(F_{p,max} - F_p\right) \tag{18}$$

The parameters in equation (18) need to be determined by equations (13), (14), (16) and (17). **Figure 6** shows the local parameter sensitivity of π_{F_p}, which is determined by measuring the change of the model output $\Delta\pi_{F_p}$ if one of the 6 parameters is increased by 1% of its value, while all other parameters are kept constant (Hamby, 1994). Assuming $F_p = 0$ and different values

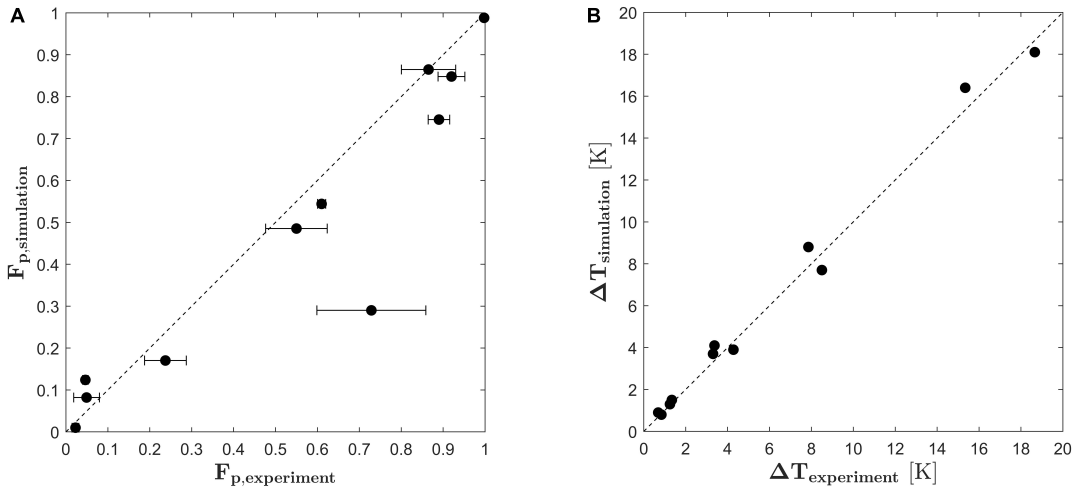

FIGURE 7 | Parity plots of the fraction of perforated cells F_p **(A)** and the average temperature increase **(B)** in the validation experiment versus the results obtained by CFD simulation. Error bars indicate the standard deviation of the experimental runs.

for E and T, the highest sensitivity of the model is found for changes of the parameters A_c, and B_c, which relate the reaction rate constant to E and T. This result reflects the structure of equation (13) and the respective linear or exponential impact of the parameters. If F_p is increased, the sensitivity of the model to A_c, and B_c decreases linearly but the model remains most sensitive toward A_c, and B_c, which have therefore the largest impact on the source term.

Validation of the Kinetic Model

In order to validate the PEF process model and the derived kinetic model for cell electroporation, experiments were conducted in a pilot scale colinear treatment chamber and compared to the simulation results of the similar treatment plant. Therefore, equation (18) was implemented into the finite volume code Ansys CFX19 together with equations (13), (14), (16) and (17) and used to calculate the degree of cell disruption in a colinear treatment chamber by solving equations (1)–(7). The results for the fraction of perforated cells obtained in the validation experiment are plotted in **Figure 7A** against the results obtained by the CFD simulations. As being indicated by the angle bisector, the simulated cell permeabilization is in good agreement to the experiments. Some deviations can be observed for the inlet temperature of 30°C and the highest specific energy inputs (for example $F_{p,exp}$ = 0.9 and $F_{p,sim}$ = 0.75). Here, the model underpredicts the experimental results. One possible explanation is that the average temperature increase for this condition was larger than 10 degrees and therefore, the outlet temperature was almost at 50°C. Since this is beyond the calibrated range of the temperature (20–40°C), the enhancement of the PEF effect through the higher temperature might be underestimated for these conditions. Furthermore, the critical temperature for thermally induced autolysis of *Chlorella vulgaris* was observed to be 55°C (Postma et al., 2016). At high treatment intensities, these temperatures can be reached or even exceeded locally within the chamber so that an additional thermal effect on the cell viability might be possible, which however is not included in the presented model. **Figure 7A** shows also that one point clearly deviates from the experimental data. Because the simulated result is in line with the remaining data and also the predicted temperature increase matches the experiment (see **Figure 7B**), it is likely that the deviation between simulated and measured cell permeabilization is caused by an experimental error, which is also indicated by the large standard deviation of this data point.

The general validity of the PEF process model was tested by comparing the predicted temperature increase in the treatment chamber with the measured data. The results are plotted in **Figure 7B**. Again, the simulation results agree in a good way with the experimental data, which means that the specific energy input in the simulation matches the specific energy input in the experiments.

In conclusion, one can say that the good agreement between the results of the CFD simulation and the experimental data in a colinear treatment chamber shows the validity of the derived kinetic model. It should be emphasized that the kinetic model was calibrated with data being obtained in batch experiments in laboratory electroporation cuvettes. On the contrary, the model validation was not only performed on the larger pilot scale but also in a continuous treatment chamber, for which the occurrence of inhomogeneous treatment conditions is well known. Therefore, the study demonstrates the potential of the proposed approach as a method to transfer data from a small to a larger scale. Since the model is independent of the investigated treatment chamber design, it can be used to design and optimize new treatment chambers for the treatment of microalgae.

Results of the Numerical Parameter Study

After validation, the PEF process model can be applied to study the effect of different process conditions on the

degree of cell permeabilization. For that purpose, a numerical parameter study is conducted as described in section "Numerical Parameter Study."

The results of the numerical simulations are exemplary shown in **Figure 8** for one of the simulated cases ($U = 15$ kV, $T_I = 298.15$ K, $\dot{V} = 2.50 \cdot 10^6 \mathrm{m}^{-3}\ \mathrm{s}^{-1}$). **Figure 8A** shows the evolution of the fraction of perforated cells F_p in the treatment chamber. In the first treatment zone about 45% of all cells are permeabilized and the highest inactivation occurs in regions close to the wall where the flow velocity is low. In addition, a high fraction of permeabilized cells can be found behind the insulators where cells are trapped in recirculation zones with high temperature (see **Figures 8B,C**). The second plot shows the flow velocity magnitude, which follows the typical patterns of laminar flow with the lowest magnitudes near the wall of the chamber and the largest in the center of the pipe. This corresponds to a shorter treatment time for cells which are passing the treatment zone in the middle of the insulators. Therefore, it is obvious that the inactivation is lower in the center of the treatment chamber. This effect is further enhanced because the electric field strength is stronger near the insulator walls (see **Figure 8D**).

The specific energy input is of major interest for PEF treatment. It can be calculated per kg of cell suspension by integrating the local energy input over the volume of the treatment chamber, which yields the expression

$$w_{spec} = \frac{\tau f}{\dot{m}} \int_V \sigma\,(T)\, E dV \tag{19}$$

Herein, $\dot{m}$ is the mass flow rate of the liquid and V the volume the chamber. Since preheating contributes to the overall energy demand, the total energy input w_{total} should be calculated as

$$w_{Total} = w_{spec} + c_p \Delta T \tag{20}$$

Herein stands ΔT for the temperature difference between a reference temperature (in this case chosen as 20°C) and the actual treatment temperature at the chamber inlet. An average value for the heat capacity was used for the calculation of the energy demand for preheating of the cell suspension. **Figure 9A** depicts the fraction of perforated cells versus the electric energy input. For the complete permeabilization of the cell suspension, an energy input of at least 64.64 kJ kg^{-1} is necessary. This is around three times more than the energy input which was necessary for a full perforation in the batch experiments (see section "Experiments in Electroporation Cuvettes"). This dramatic increase can be explained by the previously discussed inhomogeneous treatment conditions in the chamber. Furthermore, the residence time within the treatment zone inside the two isolators is short so that the number of applicable pulses is limited. For the treatment chamber under investigation, mean residence times of 0.062 s, 0.0417 s and 0.0313 s were calculated for volume flows of 1.66 ml s^{-1}, 2.5 ml s^{-1} and 3.33 ml s^{-1}, respectively. This corresponds to a maximum of 22 pulses on average at the lowest flow rate and the highest pulse repetition rate (200 Hz). Due to limitations of the used equipment, the maximum applicable electric field strength is 22.8 kV cm^{-1}. Regarding the results of section "Experiments in Electroporation Cuvettes," it seems likely that the required specific energy input for permeabilizing all cells of *Chlorella vulgaris* could be reduced by applying higher voltages. However, the example makes clear that the design of the treatment chamber is fundamental for energy efficient processing and further developments in this direction are needed.

The variance of the data in **Figure 9A** can be explained by the different treatment temperatures. If the data are plotted with respect to the total energy input, the variance within each group almost disappears (see **Figure 9B**). It can be observed that the overall energy input for a full perforation is more or less similar for all inlet temperatures. Therefore, preheating might be a good option to improve the cell permeabilization in case of technical limitations of the pulse generator. On the other hand, it was stated before that the extraction of thermosensitive cell valuables might be the target of the process and that it might be favorable to choose a lower inlet temperature to remain their functionality. Nevertheless, the temperature increase for a full perforation at an inlet temperature of 20°C was 31°C ($T_{outlet} = 51$°C), 28.87°C for an inlet temperature of 25°C ($T_{outlet} = 53.87$°C) and only 16.11°C for an inlet temperature of 30°C ($T_{outlet} = 46.1$°C). The results show that finding optimal conditions is not always straightforward and that numerical simulation can be a tool to support the process design.

DISCUSSION

Discussion of Experiments in Electroporation Cuvettes

During the treatment of microalgae cells in electroporation cuvettes, it was observed that the maximum achievable fraction of permeabilized cells depends on the applied treatment conditions. An explanation for the observed maximum degree of cell permeabilization is the dependency of the transmembrane potential on the cell size (Neumann, 1996). Even if the mechanism of pore formation is not fully understood, it is consensus that a critical transmembrane potential must be exceeded to induce pore formation (Zimmermann et al., 1976; Abidor et al., 1979). Because the size of cells within a population is never unique but follows a size distribution, a simple explanation for the observed results could be that the critical transmembrane potential was not exceeded for a certain proportion of the cell population. The cell size distribution was also measured for some samples during the experiments and the obtained results indicate a correlation between $1 - F_{p,max}$ and the fraction of the cell population with size larger than a critical value. However, the results are preliminary and further experiments must be carried out to substantiate the hypothesis that incomplete cell perforation is linked to the cell size distribution under certain treatment conditions. The observed phenomena of converging to a maximum value for the fraction of perforated cells under certain conditions is in good agreement to the data of Martínez et al. (2019). They investigated the permeability of *Porphyridium cruentum* cells to PI as a function of electric field strength and the

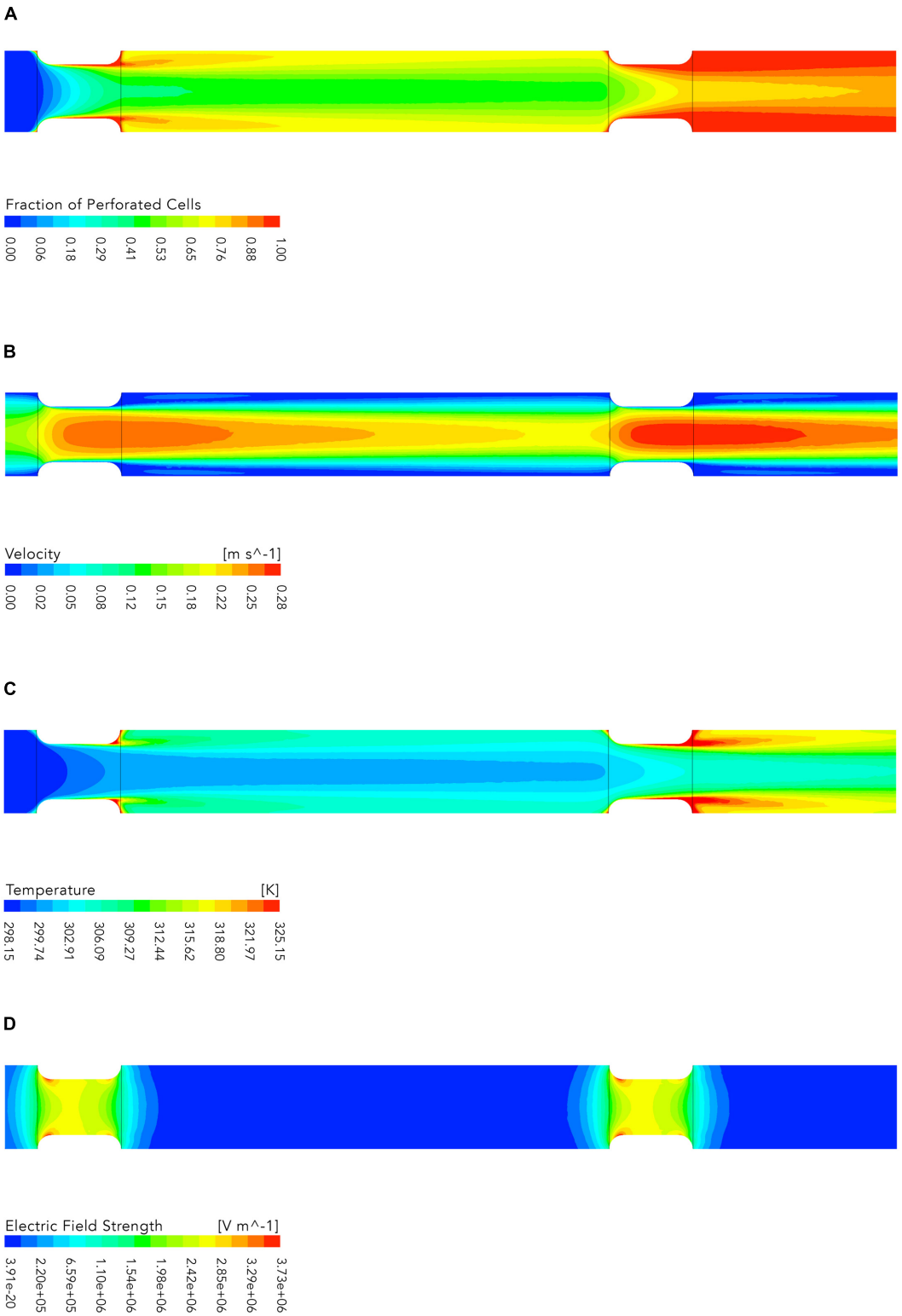

FIGURE 8 | Contour plots of the fraction of perforated cells **(A)**, flow velocity **(B)**, temperature **(C)**, and electric field strength **(D)**, respectively. The plots show the middle plane of the colinear treatment chamber. The flow is from left to right. The electric energy input w_{spec} for the shown case was 58.62 $kJ\ kg^{-1}$ ($U = 15\ kV$, $T_l = 298.15\ K$, $\dot{V} = 2.50 \cdot 10^{-6}\ m^{-3}\ s^{-1}$). Note that the plots depict not the entire simulated domain (see **Figure 1**), since the parts not shown contain no additional relevant information.

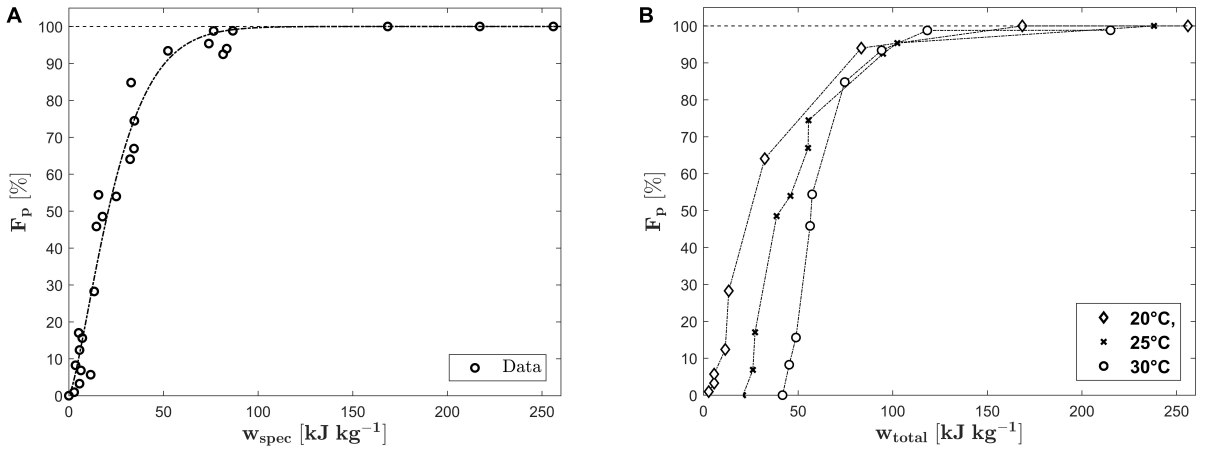

FIGURE 9 | Fraction of perforated cells (F_p) as a function of the electric energy input w_{spec} **(A)**. The dash dotted line indicates the best fit of the data by the Weibull distribution function. Plot **(B)** shows the fraction of perforated cells versus the total energy input w_{total}.

treatment time. In this work it was also shown that the increase of the treatment time did not increase the number of PI-stained cells at certain treatment conditions.

At the lowest treatment intensities, the maximum degree of cell permeabilization was almost not measurable. It is possible that a larger number of cells was permeabilized under these conditions but that resealing of the pores took place before the fluorescent dye was added. For example, Luengo et al. (2014) showed that the addition of PI before the PEF treatment led to a higher proportion of stained cells in comparison to the addition of the dye after the treatment. This means that even at a low electric field strength, a certain part of the cells can be reversibly perforated and therefore becomes accessible for PI, which might be interesting for cell milking applications (Buchmann et al., 2019). However, the concept of microalgae milking has not been proven yet to work at relevant scale and PEF treatment is usually applied to reduce the mass transfer resistance of cells in order to improve the extraction of valuable cell contents.

Resealing is not the only mechanism which affects the accessibility of fluorescent dyes like PI to cells after PEF. Kennedy et al. (2008) observed a rise in the fluorescence intensity over up to 500 s after the treatment and PI addition. Similar results were found by Sweeney et al. (2018b) who observed especially at low treatment intensities an increasing fluorescence intensity for a certain fraction of the treated cells during a time interval of more than 5 min after the treatment and PI addition. The authors attribute their observations to a number of possible reasons, namely diffusive transport of PI into the cells, the formation dynamics of the PI-nucleic acid-complex in a cell and the dynamic closure (Kennedy et al., 2008) or formation of pores after the treatment (Sweeney et al., 2018b). For the development of kinetic models, it is therefore important to use accurate staining protocols, which ensure the correct detection of the permeabilized cell fraction, even at low treatment intensities. The applied experimental protocol for the PI staining of *C. vulgaris* was optimized by Design of Experiments with the independent variables PI concentration per biomass, temperature and time. Since the time duration between the treatment and the measurement in the flow cytometer was about 30 min, it can be expected on basis of the available knowledge that the electroporated fraction of the cell culture remains stable for a suitable time interval and therefore that the measured data provides reliable information about the impact of different treatment conditions on the fraction of permeabilized cells.

Discussion of Kinetic Modeling and Numerical Simulation as Tools for Electroporation Process Development and Scale-Up

The good agreement between the simulation results and the performed experiments in a colinear treatment chamber show the validity of the developed process model. This further proves that simulation is a valid tool to transfer data from a small cuvette scale to a larger scale, even if the design of the treatment chamber and the process operation mode change. Therefore, modeling and simulation can be considered as important tools for the process scale-up or for the design of new treatment chambers for PEF processing. This opens the possibility to develop tailored geometries for the treatment of microalgae with a high throughput at the industrial scale.

For the scale-up it is important to consider process homogeneity and energy requirements, which also depend on the configuration of the treatment chamber. The presented experimental results indicate that a minimum specific energy input of 19.6 kJ kg^{-1} is necessary to perforate 100% of the cells in electroporation cuvettes. These results are in good agreement with the work of Rego et al. (2015), who treated *Chlorella* cells in a continuous treatment chamber with a parallel plate electrode configuration. According to their results, about 20 kJ kg^{-1} were necessary for permeabilizing 100% of the treated cells. In this case, the good comparability of a batch and a continuous treatment chamber may be due to the parallel plate arrangement, which however is not suitable for industrial applications since

this configuration has a lower electrical resistance and therefore a high current flow. Therefore, higher energy inputs are necessary to reach the required electric field strength in a treatment chamber with a parallel plate configuration (Jaeger et al., 2009). According to the presented simulation results, at least 64.64 kJ kg^{-1} are necessary to achieve the complete perforation of the cell culture in the investigated colinear arrangement. By the best knowledge of the authors, no work was published which investigates the treatment of *Chlorella vulgaris* in a colinear treatment chamber at pilot scale so that it is not possible to compare the measured data with the literature. However, the mentioned discrepancy between different setups at different scales shows on the one hand that numerical simulation can serve as a useful tool for the development and planning of industrial biorefinery concepts because estimates of the required energy input and process conditions can be achieved *a priori*. On the other hand, the energy requirement for treating microalgae can be potentially reduced and additional work is needed to study microalgae cell permeabilization at scales beyond the lab scale and to develop energy efficient treatment chambers. This is particularly of interest since the energy input scales linearly with temperature increase. The presented simulation results for different PEF treatment conditions indicate a large effect of the local temperature magnitude and the flow field on the cell membrane permeabilization of *Chlorella vulgaris*. If mass transfer enhancement for the extraction of valuable compounds is the goal of the process, long residence times and the exposure to high temperatures may lead to a loss of thermally sensitive products which in turn entails a lower economic efficiency. It is therefore questionable whether a colinear treatment chamber is the best option for treating microalgae. Numerical simulation and validated virtual engineering are suitable tools to develop new treatment chambers which avoid the occurrence of temperature hotspots. According to the presented results, the improvement of the flow field might be a good starting point to create new treatment chambers for the electroporation of microalgae.

Nevertheless, several practical aspects need to be considered when models like the proposed one shall be used for process or plant design. First, one should consider the pulse shape in the real process. Since the impedance of the treatment chamber might not fit to the pulse generator, reflection can occur. Therefore, the real pulse applied to the suspension might be different from the perfect rectangular one which is considered in the simulation. As stated in section "PEF Systems and Experimental Design," an overshoot of the voltage and subsequent ringing was observed during the conducted experiments. These features of the pulse are not resolved by the numerical model. Instead, it considers the time-averaged power input, which is the power input per pulse being scaled with the pulse repetition rate, see equation (4) and definitions in section "Governing Equations." The comparison between experiments and CFD simulation indicates that the most important factors for the prediction of cell permeabilization (**Figure 7A**) and specific energy input (**Figure 7B**) are correct values for the time-averaged voltage during a single pulse and the energy per pulse under the investigated conditions. It can be expected that this conclusion is valid up to a certain limit but also that the numerical model does not reflect the real conditions anymore if the difference between real and perfect pulses becomes too large. Consequently, the prediction of cell permeabilization will also deviate from the experimental reality.

Second, the results of this study indicate that thermally induced autolysis might take place in real processing. For *Chlorella vulgaris* this is the case at temperatures higher than 55°C (Postma et al., 2016). Since such effects are not considered in the proposed model, thermal autolysis can explain deviations to experiments if the inlet temperature or the electric energy input are too high.

Third, the dependency of the PEF response on the growth phase is known for a number of other organisms such as *Saccharomyces cerevisiae* (Molinari et al., 2004). It is thinkable that the time of cell harvest and the respective growth phase have an impact on the predictive capability of the developed kinetic model. In that case it would be crucial for a successful process design to know the harvesting point and the constitution of a cell culture before calibrating kinetic models for cell perforation. In the present work, cells were harvested in the late exponentially phase, what should be considered if the proposed model is used by other scientists or process developers.

Fourth, it should be mentioned that the model calibration was done at a dry mass content of 1 g l^{-1}. Nevertheless, it was shown that the PEF treatment of microalgae is independent of the biomass concentration up to concentrations 160 g l^{-1} for Auxenochlorella protothecoides (Goettel et al., 2013) and 40 g l^{-1} for Chlorella vulgaris (Rego et al., 2015) (higher concentrations were not tested in the cited papers). Based on these results, the validity of the proposed model at higher biomass concentrations seems likely, although it should be proved in future work. Also, it must be shown whether this assumption is valid for dry mass concentration higher than 40 g l^{-1}, which are of interest for industrial applications because the specific energy input per unit of dry biomass decreases at higher biomass concentrations. Even if the cell concentration has no direct impact on the perforation kinetics, it should be considered since the effective viscosity and the flow behavior of the cell suspension changes at higher biomass concentration. This entails an indirect effect on the degree of perforated cells, due to its dependency on the residence time distribution, which again is affected by the suspension rheology. Even if this point can be addressed easily in simulations with suitable data for the concentration dependency of the viscosity at hand (Buchmann et al., 2018), it should be kept in mind in the case that the cell concentration is changed.

Lastly, the development of kinetic models requires a method for the detection of cell permeabilization. In this work, PI staining and flow cytometry were the chosen for this task. With these methods, the detection of cells in which the fluorescent dye has been penetrated is an all or nothing event and therefore no statement regarding the degree of perforation of individual cells can be made. In other words: after a sufficient staining time, the method provides information whether a cell is permeabilized, but it is not suitable to give an answer to the question how much a cell is permeabilized. As discussed in the previous section, the uptake kinetics of PI are determined by the permeabilized fraction of the cell surface and its evolution in time (Kennedy et al., 2008).

It can be expected that similar dependencies exist for the molecular mass transfer of other molecules than PI. Since the enhancement of solute mass transfer is the major application of PEF in the context of microalgae biorefinery, information about the relation between PEF treatment conditions and the consequential mass transfer kinetics might be of interest. Modeling and simulation turn out to be suitable tools for this purpose as well. In literature, authors suggest different approaches for relating the treatment conditions directly to the transport of solutes, which represents an extension in comparison to the presented model. Thereby, concentration gradients as driving forces (Mahnič-Kalamiza et al., 2014) and the transport resistance must be considered. The latter is related to the dynamics of pore formation and their size distribution (Krassowska and Filev, 2007; Sweeney et al., 2018a), which in turn determine the membrane permeability for specific solutes. An alternative approach to capture this effect is the introduction of a solute-specific hindering coefficient (Mahnič-Kalamiza et al., 2014). Even if these approaches are not formulated specifically for microalgae, the underlying concepts seem well applicable and provide beneficial approaches for future work in the field of utilizing PEF for biorefinery concepts. Nevertheless, new studies also show that the mass transfer is further enhanced by simply incubating the permeabilized cells after the PEF treatment. The associated decrease of the transport resistance is believed to be caused by an enzymatically driven autolysis in response to PEF-induced cell death (Silve et al., 2018a; Jaeschke et al., 2019; Scherer et al., 2019). Therefore, effects on short and on long time scales should be considered for the goal of improving the efficiency of microalgae biorefining by applying PEF technology.

CONCLUSION

The broad commercial breakthrough of microalgae as a resource for versatile products in the food and feed industry and in industrial biotechnology is limited by the production costs. Therefore, it is crucial to find new cost and energy saving technologies for the downstream processing. The presented work proposes an approach for this objective based on modeling and numerical simulation of cell permeabilization by Pulsed Electric Fields. Simulations are highly desirable because they can contribute to reduce costs for the collection of data being required for process scale-up. The proposed approach follows the idea that data for the calibration of models for cell disruption kinetics can be gained in laboratory work at the smallest scale in electroporation cuvettes. Once the kinetic is adequately described, numerical simulation models offer flexible tools for process design, scale-up and optimization of operation conditions. The principal capability of this approach was demonstrated by comparing the results of simulations and experiments for the PEF treatment of *Chlorella vulgaris* in a pilot scale collinear treatment chamber. Therefore, the present work provides the first contribution showing the applicability of kinetic modeling and numerical simulation for designing PEF processes for the purpose of biorefining microalgae biomass.

Future work should target the enhancement of the treatment efficiency by designing new treatment chambers. With the proposed modeling approach, new designs can be compared easily with regard to their potential for energy efficient cell membrane permeabilization. In the end, numerical simulation cannot replace the manufacturing of prototypes, but it can help to find efficient designs at reduced cost for the process development.

DATA AVAILABILITY STATEMENT

The datasets generated for this study are available on request to the corresponding author.

AUTHOR CONTRIBUTIONS

JK and CM drafted the manuscript. JK conducted the experiments, analyzed experimental and simulation data, calibrated and implemented the kinetic model, and performed numerical simulation. CM conceptualized the study and supervised the experimental and numerical work including data analysis and model development. CR critically revised the manuscript, improved the work with important intellectual content, and took responsibility for the integrity of the study as a whole. All authors read and approved the submitted manuscript.

ACKNOWLEDGMENTS

The authors gratefully acknowledge Stephanie Eva Haas for developing the PI staining protocol in the frame of her Bachelor thesis and Tobias Horneber for helpful discussions on numerical issues.

REFERENCES

Abidor, I. G., Arakelyan, V. B., Chernomordik, L. V., Chizmadzhev, Y. A., Pastushenko, V. F., and Tarasevich, M. P. (1979). Electric breakdown of bilayer lipid membranes. *J. Electroanal. Chem. Inter. Electrochem.* 104, 37–52. doi: 10.1016/S0022-0728(79)81006-2

Aouir, A., Amiali, M., Kirilova-Gachovska, T., Benchabane, A., and Bitam, A. (2015). "The effect of pulsed electric field (PEF) and ultrasoud (US) technologies on the extraction of phycopiliproteins from *Arthrospira platensis*," in *Proceedings of the 2015 IEEE Canada International Humanitarian Technology Conference (IHTC2015)* (Ottawa, ON: IEEE), 1–4.

Atkins, P. W., and de Paula, J. (2006). *Atkins' Physical Chemistry*. Oxford: Oxford University Press.

Becker, E. W. (2007). Micro-algae as a source of protein. *Biotechnol. Adv.* 25, 207–210. doi: 10.1016/j.biotechadv.2006.11.002

Buchmann, L., Bloch, R., and Mathys, A. (2018). Comprehensive pulsed electric field (PEF) system analysis for microalgae processing. *Bioresour. Technol.* 265, 268–274. doi: 10.1016/j.biortech.2018.06.010

Buchmann, L., Brändle, I., Haberkorn, I., Hiestand, M., and Mathys, A. (2019). Pulsed electric field based cyclic protein extraction of microalgae towards closed-loop biorefinery concepts. *Bioresour. Technol.* 291, 121870. doi: 10.1016/j.biortech.2019.121870

Capello, C., Fischer, U., and Hungerbühler, K. (2007). What is a green solvent? A comprehensive framework for the environmental assessment of solvents. *Green Chem.* 9, 927–934. doi: 10.1039/b617536h

Caporgno, M. P., and Mathys, A. (2018). Trends in microalgae incorporation into innovative food products with potential health benefits. *Front. Nutr.* 5:58. doi: 10.3389/fnut.2018.00058

Carullo, D., Abera, B. D., Casazza, A. A., Donsì, F., Perego, P., Ferrari, G., et al. (2018). Effect of pulsed electric fields and high pressure homogenization on the aqueous extraction of intracellular compounds from the microalgae *Chlorella vulgaris*. *Algal Res.* 31, 60–69. doi: 10.1016/j.algal.2018.01.017

Coustets, M., Joubert-Durigneux, V., Hérault, J., Schoefs, B., Blanckaert, V., Garnier, J.-P., et al. (2015). Optimization of protein electroextraction from microalgae by a flow process. *Bioelectrochemistry (Amster. Netherl.)* 103, 74–81. doi: 10.1016/j.bioelechem.2014.08.022

Crowe, C. T., Schwarzkopf, J. D., Sommerfeld, M., and Tsuji, Y. (2011). *Multiphase Flows with Droplets and Particles*. Boca Raton, FL: CRC Press.

D'Hondt, E., Martín-Juárez, J., Bolado, S., Kasperoviciene, J., Koreiviene, J., Sulcius, S., et al. (2017). "Cell disruption technologies," in *Microalgae-Based Biofuels and Bioproducts: From Feedstock Cultivation to End-Products*, eds C. Gonzalez-Fernandez and R. Muñoz (Kindlington: Woodhead Publishing), 133–154.

Fiala, A., Wouters, P. C., van den Bosch, E., and Creyghton, Y. L. M. (2001). Coupled electrical-fluid model of pulsed electric field treatment in a model food system. *Innov. Food Sci. Emerg. Technol.* 2, 229–238. doi: 10.1016/S1466-8564(01)00042-X

Gerlach, D., Alleborn, N., Baars, A., Delgado, A., Moritz, J., and Knorr, D. (2008). Numerical simulations of pulsed electric fields for food preservation: a review. *Innov. Food Sci. Emerg. Technol.* 9, 408–417. doi: 10.1016/j.ifset.2008.02.001

Glaser, R. W., Leikin, S. L., Chernomordik, L. V., Pastushenko, V. F., and Sokirko, A. I. (1988). Reversible electrical breakdown of lipid bilayers: formation and evolution of pores. *Biochim. Biophys. Acta Biomembr.* 940, 275–287. doi: 10.1016/0005-2736(88)90202-7

Goettel, M., Eing, C., Gusbeth, C., Straessner, R., and Frey, W. (2013). Pulsed electric field assisted extraction of intracellular valuables from microalgae. *Algal Res.* 2, 401–408. doi: 10.1016/j.algal.2013.07.004

Grimi, N., Dubois, A., Marchal, L., Jubeau, S., Lebovka, N. I., and Vorobiev, E. (2014). Selective extraction from microalgae *Nannochloropsis* sp. using different methods of cell disruption. *Bioresour. Technol.* 153, 254–259. doi: 10.1016/j.biortech.2013.12.011

Günerken, E., D'Hondt, E., Eppink, M. H. M., Garcia-Gonzalez, L., Elst, K., and Wijffels, R. H. (2015). Cell disruption for microalgae biorefineries. *Biotechnol. Adv.* 33, 243–260. doi: 10.1016/j.biotechadv.2015.01.008

Hamby, D. M. (1994). A review of techniques for parameter sensitivity analysis of environmental models. *Environ. Monitor. Assess.* 32, 135–154. doi: 10.1007/BF00547132

Jaeger, H., Meneses, N., and Knorr, D. (2009). Impact of PEF treatment inhomogeneity such as electric field distribution, flow characteristics and temperature effects on the inactivation of *E. coli* and milk alkaline phosphatase. *Innov. Food Sci. Emerg. Technol.* 10, 470–480. doi: 10.1016/j.ifset.2009.03.001

Jaeschke, D. P., Mercali, G. D., Marczak, L. D. F., Müller, G., Frey, W., and Gusbeth, C. (2019). Extraction of valuable compounds from Arthrospira platensis using pulsed electric field treatment. *Bioresour. Technol.* 283, 207–212. doi: 10.1016/j.biortech.2019.03.035

Kennedy, S. M., Ji, Z., Hedstrom, J. C., Booske, J. H., and Hagness, S. C. (2008). Quantification of electroporative uptake kinetics and electric field heterogeneity effects in cells. *Biophys. J.* 94, 5018–5027. doi: 10.1529/biophysj.106.103218

Krassowska, W., and Filev, P. D. (2007). Modeling electroporation in a single cell. *Biophys. J.* 92, 404–417. doi: 10.1529/biophysj.106.094235

Lam, G. P., Postma, P. R., Fernandes, D. A., Timmermans, R. A. H., Vermuë, M. H., Barbosa, M. J., et al. (2017a). Pulsed electric field for protein release of the microalgae chlorella vulgaris and neochloris oleoabundans. *Algal Res.* 24, 181–187. doi: 10.1016/j.algal.2017.03.024

Lam, G. P., van der Kolk, J. A., Chordia, A., Vermuë, M. H., Olivieri, G., Eppink, M. H. M., et al. (2017b). Mild and selective protein release of cell wall deficient microalgae with pulsed electric field. *ACS Sustain. Chem. Eng.* 5, 6046–6053. doi: 10.1021/acssuschemeng.7b00892

Lam, G. P., Vermuë, M. H., Eppink, M. H. M., Wijffels, R. H., and van den Berg, C. (2018). Multi-product microalgae biorefineries: from concept towards reality. *Trends Biotechnol.* 36, 216–227. doi: 10.1016/j.tibtech.2017.10.011

Lindgren, M., Aronsson, K., Galt, S., and Ohlsson, T. (2002). Simulation of the temperature increase in pulsed electric field (PEF) continuous flow treatment chambers. *Innov. Food Sci. Emerg. Technol.* 3, 233–245. doi: 10.1016/S1466-8564(02)00044-9

Luengo, E., Condón-Abanto, S., Álvarez, I., and Raso, J. (2014). Effect of pulsed electric field treatments on permeabilization and extraction of pigments from *Chlorella vulgaris*. *J. Membr. Biol.* 247, 1269–1277. doi: 10.1007/s00232-014-9688-2

Luengo, E., Martínez, J. M., Bordetas, A., Álvarez, I., and Raso, J. (2015). Influence of the treatment medium temperature on lutein extraction assisted by pulsed electric fields from *Chlorella vulgaris*. *Innov. Food Sci. Emerg. Technol.* 29, 15–22. doi: 10.1016/j.ifset.2015.02.012

Mahnič-Kalamiza, S., Miklavčič, D., and Vorobiev, E. (2014). Dual-porosity model of solute diffusion in biological tissue modified by electroporation. *Biochim. Biophys. Acta* 1838, 1950–1966. doi: 10.1016/j.bbamem.2014.03.004

Martínez, J. M., Delso, C., Álvarez, I., and Raso, J. (2019). Pulsed electric field permeabilization and extraction of phycoerythrin from *Porphyridium cruentum*. *Algal Res.* 37, 51–56. doi: 10.1016/j.algal.2018.11.005

Martínez, J. M., Luengo, E., Saldaña, G., Álvarez, I., and Raso, J. (2017). C-phycocyanin extraction assisted by pulsed electric field from *Artrosphira platensis*. *Food Res. Inter. (Ottawa Ont.)* 99, 1042–1047. doi: 10.1016/j.foodres.2016.09.029

Meneses, N., Jaeger, H., Moritz, J., and Knorr, D. (2011). Impact of insulator shape, flow rate and electrical parameters on inactivation of *E. coli* using a continuous co-linear PEF system. *Innov. Food Sci. Emerg. Technol.* 12, 6–12. doi: 10.1016/j.ifset.2010.11.007

Molinari, P., Pilosof, A. M. R., and Jagus, R. J. (2004). Effect of growth phase and inoculum size on the inactivation of *Saccharomyces cerevisiae* in fruit juices by pulsed electric fields. *Food Res. Inter.* 37, 793–798. doi: 10.1016/j.foodres.2004.03.010

Nehmé, R., Atieh, C., Fayad, S., Claude, B., Chartier, A., Tannoury, M., et al. (2017). Microalgae amino acid extraction and analysis at nanomolar level using electroporation and capillary electrophoresis with laser-induced fluorescence detection. *J. Separat. Sci.* 40, 558–566. doi: 10.1002/jssc.201601005

Neumann, E. (1996). "Gene delivery by membrane electroporation," in *Electrical Manipulation of Cells*, eds P. T. Lynch and M. R. Davey (Boston, MA: Springer), 157–183. doi: 10.1007/978-1-4613-1159-1_8

Parniakov, O., Barba, F. J., Grimi, N., Marchal, L., Jubeau, S., Lebovka, N., et al. (2015). Pulsed electric field and pH assisted selective extraction of intracellular components from microalgae *Nannochloropsis*. *Algal Res.* 8, 128–134. doi: 10.1016/j.algal.2015.01.014

Pataro, G., Goettel, M., Straessner, R., Gusbeth, C., Ferrari, G., and Frey, W. (2017). Effect of PEF treatment on extraction of valuable compounds from microalgae *C. vulgaris*. *Chem. Eng. Transact.* 2017, 67–72.

Postma, P. R., Pataro, G., Capitoli, M., Barbosa, M. J., Wijffels, R. H., Eppink, M. H. M., et al. (2016). Selective extraction of intracellular components from the microalga *Chlorella vulgaris* by combined pulsed electric field-temperature treatment. *Bioresour. Technol.* 203, 80–88. doi: 10.1016/j.biortech.2015.12.012

Raso, J., Frey, W., Ferrari, G., Pataro, G., Knorr, D., Teissie, J., et al. (2016). Recommendations guidelines on the key information to be reported in studies of application of PEF technology in food and biotechnological processes. *Innov. Food Sci. Emerg. Technol.* 37, 312–321. doi: 10.1016/j.ifset.2016.08.003

Rauh, C., Baars, A., and Delgado, A. (2009). Uniformity of enzyme inactivation in a short-time high-pressure process. *J. Food Eng.* 91, 154–163. doi: 10.1016/j.jfoodeng.2008.08.019

Rauh, C., Krauss, J., Ertunc, Ö, Delgado, A., Simos, T. E., Psihoyios, G., et al. (2010). "Numerical simulation of non-thermal food preservation," in *AIP Proceedings*, ed. AIP Publishing (Rhodes: AIP Conference Proceedings), 1692–1695.

Rego, D., Costa, L., Pereira, M. T., and Redondo, L. M. (2015). Cell membrane permeabilization studies of *Chlorella* sp. by pulsed electric fields. *IEEE Transact. Plasma Sci.* 43, 3483–3488. doi: 10.1109/TPS.2015.2448660

Ruiz, J., Olivieri, G., de Vree, J., Bosma, R., Willems, P., Reith, J. H., et al. (2016). Towards industrial products from microalgae. *Energy Environ. Sci.* 9, 3036–3043. doi: 10.1039/C6EE01493C

Sadik, M. M., Yu, M., Zheng, M., Zahn, J. D., Shan, J. W., Shreiber, D. I., et al. (2014). Scaling relationship and optimization of double-pulse electroporation. *Biophys. J.* 106, 801–812. doi: 10.1016/j.bpj.2013.12.045

Saulis, G. (2010). Electroporation of cell membranes: the fundamental effects of pulsed electric fields in food processing. *Food Eng. Rev.* 2, 52–73. doi: 10.1007/s12393-010-9023-3

Saulis, G., and Venslauskas, M. S. (1993). Cell electroporation: Part 1. theoretical simulation of the process of pore formation in a cell. *Bioelectrochem. Bioenerg.* 32, 221–235. doi: 10.1016/0302-4598(93)80047-X

Scherer, D., Krust, D., Frey, W., Mueller, G., Nick, P., and Gusbeth, C. (2019). Pulsed electric field (PEF)-assisted protein recovery from *Chlorella vulgaris* is mediated by an enzymatic process after cell death. *Algal Res.* 41:101536. doi: 10.1016/j.algal.2019.101536

Silve, A., Kian, C. B., Papachristou, I., Kubisch, C., Nazarova, N., Wüstner, R., et al. (2018a). Incubation time after pulsed electric field treatment of microalgae enhances the efficiency of extraction processes and enables the reduction of specific treatment energy. *Bioresour. Technol.* 269, 179–187. doi: 10.1016/j.biortech.2018.08.060

Silve, A., Papachristou, I., Wüstner, R., Sträßner, R., Schirmer, M., Leber, K., et al. (2018b). Extraction of lipids from wet microalga *Auxenochlorella protothecoides* using pulsed electric field treatment and ethanol-hexane blends. *Algal Res.* 29, 212–222. doi: 10.1016/j.algal.2017.11.016

Sweeney, D. C., Douglas, T. A., and Davalos, R. V. (2018a). Characterization of cell membrane permeability in vitro part II: computational model of electroporation-mediated membrane transport. *Technol. Cancer Res. Treat.* 17:1533033818792490. doi: 10.1177/1533033818792490

Sweeney, D. C., Weaver, J. C., and Davalos, R. V. (2018b). Characterization of cell membrane permeability in vitro part I: transport behavior induced by single-pulse electric fields. *Technol. Cancer Res. Treat.* 17:1533033818792491. doi: 10.1177/1533033818792491

Toepfl, S., Heinz, V., and Knorr, D. (2007). High intensity pulsed electric fields applied for food preservation. *Chem. Eng. Process. Process Intensif.* 46, 537–546. doi: 10.1016/j.cep.2006.07.011

United Nations- Department of Economic and Social Affairs (2017). *World Population Projected to Reach 9.8 Billion in 2050, and 11.2 Billion in 2100 | UN DESA | United Nations Department of Economic and Social Affairs*. Available online at: https://www.un.org/development/desa/en/news/population/world-population-prospects-2017.html (accessed 20 February, 2019).

Wölken, T., Sailer, J., Maldonado-Parra, F. D., Horneber, T., and Rauh, C. (2017). "Application of numerical simulation techniques for modeling pulsed electric field processing," in *Handbook of Electroporation*, ed. D. Miklavcic (Cham: Springer International Publishing), 1–31. doi: 10.1007/978-3-319-26779-1_42-1

Zbinden, M. D. A., Sturm, B. S. M., Nord, R. D., Carey, W. J., Moore, D., Shinogle, H., et al. (2013). Pulsed electric field (PEF) as an intensification pretreatment for greener solvent lipid extraction from microalgae. *Biotechnol. Bioeng.* 110, 1605–1615. doi: 10.1002/bit.24829

Zimmermann, U., Pilwat, G., Beckers, F., and Riemann, F. (1976). Effects of external electrical fields on cell membranes. *Bioelectrochem. Bioenerg.* 3, 58–83. doi: 10.1016/0302-4598(76)85007-6

Zocher, K., Banaschik, R., Schulze, C., Schulz, T., Kredl, J., Miron, C., et al. (2016). Comparison of extraction of valuable compounds from microalgae by atmospheric pressure plasmas and pulsed electric fields. *Plasma Med.* 6, 273–302. doi: 10.1615/PlasmaMed.2017019104

Conflict of Interest: The authors declare that the research was conducted in the absence of any commercial or financial relationships that could be construed as a potential conflict of interest.

Copyright © 2020 Knappert, McHardy and Rauh. This is an open-access article distributed under the terms of the Creative Commons Attribution License (CC BY). The use, distribution or reproduction in other forums is permitted, provided the original author(s) and the copyright owner(s) are credited and that the original publication in this journal is cited, in accordance with accepted academic practice. No use, distribution or reproduction is permitted which does not comply with these terms.

APPENDIX A

The biophysical meaning of the parameters in equation (11) shall be briefly described. For the reader's convenience, the equation is rewritten.

$$k_f = A_c\left[s^{-1}\right]\ \exp\left(-\frac{B_c\,[K]}{T}\right) \times \int_{-1}^{1} exp\left[\left(\frac{C_c\left[K\ V^{-1}\right]}{T}\right)\cdot\left(\frac{3}{2}E^2 D_c\,[m]\cdot \text{y-E}_c\,[V]\right)^2\right] dy \tag{21}$$

In order to reduce the parameters of the original model as stated by Saulis (2010), the following substitutions were made

$$A_c = \frac{2\pi\nu a^2}{a_l} \tag{22}$$

$$B_c = \frac{\Delta W_f\,(0)}{k_B} \tag{23}$$

$$C_c = \frac{\pi C_m\left(\frac{\varepsilon_W}{\varepsilon_M} - 1\right)}{2k_B} r_*^2 \tag{24}$$

$$D_c = ay \tag{25}$$

$$E_C = \Phi_0 \tag{26}$$

The symbols in Equations (22–26) have the following meaning: ν is the natural fluctuation frequency of the lipid molecules in the cell membrane, a is the cell radius, a_l the area of a lipid molecule, $\Delta W_f\,(0)$ is the energy barrier for pore formation at a transmembrane potential of 0 V, k_B is the Boltzmann constant, C_m is the cell membrane capacity, ε_W and ε_M stand for the relative permittivity of water and the cell membrane, r_* is the radius of a pore corresponding to the maximum of the energy barrier at given transmembrane potential, y is the substitute for the integration variable which reads as $\cos(\rho)$ where ρ is the angle to the surface normal and Φ_0 is the resting potential of the cell.

frontiers in Bioengineering and Biotechnology

ORIGINAL RESEARCH
published: 17 April 2020
doi: 10.3389/fbioe.2020.00297

Pulsed Electric Field Extraction of α and β-Acids From Pellets of *Humulus lupulus* (Hop)

*George Ntourtoglou[1], Evangelia Anastasia Tsapou[1], Fotini Drosou[1], Eleni Bozinou[2], Stavros Lalas[2], Panagiotis Tataridis[1] and Vassilis Dourtoglou[1]**

[1] Department of Wine, Vine and Beverage Sciences, University of West Attica, Athens, Greece, [2] Department of Food Science and Nutrition, University of Thessaly, Karditsa, Greece

This paper investigates the process of extracting hop pellets (hops) utilizing the pulsed electric field (PEF) technique and the contrasting effects of the technique between two distinct hop varieties (one bitter and one aromatic). The effect of PEF on the extraction was evaluated by measuring the concentration of α-acids and β-acids (humulones and lupulones). Regarding the aromatic character, the hop's volatile caryophyllene, humulene and β-myrcene were analyzed both with and without employing the PEF treatment. In order to analyze the acids and the volatile fraction, the analytical method of UV–vis spectrophotometry was applied followed by gas chromatography coupled with mass spectrometry. For the second technique, the extracts were previously purified through a Graphitized Carbon Black syringe for Solid Phase Extraction. The results revealed that PEF had a positive impact on the alpha acids of bitter hops by increasing the extraction rate of these acids by 20%, while the volatiles demonstrated an increase of 5.6 and 7.4% for humulene and caryophyllene, respectively. Concerning the aromatic variety of hops, the PEF treatment appeared to have no noteworthy effects.

Keywords: hops, pulsed electric field, α-acids, β-acids, extraction, SPE

OPEN ACCESS

Edited by:
Eugene Vorobiev, University of Technology Compiegne, France

Reviewed by:
Vivek Sharma, Chandigarh University, India
Amine Moubarik, Université Sultan Moulay Slimane, Morocco

***Correspondence:**
Vassilis Dourtoglou
vdourt@uniwa.gr

Specialty section:
This article was submitted to Industrial Biotechnology, a section of the journal Frontiers in Bioengineering and Biotechnology

Received: *25 September 2019*
Accepted: *20 March 2020*
Published: *17 April 2020*

Citation:
Ntourtoglou G, Tsapou EA, Drosou F, Bozinou E, Lalas S, Tataridis P and Dourtoglou V (2020) Pulsed Electric Field Extraction of α and β-Acids From Pellets of Humulus lupulus (Hop). Front. Bioeng. Biotechnol. 8:297. doi: 10.3389/fbioe.2020.00297

INTRODUCTION

Hop pellets are renowned for contributing to the bitterness of the taste and the enrichment of aroma in beer. They come from the plant *Humulus lupulus* and, specifically, from its female cone. The genus is represented by two species; the Humulus, the common hops (*H. lupulus* L.), and the Japanese hops (*H. japonicus* Sieb. and Zuce.). The Humulus genus particularly, belongs to the family of the Cannabinaceae (Steinhaus and Schieberle, 2000). Hops complement beer in a complex way due to their chemical composition, which varies depending on the variety used, the cultivation techniques and the extraction that occurs during the processing of the beer. In air-dried hop cones, water accounts for 10%, total resins for 15%, essential oils 0.5–2%, tannins 4%, monosaccharides 2%, proteins 15%, ash 8% and cellulose 43% (Stevens, 1967). Additionally, it is remarkable to mention that hops have been used in folk medicine in the past since they possess a broad spectrum of medico-pharmaceutical properties. The hop pellets are financially exploited primarily by the beer industry.

Hop resins include hard resins, soft resins and uncharacterized resins. Hard resins make up the part of the total resins which is insoluble in low boiling paraffinic solvents. Soft resins contrastively, are the fraction of total resins soluble in low boiling paraffinic hydrocarbons and mainly include the

α-acids and the β-acids. The α-acids consist of humulones, cohumulones and adhumulones while the β-acids include lupulones, colupulones and adlupulones (Stevens, 1967). There is also another part of the resins which are uncharacterized. This fraction is the portion of the soft resin remaining after precipitation of α-acids with lead acetate and crystallization of β-acids (Stevens, 1967; Kunze, 2004).

Another important constituent of the hop flower, is the essential oils located within the hop cone. This fraction is also known as "hop oil" and is mainly composed by the volatile aromatic compounds. The total oil content depends on the variety of hop and varies between 0.1 and 2.0% by dry weight (Stevens, 1967). In this fraction more than 400 hop flavor components have been identified in majority monoterpenes (C_{10}) and sesquiterpenes (C_{15}). The main volatiles in hops cultivars are myrcene, α-humulene and β-caryophyllene, which account for 80% (Rettberg et al., 2018). Myrcene varies from variety to variety and can contain from 10 to 72% of the "hop oil". This compound bestows the green fresh note with resinous aspects (Steinhaus and Schieberle, 2000; Nance et al., 2011). Myrcene's oxidation forms many terpenoids, such as linalool, geraniol, citral, a-terpineol and carvone, known for their augmenting effects on the aroma (Dieckmann and Palamand, 1974; Rettberg et al., 2018). With respect to α-humulene (15–42% of the essential oil of hops) and β-caryophyllene (2.8–18.2% of the essential oil), they are known for their woody and spicy odor (Peacock and Deinzer, 1981; Nickerson and Van Engel, 1992; Peacock and McCarty, 1992; Eyres and Dufour, 2009).

Conventional extraction methods require extended extraction times, high purity solvents, often offer low extraction selectivity and, finally, in some cases are responsible for the thermal decomposition of sensitive compounds (Bozinou et al., 2019). For the above reasons, new extraction techniques have been introduced. These methods include ultrasonic waves (Hossain et al., 2014; Bimakr et al., 2017), gamma irradiation (Gyawali et al., 2006; Pinela et al., 2014) and electric fields, including the pulsed electric field (PEF) (Delsart et al., 2012; Zhang et al., 2012). These methods are already applied to other crops of commercial interest such as grapes, onions, potatoes, etc.

New technologies, such as PEFs and high voltage electric discharges (HVED), have been proposed for microbial inactivation of food liquids (Delsart et al., 2015), for the extraction of compounds from Chardonnay grapes (Grimi et al., 2009) or other fruits, such as apples (Grimi et al., 2011). HVEDs have also been proposed for the extraction of polyphenols and other compounds with antioxidant activity (Boussetta et al., 2009; Boussetta et al., 2011).

The application of PEF has principally been used as a non-thermal treatment of liquid foods aiming to the inactivation of microorganisms (Grahl and Markl, 1996; Alvarez et al., 2003). The microbial inactivation is a function of food composition which depends on the composition of the solution and the electrical parameters (Heinz et al., 2003; Touya, 2005; Vorobiev and Lebovka, 2010). Other researchers have introduced electric field treatment for the acceleration of aging of young wine thanks to the extraction of flavor compounds from wood (Zeng et al., 2008; Drosou et al., 2017).

The disruption of the cell membrane due to electroporation is caused by the high intensity of the fields induced by PEF. This disturbance of the architectural structure of the membrane and the disorganization of the integrity of microbial or plant cells, lead to complex phenomena such as cell lysis or the fusion of protoplasts. When the transmembrane potential exceeds a critical value, generally around 0.8 to 1 V (Zimmermann, 1986), pore formation occurs in the cell membrane and certain metabolites diffuse in the extracellular medium. This state can be transient and reversible if the applied field remains below a certain level (Cukjati et al., 2007). On the other hand, the electropermeabilization of cells must be irreversible when the objective is the inactivation of microbial cells.

The PEF treatment system is not a simple device and consists of a high voltage source, in some cases a capacitor bank, a switch and the treatment chamber. The PEF treatment chamber comprises two or more electrodes, filled with the material to be treated and it is constructed so that the electric field acting on the mass of the product to be treated is as homogeneous as possible (Maged and Ayman, 2012).

Hops are the most complex and costly raw material used in brewing. Of all the herbs that have been used to flavor and preserve beer over the ages, only the hop (*H. lupulus* L.) is now regarded as an essential raw material in brewing throughout the world.

In 2017, 148,603 tons of hops were produced worldwide (FAO). The majority was produced in the United States, with a total of 47,000 tons. Considerable amounts were also produced in Ethiopia and Germany yielding up to 38,000 and 32,000 tons, respectively. The estimated needs for α-acids are calculated up to 8,000 tons, and the average price is valued approximately at 8 United States $ per kg. Demands for alpha acids are estimated on the basis that an average of 4.1 g is needed per hectoliter of beer (European Commission). Hop content varies depending on the type of beer, particularly considering its bitterness, and the variety of hop used. Hop content displays a steady decline in percentage annually (it still stood at 6.3 g alpha per hectoliter in 1995) due to the consumers' growing preference for less bitter beers, and the technological progress that this preference has brought about. Different brewing techniques have been developed to enhance the extraction of volatiles and acids in hopped beers. The most significant contribution of hops to beer flavoring is that of the so-called soft resins, principally the alpha acids (also known as humulones), which are ultimately responsible for the characteristic bitterness in the taste.

Analytically, the aroma of hops and the flavor of hoppy beers cannot be measured by the quantification of a single odorant; moreover, the selection of several key compounds or a comprehensive characterization (profiling) is of great importance. Analysis of hops and beer is challenging.

This study determines the effect of PEF treatment on two hop varieties for the extraction of bitter acids and volatiles. No previous studies have been published on this field to the extent of our knowledge. Additionally, research on the divergent effects of the treatment on two separate hop varieties (bitter and aromatic), was carried out.

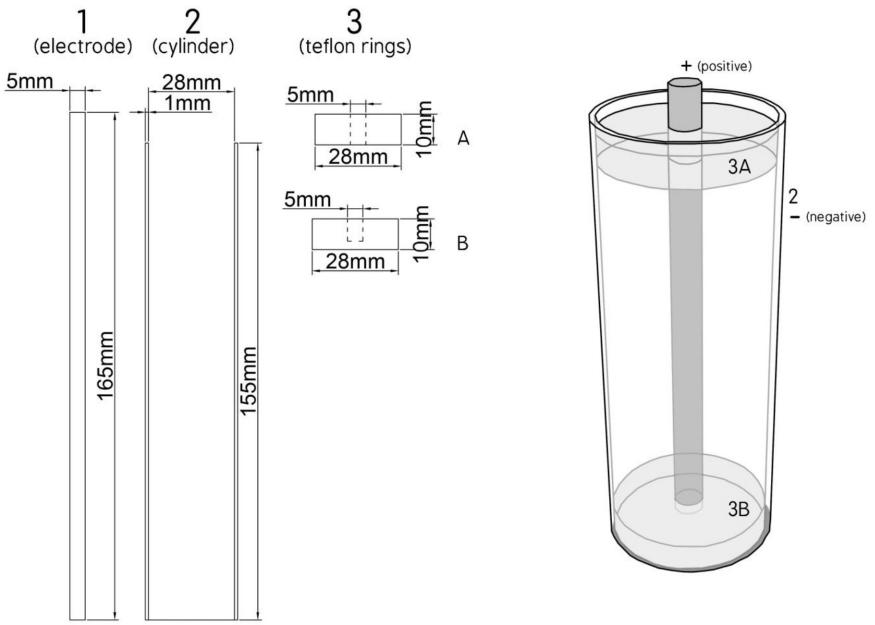

FIGURE 1 | View of treatment chamber.

MATERIALS AND METHODS

Plant Material

The two different varieties of hop cones (pelletized) used in this study were purchased by the Macedonian Thrace Brewery S.A. (Athens, Greece). The first variety was bitter, known for its high content in "bitter" acids. The second variety was aromatic, known for its high quality of essential oils. The characteristics of the two varieties were determined (using the methods described below).

Moisture Content Determination

For the determination of the dry matter content of hops, an established method regarding the moisture content of hops and hop products by European Brewery Convention, 2006 (EBC, 7.2, 1998) was employed. After being weighted, the samples were dried in a vacuum oven in 85°C for 6 h. The moisture percentage was determined according to the following equation: Moisture in, hops was calculated as:% = $\frac{\text{loss in } wt \times 100}{wt \text{ of sample}}$ (loss in wt × 100)/(wt of sample).

Hop Storage Index (HSI)

The determination of HSI was carried out according to the American Society of Brewing Chemists and specifically the Method of Analysis HOPS-6.A, where, the oxidative decrease in both α- and β-acids content during storage is determined by the progressive increase in the ratio of absorbance at 275–325 nm. Such loss in α- and β-acids and increase in the hop storage index (HSI) ratios may reflect unfavorably on the utility and quality of the hops.

The HSI was calculated on a ratio of absorbance at 275 nm (A_{275}) to the absorbance at 325 nm (A_{325}) after PEF treatment and compared to the same ratio without PEF (control).

Chemicals

The dichloromethane, chloroform, sodium chloride, ethyl acetate, methanol, N-pentane, anhydrous sodium sulfate and 2-octanol used were purchased from the Chem Lab (Zedelgem, Belgium).

PEF Equipment

The PEF equipment used was provided by Val-Electronic (Athens, Greece), and included the static bench scale system, reported previously (Bozinou et al., 2019), accompanied by another high voltage power generator (from Eisco, India). The model of the batch processing chamber (TC) was adapted from a design of cylinder type electrodes (Ohshima and Sato, 2004) and consists of a coaxial stainless steel electrode [5 mm in diameter and 165 mm high, **Figure 1**(1)] placed inside a bronze cylinder [1 mm thick, 155 mm high and 30 mm outer diameter **Figure 1**(2)] with a closed flat bottom. In this cylinder are placed two teflon rings (28 mm diameter and 10 mm thick **Figure 1**(3), one at the bottom **Figure 1**(3B) and another at the top **Figure 1**(3A) with a hole in the middle to pass the electrode which serve to isolate the electrode of the outer bronze cylinder (**Figure 1**).

The electric field strength E is evaluated as $E = U/d$, where "U" is the applied voltage and "d" is the distance between the electrode and the bronze cylinder (d = 12.4 mm).

For each case, the treatment was calculated as:

$$t = (\text{ti} + \text{tp}) \times \text{P}$$

ti = pulse duration (sec) tp = pause time (sec)

P = number of pulses.

For GC-MS analysis the extraction solvent was methanol. For UV–vis analysis the extraction solvents were methanol, toluene and water. For the capacitance measurement the solvents were methanol, water and ethanol. For the extraction method with water the electric field strength was E = 2.42 kV/cm, t = 30 min (ti = 1 μs, tp = 1 s, 1800 pulses), while for all the others solvents the treatment conditions were E = 1.13 kV/cm, t = 30 min (ti = 1 μs, tp = 1 s, 1800 pulses).

For the combination "treatment chamber- sample" there was no dielectric breakdown until the electric field strength of 2.5 kV/cm for 56 μF capacitance of the discharge capacitor. On these grounds, 1.15 to 2.5 kV/cm were used during this work. In order to select the number of pulses, UV–vis determinations were utilized to quantify the difference between treated samples and controls. Absorbance was measured every 900 pulses. Accordingly, the number of pulses selected was 1800. The pulse width was approximately 1 μs and the frequency of the pulse was 1 Hz. Treatment time was 0.75 ms. The temperature raise caused by the treatment was negligible ($<1°C$).

Sample Preparation for PEF and Control Treatments

Around 6 g of hop pellets were grounded to a fine powder using a grinding bowl. A 2.5 g amount of this powder was weighed in a Schott Duran laboratory bottle (100 mL) with Teflon-lined screw cap, and then, 50 mL of methanol was added (same procedure for the other solvents). For the control, another identical sample was prepared and both they left at 25°C for 30 min. Then, one sample was transferred to the treatment cell for PEF and the other was used for control. After the treatment (30 min) both samples were gravity filtered to remove the plant material and the filtrate (hop extract) was transferred into a vial (20 mL) for analysis as described below.

For the experiment with hydrated hop pellets, an additional step was added for the two samples (treated and control) which consist of a 30-min hydration in HPLC water before treatment in methanol or water.

For the evaluation of the treatment time on the extractability of the acids, the extraction medium was methanol. Treatments of 15, 30, 45, and 60 min (increments of 900 pulses) were performed. And at the end of each time, the treated hop pellets were filtered and processed as described above. The same procedure was also carried out for the control sample.

In all treatments, care must be taken to keep the temperature below the boiling point of the solvent used.

α- and β-Acids Determination Using UV–Vis Spectra

The method used was adapted from Alderton et al. (1954) and Egts et al. (2012). Specifically, in a 25 mL volumetric flask, 50 μL of the filtrate was added to a methanolic solution of NaOH (0.5 mL of 6M NaOH in 250 mL of methanol) and the complete spectrum (520 to 210 nm) was recorded against a solution of methanol in methanolic NaOH (50 μL:25 mL) as a blanc. The formulas used to find α-acid, β-acid and a third component (comp 3) are the following:

$$A_{355} = 31.8C_{\alpha} + 46.0C_{\beta} + 1.0C_{comp3}$$

$$A_{325} = 38.1C_{\alpha} + 33.1C_{\beta} + 1.5C_{comp3}$$

$$A_{275} = 9.0C_{\alpha} + 3.7C_{\beta} + 3.1C_{comp3}$$

where A_{355}, A_{325}, and A_{275} stand for the absorbance of the three analytical wavelengths and C_{α}, C_{β}, and C_{comp3} stand for the concentrations (in mg/L) of the α-acids, β-acids, and the third component, respectively (Egts et al., 2012).

α-Acids, β-Acids and Terpenes, Determination Using GC-MS

Prior to GC-MS analysis, the hop extracts were purified by applying a solid phase extraction treatment (SPE) using a graphite carbon black syringe (GCB). The syringe was first washed with 10 mL of dichloromethane (DCM) and then conditioned with 10 mL of methanol and 10 mL of deionized water under vacuum to the point of complete dryness. After that, 5 mL of methanolic hop extract was added with 3 mL of distilled water to the GCB syringe. The vacuum was then adjusted to give a flow of 10 mL/min and the cartridges were dried under full vacuum for 10 min. When the cartridges were dried, they were eluted with 5 mL ethyl acetate and 5 mL DCM. The eluents were collected, then dried over sodium sulfate and filtered before adding 50 μL of the internal standard (2-octanol 2500 ppm diluted in the pentane). The sample was then concentrated into a flash evaporator to 1 mL and 1 μL of the sample was injected to the GC-MS.

Capacitance of the Treatment Chamber

In order to measure the capacitance of the treatment chamber, the chamber was consecutively filled with the materials used in the experiments. To achieve a correct capacitance measurement, the treatment chamber must be electrically discharged. For each of the materials the value of the capacitance was measured with a digital capacitance meter (ProsKit MT-5110, Prokit's Industries Co. Ltd., Taiwan) with precision ± 0.5%.

Gas Chromatography/Mass Spectrometry Analysis

The instrumentation, the column and the conditions of GC-MS used were previously described by Drosou et al. (2017).

DPPH• Assay

The antioxidant activity of hop extracts was determined using the DPPH• assay. A slightly modified method of Blois (1958) was adopted. At first, the samples were properly diluted in methanol or ethanol (1:10). An aliquot of 0.1 mL of each diluted extract was added to 3.9 mL of DPPH• radical solution (0.0029 g/100 mL methanol) and the solution was then vortexed. After 20 min of remaining in the darkness, the absorbance of each mixture was measured at 515 nm. Pure methanol with the DPPH• radical

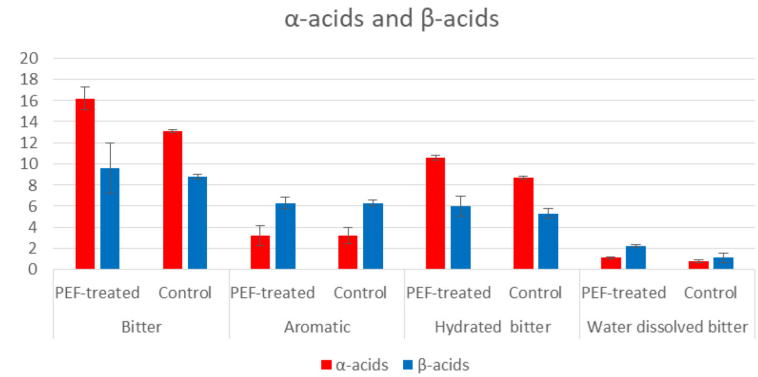

FIGURE 2 | % extraction of α-acids and β-acids determined by UV–vis spectrophotometer.

was used as control. All samples were prepared in triplicate. Percentage of inhibition of DPPH• radical I (%) of each hop extract was calculated according to the following equation:

$$I\,(\%) = \left[\frac{A_{\text{blank}} - A_{\text{sample}}}{A_{\text{blank}}}\right] \times 100,$$

where A_{blank} stands for the absorbance of DPPH• with methanol instead of sample and A_{sample} is the absorbance of DPPH• after the reaction with hop extracts.

TABLE 1 | Hop moisture, hop storage index (HSI), α- and β-acids content and α-acids losses.

	Hop variety	
	Aromatic	**Bitter**
Moisture (%)	9.47	9.06
HSI	0.43	0.29
α-acids (%)	2.30	10.80
β-acids (%)	3.20	8.40
α-acids losses (%)	105.36	91.87

Statistical Analysis

Results are displayed as means of triplicate determinations. Statistical analysis was carried out using the Excel 2013 (Microsoft, United States) software. Standard deviation for the concentrations of α- and β-acids was calculated and presented in **Tables 5**, **6** and in **Figure 2**.

Risk Assessment

Treatments in organic solvents should be done with caution. In general, in the absence of water or even in binary water-flammable organic solvent systems, the flash point of the solvent or mixture should be taken into account; the temperature should not be increased, preferably at room temperature and the treatment should be carried out in closed systems. Avoid electrical sparks around the treatment chamber.

RESULTS AND DISCUSSION

Hop Storage Index (HSI)

The physical and chemical values of the two varieties were determined prior to the PEF treatment in order to acquire knowledge on the composition of hop samples. As it was reported by Roberts (2016), HIS is a measure

TABLE 2 | Analysis of spectra from UV–vis.

		Bitter, methanol extracted		**Aromatic, methanol extracted**		**Bitter, hydrated and methanol extracted**		**Bitter, hydrated and water extracted**	
		PEF-treated	**Control**	**PEF-treated**	**Control**	**PEF-treated**	**Control**	**PEF-treated**	**Control**
Absorbance in nm	275	0.534	0.396	0.246	0.242	0.345	0.266	0.161	0.104
	325	0.918	1.153	0.425	0.422	0.712	0.589	0.185	0.102
	355	0.903	1.139	0.455	0.452	0.686	0.575	0.183	0.097
Acids	α-acids	16.2%	13.1%	3.2%	3.2%	10.6%	8.7%	1.1%	0.8%
	β-acids	9.6%	8.8%	6.3%	6.3%	6%	5.3%	2.2%	1.1%
Increase with PEF treated for	α-acids	24%		0%		21%		100%	
	β-acids	9%		1%		14%		120%	
HSI		0.58	0.34	0.57	0.57	0.48	0.44	0.87	1.01

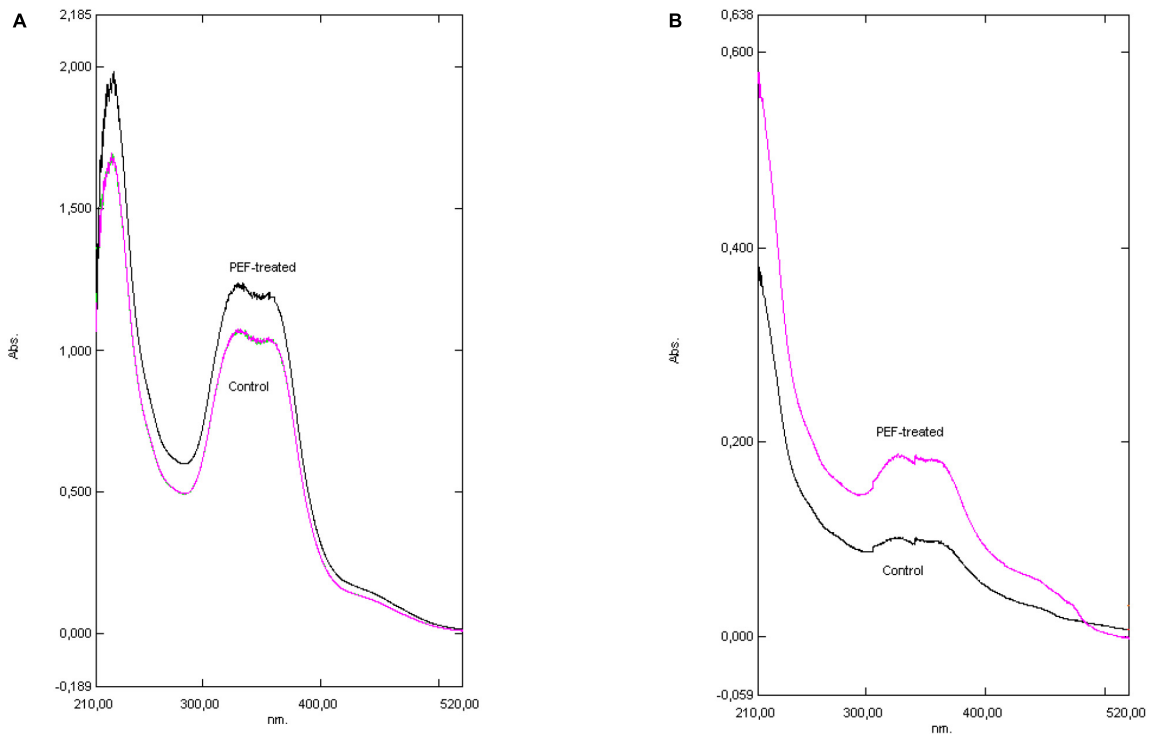

FIGURE 3 | The effect of extraction media. Basic methanolic **(A)** versus Water **(B)**. For the quantification of the acids' absorbance at 275, 325, and 355 nm was used. **(A)** The UV–vis spectrum of both samples, PEF treated and Control (bitter hop was suspended in methanol). **(B)** The UV–vis spectrum of both samples, PEF treated and Control (bitter hop was suspended in water).

of the degradation and can be used to quantify the losses of α-acids and β-acids during treatment. As it is shown in **Table 1**, HIS values (0.3–0.4) in bitter and aromatic hop are low, indicating a fresh raw material, as stated by Van Holle et al. (2017). Following PEF treatment, extracts were subjected to an analysis based on their UV–vis spectra.

As it can be observed (**Table 1**) the bitter hop variety had a 249% higher concentration of total acids compared to the aromatic one. The α-acids are the precursors of iso-α-acids which are formed in the boiling wort resulting in the bitterness of beer. Specifically, the α-acids had 370% higher concentration compared to the aromatic, while for β-acids the concentration was 162%. The results above, partially clarify the difference observed in the extractability using PEF. After PEF treatment, the HSI level varied with the extraction media. In samples treated with methanol the value was 0.58, while for those treated with water, it was 0.87 (0.34 and 1.01 for the control sample, respectively) (**Table 2**). It appears quite evidently, that following the processes of extraction and treatment with PEF, there is an increase in HSI in both bitter and aromatic varieties but in insignificantly low values indicating that PEF has not any deleterious effects in the raw material. These values of course, are merely results of comparison between hop samples and not between different extraction media, in which differences of solubility drastically influence the final result.

Effect of PEF on the Extractability of α- and β-Acids

Hop pellets from the *H. lupulus* plant contain both α-acids (humulones) and β-acids (lupulones) as well as many other compounds that interfere in the UV–vis spectrum (**Figures 2**, **3**). The isomerization of α-acids to iso-α-acids during boiling is a process which strongly influences the taste of beer. The iso-α-acids are responsible for the distinct bitterness of the taste. The positive effect of the PEF treatment lies in the increase in the extractability of the α-acids which are then isomerized into iso-α-acids. The method applied for visualizing the PEF effect is a three-component analysis (Egts et al., 2012; **Figure 3**). Therefore, in order to determine the impact of the samples of hops treated with PEF, a spectrophotometric plot was followed to quantify the acids α and β, as well as those of the third component (iso-α-acids, etc.).

The spectra obtained from UV–vis plot are shown in **Figures 3A,B** and the calculated results are presented

TABLE 3 | Content (mg/L) in α-acids and β-acids of toluene extracted bitter hop with UV–vis analysis.

Acids	Control	PEF treated	Difference
α-acids	11.8	25.8	118.03%
β-acids	7.8	14.5	85.39%

in **Table 2**. The spectra presented refer to treatment of bitter hop in methanol and in water. The decrease of the absorbance is attributed to the acids' low solubility in water; nevertheless, the shape of the curve is the same in both treatment media, where the hop exhibits a similar physical and chemical response.

The spectra obtained from the UV–vis plot are presented in **Figures 3A,B** and the calculated results are presented in **Table 2**. The spectra presented refer to the treatment of bitter hop pellets in methanol and in water. The decrease in absorbance is attributed to the low solubility of acids in water; however, the shape of the curve is the same in both processing media, where the hop pellets have a similar physical and chemical response.

According to the results shown in **Table 2**, the difference of the α-acids and β-acids regarding the bitter hop are ranked between 9.1 and 23.7%. More specifically, the α-acids of the PEF treated sample were 23.7% higher than those of the control displaying in this manner the positive aspects of this treatment. As it has already been mentioned, humulones are isomerized into iso-α-acids, while the β-acids (also 9.1% higher) are mostly oxidized rather than isomerized. It was also observed, by employing different extraction media (solvents) or different varieties of hop, the results exhibited significant deviations (**Figure 2**). The aromatic hop (low concentration of α-acids and β-acids), under the same experimental conditions, showed no differences in PEF treatment and control. Finally, in order to examine the significance of the absence of water in the dried hop, the hops were hydrated for 30 min before treatment. This process produced similar results but with lower concentration in acids in comparison with the sample that was not hydrated. The aforementioned results are summarized in **Tables 2**, **3**. During this process, methanol was used as solvent with the purpose to evaluate

TABLE 4 | Capacity of PEF treatment chamber with different solvents.

Sample	Capacitance (μF)	Water (mL)/methanol or ethanol (mL)/plant material (gr)
Water suspended hop	56.0	50/0/2.5
Methanol with hydrated hop	27.9	25/25/2.5
Methanol with dried hop	14.9	0/50/2.5
Ethanol with hydrated hop	24.2	25/25/2.5
Ethanol with dried hop	54.0	0/50/2.5

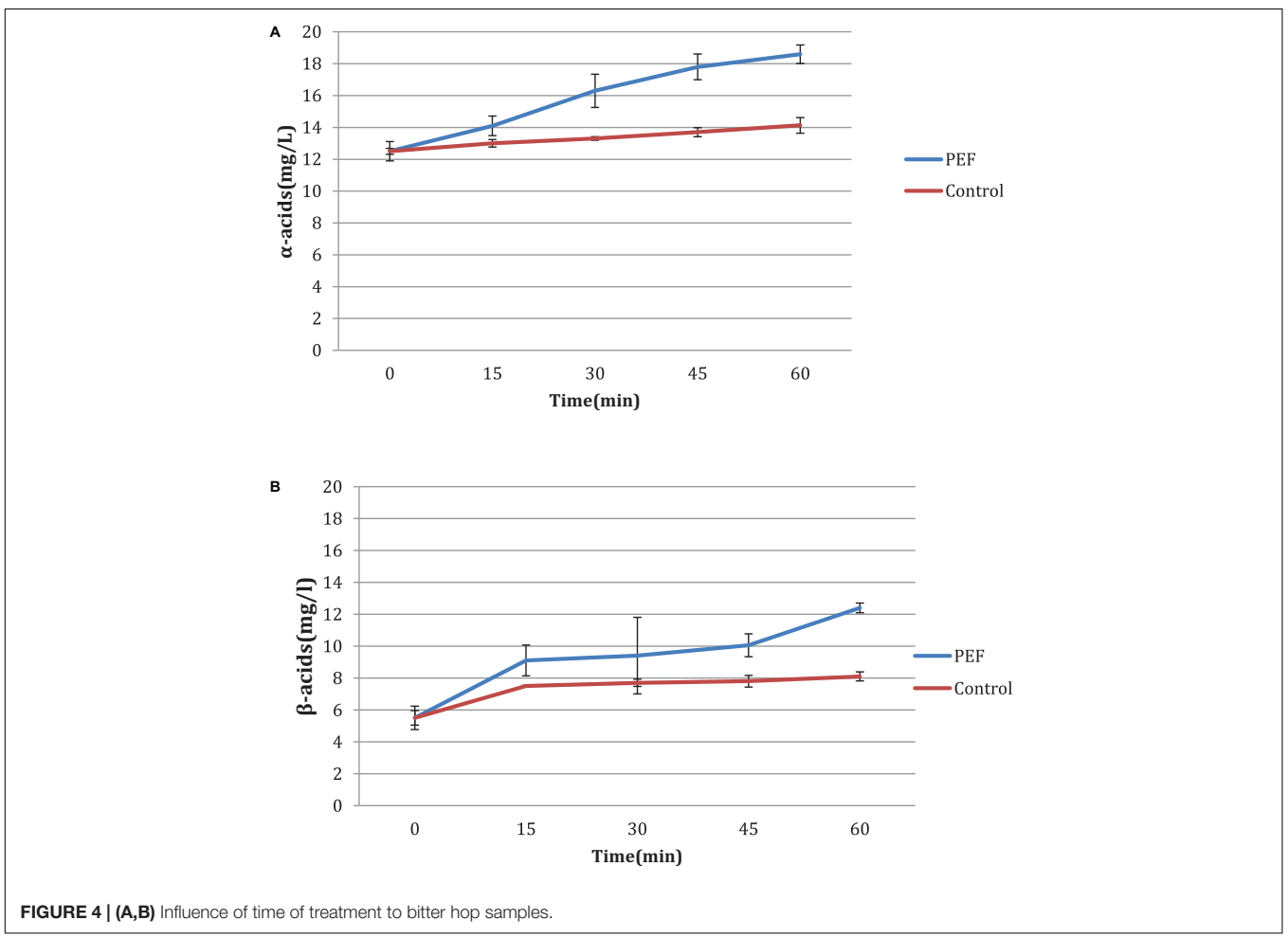

FIGURE 4 | (A,B) Influence of time of treatment to bitter hop samples.

the PEF treatment. The extractability in methanol is intermediate between non-polar solvents like toluene and polar solvents like water.

Capacity of PEF Treatment Chamber and the Effect of Extraction Media

When the processing chamber is filled with a liquid or solid element, it becomes a capacitor. The electrodes become the conductors and the sample, which is being processed, the dielectric. The higher the conductivity of the product, the easier the electrical current flows. Thus, for high conductivity samples, a lower voltage should be used to avoid sparks. The capacity in water is much higher than the electric capacity in solvents such as methanol or ethanol (**Table 4**).

Most studies in the literature that assess the composition and release of hop ingredients in wort have been carried out with solvents such as methanol or other non-polar solvents (pentane and toluene). During the production of beer, the extraction of the hop constituents takes place in an almost hydro environment. In view of this, this study was carried out using aqueous media combined with pure methanol. The hop pellets were hydrated with pure HPLC water, and then suspended in methanol or pure water before treatment with PEF. In all these environments, the capacity of the processing cell was measured.

The hydrated hop results (**Figure 3B**) showed a week absorbance after PEF treatments across all spectra. By comparing the percentage of α- and β-acids extracted from hydrated bitter hops, we can conclude that due to their insolubility, the concentration of humulones and lupulones was much lower for PEF and the control samples and, consequently, their absorbance showed lower values. However, by examining their differences in percentages (**Table 2**), it can be concluded that the relative extractability due to PEF in water of acids and other compounds is higher than in non-polar solvents.

Time Influence

An additional experiment was carried out to measure the influence of the duration of the PEF, as well as the differences between the two varieties, aromatic and bitter. It is observed that in the bitter, the acid concentration increases with the treatment time (**Figures 4A,B**) with or without PEF treatment. The variety of hops seems to have a significant effect on the final results. As shown in **Figures 5A,B**, the aromatic hops treated with PEF did

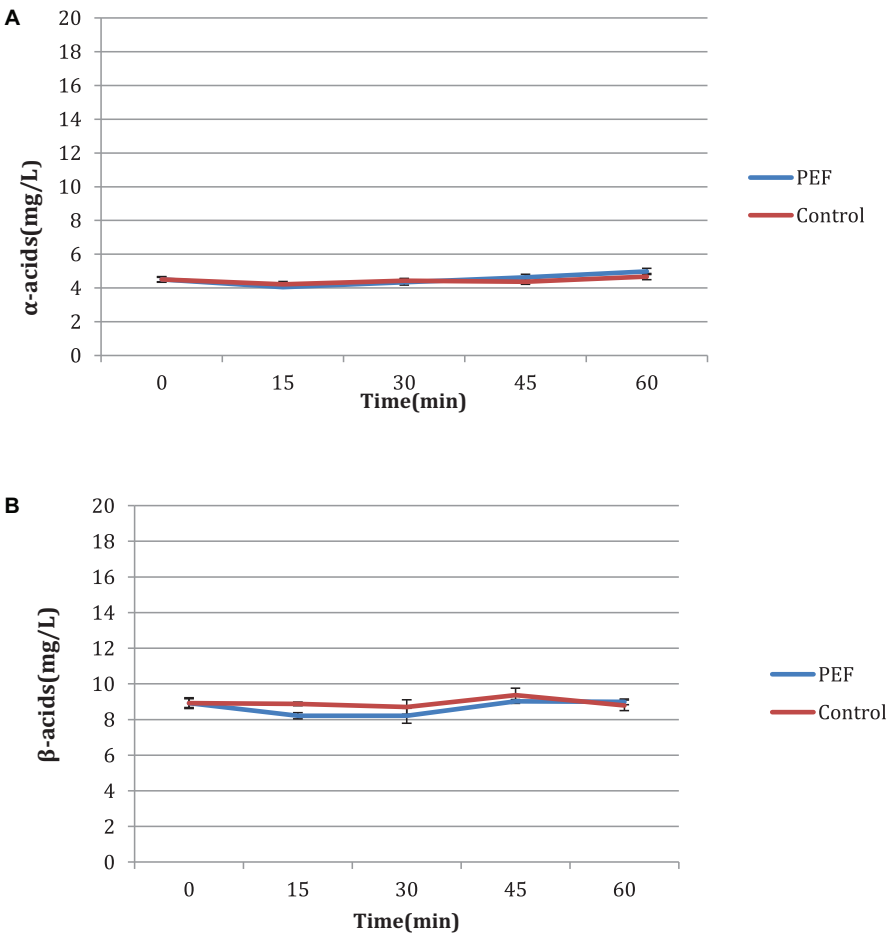

FIGURE 5 | (A,B) Influence of time of treatment to aromatic hop samples.

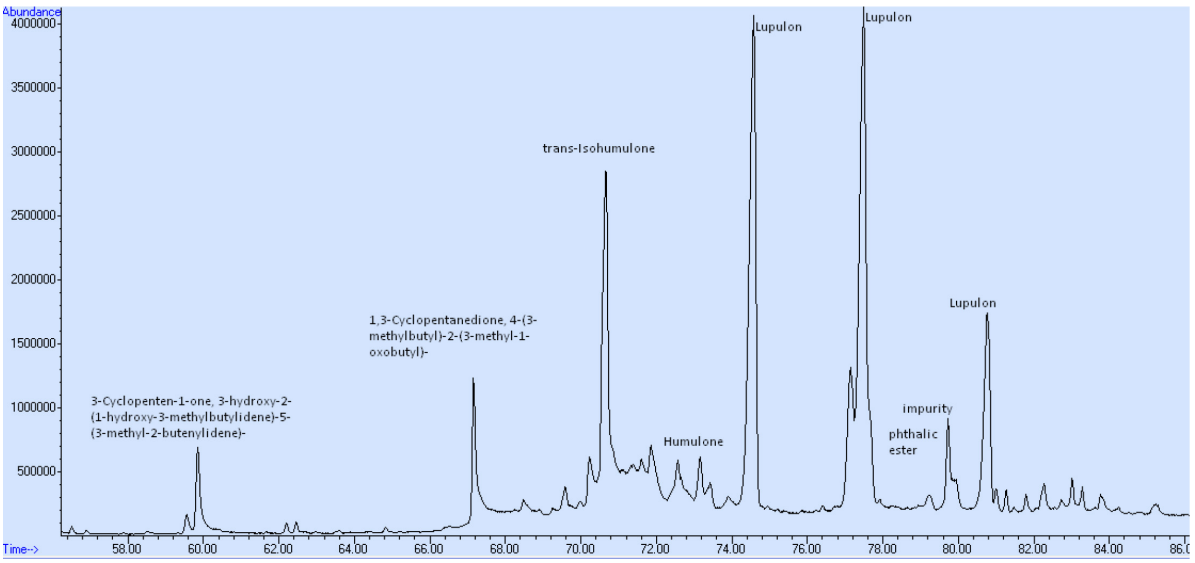

FIGURE 6 | GC-MS analysis after purification thought SPE.

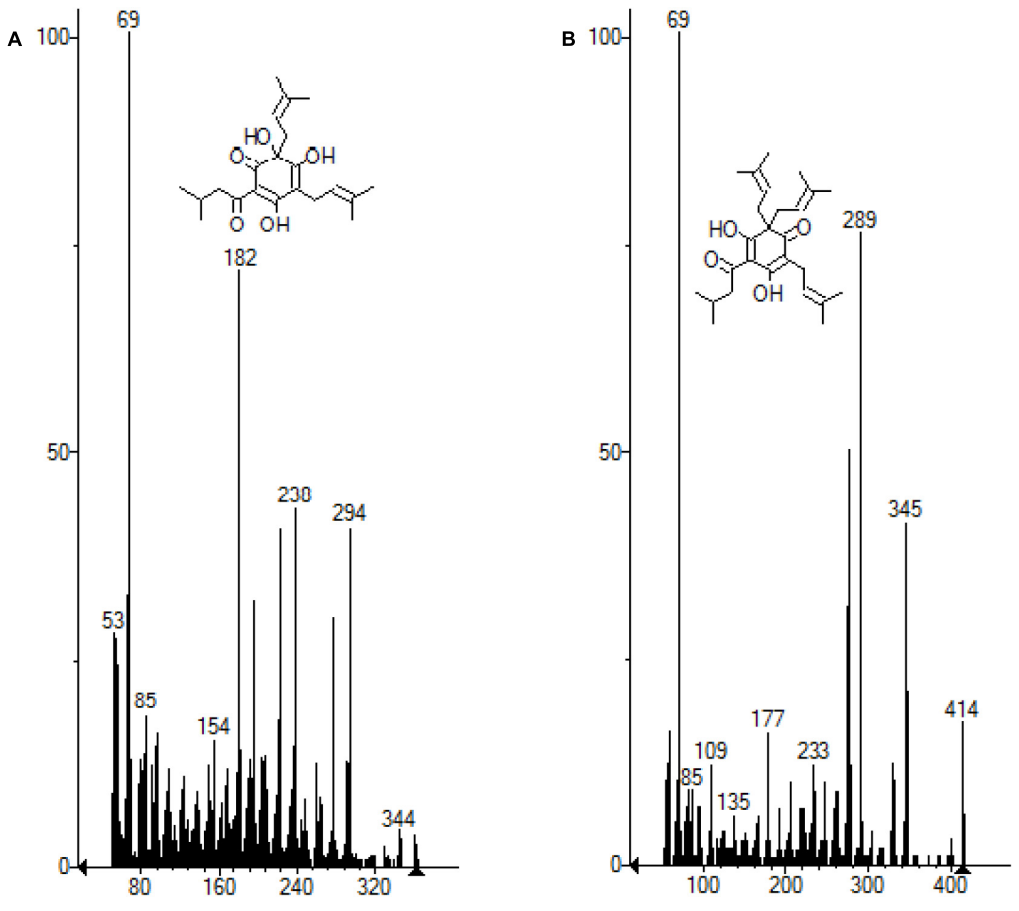

FIGURE 7 | (A) Molecule of the humulone subtracted from the MS chromatogram. **(B)** Molecule of lupulon subtracted from the MS chromatogram.

not show any particular difference compared to the control. In addition, over time, the control samples and the samples treated with PEF have a negligible increase in the concentration of α and β-acids. We can deduce that in aromatic hops, the acids are mainly in free form unlike bitter, in which an amount of acids is probably localized in plant cells and is released after cell rupture with PEF.

Volatile Analysis

The impact of the application of PEF in volatile compounds of bitter hops is presented in **Table 5**, while the average of the α and β-acids from the GC-MS analysis (compared to the spectrophotometric analysis) in **Table 6**. In order to avoid contamination of the GC column, an intermediate purification step was applied, using a solid phase extraction column (SPE). This purification step was carried out in order to avoid liquid-liquid extraction of the treated samples and thus avoid deterioration of the GC columns with waxes and non-volatile hop resins (Stevens, 1967; American Society of Brewing Chemists, 1992, Eri et al., 2000). The hops are rich in resins which are easily extracted by non-polar solvents and thus deteriorate the GC columns during analysis.

Myrcene, β-caryophyllene and α-humulene are the most abundant terpenes in hops. In dry granules, their aroma is persistent and characteristic. In beer, they are lost as odor descriptors. They are also insoluble in wort and beer but their oxidation leads to derivative compounds, such as their epoxides (for example humulene epoxide) or humulol alcohols, which appear in the final product depending on the time of adding hops.

As previously mentioned, sesquiterpenes such as humulene, caryophyllene and β-pinene (oxidation product of myrcene) are the main constituents of essential oil of fresh hops. More specifically, it is evident (**Table 5**) that the application of PEF has a small but significant increase in the concentration of these compounds. In particular, in the control samples, the humulene, caryophyllene and β-pinene had a concentration of 0.89, 0.27, and 0.09 mg/L, while in the treated samples at PEF, there was an increase of 0.94, 0.29, and 0.08 mg/L, respectively. The application of PEF had a limited influence on the concentration of these volatile compounds and mainly in the monoterpens. The oxygenated fractions of the hop aroma (Deinzer and Yang, 1994) can be synergistic by contributing to the "hops" of beer (Siebert, 1994). All of these compounds have an active flavor in beer with very low flavor thresholds (ppb) and depending on when they are added, they play an important role in the character of hops (Preis and Mitter, 1995). From this point of view, even a slight increase in terpene precursors (humulene, caryophyllene and myrcene) is important for the final hoppy taste of beer.

Liquid-liquid extraction involves a heating step which can degrade the initial profile of volatiles. The SPE method used before the GC-MS analysis allowed a clear separation of the compounds and a "clean" chromatogram, as shown in **Figure 6**. The molecules of the main acids (humulone and lupulone) of the MS chromatogram are presented in the **Figures 7A,B**. **Table 5** shows the effect of PEF on the (average) concentration of α and β-acids in bitter hop varieties. The concentration of acids should be higher in bitter hops. The extraction of α and β-acids soluble in methanol also increases with the application of PEF, with

TABLE 5 | Volatile analysis (mg/L) of bitter hop with or without PEF treatment.

Compound	Pef treated		Control	
	Average	S.D.	Average	S.D.
β-Myrcene	0.083	0.052	0.092	0.003
2-octanol	0.125	0.000	0.125	0.000
Caryophyllene	0.290	0.175	0.266	0.070
β-Cubebene	0.019	0.009	n.d.	
Humulene	0.943	0.578	0.889	0.203
γ-Muurolene	0.023	0.015	0.022	0.019
γ-Cadinene	0.032	0.004	0.023	0.006
β-Cadinene	0.008	0.002	n.d.	
α-Cadinene	0.008	0.005	0.008	0.003
δ-Cadinene	0.069	0.040	n.d.	
Geranyl isobutyrate	n.d.*		0.034	0.019
Hexadecane	0.036	0.008	0.023	0.002
Humulene epoxide 2	n.d.		0.025	0.006
Hexadecanoic acid methyl ester	0.053	0.021	0.047	0.010
Dehydro-cohumulinic acid or 3-Hydroxy-2-isobutyryl-5-(3-methyl-2-butenyl)-2,4-cyclopentadien-1-one	0.069	0.033	0.335	0.277
3-hydroxy-2-(1-hydroxy-3-methylbutylidene)-5-(3-methyl-2-butenylidene)-3-Cyclopenten-1-one	0.510	0.159	1.754	1.333
Linoleic acid methyl ester	0.036	0.019	0.032	0.006
Humulone	0.498	0.130	0.837	0.045
Isohumulone	5.977	1.134	4.325	0.275
Lupulone	16.630	2.498	11.269	0.926

**n.d. = Not detected.*

TABLE 6 | Averages (mg/L) of α- and β-acids of bitter hop PEF treated and control samples extracted with methanol.

Method	Acids	Pef Treated		Control		Increase (%)
		Average	S.D.	Average	S.D.	
GC-MS	α-acids	6.4	1.0	5.2	0.2	25.45
	β-acids	16.6	2.5	11.3	0.9	47.56
UV–vis	α-acids	16.2	1.0	13.1	0.1	23.66
	β-acids	9.6	2.4	8.8	0.2	9.09

TABLE 7 | Percentage of inhibition of DPPH• radical (I%) of hop extracts.

Sample	*I%*	
	PEF treated	Control
Hydrated (bitter)	70.27	69.89
Methanol (bitter)	73.19	83.35
Methanol (aromatic)	82.47	81.32

the intensity of the electric field and with the extension of the duration of the treatment.

As indicated in the samples treated with PEF, the bitter acids in the sample had a concentration 40.66% higher than that of the control. More specifically, the samples treated with PEF had a higher concentration compared to the control (25.45 and 47.56% of α and β-acids, respectively). This result is of capital importance since the aim of bitter hops is to strengthen bitterness.

DPPH•

The treated extracts maintained their antiradical activity (**Table 7**) and, in the case of extracted methanol, an increase of about 10% was observed. The water treated samples demonstrated almost the same antiradical activity. The low water extractability probably does not allow the proper evaluation of the results.

CONCLUSION

In conclusion, this study aimed to extract α-acids and β-acids of two different varieties of hops using PEF. During these experiments, different solvents and different methods of analysis were used. According to the results, samples of hops treated with PEF showed higher concentrations of humulones and lupulones (the main representatives of α-acids and β-acids, respectively). PEF conditions (1.5 kV/cm; 15 μs and 1800 pulses) increased the total bitter acids (a + β) and sesquiterpenes extraction from bitter hop approximatively by 1.3 times. The PEF treatment enhanced the extraction of α-acids from 21 to 100% and from 9 to 120% for β-acids. The amount of extracted acids was a function of the solvent and the time of treatment. PEF treatment of hop pellets did not cause any substantial changes in HSI that would indicate possible further degradation. Hops maintained their antiradical activity, which, in some cases, was increased. Therefore, it can be concluded that the extraction of α- and β-acids was enhanced by PEF application and should be further investigated in order to optimize their concentration by utilizing water base solvents or by minimizing the time of the PEF treatment in pilot plant conditions before industrial applications.

DATA AVAILABILITY STATEMENT

All datasets generated for this study are included in the article/supplementary material.

AUTHOR CONTRIBUTIONS

GN: conception and execution of the PEF work. ET: analysis of GC-MS. FD: analysis of hop and antioxidant properties. EB: writing – review and editing. SL, PT, and VD: materials and methods setup.

FUNDING

This research has been co-financed by the European Union and Greek national funds through the Operational Program Competitiveness, Entrepreneurship and Innovation, under the call RESEARCH – CREATE – INNOVATE (project code: T1EDK-03762).

REFERENCES

Alderton, G., Bailey, G. R., Lewis, J. C., and Stitt, F. (1954). Spectrophotometric determination of humulone complex and lupulone in hops. *Anal. Chem.* 26, 983–992. doi: 10.1021/ac60090a010

Alvarez, I., Pagan, R., Condon, S., and Raso, J. (2003). The influence of process parameters for the inactivation of Listeria monocytogenes by pulsed electric fields. *Intern. J. Food Microbiol.* 87, 87–95. doi: 10.1016/s0168-1605(03)00056-4

American Society of Brewing Chemists (1992). *Methods of Analysis*, 8th Edn, St. Paul, MN: ASBC.

Bimakr, M., Ganjloo, A., Zarringhalam, S., and Ansarian, E. (2017). Ultrasound-assisted extraction of bioactive compounds from *Malva sylvestris* leaves and its comparison with agitated bed extraction technique. *Food Sci. Biotechnol.* 26, 1481–1490. doi: 10.1007/s10068-017-0229-5

Blois, M. S. (1958). Antioxidant determinations by the use of a stable free radical. *Nature* 181, 1199–1200. doi: 10.1038/1811199a0

Boussetta, N., Lanoiselle, J.-L., Bedel-Cloutour, C., and Vorobiev, E. (2009). Extraction of soluble matter from grape pomace by high voltage electrical discharges for polyphenol recovery: effect of sulphur dioxide and thermal treatments. *J. Food Eng.* 95, 192–198. doi: 10.1016/j.jfoodeng.2009.04.030

Boussetta, N., Vorobiev, E., Deloison, V., Pochez, F., Falcimaigne-Cordin, A., and Lanoiselle, J.-L. (2011). Valorisation of grape pomace by the extraction of phenolic antioxidants: application of high voltage electrical discharges. *Food Chem.* 128, 364–370. doi: 10.1016/j.foodchem.2011.03.035

Bozinou, E., Karageorgou, I., Batra, G., Dourtoglou, V. G., and Lalas, S. I. (2019). Pulsed electric field extraction and antioxidant activity determination of *Moringa oleifera* dry leaves: α comparative study with other extraction techniques. *Beverages* 5:8. doi: 10.3390/beverages5010008

Cukjati, D., Batiuskaite, D., André, F., Miklavcic, D., and Mir, L. M. (2007). Real time electroporation control for accurate and safe in vivo non-viral gene therapy. *Bioelectrochemistry* 70, 501–507. doi: 10.1016/j.bioelechem.2006.11.001

Deinzer, M., and Yang, X. (1994). Hop aroma: character impact compounds found in beer, methods of formation of individual compounds. *Proc. Eur. Brew. Convent.* 22, 1–17.

Delsart, C., Ghidossi, R., Poupot, C., Cholet, C., Grimi, N., and Vorobiev, E. (2012). Enhanced extraction of phenolic compounds from merlot grapes by pulsed electric field treatment. *Am. J. Enol. Viticult.* 63:2. doi: 10.5344/ajev.2012.11088

Delsart, C., Grimi, N., Boussetta, N., Miot Sertier, C., Ghidossi, R., Vorobiev, E., et al. (2015). Impact of pulsed-electric field and high-voltage electrical discharges on red wine microbial stabilization and quality characteristics. *J. Appl. Microbiol. I* 120, 152–164. doi: 10.1111/jam.12981

Dieckmann, R. H., and Palamand, R. S. (1974). Autoxidation of some constituents of hops. i. monoterpene hydrocarbon myrcene. *J. Agr. Food Chem.* 22, 498–503. doi: 10.1021/jf60193a033

Drosou, F., Yang, E., Marinea, M., Dourtoglou, E. G., Chatzilazarou, A., and Dourtoglou, V. G. (2017). "An assessment of potential applications with pulsed electric field in wines," in *Proceeding of the 40th World Congress of Vine and Wine*, Sofia.

Egts, H., Durben, D. J., Dixson, J. A., and Zehfus, M. H. (2012). A multicomponent UV analysis of α- and β-acids in hops. *J. Chem. Educ.* 89, 117–120. doi: 10.1021/ed1010536

Eri, S., Khoo, B. K., Lech, J., and Hartmann, T. G. (2000). Direct thermal desorption-gas chromatography and gas chromatography-mass spectrometry profiling of hop (*Humulus lupulus* L.) essential oils in support of varietal characterization. *J. Agric. Food Chem.* 48, 1140–1149. doi: 10.1021/jf9911850

European Brewery Convention (2006). *Analytica-EBC; Fachverlag Hans Carl, 2006; Section 7 Hops, Methods 7.2, 7.10 and 7.12*. Nuernberg: EBC.

Eyres, G. T., and Dufour, J. P. (2009). "Hop essential oil: analysis, chemical composition and odor characteristics," in *Beer in Health and Disease Prevention*, ed. V. R. Preedy (Cambridge, MA: Academic Press), 239–254. doi: 10.1016/B978-0-12-373891-2.00022-5

Grahl, T., and Markl, H. (1996). Killing of microorganisms by pulsed electric fields. *Appl. Microbiol. Biotechnol.* 45, 148–157. doi: 10.1007/s002530050663

Grimi, N., Lebovka, N. I., Vorobiev, E., and Vaxelaire, J. (2009). Effect of a pulsed electric field treatment on expression behavior and juice quality of chardonnay grape. *Food Biophys.* 4, 191–198. doi: 10.1007/s11483-009-9117-8

Grimi, N., Mamouni, F., Lebovka, N., Vorobiev, E., and Vaxelaire, J. (2011). Impact of apple processing modes on extracted juice quality: pressing assisted by pulsed electric fields. *J. Food Eng.* 103, 52–61. doi: 10.1016/j.jfoodeng.2010.09.019

Gyawali, R., Seo, H. Y., Lee, H. J., Song, H. P., Kim, D. H., Byun, M. W., et al. (2006). Effect of g-irradiation on volatile compounds of dried Welsh onion (*Allium fistulosum* L.). *Radiat. Phys. Chem.* 75, 322–328. doi: 10.1016/j.radphyschem.2005.07.001

Heinz, V., Toepfl, S., and Knorr, D. (2003). Impact of temperature on lethality and energy efficiency of apple juice pasteurization by pulsed electric fields treatment. *Innov. Food Sci. Emerg. Technol.* 4, 167–175. doi: 10.1016/s1466-8564(03)00017-1

Hossain, M. B., Tiwari, B. K., Gangopadhyay, N., O'Donnell, C. P., Brunton, N. P., and Rai, D. K. (2014). Ultrasonic extraction of steroidal alkaloids from potato peel waste. *Ultrason. Sonochem.* 21, 1470–1476. doi: 10.1016/j.ultsonch.2014.01.023

Kunze, W. (2004). *Technology Brewing and Malting*. Berlin: VLB.

Maged, E. A. M., and Ayman, H. A. E. (2012). *Pulsed Electric Fields for Food Processing Technology*. London: IntechOpen.

Nance, M., Setzer, R., and William, N. (2011). Volatile components of aroma hops (*Humulus lupulus* L.) commonly used in beer brewing. *J. Brew. Distill.* 2, 16–22.

Nickerson, G. B., and Van Engel, L. (1992). Hop aroma component profile and the aroma unit. *J. Am. Soc. Brew. Chem.* 50, 77–81. doi: 10.1094/asbcj-50-0077

Ohshima, T., and Sato, M. (2004). Bacterial sterilization and intracellular protein release by a pulsed electric field. *Adv. Biochem. Engin. Biotechnol.* 90, 113–133. doi: 10.1007/b94194

Peacock, V. E., and Deinzer, M. L. (1981). Chemistry of hop aroma in beer. *J. Am. Soc. Brew. Chem.* 39, 136–141. doi: 10.1094/asbcj-39-0136

Peacock, V. E., and McCarty, P. (1992). Varietal identification of hops and hop pellets. *Techn. Q. Master Brew. Assoc. Am.* 29, 81–85.

Pinela, J., Antonio, A. L., Cabo Verde, S., Barreira, J. C. M., Carvalho, A. M., Oliveira, M. B. P. P., et al. (2014). "Effects of gamma irradiation and extraction method in the antioxidant potential of wild and commercial *Tuberaria lignosa* samples," in *Proceedings of the International Symposium on Food Safety and Quality: Applications of Nuclear and Related Techniques - IAEA CN-222At*, Viena.

Preis, F., and Mitter, W. (1995). The rediscovery of first wort hopping. *Brauw. Intern.* 13, 308–315.

Rettberg, N., Biendl, M., and Garbe, L. A. (2018). Hop aroma and hoppy beer flavor: chemical backgrounds and analytical tools: a review. *J. Am. Soc. Brew. Chem.* 76, 1–20. doi: 10.1080/03610470.2017.1402574

Roberts, T. R. (2016). "Hops," in *Brewing Materials and Processes: A Practical Approach to Beer Excellence*, ed. C. W. Bamforth (Cambridge, MA: Academic Press), 47–75. doi: 10.1016/C2013-0-13349-1

Siebert, K. J. (1994). "Sensory analysis of hop oil-derived compounds in beer; flavor effects of individual compounds. Quality control," in *Proceedings of the Monograph XXII E.B.C. Symposium on Hops. European Brewery Convention*, Zoeterwoude.

Steinhaus, M., and Schieberle, P. (2000). Comparison of the most odor active compounds in fresh and dried hop cones (*Humulus lupulus* L. variety spalter select) based on GC-olfactometry and odor dilution techniques. *J. Agr. Food Chem.* 48, 1776–1783. doi: 10.1021/jf990514l

Stevens, R. (1967). The chemistry of hop constituents. *Chem. Rev. Am. Soc.* 67, 19–71. doi: 10.1021/cr60245a002

Touya, G. (2005). *Contribution à l'étude Expérimentale des Décharges Électriques Dans L'eau Et des Ondes De Pression Associées. Réalisation d'un Prototype Industriel 100 Kj Pour le Traitement de Déchets Par Puissances Électriques Pulsées*. Ph.D. thesis, Université de Pau et des Pays de l'Adour, Pau.

Van Holle, A., Van Landschoot, A., Roldán-Ruiz, I., Naudts, D., and Keukeleire, D. (2017). The brewing value of amarillo hops (*Humulus lupulus* L.) grown in northwestern USA: a preliminary study of terroir significance. *Instit. Brew. Distil.* 123, 312–318. doi: 10.1002/jib.433

Vorobiev, E., and Lebovka, N. (2010). Enhanced extraction from solid foods and biosuspensions by pulsed electrical energy. *Food Eng. Rev.* 2, 95–108. doi: 10.1007/s12393-010-9021-5

Zeng, X. A., Yu, S. J., Zhang, L., and Chen, X. D. (2008). The effects of AC electric field on wine maturation. *Innov. Food Sci. Emerg. Technol.* 9, 463–468. doi: 10.1016/j.ifset.2008.03.002

Zhang, B., Zeng, X. A., Sun, D., Yu, S. J., Yang, M. F., and Ma, S. (2012). Effect of electric field treatments on brandy aging in oak barrels. *Food Bioprocess Technol.* 6, 1635–1643. doi: 10.1007/s11947-012-0788-7

Zimmermann, U. (1986). Electrical breakdown, electropermeabilization and electrofusion. *Rev. Physiol. Biochem. Pharmacol.* 105, 175–256. doi: 10.1007/bfb0034499

Conflict of Interest: The authors declare that the research was conducted in the absence of any commercial or financial relationships that could be construed as a potential conflict of interest.

Copyright © 2020 Ntourtoglou, Tsapou, Drosou, Bozinou, Lalas, Tataridis and Dourtoglou. This is an open-access article distributed under the terms of the Creative Commons Attribution License (CC BY). The use, distribution or reproduction in other forums is permitted, provided the original author(s) and the copyright owner(s) are credited and that the original publication in this journal is cited, in accordance with accepted academic practice. No use, distribution or reproduction is permitted which does not comply with these terms.

frontiers in Bioengineering and Biotechnology

ORIGINAL RESEARCH
published: 30 April 2020
doi: 10.3389/fbioe.2020.00340

Development of a Continuous Pulsed Electric Field (PEF) Vortex-Flow Chamber for Improved Treatment Homogeneity Based on Hydrodynamic Optimization

Felix Schottroff[1], Justus Knappert[2], Pauline Eppmann[2], Anna Krottenthaler[1], Tobias Horneber[2], Christopher McHardy[2], Cornelia Rauh[2] and Henry Jaeger[1]*

[1] Institute of Food Technology, Department of Food Science and Technology, University of Natural Resources and Life Sciences (BOKU), Vienna, Austria, [2] Institute of Food Technology and Food Chemistry, Department of Food Biotechnology and Food Process Engineering, Technische Universität Berlin, Berlin, Germany

OPEN ACCESS

Edited by:
Saša Haberl Meglič, University of Ljubljana, Slovenia

Reviewed by:
Nikolai I. Lebovka, Institute of Biocolloidal Chemistry (named after F.D. Ovcharenko), Ukraine
Jianye Xia, East China University of Science and Technology, China

***Correspondence:**
Felix Schottroff
felix.schottroff@boku.ac.at

Specialty section:
This article was submitted to Bioprocess Engineering, a section of the journal Frontiers in Bioengineering and Biotechnology

Received: *06 December 2019*
Accepted: *27 March 2020*
Published: *30 April 2020*

Citation:
Schottroff F, Knappert J, Eppmann P, Krottenthaler A, Horneber T, McHardy C, Rauh C and Jaeger H (2020) Development of a Continuous Pulsed Electric Field (PEF) Vortex-Flow Chamber for Improved Treatment Homogeneity Based on Hydrodynamic Optimization. Front. Bioeng. Biotechnol. 8:340. doi: 10.3389/fbioe.2020.00340

Pulsed electric fields (PEF) treatment is an effective process for preservation of liquid products in food and biotechnology at reduced temperatures, by causing electroporation. It may contribute to increase retention of heat-labile constituents with similar or enhanced levels of microbial inactivation, compared to thermal processes. However, especially continuous PEF treatments suffer from inhomogeneous treatment conditions. Typically, electric field intensities are highest at the inner wall of the chamber, where the flow velocity of the treated product is lowest. Therefore, inhomogeneities of the electric field within the treatment chamber and associated inhomogeneous temperature fields emerge. For this reason, a specific treatment chamber was designed to obtain more homogeneous flow properties inside the treatment chamber and to reduce local temperature peaks, therefore increasing treatment homogeneity. This was accomplished by a divided inlet into the chamber, consequently generating a swirling flow (vortex). The influence of inlet angles on treatment homogeneity was studied (final values: radial angle $\alpha = 61°$; axial angle $\beta = 98°$), using computational fluid dynamics (CFD). For the final design, the vorticity, i.e., the intensity of the fluid rotation, was the lowest of the investigated values in the first treatment zone (1002.55 1/s), but could be maintained for the longest distance, therefore providing an increased mixing and most homogeneous treatment conditions. The new design was experimentally compared to a conventional co-linear setup, taking into account inactivation efficacy of *Microbacterium lacticum* as well as retention of heat-sensitive alkaline phosphatase (ALP). Results showed an increase in *M. lacticum* inactivation (maximum Δlog of 1.8 at pH 7 and 1.1 at pH 4) by the vortex configuration and more homogeneous treatment conditions, as visible by the simulated temperature fields. Therefore, the new setup can contribute to optimize PEF treatment conditions and to further extend PEF applications to currently challenging products.

Keywords: pulsed electric fields (PEF), treatment chamber design, proof of concept, process optimization, numerical simulation, differentiation of thermal and electric field effects, non-thermal inactivation of microorganisms, effects of PEF on alkaline phosphatase

INTRODUCTION

Pulsed electric fields (PEF) treatment is a process increasingly used in food and biotechnology, as the resulting electroporation can cause damage to membranes of biological cells, which consequently enables a variety of different applications including gene transfer, enhancement of mass transfer and extraction, as well as non-thermal decontamination with a reduced thermal load (Kotnik et al., 2015).

For the continuous PEF treatment of liquids, the most commonly used type of treatment chamber is the so-called co-linear electrode configuration, involving ring-shaped electrodes and insulators in an alternating order. This configuration is characterized by a relatively high electrical resistance, thus enabling high electric field strength levels necessary for many cell disruption tasks while limiting electrical current flow, energy input and the associated temperature increase ($\Delta T = W_{spec} c_p^{-1}$; with ΔT: temperature increase, W_{spec}: specific electric energy input, c_p: specific heat capacity at constant pressure), especially for products with a higher electrical conductivity (Toepfl, 2006). However, due to this design, the electric field is not equally distributed within the chamber. In fact, highest current densities are present at the inner walls of the chamber (Jaeger et al., 2009; Reineke et al., 2015; Woelken et al., 2017). Moreover, as treatments usually operate under laminar flow conditions, this also corresponds to the position with the lowest flow velocity, therefore leading to local electric field and temperature peaks, accompanied by possible negative effects on heat-sensitive compounds of the product to be treated. This is of special relevance for the reduction of the microbial load in bioactive products, like protein or enzyme solutions (Schottroff et al., 2019), as the occurring electric field and temperature inhomogeneities can contribute to a reduced inactivation of microorganisms, and an increased thermal destruction of valuable compounds, respectively. Especially at neutral pH, without the presence of additional anti-microbial hurdles (Leistner, 1995) and for challenging products with higher viscosities or contents of protective ingredients, this can have pronounced negative implications on the quality of the treated product, as a high level of energy input and an associated occurrence of pronounced hot spots may be necessary to achieve the desired microbial log reduction. Limitations regarding the processability of such products and negative implications on bioactive compounds have been shown earlier (Schottroff et al., 2020).

Some approaches have already been undertaken to improve homogeneity during continuous PEF treatment or to reduce thermal effects, e.g., by optimization of insulator designs (Buckow et al., 2011), use of a static mixer (Jaeger et al., 2009), or electrode cooling (Saldaña et al., 2010; Meneses et al., 2011a). However, none of these approaches have been implemented on an industrial scale so far, due to mechanical stress and reduced cleaning-in-place ability of static mixers and limitations in upscaling considering heat transfer of cooled electrodes.

In order to overcome these limitations, a so-called vortex treatment chamber was designed and optimized using CFD, aiming to improve mixing inside the chamber, but also being scalable. For this purpose, the flow-through chamber was planned in such a way that the product inlet was divided and shifted, so that the product was inserted into the chamber at a certain angle, creating a swirling flow which should affect the exposure of individual fluid volume elements to the electric field. As a result, the temperature peaks within the treatment chamber were supposed to be reduced. This was verified by numerical simulations of the flow, electric field and temperature distributions. Based on these outcomes, inactivation of the heat-resistant bacterium *Microbacterium lacticum* and the heat-sensitive enzyme alkaline phosphatase (ALP) was investigated. Microbial inactivation levels and retention of bioactivity of the enzyme were subsequently evaluated. Thus, the vortex design was experimentally characterized, in comparison to the current standard-configuration, i.e., the co-linear treatment chamber, in order to proof the concept of more homogeneous treatment conditions in a continuous swirling flow PEF chamber.

Abbreviations: A, enzyme activity [U/L]; A_0, initial enzyme activity [U/L]; ALP, alkaline phosphatase; $c(t)$, concentration profile [mol/L]; c_0, initial concentration [mol/L]; c_p, specific heat capacity at constant pressure [J/(kg K)]; $c_{chamber}$, conversion factor for continuous chambers [1/m]; CFD, computational fluid dynamics; CFU, colony forming units; D, decimal reduction time [min]; $D_{T_{ref}}$, decimal reduction time at reference temperature [min]; E, electric field strength [V/m]; $E_r(t)$, residence time distribution function [−]; E_a, activation energy [J/mol]; E_{avg}, average electric field strength [V/m]; Eq., equation; $F(t)$, cumulated residence time function [−]; f_p, pulse repetition rate [Hz]; g, gravitational acceleration [m/s^2]; $k(T)$, Arrhenius rate constant function [1/s]; k_T, Arrhenius rate constant for temperature T [1/s]; k_0, rate constant for 1/T → 0 [1/s]; $\dot{m}$, mass flow [kg/s]; N_0, initial microbial counts [CFU/mL]; N_t, microbial counts after the treatment [CFU/mL]; p, static pressure [Pa]; p_{in}, inlet pressure [Pa]; p_{out}, outlet pressure [Pa]; Δp, pressure loss [Pa]; PEF, pulsed electric fields; POM, polyoxymethylene; R, universal gas constant [J/(mol K)]; RA, residual activity [−]; t, time [min]; $\bar{t}$, mean residence time [min]; T, temperature [K]; [°C]; T_{ref}, reference temperature [K]; [°C]; TSA, tryptic soy agar; TSB, tryptic soy broth; RA, residual activity [−]; r_{RA}, reaction term considering inactivation [−]; U, voltage [V]; **u**, flow velocity vector [m/s]; u_{in}, mean inlet flow velocity [m/s]; u_{out}, mean outlet flow velocity [m/s]; W_{spec}, total specific energy input [J/kg]; z, z-value [°C]; α, inlet angle of vortex chamber; β, inlet angle of vortex chamber; σ, electrical conductivity [S/m]; σ^2_{var}, variance [s^2]; λ, thermal conductivity [W/(m K)]; μ, dynamic viscosity [Pa s]; ρ, mass density [kg/L]; τ, stress tensor [Pa]; τ_p, pulse width [μs]; Φ, electric potential [V]; **ω**, vorticity vector [1/s].

MATERIALS AND METHODS

Standard and Modified Chamber Geometry

Two different PEF treatment chamber configurations were used in this study – the standard co-linear treatment chamber as well as the newly developed vortex chamber. Both chambers consist of an alternating sequence of electrodes and insulators. The center of each treatment chamber is formed by the hollow high voltage electrode, which is surrounded by two hollow disk-shaped insulators and two terminal ground electrodes, at the inlet or outlet, respectively. The two treatment chambers differ by the design of the inlet, i.e., the bottom ground electrode as well as

the first insulator, with the remaining configuration being identical (**Figure 1**).

Figure 2 depicts a schematic of the standard co-linear treatment chamber and a base configuration of the vortex treatment chamber. The co-linear treatment chamber has an inner pipe diameter of 6 mm that is reduced to 4 mm within the insulators. The chamber consists of two identical treatment zones, i.e., the volume inside the insulators where the electric field exposure takes place, with a length of 4 mm each, see also **Figure 1**.

The modified chamber geometry differs therefore in the design of the first treatment zone. In order to enhance the homogeneity of the treatment, the central inflow was split into two inlets through which the liquid was introduced into the bottom insulator. This configuration causes a rotation of the liquid within the chamber and potentially reduces over-processing in stagnation zones. Each inlet is characterized by two angles, α and β, which determine the position of the respective inlet pipes (2 mm inner diameter each) with respect to the chamber. The second treatment zone is identical

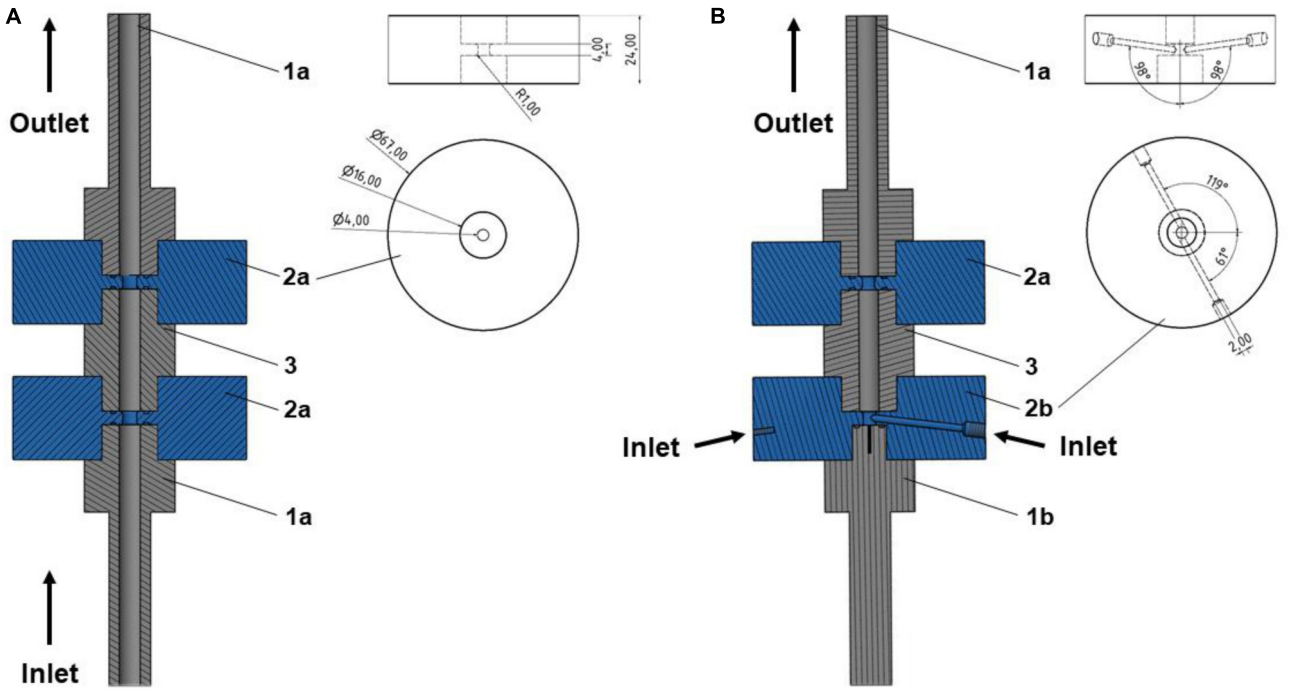

FIGURE 1 | Cross sections of the two different designs used in this study, i.e., co-linear **(A)** and vortex **(B)** PEF treatment chamber configurations, including the final dimensions. Depicted are the flow-through ground (1a) and high voltage (3) electrodes, and disk-shaped flow-through insulators (2a). For the vortex configuration, a solid ground electrode (1b) and the specific bottom insulator design (2b) were implemented. The remaining configuration was unchanged. More information on the co-linear chamber and further dimensions are provided by Meneses et al. (2011a).

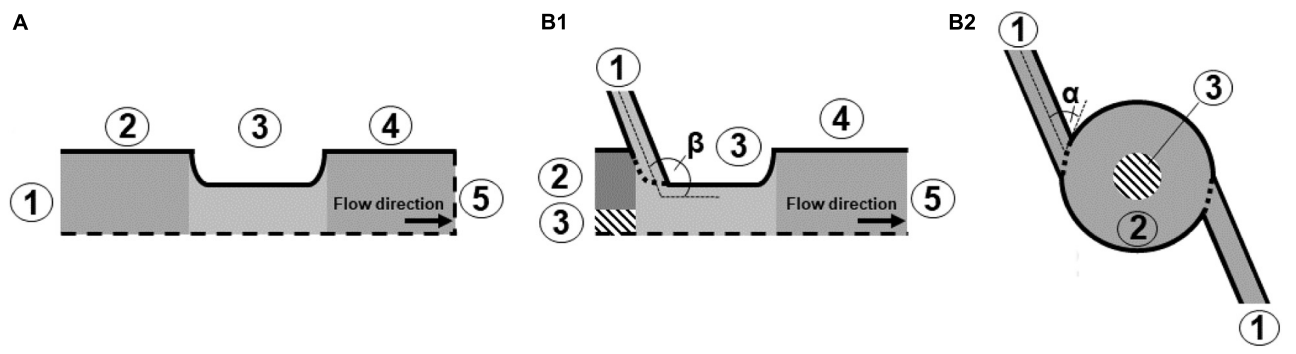

FIGURE 2 | Schematic drawing of the simulated domain for co-linear **(A)** and vortex **(B1)** configurations, and bottom view of the vortex treatment chamber **(B2)**. Further depicted are the varied inlet angles, α and β, as well as the boundaries (1–5). The values of the boundaries are summarized in **Table 2**. The dashed lines indicate symmetry lines.

to the co-linear treatment chamber (**Figure 1**). For both chambers, the total treatment volume inside the two insulators was 100.5 μL.

Thermofluiddynamical Model of the PEF Process

In order to simulate the PEF process, the bacterial and enzyme suspensions were treated as incompressible, single-phase fluids, i.e., the effect of the cells and molecules on the flow, temperature, and electric field was neglected. This assumption is justified due to the low volume fraction of cells and enzymes, their small size and consequently their negligible impact on the transport of momentum and energy (Crowe et al., 2011). Moreover, for the mass flows under consideration, laminar flow conditions can be expected for all investigated conditions. This estimate is based on the magnitude of the Reynolds number within the smallest and largest diameters of the geometry and the consideration of the respective mean flow velocities. Based on these estimates, the thermofluiddynamical model for the PEF treatment contains equations for the conservation of mass, momentum, energy, and electric charges. In addition, a first order kinetic model for thermal inactivation was included in order to estimate the contribution of thermal effects on the overall inactivation during the treatment. The equation of mass conservation for an incompressible fluid reads

$$\nabla \cdot \boldsymbol{u} = 0, \tag{1}$$

where $\boldsymbol{u}$ is the fluid velocity vector. The equation for momentum conservation reads

$$\frac{\partial \rho \boldsymbol{u}}{\partial t} + \nabla \cdot (\rho \boldsymbol{u}\boldsymbol{u}^T) = -\nabla p + \nabla \cdot \tau + \rho \boldsymbol{g}. \tag{2}$$

Herein, t stands for time, ρ for mass density of the fluid, p is the local static pressure, $\boldsymbol{g}$ the vector of gravitational acceleration and τ the stress tensor, which for an incompressible fluid is given as

$$\tau = \mu(\nabla \boldsymbol{u} + (\nabla \boldsymbol{u})^T), \tag{3}$$

where μ is the dynamic viscosity. The energy conservation equation reads

$$c_p \frac{\partial \rho T}{\partial t} + c_p \nabla \cdot (\rho \boldsymbol{u} T) = \nabla \cdot (\lambda \nabla T) + \tau_p f_p \sigma E^2. \tag{4}$$

Herein, T is the local absolute temperature, c_p the specific heat capacity of the fluid and λ the thermal conductivity. The last term of Eq. 4 covers the Joule heating of the liquid during the electric pulse. The rate of energy production is given as the product of pulse width τ_p and pulse repetition rate f_p of the electric pulse, local electrical conductivity σ and the squared local electric field strength E. The latter can be calculated by solving the conservation equation of electric charges, which reads

$$\nabla \cdot (\sigma \nabla \Phi) = 0. \tag{5}$$

In Eq. 5, Φ is the electric potential, which is related to the electric field strength by

$$E = -\nabla \Phi. \tag{6}$$

Additionally, the thermal inactivation of the used microbial cells and enzymes was modeled. Therefore, a transport equation for the residual activity RA of the biological species was considered (Rauh et al., 2009), which reads

$$\frac{\partial RA}{\partial t} + \nabla \cdot (\boldsymbol{u} RA) = r_{RA} \tag{7}$$

where r_{RA} is a reaction term considering the reduction of RA by thermal inactivation. The reaction is modeled as a first order kinetic, as described elsewhere (Jaeger et al., 2010; Dumitraşcu et al., 2015), thus

$$r_{RA} = -k(T)RA. \tag{8}$$

The kinetic parameter $k(T)$ includes the temperature dependency of the inactivation rate by the Arrhenius equation:

$$k(T) = \frac{2.303}{D_{T_{ref}}} \exp\left(-\frac{2.303T^2}{z}\left(\frac{1}{T} - \frac{1}{T_{ref}}\right)\right) = k_0 \exp\left(-\frac{E_\alpha}{RT}\right) \tag{9}$$

Here, $D_{T_{ref}}$ represents the D-value at reference temperature T_{ref} and z is the z-value of *M. lacticum* (see section "Microbiological Procedures") or ALP (see section "Quality Analysis"), respectively. The definitions of D and z-values are given in Eqs. 10 and 11. With this regard, the D-value represents the decimal reduction time, i.e., the time needed at a constant temperature T to reduce the initial microbial population (N_0) by 90%, taking into account treatment time t and the corresponding inactivation (N_t). In a similar manner, the z-value describes the temperature increase or decrease needed to reduce or raise the inactivation time, i.e., the D-value, by 90%, based on a reference temperature T_{ref} and another temperature level T, as well as the corresponding D-values, $D_{T_{ref}}$ and D_T. Moreover, the activation energy E_a (see Eq. 9) was derived from the Arrhenius plot, from the natural logarithm (ln $k(T)$) of the individual, temperature-dependent rate constants (Eq. 12) plotted over $1/T$. In this context, k_o refers to the rate constant for $1/T \rightarrow 0$ and R gives the universal gas constant, i.e., 8.314 J/(mol K).

$$D_T = \frac{t}{\log N_0 - \log N_t} \tag{10}$$

$$z = \frac{T - T_{ref}}{\log D_{T_{ref}} - \log D_T} \tag{11}$$

$$k_T = \frac{2.303}{D_T} \tag{12}$$

The material properties of the liquid used for the simulations are summarized in **Table 1**. In this regard, all material properties except from the electrical conductivity were assumed to be

TABLE 1 | Material properties of the Ringer's solution used as the treatment medium for the trials, as deployed in the CFD simulation.

Property	Symbol	Value	Unit
Density	ρ	999.9	kg/m^3
Viscosity	μ	1.0	mPas
Heat capacity	c_p	4184.52	J/(kgK)
Thermal conductivity	λ	599.35×10^{-3}	W/(mK)
Electrical conductivity	$\sigma(T)$	$0.0073T[°C]+0.1874$	S/m

Values derived from VDI Heat Atlas (VDI, 2010), conductivity was self-determined.

constant and independent from temperature. In case of the electrical conductivity, a linear relationship with respect to the temperature was assumed (Woelken et al., 2017), according to experimental measurements. Consequently, the electric and temperature fields were coupled to each other.

Eqs. 1–7 can be solved numerically with proper boundary conditions, which are summarized in **Table 2**. The positions of the boundaries are shown by their numbers in **Figure 2**. In brief, the fluid is assumed to flow into the treatment chamber with a parabolic velocity profile, corresponding to the average velocity u_{in}, and a constant temperature. The walls of the chamber are considered adiabatic, which is a reasonable assumption, since they are usually covered by an insulating material. In addition, the common no-slip condition is applied at the walls. A constant pressure and a vanishing temperature gradient are assumed at the outlet of the chamber. For the electric field, the voltage at the high voltage and grounding electrodes were set to $U = U_0$ and $U = 0$ V, respectively. At the chamber inlets and outlets, as well as at the insulating walls of the chamber, a zero-gradient condition was set for the electric potential. For the residual activity, a value of $RA = 1$ was set at the chamber inlet, which is equivalent to $\log(N/N_0)$. At the outlet, a zero gradient condition was set for the residual activity.

TABLE 2 | Boundary conditions on the positions indicated by the numbers in **Figure 2**.

Boundary and number	Condition
Flow model	
Inlet (1)	$u_{in} = \frac{4\dot{V}}{\pi d_{inlet}^2}$
Outlet (5)	$p_{stat} - p_{ref} = 0$
Walls (2, 3, 4)	$\boldsymbol{u} = 0$
Thermal model	
Inlet (1)	$T = T_0$
Outlet (5)	$\nabla T = 0$
Walls (2, 3, 4)	$q = -\lambda\nabla T = 0$
Electrostatic model	
High voltage electrode (4)	$U = U_0$
Grounding (2)	$U = 0$
Insulator (3)	$\sigma\nabla\phi = 0$
Inlet (1)	$\sigma\nabla\Phi = 0$
Outlet (5)	$\sigma\nabla\Phi = 0$
Inactivation model	
Inlet (1)	$RA = 1$
Outlet (5)	$\nabla RA = 0$
Walls (2, 3, 4)	$q_{RA} = 0$

In order to solve Eqs. 1–7 numerically, the domain was discretized after a grid convergence study in 810,812 volume elements by means of the software Ansys Meshing 19.2. The solution of the model was obtained by transient simulations of the flow with the finite volume code ANSYS CFX 19.2 (ANSYS, Inc., Canonsburg, United States). The simulations where initialized with a steady-state solution of the flow and subsequently improved by performing a time-resolved transient simulation with similar conditions. The total simulation time was set to 3 s, which is approximately four times the average residence time of a fluid element in the treatment chamber. After this time, the properties of the flow changed less than 0.5% within a time period of 0.2 s, so that the flow and the treatment conditions can be assumed as steady and therefore representative for the treatment.

Optimization of Chamber Design

Simulation studies were performed in order to determine the design of the new treatment chamber. This was done by a systematic variation of the angle α between 61° and 90°, while β was held constant at 98° because of manufacturing restrictions. This is supported by preliminary simulation studies in which no clear relation of the treatment conditions and β was detected.

For the assessment of the different geometries, three major quantities were evaluated. According to the working hypothesis, a large magnitude of the vorticity

$$\omega = |\nabla \times \boldsymbol{u}| \tag{13}$$

corresponds to a more homogeneous treatment. As an integral measure for the vorticity, the volumetric average was calculated within each of the two treatment zones of the chamber geometry, which are indicated by the light gray area in **Figure 1**. From an integral point of view, the total specific energy input

$$W_{spec} = \frac{1}{\dot{m}} f_p \tau_p \int_V \sigma E^2 dV \tag{14}$$

and the pressure loss between the inlet and outlet of the chamber

$$\Delta p = (p_{in} - p_{out}) + \frac{\rho}{2}(u_{in}^2 - u_{out}^2) \tag{15}$$

are important quantities and therefore evaluated for the different treatment chambers. It should be noted that W_{spec} only differs between the different designs because of the temperature-dependency of the electrical conductivity.

Prototyping

Based on the obtained results of the simulation, a prototype of the vortex treatment chamber configuration was designed using 3D CAD (Inventor, Autodesk, Corp., San Rafael, United States). For reasons of comparability, the co-linear configuration was modified accordingly (see **Figure 1**). For this purpose, the hollow flow-through ground electrode was replaced by a solid bottom electrode of the same dimensions, including a

non-conductive center (Acrifix, Evonik Performance Materials GmbH, Darmstadt, Germany) of 2 mm diameter, to limit the present currents, as determined by simulation. The inlet of the cell was implemented through the bottom insulator, by two opposing inlet holes of 2 mm diameter each, compared to 4 mm inner diameter of the insulator. The inlet drillings featured the determined angles (α and β). The corresponding inlet tubing (Festo AG & Co. KG, Esslingen, Germany) was connected via screw-in hose nozzles (Festo AG & Co. KG, Esslingen, Germany). The further parts and dimensions of the treatment chamber were identical to those of the co-linear configuration (see Meneses et al., 2011a for further details and dimensions). All electrodes were produced from V2A stainless steel, the insulators consisted of polyoxymethylene (POM).

Microbiological Procedures

Microbacterium lacticum D84 (EF204392), an isolate from heat-treated extended shelf life milk, was used as a heat-resistant model bacterium for the microbiological trials. This strain was determined to be the most heat resistant from a set of available vegetative microorganisms in preliminary screening studies, including six different heat-resistant *M. lacticum* isolates, based on determination of D-values (data not shown). Due to the pronounced heat resistance, *M. lacticum* is a suitable indicator for electroporation phenomena within a wide temperature range, since superimposing thermal inactivation effects become relevant at higher temperatures only.

A single colony of *M. lacticum* was inoculated in 1 mL of tryptic soy broth (TSB; VWR International SPRL/BVBA, Leuven, Belgium) and incubated over night at 37°C. Subsequently, this overnight culture was inoculated 1:100 in TSB and incubated for 24 h at 37°C without shaking, to obtain cells in the early stationary phase. This working culture was centrifuged at 2700 *g* for 10 min at 20°C and washed three times in $\frac{1}{4}$ strength Ringer's solution (Merck KGaA, Darmstadt, Germany). Final inoculation was carried out in appropriate amounts of sterile, diluted Ringer's solution at pH 4 and 7, with a defined electrical conductivity of 3.0 mS/cm. The pH was adjusted using 10% lactic acid (Sigma Aldrich, St. Louis, MO, United States). Initial counts were in the range of 10^7 colony forming units (CFU) per mL.

After each treatment, 50 μL of the untreated (N_0) as well as the treated (N) microbial suspensions were plated on tryptic soy agar (TSA) in duplicate. Plates were incubated at 37°C for 48 h. Cell counts were consecutively determined and inactivation levels were expressed as $\log_{10}(N/N_0)$. In the following parts of the manuscript, $\log_{10}$ will simply be referred to as log. All trials were carried out in triplicate.

Quality Analysis

In order to determine the effects of temperature during continuous PEF treatment, bovine alkaline phosphatase (ALP; CAS number 9001-78-9, AppliChem GmbH, Darmstadt, Germany), an enzyme found, e.g., in milk, was exemplarily used as a representative for heat-sensitive bioactive molecules. ALP was dissolved in diluted Ringer's solution (3.0 mS/cm) at pH 4 and 7. Enzyme activity was determined using a colorimetric assay (Amplite Alkaline Phosphatase Assay Kit, AAT Bioquest, Sunnyvale, CA, United States) according to the manufacturer's specifications. Enzyme activity was expressed as mU/mL and enzyme inactivation was calculated as the residual activity (*RA*), i.e., as A/A_0, from the initial (A_0) activity and the activity after the treatment (A). Initial enzyme activity was 160 mU/mL. All trials and analyses were carried out in triplicate.

Thermal Reference Data

In order to obtain data on the heat sensitivity of *M. lacticum* and ALP, thermal reference trials were carried out, using different temperature-time combinations. This was accomplished by enclosing 80 μL of microbial suspension or enzyme solution in small glass capillaries (d_i = 1 mm, d_a = 1.3 mm, L = 100 mm, Kleinfeld Labortechnik GmbH, Gehrden, Germany). Capillaries were heat-sealed using a bunsen burner, while simultaneously being cooled (Haas et al., 1996; Reineke et al., 2015). Capillaries were immersed into a water bath at the respective temperature for predefined holding times and immediately cooled in ice water after the treatment. Capillaries were opened by means of disinfected pliers, the contents were withdrawn using a 200 μL pipette and analyzed as mentioned above.

Thermal-only inactivation data were linearly modeled and mathematically described, using D and z-values (Eqs. 10 and 11) for microorganisms, values for ALP were calculated analogously, by replacing the microbial counts with the corresponding *RA*.

Characterization of the Newly Developed and Standard Co-linear Treatment Chambers

For the evaluation of the two treatment chamber configurations, the vortex and co-linear designs were experimentally compared, considering their similarity in residence time behavior as well as their individual efficacy for inactivation and retention of heat-sensitive matrix compounds.

Continuous Treatments

The used continuous PEF setup (**Figure 3**) consisted of a screw pump with an inlet vessel (MDC 006-12, Seepex GmbH, Bottrop, Germany), coil heat exchangers for preheating and cooling (self-built) and the co-linear or vortex PEF chamber. Inlet and outlet temperatures were measured before and 110 mm after the treatment chamber, in the center of the pipe. The system is described in more detail by Schottroff et al. (2019).

As the electric field inside of flow-through treatment chambers is inhomogeneously distributed (Toepfl, 2006; Jaeger et al., 2009), a trivial relation of voltage and electrode distance is inadequate to describe the present electric field strength (E) during the treatment. Therefore, an average electric field strength (E_{avg}) can be derived from simulations, employing a design-specific conversion factor ($c_{chamber}$), which enables the calculation of E_{avg} from the applied voltage (Eq. 16). For the used co-linear treatment chamber configuration, $c_{chamber}$ amounts to 1.6 (Jaeger et al., 2009). The setup was designed in such a way that the average electric field strength remained constant for both treatment chamber configurations (**Table 3**).

$$E_{avg} = c_{chamber} U \tag{16}$$

For the trials, the continuous system was started using saline solution of the same electrical conductivity than the *M. lacticum* suspensions or ALP solutions (3.0 mS/cm), and once a steady state was reached, the product inlet was changed to the liquid to be treated. After the determined residence time (see section "Overall Residence Time Distribution"), samples were gathered and placed on ice until further analysis. In-between parameter changes, a corresponding fraction of the residence time had to pass by. Details on the setup of the process are reported elsewhere (Schottroff et al., 2019). The used process parameters are given in **Table 3**.

Overall Residence Time Distribution

Residence time distribution profiles were obtained in both setups. After connection of the individual treatment chamber, the pump was started with tap water and the inlet was abruptly changed to saline solution of a defined electrical conductivity (3.0 mS/cm). From this starting point on, samples were taken every 30 s and the electrical conductivity was determined (EL3 handheld conductivity meter, Mettler Toledo, Columbus, United States). By interpretation of the electrical conductivity as the concentration of ions, $c(t)$, the dimensionless cumulated residence time $F(t)$ as well as the residence time distribution function $E_r(t)$ could be calculated (Eqs. 17 and 18). From these curves, the mean residence time $\bar{t}$ (Eq. 19), as well as the variance σ^2_{var} were derived (Eq. 20). In Eqs. 17–20, c stands for concentration and t gives the time. Subscripted 0 refers to initial values.

$$F(t) = \frac{c(t)}{c_0} \tag{17}$$

$$E_r(t) = \frac{dF(t)}{dt} \tag{18}$$

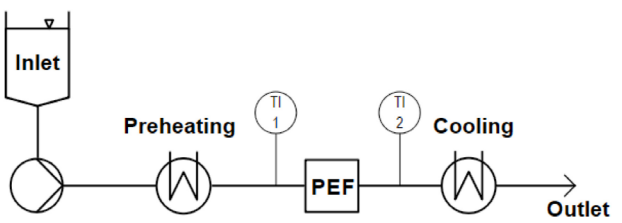

FIGURE 3 | Scheme of the used continuous PEF equipment, including an inlet tank, a screw pump, heat exchangers for preheating and cooling, inlet (TI 1) and outlet (TI 2) temperature sensors, and the PEF treatment chamber (co-linear or vortex configuration).

$$\bar{t} = \int_0^\infty t E_r(t) dt \tag{19}$$

$$\sigma^2_{var} = \int_0^\infty t^2 E_r(t) dt - \bar{t}^2 \tag{20}$$

Differentiation of Thermal and Electric Field Effects

In order to evaluate the individual thermal and electric field effects of the two treatment chamber configurations, the thermal-only inactivation of *M. lacticum* or ALP during the treatment was calculated by solving the thermofluiddynamical model as given by Eqs. 1–9, under consideration of the respective measured thermal reference data. The effects of the electric field alone could consequently be evaluated from the difference of experimentally determined inactivation (which is a mixture of thermal and electric field effects) and the calculated thermal-only inactivation, see Eq. 21 (Jaeger et al., 2010; Reineke et al., 2015). Inactivation of ALP was calculated equivalently.

$$\log\left(\frac{N}{N_0}\right)_{PEF} = \log\left(\frac{N}{N_0}\right)_{experimental} - \log\left(\frac{N}{N_0}\right)_{thermal} \tag{21}$$

Data Processing, Visualization, and Statistical Analysis

Analytical data were processed in Microsoft Excel (Microsoft, Corp., Redmond, WA, United States) and visualized using SigmaPlot 14 (Systat Software, Inc., San Jose, CA, United States). Statistical analyses (Student's t-test) were performed using Statgraphics Centurion XVII (Statpoint Technologies, Inc., Warrenton, VA, United States).

RESULTS AND DISCUSSION

Thermal References

Microbacterium lacticum and ALP were thermally inactivated in order to obtain data for the simulation of thermal-only effects during PEF treatment. The correspondingly determined D and z-values, as well as activation energies are displayed in **Table 4**. Considering the values for *M. lacticum*, inactivation took 122% longer at neutral pH than at pH 4 (180.6 vs. 81.2 s) at 80°C. This effect was distinctly less pronounced for higher temperatures, where slightly increased values were observed, i.e., 48% at 85°C (28.8 vs. 19.4 s) and 16% at 90°C (3.6 vs. 3.1 s). The z-values, on the other hand, were relatively similar, with values of 7.0 and 5.9°C at pH 4 and 7, respectively. Likewise, the activation energy

TABLE 3 | Used PEF parameters for the different trials, including voltage (U), average electric field strength (E_{avg}), maximum current (I_{max}), pulse width (τ_p), maximum pulse repetition rate ($f_{p,max}$), used mass flow ($\dot{m}$), inlet temperature (T_{in}) as well as maximum outlet temperature ($T_{out,max}$).

PEF chamber	U_0 [kV]	E_{avg} [kV/cm]	$c_{chamber}$ [1/cm]	I_{max} [A]	τ_p [µs]	$f_{p,max}$ [Hz]	$\dot{m}$ [kg/h]	T_{in} [°C]	$T_{out,max}$ [°C]
Co-linear	20	32	1.60	62	3	130	7.0	50	87
Vortex	18.1	32	1.77	62	3	130	7.0	50	87

Further given are the conversion factors ($c_{chamber}$) for the determination of average electric field strength from the applied voltage, depending on the individual treatment chamber design. Value for the co-linear chamber was determined by Jaeger et al. (2009).

TABLE 4 | Thermal inactivation data of *M. lacticum* and ALP.

Indicator	pH [–]	T [°C]	D_T [s]	z [°C]	E_a [kJ/mol]
M. lacticum	4	80	81.2	7.0	350.1
		85	19.4		
		90	3.1		
	7	80	180.6	5.9	393.8
		85	28.8		
		90	3.6		
ALP	4	67	312.5	13.0	180.1
		72	277.8		
		77	28.6		
		82	36.6		
		87	10.4		
	7	67	256.4	13.9	169.3
		72	185.2		
		77	37.7		
		82	29.9		
		87	10.0		

Values were determined as described in section "Thermal Reference Data."

at pH 4 (350.1 kJ/mol) was lower than at pH 7 (393.8 kJ/mol), thus also indicating a facilitated inactivation at pH 4. The reason for this increased inactivation is most likely a consequence of the additional antimicrobial hurdle present in form of the low pH in combination with heat (Leistner, 1995). On the other hand, it was observed that a longer contact time (approximately $>$ 1 h) of bacteria and low-pH medium led to a drastic increase of the heat resistance, implying the occurrence of cross-protective effects (Ryu and Beuchat, 1998). Therefore, the contact time was carefully considered for the trials and kept below 30 min.

Considering ALP inactivation, it was observed that enzyme activity was lower at pH 4, due to the severe deviation from the optimum pH range of 7–9 (Ross et al., 1951). However, by expressing enzyme inactivation based on the initial activity, this fact could be compensated for the calculation of the kinetics. In contrast to *M. lacticum*, thermal inactivation of ALP was slightly increased at neutral pH, compared to pH 4, although the differences between the two values were not as pronounced as for the bacterium. Increase of inactivation was in the range of 33% (72°C; 277.8 vs. 185.2 s) to 3.5% (87°C; 10.4 vs. 10.0 s), based on the comparison of D-values. The z-values also only differed by 5.9%, with values of 13.0°C and 13.9°C, for pH 4 and 7, respectively. Moreover, the activation energy of 169.3 kJ/mol at pH 7 also indicates a facilitated enzyme inactivation at that pH level, compared to pH 4 (180.1 kJ/mol; ΔE_a of 6.4%).

These values were further used for the calculation of thermal inactivation occurring in the individual PEF chambers (see section "Thermofluiddynamical Model of the PEF Process").

Design Optimization of the Vortex Treatment Chamber

Figure 4 compares the simulated features of PEF processing between the vortex chamber design and the common co-linear design. The assumed processing conditions for the simulations were a liquid mass flow $\dot{m} = 10.2$ kg/h, liquid temperature $T_{in} = 20$°C, applied voltage $U_0 = 20$ kV, pulse repetition rate $f_p = 105$ Hz, and pulse width $\tau_p = 3$ µs. The set of parameters represents typical conditions for a pilot-scale PEF treatment and was therefore chosen as a test case for the comparison of the treatment chamber characteristics. The computed flow and temperature patterns in the co-linear chamber agree to the descriptions in the literature (Jaeger et al., 2009; Woelken et al., 2017) and are characterized by parallel streamlines and the formation of a liquid jet behind the treatment zones. This flow pattern creates a recirculation zone behind the insulators, where local temperature maxima can be found. Besides, the temperature is the lowest in the center of the chamber because of the faster convective transport of thermal energy in the direction of the liquid flow. In the modified treatment chamber, a swirling flow regime was created, as expected. The swirling flow was even maintained within and behind the second treatment zone so that no recirculation zones evolved, unlike the co-linear chamber. Consequently, the temperature distribution was distinctly more homogeneous across the cross-section of the pipe in the whole treatment chamber. The distribution of the electric field in the second treatment zone is similar in both chambers due to the equivalent design. In contrast, the electric field strength in the first treatment zone is found to be higher in the vortex design, due to the different arrangement of the electrodes.

Table 5 summarizes the conditions in the treatment chamber for different values of the angle α. For comparison, simulation results for the conventional co-linear configuration are also reported. The swirling flow can be characterized in terms of the vorticity, which is a measure of the strength of the fluid rotation. According to the simulated results, the average vorticity in the first treatment zone becomes the highest for $\alpha = 65^\circ$ (1320.12 1/s). Among the different simulated designs, the vorticity in the first treatment zone varied by 25% with respect to the maximum value, whereas the minimum value was found for $\alpha = 61^\circ$ (1002.55 1/s). However, it can also be observed that for $\alpha = 61^\circ$ the swirling flow can be maintained for a longer period, which is reflected by the highest vorticity in the second treatment zone (434.16 1/s), while it is the lowest for $\alpha = 65^\circ$ (260.26 1/s). Generally, it was observed that the difference of the average vorticity between treatment zones 1 and 2 is linearly correlated with the average vorticity in the first treatment zone ($R^2 = 0.9946$), or, in other words, the higher the average vorticity in the first treatment zone the faster it decays within the treatment chamber. This also corresponds to the estimated pressure loss over the treatment chamber, which is positively correlated to the average vorticity in the first treatment zone. Therefore, under the simulated conditions, the maximum pressure loss was found for $\alpha = 65^\circ$ (367.05 Pa), while the pressure loss for $\alpha = 61^\circ$ was about 20% lower (296.31 Pa). The pressure loss of the co-linear treatment chamber was estimated to be in a similar order of magnitude (327.54 Pa).

In comparison to the co-linear chamber (76.64 kJ/kg), a significantly higher specific energy input W_{spec} was observed in all configurations of the modified chamber (103.37–105.12 kJ/kg) if the applied voltage is similar in both chambers. This observation can be explained by the more homogeneous temperature distribution in the modified treatment chamber, as it increases

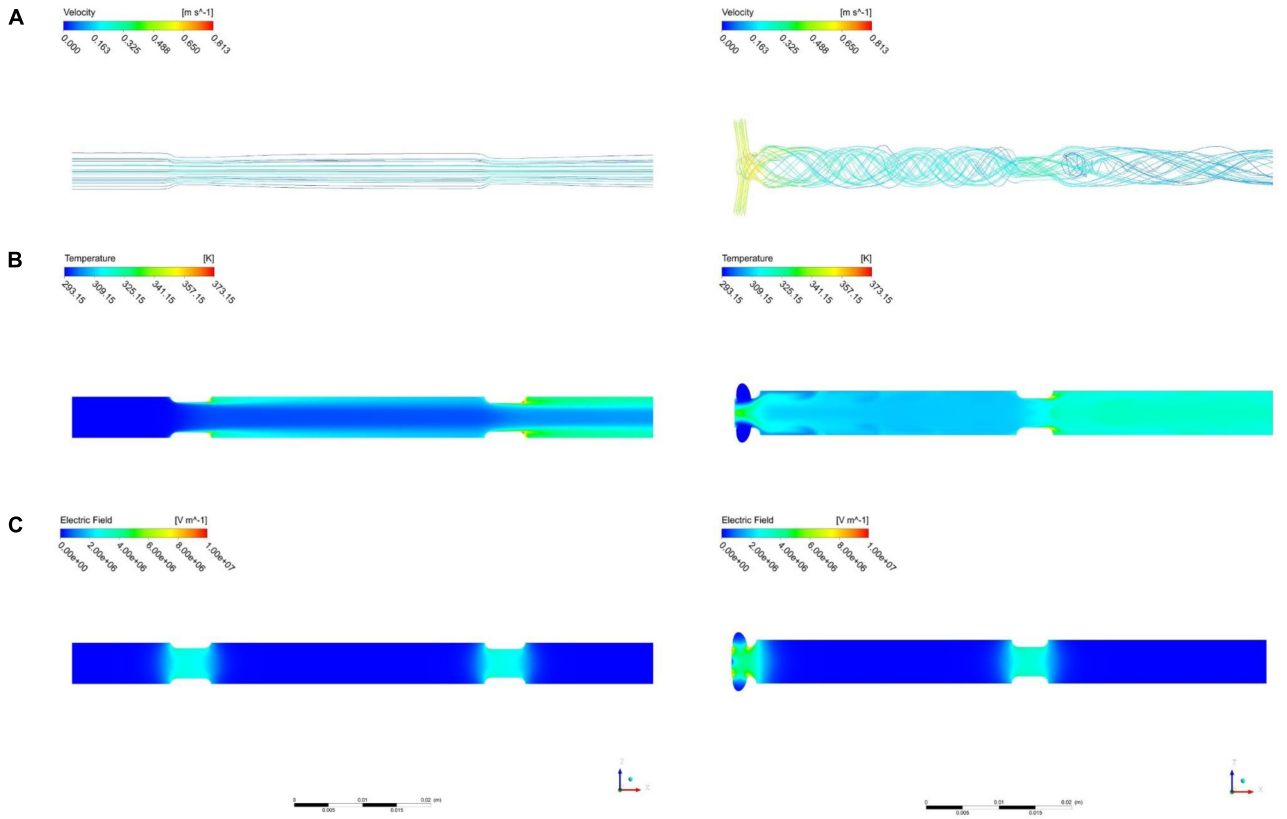

FIGURE 4 | Comparison of the co-linear (left) and the vortex (right, $\alpha = 61^{\circ}$) treatment chambers, including velocity streamlines **(A)** with colors indicating the fluid velocity, temperature distribution **(B)**, as well as electric field strength **(C)**. Assumed processing conditions: $\dot{m} = 10.2$ kg/h, $T_{in} = 20°C$, $E_{avg} = 32$ kV/cm, $f_p = 105$ Hz, $\tau_p = 3$ µs. Note that the scale on the left and right side of the figure is different, as indicated by the scale bar at the bottom.

TABLE 5 | Characteristics of the flow and treatment conditions in the two different treatment chambers.

Design	Angle α [°]	W_{spec} [kJ/kg]	ΔT [K]	ω [1/s] Zone 1	ω [1/s] Zone 2	Δω [1/s]	Δp [Pa]
Vortex	90	103.51	24.06	1170.41	331.03	389.38	324.14
	85	103.27	24.23	1184.92	319.47	865.45	326.01
	80	102.87	24.41	1211.37	302.01	909.36	331.12
	75	102.79	24.05	1222.30	287.41	934.87	341.66
	70	102.56	24.47	1249.92	266.76	983.16	353.86
	65	101.00	24.73	1320.12	260.21	1059.91	367.05
	61	105.03	24.84	1002.55	434.16	568.39	396.31
Co-linear	–	76.64	21.75	177.16	206.03	−28.87	327.54

the electrical conductivity in the treatment zone and therefore the current and the associated energy input in areas of high electric field strength. The results show that the general design of the chamber is more important than the impact of the angle α on the overall energy input, as W_{spec} differs less than 1.6% between all configurations of the vortex treatment chamber but about 25% between the conventional co-linear and the vortex designs.

The simulation results indicate that the vortex treatment chamber is superior over the co-linear treatment chamber. In accordance to the obtained results, the chamber geometry with $\alpha = 61^{\circ}$ was chosen for the experimental investigations, since it unifies the highest specific energy input and the lowest pressure loss, which are both important parameters for future industrial applications.

Previously published studies on improvement of treatment homogeneity during PEF processing optimized the inner insulator geometry (Buckow et al., 2011; Meneses et al., 2011b; Woelken et al., 2017), applied electrode cooling (Meneses et al., 2011a), or implemented a static mixer in the treatment chamber (Jaeger et al., 2009). The treatment chambers investigated were already equipped with an optimized insulator geometry, as described by Meneses et al. (2011b). Although the electric field and flow are influenced to a certain extent, there was still room for improvement. Electrode cooling was not further

considered, as especially for upscaling applications the heat transfer was determined to be insufficient (data not shown). Moreover, a static mixer was investigated in preliminary studies, but also turned out to be impracticable due to reduced cleanability (data not shown). Therefore, the vortex treatment chamber configuration is a promising approach for improvement of treatment homogeneity, while compensating the above-mentioned issues.

Characterization and Comparison of the Used Setups

The overall residence time distribution between inlet and outlet of the continuous PEF system (**Figure 3**) was evaluated, in order to ensure comparable treatment conditions for the two different process setups. Both setups showed a distinctly similar, almost identical residence time behavior (**Figure 5**), with mean residence times $\bar{t}$ of 316.4 s and 312.2 s for the co-linear and vortex-chamber, respectively, and corresponding variance σ^2_{var} of 37321.4 s^2 and 35945.8 s^2. The overall mean residence time of the vortex configuration was therefore 4.2 s shorter compared to the co-linear configuration. This could be due to the accomplished alteration of the inlet, using small plastic tubes (see section "Prototyping"), compared to the little larger metal tubing of the co-linear configuration (see **Figure 1**). However, the design of the vortex treatment chamber has been modified in such a way that maximum similarity of the two chambers was ensured, i.e., the configuration above the bottom insulator as well as the outlet tubing remained unchanged. This implies that an important variable of the continuous process, the holding time of the product at T_{out} after the treatment chamber (Schottroff et al., 2019), remained unchanged and as low as possible. Therefore, similar additional thermal effects on the product are expected and the two chambers can directly be compared in experiments.

In order to compare the outcomes of experiments and simulations, **Figure 6** shows the measured and simulated temperatures after the treatment chambers with respect to the specific energy input. For the vortex chamber, the simulation matches the experiments well, although the temperature measurement was conducted 110 mm behind the chamber outlet. This indicates that the temperature in the pipe remains constant in good approximation and that heat transfer out of the system through the pipe wall is negligible. In case of the co-linear configuration, however, slightly higher outlet temperatures of 1–2°C above those being actually measured were determined by simulation. The deviation might be caused by experimental errors of the temperature measurement, heat transfer from the fluid to the surroundings during its passage from the treatment chamber to the temperature sensor, or slight deviations between the geometry of the chamber being used in the experiments and the simulated geometry. Since the temperatures agree fairly well between experiments and simulation under all conditions, it is

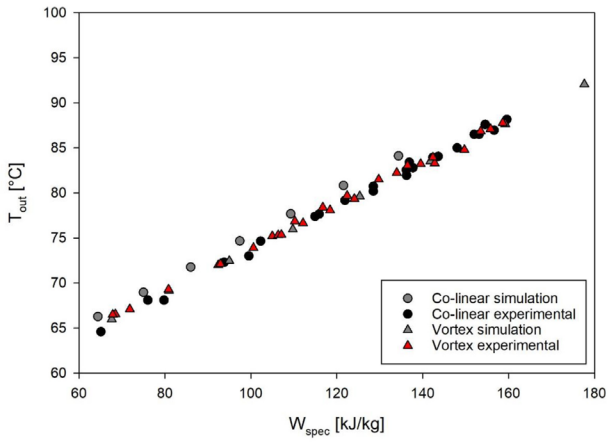

FIGURE 6 | Comparison of outlet temperatures and specific energy input, as determined by experiments and simulation. Depicted experimental data points are derived from all accomplished trials with *M. lacticum* and ALP, respectively. Corresponding process parameters are given in **Table 3**.

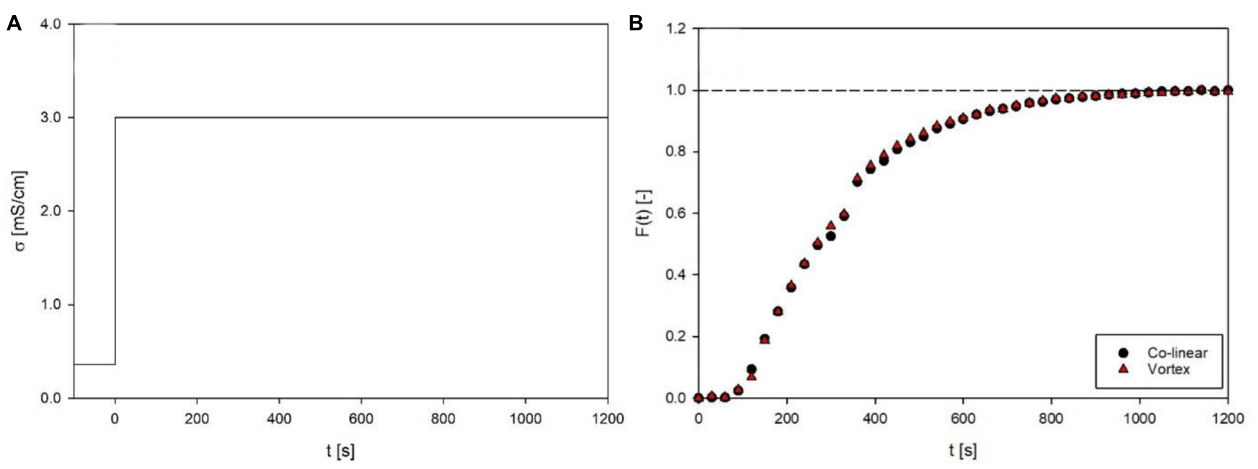

FIGURE 5 | Inlet function **(A)** and response function **(B)** of the residence time distribution for co-linear and vortex chambers at a flow rate of 7 L/h. Given are electrical conductivity (σ) and the calculated dimensionless residence time function $F(t)$ over time. Data points depict the average of three independent replicates.

expected that the CFD model allows to derive an estimate of the thermal effects of PEF on *M. lacticum* and ALP.

Performance for Microbial Inactivation

Figure 7 shows the achieved inactivation kinetics of *M. lacticum* in the co-linear and vortex PEF systems. At pH 4, the progressions of the kinetics are relatively similar, except for the highest energy input level of the vortex chamber (149.7 kJ/kg), where an additional inactivation of 1.1 log could be achieved. At pH 7, however, a distinctly increased inactivation was observed by the vortex configuration for most energy input levels, with a maximum increase of 1.8 log (143 kJ/kg).

The reason for the similar curve progression at pH 4 (**Figure 7A**) may be that the inactivation effect of PEF is superimposed by the effects of the low pH (García et al., 2005; Schottroff et al., 2019), which acts as an additional antimicrobial hurdle (Leistner, 1995). Therefore, even the occurrence of reversible pores in the membrane might be sufficient for an inactivation to occur, due to disturbance of the intracellular pH of the microorganism potentially associated with cell death, also at less severe processing conditions, which the cell would usually be able to survive in a more favorable environment (Toepfl, 2006). The reason for the significant increase ($p < 0.05$) in inactivation for the last kinetic point of the vortex chamber (149.7 kJ/kg) could be that for this relatively high energy input level electroporation was distinctly enhanced, exceeding the mixed effects of electric field and low pH, considering that also at pH 7 the increase in inactivation by the vortex chamber was maximized in this range of energy input levels.

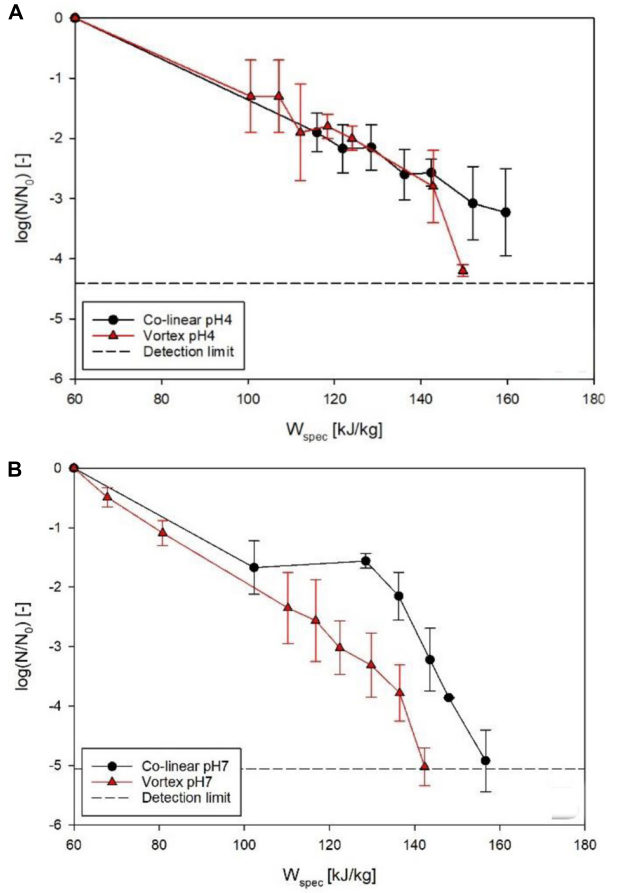

FIGURE 7 | Comparison of *M. lacticum* inactivation kinetics of co-linear (black circles) and vortex (red triangles) configuration at pH 4 **(A)** and pH 7 **(B)**. Data points depict average values, error bars represent the standard deviation.

In comparison, at pH 7, a significant increase ($p < 0.05$) in inactivation was shown for almost all energy input levels in the vortex configuration (**Figure 7B**). This leads to the conclusion that, in general, the vortex configuration produces a larger fraction of lethally injured cells, reducing the amount of sub-lethal injury. This is a beneficial attribute, as especially at neutral pH, inactivation of microorganisms by PEF may be difficult, due to the lack of additional hurdles and possible recovery of sublethally injured cells after the treatment (Schottroff et al., 2019, 2020). Moreover, the increased inactivation, especially at neutral pH, can be interpreted as a further confirmation of the increased temperature homogeneity in the vortex chamber, therefore potentially promoting possible synergistic microbial inactivation effects of temperature and electric field (Jayaram et al., 1991), by reduction of local cold spots inside the chamber.

With regard to the thermal effects of PEF, **Figure 8** shows contour plots of the thermal inactivation N/N_0 (linear scale) in the co-linear and vortex chambers for a pulse repetition rate of 100 Hz and treatment conditions as defined in **Table 3**. In case of the co-linear chamber, it can clearly be seen that the thermal inactivation occurs in the boundary layers. The residual activity in the recirculation zone after the second insulator is even close to zero due to the long residence time and high local temperature. In contrast, the inactivation pattern in the vortex treatment chamber is distinctly different and the highest thermal inactivation can be found in the vortex core between the two treatment zones. It was observed that reverse flow toward the vortex core occurs, which causes a higher residence time of some cells in the treatment chamber, and therefore an increased thermal inactivation. However, the exposure of the product to heat seems more homogeneous in the vortex chamber due to the improved mixing.

In general, it is found that the thermal inactivation of *M. lacticum* does not take place to a significant degree and the computed values for the thermal inactivation at pH 7 are lower than 0.35 log cycles under all conditions in both treatment chambers (co-linear chamber: $RA = 0.49$ at $f_p = 70$ Hz, $RA = 0.47$ at $f_p = 120$ Hz; vortex chamber: $RA = 0.61$ at $f_p = 70$ Hz, $RA = 0.59$ at $f_p = 120$ Hz, all values in linear scale). It is also seen that the simulation of the thermal inactivation indicates a higher thermal load in the co-linear chamber in comparison to the vortex design, which becomes visible by the lower residual activity.

Quality Effects on Heat-Sensitive Matrix Compounds

In terms of enzyme inactivation, the effects of the individual treatment chamber designs are less obvious (**Figure 9**). At pH 4

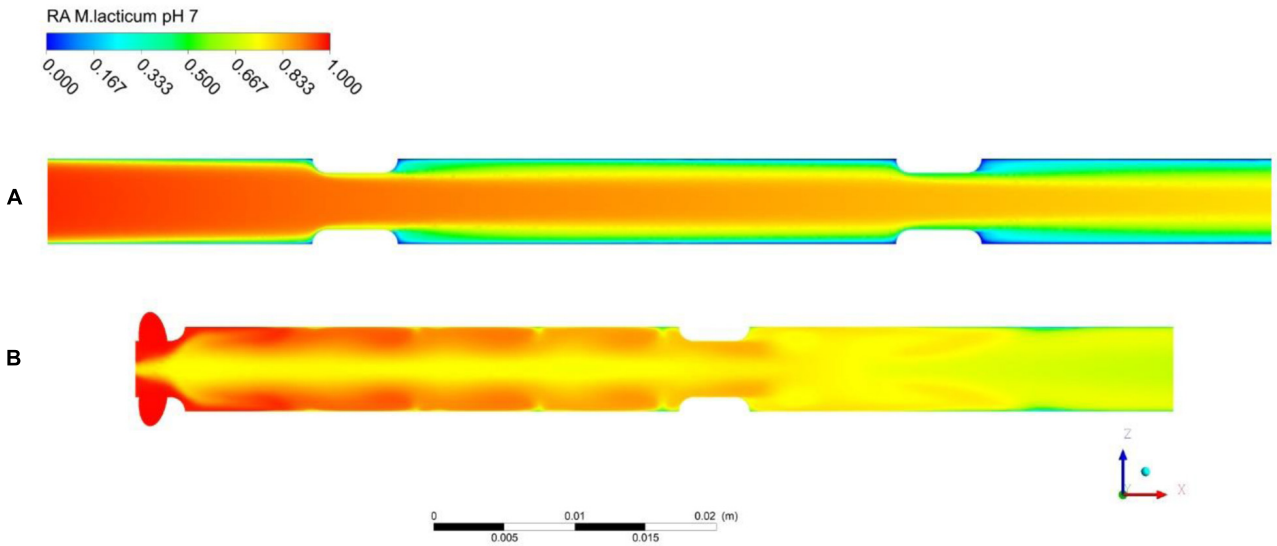

FIGURE 8 | Simulated total inactivation based on residual activity (RA) of *M. lacticum* at pH 7 inside the co-linear **(A)** and vortex **(B)** treatment chamber configurations. Assumed processing conditions: $\dot{m} = 7$ kg/h, $T_{in} = 50°C$, $E_{avg} = 32$ kV/cm, $f_p = 100$ Hz, $\tau_p = 3$ µs. Note that microbial inactivation is expressed in linear scale.

(**Figure 9A**), the data points of the vortex chamber are located slightly above the data points of the co-linear configuration, thus indicating a minor decrease in enzyme inactivation in this treatment chamber. However, this only indicates a trend and is not statistically significant ($p > 0.05$). At pH 7, however, no difference could be determined at all, i.e., enzyme inactivation was equivalent for the co-linear and vortex chambers, independent of the respective energy input level (**Figure 9B**). Consequently, the quality of PEF-treated enzyme solutions by the vortex treatment chamber configuration is neither better nor worse than the quality of products processed by the conventional co-linear design. However, it has to be mentioned that the enzyme activities were determined by use of an enzyme kit, thus the precision of the measurement may be limited. Therefore, smaller variations between data points may not be detectable. In future research, more precise methods or a different product quality parameter should be deployed.

The overall measured effect of the PEF treatment on ALP can be expected to be a combination of electric field effects in the treatment chamber, thermal effects in the treatment chamber, and thermal effects in the pipe between the treatment chamber and the heat exchanger for cooling. The numerical simulation of the thermal inactivation in the vortex treatment chamber shows that the thermal inactivation explains 15–20% loss of activity (pH 4: $RA = 0.81$ at $f_p = 70$ Hz, $RA = 0.79$ at $f_p = 120$ Hz; pH 7: $RA = 0.85$ at $f_p = 70$ Hz, $RA = 0.83$ at $f_p = 120$ Hz). Although the simulation predicts steadily decreasing enzyme activities with increasing specific energy input, the differences between the individual simulations are not large enough to explain the overall inactivation observed in the experiments. For the co-linear arrangement, the simulation predicts a higher loss of ALP activity due to thermal effects. The residual activity takes values between 0.70 and 0.71, so that about 30% of the measured activity loss can be explained by thermal effects within the treatment chamber (pH 4: $RA = 0.71$ at $f_p = 70$ Hz, $RA = 0.70$ at $f_p = 120$ Hz; pH 7: $RA = 0.70$ at $f_p = 70$ Hz, $RA = 0.70$ at $f_p = 120$ Hz). Therefore, the thermal load in the vortex treatment chamber itself is considered to be lower in comparison to the co-linear design, which is an important finding in view of quality characteristics.

However, in both chambers, the decrease of enzyme activity is almost constant due to the short residence times (<1 s) and the simulation of the thermal inactivation of ALP within the respective treatment chambers could not explain the overall activity loss and its dependency on the treatment intensity as determined in the experiments (**Figures 9A,B**). By considering the measured temperature after the treatment chamber and the mean residence time of the enzyme between the treatment chamber and the cooling, the degree of thermal damage in the pipe can be estimated from the first order thermal inactivation kinetics of ALP as given by Eqs. 8 and 9. According to **Figure 6**, the measured temperature matches the simulated temperature at the outlet of the treatment chamber very well and therefore is a suitable estimate for the temperature in the pipe. The mean residence time in the pipe was determined experimentally to be 14.53 s. **Figure 9C** depicts the contribution of the different effects toward the loss of activity in relation to the overall effect, with respect to the specific energy input during the treatment in the vortex treatment chamber at pH 4. Similar results were obtained for the treatment at pH 7 (data not shown). It is seen that at low treatment intensities (<110 kg/kJ), the thermal load in the treatment chamber exceeds the effect in the pipe, while at higher treatment intensities the thermal damage of the enzyme in the pipe after the treatment chamber becomes the dominating feature. However, the total thermal effect still cannot explain the total measured loss of activity, which indicates that the electric field itself may have a limited effect on the enzyme activity.

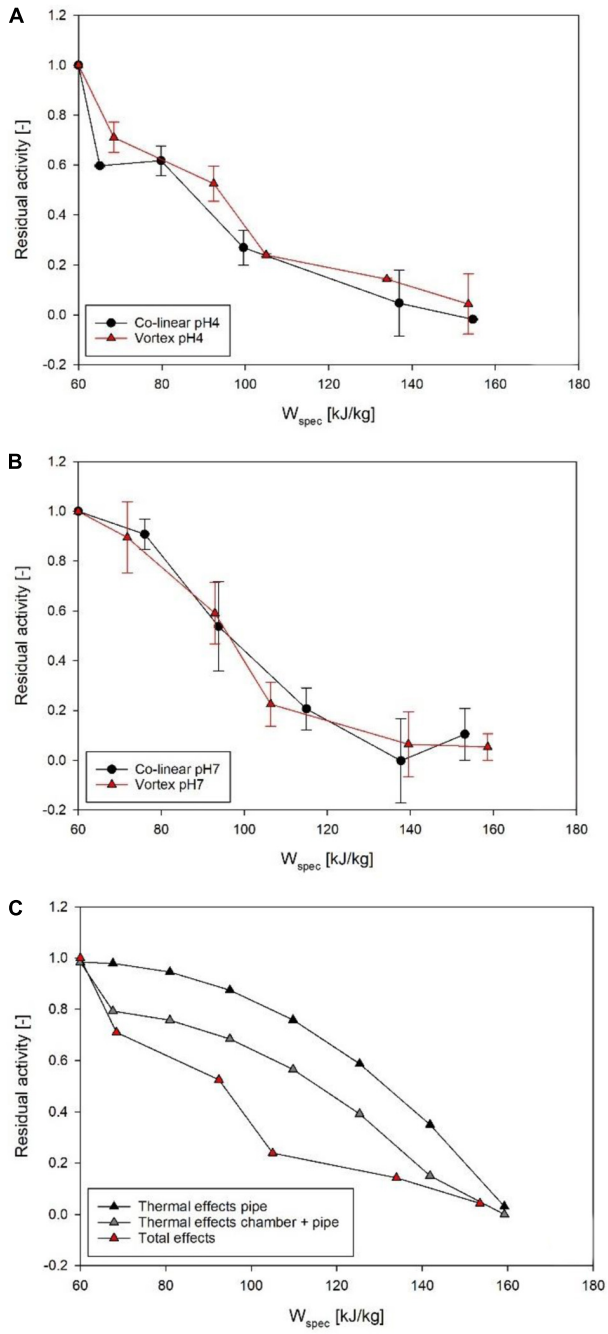

FIGURE 9 | Comparison of ALP inactivation kinetics of co-linear (black circles) and vortex (red triangles) configuration at pH 4 **(A)** and pH 7 **(B)**. Data points depict average values, error bars represent the standard deviation. Further depicted **(C)** is the total inactivation in the vortex chamber at pH 4, and the thermal effects occurring in the pipe after the treatment chamber, as well as inside the treatment chamber and in the pipe, as determined by mathematical modeling and simulation.

It is reported that the activity of ALP may be reduced by a PEF treatment, depending on the field strength and the number of pulses (Castro et al., 2001; Poojary et al., 2017; Giteru et al., 2018). Using electroporation cuvettes, Castro et al. (2001) reported a reduction of ALP activity for field strengths as low as 13.2 kV/cm, with residual activities of 0.7 for 10 pulses, to 0.1 for 70 pulses. Temperature increase due to electric current flow was not reported. As the electric field strengths applied during the present study well surpassed these reported field strengths, non-thermal effects of PEF on ALP can be assumed. Recent studies used more controlled process conditions and reported differences between the thermal-only and the overall effects, depending on the treatment intensity. Jaeger et al. (2010) showed limited electric field effects on ALP, with around 20% increase in enzyme inactivation compared to heat alone. Electric field effects in a similar order of magnitude (up to 12%) were also reported for Lactoperoxidase (Buckow et al., 2012).

CONCLUSION

The swirl flow generated in the newly designed vortex treatment chamber was shown to contribute to an increased treatment homogeneity. This could be visualized by the simulated temperature fields inside the chamber but also experimentally determined, by showing an increased microbial inactivation of *M. lacticum*, compared to the standard co-linear configuration. ALP was used as a heat-sensitive quality parameter, but the retention of this enzyme did not significantly increase. However, this could also be related to the relatively high variation of the analytical method (enzyme kit). Therefore, further research on the possible benefits of the vortex treatment chamber for quality retention should be carried out.

Nevertheless, it can be stated that hydrodynamic optimization can be a useful tool to increase PEF treatment homogeneity. During the individual trials, it was noticeable that for high energy input levels, the performance of the vortex chamber was distinctly more stable than the co-linear configuration, i.e., that arcing could be drastically reduced, which is an indication of reduced local electric field and temperature peaks. Also considering the performance for non-thermal inactivation effects on bacteria at a neutral pH, which is usually difficult to achieve (Schottroff et al., 2019), the new configuration performed comparably well. Therefore, it can be concluded that further studies using the vortex configuration and a further optimization of the system are promising, especially for the improvement of the inactivation of microorganisms by PEF at neutral pH.

Open points considering the vortex treatment chamber design are related to the further understanding of the process characteristics. Needless to say, that the design itself can be further optimized with respect to the treatment homogeneity, manufacturing or hygienic design. The design of the vortex treatment chamber was also fully based on modeling and numerical simulations, which naturally do not perfectly cover all process features. For example, in the present model the temperature dependency of some material

properties was not considered in order to reduce the numerical costs of the simulation. Therefore, an additional experimental characterization of the flow and mixing in the treatment chamber should be carried out in order to validate the numerical model and to further improve its accuracy. In this regard, particle image velocimetry and particle tracking velocimetry could be suitable tools for such investigations. Open questions are also related to changes of flow and temperature distributions under different process conditions. Also, the material properties of the product, especially viscosity, will have a large impact on the process and the applicability of the new chamber design and its underlying principle of operation. For simple pipe configurations it is known that the decay of laminar swirl velocity is a function of the Reynolds number (Yao and Fang, 2012) and therefore an evaluation of the treatment conditions in terms of the Reynolds and Prandtl numbers should be part of further research on the PEF process within the vortex treatment chamber. Finally, further investigations should also address the question of upscaling. This naturally affects the flow in the treatment chamber, but also the distribution and strength of the electric field. Well-defined electric fields only exist for some simple geometric arrangements like parallel-plate configurations. However, for engineering purposes there is a need for correlations which help to estimate important parameters of the treatment (e.g., average or peak electric field strength) for different chamber designs and process scales. To date, such correlations do not exist and further studies are therefore necessary.

DATA AVAILABILITY STATEMENT

The datasets generated for this study are available on request to the corresponding author.

AUTHOR CONTRIBUTIONS

FS and HJ developed the idea for the study. FS, TH, and HJ were involved in the planning of study. TH, PE, JK, CM, and CR planned and conducted the modeling and simulation and analyzed the resulting data. FS and AK acquired and analyzed the experimental data. FS, JK, and CM wrote the manuscript. HJ and CR proofread the manuscript and contributed to discussions during the development of the study and the manuscript.

ACKNOWLEDGMENTS

The authors acknowledge the assistance of Axel Perotin and Benjamin Illmer during the experiments. Furthermore, the authors thank Beatrix Stessl and Martin Wagner (University of Veterinary Medicine Vienna) for providing the *Microbacterium lacticum* isolate. The experimental part of the study was supported by the BOKU Core Facility Food & Bio Processing and part of the equipment used in this study was financed by EQ BOKU VIBT GmbH and belongs to the Center for Preservation and Aseptic Processing.

REFERENCES

Buckow, R., Baumann, P., Schroeder, S., and Knoerzer, K. (2011). Effect of dimensions and geometry of co-field and co-linear pulsed electric field treatment chambers on electric field strength and energy utilisation. *J. Food Eng.* 105, 545–556. doi: 10.1016/j.jfoodeng.2011.03.019

Buckow, R., Semrau, J., Sui, Q., Wan, J., and Knoerzer, K. (2012). Numerical evaluation of lactoperoxidase inactivation during continuous pulsed electric field processing. *Biotechnol. Prog.* 28, 1363–1375. doi: 10.1002/btpr.1582

Castro, A. J., Swanson, B. G., Barbosa-Cánovas, G. V., and Zhang, Q. H. (2001). "Pulsed electric field modification of milk alkaline phosphatase activity," in *Electric Fields in Food Processing*, eds G. V. Barbosa-Cánovas and Q. H. Zhang (Lancaster: Technomic), 65–82. doi: 10.1201/9780429133459-5

Crowe, C. T., Schwarzkopf, J. D., Sommerfeld, M., and Tsuji, Y. (2011). *Multiphase Flows with Droplets and Particles*. Boca Raton: CRC Press.

Dumitraşcu, L., Stănciuc, N., Aprodu, I., Ciuciu, A.-M., Alexe, P., and Bahrim, G. E. (2015). Monitoring the heat-induced structural changes of alkaline phosphatase by molecular modeling, fluorescence spectroscopy and inactivation kinetics investigations. *J. Food Sci. Technol.* 52, 6290–6300. doi: 10.1007/s13197-015-1719-1

García, D., Gómez, N., Mañas, P., Condón, S., Raso, J., and Pagán, R. (2005). Occurrence of sublethal injury after pulsed electric fields depending on the micro-organism, the treatment medium ph and the intensity of the treatment investigated. *J. Appl. Microbiol.* 99, 94–104. doi: 10.1111/j.1365-2672.2005.02611.x

Giteru, S. G., Oey, I., and Ali, M. A. (2018). Feasibility of using pulsed electric fields to modify biomacromolecules: a review. *Trends Food Sci. Technol.* 72, 91–113. doi: 10.1016/j.tifs.2017.12.009

Haas, J., Behsnilian, D., and Schubert, H. (1996). Determination of the heat resistance of bacterial spores by the capillary tube method. I. Calculation of two borderline cases describing quasi-isothermal conditions. *LWT Food Sci. Technol.* 29, 197–202. doi: 10.1006/fstl.1996.0029

Jaeger, H., Meneses, N., and Knorr, D. (2009). Impact of PEF treatment inhomogeneity such as electric field distribution, flow characteristics and temperature effects on the inactivation of *E. coli* and milk alkaline phosphatase. *Innovat. Food Sci. Emerg. Technol.* 10, 470–480. doi: 10.1016/j.ifset.2009.03.001

Jaeger, H., Meneses, N., Moritz, J., and Knorr, D. (2010). Model for the differentiation of temperature and electric field effects during thermal assisted PEF processing. *J. Food Eng.* 100, 109–118. doi: 10.1016/j.jfoodeng.2010.03.034

Jayaram, S., Castle, G. S. P., and Margaritis, A. (1991). "Effects of high electric field pulses on *Lactobacillus brevis* at elevated temperatures," in *Proceedings of the Conference Record of the 1991 IEEE Industry Applications Society Annual Meeting*, Dearborn, MI.

Kotnik, T., Frey, W., Sack, M., Haberl Meglic, S., Peterka, M., and Miklavcic, D. (2015). Electroporation-based applications in biotechnology. *Trends Biotechnol.* 33, 480–488. doi: 10.1016/j.tibtech.2015.06.002

Leistner, L. (1995). "Principles and applications of hurdle technology," in *New Methods of Food Preservation*, ed. G. W. Gould (Boston, MA: Springer), 1–21. doi: 10.1007/978-1-4615-2105-1_1

Meneses, N., Jaeger, H., and Knorr, D. (2011a). Minimization of thermal impact by application of electrode cooling in a co-linear PEF treatment chamber. *J. Food Sci.* 76, E536–E543.

Meneses, N., Jaeger, H., Moritz, J., and Knorr, D. (2011b). Impact of insulator shape, flow rate and electrical parameters on inactivation of *E. coli* using a continuous co-linear PEF system. *Innovat. Food Sci. Emerg. Technol.* 12, 6–12. doi: 10.1016/j.ifset.2010.11.007

Poojary, M. M., Roohinejad, S., Koubaa, M., Barba, F. J., Passamonti, P., Režek Jambrak, A., et al. (2017). "Impact of pulsed electric fields on enzymes," in *Handbook of Electroporation*, ed. D. Miklavčič (Cham: Springer International Publishing), 2369–2389. doi: 10.1007/978-3-319-32886-7_173

Rauh, C., Baars, A., and Delgado, A. (2009). Uniformity of enzyme inactivation in a short-time high-pressure process. *J. Food Eng.* 91, 154–163. doi: 10.1016/j.jfoodeng.2008.08.019

Reineke, K., Schottroff, F., Meneses, N., and Knorr, D. (2015). Sterilization of liquid foods by pulsed electric fields–an innovative ultra-high temperature process. *Front. Microbiol.* 6:400. doi: 10.3389/fmicb.2015.00400

Ross, M. H., Ely, J. O., and Archer, J. G. (1951). Alkaline phosphatase activity and pH optima. *J. Biol. Chem.* 192, 561–568.

Ryu, J.-H., and Beuchat, L. R. (1998). Influence of acid tolerance responses on survival, growth, and thermal cross-protection of *Escherichia coli* O157:H7 in acidified media and fruit juices. *Intern. J. Food Microbiol.* 45, 185–193. doi: 10.1016/s0168-1605(98)00165-2

Saldaña, G., Puértolas, E., Álvarez, I., Meneses, N., Knorr, D., and Raso, J. (2010). Evaluation of a static treatment chamber to investigate kinetics of microbial inactivation by pulsed electric fields at different temperatures at quasi-isothermal conditions. *J. Food Eng.* 100, 349–356. doi: 10.1016/j.jfoodeng.2010.04.021

Schottroff, F., Gratz, M., Krottenthaler, A., Johnson, N. B., Bédard, M. F., and Jaeger, H. (2019). Pulsed electric field preservation of liquid whey protein formulations – Influence of process parameters, pH, and protein content on the inactivation of *Listeria innocua* and the retention of bioactive ingredients. *J. Food Eng.* 243, 142–152. doi: 10.1016/j.jfoodeng.2018.09.003

Schottroff, F., Johnson, K., Johnson, N. B., Bédard, M. F., and Jaeger, H. (2020). Challenges and limitations for the decontamination of high solids protein solutions at neutral pH using pulsed electric fields. *J. Food Eng.* 268:109737. doi: 10.1016/j.jfoodeng.2019.109737

Toepfl, S. (2006). *Pulsed Electric Fields (PEF) for Permeabilization of Cell Membranes in Food- and Bioprocessing – Applications, Process and Equipment Design and Cost Analysis*. Berlin: Berlin Institute of Technology.

VDI (2010). *VDI Heat Atlas*. New York, NY: Springer Publishing.

Woelken, T., Sailer, J., Maldonado-Parra, F. D., Horneber, T., and Rauh, C. (2017). "Application of numerical simulation techniques for modeling pulsed electric field processing," in *Handbook of Electroporation*, ed. D. Miklavcic (Basel: Springer International Publishing).

Yao, S., and Fang, T. (2012). Analytical solutions of laminar swirl decay in a straight pipe. *Commun. Nonlinear Sci. Numer. Simul.* 17, 3235–3246. doi: 10.1016/j.cnsns.2011.11.038

Conflict of Interest: The authors declare that the research was conducted in the absence of any commercial or financial relationships that could be construed as a potential conflict of interest.

Copyright © 2020 Schottroff, Knappert, Eppmann, Krottenthaler, Horneber, McHardy, Rauh and Jaeger. This is an open-access article distributed under the terms of the Creative Commons Attribution License (CC BY). The use, distribution or reproduction in other forums is permitted, provided the original author(s) and the copyright owner(s) are credited and that the original publication in this journal is cited, in accordance with accepted academic practice. No use, distribution or reproduction is permitted which does not comply with these terms.

frontiers in Bioengineering and Biotechnology

ORIGINAL RESEARCH
published: 13 May 2020
doi: 10.3389/fbioe.2020.00443

Electroporation as a Solvent-Free Green Technique for Non-Destructive Extraction of Proteins and Lipids From *Chlorella vulgaris*

*Tina Eleršek[1], Karel Flisar[2], Blaž Likozar[3], Marina Klemenčič[4], Janvit Golob[4], Tadej Kotnik[2] and Damijan Miklavčič[2]**

[1] Department of Genetic Toxicology and Cancer Biology, National Institute of Biology, Ljubljana, Slovenia, [2] Faculty of Electrical Engineering, University of Ljubljana, Ljubljana, Slovenia, [3] National Institute of Chemistry, Ljubljana, Slovenia, [4] Faculty of Chemistry and Chemical Technology, University of Ljubljana, Ljubljana, Slovenia

Proteins extracted from microalgae for food, personal care products and cosmetics must be of high purity, requiring solvent-free extraction techniques despite their generally considerably lower protein yield and higher energy consumption. Here, three such approaches for green extraction of proteins from *Chlorella vulgaris* were evaluated: ultrasound, freeze-thawing, and electroporation; chemical lysis was used as positive control (maximal achievable extraction), and no extraction treatment as negative control. Compared to chemical lysis, electroporation yielded the highest fraction of extracted protein mass in the supernatant (≤27%), ultrasound ≤24%, and freeze-thawing ≤15%. After a growth lag of several days, electroporated groups of algal cells started to exhibit growth dynamics similar to the negative control group, while no growth regeneration was detected in groups exposed to ultrasound, freeze-thawing, or chemical lysis. For electroporation as the most efficient and the only non-destructive among the considered solvent-free protein extraction techniques, simultaneous extraction of intracellular algal lipids into supernatant was then investigated by HPLC, proving relatively low-yield (≤7% of the total algal lipid mass), yet feasible for glycerides (tri-, di-, and mono-) as well as other fatty acid derivatives. Our results show that electroporation, though lower in extraction yields than chemical lysis or mechanical disintegration, is in contrast to them a technique for largely debris-free extraction of proteins from microalgae, with no need for prior concentration or drying, with feasible growth regeneration, and with potential for simultaneous extraction of intracellular algal lipids into the supernatant.

Keywords: electroporation, lipid extraction method, microalgae, protein extraction and processing, solvent-free extraction

OPEN ACCESS

Edited by:
Ao Xia,
Chongqing University, China

Reviewed by:
Michel Eppink,
Wageningen University & Research, Netherlands
Kit Wayne Chew,
Xiamen University, Malaysia, Malaysia

****Correspondence:***
Damijan Miklavčič
damijan.miklavcic@fe.uni-lj.si

Specialty section:
This article was submitted to Bioprocess Engineering, a section of the journal Frontiers in Bioengineering and Biotechnology

Received: *16 March 2020*
Accepted: *17 April 2020*
Published: *13 May 2020*

Citation:
Eleršek T, Flisar K, Likozar B, Klemenčič M, Golob J, Kotnik T and Miklavčič D (2020) Electroporation as a Solvent-Free Green Technique for Non-Destructive Extraction of Proteins and Lipids From Chlorella vulgaris. Front. Bioeng. Biotechnol. 8:443. doi: 10.3389/fbioe.2020.00443

INTRODUCTION

Green, solvent-free, and preferably non-destructive extraction of natural chemical compounds from microorganisms is among the key concepts in meeting the 21st century challenges of protecting both the environment and the consumers. Green extraction is the umbrella term for innovative energy-efficient and environment-friendly extraction techniques that minimize the use of conventional solvents, replacing them with biosolvents and/or renewable natural products, and

thus enabling production of safe and high-quality extracts (Chemat et al., 2012). If the extraction process is designed as to avoid the use of solvents altogether, this renders both the extracts and the leftovers free of solvent residuals, reducing both the health risk to consumers and the environmental footprint, as well as raising the extract purity to the levels required for food, personal care and cosmetics. Finally, if the extraction method is refined to also be non-destructive, so that the population of microorganisms from which the compounds are extracted retains the ability for cell growth regeneration, this reduces the amount of waste resulting from the extraction and thus further benefits the environmental footprint.

Naturally occurring algae are of great importance for aquatic ecosystems stability, O_2 emission and CO_2 sequestration, and are already established in wastewater treatment and in some biotechnological applications (Becker, 2007; Aschemann-Witzel et al., 2013). It is gradually also becoming evident that microalgae are promising organisms for sustainable biotechnological processes in which bio-refinery concepts are integrated with natural (sun, water, CO_2), renewable (algal biomass), and/or recyclable (wastewater, nutrients) components (Golberg et al., 2016; Buchmann et al., 2019). In particular, microalgae can serve as a potential source of energy (Hannon et al., 2010), food (Draaisma et al., 2013), feed (Skrede et al., 2011), cosmetics, and pharmaceuticals (Olaizola, 2003a; Olaizola, 2003b) due to their higher photosynthetic efficiency, higher biomass production and faster growth compared to other energy crops (Widjaja et al., 2009). Microalgae can also be converted directly into energents such as biodiesel, which makes them a promising source of renewable energy (Gouveia and Oliveira, 2009; Halim et al., 2012). Moreover, microalgae are an attractive food/feed and food-supplement source, as they are rich in proteins, peptides, carbohydrates, lipids, omega 3 fatty acids, trace elements and other essential nutrients with protective and detoxifying roles (vitamins, minerals, pigments) (Wijffels et al., 2010; Gong and Jiang, 2011; Cuellar-Bermudez et al., 2015).

Under certain conditions, protein content in microalgae can represent as much as 60% of the biomass (Becker, 2007; Draaisma et al., 2013). Cells that produce these high-value proteins can be grown under controlled environmental conditions in photobioreactors (Walker et al., 2005) without adverse effects to the environment (Pulz and Gross, 2004). Microalgal proteins are of high quality and comparable to conventional plant proteins (FAO/WHO, 1973; Becker, 2007). In comparison to conventional protein-rich crops, microalgae have higher areal productivity, they can be grown in sea water and thus do not require arable land, exhibit no need for pesticides, are generally easily cultivated, and have no adverse effect on biodiversity (Godfray et al., 2010; Tilman et al., 2011).

Microalgae as protein source for food, however, have certain drawbacks. Similarly to plant crops, all algal products are poorly digested by humans (and all other non-ruminant animals), because algae (as plants) possess a rigid cell wall composed predominantly of cellulose. For effective availability of algal proteins in food, a post-harvesting treatment resulting in disruption of the cell wall must therefore be employed (Safi et al., 2012). For microalgae to become an established and widely used protein source in nutrition, these post-harvesting treatments must be acceptable economically (McMillan et al., 2013) and from the aspect of the resulting food microstructure, which affects the bioavailability of nutrients including proteins (Parada and Aguilera, 2007). But most importantly, the proteins extracted from microalgae for food – as well as for personal care products and cosmetics – must be of high purity, requiring solvent-free extraction techniques despite their generally lower protein yield and higher energy consumption. This clearly disqualifies chemical extraction techniques.

Among physical extraction techniques, bead-milling, high-pressure homogenization, ultrasonication, and freeze-thawing have all proved effective in protein extraction from microalgae (Hopkins, 1991; Middelberg, 1995; Doucha and Livansky, 2008; Günerken et al., 2015; Postma et al., 2015), and ultrasonication was also found effective in lipid extraction (Prabakaran and Ravindran, 2011). However, all these approaches generally result in cell lysis and disintegration. As a consequence, they all yield a mix of extracted proteins and structural debris of the microalgae (lipids from their cellular and intracellular membranes and the fragments of their cell wall), affecting the solubilization of the extracted proteins (Shen et al., 2008), as well as necessitating further fractionation and purification (Vanthoor-Koopmans et al., 2013).

In contrast, in electroporation, where exposure of cells to short high-voltage electric pulses is used to increase their permeability (Kotnik et al., 2019), pulse amplitude and duration highly optimizable for the permeabilizing effect to be limited and reversible, with the cells retaining their viability and integrity, so that the extract is largely free of the structural debris (Kotnik et al., 2015). Further fine-tuning of pulse parameters can also increase the selectivity of extraction to proteins or lipids (Coustets et al., 2013; Grimi et al., 2014); the reports of electroporation-based extraction of various biomolecules from various microalgae are summarized in **Table 1**. In comparison to ultrasonication and freeze-thawing, as well as high-pressure homogenization, electroporation was also reported to be the most economical in energy consumption (Wijffels et al., 2010; Goettel et al., 2013). And finally, when reversible and thus non-destructive, electroporation allows for the microorganisms to regenerate after extraction, reducing the amount of waste and thus the burden on the environment.

In this paper, we investigate, evaluate and compare ultrasound, freeze-thawing, and electroporation as three non-thermal, solvent-free approaches for extraction of proteins from the microalga *Chlorella vulgaris*; we use chemical lysis as the positive control (maximal achievable extraction), and absence of extraction treatment as the negative control. We demonstrate that electroporation allows largely debris-free extraction of proteins and lipids from microalgae, with feasible growth regeneration.

MATERIALS AND METHODS

Algal Growth in Photobioreactor

Unicellular microalga *Chlorella vulgaris* SAG 211-11b was inoculated in 50 ml flasks. When cell culture reached stationary

TABLE 1 | Reports of electroporation-based extraction techniques from microalgae.

References	Species	Extracted molecules	Voltage amplitude (kV)	Distance between electrodes (mm)	Pulse duration (ms)	Number of pulses	Pulse repetition frequency (Hz)
Coustets et al., 2013	*C. vulgaris, N. salina*	Proteins	1.8	3 or 6	2	15	NR
Grimi et al., 2014	*Nannochloropsis* sp.	Proteins	20	NR	1–4	NR	NR
Coustets et al., 2015	*C. vulgaris, H. pluvialis, N. salina*	Proteins	1.8	3 or 6	2	9	NR
Postma et al., 2016	*C. vulgaris*	Carbohydrates, proteins	8	4	0.005	NR	50–200
Parniakov et al., 2015	*Nannochloropsis* sp.	Phenols, chlorophylls	20	20	0.01	400	NR
t'Lam et al., 2017	*C. vulgaris, N. oleoabundans*	Proteins	1.6–3	2	0.05–5	1–40	120–964
Safi et al., 2017	*N. gaditana*	Proteins	1.6–13.5	NR	5	2 or 10	NR
Carullo et al., 2018	*C. vulgaris*	Carbohydrates, proteins	20	4	1–10	NR	1–1000
Bodénès et al., 2019	*C. reinhardtii*	Lipids	0–0.7	1	0.005–0.5	10	10

NR, not reported; C. reinhardtii, Chlamydomonas reinhardtii; C. vulgaris, Chlorella vulgaris; H. pluvialis, Haematococcus pluvialis; N. gaditana, Nannochloropsis gaditana; N. oleoabundans, Neochloris oleoabundans; N. salina, Nannochloropsis salina.

phase, cells were transferred to a 20 L laboratory photobioreactor for 2 to 3 weeks (the tubular part of bioreactor at illumination 300–350 μmol photons/m^2s, flow rate 720 mL/min). The alga was grown in Jaworski's medium (Schlösser, 1982) with 16 h illumination per day, constant mixing, and automated measurements of temperature (kept in the interval 22 ± 2°C), O_2 concentration (kept above 7 mg/L) and pH value (kept in the interval 6.5–7.5) every 10 min. Every second day, cell density, morphology and potential cell malformalities were checked under the microscope. Nutrient concentrations (NO_3^-, PO_4^{3-}, SO_4^{2-}) were also monitored spectrophotometrically (HI83225, Hanna Instruments). To avoid limitation of protein synthesis due to limited availability of nitrogen in the media, nitrogen source ($NaNO_3$ at concentration 124 mg/L) was added when nitrogen values dropped below 70% of initial concentrations (usually every 7–10 days of cultivation).

Extraction

When algal culture was reaching the end of exponential growth phase (in our conditions at app. 10^7 cells/mL), aliquotes of algal suspension (8 × 0.5 L) were used for each of the treatments, with their quantitative parameters and abbreviations used henceforth specified in **Table 2**. For electroporation, the experimental setup, a snapshot of monitored unipolar square wave pulse voltage and current, and the flow chamber are schematically presented in **Figure 1**. The conductivity at the beginning of the experiments was in the range 185–273 μS/cm. All treatments were performed at room temperature, except ultrasonication where samples were put on ice during the exposure to avoid excessive heating.

After every treatment, algal suspension was centrifuged (5000 rpm, 10 min) to allow the algal pellet (i.e., the centrifugate) and the supernatant to be analyzed separately. Cell density, conductivity, temperature, dry weight and protein and lipid content were measured before and after each treatment (after treatment separately for supernatant and algal pellet). Cell density and morphology were assessed microscopically with Bürker-Türk hemocytometer. Conductivity and temperature were measured with a multi sonde (Multi 3420 SETF, WTW). Dry weight was measured by weighing glass fiber filters (Sartorius GF/C) before and after filtration of 100 ml of algal suspensions with a known number of cells after drying at 105°C for 2 h. Dry weight was compared to weight of liophylised algal culture to validate the dry weight data.

Extracted Proteins Quantification

Extracted protein content was quantified by a modified Bradford Assay (Bradford, 1976). Protein samples with protein content in range 1–25 μg were diluted with distilled water to final volume of 900 and 200 μl of Bradford reagent was added and mixed. The absorbance at 595 nm against blank sample (900 μl of distilled water + 200 μl Bradford reagent) was measured after 5 min incubation. The protein amount was determined from

TABLE 2 | Extraction treatments used.

Abbreviation	Treatment	Exposure and parameters for 0.5 L of algal suspensions (0.4 g d.w./L of suspension)	
NC	Negative control	Algal suspension left on the laboratory desk for 30 min	
PC	Positive control	Detergent added (2,5% sodium dodecyl sulfate, Sigma-Aldrich) for 10 min	
US	Ultrasonication	Ultrasonic homogenizer Cole and Parmer, Chicago Ilinois, 40 W for 10 min, on ice in parts of 50 ml at once	
FT	Freeze-thawing	3 times slow freezing overnight at −20°C and thawing at 22°C	
EL1	Electroporation 1	Circulating in electro flow chamber, flow 0.72 L/min, 10 Hz, 30 min.	3 kV, 100 μs, i ≈ 300 mA
EL2	Electroporation 2		4 kV, 100 μs, i ≈ 550 mA
EL3	Electroporation 3		3 kV, 1 ms, i ≈ 400 mA
EL4	Electroporation 4		4 kV, 1 ms, i ≈ 550 mA

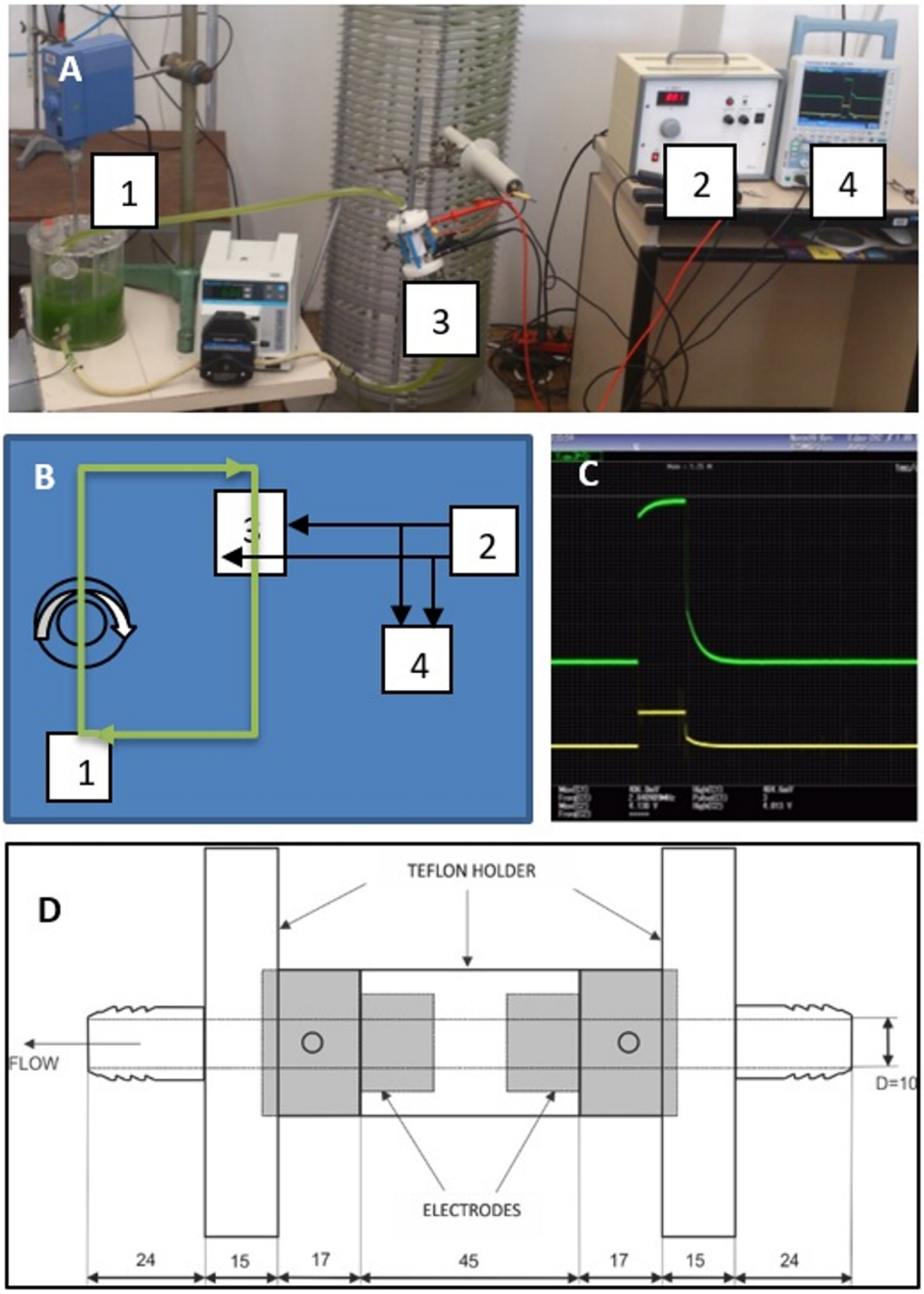

FIGURE 1 | (A) The setup: algal photobioreactor (1) coupled with electroporation device (2) through the flow chamber (3), and electric pulses monitored by oscilloscope (4). **(B)** Schematic presentation of the components as labeled in panel **(A)**. **(C)** An psciloscope snapshot of the monitored unipolar square wave pulse for the setting EL4 as specified in **Table 2** (green curve: voltage reaching the amplitude of 4 kV; yellow curve: electric current reaching the amplitude of 550 mA). **(D)** The flow chamber for electroporation of the algal suspension, with the gray areas representing the electrodes (design by Gianpiero Pataro, University of Salerno-UNISA).

the calibration line prepared using solutions of bovine serum albumin (BSA) in amounts ranging from 1 to 25 μg.

Extracted Lipids Quantification

Lipids released from algae into the non-polar phase were quantified by measuring liquid component concentrations. Each sample of supernatant was vigorously shaken, and a volume of 50 mL was pipetted into a 250 mL flask, to which 50 mL of a mix (1.6:1 volume ratio) of n-hexane (LiChrosolv, Merck) and isopropanol (LiChrosolv, Merck) was added. Immediately after preparation, all samples of algal pellets were shaken intensely in isopropanol for at least 5 min, and then treated in an ultrasound

bath unit for 1 h, where the temperature of samples reached 35°C. Over the night, they were left at room temperature. In the morning, the samples were intensely shaken again and treated in ultrasound bath for another hour. After 5 h of samples rest at room temperature, 3–4 separated phases were visible. In all cases 1 mL of the present most upper phase was filtered through 2 μm syringe filter (Chromafil O-20/25 PTFE, Macherey-Nagel) into the 1.5 mL HPLC vial. The presences of lipid molecules were confirmed by HPLC as described elsewhere (Likozar and Levec, 2014a,b; Likozar et al., 2016).

RESULTS AND DISCUSSION

Cultivation in Photobioreactor for High Biomass Yield

Our cultivation method in photobioreactor for green alga *Chlorella vulgaris* led to high biomass yield (up to 0.4 g/L) which is the basic prerequisite for an extraction technique to be deemed efficient. Balanced nutrient composition and non-limiting source of nitrogen are key elements for maximal protein production, therefore it was assumed reasonable to add nitrogen source during algal growth when nitrogen values in surrounding media dropped under 70% of initial concentrations. For all experiments, direct algal suspension was used, with no concentration of cells prior to extraction. Elemental composition of the medium used and of the main nutrients in *C. vulgaris* are shown in **Table 3**.

Protein Extraction

The decrease and growth regeneration after the treatments is shown in **Figure 2**. Since microscopic observations can not detect all cell changes or injuries and each round green shape is counted as a cell, for further experiments flow cytometry as cell counting method should be employed, providing additional information about cell size, granulation and autofluorescence

TABLE 3 | The elemental composition medium composition and main nutrients (C, carbon; O, oxygen; H, hydrogen; N, nitrogen; P, phosphorous; Na, sodium; Mg, magnesium; S, sulfur) in *C. vulgaris*.

Elements	% in *Chlorella* cell (Oh-Hama, 1988)	Jaworski's medium (%)
C	51.4–72.6	2%
O	11.6–28.5	62%
H	7.0–10.0	3%
N	6.2–7.7	8%
P	1.0–2.0	3%
Na	0.85–1.62	18%
Mg	0.36–0.80	1%
S	0.28–0.39	2%

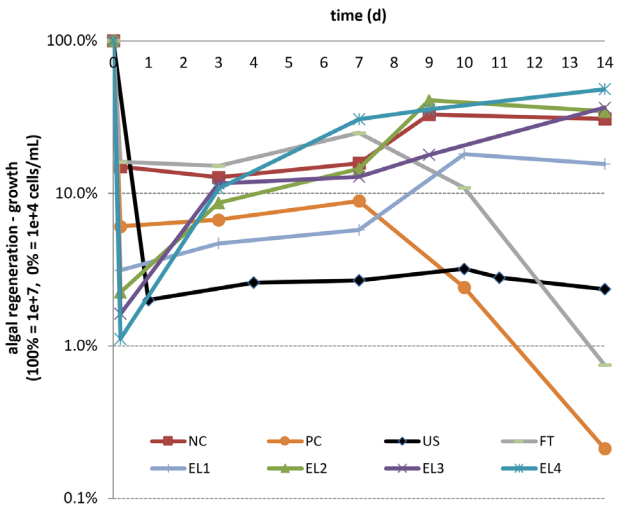

FIGURE 2 | Growth regeneration (average values, calculated from cells per ml ranging from max 1e + 07 = 100% to min 1e + 04 = 0%) after different extraction techniques (abbreviations as in **Table 2**). The first assessment was performed at about 0.5 h after the treatment. After the lag growth phase of several days, the populations of electroporated algal cells (EL1–EL4) resumed growth with the same dynamic as control cells, while no such effect was observed with PC, FT, or US treatment.

of photosynthetic pigments. Temperature and conductivity measurements are presented in **Table 4**.

After each of the investigated extraction treatments, the conductivity increased; in the positive control (PC) with detergent addition, conductivity increased more than 6-fold (by 637%), while after the electroporation, conductivity increased proportionally to the energy input; except for PC, the increase was the highest with EL4 at 23% (**Figure 3**). Membrane conductivity and cell suspension conductivity increased (**Table 4**), due to ions release from cells into the medium due to concentration gradient and membrane increased permeability, which is a consequence of electroporation (Pavlin et al., 2005).

Similarly to conductivity, after electroporation also temperature increased proportionally to the energy input; the temperature increase was the highest with EL4 at 13 ± 6°C (**Table 4**). After centrifugation there was no difference in algal pellets (centrifugates) between different treatments; the pellets represented on average 4 ± 1% of total volume (and 82 ± 15% of total weight) of algal culture, which has been treated with US, FT, EL1, EL2, EL3 or EL4.

Protein content (in mg/L of algal suspension) was calculated to the measured dry weight of algal cultures for every treatment, separately for pellet and supernatant (**Table 5**). In all treatments except US, the mass of the pellet and supernatant were of the same order of magnitude, while with US the pellet was much smaller, reflecting much higher degree of cell fragmentation into debris too small to settle into a pellet upon centrifugation, and resulting in the much higher relative protein content in the supernatant relative to the pellet. In EL1–EL4, Western blot with Coomassie staining performed on the supernatant revealed that the extracted proteins sizes were between 35 and 55 kDa.

TABLE 4 | Average temperature (°C) and conductivity (μS/cm) ± standard deviation, before and after every treatment.

Abbreviation *	Treatment	Conductivity		Temperature	
		Before	After	Before	After
NC	Negative control	223.0 ± 36.6	225.5 ± 34.1	22.4 ± 0.5	22.4 ± 0.5
PC	Positive control	225.7 ± 44.4	1715.7 ± 862.4	22.3 ± 0.3	23.7 ± 0.6
US	Ultrasonication	222.0 ± 4.2	224.8 ± 5.9	21.7 ± 0.9	26.6 ± 3.4
FT	Freeze-thawing	222.0 ± 4.2	232.7 ± 10.3	21.6 ± 0.6	22.0 ± 0.0
EL1	Electroporation 1	227.5 ± 36.4	237.3 ± 33.0	23.1 ± 0.9	25.1 ± 0.7
EL2	Electroporation 2	228.0 ± 35.3	242.5 ± 30.8	22.6 ± 1.4	25.2 ± 0.2
EL3	Electroporation 3	227.0 ± 45.3	263.0 ± 41.1	22.3 ± 1.5	29.6 ± 2.0
EL4	Electroporation 4	226.7 ± 44.0	278.3 ± 53.4	22.3 ± 1.5	35.0 ± 5.1

see **Table 2 for treatment parameters.*

The highest concentration of extracted proteins was obtained in the positive control (PC – chemical lysis), with EL2-EL4 reaching up to 27%, US up to 24%, and FT up to 15% of the yield obtained in PC, respectively (**Figure 4A**). The fraction of the total proteins extracted into the supernatant was also the highest in PC at 30% (with the remaining 70% in the pellet), while with EL2–EL4 it was up to 8%, US up to 7%, and FT up to 5% of the total proteins extracted (**Figure 4B**). While these yields may seem poor, we must bear in mind that PC – especially with alkaline solvents – dissolves not only the cell membrane but also the

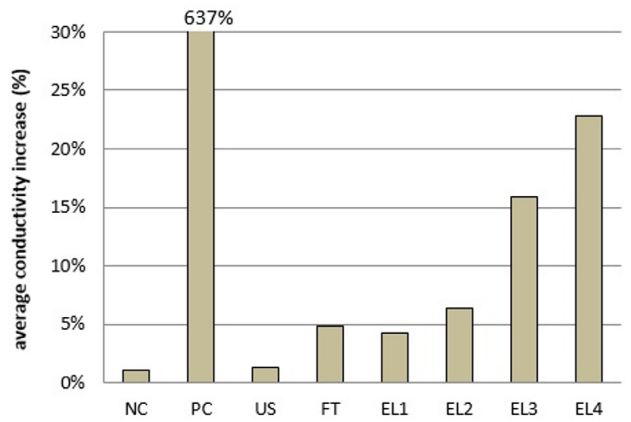

FIGURE 3 | Average electrical conductivity increase for different extraction treatments. NC, negative control; PC, positive control; US, ultrasound; FT, freeze-thaw; EL, electroporation (abbreviations EL1–EL4 as in **Table 2**).

TABLE 5 | Protein (P) content in mg/L of algal suspension and g/g dry weight of algal cultures, separately for pellet (p) and supernatant (s) of different treatments.

	Average P (mg/L)		Average P (g/g dry weight)		Relative P (%)
Treatment*	p	s	p	s	s:p
NC	150.0	7.9	2.9	0.3	11
PC	203.9	89.7	3.9	1.7	43
US	166.5	13.4	2.1	4.9	237
FT	68.1	3.3	2.0	0.2	12
EL1	211.7	11.4	4.0	0.5	12
EL2	168.3	11.8	2.4	0.6	25
EL3	136.9	12.5	2.2	0.7	32
EL4	149.5	13.1	2.3	0.9	38

see **Table 2.*

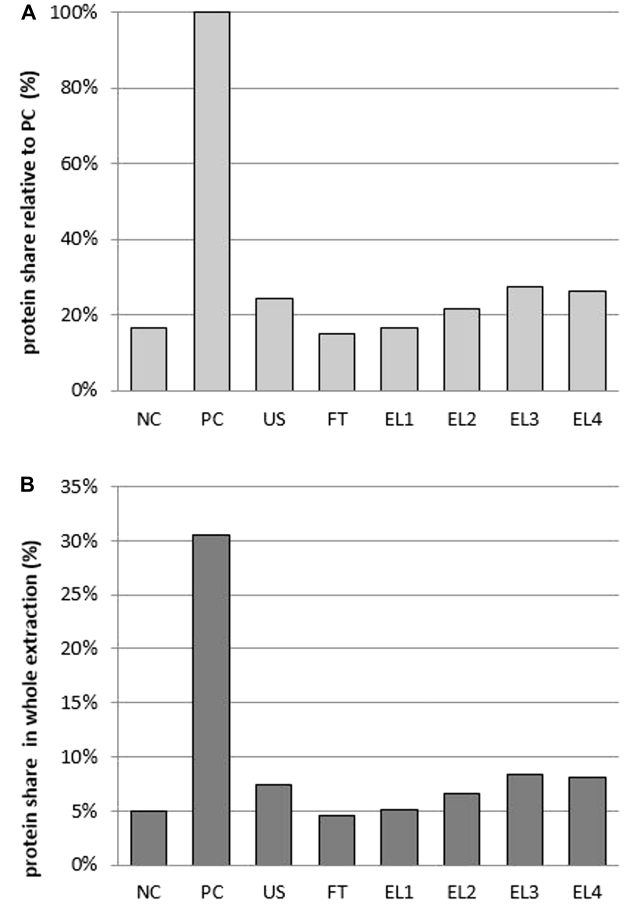

FIGURE 4 | (A) The fraction of extracted protein concentration relative to the positive control. **(B)** The fraction of the total proteins extracted into the supernatant. NC, negative control; PC, positive control; US, ultrasound; FT, freeze-thaw; EL, electroporation (abbreviations EL1–EL4 as in **Table 2**).

cell wall, resulting both in release of previously bound proteins into the supernatant and in complete disintegration of the cell that litters the extract with cells' structural debris. The latter is largely the case also for US, and partly for FT, while in EL the permeabilizing effect can be limited and reversible, with the cells retaining their viability and integrity, and the extract is largely free of this debris.

Algal Growth Regeneration

Successful treatment for extraction of substances from algal cells, where a subpopulation of cells would still remain viable, is based on compromise to disrupt the algal cells sufficiently as to extract compounds, yet mildly enough as to not kill all the cells (reversible permeabilization of algal membrane). In this way, the source of biomass, water and nutrients is recyclable, making the approach non-destructive and contributing to the sustainability of resources for a growing world population (Buchmann et al., 2019). Our findings indicate that after the lag growth phase of a few days, the population of electroporated algal cells grows with the same dynamics as control cells, while this in not true for PC, FT, and US treatment, where growth regeneration could not be reached (see **Figure 2**). Certainly, the viable fraction of biomass also contained reversibly electroporated microalgae, from which there was also some extraction/leakage into the supernatant, which contributed to the initial lag and gradual approach of post-exposure growth rate to the pre-exposure levels (and thus to the biomass regaining its full quality and functionality).

Simultaneous Protein and Lipid Extraction

In some end-user applications of value-added algal substances, it is desired that proteins and lipids are extracted at the same time (e.g., in mixed algae extracts used as a renewable agriculture or aquaculture feedstock). Thus for electroporation as the most yield-efficient and the only non-destructive among the considered solvent-free protein extraction techniques, two preliminary experiments of simultaneous protein/lipid extraction were also investigated, by HPLC, using the same electroporation protocols as above. Although in comparison to glyceryl trioleate model, as a HPLC standard, up to six different oleaginous peaks could be detected in the supernatants of electroporated algal cultures (none in other control samples), the quantities were relatively low, with the fraction of extracted lipids in the supernatant comprising only up to 7% of their total extracted mass (with the remaining 93% in the pellet). As anticipated, positive control revealed 21 different peaks, since cells were lysed with detergent (**Table 6**). Interestingly, the cumulative lipid quantities in NC pellet sample were up to 6.6 g/L, but for electroporation, up to 27.5 g/L (**Table 6**). Increasing the time after electroporation treatment process, combined with centrifugation, may increase yields further. Regarding components, tri-, di- and mono-glycerides were obtained, as well as other fatty acid derivatives, with the distribution of the latter affected by culture. Fractionation of proteins and lipids from the extract could be performed by separation of the water-soluble fraction containing proteins, and subsequent extraction of lipids from the residual by elution in ethanol (Golberg et al., 2016).

TABLE 6 | Concentration (g/L) and number of different lipid substances (HPLC peaks) extracted from *C. vulgaris* after electroporation, separately for pellet and supernatant; NC negative control, PC positive control.

Treatment*	Number of peaks in pellet	Lipids (g/L) in pellet	Number of peaks in supernatants	Lipids (g/L) in supernatants
NC	13	6.6	0	0
PC	21	39.1	0	0
EL1	9	21.6	6	1.2
EL2	8	18.1	5	0.7
EL3	13	27.5	5	0.7
EL4	4	9.6	5	0.7

see **Table 2.*

CONCLUSION

Electroporation, though lower in extraction yields than chemical lysis or mechanical disintegration, is in contrast to them a technique for largely debris-free extraction of proteins from microalgae, with no need for prior concentration or drying, with feasible growth regeneration, and with potential for simultaneous extraction of intracellular algal lipids into the supernatant. While we demonstrated the use of electroporation for extraction of proteins and lipids as primary microalgae products, for the scope of biorefineries other studies have shown it is a promising method for simultaneous extraction of various additional valuable products, ranging from vitamins and carbohydrates (Mahnič-Kalamiza et al., 2014; Postma et al., 2016) to phenols and chlorophylls (Parniakov et al., 2015). This approach furthermore has large potential for upscaling, which is important for industrial use (Kotnik et al., 2015). Regarding the extent of regeneration, further lifecycle analysis will be necessary for it to be broadly recognized. As irreversible electroporation also inactivates microorganisms including pathogens, this approach can simultaneously reduce the risk of infection that is otherwise a common biotechnological problem (Rego et al., 2015).

DATA AVAILABILITY STATEMENT

All datasets generated for this study are included in the article/supplementary material.

AUTHOR CONTRIBUTIONS

TE, JG, and DM conceptualized the study. KF developed the generator of electric pulses. TE and MK conducted the experiments, analyzed the data and interpreted the results on protein extraction. BL conducted the experiments, analyzed the data and interpreted the results on lipid extraction. DM supervised the experimental work. DM and TK critically revised

the results, their interpretation, and improved the manuscript with important intellectual content. All authors have read and approved the submitted manuscript.

FUNDING

The research was supported financially by the Slovenian Research Agency (ARRS) grants P2-0249 and IP-0510, and conducted in the scope of the LEA EBAM Electroporation in Biology and Medicine European Associated Laboratory.

ACKNOWLEDGMENTS

The authors would like to thank Karmen Stanič, Tjaša Čeh, Anja Hajsan, and Anja Zakrajšek for their valuable technical support for the experimental work.

REFERENCES

Aschemann-Witzel, J., Maroscheck, N., and Hamm, U. (2013). Are organic consumers preferring or avoiding foods with nutrition and health claims? *Food Qual. Prefer.* 30, 68–76. doi: 10.1016/j.foodqual.2013.04.011

Becker, E. W. (2007). Micro-algae as a source of protein. *Biotechnol. Adv.* 25, 207–210. doi: 10.1016/j.biotechadv.2006.11.002

Bodénès, P., Bensalem, S., Français, O., Pareau, D., Pioufle, B., and Lopes, F. (2019). Inducing reversible or irreversible pores in *Chlamydomonas reinhardtii* with electroporation: impact of treatment parameters. *Algal Res.* 37, 124–132. doi: 10.1016/j.algal.2018.11.016

Bradford, M. M. (1976). A rapid and sensitive method for the quantitation of microgram quantities of protein utilizing the principle of protein-dye binding. *Anal. Biochem.* 72, 248–254. doi: 10.1016/0003-2697(76)90527-3

Buchmann, L., Brändle, I., Haberkorn, I., Hiestand, M., and Mathys, A. (2019). Pulsed electric field based cyclic protein extraction of microalgae towards closed-loop biorefinery concepts. *Bioresour. Biotechnol.* 291:121870. doi: 10.1016/j.biortech.2019.121870

Carullo, D., Abera, B. D., Casazza, A. A., Donsi, F., Perego, P., Ferrari, G., et al. (2018). Effect of pulsed electric fields and high pressure homogenisation on the aqueous extraction of intracellular compounds from the microalgae *Chlorella vulgaris*. *Algal Res.* 31, 60–69. doi: 10.1016/j.algal.2018.01.017

Chemat, F., Vian, M. A., and Gravotto, G. (2012). Green extraction of natural products: concept and principles. *Int. J. Mol. Sci.* 13, 8615–8627. doi: 10.3390/ijms13078615

Coustets, M., Al-Karablieh, N., Thomsen, C., and Teissie, J. (2013). Flow process for electroextraction of total proteins from microalgae. *J. Membrane Biol.* 246, 751–760. doi: 10.1007/s00232-013-9542-y

Coustets, M., Joubert-Durigneux, V., Hérault, J., Schoefs, B., Blanckaert, V., Garnier, J. P., et al. (2015). Optimization of protein electroextraction from microalgae by a flow process. *Bioelectrochemistry* 103, 74–81. doi: 10.1016/j.bioelechem.2014.08.022

Cuellar-Bermudez, S. P., Aguilar-Hernandez, I., Cardenas-Chavez, D. L., Ornelas-Soto, N., Romero-Ogawa, M. A., and Parra-Saldivar, R. (2015). Extraction and purification of high-value metabolites from microalgae: essential lipids, astaxanthin and phycobiliproteins. *J. Microbiol. Biotechnol.* 8, 190–209. doi: 10.1111/1751-7915.12167

Doucha, J., and Livansky, K. (2008). Influence of processing parameters on disintegration of *Chlorella* cells in various types of homogenizers. *Appl. Microbiol. Biotechnol.* 81, 431–440. doi: 10.1007/s00253-008-1660-6

Draaisma, R. B., Wijffels, R. H., Slegers, P. M. E., Brentner, L. B., Roy, A., and Barbosa, M. J. (2013). Food commodities from microalgae. *Curr. Opin. Biotechnol.* 24, 169–177. doi: 10.1016/j.copbio.2012.09.012

FAO/WHO (1973). *Energy and Protein Requirement: Report of a Joint FAO/WHO ad hoc* Expert Committee, Vol. 52. Geneva: FAO.

Godfray, H. C. J., Beddington, J. R., Crute, I. R., Haddad, L., Lawrence, D., Muir, J. F., et al. (2010). Food security: the challenge of feeding 9 billion people. *Science* 327, 812–818. doi: 10.1126/science.1185383

Goettel, M., Eing, C., Gusbeth, C., Straessner, R., and Frey, W. (2013). Pulsed electric field assisted extraction of intracellular valuables from microalgae. *Algal Res.* 2, 401–408. doi: 10.1016/j.algal.2013.07.004

Golberg, A., Sack, M., Teissié, J., Pataro, G., Pliquett, U., Saulis, G., et al. (2016). Energy-efficient biomass processing with pulsed electric fields for bioeconomy and sustainable development. *Biotechnol. Biofuels* 9:94. doi: 10.1186/s13068-016-0508-z

Gong, Y., and Jiang, M. (2011). Biodiesel production with microalgae as feedstock: from strains to biodiesel. *Biotechnol. Lett.* 33, 1269–1284. doi: 10.1007/s10529-011-0574-z

Gouveia, L., and Oliveira, A. C. (2009). Microalgae as a raw material for biofuels production. *J. Ind. Microbiol. Biotechnol.* 36, 269–274. doi: 10.1007/s10295-008-0495-6

Grimi, N., Dubois, A., Marchal, L., Jubeau, S., Lebovka, N., and Vorobiev, E. (2014). Selective extraction from microalgae *Nannochloropsis* sp. using different methods of cell disruption. *Bioresour. Technol.* 153, 254–259. doi: 10.1016/j.biortech.2013.12.011

Günerken, E., D'Hondt, E., Epping, M. H. M., Garcia-Gonyaley, L., Elst, K., and Wijffels, R. H. (2015). Cell disruption for microalgae biorefineries. *Biotechnol. Adv.* 33, 243–260. doi: 10.1016/j.biotechadv.2015.01.008

Halim, R., Harun, R., Danquah, M. K., and Webley, P. A. (2012). Microalgal cell disruption for biofuel development. *Appl. Energy* 91, 116–121. doi: 10.1016/j.apenergy.2011.08.048

Hannon, M., Gimpel, J., Tran, M., Rasala, B., and Mayfield, S. (2010). Biofuels from algae: challenges and potential. *Biofuels* 1, 763–784. doi: 10.4155/bfs.10.44

Hopkins, T. R. (1991). Physical and chemical cell disruption for the recovery of intracellular proteins. *Bioprocess Technol.* 12, 57–83.

Kotnik, T., Frey, W., Sack, M., Haberl Meglič, S., Peterka, M., and Miklavčič, D. (2015). Electroporation-based applications in biotechnology. *Trends Biotechnol.* 33, 480–488. doi: 10.1016/j.tibtech.2015.06.002

Kotnik, T., Rems, L., Tarek, M., and Miklavčič, D. (2019). Membrane electroporation and electropermeabilization: mechanisms and models. *Annu. Rev. Biophys.* 48, 63–91. doi: 10.1146/annurev-biophys-052118-115451

Likozar, B., and Levec, J. (2014a). Effect of process conditions on equilibrium, reaction kinetics and mass transfer for triglyceride transesterification to biodiesel: experimental and modeling based on fatty acid composition. *Fuel Process. Technol.* 122, 30–41. doi: 10.1016/j.fuproc.2014.01.017

Likozar, B., and Levec, J. (2014b). Transesterification of canola, palm, peanut, soybean and sunflower oil with methanol, ethanol, isopropanol, butanol and tert-butanol to biodiesel: modelling of chemical equilibrium, reaction kinetics and mass transfer based on fatty acid composition. *Appl. Energy* 123, 108–120. doi: 10.1016/j.apenergy.2014.02.046

Likozar, B., Pohar, A., and Levec, J. (2016). Transesterification of oil to biodiesel in a continuous tubular reactor with static mixers: modelling reaction kinetics, mass transfer, scale-up and optimization considering fatty acid composition. *Fuel Process. Technol.* 142, 326–336. doi: 10.1016/j.fuproc.2015.10.035

Mahnič-Kalamiza, S., Vorobiev, E., and Miklavčič, D. (2014). Electroporation in food processing and biorefinery. *J. Membrane Biol.* 247, 1279–1304. doi: 10.1007/s00232-014-9737-x

McMillan, J. R., Watson, I. A., Ali, M., and Jaafar, W. (2013). Evaluation and comparison of algal cell disruption methods: microwave, water bath, blender, ultrasonic and laser treatment. *Appl. Energy* 103, 128–134. doi: 10.1016/j.apenergy.2012.09.020

Middelberg, A. P. J. (1995). Process-scale disruption of microorganisms. *Biotechnol. Adv.* 13, 491–551. doi: 10.1016/0734-9750(95)02007-P

Olaizola, M. (2003a). Commercial development of microalgal biotechnology: from the test tube to the marketplace. *Biomol. Eng.* 20, 459–466. doi: 10.1016/S1389-0344(03)00076-5

Olaizola, M. (2003b). Microalgal removal of CO2 from flue gases: changes in medium pH and flue gas composition do not appear to affect the photochemical yield of microalgal cultures. *Biotechnol. Bioprocess Eng.* 8, 360–367. doi: 10.1007/BF02949280

Parada, J., and Aguilera, J. M. (2007). Food microstructure affects the bioavailability of several nutrients. *J. Food Sci.* 72, 21–32. doi: 10.1111/j.1750-3841.2007.00274.x

Parniakov, O., Apicella, E., Koubaa, M., Barba, F. J., Grimi, N., Lebovka, N., et al. (2015). Ultrasound-assisted green solvent extraction of high-added value compounds from microalgae *Nannochloropsis* spp. *Bioresour. Technol.* 198, 262–267. doi: 10.1016/j.biortech.2015.09.020

Pavlin, M., Kandušer, M., Reberšek, M., Pucihar, G., Hart, F. X., Magjareviæ, R., et al. (2005). Effect of cell electroporation on the conductivity of a cell suspension. *Biophys. J.* 88, 4378–4390. doi: 10.1529/biophysj.104.048975

Postma, P. R., Miron, T. L., Olivieri, G., Barbosa, M. J., Wijffels, R. H., and Epping, M. H. M. (2015). Mild disintegration of the green microalgae *Chlorella vulgaris* using bead milling. *Bioresour. Technol.* 184, 297–304. doi: 10.1016/j.biortech.2014.09.033

Postma, P. R., Pataro, G., Capitoli, M., Barbosa, M. J., Wijffels, R. H., Eppink, M. H. M., et al. (2016). Selective extraction of intracellular components from the microalga *Chlorella vulgaris* by combined pulsed electric field - temperature treatment. *Bioresour. Technol.* 203, 80–88. doi: 10.1016/j.biortech.2015.12.012

Prabakaran, P., and Ravindran, A. D. (2011). A comparative study on effective cell disruption methods for lipid extraction from microalgae. *Lett. Appl. Microbiol.* 53, 150–154. doi: 10.1111/j.1472-765X.2011.03082.x

Pulz, O., and Gross, W. (2004). Valuable products from biotechnology of microalgae. *Appl. Microbiol. Biotechnol.* 65, 635–648. doi: 10.1007/s00253-004-1647-x

Rego, D., Redondo, L. M., Geraldes, V., Costa, L., Navalho, J., and Pereira, M. T. (2015). Control of predators in industrial scale microalgae cultures with pulsed electric fields. *Bioelectrochemistry* 103, 60–64. doi: 10.1016/j.bioelechem.2014.08.004

Safi, C., Cabas Rodriguez, L., Mulder, W. J., Engelen-Smit, N., Spekking, W., van den Broek, L. A. M., et al. (2017). Energy consumption and water-soluble protein release by cell wall disruption of *Nannochloropsis gaditana*. *Bioresour. Technol.* 239, 204–210. doi: 10.1016/j.biortech.2017.05.012

Safi, C., Charton, M., Pignolet, O., Silvestre, F., Vaca-Garcia, C., and Pontalier, P. Y. (2012). Influence of microalgae cell wall characteristics on protein extractability and determination of nitrogen-to-protein conversion factors. *J. Appl. Phycol.* 25, 523–529. doi: 10.1007/s10811-012-9886-1

Schlösser, U. G. (1982). Sammlung von algenkulturen. *Ber. Deutsch. Bot. Ges.* 95, 181–276. doi: 10.1111/j.1438-8677.1982.tb02862.x

Shen, L., Wang, X., Wang, Z., Wu, Y., and Chen, J. (2008). Studies on tea protein extraction using alkaline and enzyme methods. *Food Chem.* 107, 929–938. doi: 10.1016/j.foodchem.2007.08.047

Skrede, A., Mydland, L. T., Ahlstrøm, Ø, Reitan, K. I, and Øverland, M. (2011). Evaluation of microalgae as sources of digestible nutrients for monogastric animals. *J. Animal Feed Sci.* 20, 131–142. doi: 10.22358/jafs/66164/2011

Tilman, D., Balzer, C., Hill, J., and Befort, B. L. (2011). Global food demand and the sustainable intensification of agriculture. *Proc. Natl. Acad. Sci. U.S.A.* 108, 20260–20264. doi: 10.1073/pnas.1116437108

t'Lam, G. P., Postma, P. R., Fernandes, D. A., Timmermans, R. A. H., Vermuë, M. H., Barbosa, M. J., et al. (2017). Pulsed electric field for protein release of the microalgae *Chlorella vulgaris* and *Neochloris oleoabundans*. *Algal Res.* 24A, 181–187. doi: 10.1016/j.algal.2017.03.024

Vanthoor-Koopmans, M., Wijffels, R. H., Barbosa, M., and Eppink, M. H. M. (2013). Biorefinery of microalgae for food and fuel. *Bioresour. Technol.* 135, 142–149. doi: 10.1016/j.biortech.2012.10.135

Walker, T. L., Purton, S., Becker, D. K., and Collet, C. (2005). Microalgae as bioreactors. *Plant Cell Rep.* 24, 629–641. doi: 10.1007/s00299-005-0004-6

Widjaja, A., Chien, C. C., and Ju, Y. H. (2009). Study on increasing lipid production from fresh water microalgae *Chlorella vulgaris*. *J. Taiwan Inst. Chem. Eng.* 40, 13–20. doi: 10.1016/j.jtice.2008.07.007

Wijffels, R. H., Barbosa, M., Michel, H. M., and Eppink, M. H. M. (2010). Microalgae for the production of bulk chemicals and biofuels. *Biofuels Bioprod. Bioref.* 4, 287–295. doi: 10.1002/bbb.215

Conflict of Interest: The authors declare that the research was conducted in the absence of any commercial or financial relationships that could be construed as a potential conflict of interest.

Copyright © 2020 Eleršek, Flisar, Likozar, Klemenčič, Golob, Kotnik and Miklavčič. This is an open-access article distributed under the terms of the Creative Commons Attribution License (CC BY). The use, distribution or reproduction in other forums is permitted, provided the original author(s) and the copyright owner(s) are credited and that the original publication in this journal is cited, in accordance with accepted academic practice. No use, distribution or reproduction is permitted which does not comply with these terms.

frontiers in Bioengineering and Biotechnology

ORIGINAL RESEARCH
published: 19 May 2020
doi: 10.3389/fbioe.2020.00396

Development of a Multi-Pulse Conductivity Model for Liver Tissue Treated With Pulsed Electric Fields

Yajun Zhao[1,2], Shuang Zheng[3,4], Natalie Beitel-White[2,5], Hongmei Liu[3,4], Chenguo Yao[3,4] and Rafael V. Davalos[1,2]*

[1] Department of Biomedical Engineering and Mechanics, Virginia Tech, Blacksburg, VA, United States, [2] Bioelectromechanical Systems Laboratory, Virginia Tech, Blacksburg, VA, United States, [3] State Key Laboratory of Power Transmission Equipment and System Security and New Technology, Chongqing University, Chongqing, China, [4] School of Electrical Engineering, Chongqing University, Chongqing, China, [5] Department of Electrical and Computer Engineering at Virginia Tech, Blacksburg, VA, United States

Pulsed electric field treatment modalities typically utilize multiple pulses to permeabilize biological tissue. This electroporation process induces conductivity changes in the tissue, which are indicative of the extent of electroporation. In this study, we characterized the electroporation-induced conductivity changes using all treatment pulses instead of solely the first pulse as in conventional conductivity models. Rabbit liver tissue was employed to study the tissue conductivity changes caused by multiple, 100 μs pulses delivered through flat plate electrodes. Voltage and current data were recorded during treatment and used to calculate the tissue conductivity during the entire pulsing process. Temperature data were also recorded to quantify the contribution of Joule heating to the conductivity according to the tissue temperature coefficient. By fitting all these data to a modified Heaviside function, where the two turning points (E_0, E_1) and the increase factor (A) are the main parameters, we calculated the conductivity as a function of the electric field (E), where the parameters of the Heaviside function (A and E_0) were functions of pulse number (N). With the resulting multi-factor conductivity model, a numerical electroporation simulation can predict the electrical current for multiple pulses more accurately than existing conductivity models. Moreover, the saturating behavior caused by electroporation can be explained by the saturation trends of the increase factor A in this model. The conductivity change induced by electroporation has a significant increase at about the first 30 pulses, then tends to saturate at 0.465 S/m. The proposed conductivity model can simulate the electroporation process more accurately than the conventional conductivity model. The electric field distribution computed using this model is essential for treatment planning in biomedical applications utilizing multiple pulsed electric fields, and the method proposed here, relating the pulse number to the conductivity through the variables in the Heaviside function, may be adapted to investigate the effect of other parameters, like pulse frequency and pulse width, on electroporation.

Keywords: pulsed electric field, electroporation, dynamic process, cumulative effect, tissue conductivity, tumor ablation, treatment planning

OPEN ACCESS

Edited by:
Saša Haberl Meglič, University of Ljubljana, Slovenia

Reviewed by:
Udi Sarig, Technion Israel Institute of Technology, Israel
Bor Kos, University of Ljubljana, Slovenia

****Correspondence:***
Yajun Zhao
yajun@vt.edu

Specialty section:
This article was submitted to Industrial Biotechnology, a section of the journal Frontiers in Bioengineering and Biotechnology

Received: *03 December 2019*
Accepted: *08 April 2020*
Published: *19 May 2020*

Citation:
Zhao Y, Zheng S, Beitel-White N, Liu H, Yao C and Davalos RV (2020) Development of a Multi-Pulse Conductivity Model for Liver Tissue Treated With Pulsed Electric Fields. Front. Bioeng. Biotechnol. 8:396. doi: 10.3389/fbioe.2020.00396

INTRODUCTION

Electroporation is a bioelectric phenomenon that employs high intensity, short duration pulsed electric fields (PEFs) to create reversible or irreversible defects in the cell membrane (Weaver and Chizmadzhev, 1996). Reversible electroporation (RE) occurs when the cell is able to recover from these defects and maintain high viability following treatment; alternatively, beyond a certain threshold, the process is irreversible and leads to cell death (termed irreversible electroporation, IRE) (Kotnik et al., 2012). Both RE and IRE are emerging oncological therapies (Mir et al., 1991; Yao et al., 2004; Davalos et al., 2005; Onik and Rubinsky, 2010). Electrochemotherapy (ECT) and gene electrotransfer (GET) utilize RE while IRE is mostly used as a non-thermal tumor ablation modality (Golberg and Yarmush, 2013; Haberl et al., 2013; Yarmush et al., 2013). Recently, another improved type of IRE termed high-frequency IRE (HFIRE) (Arena et al., 2011; Sano et al., 2015, 2018) was proved to ablate tumors with a benefit of mitigating muscle contraction and showed some promising results (Dong et al., 2018; DeWitt et al., 2019).

Therapeutic efficacy in either of these therapies is dependent on adequate coverage of the target area with electric fields capable of inducing electroporation; thus, clinicians are in need of tools capable of providing information regarding ablation outcome. In addition to post-treatment imaging using ultrasound, computed tomography (CT), or magnetic resonance imaging (MRI) (Onik and Rubinsky, 2010; Sommer et al., 2013; Ting et al., 2016), real-time evaluation of the ablation outcome has been proposed in recent studies (Ivorra et al., 2009; Zhao et al., 2018b). Pre-treatment visualization of the expected treatment zone also aids in achieving complete ablation (Edd and Davalos, 2007). However, the size and shape of the ablation are influenced by a number of factors, including electrode spacing and exposure, applied voltage, pulsing protocol, and tissue properties. These factors can be accounted for by using numerical models to predict the treatment zone (Neal et al., 2012). Pre-treatment planning models must account for the dynamic change in conductivity of the target tissue. This non-linearity is due to the nature of electroporation, in which low-resistance pathways form in cellular membranes within the target tissue. This change in resistance is dependent on the local electric field strength, causing a redistribution in the electric field (Davalos et al., 2004; Sel et al., 2005) and thus the expected treatment zone. Several studies have investigated this redistribution of the electric field caused by dynamic conductivity (Sel et al., 2005; Neal et al., 2012; Corovic et al., 2013; Zhao et al., 2018a), however, most of these studies only use the first treatment pulse to quantify the change of conductivity as a function of electric field. The effects induced by subsequent pulses are approximately reflected by the temperature rise in some studies (Garcia et al., 2010, 2011; Neal et al., 2012; Zhao et al., 2018a). In reality, electroporation causes cell membranes to become more permeable to ions, increasing the bulk conductivity. This effect can be enhanced as more pulses are applied. In this respect, electroporation can be viewed as a cumulative process, which means the pulse number should be incorporated into the conductivity model, making the numerical model more realistic. Langus et al. developed a model that described the dynamic conductivity as a function of electric field, temperature, and time (Langus et al., 2016). This model is complex, though it was well verified in reversible studies that employ eight pulses. In the case of multi-pulse IRE treatments, which employ dozens of pulses, to our knowledge, no study has developed a model that incorporates all three aspects.

In the present study, the often-used Heaviside function was employed to characterize the dynamic development of the conductivity as a function of electric field, temperature, and pulse number. Flat plate electrodes were used to deliver pulses to rabbit liver samples. The resulting voltage and current data were recorded to calculate the conductivity based on the constant shape factor of the flat plate electrodes, and the recorded temperature rise was used to quantify its contribution to the conductivity. The relationship between electric field strength and conductivity was then quantified using the Heaviside function, with the parameters as functions of pulse number. Finally, the dynamic conductivity model was used in a computational model employing the finite element method to predict the pulsed electrical current induced by multiple pulses. These results were compared to those obtained by using an existing conductivity model (Neal et al., 2012). The conductivity model presented in this study will be useful for developing a time-domain numerical model to study the electroporation process accounting for pulse number, electric field, and temperature.

MATERIALS AND METHODS

Experimental Setup

Rabbit liver was obtained from the Experimental Animal Center of Chongqing Medical University. All procedures were in agreement with the Ethics Committee of Chongqing Medical University. The livers were acquired within 5 min of sacrifice and all tests were conducted within 1 h of organ procurement to prevent the effects of tissue degradation. Livers were placed in phosphate-buffered saline (PBS) in a cooler with ice before treatment to reduce the effect of metabolism on the tissue properties. Prior to the measurement, the liver samples were removed from the PBS and dried using paper tissue. Then they were cut into small pieces and filled in a 3D printed, polylactic acid (PLA) cylindrical mold as shown in **Figure 1A**. Every liver can be used to prepare about 6 samples, and 8 livers in total were used for this study. The mold features a slot for placement of a Luxtron m600 OEM fiber optic probe (FOT Lab Kit, LumaSense Technologies, Santa Clara, CA, United States), and the tissue temperature was sampled at 1 Hz. At the top center of the mold, there is a cylindrical space with a diameter of 1 cm and a height of 5 mm in which the tissue sample was placed. A total of 90 pulses were delivered for each experiment with an inter-pulse delay of 1 s and a pulse width of 100 μs. Applied electric field magnitude was varied for conductivity modeling: 100, 200, 400, 600, 800, 1,200, 1,400, 1,600, 1,800, 2,000, and 2,800 V/cm, while the magnitudes of 500, 1,000, 1,500, and 2,500 V/cm were used to verify the conductivity model. Every pulse magnitude was tested in 3 samples. All voltage and current data were recorded by an oscilloscope (WavePro 760Zi-A, Teledyne LeCroy Inc.,

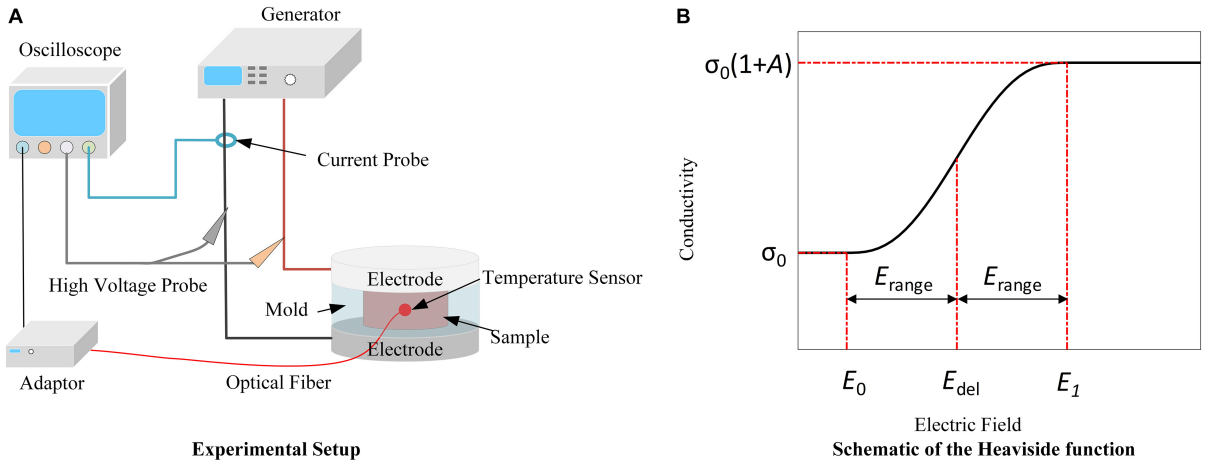

FIGURE 1 | Schematics of the experimental setup **(A)** and the Heaviside function **(B)**. **(A)** Delivery of PEFs through flat plate electrodes enables conductivity measurements during multi-pulse treatments. Temperature is recorded by the fiber optic sensor to account for its contribution to the conductivity. **(B)** Due to electroporation, the tissue conductivity will change from its initial value (σ_0) to the final value [$\sigma_0(1 + A)$] with the transition zone from $E_{del}-E_{range}$ (E_0) to $E_{del} + E_{range}$ (E_1).

New York, NY, United States) with a high voltage probe (PPE-5 kV) and a current sensor (Pearson 6600, Pearson Electronics Inc., Palo Alto, CA, United States). The temperature was recorded by the fiber optic sensor, and the adaptor was connected to the oscilloscope with TrueTemp software installed. The experimental setup is shown in **Figure 1A**. Since 100 μs pulses were applied in this study, the transient capacitive current was not considered, and the conductivity was calculated using the average voltage and current from the last 4 μs of each pulse (**Supplementary Figure S1**). The conductivity of the tissue was obtained by (1):

$$\sigma = \frac{I \cdot L}{U \cdot S} \quad (1)$$

Where U(V) and I(A) are the averages of the last 4 μs of the recorded voltage and the current, respectively, L(m) is the thickness of the sample and S(m^2) is the cross-sectional area of the sample.

Dynamic Model of Conductivity

At the end of each consecutive pulse, the calculated conductivity at different electric fields can be described. For each of the 90 pulses, a Heaviside function (2) describing conductivity as a function of electric field was fit to the experimental data (Zhao et al., 2018a).

$$\sigma(|E|, T) = \sigma_0 \cdot \left(1 + A \cdot flc2hs\left(E - E_{del}, E_{range}\right) + \alpha \cdot (T - T_0)\right) \quad (2)$$

Here, σ_0(S/m) is the initial conductivity of the tissue before treatment, A is the increase factor of the conductivity after treatment, *flc2hs* is the Heaviside function, E_{del}(V/m) and E_{range}(V/m) define the transition zone (**Figure 1B**); and the exact expression of the function can be found in the **Supplementary Material S2**. In (2), the value of $\sigma_0 \cdot A \cdot flc2hs\ (E-E_{del}, E_{range})$ changes from 0 to $\sigma_0 \cdot A$ with the transition from $E_{del}-E_{range}$, defined as E_0(V/m), to $E_{del} + E_{range}$, defined as E_1(V/m). This term is used to describe the contribution of electroporation to conductivity. More information about these parameters can be found in Zhao et al. (2018a). E is the electric field magnitude (V/m), and α(1/°C) is the coefficient that reflects the conductivity change due to temperature variation. Here, the value of 2% was chosen from the literature (Duck, 2013). T(°C) is the real-time tissue temperature, and T_0 is the initial temperature before treatment, set to 24°C. The temperature data for fitting were from our measurements. Therefore, the three terms on the right side of the equation quantify the tissue's intrinsic electrical properties (σ_0), electroporation effect ($\sigma_0 \cdot A$), and temperature effect [$\sigma_0 \cdot \alpha(T-T_0)$], respectively.

After fitting the conductivity and electric field data to the Heaviside function, the value of the main variables (A_i, E_{del_i}, and E_{range_i}, where i is the pulse number from 1 to 90) in the conductivity model for each pulse number was determined. E_0 and E_1 are the two turning points of the curve, indicating the points at which the conductivity begins to increase and begins to saturate, respectively. The change of these two variables with pulse number is intuitive; with more pulses applied, the tissue would be easier to electroporate, which means lower electric fields (turning points) can induce the conductivity change resulting from electroporation. Therefore, our hypothesis is that the asymptote of E_0, the electric field where tissue conductivity starts to change, approaches zero when the pulse number tends to infinity. According to analysis from the **Supplementary Material S3**, E_1 does not change much with pulse number (< 5%). Thus, E_0 was chosen as the fitting parameter in lieu of E_{del} and E_{range}. The following data fitting was conducted to establish models for E_0 and A, which are treated as functions of pulse number. This process served as a bridge to build the relationship between the pulse number and the tissue conductivity variation caused by PEFs. According to the trends of these variables, the symmetrical sigmoidal function (3) was used to describe the relationship between A and the pulse number

(Lin et al., 2012), while the change of E_0 with pulse number was reflected by Equation (4).

$$A = a_1\left(1-\left(1+N\cdot b_1^{-1}\right)^{-c_1}\right),\quad (a_1, b_1,\ c_1 > 0) \tag{3}$$

$$E_0 = a_2 N^{-1} + b_2 e^{-c_2 N},\quad \left(a_2, b_2,\ c_2 \geq 0\right) \tag{4}$$

Here, N is the pulse number, and $a_{(1,2)}$, $b_{(1,2)}$, and $c_{(1,2)}$ are coefficients determined by data fitting. MATLAB (R2018b, MathWorks) and Excel (Microsoft Office Professional Plus 2019) were used to perform the curve fitting and data analysis, respectively.

Validation of the Conductivity Model

The pulse parameters with varied electric field magnitude (500, 1,000, 1,500, 2,500 V/cm) were used to verify the conductivity model by comparing the experimental current outputs and the numerical results. Two cylinders with diameters of 2 cm and thicknesses of 2 mm were built in COMSOL Multiphysics (v.5.4, Stockholm, Sweden) as two flat plate copper electrodes. Another cylinder with 2 cm diameter, 5 mm height and a 1 cm diameter through-hole in the center was constructed to represent the 3D printed mold used in experiments. The tissue sample was modeled as a cylinder with a diameter of 1 cm and a height of 5 mm. The Laplace equation was used to solve for the electrical potential, and the electric field distribution was obtained by taking the gradient of the electrical potential:

$$\nabla\cdot\left(\sigma\left(E, N, T\right)\nabla\varphi\right) = 0 \tag{5}$$

$$E = -\nabla\varphi \tag{6}$$

Here, $\sigma\ (E, N, T)$ is the tissue conductivity which is a function of electric field, pulse number, and temperature; E is the electric field, N is the pulse number and T is the temperature.

Temperature in the finite element model was calculated by a modified heat conduction equation including the Joule heating term:

$$\nabla\cdot\left(k\nabla T\right) + \frac{\sigma\left|\nabla\varphi\right|^2\cdot d}{\tau} = \rho c_p\frac{\partial T}{\partial t} \tag{7}$$

Here, k is the thermal conductivity of the tissue, c_p is the tissue heat capacity, ρ is the tissue density, and $\sigma|\nabla\varphi|^2$ is the Joule heating term which was scaled according to the pulse width d divided by the period τ, averaging the heating over the entire treatment (Neal et al., 2012). Since the tissue sample and the contacting area between the electrodes and the tissue are relatively small, the generated Joule heating will not have a significant effect on the outside boundary of the electrodes and the mold. Therefore, the outside boundary of the electrodes and the mold was set to room temperature, 24°C. The blood perfusion and metabolic heat were not included since the studies were conducted *ex vivo*. Parameters values used here are shown in **Table 1**.

To determine the impact of incorporating multiple pulse tissue conductivity parameters in the proposed model, a comparison was made to the existing conventional conductivity model, $\sigma(E, T)$, where the tissue conductivity is determined following the first pulse. From the proposed model, the conventional conductivity model can be obtained by setting the pulse number, N, to 1 pulse; subsequent increases in tissue conductivity are then attributed solely to Joule heating effects (Garcia et al., 2010, 2011; Neal et al., 2012; Zhao et al., 2018a). The normal current density over the middle plane of the tissue which was in parallel with the electrodes was integrated to obtain the total current delivered to the tissue (Equation 8), which was used to compare the agreement of the results between simulation and experiments.

$$I_s = \iint \text{ec.normJ} \tag{8}$$

Here, ec.normJ is the magnitude of current density perpendicular to the middle plane of the tissue which is in parallel with the flat plate electrodes. I_s is the calculated current that is used to compare with the experimental results.

The error between the experimental data and the simulated results was described by the root-mean-square error (RMSE) (Barnston, 1992):

$$RMSE = \left[\sum_{i=1}^{n}\left(f_i - y_i\right)^2/n\right]^{1/2} \tag{9}$$

Here, n is the total applied pulse number. f_i is the simulated results, and y_i is the data from the experiments. A smaller RMSE indicates lower error between the simulation results and the experimental results, demonstrating a more accurate prediction.

RESULTS AND DISCUSSION

In this study, we applied 90, 100 μs pulses to capture the dynamic change of tissue conductivity caused by electroporation. The initial transient tissue response, mostly capacitive current, to the pulses was not included in calculating the tissue conductivity change caused by electroporation (Neal et al., 2012). The tissue conductivity during each pulse was quantified by the end of each voltage and current pulse (details can be found in the **Supplementary Material S1**). The conductivity and temperature change with pulse number at different electric fields is shown in **Figure 2** (only 4 magnitudes are shown). With higher electric field and more pulses applied, the tissue conductivies and temperature rise increase. The dynamic behavior of each conductivity curve in **Figure 2** can be divided into two parts: first, the non-linear change happens during the first few dozen pulses, which mainly reflects the cumulative effect of multiple pulses on electroporation. However, this non-linear behavior could not be captured by the conventional conductivity model which was based solely on the first pulse (the electroporation effect), and the temperature rise (cumulative effect of multiple pulses). After the initial non-linearity, the tissue conductivity seems to increase linearly with pulse number, potentially indicating that the electroporation effect saturated, and the increase in conductivity is likely attributed to increases in temperature. This non-linear process might provide insight into the electroporation process in tissue. In this study, we quantified this non-linear process by creating mathematical models.

TABLE 1 | Material properties used for the simulation.

Material	Parameter	Value	Unit	References
Liver	ρ, density	1,079	kg/m^3	Zhao et al., 2018a
	c_p, heat capacity	3,540	J/kg/K	Zhao et al., 2018a
	k, thermal conductivity	0.52	W/m/K	Zhao et al., 2018a
PLA	ρ, density	1,252	kg/m^3	Farah et al., 2016
	c_p, heat capacity	1,590	J/kg/K	Farah et al., 2016
	k, thermal conductivity	0.11	W/m/K	Farah et al., 2016
	σ, electrical conductivity	1e–16	S/m	Zenkiewicz et al., 2011
Electrode (Copper)	ρ, density	8,960	kg/m^3	Comsol Material Library
	c_p, heat capacity	385	J/kg/K	Comsol Material Library
	k, thermal conductivity	400	W/m/K	Comsol Material Library
	σ, electrical conductivity	5.998e7	S/m	Comsol Material Library

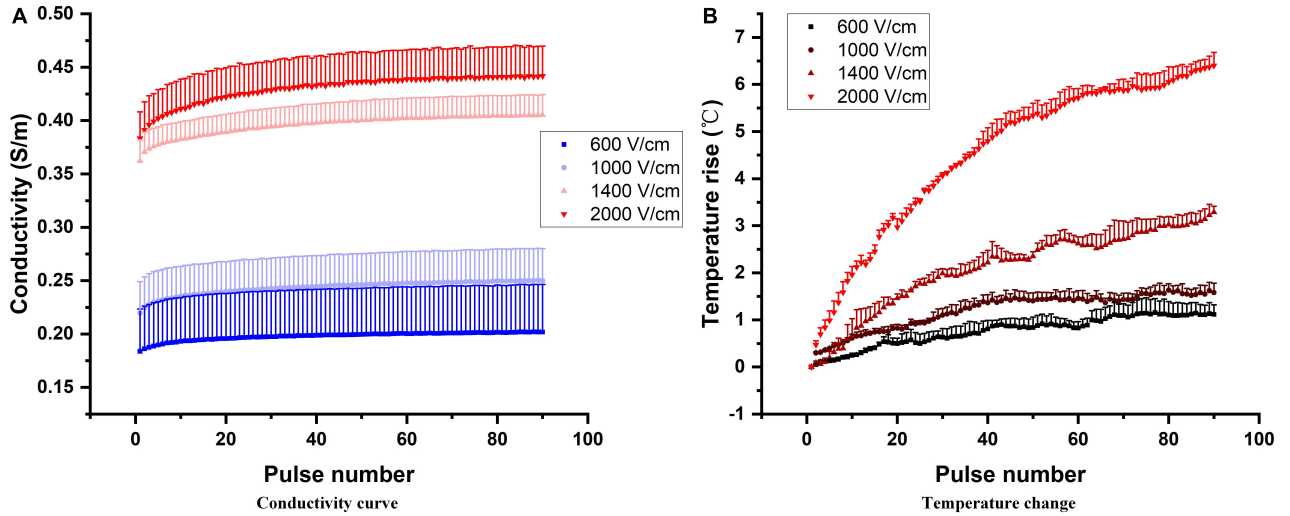

FIGURE 2 | Conductivity dependency on pulse number at different electric field magnitudes **(A)**. Increasing electric field magnitudes cause a vertical shift in multi-pulse conductivity. Pulse number also has an effect on the dynamic behavior of the conductivity, as reflected in the non-linear increase during the first few dozen pulses and nearly linear increase with the subsequent pulses. The temperature rise at those corresponding pulse parameters is shown **(B)**.

Data Fitting Results

The tissue conductivity change during electroporation is a suitable indirect method to help us further understand the dynamic process of electroporation (Sel et al., 2005; Neal et al., 2012; Zhao et al., 2018a). In this study, all treatment voltage and current pulses were recorded to obtain the tissue conductivity change during the entire treatment process. **Figure 3** shows the tissue conductivity at different electric field strengths at 4 specific pulse numbers. The experimental data were fitted using (2) at each pulse number, and the fitted curves are shown as the solid line in **Figure 3**. The coefficients of determination, R^2, for all 90 curves (data were shown in the **Supplementary Material S4**) were above 0.85 which indicates acceptable data fitting accuracy. As more pulses are applied, the conductivities at higher electric fields were a little upward shift rather than flat which was caused by the temperature rise. At lower electric field strengths, the tissue was not electroporated, and the conductivity at these fields was the initial conductivity of the tissue. After data fitting, the results showed that the initial conductivity for different pulse numbers did not change significantly, as expected. The initial conductivity for (2) was determined as the average of all the initial values of conductivity for different pulse numbers, calculated to be 0.137 S/m in this study.

After fitting the conductivity data, the change in the variables (A, E_0) with increasing pulse number was obtained, as shown in **Figure 4**. Each hollow circle in the figure represents a value of A or E_0 determinted by the data fitting using Equation (2) for a specific pulse number. Therefore, there are 90 values of A and E_0, respectively. The coefficients of determination R^2 for each curve fit are shown below each figure, which indicates successful fitting results for these two parameters.

The obtained equations for these two parameters are shown below:

$$A = 2.3919 \times \left(1 - \left(1 + N \cdot 0.0018^{-1}\right)^{-0.2802}\right) \quad (10)$$

$$E_0 = 8.0861 \times 10^3 N^{-1} + 2.9056 \times 10^4 e^{-0.0027N} \, (V/m) \quad (11)$$

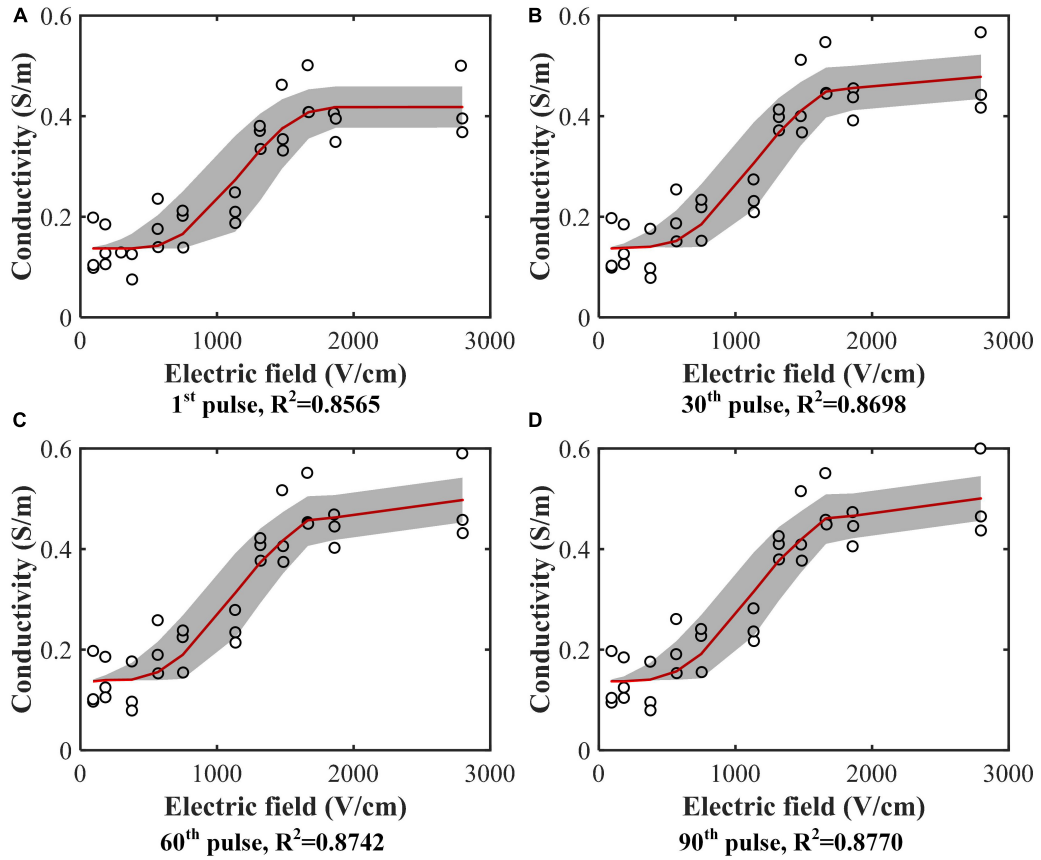

FIGURE 3 | Conductivity data (hollow circle) from experiments with the fitted curves [red solid line, Equation (2)]. Conductivity values were calculated at each electric field magnitude at the **(A)** 1st pulse, **(B)** 30th pulse, **(C)** 60th pulse, and **(D)** 90th pulse. Curves were fitted for each case. The gray band is the 95% confidence interval of the fitting. All the fitting results can be found in the **Supplementary Material S4**.

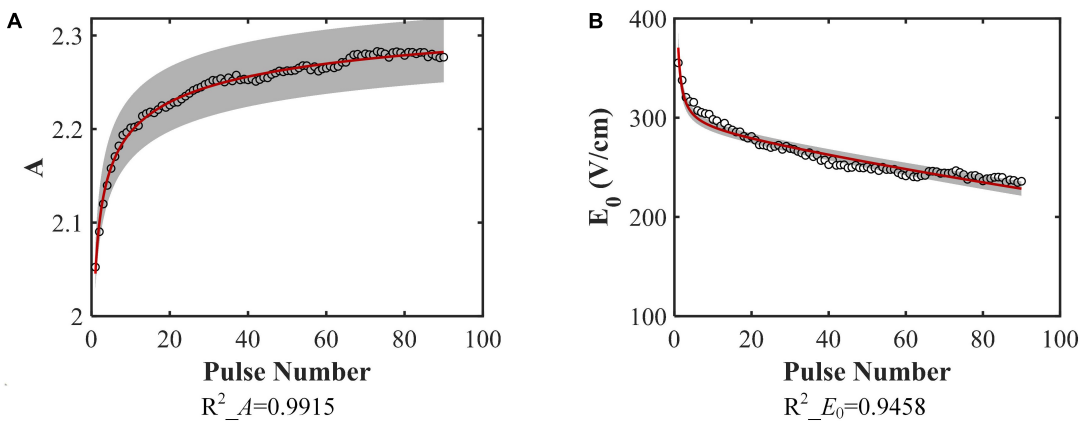

FIGURE 4 | Model parameters. **(A)** *A*, **(B)** E_0 change with increasing pulse number and the data fitting results [**A:** Equation (3), **B:** Equation (4)]. The coefficients of determination of the fitting are given below each figure. The gray band is the 95% confidence interval of the fitting. They don't include 0, indicating that they are significantly different from 0.

where N is the pulse number. From these equations, the top and bottom limits for each parameter are readily identifiable. Since N must be a non-negative integer, the lower limit for these parameters will be obtained at $N = 0$, which means no pulses are applied. When $N = 0$, $A = 0$, and E_0 tends to infinity. The upper limit can be obtained when

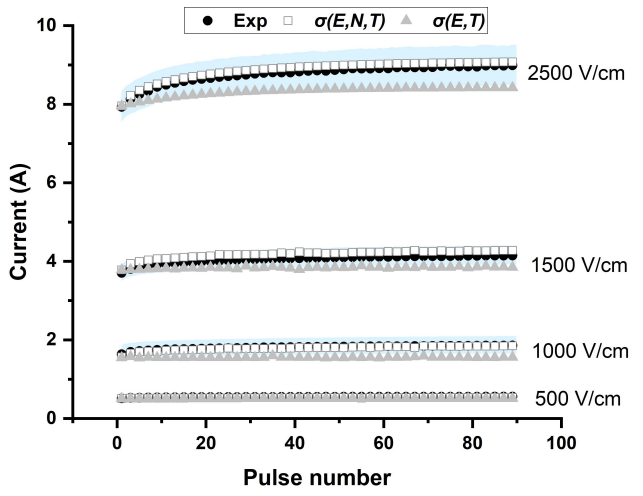

FIGURE 5 | The presented conductivity model [σ(*E*, *N*, *T*)] predicts the experimental current more accurately than the conventional model [σ(*E*, *T*)]. The experimental data are plotted as the mean (black solid circle) and standard deviation (light blue shadow).

N tends to infinity; in this case, $A = 2.3919$, and E_0 tends toward 0.

Validation of Outcome and Comparison With Conventional Conductivity Model

The conductivity model in this study, which is a function of electric field, pulse number, and temperature, can be obtained by inserting (10–11) into (2). To verify the model, the experimental results of the selected pulse parameters were compared to the numerical results. To compare the conductivity model proposed in this study, σ(*E*, *N*, *T*), and the conventional conductivity model, σ(*E*, *T*), the electrical current calculated using these two models in COMSOL and the experimental data at different pulse numbers are shown in **Figure 5**. As expected, the current obtained from the conventional model was almost linear with increasing pulse number. The non-linear portion during the first 20–30 pulses cannot be replicated by the conventional conductivity model but is captured using the σ(*E*, *N*, *T*) model. These results show that the conductivity model developed herein can describe the electroporation process for multiple pulses more accurately than σ (*E*, *T*).

Figure 6 presents the relative errors which were calculated at each point (pulse number) using the simulated data and the averaged experimental data (black solid circle in **Figure 5**). **Table 2** shows the RMSE values for four electric field magnitudes which are used to verify the conductivity model. From **Figure 6**, the relative errors for σ(*E*, *N*, *T*) are all below 0.05. In **Table 2**, RMSEs for σ(*E*, *N*, *T*) are all smaller than those of σ(*E*, *T*). Both the results show that the predicted data using σ(*E*, *N*, *T*) has lower errors than the data obtained by σ(*E*, *T*). At lower electric field magnitude, both of these models have low RMSE values; this is likely due to a lesser extent of tissue electroporation. Therefore, cumulative electroporation effects are not obvious. For higher electric field magnitude, the error of σ(*E, T*) increases sharply after the first few dozen pulses since the cumulative effect is not included.

Parameter Variation of Conductivity Model

In this study, the Heaviside function with a continuous second derivative was used to describe the change of tissue conductivity with different pulse parameters. Excluding the effect of the temperature, the conductivity variation caused by electroporation will change from σ_0 to $\sigma_0(1 + A)$. From **Figure 4A**, with the application of multiple pulses, A will change from its initial value to its asymptote with a value of 2.3919, which indicates that the conductivity change resulting from electroporation will be saturated at the value of 0.465 S/m for rabbit liver tissue. This conclusion is also consistent with previous work indicating that when tissue is completely electroporated, the conductivity will cease changing due to electroporation (Ivorra and Rubinsky, 2007; Maor et al., 2009). Some studies reported that the ablation zone of IRE tended to be saturated after dozens of pulses (Miklovic et al., 2017) which could reflect the saturation behavior too.

The conductivity curve excluding the temperature effect can clearly reflect the electroporation process, as shown in **Figure 7**. After the first few dozen pulses, the plateau of each curve, $\sigma_0(1 + A)$, begins to saturate, indicative of a change in A with pulse number. The first inflection point moves to a lower value with a higher pulse number which can also be seen from the change in E_0. The variation of the inflection point indicates that lower electric fields can induce tissue conductivity changes when more pulses are applied, which means that the tissue will be easier to electroporate with more pulses applied. This might be an explanation of the observation that the electric field threshold for IRE was lower with more pulses applied (Bonakdar et al., 2015; Bhonsle et al., 2016; Zhao et al., 2018a).

Figure 5 shows that the model proposed in this study can describe the electroporation process more accurately than the typically used conductivity model. The proposed conductivity model which includes the effect from electric field, pulse number, and temperature can help us understand the electroporation process at the tissue level, and would result in more precise treatment planning. In this study, a non-linear process is obvious during the first few dozen pulses (∼30 pulses); however, this does not necessarily ensure that ∼30 pulses can induce irreversible electroporation. Since the recovery process was not evaluated in this study, more pulses are most likely needed to maintain the electroporation effect and create a relatively stable irreversible electroporation outcome. Future work should pay more attention to the recovery process of the tissue after electroporation. Incorporating these effects will allow for the optimization of pulse parameters (pulse magnitude, pulse number, et al.) which need to be applied to induce expected irreversible electroporation effects.

The success of IRE treatment depends on a good treatment planning of IRE. Olivier Gallinato et al. (2019) proposed a numerical workflow of IRE based on the real clinical situation

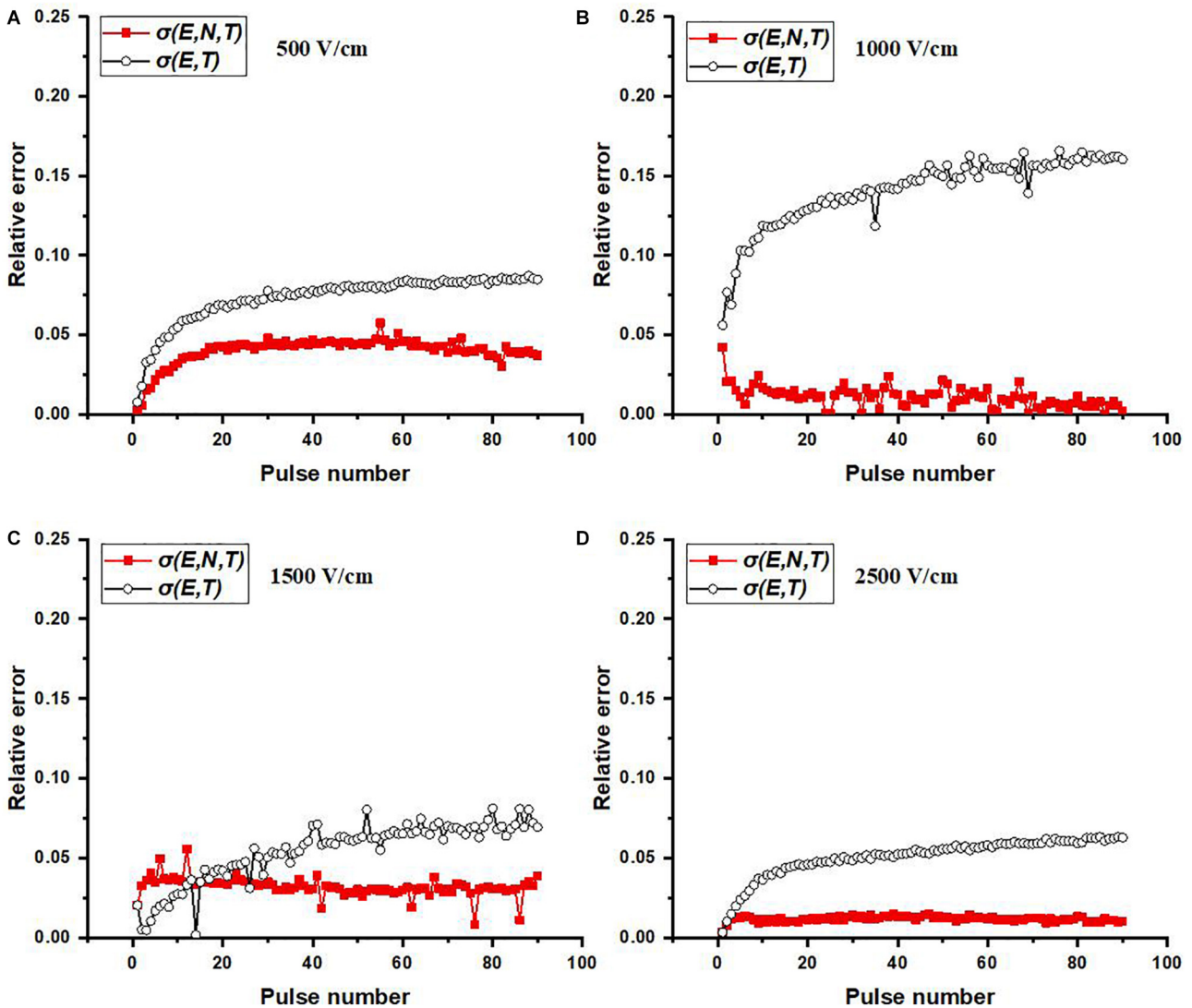

FIGURE 6 | Relative errors at each pulse number for varied electric field magnitudes: **(A)** 500, **(B)** 1,000, **(C)** 1,500, and **(D)** 2,500 V/cm. Relative error at each pulse number is calculated by | simulated value – averaged experimental value| /averaged experimental value.

TABLE 2 | Root-mean-square error between simulated and experimental results based on two conductivity models.

Conductivity model	RMSE			
	500 V/cm	1,000 V/cm	1,500 V/cm	2,500 V/cm
$\sigma(E, N, T)$	0.0592	0.3724	0.4593	0.8404
$\sigma(E, T)$	0.0839	0.5800	0.5678	1.1423

(placement of electrodes and the response current) which should be the future trend to make patient-specific treatment planning. The significant part of making treatment planning is the calculation of the electric field distribution which is affected by the tissue conductivity distribution during the treatment. Damien Voyer et al. (2018) recently built a dynamic model of tissue electroporation based on the equivalent circuit approach at the tissue level. By their model, the electroporation models at cell and tissue levels can be linked, which is good for us to understand the electroporation process in tissue. This model was validated by the first pulse; applications with more pulses, such as 90 pulses for IRE, still need to be further studied. In the present study, the conductivity model can be used to predict the current for 90 pulses accurately. However, this is only valid for the current at the end of the pulse rather than the entire pulse.

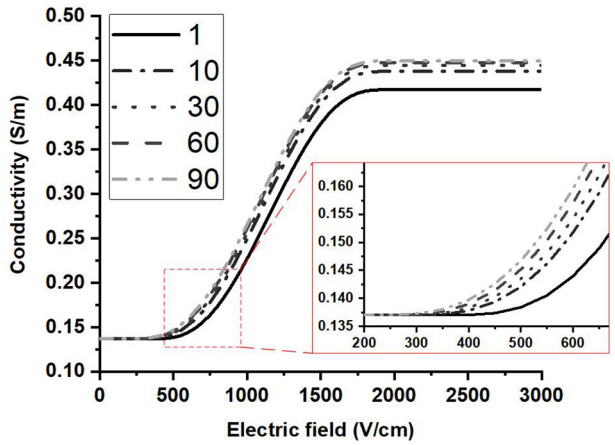

FIGURE 7 | Conductivity vs. electric field curves are shown at different pulse numbers based on the proposed conductivity model. The contribution of the temperature change to the conductivity was not included. The plateau of each curve saturates after a few dozen pulses.

In the chosen conductivity model (2), the parameter A incorporates changes due to electroporation, that is, the formation of new current pathways through cell membranes. We expect that this effect would also be influenced by temperature rise. Some studies use an alternate expression (12) to describe the contribution of the temperature rise to the conductivity (O'Brien et al., 2018, 2019):

$$\sigma(|E,|T) = \sigma_0 \cdot (1 + A \cdot flc2hs\left(E - E_{\text{del}}, E_{\text{range}}\right)(1 + \alpha \cdot (T - T_0)) \quad (12)$$

In this equation, the influence of temperature rise is based on the conductivity after electroporation; however, in the present study, the temperature rise was calculated based on the initial temperature. Calculating temperature effect in this manner will overestimate the contribution of the temperature to some extent, which will make A decrease with pulse number within a certain pulse number range. In the present study, we calculated the temperature effect based on the initial conductivity which will consequently underestimate the effect, as part of the temperature effect was incorporated into A. This issue is also one of the reasons we mentioned later that it is difficult to completely decouple the temperature and the electroporation effects. However, with the conductivity model proposed in this study, the trends of A can still represent the cumulative effect of electroporation, leading us to choose Equation (2).

Limitations of This Study

This study proposed a method to build the relationship between the conductivity changes of PEF-treated tissue and the pulse parameters (pulse number, electric field, and temperature) which accounts for the cumulative effects of pulses. Using the presented model, the change of the parameters A and E_0 can be easily understood and used to explain some experimental results. Another limitation is our assumption of the often-used pulsing frequency of 1 Hz. The model might change with the pulsing frequency. However, this method might be still effective, and the effects of the pulsing frequency could be incorporated into the model. Additionally, this is an *ex vivo* study and only tested liver tissue. *In vivo* studies are needed, and more tissues need to be verified in the future. Finally, from **Figure 5**, at 2,500 V/cm, the numerically calculated current with our model $\sigma(E, N, T)$ at higher pulse number was slightly larger than experimental current, but still closer than the prediction from the conventional model $\sigma(E, T)$, which also can be found from the relative errors of **Figure 6**. This might be caused by our assumption of the tissue temperature coefficient. In the literature, α has been reported to be between 1 and 3% for soft tissue (Duck, 2013) and may vary based on tissue type and temperature. The conductivity model we used here incorporates an α value of 2%, which led to a trend in A which was consistent with what we would expect with cumulative electroporation effects. However, it should be noted that without knowing the exact α, our experimental setup made it impossible to completely decouple the contributions from the electroporation and thermal effects in the model. In the future, the dynamic change of temperature coefficient α should be further investigated. By incorporating these efforts, the cell death model of IRE (Golberg and Rubinsky, 2010; Garcia et al., 2014) and the multi-pulse conductivity model proposed here, the more accurate ablation zone of IRE can be predicted.

CONCLUSION

In this study, the cumulative conductivity model as a function of electric field, pulse number, and temperature for rabbit liver tissue was established. By using this model, the simulated electrical currents at different pulse numbers were in good agreement with experimental results. The presented model demonstrated closer predictions of experimental current than an existing conventional conductivity model. Also, the non-linear process of electroporation can be partly described by changes in the parameters of the model. The electroporation process yields an obvious tissue conductivity change during the first few dozens of pulses (~30) and tends to saturate. While the pulse number was considered in this study, the method proposed here can be easily transferred to investigate the effect of other parameters on dynamic conductivity changes.

DATA AVAILABILITY STATEMENT

The datasets generated for this study are available on request to the corresponding author.

ETHICS STATEMENT

The animal study was reviewed and approved by Ethics Committee of Chongqing Medical University.

AUTHOR CONTRIBUTIONS

YZ, CY, and RD designed the experiments and directed the modeling process. YZ, SZ, and HL performed the experiments and analyzed the data. YZ, SZ, and NB-W established the conductivity model and ran the numerical simulation. YZ and NB prepared the manuscript. All the authors read and approved the final manuscript.

FUNDING

This work was supported by grants from the National Institute of Health award R01 CA240476 and the National Natural Science Foundation of China (51877022).

ACKNOWLEDGMENTS

We acknowledge support from the Institute for Critical Technology and Applied Science (ICTAS) and the Center for Engineered Health (CEH) at Virginia Tech for their support of this research.

SUPPLEMENTARY MATERIAL

The Supplementary Material for this article can be found online at: https://www.frontiersin.org/articles/10.3389/fbioe.2020.00396/full#supplementary-material

FIGURE S1 | Typical current waveform during electroporation. Shown here is the response current of 1000 V which is 2000 V/cm in our study.

FIGURE S2 | Dependency of E_0, E_1, and A with pulse number obtained by fitting the experimental data to equation (2).

FIGURE S3 | E_1 changes little with pulse number when compared with A and E_0 after fitting the conductivity data to the Heaviside function for all 90 pulses. The percent changes of E_0, E_1, and A at different pulse numbers were calculated using Equation (1).

TABLE S1 | Fitting results of A and E_0.

REFERENCES

Arena, C. B., Sano, M. B., Rossmeisl, J. H., Caldwell, J. L., Garcia, P. A., Rylander, M. N., et al. (2011). High-frequency irreversible electroporation (H-FIRE) for non-thermal ablation without muscle contraction. *Biomed. Eng. Online* 10:102. doi: 10.1186/1475-925X-10-102

Barnston, A. G. (1992). Correspondence among the correlation, RMSE, and Heidke forecast verification measures; refinement of the Heidke score. *Weather Forecast.* 7, 699–709. doi: 10.1175/1520-0434(1992)007<0699:catcra>2.0.co;2

Bhonsle, S., Bonakdar, M., Neal, R. E., Aardema, C., Robertson, J. L., Howarth, J., et al. (2016). Characterization of irreversible electroporation ablation with a validated perfused organ model. *J. Vasc. Int. Radiol.* 27, 1913.e2–1922.e2.

Bonakdar, M., Latouche, E. L., Mahajan, R. L., and Davalos, R. V. (2015). The feasibility of a smart surgical probe for verification of IRE treatments using electrical impedance spectroscopy. *IEEE Trans. Biomed. Eng.* 62, 2674–2684. doi: 10.1109/tbme.2015.2441636

Corovic, S., Lackovic, I., Sustaric, P., Sustar, T., and Rodic, T. (2013). Modeling of electric field distribution in tissues during electroporation. *BioMed. Eng. Online* 2:16. doi: 10.1186/1475-925x-12-16

Davalos, R. V., Mir, L., and Rubinsky, B. (2005). Tissue ablation with irreversible electroporation. *Anna. Biomed. Eng.* 33, 223–231.

Davalos, R. V., Otten, D. M., Mir, L. M., and Rubinsky, B. (2004). Electrical impedance tomography for imaging tissue electroporation. *IEEE Trans. Biomed. Eng.* 51, 761–767. doi: 10.1109/tbme.2004.824148

DeWitt, M. R., Lattouche, E., Kaufman, J. D., Fesmire, C. C., Swet, J., Kirks, R., et al. (2019). Simplified non-thermal tissue ablation with a single insertion device enabled by bipolar high-frequency pulses. *IEEE Trans. Biomed. Eng.*

Dong, S., Wang, H., Zhao, Y., Sun, Y., and Yao, C. (2018). First human trial of high-frequency irreversible electroporation therapy for prostate cancer. *Technol. Cancer Res. Treatm.* 17:533033818789692.

Duck, F. A. (2013). *Physical Properties of Tissues: a Comprehensive Reference Book*. Cambridge, MA: Academic press.

Edd, J. F., and Davalos, R. V. (2007). Mathematical modeling of irreversible electroporation for treatment planning. *Technol. Cancer Res. Treatm.* 6, 275–286. doi: 10.1177/153303460700600403

Farah, S., Anderson, D. G., and Langer, R. (2016). Physical and mechanical properties of PLA, and their functions in widespread applications - A comprehensive review. *Adv. Drug Deliv Rev.* 107, 367–392. doi: 10.1016/j.addr.2016.06.012

Gallinato, O., de Senneville, B. D., Seror, O., and Poignard, C. (2019). Numerical workflow of irreversible electroporation for deep-seated tumor. *Phys. Med. Biol.* 64:055016. doi: 10.1088/1361-6560/ab00c4

Garcia, P. A., Davalos, R. V., and Miklavcic, D. (2014). A numerical investigation of the electric and thermal cell kill distributions in electroporation-based therapies in tissue. *PLoS One* 9:e103083. doi: 10.1371/journal.pone.0103083

Garcia, P. A., Rossmeisl, J. H., Neal, R. E., Ellis, T. L., and Davalos, R. V. (2011). A parametric study delineating irreversible electroporation from thermal damage based on a minimally invasive intracranial procedure. *Biomed. Eng. Online* 10:34.

Garcia, P. A., Rossmeisl, J. H., Neal, R. E., Ellis, T. L., Olson, J. D., Henao-Guerrero, N., et al. (2010). Intracranial nonthermal irreversible electroporation: in vivo analysis. *J. Membr. Biol.* 236, 127–136. doi: 10.1007/s00232-010-9284-z

Golberg, A., and Rubinsky, B. (2010). A statistical model for multidimensional irreversible electroporation cell death in tissue. *Biomed. Eng. Online* 9:13. doi: 10.1186/1475-925X-9-13

Golberg, A., and Yarmush, M. L. (2013). Nonthermal irreversible electroporation: fundamentals, applications, and challenges. *IEEE Trans. Biomed. Eng.* 60, 707–714. doi: 10.1109/tbme.2013.2238672

Haberl, S., Miklavcic, D., Sersa, G., Frey, W., and Rubinsky, B. (2013). Cell Membrane electroporation-Part 2: the applications. *IEEE Electr. Insul. Mag.* 29, 29–37. doi: 10.1109/Mei.2013.6410537

Ivorra, A., Al-Sakere, B., Rubinsky, B., and Mir, L. M. (2009). In vivo electrical conductivity measurements during and after tumor electroporation: conductivity changes reflect the treatment outcome. *Phys. Med. Biol.* 54, 5949–5963. doi: 10.1088/0031-9155/54/19/019

Ivorra, A., and Rubinsky, B. (2007). In vivo electrical impedance measurements during and after electroporation of rat liver. *Bioelectrochemistry* 70, 287–295. doi: 10.1016/j.bioelechem.2006.10.005

Kotnik, T., Kramar, P., Pucihar, G., Miklavcic, D., and Tarek, M. (2012). Cell membrane electroporation-part 1: the phenomenon. *Electr. Insul. Mag. IEEE* 28, 14–23. doi: 10.1109/mei.2012.6268438

Langus, J., Kranjc, M., Kos, B., Šuštar, T., and Miklavčič, D. (2016). Dynamic finite-element model for efficient modelling of electric currents in electroporated tissue. *Sci. Rep.* 6:26409.

Lin, D., Shkedy, Z., Yekutieli, D., Amaratunga, D., and Bijnens, L. (2012). *Modeling Dose-Response Microarray data in Early Drug Development Experiments Using R: Order-Restricted Analysis of Microarray Data*. Berlin: Springer Science & Business Media.

Maor, E., Ivorra, A., and Rubinsky, B. (2009). Non thermal irreversible electroporation: novel technology for vascular smooth muscle cells ablation. *PLoS One* 4:e4757. doi: 10.1371/journal.pone.0004757

Miklovic, T., Latouche, E. L., DeWitt, M. R., Davalos, R. V., and Sano, M. B. (2017). A comprehensive characterization of parameters affecting high-frequency

irreversible electroporation lesions. *Ann. Biomed. Eng.* 45, 2524–2525. doi: 10.1007/s10439-017-1889-2

Mir, L. M., Belehradek, M., Domenge, C., Orlowski, S., Poddevin, B., Belehradek, J. J., et al. (1991). Electrochemotherapy, a new antitumor treatment: first clinical trial. *C. R. Acad. Sci. III* 313, 613–618.

Neal, R. E. II, Garcia, P. A., Robertson, J. L., and Davalos, R. V. (2012). Experimental characterization and numerical modeling of tissue electrical conductivity during pulsed electric fields for irreversible electroporation treatment planning. *IEEE Trans. Biomed. Eng.* 59, 1076–1085. doi: 10.1109/TBME.2012.2182994

O'Brien, T. J., Bonakdar, M., Bhonsle, S., Neal, R. E., Aardema, C. H. Jr., Robertson, J. L., et al. (2018). Effects of internal electrode cooling on irreversible electroporation using a perfused organ model. *Int. J. Hyperther.* 35, 44–55. doi: 10.1080/02656736.2018.1473893

O'Brien, T. J., Lorenzo, M. F., Zhao, Y., Neal, I. R. E., Robertson, J. L., Goldberg, S. N., et al. (2019). Cycled pulsing to mitigate thermal damage for multi-electrode irreversible electroporation therapy. *Int. J. Hyperthermia* 36, 953–963. doi: 10.1080/02656736.2019.1657187

Onik, G., and Rubinsky, B. (2010). *Irreversible Electroporation: First Patient Experience Focal Therapy of Prostate Cancer*. Berlin: Springer.

Sano, M. B., Arena, C. B., Bittleman, K. R., DeWitt, M. R., Cho, H. J., Szot, C. S., et al. (2015). Bursts of bipolar microsecond pulses inhibit tumor growth. *Sci. Rep.* 5:14999.

Sano, M. B., Fan, R. E., Cheng, K., Saenz, Y., Sonn, G. A., Hwang, G. L., et al. (2018). Reduction of muscle contractions during irreversible electroporation therapy using high-frequency bursts of alternating polarity pulses: a laboratory investigation in an ex vivo swine model. *J. Vasc. Int. Radiol.* 29, 893.e4–898.e4.

Sel, D., Cukjati, D., Batiuskaite, D., Slivnik, T., Mir, L. M., and Miklavcic, D. (2005). Sequential finite element model of tissue electropermeabilization. *IEEE Trans. Biomed. Eng.* 52, 816–827. doi: 10.1109/tbme.2005.845212

Sommer, C. M., Fritz, S., Wachter, M. F., Vollherbst, D., Stampfl, U., Bellemann, N., et al. (2013). Irreversible electroporation of the pig kidney with involvement of the renal pelvis: technical aspects, clinical outcome, and three-dimensional CT rendering for assessment of the treatment zone. *J. Vasc. Int. Radiol.* 24, 1888–1897. doi: 10.1016/j.jvir.2013.08.014

Ting, F., Tran, M., Böhm, M., Siriwardana, A., Van Leeuwen, P., Haynes, A., et al. (2016). Focal irreversible electroporation for prostate cancer: functional outcomes and short-term oncological control. *Prost. Cancer Prost. Dis.* 19, 46–52. doi: 10.1038/pcan.2015.47

Voyer, D., Silve, A., Mir, L. M., Scorretti, R., and Poignard, C. (2018). Dynamical modeling of tissue electroporation. *Bioelectrochemistry* 119, 98–110. doi: 10.1016/j.bioelechem.2017.08.007

Weaver, J. C., and Chizmadzhev, Y. A. (1996). Theory of electroporation: a review. *Bioelectrochem. Bioenerget.* 41, 135–160. doi: 10.1016/s0302-4598(96)05062-3

Yao, C., Sun, C., Mi, Y., Xiong, L., and Wang, S. (2004). Experimental studies on killing and inhibiting effects of steep pulsed electric field (SPEF) to target cancer cell and solid tumor. *Plasma Sci. IEEE Trans.* 32, 1626–1633. doi: 10.1109/tps.2004.832621

Yarmush, M. L., Golberg, A., Serša, G., Kotnik, T., and Miklavčič, D. (2013). Electroporation-based technologies for medicine: principles, applications, and challenges. *Annu. Rev. Biomed. Eng.* 16, 295–320. doi: 10.1146/annurev-bioeng-071813-104622

Zenkiewicz, M., Richert, J., Rytlewski, P., and Richert, A. (2011). Selected electrical and thermal properties of polylactide/graphite composites. *Polimery* 56, 489–493. doi: 10.14314/polimery.2011.489

Zhao, Y., Bhonsle, S., Dong, S., Lv, Y., Liu, H., and Safaai-Jazi, A. (2018a). Characterization of conductivity changes during high-frequency irreversible electroporation for treatment planning. *IEEE Trans. Biomed. Eng.* 65, 1810–1819. doi: 10.1109/TBME.2017.2778101

Zhao, Y., Liu, H., Bhonsle, S. P., Wang, Y., Davalos, R. V., and Yao, C. (2018b). Ablation outcome of irreversible electroporation on potato monitored by impedance spectrum under multi-electrode system. *Biomed. Eng. Online* 17:126. doi: 10.1186/s12938-018-0562-9

Conflict of Interest: RD and NB-W have pending and accepted patents on IRE.

The remaining authors declare that the research was conducted in the absence of any commercial or financial relationships that could be construed as a potential conflict of interest.

Copyright © 2020 Zhao, Zheng, Beitel-White, Liu, Yao and Davalos. This is an open-access article distributed under the terms of the Creative Commons Attribution License (CC BY). The use, distribution or reproduction in other forums is permitted, provided the original author(s) and the copyright owner(s) are credited and that the original publication in this journal is cited, in accordance with accepted academic practice. No use, distribution or reproduction is permitted which does not comply with these terms.

frontiers in Bioengineering and Biotechnology

ORIGINAL RESEARCH
published: 23 July 2020
doi: 10.3389/fbioe.2020.00819

Proof-of-Concept of Electrical Activation of Liposome Nanocarriers: From Dry to Wet Experiments

Laura Caramazza[1,2†], Martina Nardoni[3†], Annalisa De Angelis[2], Patrizia Paolicelli[3], Micaela Liberti[1,2], Francesca Apollonio[1,2] and Stefania Petralito[3]*

[1] ICEmB at DIET, Sapienza University of Rome, Rome, Italy, [2] Center for Life Nano Science@Sapienza, Istituto Italiano di Tecnologia, Rome, Italy, [3] Department of Drug Chemistry and Technologies, Sapienza University of Rome, Rome, Italy

The increasing interest toward biocompatible nanotechnologies in medicine, combined with electric fields stimulation, is leading to the development of electro-sensitive smart systems for drug delivery applications. To this regard, recently the use of pulsed electric fields to trigger release across phospholipid membranes of liposomes has been numerically studied, for a deeper understanding of the phenomena at the molecular scale. Aim of this work is to give an experimental validation of the feasibility to control the release from liposome vesicles, using nanosecond pulsed electric fields characterized by a 10 ns duration and intensity in the order of MV/m. The results are supported by multiphysics simulations which consider the coupling of three physics (electromagnetics, thermal and pore kinetics) in order to explain the occurring physical interactions at the microscopic level and provide useful information on the characteristics of the train of pulses needed to obtain quantitative results in terms of liposome electropermeabilization. Finally, a complete characterization of the exposure system is also provided to support the reliability and validity of the study.

Keywords: nanosecond pulsed electric fields, liposome vesicles, controlled release, electroporation, electropermeabilization, exposure systems, multiphysics modeling

OPEN ACCESS

Edited by:
Saša Haberl Meglič, University of Ljubljana, Slovenia

Reviewed by:
Nuno F. Azevedo, University of Porto, Portugal
Xiaobo Liu, The University of Hong Kong, Hong Kong

***Correspondence:**
Francesca Apollonio
francesca.apollonio@uniroma1.it

[†] These authors have contributed equally to this work

Specialty section:
This article was submitted to Bioprocess Engineering, a section of the journal Frontiers in Bioengineering and Biotechnology

Received: *15 April 2020*
Accepted: *26 June 2020*
Published: *23 July 2020*

Citation:
Caramazza L, Nardoni M, De Angelis A, Paolicelli P, Liberti M, Apollonio F and Petralito S (2020) Proof-of-Concept of Electrical Activation of Liposome Nanocarriers: From Dry to Wet Experiments. Front. Bioeng. Biotechnol. 8:819. doi: 10.3389/fbioe.2020.00819

INTRODUCTION

In the last few decades, there has been great interest in developing drug delivery systems involving the use of liposomal nanodevices carriers, as promising tools either for treatment of cancer diseases (Rosenblum et al., 2018; Senapati et al., 2018; Riley et al., 2019) or for non-cancer ones such as cardiovascular, neurological and autoimmune disorders, respiratory system diseases, skin illness (Bayat et al., 2020; Moncalvo et al., 2020). Liposomes are like toolboxes of lipids which can be manipulated, tuned and manufactured to demand in order to control their biochemical characteristics in terms of dimension, composition and drug release rate. Since the pioneering research of Bangham and Horne (1964), liposomes have attracted great attention in the field of drug delivery for their excellent biocompatibility (Williams, 2008), biodegradability, almost no toxicity, low immunogenicity, ability to incorporate hydrophilic and hydrophobic agents, controlled release properties, high stability, improved therapeutics efficacy, reproducible scale-up and manufacturing (Akbarzadeh et al., 2013; Allen and Cullis, 2013; Bozzuto and Molinari, 2015).

From the first generation to date, conventional liposomes were typically composed of phospholipids and cholesterol. The novel generation of lipid vesicles is based on: (i) functionalized

surface to specifically reach the selected cell or tissue – ligand targeted liposomes – (Daeihamed et al., 2017), (ii) deformed and elastic structure in order to be administered via transdermal and oral routes – transfersome – (Bayat et al., 2020), and (iii) ability to be triggered by an external or internal stimulus such as pH, temperature, redox potential, enzymes, electrolyte concentration and ultimately even magnetic fields to achieve a spatiotemporal control of drug release – smart delivery system – (Murdan, 2003; Spera et al., 2014, 2015; Kim and Lee, 2017; Nardoni et al., 2018; Liu and An, 2019; Yuba, 2020). This last characteristic is particularly promising in the evolution of liposome technology, because one can think of electromagnetic fields as actuators; in practice it will allow engineers to design a rational and remote control of the release thus making liposome vesicles a reservoir of the drug or molecule to be released on site and on-demand.

Recently, an attempt to evaluate a stimulus-dependent response of giant unilamellar lipid vesicles (GUV) using a series of electric field pulses of micro- to millisecond duration, has been demonstrated to be successful in electrodeformation, electrofusion and electroporation in the membranes of these vesicles (Karal et al., 2019). Authors proved that the results of pore formation at different electrical-induced membrane tensions are in agreement with those reported for mechanical-induced ones. Similar results have been reported in Perrier et al. (2018), where it was observed an ejection of fluid-phase lipids concomitant with a GUV size decrease.

In spite of the interesting and promising results, the electric fields used in these works are those typical of irreversible electroporation which, when applied to cells or tissues, imply the creation of permanent and hence lethal nanopores in the cell membrane disrupting cellular homeostasis thus causing cell death. A more versatile and powerful approach could be to use electric field pulses not disrupting the cells to which they are applied. This is the well-known electropermeabilization process, which is based on the creation of transient pores in the phospholipid bilayer. Nowadays, this is becoming a technology platform for enhancing the transmembrane transport of drugs, genetic materials, and other molecules in the areas of medicine, food processing, and in some environmental applications (Kotnik et al., 2015; Perrier et al., 2017).

In particular nanosecond pulsed electric fields (nsPEFs) seem to be promising in this sense; the challenge in the application of nsPEFs relies in the possibility to cause both the cells and the liposomes membranes electroporation without triggering irreversible damage of cells. In such a way, liposome poration could permit the drugs release in the extracellular medium, close to the cells, and an easy uptake of the drugs by the electroporated cells could be achieved. Thanks to the similarity between cellular and liposomal membranes (Breton et al., 2012, 2015; Portet et al., 2012) and considering the second-order model of induced transmembrane voltage (Postow and Polk, 1996; Kotnik and Miklavčič, 2000; Merla et al., 2012), such pulsed electric fields with high frequency content could be used as a promising external trigger to obtain simultaneous and reversible electropermeabilization of both cell and liposome membranes, thus overcoming the limitation of the well-known transmembrane dependence on the radius of the microscopic structures for pulses with a lower frequency spectral content. Authors have already shown through a theoretical study the possibility of nsPEFs to induce a simultaneous electroporation of cell and liposomes using small unilamellar lipid vesicles of the order of hundreds of nm (Denzi et al., 2017a,b).

In this paper we experimentally prove that nsPEFs can trigger the release of a fluorescent dye used as a hydrophilic model drug molecule contained in the aqueous core of unilamellar liposomes, using a fully characterized and controllable experimental bench. The real-time monitoring of the dye fluorescence gives direct information on the concentration of the compound escaped from the vesicles and hence provides an estimate of the increased permeability of the lipid membrane induced by nsPEFs application.

The setup of the experiments was accompanied by its full characterization in order to obtain complete reliability and control of the experimental data. The measurements involved both the nsPEFs generation and delivery, and the temperature acquisition during the experiments; the same characterization has been obtained via simulations, ensuring the same operative exposure conditions for the liposome samples. The experimental results obtained on liposomes permeabilization are further investigated by multiphysics simulations which, exploring these physical interactions, represent a guide to achieve quantitative results when exposing nanosized liposomes to nsPEFs. This study is aimed at establishing a powerful tool to predict the results of advanced experiments on modulating nsPEFs parameters. Thus, starting from these combined numerical and experimental outcomes, future *in vitro* experiments could be performed first on cells and then on both liposomes and cells to experimentally investigate compounds release from liposomes and their uptake inside cells.

MATERIALS AND METHODS

Materials

Egg phosphatidylcholine (Egg-PC) Lipoid 80 E from Lipoid GmbH (Germany) was kindly offered by AVG Srl (Italy). 4-(2-hydroxyethyl)-1-piperazine ethanesulfonic acid (HEPES), 5-(6) carboxyfluorescein [5-(6) CF], Triton X-100 (TX-100), Sephadex G-50 medium grade, hydrochloric acid (HCl), ammonium thiocyanate and sodium hydroxide (NaOH) were purchased from Sigma Aldrich (Italy). Chloroform ($CHCl_3$) was obtained from Merck (Italy). Bidistilled water, sodium chloride (NaCl), ethanol, thiocyanatoiron and 1,2-dichloroethane were supplied by CARLO ERBA Reagents (Italy). Cyclopore polycarbonate membrane filters Whatman® were purchased from Cyclopore Track Etched Membrane.

Liposome Preparation and Characterization

According to the thin film hydration method (Petralito et al., 2012), Egg-PC was dissolved in a round bottom flask containing 3 mL of $CHCl_3$. The organic solvent was evaporated under reduced pressure until a thin lipid film was formed on the

flask bottom, using a rotavapor. Any trace of solvent was further removed keeping the flask under reduced pressure for 2 h. The dry lipid film was then hydrated with 5 mL of the 5-(6) CF dye solution, 50 mM in HEPES buffer (σ = 0.0304 ± 0.0041 S/m, 10 mM, pH = 7.4). The buffer properties have been chosen in accordance with the literature on electroporation (Silve et al., 2016; Denzi et al., 2017b). Five consecutive freezing/thawing cycles in a dry ice-ethanol bath were performed to increase the trapped volume of multilamellar preparations. The obtained vesicles were downsized by sequential extrusion to form unilamellar liposomes. This step was performed through polycarbonate membrane filters of decreasing pore size (0.8–0.4 μm) up to five times in order to obtain a narrow size distribution. To remove the unencapsulated fluorescent dye, the sample was subjected to a size exclusion chromatography (SEC) with a Sephadex G-50 column. After the preparation, a physico-chemical characterization has been carried out in terms of both sizing (hydrodynamic diameter and size distribution) and ζ-potential, using a Zetasizer Nano ZS 90 (Malvern Instruments Ltd., Malvern, United Kingdom), at the constant temperature of 25°C, in order to ensure homogeneous size distribution and shape, with good time stability.

Evaluation of Liposome Membrane Permeabilization

The effect of nsPEFs application on the liposomal vesicles membranes was evaluated through the carboxyfluorescein release method relying on the de-quenching of the encapsulated hydrophilic marker 5-(6) CF from the inner compartment of the liposomes to the bulk of the suspension.

When a defect forms in a liposome containing internal 5-(6) CF, its release is detected quantitatively as an increase in fluorescence. The fluorescence intensity measurements were performed in time drive modality scanning the samples with a spectrofluorometer (LS 50B Perkin Elmer, United States), using the λ_{ex} and λ_{em} maxima (λ_{ex} = 492 nm and λ_{em} = 512 nm) previously determined, up to 2 h and 30 min after the exposure. At the end of the entire set of measurements, the liposomal vesicles were completely destroyed by adding a lytic concentrated solution of the non-ionic detergent TX-100 (30% w/V) in order to evaluate the total amount of 5-(6) CF entrapped. The percentage release of the hydrophilic dye was calculated with the following equation:

$$5-(6)\,\text{CF released}\ (\%) = \frac{\text{I}\,(\text{t}) - \text{I}\,(\text{t}_{\text{ref}})}{\text{I}\,(\text{t}_{\text{max}}) - \text{I}\,(\text{t}_{\text{ref}})} \times 100 \qquad (1)$$

where, I(t_{ref}) is the initial fluorescence intensity of the dye in the bulk suspension, I(t) represents the fluorescence intensity recorded at each sampling time and I(t_{max}) corresponds to the maximum intensity after the lysis of the liposomes with TX-100. All the measurements were performed in triplicate and the results are reported as mean ± standard deviation.

nsPEFs Exposure Setup: Experimental Characterization and Numerical Modeling

The system used to perform the nsPEFs exposure was composed by a standard electroporation cuvette (1002561E, BioGenerica, Italy), hosting a fixed volume of the prepared liposomal suspension, placed in the 11 mm-gap between the two brass electrodes of the cuvette holder, that are suitable connected to a HN coaxial cable, as first designed and developed in Denzi et al. (2017b). To mechanically stabilize the structure, avoiding any air gaps between the holder and the standard cuvette, they were attached with a clamp. This exposure system was then completed with a second HN coaxial cable that was connected to the FID generator (FPG 10-1 NM10, FID Technologies, Germany) (see **Figure 1A**). The 10 ns pulses produced by the generator were delivered to the liposomal suspension placed in the 1 mm-gap cuvette electrodes, reaching electric field amplitudes in the order of MV/m.

The electrical signal delivered by the pulse generator was recorded using an oscilloscope (RTO2014, Rohde & Schwarz, Germany) connected to the source through a chain of four attenuators. Moreover, the electrical signal reaching the cuvette was monitored in time during each experiment. In particular, the voltage established between the two electrodes of the cuvette was measured using two HV-probes (TT-HVP 2739, Testec, Germany) connecting the exposure structure to the oscilloscope. The HV probes are characterized by a band width ranging from DC to 220 MHz and a rise time of 1.6 ns. The exposure setup is shown in **Figure 1A**. The electric field applied to the sample is given by the ratio of the voltage at the electrodes and the 1 mm distance.

The temperature of the sample placed in the cuvette has been monitored during the exposure using an infrared (IR) thermal camera A325 (FLIR Systems, United States) which has a thermal sensitivity <0.07 at 30°C. This camera is able to measure the temperature in the range −20 to 120°C with an accuracy of ±2%. The thermal images are composed by over 76000 individual picture elements, with a frame rate up to 60 Hz. The use of this thermal camera allows the acquisition of both thermographic images and non-contact measurements of the temperature, avoiding any interactions with the analyzed sample. A FLIR Research IR software is used both to control the real-time thermal analysis and to post-elaborate the recorded data.

Numerical modeling of the exposure setup has been investigated in order to support the experimental data and to give theoretical support to the whole procedure. The electric field distribution in the cuvette containing the buffer and the temperature profile in time during the nsPEFs was solved using the software COMSOL Multiphysics v. 5.3. A 3D model of the exposure system with realistic geometrical dimension was implemented. The cuvette was filled with a solution characterized by a relative permittivity of 85 and a conductivity of 0.03 S/m, as the dielectric properties of the HEPES buffer solution. The conductivity value of the buffer solution was confirmed with measurements with a Precision LCR Meter E4980A from Agilent, as in Denzi et al. (2017a). The multiphysics problem was

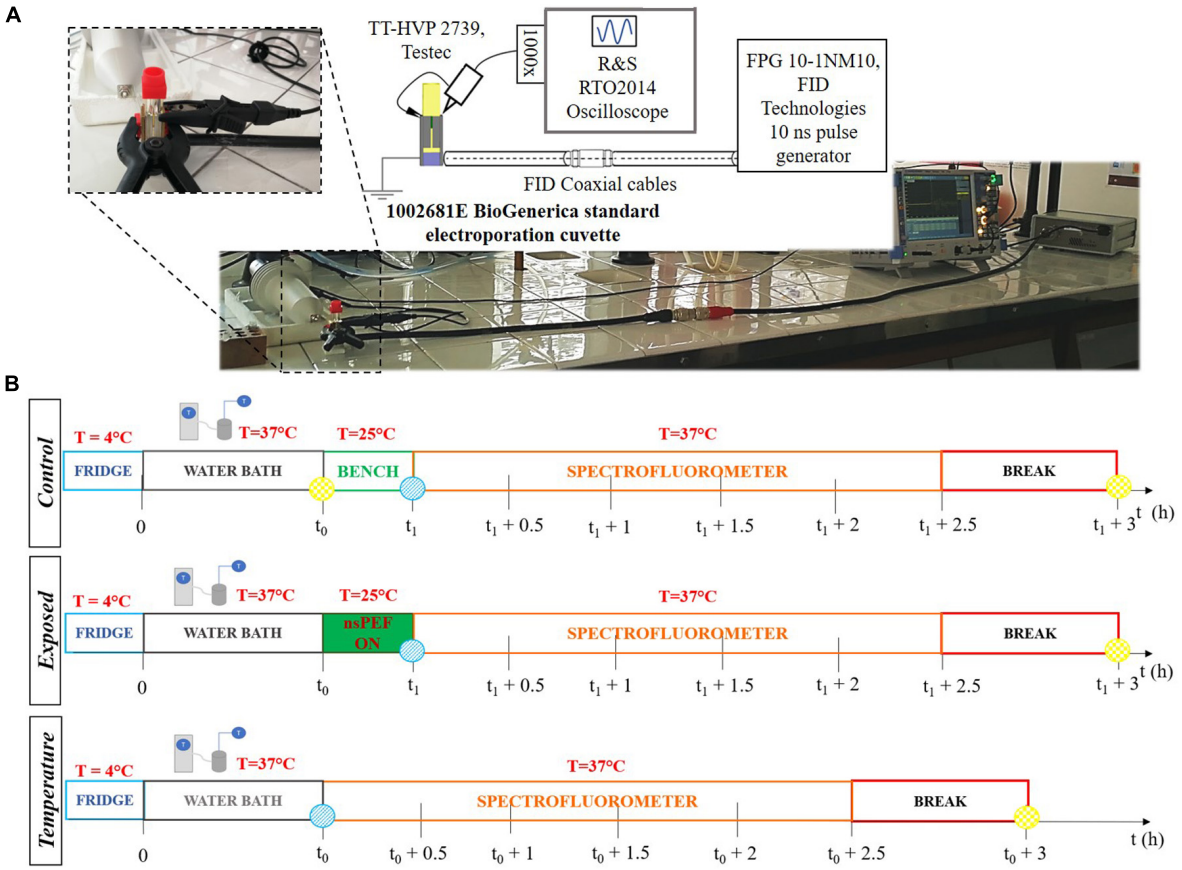

FIGURE 1 | (A) Exposure setup configuration and picture of the laboratory equipment used to perform the experiments. The generator is connected through two coaxial cables and a transition to the cuvette. The cuvette is filled with the liposomal suspension sample. The signal at the load is monitored in time with the R&S oscilloscope and two Testec HV probes. **(B)** Experimental protocol tuned to expose liposomal vesicles to a sequence of pulses, with a nanosecond duration and intensities in the order of MV/m. The three timelines represent the procedure performed for each sample. The t_0 = 0.5 h is the thermal equilibration period, while t_1 = (t_0 + 0.28 h) is the start of the exposure. The times t_0 and (t_1 + 3 h) are, respectively, the reference time (blue point) and the maximum fluorescence time (yellow point) used to evaluate the electrical signal effect on the liposomes. The starting time for fluorescence analysis is t_1.

solved by coupling two modules, in a Time Dependent study. The quasi-static electromagnetic problem was solved using the AC/DC modules in Electric Currents mode. The square pulse excitation, with 10 ns duration and 2 ns rise/fall time, was applied to the cuvette electrode, the brass electrode and the central pin, connected together. The ground terminal was set to the external sock and to both the cuvette and the second brass electrode connected together. Temperature increase in the buffer solution due to the electromagnetic signal, has been evaluated using the electromagnetic heating module in the Joule heating mode, starting from 25°C as initial room temperature value of the suspension.

Experimental Protocol

Liposomal samples were prepared 24 h before the experiments and they were stored overnight in a refrigerator at 4°C. As reported in **Figure 1B**, the experimental protocol was characterized by the following steps: (1) thermal equilibration at 37°C of the sample up to t_0 = 30 min using a cryostat water bath; (2) application of the electrical signal (nsPEFs ON) placing the sample in the electroporation cuvette for a period of time of about 17 min at room temperature (ending at $t_1 = t_0 + 17$ min); (3) analysis of the fluorescent dye release: during this step the sample is placed in a quartz cuvette and accommodated in the spectrofluorometer at the controlled temperature of 37°C and the fluorescence measurements were performed monitoring in time up to 2.5 h after the exposure; (4) complete lysis of the liposomes in order to evaluate the maximum fluorescence of the dye entrapped in the sample. The exposures have been carried out using the protocol parameters reported in **Table 1**, thus setting the generator at 9 kV and a pulse repetition frequency (PRF) of both 2 and 4 Hz for a period of time of about 17 min, thus exposing the liposomal sample to 2000 and 4000 pulses, respectively. Exposure parameters such as number of pulses, period of exposure and PRF have been chosen considering the literature (Silve et al., 2014; Lamberti et al., 2015). For the control samples procedure in step (2) the control was placed on the bench near the exposure system, while for the temperature control the operating temperature has been set to 37°C. Eight independent exposure experiments have been performed with 2000 pulses, and

TABLE 1 | Operative conditions of the exposures for a dose-effect electropermeabilization evaluation.

Electrical Parameters					
# set-up	**# nsPEFs**	**PRF (Hz)**	**Voltage (kV)**	**FWHM (ns)**	**Rise/Fall time (ns)**
1	2000	2	9	10	2
2	4000	4	9	10	2

four experiments with 4000 pulses, each exposed sample has been tested simultaneously with its control.

Numerical Simulation of Liposome Membranes Electropermeabilization

2D numerical simulations have been performed to model a mixture of liposomes in solution with COMSOL Multiphysics software v. 5.3. **Figure 2** displays the 2D rectangular box representing the external buffer medium, 2.30 μm in width and 9.34 μm in height, where a random distribution of liposomes of 266 nm in diameter and a membrane thickness of 5 nm were placed, according to the experimental liposomes dimension. The distribution of 156 liposomes was obtained by a random distribution program built in MATLAB, avoiding the superposition of vesicles. Periodic conditions were set on the top and bottom of the box. The simulations were performed considering the left side of the box as the ground electrode and the right one excited by a train of pulses of 10 ns duration and rise/fall times of 2 ns, spaced in time of 250 ms to simulate the liposome exposure to a train of pulses delivered at 4 Hz.

The quasi-static electromagnetic problem was solved in the Electric Currents mode and coupled with two other modules. Boundary conditions were imposed on liposome membranes as contact impedance and the formation of pores on the membranes was studied solving in the Boundary ODEs and DAEs mode the asymptotic equation, firstly proposed by DeBruin and Krassowska (1998), and used in literature (DeBruin and Krassowska, 1999; Neu and Krassowska, 1999; Mercadal et al., 2016; Caramazza et al., 2019). Specifically, the pore formation across a membrane is determined by the transmembrane potential induced by the electrical stimulus. In accordance with the asymptotic model, the membrane conductivity changes are also determined by a series of parameters i.e., pore conductivity as reported in studies on synthetic membranes (He and Kyu, 2016; Liu et al., 2018; Zhang et al., 2019), transmembrane potential (TMP) and temperature, as reported in DeBruin and Krassowska (1999), Retelj et al. (2013). To this regard, the temperature distribution in the simulation box was evaluated in time by coupling the Heat Transfer in fluid module with the AC/DC module. A thin layer condition was set on liposome membranes to take into account their thermal properties and behavior. In **Table 2** the material properties that were set in the simulations are reported according with the experimental data and literature (Merla et al., 2012; Caramazza et al., 2019). All the parameters used for the pore kinetics model are reported in Mercadal et al. (2016) and Retelj et al. (2013).

Statistical Analysis

All the reported data came from measurements done at least in triplicate for each sample of a single experiment. All statistical

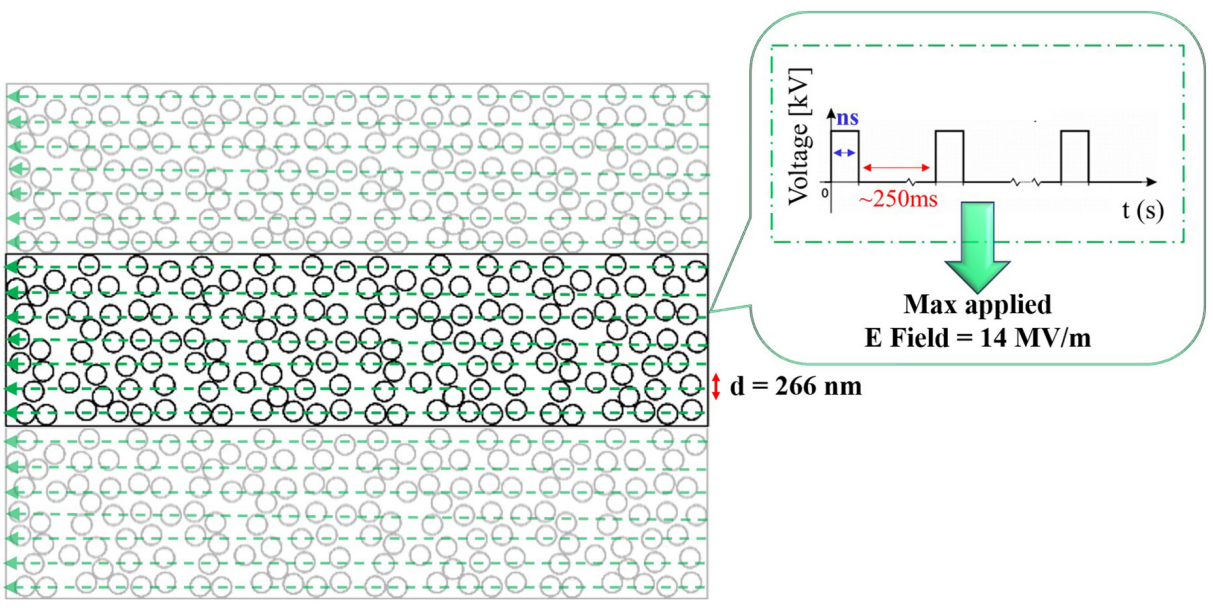

FIGURE 2 | 2D geometrical model of a randomly packed distribution of 156 liposomes, characterized by a diameter of 266 nm. The signal applied to the liposomes is reported in the inset and it represents the experimental train of nsPEFs delivered by the ns generator, each pulse is characterized by a 10 ns duration and 14 MV/m as maximum electric field amplitude. On the top and bottom boundaries periodic conditions were set, thus the simulation box is ideally replicated.

TABLE 2 | Dielectric and thermal properties used to represent each material compartment in the microdosimetric simulations.

Material properties	External medium	Membrane	Internal medium
σ [S/m]	0.03	1.1×10^{-7}	0.35
ε_r	85	11.7	85
Cp [J/(kg K)]	4185.5	2000	4185.5
ρ [kg/m^3]	993.2	951.1	993.2
k [W/(m K)]	0.62	0.2	0.62

analyses were performed with one-way ANOVA to determine significant differences in the experimental data. The maximum *p*-value that was considered statistically significant was 0.05. As regards the outcomes of the signal characterization with HV probes, a program has been built in MATLAB software to analyze the sequence of pulses in terms of rise and fall times, duration and amplitude of each pulse of the delivered sequence, determining the mean values and the standard deviations.

RESULTS

Physicochemical features of the obtained liposomes with a diameter of 267.91 ± 1.71 nm are reported in **Supplementary Table S1**, showing hydrodynamic diameter, size distribution, ζ-potential, entrapment efficiency, structured phospholipid in vesicles. All measurements were performed at a scattering angle of 90° and were thermostatically controlled at 25°C. The samples were opportunely diluted with 10 mM HEPES (pH = 7.4) as in Petralito et al. (2012).

Electrical Activation of the Release by nsPEFs

Figure 3A reports the major result of this study showing a significant increase in both exposure conditions, just afterward exposure and, then, after 2.5 h. According to the established experimental protocol, the release profile of the 5-(6) CF dye was studied after the nsPEFs stimulation of the sample and then the results were compared with the related controls, with no electrical signal application.

Figure 3A shows the percentage of the 5-(6) CF release at the starting time after exposure (t_1 of **Figure 1B**, as described in section "Experimental protocol") and at 2.5 h after t_1 for exposed and control samples, comparing the experiments applying 2000 and 4000 ns pulses. The results are reported as the mean ± the standard deviation of the experiments and the statistical analysis shows that the difference between exposed and control samples is significant at all times with *p*-values < 0.001, thus confirming the effect of nsPEFs on the membrane of nanosized liposomal vesicles. The release of the fluorescent dye increases in time, as can be observed in **Figure 3B** reaching, after the 2.5 h of post-exposure, a value of 19.6 ± 3.3% confirming the role of electrical activation in the leakage of these vesicles. As it can be seen from **Figure 3C**, where the values of percentage of the 5-(6) CF release are reported for selected times in the case of 4000 pulses, the increase versus time of the control samples is almost constant between 0.8 and 1.1% every 0.5 h, while, after the first hour, the increase of the exposed sample rises significantly. For 4000 pulses applied, the difference between the exposed and the control starts slightly above 8% just at the end of the exposure and reaches around 13% at 2.5 h, while for the 2000

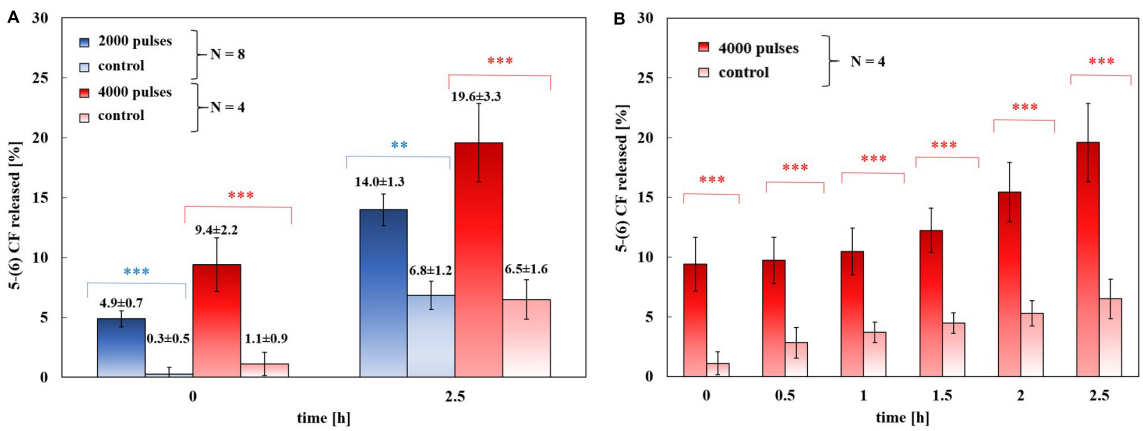

C

time [h]	0	0.5	1	1.5	2	2.5
exposed	9.4±2.2	9.7±1.9	10.5±1.9	12.2±1.8	15.4±2.5	19.6±3.3
control	1.1±0.9	2.8±1.3	3.7±0.8	4.5±0.8	5.3±1.1	6.5±1.6

FIGURE 3 | Experimental release of the 5-(6) CF in percentage. **(A)** Dose-effect evaluation: 8 trails of exposed samples at 2000 pulses at 2 Hz train (blue) and 4 trails of exposed samples at 4000 pulses at 4 Hz train (red), with their controls (light blue and light red, respectively), at 0 and 2.5 h after the exposure. The differences between the exposed samples and their control are always statistically significant with a $p < 0.01$ or $p < 0.001$. **(B)** The results of a set of four exposures using 4000 pulses and a PRF of 4 Hz and their controls, (8 samples). The release of the 5-(6) CF is shown at 0, 0.5, 1, 1.5, 2, and 2.5 h after the exposure, values reported in panel **(C)**. At each time the difference between the exposed and the control values is significant with a $p < 0.001$. **(C)** Values of 5-(6) CF experimental release at the selected times for both 4000 pulses exposed samples and the controls.

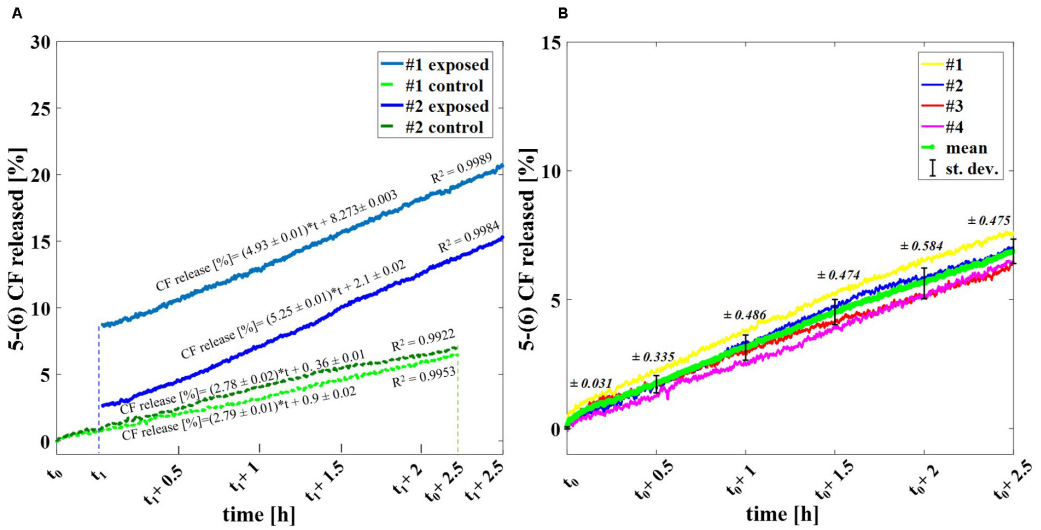

FIGURE 4 | Profile in time of the experimental release of the fluorescent dye. **(A)** Percentage release of 5–(6) CF monitored in time up to 2.5 h for four different trials: two exposed samples using 2000 pulses and 2 Hz (dark and light blue) and two temperature control samples (dark and light green). **(B)** Spontaneous release of 5-(6) CF from liposomes due to the operative temperature of 37°C up to 2.5 h via spectrofluorimetry. A set of four different trails is reported (yellow, blue, red, magenta) with the calculated mean curve (green) and the standard deviation values as bars.

pulses the exposed versus control differences are slightly smaller but still statistically significant. Going into a deeper analysis in time, this effect is observed also in the case of 2000 pulses, looking at **Figure 4**, which reports the profile in time of the fluorescent dye release. **Figure 4A** reports the percentage release of 5–(6) CF monitored in time up to 2.5 h for four different trials: two exposed samples using 2000 pulses and 2 Hz (dark and light blue) and two temperature control samples (dark and light green). It is possible to observe the slopes of the curves of the two exposed samples 4.93 ± 0.01 and 5.25 ± 0.01 with respect to the slopes of the control ones, around 2.79 ± 0.01; this means that the electric pulse train is able to destabilize the membrane of the liposomes so that the dye was slowly released from the liposomes for hours after the end of the exposure. The spontaneous leakage from the vesicles due to the environmental temperature of 37°C causes an effect similar to the control (**Figure 4B**) determining a leakage of about 7% after 2.5 h, much smaller than the effect of the dye released from the exposed samples, ranging from 15% (2000 pulses) to 20% (4000 pulses). Finally, it is important to underline that the nsPEFs application did not lead to the liposomes rupture, as demonstrated by the hydrodynamic diameter data obtained before and after the pulse application, as reported in **Supplementary Figure S1A**. The data reported have been obtained using a pretreatment temperature of 37°C, considering the future application for the human body, but similar results have been obtained also using a pretreatment temperature of 25°C and then applying 2000 pulses in **Supplementary Figure S1B**.

Characterization of the Experimental Bench

A full characterization of the experimental bench was performed in order to obtain complete reliability and control of the experimental data. As first step in the analysis of the experimental bench performance, the electrical signal delivered by the generator has been recorded. The result of a single recorded pulse is compared with the ideal trapezoidal pulse with a duration of 10 ns and rise and fall times of about 2 ns, as reported in **Figure 5A**. The two blue curves (solid and dashed, respectively for the experimental and ideal signal) are in good agreement with each other, with a cross-correlation coefficient = 0.9931. **Figure 5B** represents the mean electric field (dark green solid line) with the standard deviation (light green shadow) evaluated in the cuvette, measured from the voltage acquired with the two Testec HV probes (see inset **Figure 1A**) when the 4000 pulses train is applied on the liposomal suspension with a PRF of 4 Hz. The signal maintains a 10 ns duration and the very good repeatability of the pulses sequence is represented by the low standard deviation of the curve; the maximum intensity of the electric field in time inside the cuvette is about 14 MV/m, with 9 kV from the generator. More information about the parameter values in terms of mean and standard deviation of the acquired signals are reported in **Supplementary Table S2**.

As reported in the inset of **Figure 1A** the nsPEFs signal is delivered to the sample using an *ad hoc* exposure system hosting the cuvette for electroporation. A numerical study has been carried out using COMSOL Multiphysics as explained in section "Materials and Methods" and considering a 3D model of the system, shown in **Figure 6A** where the cuvette, the transition from the coaxial cable to the brass parallel plates electrodes and the cable itself are modeled. Specifically, in **Figures 6B,C** are reported the electric field distributions inside the sample holder for two coordinate planes parallel and perpendicular to the electrodes, showing a homogeneous electric field of 14 MV/m at t = 10 ns, corresponding to the last time instant at the maximum intensity of the pulse.

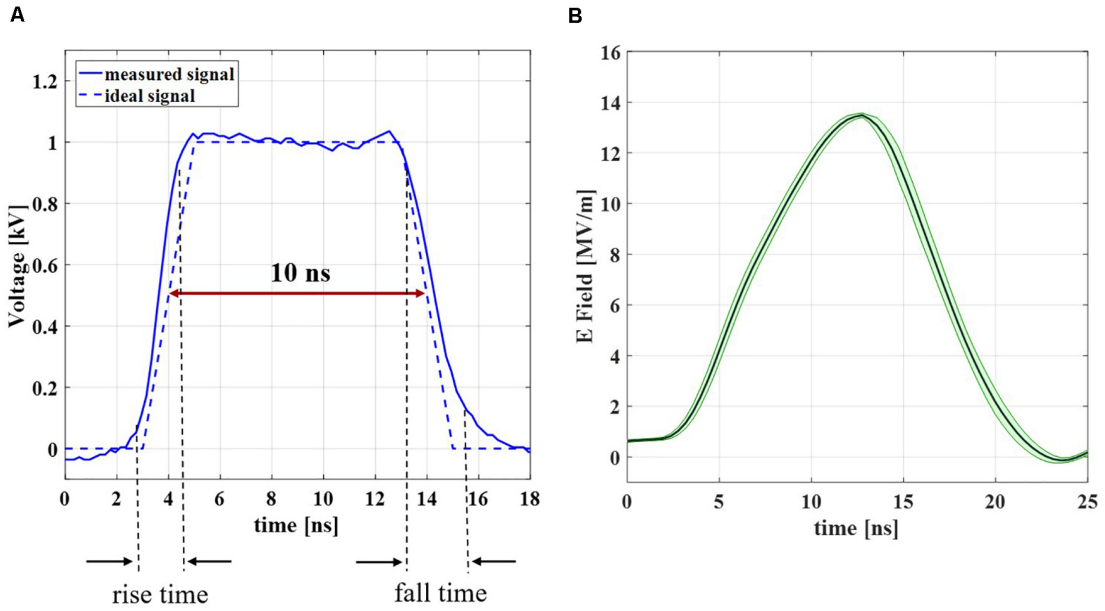

FIGURE 5 | Experimental signal characterization results. **(A)** Measured signal at the generator (blue solid line) in comparison with the ideal signal (blue dashed line). **(B)** Measured electric field inside the 1 mm-gap cuvette during the exposure to a train of 4000 pulses with a PRF of 4 Hz. The results are reported as the mean curve (dark green solid line) ± standard deviation (light green shadow).

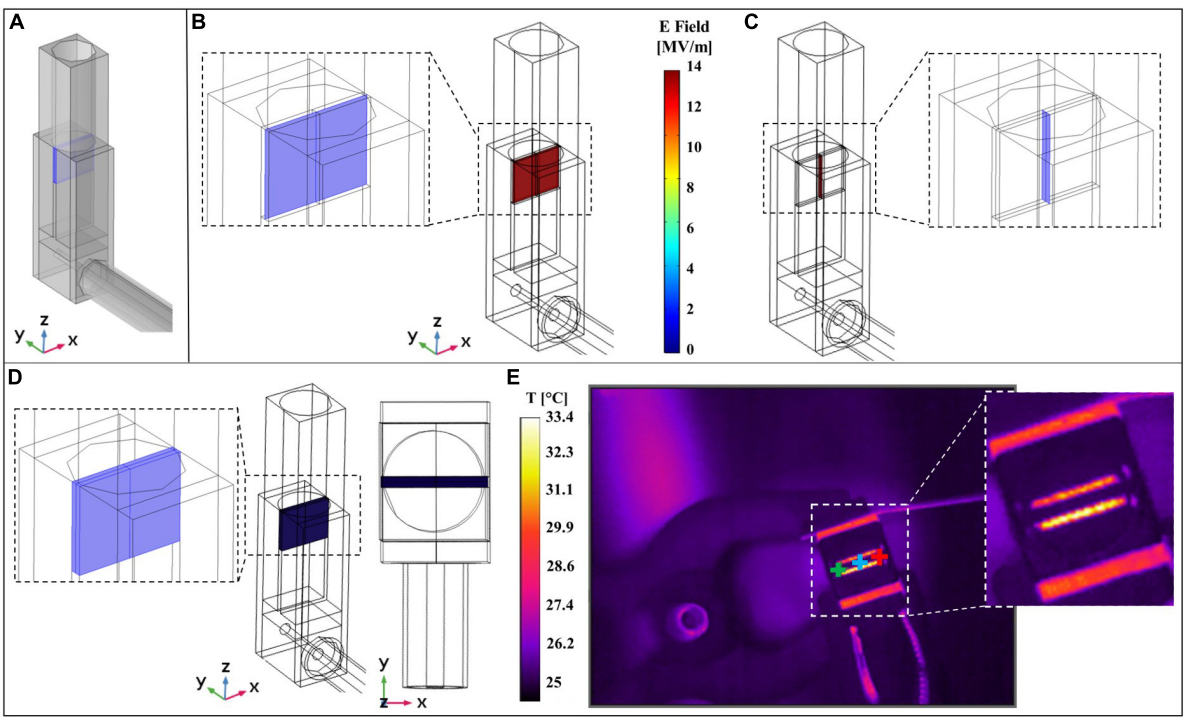

FIGURE 6 | Comparison of simulated and experimental results. **(A)** 3D model of the experimental system used to perform multiphysics simulations. **(B)** Simulated electric field distribution inside the cuvette at t = 10 ns is homogeneous on the central slice parallel to the electrodes (the slice is represented in the left inset). **(C)** Simulated electric field distribution inside the cuvette at t = 10 ns is homogeneous on the central slice perpendicular to the electrodes (the slice is represented in the right inset). **(D)** Homogeneous simulated temperature distribution inside the volume of the solution sample placed in the cuvette, lateral and top view of the exposure system. **(E)** Image experimentally recorded with the thermal camera during the exposure to nsPEFs on the right, with three cursors point (green, blue, and red). A zoom of the image without cursors is reported in the right inset.

Finally, the exposure system has been characterized in terms of temperature distribution comparing measurements and simulations. This is a crucial point since it is mandatory to monitor that the application of nsPEFs does not induce an increase of temperature in the sample thus becoming a confounding element in the interpretation of the final outcome. IR image of the system acquired with the thermal camera during the exposure is reported in **Figure 6E**, where three cursors point (green, blue, and red) are highlighted; in the inset is reported the temperature acquisition of the top of the cuvette hosting the solution. It is possible to observe that the temperature of the solution is around 25°C while electrodes reach a temperature of 33°C. The simulated 3D temperature distribution in the cuvette volume at 10 ns is reported in **Figure 6D**. As expected, the temperature distribution is homogeneous in the volume solution with a value comparable to the one acquired experimentally.

The behavior of the three cursors in time is reported in **Figure 7A** for the whole duration of the exposure (around 17 min) with an acquisition frame frequency of 16.3 Hz. It is possible to observe that apart from higher peak values of almost 26°C the temperature inside the sample holder fluctuates between 24.6 and 25.2°C showing a negligible temperature increase induced by the application of the field. Even if during the 10 ns of the pulse application the electric field is extremely high (14 MV/m), during the remaining 250 ms the field is OFF, therefore eventual local peaks of the temperature in the solution drop rapidly and as a whole the temperature remains quite stable around 25°C. This can be seen in **Figure 7B** where a zoom of temperature data coming from cursor #1 up to 1.25 s is reported representing the first 40 pulses of the applied signal. Similarly, for the numerical study (see **Figure 7C**), the temperature of the external buffer is reported during the application of the 40th pulse, as the worst-case scenario. At 1 s the temperature profile (yellow curve) suddenly responds to the electric field stimulus; in the inset (**Figure 7D**) is reported a zoom of the temperature profile for the 40th pulse simulation: pulse ON at $t = 0$ ns, pulse OFF from $t = 12$ to 800 ns. The yellow curve increases of about 0.04°C and then it starts decreasing when the pulse is turned off, from $t = 12$ to 800 ns.

Multiphysics Modeling of the Liposome Suspension

The main physical quantities involved in the interaction of electric field pulses and liposomes have been evaluated by means of a thorough numerical modeling. The simulations have been performed using up to 40 applied pulses with a PRF of 4 Hz and a maximum amplitude of about 14 MV/m, according to the experimental operating conditions and considering the computational costs. In fact already reproducing such conditions requires a high computational effort in terms of quasi-static solution of the electric currents module given that the total time duration of the simulation is almost 1 s with a variable time step, starting from 0.1 ns during pulse ON and gradually increasing to 0.2 ms during the pulse OFF time span.

After the first 40 pulses, an indication of nsPEFs induced destabilization can be drawn by looking at the induced TMP, the pore density distribution on the liposome membranes, the temperature distribution and the changes of the electrical conductivity in time. **Figure 8** shows a cut view from the whole initial model, reporting these quantities: E field (**Figure 8A**), pore density (**Figure 8B**), TMP (**Figure 8C**), and current density (**Figure 8D**) at the time $t = 10$ ns of the 40th applied pulse.

As expected, the electric field, normalized with respect to the maximum value applied, is higher outside the vesicles than inside, while the current density streamlines enter inside the vesicles due to the higher conductivity of the internal solution with respect to the external one, as also confirmed by the behavior of the current density norm in MA/m, of **Figure 8D**. The pore density spatial distribution on the liposome membranes shows how the effect of the electric field application is not uniform in the vesicle distribution; moreover, although somehow affected by the nsPEFs after the first 40 pulses, the poration density is still well below the threshold considered for an appreciable effect (see **Figure 8B**). Finally, the TMP distribution ranges from 0.3 to 1.1 V, showing higher values at the anode and cathode vesicles poles in line with the pore density distribution in terms of higher values (**Figure 8C**). As a whole it is possible to support the hypothesis that already after the first 40 pulses some slight effects in the coupling of the field are observable as the basis of the electroporation mechanism.

Given the computational effort to reproduce the realistic exposure for 4 Hz repetition frequency, pore density in time has been calculated in the most exposed liposome of the model, for the 40 simulated pulses (red circles) and reported in **Figure 9A**, with a third-grade polynomial fitting curve (dashed line). The extrapolation of the polynomial curve up to 4000 pulses (**Figure 9B**) clearly reveals that starting from the 570th pulse the threshold for poration is overcome. In fact, once the well-known threshold value of 10^{14} m^{-2} for the poration of lipid membrane is reached (DeBruin and Krassowska, 1999; Retelj et al., 2013; Caramazza et al., 2019), the poration can start and give rise to a breakdown mechanism. It is assumed that for 2000 or 4000 pulses the threshold is highly exceeded hence, poration of the liposomes is definitively obtained, supporting the effect experimentally proven.

Regarding a possible local thermal coupling, **Figure 10** shows the microscopic temperature distribution on the same cut view of the previous electrical distributions, during the nsPEFs application. Higher values are localized inside the liposome vesicles and in the space between vesicles, showing both the vesicle-environment and the vesicle-vesicle interactions, but still in the order of a temperature difference of 0.02°C. It is argued that, despite the non-linear physics underlying the response of the system under investigation, the increasing number of pulses will not affect the thermal safety of electroporation process, as clearly indicated by the temperature measurements reported in **Figure 7B**.

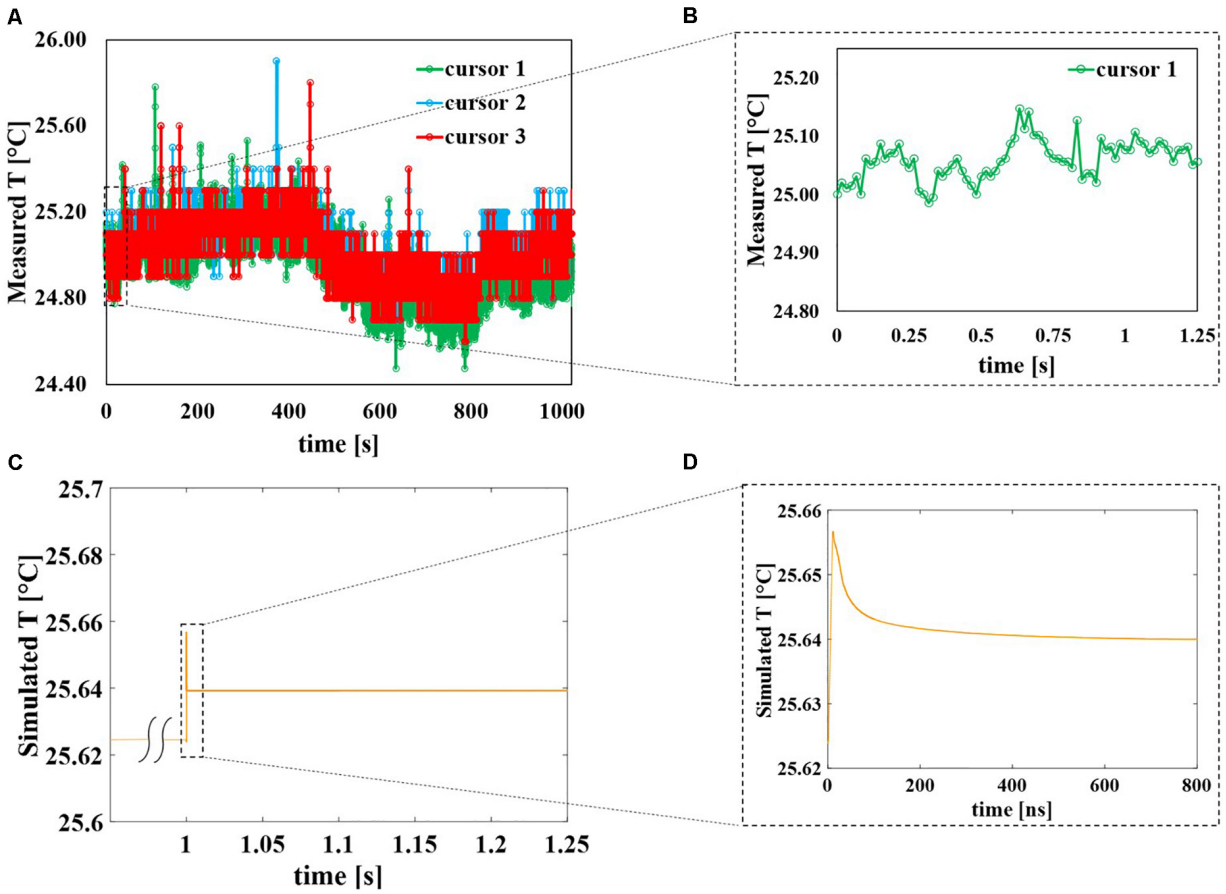

FIGURE 7 | Evolution in time of the sample temperature, comparison between experimental and numerical data. **(A)** Temperature of the solution sample experimentally measured using the thermal camera with a frame frequency of 16.3 Hz during the entire exposure of about 17 min. The peaks represent the times during which the pulses are delivered to the solution and are reported as isolated events. **(B)** Zoom of temperature experimentally measured with cursor #1 from the beginning of the exposure up to 1.25 s corresponding to the initial 40 pulses. **(C)** Simulated temperature of the sample when the 40th pulse is applied to the sample, considering the worst-case scenario. **(D)** Zoom of the simulated temperature data from t = 0 ns of the 40th pulse application up to 800 ns.

DISCUSSION

In the past several decades, together with the improvement of nanotechnology and material science, various so-called stimuli responsive carriers have been successfully developed as promising vectors for drug delivery, i.e., so that the encapsulated therapeutics molecules could be released in a spatial or temporal ("*smart*") delivery systems (Gu et al., 2018). Among the external stimuli, pulsed electric fields, as the ones used for electroporation of cells seem a promising technique to activate lipid vesicles carriers thus achieving a stimulus-sensitivity delivery of the payload encapsulated inside them. In particular the possibility to use nsPEFs, which have proven to electroporate intracellular organelles of cells, have suggested the idea to control the release from liposomes, at first electroporating liposomes once they are taken up by the cells (Perrier et al., 2017). A theoretical study already demonstrated the feasibility that internalized liposomes could be electroporated without affecting the cell viability (Retelj et al., 2013). Another approach could be to electroporate such lipid vesicles when they are in close proximity of the target cells, simultaneously electroporating both the cell and liposomes population, without compromising the cell viability. In fact, since nsPEFs are able to electroporate the cell membrane, the content released from the liposomes could be taken by the electroporated cells (Denzi et al., 2017b). However, the possibility of triggering the release of liposome content with nsPEFs remains up to now at the theoretical level, and the experimental feasibility of this approach has not been confirmed yet.

The experimental proof-of-concept presented in this paper supports the challenging issue that it is possible to electrically activate by means of nsPEFs (10 ns duration, 14 MV/m) the release of molecules entrapped in the interior of liposomes. Experimental data show that a train of pulses is required to obtain the effect; in particular 2000 pulses with a pulse repetition frequency of 2 Hz and 4000 pulses with a repetition frequency of 4 Hz. Moreover, the observed effect seems to be dose-dependent enhancing the release when increasing the number of pulses for the same duration of exposure. Temperature acquisitions during the exposure confirm that this kind of stimulus is non-thermal. The stability of the signal generated, in terms

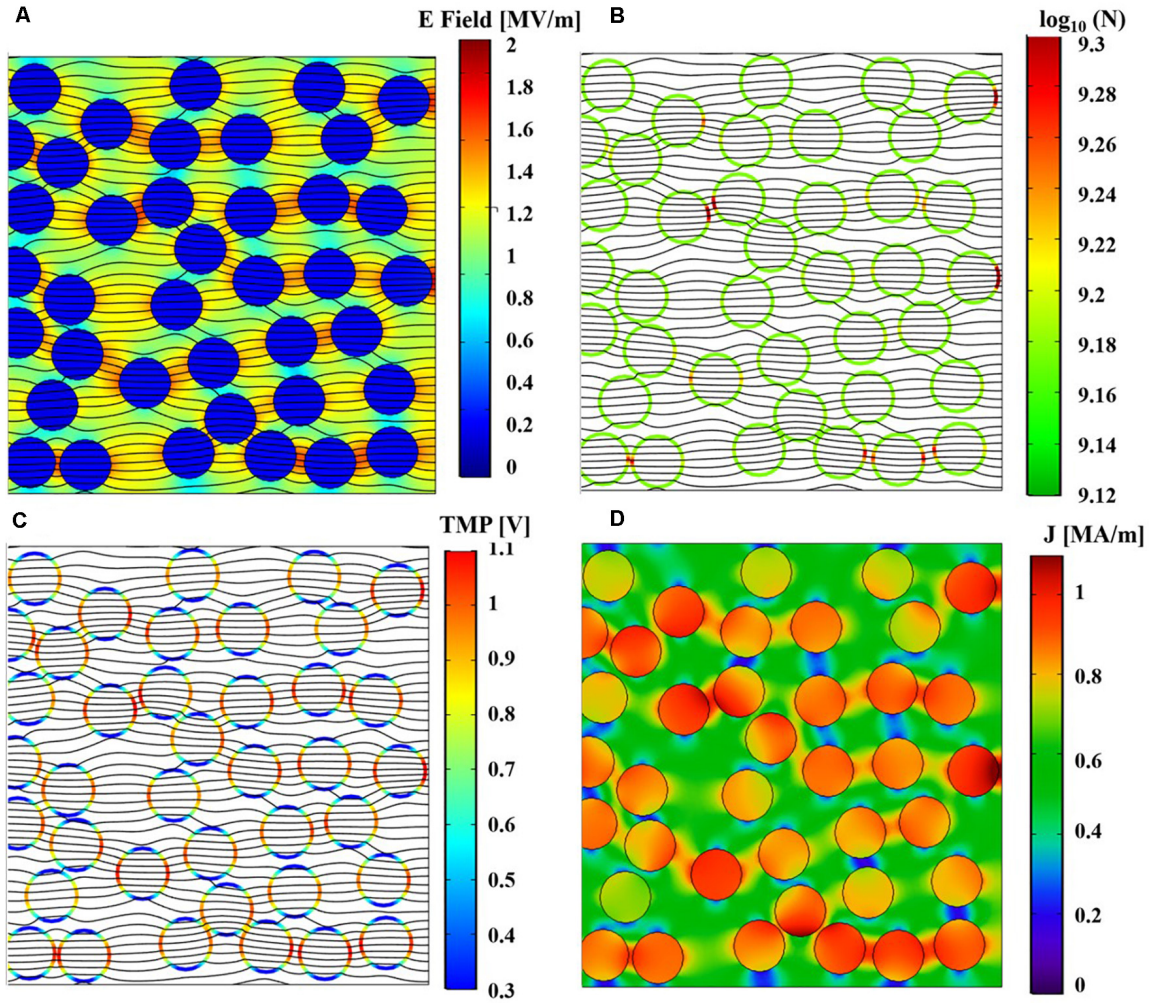

FIGURE 8 | Spatial distributions of the simulated physical quantities on a section of the simulation box at t = 10 ns of the 40th pulse application. **(A)** Simulated electric field distribution together with the current density streamlines. **(B)** Simulated pore density distribution on liposome membranes together with the current density streamlines. **(C)** Simulated TMP distribution on liposome membranes together with the current density streamlines. **(D)** Spatial distribution of the simulated density current norm.

of repetition of electric pulses, guarantees that the exposure conditions are highly reproducible and well controlled.

An effort has been made to strengthen the experimental results, providing a theoretical investigation based on a multiphysics numerical simulation of the liposome solution exposed for the first time to a realistic train of electric pulses, characterized by the temporal multiscale of a very short pulse duration (10 ns) and a much longer time interval between pulses (250 ms). This allows a better comprehension of the field interaction with the target nanocarrier suspension. In particular from the numerical simulations related to the spatial distributions of the electrical quantities involved, we suggest that there is a consistent effect of focalization due to the close proximity of liposomes each other: the closer they are the higher such effect, including the local temperature around and inside the liposomes. In fact, even if, during the extremely short duration of the pulse, a local increase in temperature could happen due to the extremely high intensity of the electric field, this would rapidly diffuse during the longer period of quiescence of the signal (250 ms), so that the average temperature of the solution will remain at a constant temperature. Moreover having obtained a proper fitting of the liposome membrane pore density curve over the train of 40 simulated pulses, and extrapolating such curve in order to have a prediction of behavior up to the experimental condition of 2000 and 4000 pulses, one finds out that, in such conditions, the liposome membranes will be electroporated having overcome the threshold of 10^{14} m^{-2} for the electroporation of lipid membranes. This is in line with the experimental result which indicates that 2000 is the minimum number of pulses to obtain a significant release of the fluorescent dye from inside the nanosized liposomes exposed.

As a whole the significance of this work findings is related to the experimental validation of the possibility to on demand trigger the release from nanosized liposomes applying

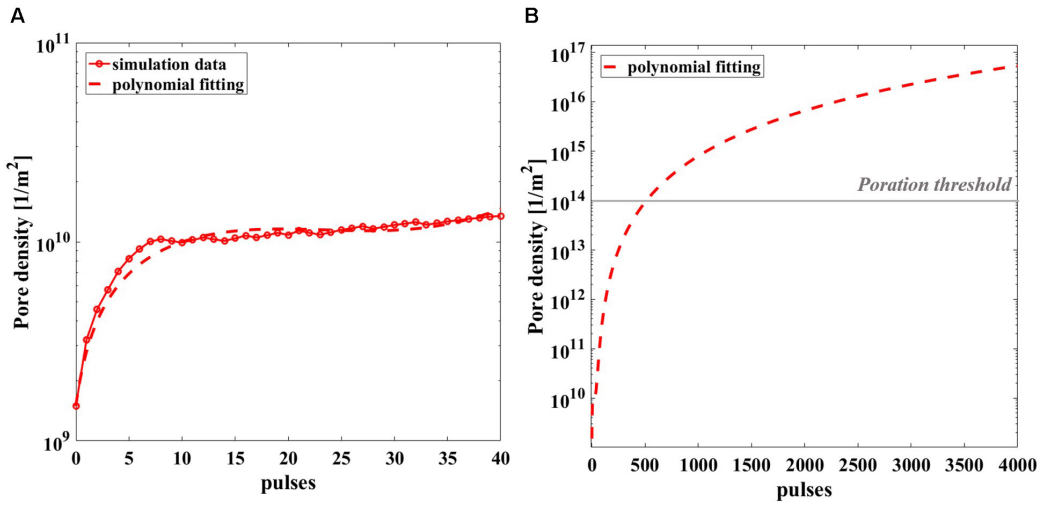

FIGURE 9 | Simulated pore density profile in time of the most exposed liposome of the model during the nsPEFs exposure. **(A)** The pore density curve obtained from the simulation (solid line with empty red circle as marker) is reported with the third-grade polynomial fitting curve (dashed line) up to 40 pulses, R^2 = 0.9207. **(B)** Polynomial fitting curve of the pore density curve extrapolated up to 4000 pulses.

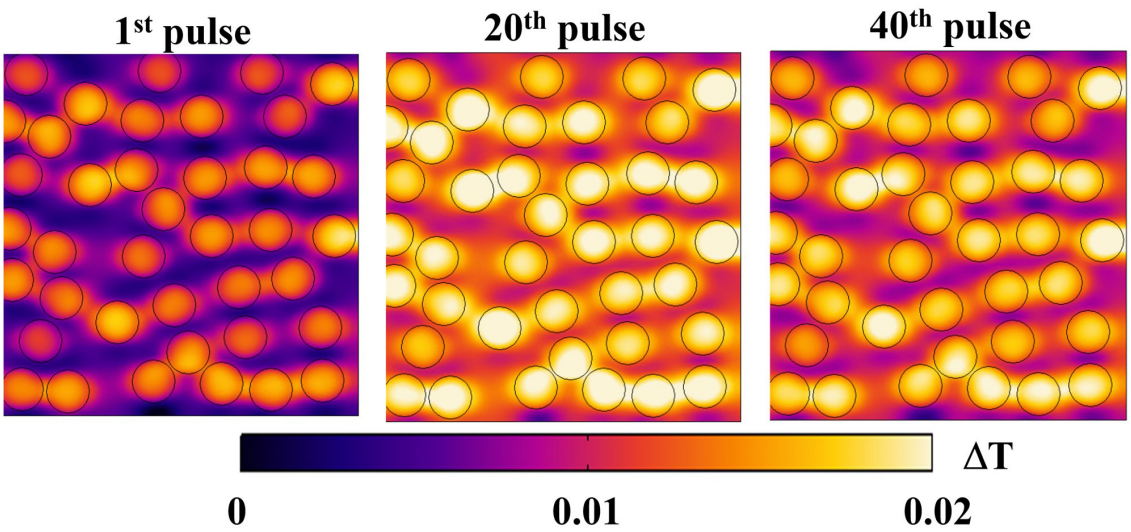

FIGURE 10 | Temperature distribution on a section of the simulation box at 10 ns for three different pulses: 1st, 20th, and 40th, respectively, in the left, central and right panels. The distribution reported as $\Delta T = T - T_{min}$ for each pulse, changes during the exposure, maintaining the trend of higher values inside the vesicles and lower values outside.

pulsed electric fields as such used for cells treatment. These outcomes open the way to the experimental application of liposomal drug delivery systems remotely activated by nsPEFs, previously studied only from a numerical point of view (Retelj et al., 2013; Denzi et al., 2017a,b). As a result of the lipid membrane destabilization, the fluorescent dye release of about 15–20% after a single treatment, is in line with literature on stimuli-sensitive drug delivery system activated by light or magnetic fields (Spera et al., 2015; Senapati et al., 2018; Liu and An, 2019). Thus, this relatively low percentage of release is useful thinking on the possibility to apply nsPEFs in a multi-dose manner. The numerical simulations confirm that liposome membrane electroporation could be achieved applying a sequence of nsPEFs with intensity in the order of MV/m and 10 ns duration. This numerical model could be a starting point to predict other exposure conditions.

CONCLUSION

In this work, the experimental feasibility of electrical activation of liposome nanocarriers with nsPEFs has been proven by looking at the release of a fluorescent dye entrapped in the vesicles.

Experiments were performed applying a train of nsPEFs (10 ns duration, 14 MV/m intensity and 2 and 4 Hz periodicity) on unilamellar liposome suspensions. Results show that liposome membranes are destabilized, allowing the release of transported compounds, in a statistically significant way up to almost 20%, and a dose-effect relationship is identified when a train of nsPEFs with higher PRF and number of pulses is applied. Multiphysics simulations have been performed in order to support the experimental data, studying the occurring mechanisms at a microscopic scale. A random distribution of liposomes was built, coupling three physical modules in order to consider the effect of nsPEFs interaction with liposome vesicles in terms of electromagnetic energy absorption, temperature distribution and pore density formation in time. The simulation results support the experiments giving an indication that not less than 500 pulses are needed to at least initiate the electroporation response. Therefore, here we prove the possibility to remotely activate nanosized liposomes with nsPEFs, with a comprehensive study in terms of both experiments and multiphysics simulations, giving a rational to design and perform an on-demand control of the release of transported compounds inside nanosized liposomes used as biocompatible reservoir, opening the way to future *in vitro* investigation.

DATA AVAILABILITY STATEMENT

All datasets presented in this study are included in the article/**Supplementary Material**.

AUTHOR CONTRIBUTIONS

FA, SP, and ML: conceptualization, funding acquisition, project administration, and supervision. LC and MN: data curation and validation. LC, FA, SP, and ML: formal analysis. LC, MN, AD, SP, and PP: investigation. FA, SP, ML, and AD: methodology. SP and PP: resources. LC, AD, FA, and ML: software. LC: visualization. All authors contributed writing, review and editing the article and approved the submitted version.

FUNDING

FA acknowledged the financial support from the Sapienza University of Rome, Research Projects, 2018 (No. RM118164282B735A). ML acknowledged the financial support from the Sapienza University of Rome, Research Projects, 2017 (No. RM11715C7DCB8473).

ACKNOWLEDGMENTS

We thank Elena della Valle and Agnese Denzi for their strong support in the identification of the strengths and weaknesses of the protocol to be applied and Caterina Merla for her fruitful discussion and suggestions. We also thank Quirino Balzano, University of Maryland, College Park, MD, United States, for his valuable suggestions in manuscript finalization. Finally authors thank the COST Action CA15211 – Atmospheric Electricity Network: coupling with the Earth System, climate and biological systems (Electronet).

SUPPLEMENTARY MATERIAL

The Supplementary Material for this article can be found online at: https://www.frontiersin.org/articles/10.3389/fbioe.2020.00819/full#supplementary-material

REFERENCES

Akbarzadeh, A., Rezaei-Sadabady, R., Davaran, S., Joo, S. W., and Zarghami, N. (2013). Liposome: classification, preparation, and applications. *Nanoscale Res. Lett.* 8:102. doi: 10.1186/1556-276X-8-102

Allen, T. M., and Cullis, P. R. (2013). Liposomal drug delivery systems: from concept to clinical applications. *Adv. Drug Deliv. Rev.* 65, 36–48. doi: 10.1016/j.addr.2012.09.037

Bangham, A. D., and Horne, R. W. (1964). Negative staining of phospholipids and their structural modification by surface-active agents as observed in the electron microscope. *J. Mol. Biol.* 8, 660–668. doi: 10.1016/s0022-2836(64)80115-7

Bayat, F., Hosseinpour-Moghadam, R., Mehryab, F., Fatahi, F., Shakeri, N., Dinarvand, R., et al. (2020). Potential application of liposomal nanodevices for non-cancer diseases: an update on design, characterization and biopharmaceutical evaluation. *Adv. Colloid Interface Sci.* 277:102121. doi: 10.1016/j.cis.2020.102121

Bozzuto, G., and Molinari, A. (2015). Liposomes as nanomedical devices. *Int. J. Nanomedicine.* 10, 975–999. doi: 10.2147/IJN.S68861

Breton, M., Amirkavei, M., and Mir, L. M. (2015). Optimization of the electroformation of giant unilamellar vesicles (GUVs) with unsaturated phospholipids. *J. Membr. Biol.* 248, 827–835. doi: 10.1007/s00232-015-9828-3

Breton, M., Delemotte, L., Silve, A., Mir, L. M., and Tarek, M. (2012). Transport of siRNA through lipid membranes driven by nanosecond electric pulses: an experimental and computational study. *J. Am. Chem. Soc.* 134, 13938–13941. doi: 10.1021/ja3052365

Caramazza, L., De Angelis, A., della Valle, E., Denzi, A., Nardoni, M., Paolicelli, P., et al. (2019). "Numerical investigations of CW electric fields on lipid vesicles for controlled drug delivery," in *Proceedings of the 2019 IEEE 49th European Microwave Conference (EuMC2019)*, Paris: IEEE, 220–223.

Daeihamed, M., Dadashzadeh, S., Haeri, A., and Akhlaghi, M. F. (2017). Potential of liposomes for enhancement of oral drug absorption. *Curr. Drug Deliv.* 14, 289–303. doi: 10.2174/1567201813666160115125756

DeBruin, K. A., and Krassowska, W. (1998). Electroporation and shock-induced transmembrane potential in a cardiac fiber during defibrillation strength shocks. *Ann. Biomed. Eng.* 26, 584–596. doi: 10.1114/1.101

DeBruin, K. A., and Krassowska, W. (1999). Modeling electroporation in a single cell. I. Effects of field strength and rest potential. *Biophys. J.* 77, 1213–1224. doi: 10.1016/S0006-3495(99)76973-0

Denzi, A., della Valle, E., Apollonio, F., Breton, M., Mir, L. M., and Liberti, M. (2017a). Exploring the applicability of nano-poration for remote control in smart drug delivery systems. *J. Membrane Biol.* 250, 31–40. doi: 10.1007/s00232-016-9922-1

Denzi, A., della Valle, E., Esposito, G., Mir, L. M., Apollonio, F., and Liberti, M. (2017b). Technological and theoretical aspects for testing electroporation on liposomes. *BioMed Res. Int.* 2017, 1–10. doi: 10.1155/2017/5092704

Gu, M., Wang, X., Toh, T., and Chow, E. (2018). Applications of stimuli-responsive nanoscale drug delivery systems in translational research. *Drug Discov. Today* 23, 931–1166. doi: 10.1016/j.drudis.2017.11.009

He, R., and Kyu, T. (2016). Effect of plasticization on ionic conductivity enhancement in relation to glass transition temperature of crosslinked polymer electrolyte membranes. *Macromolecules* 49, 5637–5648. doi: 10.1021/acs.macromol.6b00918

Karal, M. A. S., Ahamed, M. K., Rahman, M., Ahmed, M., Shakil, M. M., and Siddique-e-Rabbani, K. (2019). Effects of electrically-induced constant tension on giant unilamellar vesicles using irreversible electroporation. *Eur. Biophys. J.* 48, 731–741. doi: 10.1007/s00249-019-01398-9

Kim, K., and Lee, W. G. (2017). Electroporation for nanomedicine: a review. *J. Mater. Chem. B* 5, 2726–2738. doi: 10.1039/C7TB00038C

Kotnik, T., Frey, W., Sack, M., Haberl Meglič, S., Peterka, M., and Miklavčič, D. (2015). Electroporation-based applications in biotechnology. *Trends Biotechnol.* 33, 480–488. doi: 10.1016/j.tibtech.2015.06.002

Kotnik, T., and Miklavčič, D. (2000). Theoretical evaluation of the distributed power dissipation in biological cells exposed to electric fields. *Bioelectromagnetics* 21, 385–394. doi: 10.1002/1521-186X(200007)21:5<385::AID-BEM7<3.0.CO;2-F

Lamberti, P., Romeo, S., Sannino, A., Zeni, L., and Zeni, O. (2015). The role of pulse repetition rate in nsPEF-induced electroporation: a biological and numerical investigation. *IEEE Trans. Biom. Eng.* 62, 2234–2243. doi: 10.1109/TBME.2015.2419813

Liu, X., Shi, L., and Gu, J. D. (2018). Microbial electrocatalysis: redox mediators responsible for extracellular electron transfer. *Biotechnol. Adv.* 36, 1815–1827. doi: 10.1016/j.biotechadv.2018.07.001

Liu, Y., and An, X. (2019). Preparation, microstructure and function of liposome with light responsive switch. *Colloids Surf. B. Biointerfaces* 178, 238–244. doi: 10.1016/j.colsurfb.2018.10.068

Mercadal, B., Vernier, P. T., and Ivorra, A. (2016). Dependence of electroporation detection threshold on cell radius: an explanation to observations non compatible with schwan's equation model. *J. Membr. Biol.* 249, 663–676. doi: 10.1007/s00232-016-9907-0

Merla, C., Denzi, A., Paffi, A., Casciola, M., d'Inzeo, G., Apollonio, F., et al. (2012). Novel passive element circuits for microdosimetry of nanosecond pulsed electric fields. *IEEE Trans. Biomed. Eng.* 59, 2302–2311. doi: 10.1109/TBME.2012.2203133

Moncalvo, F., Martinez Espinoza, M. I., and Cellesi, F. (2020). Nanosized delivery systems for therapeutic proteins: clinically validated technologies and advanced development strategies. *Front. Bioeng. Biotechnol.* 8:89. doi: 10.3389/fbioe.2020.00089

Murdan, S. (2003). Electro-responsive drug delivery from hydrogels. *J. Control Release* 92, 1–17. doi: 10.1016/S0168-3659(03)00303-1

Nardoni, M., Della Valle, E., Liberti, M., Relucenti, M., Casadei, M. A., Paolicelli, P., et al. (2018). Can pulsed electromagnetic fields trigger on-demand drug release from high-tm magnetoliposomes? *Nanomaterials* 8:196. doi: 10.3390/nano8040196

Neu, J. C., and Krassowska, W. (1999). Asymptotic model of electroporation. *Phys. Rev. E* 59, 3471–3482. doi: 10.1103/PhysRevE.59.3471

Perrier, D. L., Rems, L., and Boukany, P. E. (2017). Lipid vesicles in pulsed electric fields: fundamental principles of the membrane response and its biomedical applications. *Adv. Colloid Interface Sci.* 249, 248–271. doi: 10.1016/j.cis.2017.04.016

Perrier, D. L., Rems, L., Kreutzer, M. T., and Boukany, P. E. (2018). The role of gel-phase domains in electroporation of vesicles. *Sci. Rep.* 8:4758. doi: 10.1038/s41598-018-23097-9

Petralito, S., Spera, R., Memoli, A., d'Inzeo, G., Liberti, M., and Apollonio, F. (2012). Preparation and characterization of lipid vesicles entrapping iron oxide nanoparticles. *Asia-Pac. J. Chem. Eng.* 7, 335–341. doi: 10.1002/apj.1653

Portet, T., Mauroy, C., Démery, V., Houles, T., Escoffre, J. M., Dean, D. S., et al. (2012). Destabilizing giant vesicles with electric fields: an overview of current applications. *J. Membr. Biol.* 245, 555–564. doi: 10.1007/s00232-012-9467-x

Postow, E., and Polk, C. (1996). *Handbook of Biological Effects of Electromagnetic Fields*. Boca Raton, FL: CRC Press.

Retelj, L., Pucihar, G., and Miklavcic, D. (2013). Electroporation of intracellular liposomes using nanosecond electric pulses — A theoretical study. *IEEE Trans. Biomed. Eng.* 60, 2624–2635. doi: 10.1109/TBME.2013.2262177

Riley, R. S., June, C. H., Langer, R., and Mitchell, M. J. (2019). Delivery technologies for cancer immunotherapy. *Nat. Rev. Drug Discov.* 18, 175–196. doi: 10.1038/s41573-018-0006-z

Rosenblum, D., Joshi, N., Tao, W., Karp, J. M., and Peer, D. (2018). Progress and challenges towards targeted delivery of cancer therapeutics. *Nat. Commun.* 9:1410. doi: 10.1038/s41467-018-03705-y

Senapati, S., Mahanta, A. K., Kumar, S., and Maiti, P. (2018). Controlled drug delivery vehicles for cancer treatment and their performance. *Signal Transduct. Target Ther.* 3:7. doi: 10.1038/s41392-017-0004-3

Silve, A., Guimerà Brunet, A., Al-Sakere, B., Ivorra, A., and Mir, L. M. (2014). Comparison of the effects of the repetition rate between microsecond and nanosecond pulses: electropermeabilization-induced electro-desensitization?. *Biochim. Biophys. Acta* 1840, 2139–2151. doi: 10.1016/j.bbagen.2014.02.011

Silve, A., Leray, I., Poignard, C., and Mir, L. M. (2016). Impact of external medium conductivity on cell membrane electropermeabilization by microsecond and nanosecond electric pulses. *Sci. Rep.* 6:19957. doi: 10.1038/srep19957

Spera, R., Apollonio, F., Liberti, M., Paffi, A., Merla, C., Pinto, R., et al. (2015). Controllable release from high-transition temperature magnetoliposomes by low-level magnetic stimulation. *Colloids Surf. B. Biointerfaces* 131, 136–140. doi: 10.1016/j.colsurfb.2015.04.030

Spera, R., Petralito, S., Liberti, M., Merla, C., d'Inzeo, G., Pinto, R., et al. (2014). Controlled release from magnetoliposomes aqueous suspensions exposed to a low intensity magnetic field. *Bioelectromagnetics* 35, 309–312. doi: 10.1002/bem.21841

Williams, D. F. (2008). On the mechanisms of biocompatibility. *Biomaterials* 29, 2941–2953. doi: 10.1016/j.biomaterials.2008.04.023

Yuba, E. (2020). Development of functional liposomes by modification of stimuli-responsive materials and their biomedical applications. *J. Mater. Chem. B* 8, 1093–1107. doi: 10.1039/C9TB02470K

Zhang, C., Yue, X., Mu, Y., Zuo, X., Lu, N., Luo, Y., et al. (2019). Novel pore-filling membrane based on block sulfonated poly (ether sulphone) with enhanced proton conductivity and methanol resistance for direct methanol fuel cells. *Electrochimica Acta* 307, 188–196. doi: 10.1016/j.electacta.2019.03.189

Conflict of Interest: The authors declare that the research was conducted in the absence of any commercial or financial relationships that could be construed as a potential conflict of interest.

Copyright © 2020 Caramazza, Nardoni, De Angelis, Paolicelli, Liberti, Apollonio and Petralito. This is an open-access article distributed under the terms of the Creative Commons Attribution License (CC BY). The use, distribution or reproduction in other forums is permitted, provided the original author(s) and the copyright owner(s) are credited and that the original publication in this journal is cited, in accordance with accepted academic practice. No use, distribution or reproduction is permitted which does not comply with these terms.

frontiers in Bioengineering and Biotechnology

ORIGINAL RESEARCH
published: 29 July 2020
doi: 10.3389/fbioe.2020.00857

Enzymatic Processes Triggered by PEF for Astaxanthin Extraction From *Xanthophyllomyces dendrorhous*

*Diederich Aguilar-Machado[1,2], Carlota Delso[1], Juan Manuel Martinez[1], Lourdes Morales-Oyervides[3], Julio Montañez[3] and Javier Raso[1]**

[1] Food Technology, Facultad de Veterinaria, Universidad de Zaragoza, Zaragoza, Spain, [2] Department of Food Research, Universidad Autónoma de Coahuila, Saltillo, Mexico, [3] Department of Chemical Engineering, Universidad Autónoma de Coahuila, Saltillo, Mexico

The aim of this study was to evaluate the potential of pulsed electric fields (PEF) to improve the extraction of the lipid-soluble astaxanthin from fresh biomass of a wild-type (CECT 11028) and mutant (ATCC 74219) *Xanthophyllomyces dendrorhous* strain using ethanol as solvent. Inactivation and propidium uptake studies revealed that inactivation is a good index for estimated the proportion of irreversible permeabilized cells when inactivation is higher than 70% in the two strains. Ethanol was ineffective for extracting carotenoids from the PEF-treated cells (20 kV/cm, 135 μs) of the two strains. However, after aqueous incubation of PEF-treated *X. dendrorhous* ATCC 74219 cells for 12 h, up to 2.4 ± 0.05 mg/g dried weight (d.w.) of carotenoids were extracted in ethanol. From total carotenoid extracted, around 84% corresponded to all-trans astaxanthin. The detection and quantification of esterase activity in the supernatant and the relationship between the percentage of esterase activity quantified and the amount of carotenoids extracted indicate that the extraction of astaxanthin was mediated by enzymatic esterase activity triggered by PEF during incubation. On the other hand, the formation of a large lipid globule into the cytoplasm of PEF-treated *X. dendrorhous* CECT 11028 cells during aqueous incubation prevented carotenoid extraction. The process developed in this investigation represents a more sustainable and greener method that those previously used for extracting astaxanthin from yeast.

Keywords: astaxanthin, pulsed electric field, extraction, *Xanthophyllomyces dendrorhous*, esterase, enzymatic activity

OPEN ACCESS

Edited by:
Eugene Vorobiev, University of Technology of Compiègne, France

Reviewed by:
Noppol-Leksawasdi, Chiang Mai University, Thailand
Daidi Fan, Northwest University, China

***Correspondence:**
Javier Raso
jraso@unizar.es

Specialty section:
This article was submitted to Bioprocess Engineering, a section of the journal Frontiers in Bioengineering and Biotechnology

Received: *15 April 2020*
Accepted: *02 July 2020*
Published: *29 July 2020*

Citation:
Aguilar-Machado D, Delso C, Martinez JM, Morales-Oyervides L, Montañez J and Raso J (2020) Enzymatic Processes Triggered by PEF for Astaxanthin Extraction From Xanthophyllomyces dendrorhous. Front. Bioeng. Biotechnol. 8:857. doi: 10.3389/fbioe.2020.00857

INTRODUCTION

Astaxanthin (3,3′-dihydroxy-β, β-carotene-4,4′-dione; $C_{40}H_52O_4$) is a lipid-soluble oxycarotenoid widely used in food, aquaculture, nutraceutical, cosmetic and pharmaceutical industries due to its relatively high antioxidant activity compared with other antioxidant molecules. It has been reported that astaxanthin has 10 times the antioxidant activity of β-carotene, 60 times of coenzyme Q10, and 1000 times more antioxidant activity than vitamin E (Higuera-Ciapara et al., 2006; Shah et al., 2016; Zhao et al., 2019). Astaxanthin unique chemical structure makes it a powerful antioxidant with extraordinary biological and physiological properties including cardiovascular disease prevention, strengthening the immune system and anti-tumoral, anti-inflammatory, and anti-diabetes effects (Kurihara et al., 2002; Uchiyama et al., 2002; Ohgami et al., 2003; Pashkow et al., 2008; Nagendraprabhu and Sudhandiran, 2011; Peng et al., 2012; Fakhri et al., 2018).

Currently, the main use of astaxanthin is as a feed additive for providing the characteristic pink/red color of salmons, trout, and crustaceans. Around 99% of astaxanthin available in the market is produced synthetically due to their low production cost, high purity, and high stability, and only around 1% of astaxanthin derived from a natural source. The total astaxanthin production was about 200 tons in 2014 worth 368 million euros and this is expected to encrease double in 2022 (Molino et al., 2018). However, synthetic astaxanthin has not been approved for human consumption by safety concerns related to the use of petrochemicals during its synthesis process (Li et al., 2011; Shah et al., 2016). On the other hand, natural astaxanthin has gained huge attention from researches and consumers in the last years. Studies have suggested that natural astaxanthin has around 20 times more antioxidant activity compared with the synthetic molecule (Capelli et al., 2013). The growing demand from industries and consumers has encouraged researches to demonstrate the feasibility of astaxanthin production and extraction from diverse natural sources.

The yeast *Xanthophyllomyces dendrorhous* is considered one of the most important sources of natural astaxanthin because around 84% of the total carotenoids that it synthesizes correspond to these compound (Stoklosa et al., 2018). Astaxanthin is formed as different geometrical isomers with cis and trans double bonds in the polyene chain. The yeast *X. dendrorhous* synthesize the all-trans isomer mainly, but the 9-cis and 13-cis isomers can be also found (Schmidt et al., 2011). The high-rate cell growth with short cultivation cycles, the ability to metabolize waste-based culture media, no seasonal conditions constraints and the easy manipulation of culture conditions to improve yields make the yeast *X. dendrorhous* an alternative for large scale production of natural astaxanthin (Wu et al., 2018; Villegas-Méndez et al., 2019). Generally astaxanthin production from naturally isolated strains of *X. dendrorhous* is very low (between 200 and 400 μg/g), however, some authors have developed genetic manipulations to get hyper-producer strains with yields up to 10-fold higher than the wild-type strains (Visser et al., 2003; Zhuang et al., 2020).

Xanthophyllomyces dendrorhous accumulates astaxanthin in the cytoplasm in the form of droplets associated with the cytoplasmatic membrane and fatty acids (Johnson and Gil-Hwan, 1991; Jacobson et al., 1995; Urnau et al., 2018). The presence of a thick, rigid and indigestible cell envelope, as well as the lipophilic nature of astaxanthin, are the biggest challenges in the development of efficient methodologies for extraction of this compound (Gogate and Nadar, 2015). Over the last years, several cell wall disruption processes such as chemical (acid extraction), enzymatic and physical or mechanical (ultrasound, microwave, high-pressure homogenization) methods have been evaluated to facilitate the recovery of intracellular carotenoids from *X. dendrorhous* (Choi et al., 2007; Ni et al., 2008; Michelon et al., 2012; Gogate and Nadar, 2015; Hasan et al., 2016; Urnau et al., 2018; Zhuang et al., 2020). However, those techniques present some disadvantages such as high implementation costs, long extraction time, excessive cell destruction and high cost of purification of the target molecule (Martínez et al., 2018). Furthermore, most carotenoids extraction techniques require the drying of biomass with subsequent extraction with a large amount of organic solvent. Therefore, it is desirable to develop efficient extraction methods from wet biomass using green solvents in order to achieve economical and eco-friendly processes (Martínez et al., 2019).

Pulsed electric fields (PEF) is a technique that consists in the application of an external electric field to induce the permeabilization (electroporation) of biological membranes (Kotnik et al., 2015). In contrast to other technologies that cause cell disruption, energetic requirements of PEF are low, it is easily scalable, does not result in cell disintegration, minimizing the release of cell debris and facilitating purification of the extracted compound (Kotnik et al., 2015).

Several studies have demonstrated that electroporation by PEF improve the extraction of intracellular components such as proteins, lipids, and pigments from microorganisms has been reported (Ganeva et al., 2003; Chittapun et al., 2020; Leonhardt et al., 2020). Very recently, it has been proposed that PEF not only permeabilized the cytoplasmatic membrane to enable the release of intracellular biomolecules but also trigger some enzymatic process that accelerates the autolysis and the subsequent release of intracellular components (Martínez et al., 2018, 2019; Silve et al., 2018; Scherer et al., 2019). The application of PEF technology on the recovery of intra-cellular carotenoids from *X. dendrorhous* has not been reported.

This study aimed to evaluate the effect of PEF-assisted on the extraction of astaxanthin from fresh biomass of a wild-type and a mutant hyper-producer *X. dendrorhous* strain using ethanol as solvent.

MATERIALS AND METHODS

Yeast Strains and Culture Conditions

The wild-type *X. dendrorhous* CECT 11028 and the mutant hyper-producer *X. dendrorhous* ATCC 74219 strains were obtained from the Colección Española de Cultivos Tipo (CECT) and the American Type Culture Collection (ATCC, Beltsville, MD, United States), respectively. The microorganisms were maintained in cryovials at −80°C. Yeasts were grown in 500 mL glass flask containing 250 mL of Potato-Dextrose Broth (PDB, Oxoid, Basingstoke, United Kingdom) for 6 days in a rotatory shaker (Heidolph Unimax 1010, Germany) at 200 rpm and 25°C. The inoculum was around 10^6 cells/mL defined by Thoma counting chamber.

Yeast growth was monitored by measuring the cell density at 600 nm and the cell number by the plate-counting method (PDA, Oxoid, Basingstoke, United Kingdom). Incubation time needed to obtain the maximum carotenoid production was established by determining the carotenoid production during the cultivation period using the dimethyl sulfoxide method as described below.

PEF Treatments

Pulsed electric fields unit (Modulator PG, ScandiNova, Uppsala, Sweden) used in this investigation was previously described by Saldaña et al. (2010). Before the treatments, fresh biomass of *X. dendrorhous* CECT 11028 and *X. dendrorhous* ATCC 74219

were centrifuged (Heraeus Megafuge 1.0R, United Kingdom) at 3000 × *g* for 5 min at 4°C. Next, the pellet was resuspended in a citrate-phosphate McIlvaine buffer (pH 7.0, 1 mS/cm) to a final concentration of approximately 10^8 cell/mL. The cell suspension (0.5 mL) of each strain was deposited in a static parallel-electrode tempered chamber (25 ± 1°C) with a gap of 0.25 cm and a radius of 0.8 cm employing a 1 mL sterile syringe (TERUMO, Leuven, Belgium). The cell suspension was subjected to PEF treatment of 10–60 monopolar square pulses of 3 μs pulses at electric field strength between 10 and 25 kV/cm at 0.5 Hz.

PEF Treatment Intensity Effect on Cell Inactivation and Irreversible Permeabilization

PEF treatment intensity was evaluated between 10 to 25 kV/cm at 0.5 Hz frequency. The specific energy applied during treatments ranged from 3.0 to 114.3 kJ/kg, corresponding to the minimum and maximum treatment intensity applied, respectively.

After PEF treatment, cells were plated in PDA and incubated at 25°C for 72 h. The inactivation degree was expressed as the logarithmic ratio of the initial number (N_o) of cells and the number of survivors (N_t) after different PEF treatments.

The irreversible permeabilization after PEF treatments was quantified by propidium iodide uptake technique (García-Gonzalo and Pagán, 2017). PEF-treated and untreated cells were stained after 1 h of the PEF treatments. 50 μL of PI (0.1 mg/mL) was added to 450 μL of yeast cell suspension and incubated under dark conditions for 5 min. Then, the cells were centrifugated and washed with 450 μL of phosphate-buffered saline (PBS) solution of pH 7.4 to remove the extracellular PI remained. This procedure was repeated three times.

PEF Treatment Intensity Effect on Carotenoid Extraction

Non-treated or PEF-treated yeast suspensions (10^8 cell/mL) either immediately after PEF treatment or after an incubation process ranging from 3 to 24 h at 25°C in a buffer solution of pH 7.0 were centrifuged at 3,000 × *g* for 5 min and re-suspended in ethanol at 96% for 12 h. After incubation, total carotenoids were quantified following the methodology described below.

After selecting the required incubation time in the buffer solution of pH 7.0, the kinetics of carotenoids extraction were evaluated for non-treated and PEF-treated cells at different electric field strengths (10, 15, 20, and 25 kV/cm for 135 μs).

Evaluation of the Enzymatic Activity in the Supernatant Containing Yeast

Enzymatic activity was evaluated in the supernatant of PEF-treated cells during the incubation in buffer solution. Untreated cells were used as control. Then, enzymatic thermal inactivation and its effect on carotenoids extraction were also assessed.

β-Glucanase Activity Measurement

β-glucanase activity (EC 3.2.1.6) in the supernatant of PEF-treated and untreated cells was conducted using the Megazyme Azo-barley β-glucan method (malt and bacterial β-glucanase and cellulase assay procedure, Megazyme, Ireland). Aliquots of 0.05 mL of Azo-Barley glucan substrate solution (pre-heated at 30°C) were dispensed into centrifuge tubes and incubated at 30°C for 5 min. After that, 1 mL of the supernatant of each yeast suspension was mixed with the pre-heated glucan substrate and incubated at 30°C for 10 min. After incubation, 3 mL of the precipitant solution [30.0 g of $C_2H_3NaO_2$ and 3.0 g of $ZnC_4H_6O_4$ in 1 L of ethanol (66.5%), methanol (3.5%) and water (30%)] were added and stirred vigorously. Tubes were stored at room temperature for 5 min, stirred and centrifuged (1000 × *g*, 10 min). Finally, absorbance at 590 nm of the supernatant of each sample was read against distilled water. With each set of determinations, a reaction blank was included. Enzymatic activity was calculated by correlating the malt β-glucanase standard curve on Azo Barley Glucan and absorbance from each sample.

Esterase Activity Measurement

The measurement of esterase enzymatic activity (EC 3.1.1.1) of supernatant of PEF-treated and untreated cells was performed with the colorimetric *p*-nitrophenyl chromogenic assay (Gilham and Lehner, 2005). For analysis, a stock solution of 250 mM of *p*-nitrophenyl-acetate dissolved in dichloromethane (Cl_2CH_2) was prepared. Immediately before determination, 20 μL of stock solution was diluted in 10 mL of a McIlwaine buffer (pH 8.0 and conductivity of 1 mS/cm). Then, 100 μL of the supernatant of each incubation time was added and vortexed with 1 mL of *p*-nitrophenyl-acetate solution in glass tubes and incubated at 37°C for 30 min. The liberation of p-nitrophenol was proportional to esterase activity measured spectrophotometrically at 410 nm. Distilled water was used as a blank.

Esterase Thermal Inactivation and Release of Carotenoids From Yeast

A suspension of PEF-treated cells (20 kV/cm and 135 μs) was heat-treated at 50 and 60°C ± 1°C for 5 min and incubated in a buffer solution of pH 7.0 for 12 h at 25°C. Preliminary experiments were conducted to define the temperatures levels required to inactivate esterase without affecting astaxanthin. After incubation, unheated and heat-treated PEF-treated cells were centrifugated and suspended in ethanol for carotenoids extraction during 24 h. The supernatant was analyzed to determine the amount of the esterase activity remaining after incubation. The percentage of esterase activity remained in the heat-treated samples was calculated according to the maximum esterase activity quantified in the unheated PEF-treated cell suspension after 12 h of incubation.

Analytical Methods

Total carotenoids were recovered and quantified following the methodology described by Sedmak et al. (1990). 0.5 mL of Dimethyl sulfoxide (DMSO) was added to 1.0 mL of biomass previously centrifugated. Then 0.2 mL of 0.01 M sodium phosphate and 2.0 mL of hexane: ethyl acetate (1:1) was added and vortexed for 5 min. The samples were then centrifugated for 5 min at 10,000 × *g* to separate the organic phase. Carotenoids concentration was quantified spectrophotometrically for DMSO

extraction and PEF assisted extraction. The total carotenoid yield was calculated using the equation:

$$Yx = \frac{V^*A^*10^6}{E^{1\%}*100*M} \quad (1)$$

where Yx represents the carotenoid yield (mg/g d.w.); A is the absorbance at 480 nm; V the volume of solvent used (mL); M the dry cell mass (g) and $E^{1\%}$ the specific absorptivity of solvent (2100).

For HPLC analysis, the ethanolic extract of each sample was previously evaporated in a vacuum concentrator and then resuspended in methanol/dichloromethane (3:1, v/v) for subsequent injection. Astaxanthin quantification was performed according to the method described by Yuan and Chen (1997). HPLC analysis was performed on a Varian ProStar high-performance liquid chromatograph equipped with a ProStar 240 ternary pump, an automatic ProStar 410 autosampler and a ProStar 335 photodiode array detector. The separation was performed using a reverse-phase column (LC Luna® 100 Å C18 250 × 4.6 mm; 5 μm particle size, Phenomenex, United States) with a pre-column (LC Luna 50 × 4.6 mm; 5 μm particle size, Phenomenex, United States). A single mobile phase of methanol/dichloromethane/water (80.5:17:2.5, by volume) was used during analysis. The flow rate was 1.0 mL/min with a pre-conditioned sample at 25°C. *Trans*-astaxanthin concentration was determinate by comparing the time retention of a commercial standard of *trans*-astaxanthin (Sigma, St Louis, MO, United States) with each sample analyzed.

Statistical Analysis

All experiments were performed in triplicate and presented as the average value ± standard deviation (SD). The differences were considered significant to $p < 0.05$. One-way analysis of variance (ANOVA) and Tukey test were used to determine the significant differences between treatment using Statistica 7.0 (Statsoft, Tulsa, OK, United States).

RESULTS

Sensitivity of *X. dendrorhous* CECT 11028 and *X. dendrorhous* ATCC® 74219™ to Pulsed Electric Field Treatments

The inactivation by PEF treatments of the two *X. dendrorhous* strains used in this study (CECT 11028 and ATCC 74219) varying electric field strength and treatment time is shown in **Figures 1A,B**, respectively. It can be seen that the inactivation increased with the electric field strength and treatment time above the electric field threshold that was 10 and 15 kV/cm for the strains CECT 11028 and ATCC 74219, respectively. *X. dendrorhous* ATCC 74219 presented higher resistance to PEF inactivation compared to *X. dendrorhous* CECT 11028 under the most intense treatment mainly. For example, while 1.6, 2.55 and 2.56 Log_{10} cycles of inactivation were observed after 15, 20 and 25 kV/cm and 180 μs for the CECT 11028 strain, an inactivation of 0.61, 0.81 and 1.25 Log10 cycles was obtained for *X. dendrorhous* ATCC 74219.

It is well-known that one of the effects of PEF is the loss of the selective permeability of the cell membranes as a consequence of the electroporation. Irreversible electroporation allows the uncontrolled pass of ions and macromolecules through the cell membranes leading to microbial inactivation by loss of the cellular homeostasis. **Figure 2** shows the relationship between the percentage of inactivated and irreversible permeabilized cells after the application of PEF at different intensities (10–25 kV/cm) for both strains (PI results can be viewed in the **Appendix Figure A1**). For both microorganisms, a good correlation between irreversible electroporation and inactivation was observed when the percentage of cell death was higher than 70%. On the other hand, a higher percentage of inactivated cells compared to PI permeabilized cells were observed when the inactivation was below this value. The lack of correlation between the percentage of dead and permeabilized cells when the inactivation effect was low could indicate that a certain number of inactivated cells were able to recover the integrity of their membrane even after losing their viability (García et al., 2007; Luengo et al., 2014; Martínez et al., 2018). Therefore, this proportion of inactivated cells would behave just like those non-electroporated cells during the extraction of intracellular compounds.

Carotenoid Extraction of *Xanthophyllomyces* Strains Assisted by PEF

According to the data obtained from the inactivation and permeabilization, a PEF treatment at 20 kV/cm for 135 μs that corresponds to a total specific energy of 54 kJ/kg was then selected to evaluate the effect of PEF in the carotenoids extraction from the two *X dendrorhous* strains. This PEF treatment resulted in an inactivation/permeabilization of around 80% in the cell population of the two strains.

Preliminary studies showed that when both untreated and PEF-treated cells were immediately suspended in ethanol, the presence of carotenoids in the extraction medium was deficient even after 48 h of incubation.

Then, the influence of the incubation time in a buffer solution (pH 7.0) before the extraction with ethanol was evaluated on untreated and PEF-treated cells of both *X. dendrorhous* strains. The results are shown in **Figure 3**. It can be observed that the incubation in the buffer solution was ineffective for extracting carotenoids in the PEF-treated cells of CECT 11028 strain and untreated cells of both strains. For such cases, extracted carotenoids never reached values over 0.25 ± 0.01 mg/g d.w. throughout all evaluated incubation time. Nevertheless, mutant PEF-treated cells resulted in a subsequent extraction yield of 0.88 ± 0.10 mg/g d.w. after 3 h of incubation, reaching a maximum value after 12 h of incubation (1.9 ± 0.18 mg/g d.w.). Extraction yields obtained at 24 h of incubation were not significantly different from those obtained at 12 h ($p < 0.05$). The extraction achieved after 12 h of incubation represented an improvement

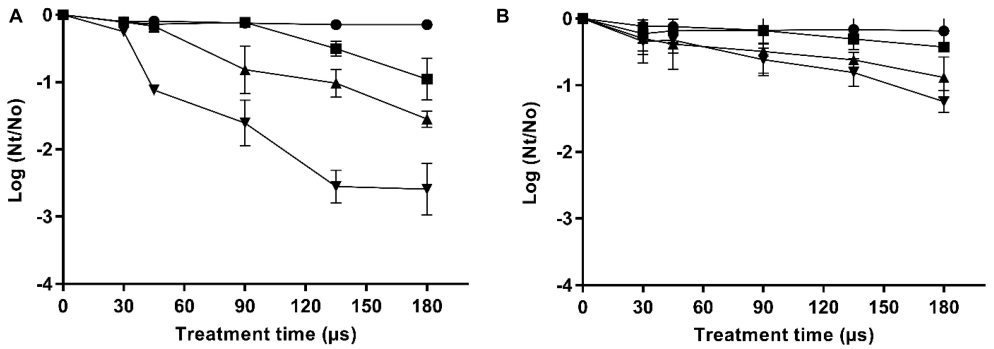

FIGURE 1 | Inactivation curves of *X. dendrorhous* CECT 11028 **(A)** and *X. dendrorhous* ATCC 74219 **(B)** by PEF at different electric fields strength. 10 kV/cm (●), 15 kV/cm (■), 20 kV/cm (▲), 25 kV/cm (▼).

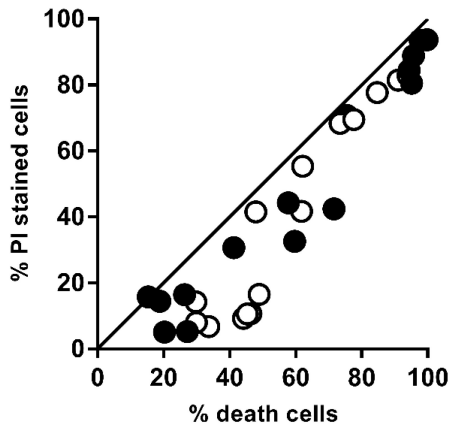

FIGURE 2 | Relationship between the percentage of irreversible permeabilized cells and the percentage of dead cells of *X. dendrorhous* CECT 11028 (●) and *X. dendrorhous* ATCC 74219 (○) after applied PEF treatments shown in **Figure 1**. The straight line with slope 1 and intercept 0 represents a perfect agreement between the percentage of PI uptake and cell death.

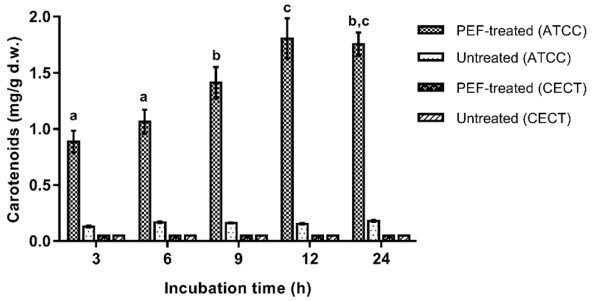

FIGURE 3 | Influence of the incubation time in buffer of pH 7.0 on the extracted carotenoids in ethanol for 12 h from untreated and PEF treated cells of *X. dendrorhous* CECT 11028 and *X. dendrorhous* ATCC 74219. Different letter indicates significant statistical differences ($p < 0.05$).

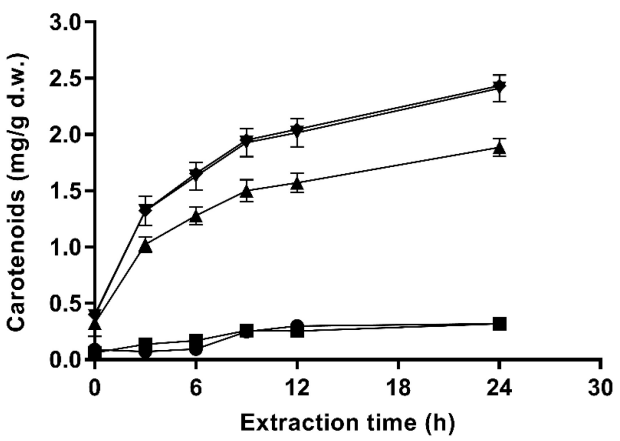

FIGURE 4 | Effect of the electric field strength on ethanolic extraction kinetics of carotenoids from and *X. dendrorhous* ATCC 74219 after 12 h of incubation in buffer of pH 7.0: 10 kV/cm (■), 15 kV/cm (▲), 20 kV/cm (▼), 25 kV/cm (♦), and untreated (●).

of more than twice the extraction yield achieved at the first 3 h of incubation and around 9.5-fold compared with untreated samples.

Since only the pre-treatment by PEF for carotenoids extraction was effective for *X. dendrorhous* ATCC 74219, only this strain was selected for subsequent studies in this section. Thereafter, the intensity of the PEF treatment and extraction time in ethanol effect on the carotenoids recovery yield was evaluated. The incubation time in buffer was kept at 12 h for such studies.

The extraction kinetics in ethanol of carotenoids from untreated and PEF-treated cells at different pulsed electric field strength (135 μs) are shown in **Figure 4**. Untreated cells and PEF-treated with the lowest applied electric field (10 kV/cm) resulted in poor extraction yields. However, significant extraction levels were obtained at electric field strength equal to or higher than 15 kV/cm. These results confirmed that it was required the irreversible electroporation of the cell membranes to be able to improve carotenoids yields from fresh biomass of *X. dendrorhous* ATCC 74219 after buffer incubation. On the other hand, an increment in the electric field strength from 20 to 25 kV/cm did not significantly affect the extraction yield, supporting the

TABLE 1 | Astaxanthin quantification by HPLC of ethanolic carotenoid extracts obtained from PEF-treated cells of *X. dendrorhous* ATCC 74219 at different treatment intensities and specific energy applied after 12 h of incubation in buffer of pH 7.0.

Electric field strength (kV/cm)	Energy applied (KJ/kg)	Yield, carotenoids (mg/g)	Extractability (%)	Yield, *trans* astaxanthin (mg/g)	*Trans*-astaxanthin (%)
10.00	13.50	0.32 ± 0.02^{a}	9 ± 0.54^{a}	0.32 ± 0.05^{a}	100 ± 0.0^{a}
15.00	31.20	1.89 ± 0.08^{b}	54 ± 2.24^{b}	1.54 ± 0.17^{b}	82 ± 0.84^{b}
20.00	54.00	2.41 ± 0.12^{c}	69 ± 3.37^{c}	1.92 ± 0.01^{c}	80 ± 0.38^{c}
25.00	85.73	2.43 ± 0.05^{c}	70 ± 1.29^{c}	2.06 ± 0.02^{c}	84 ± 0.38^{c}
Control		0.32 ± 0.02^{a}	9 ± 0.54^{a}		
Total carotenoids (DMSO)		3.50 ± 0.15^{d}	100 ± 0.0^{d}	2.81 ± 0.18^{d}	80 ± 1.69^{d}

Results are the average values of three independents experiments (mean ± standard deviation). $^{a–d}$Different letter indicates significant statistical differences ($p < 0.05$).

fact that no statistically significant differences in the number of inactivated cells were observed at this electric field strength levels during 135 μs (**Figure 1B**).

Additionally, the extraction pattern depicted in **Figure 4** shows a typical profile for solid-liquid extraction processes. The highest extraction rate was observed during the first 9 h of the process (around 80% of the total carotenoids were extracted). Then, the equilibrium seems to be reached at a lower rate.

The carotenoid extractability and trans-astaxanthin yields and the trans-astaxanthin percentage of recovered carotenoids obtained at each evaluated electric field strength levels after 12 h of buffer incubation and 24 h extraction with ethanol are shown in **Table 1**. Results for untreated samples (control), total carotenoids (extracted with DMSO) and the total specific energy applied at each electric field strength level are also shown. Total carotenoid yield recovered with the conventional method (DMSO) was 3.50 ± 0.15 mg/g d.w. Carotenoids yields ranged between 0.32 ± 0.02 and 2.43 ± 0.05 mg/g d.w. for PEF-treated cells, which corresponded to 9–70% of extractability. The carotenoid yield obtained with the control (untreated/ethanol) was 0.32 ± 0.02 mg/g d.w. (9% extractability). Thus, there was not a significant difference between the control and PEF-treated cells with an electric field level of 10 kV/cm. The highest carotenoid extraction yield was observed by applying an electric field strength in the range of 20–25 kV/cm and 135 μs, representing an extractability value of 70% of total carotenoids contained in the yeast suspension. However, at 20 kV/cm implies that 37% less energy is required in comparison with treatment at 25 kV/cm.

HPLC analysis of the carotenoid extracts showed that from the recovered carotenoids, 80–84% corresponded to *trans*-astaxanthin for PEF-treated samples (**Table 1**). Similar% *trans*-astaxanthin was obtained for the total carotenoids extracted with DMSO (80%).

Understanding Mechanism Involved in the Extraction Assisted by PEF of Carotenoid From *Xanthophyllomyces* Strains

After demonstrating the efficacy of ethanol for extracting large amounts of carotenoids from PEF-treated *X. dendrorhous* ATCC 74219 previously incubated in a buffer (pH = 7.0), studies were conducted in order to get an insight into the mechanisms involved and to be able to explain the inefficiency of PEF-treatment on the wild strain.

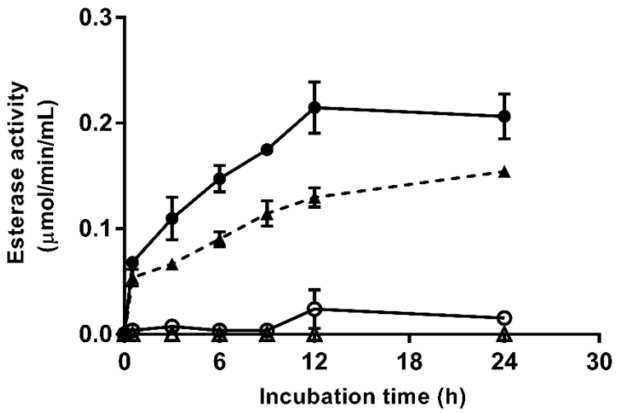

FIGURE 5 | Esterase activity during aqueous incubation at 25°C of untreated (△) and PEF-treated (▲) *X. dendrorhous* CECT 11028 cells and untreated (○) and PEF-treated (●) *X. dendrorhous* ATCC 74219 cells.

In order to verify if the PEF treatment triggered an enzymatic process that enabled the carotenoid extraction of *X. dendrorhous*, the β-glucanase and esterase activities were measured during the incubation of the untreated and PEF-treated cells (20 kV/cm and 135 μs) in a buffer of pH 7.

The β -glucanase activity was not detected in the supernatant of the suspension containing untreated or PEF-treated cells of both *X. dendrorhous* strains after 12 h of incubation at 25°C (data not showed).

Enzymatic esterase activity during aqueous incubation at 25°C of untreated and PEF-treated *X. dendrorhous* ATCC 74219 and CECT 11028 cells are shown in **Figure 5**. Esterase activity in the media containing untreated cells was negligible even after 24 h of incubation. In contrast, esterase activity in the media containing PEF-treated cells of both *X. dendrorhous* strains increased along the time, reaching the maximum activity and equilibrium after 12 h of aqueous incubation, approximately. Such results suggested that the enzyme esterase was released from the cytoplasm of the treated cells as consequence of the

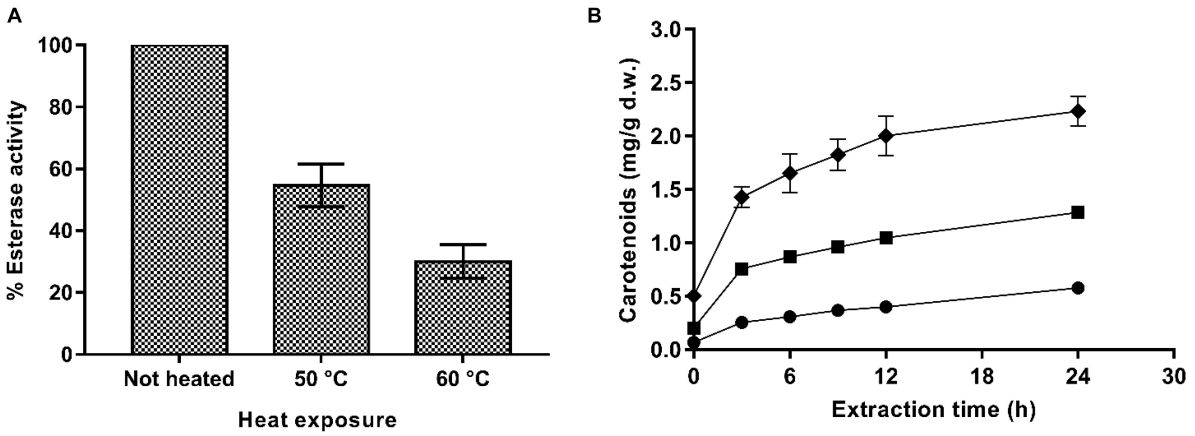

FIGURE 6 | (A) Percentage of esterase activity remaining in the supernatant containing PEF-treated (20 kV/cm, 135 μs) *X. dendrorhous* ATCC 74219 cells after 5 min of heating at 50 and 60°C. **(B)** Effect of the thermal inactivation of esterase on ethanolic extraction of carotenoids from and *X. dendrorhous* ATCC 74219 after 12 h of incubation in buffer of pH 7.0: unheated (♦) and heat-treated at 50°C (■), 60°C (●). The 100% of esterase activity represent the maximum esterase activity quantified in the unheated PEF-treated cells supernatant.

electroporation caused by PEF. However, despite the higher enzymatic activity detected in the ATCC 74219 strain, the fact that esterase activity was detected during the aqueous incubation of both strains makes unclear whether the esterase enzyme is involved in the mechanisms of the extraction assisted by PEF.

Thus, to confirm this hypothesis, an experiment consisting of exposing the PEF-treated *X. dendrorhous* ATCC 74219 cells to a heat treatment before incubation in buffer of pH 7.0 to denaturalize esterase enzyme was conducted. Percentages of esterase activity remaining in the supernatant containing PEF-treated cells treated for 5 min at 50 and 60°C after 12 h of incubation in buffer are shown in **Figure 6A**. Extraction curves of carotenoids from PEF-treated cells treated at 50 and 60°C after 12 h of buffer incubation and subsequent extraction in ethanol are compared with the carotenoid extraction from unheated cells in **Figure 6B**.

Results showed that the thermal treatment effectively inactivated the esterase enzyme, decreasing its activity in the supernatant by 50 and 75% for the treatments applied at 50 and 60°C, respectively. Accordingly, carotenoid recovery was much lower for the heat-treated PEF-treated cells along all the extraction process. After 24 h of extraction, a decrease by 42 and 72% in the extraction yield was observed for thermally treated cells at 50 or 60°C, respectively.

The correlation between carotenoid extraction yield and the esterase activity reduction in the supernatant containing PEF-thermally treated cells would confirm that PEF assisted extraction of carotenoids was a process mediated by esterases at the evaluated conditions at least for from *X. dendrorhous* ATCC 74219. However, these results are in contrast to those observed in *X. dendrorhous* CECT 11028, where the esterase activity detected in the PEF-treated cells were not correlated with carotenoids extraction.

An optical microscopy comparation after 12 h of incubation at 25°C in a buffer of pH 7.0 of untreated and PEF-treated cells of the two strains of *X. dendrorhous* is shown in **Figure 7**. It was observed at the beginning of the incubation (data not shown), that carotenoids were located in the cytoplasm into droplet structures. Incubation for 12 h did not cause any significant change in the untreated cells of both strains. Furthermore, optical observation confirmed the higher carotenoid production by *X. dendrorhous* ATCC 74219 (3.5 ± 0.15 mg/g d.w.) compared to *X. dendrorhous* CECT 11028 (0.36 ± 0.02 mg/g d.w.). While in the hyper-producer most of the observed droplets corresponded to carotenoids in the other strain most droplets correspond to lipids.

On the other hand, significant differences were observed between the two strains when the PEF-treated cells were incubated in pH 7.0 buffer. While complete droplet disintegration was observed in *X. dendrorhous* ATCC 74219, in the case of the strain CECT 11028 incubation of the PEF-treated cells clearly led to lipid droplet fusion in a bigger droplet. In both cases, the changes in the droplets observed after incubation could be mediated by esterases, which activity was triggered by the electroporation of the cell membrane of the yeast. These observations seem to indicate that ethanol was only effective for extracting those intracellular carotenoids that are free in the cytoplasm. However, ethanolic extraction was ineffective when the carotenoids were located into droplet structures such as in untreated or PEF-treated cells before incubation in both strains or as in the CECT 11028 strain after 12 h of incubation.

DISCUSSION

Pulsed electric fields-assisted extraction of intracellular compounds is associated with the improvement of mass transfer processes trough cytoplasmic membrane once its permeability has been modified by electroporation (Puértolas et al., 2012). It is well known that irreversible modification of the selective permeability of the cytoplasmic membrane leads to the microbial inactivation (Pillet et al., 2016). Therefore, in order

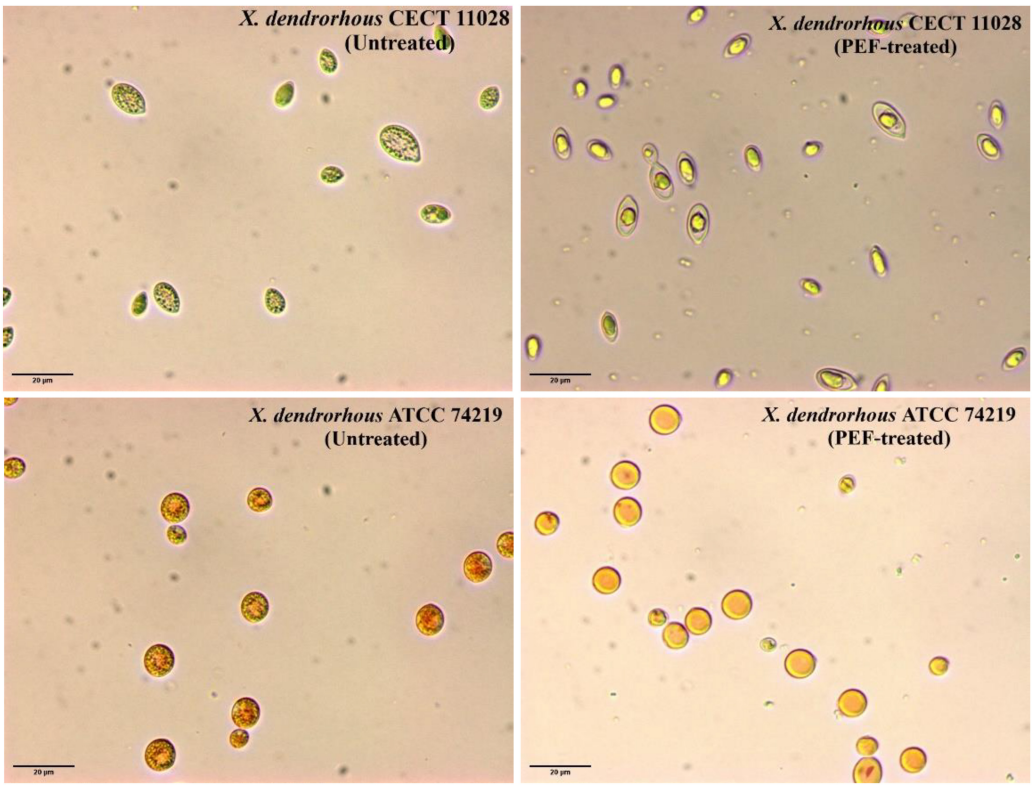

FIGURE 7 | Optical microscopy observation (600x) of untreated and PEF-treated of *X. dendrorhous* CECT 11028 and *X. dendrorhous* ATCC 74219 cells after 12 h of incubation at 25°C in a buffer of pH 7.

to identify the appropriate range of treatment conditions for irreversible electroporation, the sensitivity of the two strains to PEF treatments of different intensity was investigated (**Figure 1**). *X. dendrorhous* ATCC 74219 strain was more PEF resistant than the strain CECT 11028 and compared with other yeast, both strains showed lower sensitivity to PEF (Aronsson et al., 2005; Martínez et al., 2016). Currently, the influence of the cell envelopes surrounding the cytoplasmatic membrane on electroporation by PEF is unclear, but it has suggested that cell wall could influence the sensitivity to PEF (Aronsson et al., 2005; García et al., 2007). The highest PEF resistance could be related with the fact that oleaginous yeasts such as of *X. dendrorhous* have a higher fraction of chitin and/or mannan in the cell wall compared to non-oleaginous species that contribute to the rigidity and resistance to cell lysis (Khot et al., 2020). This rigidity and resistance to cell lysis should be higher in the ATCC 74219 strain to contain around 10 times more of carotenoids than those contained in the CECT 11028.

A small proportion of inactivated *X. dendrorhous* cells were impermeable to PI after application of mild intensity PEF treatments that caused low inactivation. This observation, previously reported by other authors, suggests that in these cells, the pore resealing is a physical process rather than a process with biosynthetic requirements (Martínez et al., 2018). Therefore, quantification of the proportion of inactivated cells is a suitable index for estimation of the number of irreversible electroporation cells when the inactivation is higher of a given value, that in the case of the strains of *X. dendrorhous* investigated was around 70%.

In order to develop a sustainable and cost-efficient overall bioprocess, carotenoids were extracted from wet biomass of *X. dendrorhous* (avoiding too high costs derived from drying) and ethanol was used as a solvent. Ethanol is a polar water-soluble solvent that is less toxic and greener than others used for extracting lipophilic compounds such as hexane, dichloromethane or chloroform (Saini and Keum, 2018).

The water solubility of ethanol in water should allow its diffusion through the cell wall and cell membrane and reaching the carotenoids located in the cytoplasm of *X. dendrorhous*. However, ethanol was inefficient for extracting carotenoids from the two investigated strains, even when around 80% of the population cells were irreversibly electroporated. This observation suggested that ethanol was not able to dissolve the carotenoids located in the droplets.

As it was previously mentioned, it was suggested that PEF triggers an enzymatic process that enables the yeast autolysis, which then allows the extraction of the intracellular compounds. Thus, the subsequent studies aimed at verifying this hypothesis and increasing the recovery yields of carotenoids. By evaluating the incubation process in the buffer solution, it was shown that ethanol was effective for extracting carotenoids from PEF-treated cells of *X. dendrorhous* ATCC 74219. Recently, several authors

have reported that an aqueous incubation period after PEF treatment increased the extraction yield of carotenoids, lipids and proteins from microalgae and yeasts (Luengo et al., 2014; Dimopoulos et al., 2018; Martínez et al., 2018, 2019; Silve et al., 2018; Scherer et al., 2019). This improvement in the extraction has been attributed to enzyme-driven processes triggered by PEF that occur during the aqueous incubation period.

The efficiency of ethanol for extracting carotenoids from PEF-treated *X. dendrorhous* ATCC 74219 after buffer incubation was dependent on the proportion of cells electroporated. Increments in the electric field strength that lead to a high proportion of electroporated cells result in a higher extraction until 20 kV/cm.

HPLC quantification of astaxanthin from ethanolic extracts obtained with different PEF treatment intensities (**Table 1**) showed that up to 84% (2.06 ± 0.02 mg/g d.w.) of total carotenoids extracted corresponded to *trans*-astaxanthin. This proportion agrees with values reported in the literature for other *X. dendrorhous* strains (Johnson and Lewis, 1979; de la Fuente et al., 2010; Schmidt et al., 2011). The high yield of *trans*-astaxanthin (2.06 ± 0.02 mg/g d.w.) obtained in this study from *X. dendrorhous* ATCC 74219 was in range to other reported yields obtained for *X. dendrorhous* ATCC 74219. Amado and Vázquez (2015) reported a maximum astaxanthin specific concentration of 2.0 mg/g d.w. by culturing the same strains of *X. dendrorhous* ATCC 74219 in a low-cost media designed from marine by-products, while Stoklosa et al. (2018) reported 2.49 mg/g d.w. specific astaxanthin production by culturing the same strain in sweet sorghum juice.

The results related with the evaluation of enzymatic activities seemed to confirm that the enzymatic esterase activity triggered by PEF mediates the effective ethanolic extraction of carotenoids from PEF-treated *X. dendrorhous* ATCC 74219 at the evaluated conditions. The uncontrolled molecular transport thought the electroporated cytoplasmic membrane of the yeast could decrease the osmotic pressure of the cytoplasm as a consequence of water inlet, causing the plasmolysis of lysosomes and the liberation of hydrolytic enzymes such as esterases. These esterases could hydrolyze the triacylglycerols of lipid droplets resulting in the loss of their structure and the subsequent carotenoid release. Once the carotenoids are free in the cytoplasm, they could be dissolved in ethanol and the complex carotenoid-solvent could diffuse across the cell membrane driven by a concentration gradient. The presence of esterase activity in the supernatant containing PEF-treated cells during buffer incubation and the lower carotenoid extraction yield when esterase activity was reduced by heating, supported such hypothesis. Furthermore, the lack of effectivity in the carotenoid extraction when PEF-treated cells were immediately incubated in ethanol could be explained for esterase denaturation when exposed to high concentrations of ethanol.

Although esterase activity was also detected in the electroporated *X. dendrorhous* CECT 11028, the inefficiency of ethanol for extracting the carotenoids could be related to the changes observed in the cytoplasm of the cells after incubation (**Figure 7**). As it has been previously described for the microalga *Chlamydomonas reinhardtii*, the aqueous incubation of the PEF-treated cells clearly led to the fusion of the lipid droplets in a big globule (Bodénès et al., 2016; Bensalem et al., 2018). In addition, this big globule of lipids might content the synthesized carotenoids by the strain CECT 11028 because neither free carotenoids nor carotenoid droplets were observed in the cytoplasm after fusion. Lipid fusion of the lipid droplets did not occur in the strain ATCC 74219 probably because, as it is observed in **Figure 7** in this hyper-producer strain, most of the droplets contained in the cytoplasm correspond to carotenoids.

Due to polarity properties of ethanol, this solvent was unable to dissolve the single large lipid droplet, mainly constituted for neutral lipids with long hydrophobic fatty acid chains (Halim et al., 2012). Therefore, using a mixture of polar and non-polar solvents might allow dissolving this lipid structure, or the rupture of the cell wall should be required for carotenoid extraction from the CECT 11028 strain (Bensalem et al., 2018).

CONCLUSION

This research has demonstrated that application of PEF treatment and subsequent aqueous incubation of fresh biomass of *X. dendrorhous* ATCC 74219 allowed the ethanolic extraction of 70% of the total carotenoids which up to 84% correspond to *trans*-astaxanthin. The effective extraction depended on the proportion of electroporated cells and the hydrolytic activity of the enzyme esterase during incubation triggered by PEF. The ineffective extraction of carotenoids from *X. dendrorhous* CECT 11028 seemed to be related to the inability of ethanol to dissolve the lipids structure containing carotenoids.

In order to establish the procedure developed in this study as a sustainable method with low environmental impact for extraction of *trans*-astaxanthin, further studies are required to optimize PEF treatment, enzymatic activity and extraction conditions for improving extraction yields with the lowest energetic costs.

DATA AVAILABILITY STATEMENT

The raw data supporting the conclusions of this article will be made available by the authors, without undue reservation.

AUTHOR CONTRIBUTIONS

DA-M, JM, and JR: conception and design of the study. DA-M, CD, and JMM: acquisition of data. DA-M, LM-O, and JR: analysis and interpretation of the data. DA-M and JMM: drafting of the manuscript. LM-O, JM, and JR: critical revision of the manuscript. All authors contributed to the article and approved the submitted version.

FUNDING

DA-M acknowledges CONACyT-México for the financial support provided for conducting the Ph.D. (486828-2017). At the Universidad de Zaragoza and Universidad Autónoma de Coahuila by the scientific support.

REFERENCES

Amado, I. R., and Vázquez, J. A. (2015). Mussel processing wastewater: a low-cost substrate for the production of astaxanthin by *Xanthophyllomyces dendrorhous*. *Microb. Cell Fact.* 14:177. doi: 10.1186/s12934-015-0375-5

Aronsson, K., Rönner, U., and Borch, E. (2005). Inactivation of *Escherichia coli*, *Listeria innocua* and *Saccharomyces cerevisiae* in relation to membrane permeabilization and subsequent leakage of intracellular compounds due to pulsed electric field processing. *Intern. J. Food Microbiol.* 99, 19–32. doi: 10.1016/j.ijfoodmicro.2004.07.012

Bensalem, S., Lopes, F., Bodénès, P., Pareau, D., Français, O., and Le Pioufle, B. (2018). Understanding the mechanisms of lipid extraction from microalga *Chlamydomonas reinhardtii* after electrical field solicitations and mechanical stress within a microfluidic device. *Bioresour. Technol.* 257, 129–136. doi: 10.1016/j.biortech.2018.01.139

Bodénès, P., Lopes, F., Pareau, D., Français, O., and Le Pioufle, B. (2016). Microdevice for studying the in situ permeabilization and characterization of *Chlamydomonas reinhardtii* in lipid accumulation phase. *Algal Res.* 16, 357–367. doi: 10.1016/j.algal.2016.03.023

Capelli, B., Bagchi, D., and Cysewski, G. R. (2013). Synthetic astaxanthin is significantly inferior to algal-based astaxanthin as an antioxidant and may not be suitable as a human nutraceutical supplement. *Nutrafoods* 12, 145–152. doi: 10.1007/s13749-013-0051-5

Chittapun, S., Jonjaroen, V., Khumrangsee, K., and Charoenrat, T. (2020). C-phycocyanin extraction from two freshwater cyanobacteria by freeze thaw and pulsed electric field techniques to improve extraction efficiency and purity. *Algal Res.* 46:101789. doi: 10.1016/j.algal.2020.101789

Choi, S., Kim, J., Park, Y., Kim, Y., and Chang, H. (2007). An efficient method for the extraction of astaxanthin from the red yeast Xanthophyllomyces dendrorhous. *J. Microbiol. Biotech.* 17, 847–852.

de la Fuente, J. L., Rodríguez-Sáiz, M., Schleissner, C., Díez, B., Peiro, E., and Barredo, J. L. (2010). High-titer production of astaxanthin by the semi-industrial fermentation of *Xanthophyllomyces dendrorhous*. *J. Biotechnol.* 148, 144–146. doi: 10.1016/j.jbiotec.2010.05.004

Dimopoulos, G., Stefanou, N., Andreou, V., and Taoukis, P. (2018). Effect of pulsed electric fields on the production of yeast extract by autolysis. *Innovat. Food Sci. Emerg. Technol.* 48, 287–295. doi: 10.1016/j.ifset.2018.07.005

Fakhri, S., Abbaszadeh, F., Dargahi, L., and Jorjani, M. (2018). Astaxanthin: a mechanistic review on its biological activities and health benefits. *Pharmacol. Res.* 136, 1–20. doi: 10.1016/j.phrs.2018.08.012

Ganeva, V., Galutzov, B., and Teissié, J. (2003). High yield electroextraction of proteins from yeast by a flow process. *Analyt. Biochem.* 315, 77–84. doi: 10.1016/S0003-2697(02)00699-1

García, D., Gómez, N., Mañas, P., Raso, J., and Pagán, R. (2007). Pulsed electric fields cause bacterial envelopes permeabilization depending on the treatment intensity, the treatment medium pH and the microorganism investigated. *Intern. J. Food Microbiol.* 113, 219–227. doi: 10.1016/j.ijfoodmicro.2006.07.007

García-Gonzalo D., and Pagán R. (2017). "Detection of electroporation in microbial cells: techniques and procedures," in *Handbook of Electroporation*, ed. D. Miklavcic (Cham: Springer). doi: 10.1007/978-3-319-26779-1

Gilham, D., and Lehner, R. (2005). Techniques to measure lipase and esterase activity in vitro. *Methods* 36, 139–147. doi: 10.1016/j.ymeth.2004.11.003

Gogate, P. R., and Nadar, S. G. (2015). Ultrasound-assisted intensification of extraction of astaxanthin from *Phaffia rhodozyma*. *Indian Chem. Eng.* 57, 240–255. doi: 10.1080/00194506.2015.1026947

Halim, R., Danquah, M. K., and Webley, P. A. (2012). Extraction of oil from microalgae for biodiesel production: a review. *Biotechnol. Adv.* 30, 709–732. doi: 10.1016/j.biotechadv.2012.01.001

Hasan, M., Azhar, M., Nangia, H., Bhatt, P. C., and Panda, B. P. (2016). Influence of high-pressure homogenization, ultrasonication, and supercritical fluid on free astaxanthin extraction from β-glucanase-treated *Phaffia rhodozyma* cells. *Prep. Biochem. Biotechnol.* 46, 116–122. doi: 10.1080/10826068.2014.995807

Higuera-Ciapara, I., Felix-Valenzuela, L., and Goycoolea, F. M. (2006). Astaxanthin: a review of its chemistry and applications. *Crit. Rev. Food Sci. Nutr.* 46, 185–196. doi: 10.1080/10408690590957188

Jacobson, G. K., Jolly, S. O., Sedmak, J. J., Skatrud, T. J., and Wasileski, J. M. (1995). *Astaxanthin Over-Producing Strains Of Phaffia rhodozyma*. U.S. Patent No. 5,466,599. Washington, DC: U.S. Patent and Trademark Office.

Johnson, E. A., and Gil-Hwan, A. (1991). Astaxanthin from microbial sources. *Crit. Rev. Biotechnol.* 11, 297–326. doi: 10.3109/07388559109040622

Johnson, E. A., and Lewis, M. J. (1979). Astaxanthin formation by the yeast *Phaffia rhodozyma*. *Microbiology* 115, 173–183. doi: 10.1099/00221287-115-1-173

Khot, M., Raut, G., Ghosh, D., Alarcón-Vivero, M., Contreras, D., and Ravikumar, A. (2020). Lipid recovery from oleaginous yeasts: perspectives and challenges for industrial applications. *Fuel* 259:116292. doi: 10.1016/j.fuel.2019.116292

Kotnik, T., Frey, W., Sack, M., Meglič, S. H., Peterka, M., and Miklavčič, D. (2015). Electroporation-based applications in biotechnology. *Trends Biotechnol.* 33, 480–488. doi: 10.1016/j.tibtech.2015.06.002

Kurihara, H., Koda, H., Asami, S., Kiso, Y., and Tanaka, T. (2002). Contribution of the antioxidative property of astaxanthin to its protective effect on the promotion of cancer metastasis in mice treated with restraint stress. *Life Sci.* 70, 2509–2520. doi: 10.1016/S0024-3205(02)01522-9

Leonhardt, L., Käferböck, A., Smetana, S., de Vos, R., Toepfl, S., and Parniakov, O. (2020). Bio-refinery of *Chlorella sorokiniana* with pulsed electric field pre-treatment. *Bioresour. Technol.* 301:122743. doi: 10.1016/j.biortech.2020.12274

Li, J., Zhu, D., Niu, J., Shen, S., and Wang, G. (2011). An economic assessment of astaxanthin production by large scale cultivation of *Haematococcus pluvialis*. *Biotechnol. Adv.* 29, 568–574. doi: 10.1016/j.biotechadv.2011.04.001

Luengo, E., Condón-Abanto, S., Álvarez, I., and Raso, J. (2014). Effect of pulsed electric field treatments on permeabilization and extraction of pigments from *Chlorella vulgaris*. *J. Memb. Biol.* 247, 1269–1277. doi: 10.1007/s00232-014-9688-2

Martínez, J. M., Cebrián, G., Álvarez, I., and Raso, J. (2016). Release of mannoproteins during *Saccharomyces cerevisiae* autolysis induced by pulsed electric field. *Front. Microbiol.* 7:1435. doi: 10.3389/fmicb.2016.01435

Martínez, J. M., Delso, C., Angulo, J., Álvarez, I., and Raso, J. (2018). Pulsed electric field-assisted extraction of carotenoids from fresh biomass of *Rhodotorula glutinis*. *Innovat. Food Sci. Emerg. Technol.* 47, 421–427. doi: 10.1016/j.ifset.2018.04.012

Martínez, J. M., Gojkovic, Z., Ferro, L., Maza, M., Álvarez, I., Raso, J., et al. (2019). Use of pulsed electric field permeabilization to extract astaxanthin from the Nordic microalga *Haematococcus pluvialis*. *Bioresour. Technol.* 289:121694. doi: 10.1016/j.biortech.2019.121694

Michelon, M., de Borba, T. D. M., da Silva Rafael, R., Burkert, C. A. V., and de Medeiros Burkert, J. F. (2012). Extraction of carotenoids from *Phaffia rhodozyma*: a comparison between different techniques of cell disruption. *Food Sci. Biotechnol.* 21, 1–8. doi: 10.1007/s10068-012-0001-9

Molino, A., Rimauro, J., Casella, P., Cerbone, A., Larocca, V., Chianese, S., et al. (2018). Extraction of astaxanthin from microalga *Haematococcus pluvialis* in red phase by using generally recognized as safe solvents and accelerated extraction. *J. Biotechnol.* 283, 51–61. doi: 10.1016/j.jbiotec.2018.07.010

Nagendraprabhu, P., and Sudhandiran, G. (2011). Astaxanthin inhibits tumor invasion by decreasing extracellular matrix production and induces apoptosis in experimental rat colon carcinogenesis by modulating the expressions of ERK-2, NFkB and COX-2. *Invest. New Drugs* 29, 207–224. doi: 10.1007/s10637-009-9342-5

Ni, H., Chen, Q. H., He, G. Q., Wu, G. B., and Yang, Y. F. (2008). Optimization of acidic extraction of astaxanthin from *Phaffia rhodozyma*. *J. Zhejiang Univ. Sci. B* 9, 51–59. doi: 10.1631/jzus.B061261

Ohgami, K., Shiratori, K., Kotake, S., Nishida, T., Mizuki, N., Yazawa, K., et al. (2003). Effects of astaxanthin on lipopolysaccharide-induced inflammation *in vitro* and *in vivo*. *Invest. Ophthalmol. Vis. Sci.* 44, 2694–2701. doi: 10.1167/iovs.02-0822

Pashkow, F. J., Watumull, D. G., and Campbell, C. L. (2008). Astaxanthin: a novel potential treatment for oxidative stress and inflammation in cardiovascular disease. *Am. J. Cardiol.* 101, S58–S68. doi: 10.1016/j.amjcard.2008.02.010

Peng, J., Yuan, J. P., and Wang, J. H. (2012). Effect of diets supplemented with different sources of astaxanthin on the gonad of the sea urchin *Anthocidaris crassispina*. *Nutrients* 4, 922–934. doi: 10.3390/nu4080922

Pillet, F., Formosa-Dague, C., Baaziz, H., Dague, E., and Rols, M. P. (2016). Cell wall as a target for bacteria inactivation by pulsed electric fields. *Sci. Rep.* 6:19778. doi: 10.1038/srep19778

Puértolas, E., Luengo, E., Álvarez, I., and Raso, J. (2012). Improving mass transfer to soften tissues by pulsed electric fields: fundamentals and applications. *Annu. Rev. Food Sci. Technol.* 3, 263–282. doi: 10.1146/annurev-food-022811-101208

Saini, R. K., and Keum, Y. S. (2018). Carotenoid extraction methods: a review of recent developments. *Food Chem.* 240, 90–103. doi: 10.1016/j.foodchem.2017.07.099

Saldaña, G., Puértolas, E., Álvarez, I., Meneses, N., Knorr, D., and Raso, J. (2010). Evaluation of a static treatment chamber to investigate kinetics of microbial inactivation by pulsed electric fields at different temperatures at quasi-isothermal conditions. *J. Food Eng.* 100, 349–356. doi: 10.1016/j.jfoodeng.2010.04.021

Scherer, D., Krust, D., Frey, W., Mueller, G., Nick, P., and Gusbeth, C. (2019). Pulsed electric field (PEF)-assisted protein recovery from Chlorella vulgaris is mediated by an enzymatic process after cell death. *Algal Res.* 41:101536. doi: 10.1016/j.algal.2019.101536

Schmidt, I., Schewe, H., Gassel, S., Jin, C., Buckingham, J., Hümbelin, M., et al. (2011). Biotechnological production of astaxanthin with *Phaffia rhodozyma*/*Xanthophyllomyces dendrorhous*. *Appl. Microbiol. Biotechnol.* 89, 555–571. doi: 10.1007/s00253-010-2976-6

Sedmak, J. J., Weerasinghe, D. K., and Jolly, S. O. (1990). Extraction and quantitation of astaxanthin from *Phaffia rhodozyma*. *Biotechnol. Techn.* 4, 107–112. doi: 10.1007/BF00163282

Shah, M., Mahfuzur, R., Liang, Y., Cheng, J. J., and Daroch, M. (2016). Astaxanthin-producing green microalga *Haematococcus pluvialis*: from single cell to high value commercial products. *Front. Plant Sci.* 7:531. doi: 10.3389/fpls.2016.00531

Silve, A., Kian, C. B., Papachristou, I., Kubisch, C., Nazarova, N., Wüstner, R., et al. (2018). Incubation time after pulsed electric field treatment of microalgae enhances the efficiency of extraction processes and enables the reduction of specific treatment energy. *Bioresour. Technol.* 269, 179–187. doi: 10.1016/j.biortech.2018.08.060

Stoklosa, R. J., Johnston, D. B., and Nghiem, N. P. (2018). Utilization of sweet sorghum juice for the production of astaxanthin as a biorefinery co-product by *Phaffia rhodozyma*. *ACS Sustain. Chem. Eng.* 6, 3124–3134. doi: 10.1021/acssuschemeng.7b03154

Uchiyama, K., Naito, Y., Hasegawa, G., Nakamura, N., Takahashi, J., and Yoshikawa, T. (2002). Astaxanthin protects β-cells against glucose toxicity in diabetic db/db mice. *Redox Rep.* 7, 290–293. doi: 10.1179/135100002125000811

Urnau, L., Colet, R., Soares, V. F., Franceschi, E., Valduga, E., and Steffens, C. (2018). Extraction of carotenoids from *Xanthophyllomyces dendrorhous* using ultrasound-assisted and chemical cell disruption methods. *Can. J. Chem. Eng.* 96, 1377–1381. doi: 10.1002/cjce.23046

Villegas-Méndez, M. Á, Aguilar-Machado, D. E., Balagurusamy, N., Montañez, J., and Morales-Oyervides, L. (2019). Agro-industrial wastes for the synthesis of carotenoids by *Xanthophyllomyces dendrorhous*: mesquite pods-based medium design and optimization. *Biochem. Eng. J.* 150:107260. doi: 10.1016/j.bej.2019.107260

Visser, H., Van Ooyen, A. J., and Verdoes, J. C. (2003). Metabolic engineering of the astaxanthin-biosynthetic pathway of *Xanthophyllomyces dendrorhous*. *FEMS Yeast Res.* 4, 221–231. doi: 10.1016/S1567-1356(03)00158-2

Wu, S., Li, W., Zhou, W., Zhan, Y., Hu, C., Zhuang, J., et al. (2018). Large-scale one-step synthesis of carbon dots from yeast extract powder and construction of carbon dots/PVA fluorescent shape memory material. *Adv. Opt. Mater.* 6:1701150. doi: 10.1002/adom.201701150

Yuan, J. P., and Chen, F. (1997). Identification of astaxanthin isomers in *Haematococcus lacustris* by HPLC-photodiode array detection. *Biotechnol. Techn.* 11, 455–459. doi: 10.1023/A:1018441411746

Zhao, T., Yan, X., Sun, L., Yang, T., Hu, X., He, Z., et al. (2019). Research progress on extraction, biological activities and delivery systems of natural astaxanthin. *Trends Food Sci. Technol.* 91, 354–361. doi: 10.1016/j.tifs.2019.07.014

Zhuang, Y., Jiang, G. L., and Zhu, M. J. (2020). Atmospheric and room temperature plasma mutagenesis and astaxanthin production from sugarcane bagasse hydrolysate by *Phaffia rhodozyma* mutant Y1. *Process Biochem.* 91, 330–338. doi: 10.1016/j.procbio.2020.01.003

Conflict of Interest: The authors declare that the research was conducted in the absence of any commercial or financial relationships that could be construed as a potential conflict of interest.

Copyright © 2020 Aguilar-Machado, Delso, Martinez, Morales-Oyervides, Montañez and Raso. This is an open-access article distributed under the terms of the Creative Commons Attribution License (CC BY). The use, distribution or reproduction in other forums is permitted, provided the original author(s) and the copyright owner(s) are credited and that the original publication in this journal is cited, in accordance with accepted academic practice. No use, distribution or reproduction is permitted which does not comply with these terms.

APPENDIX

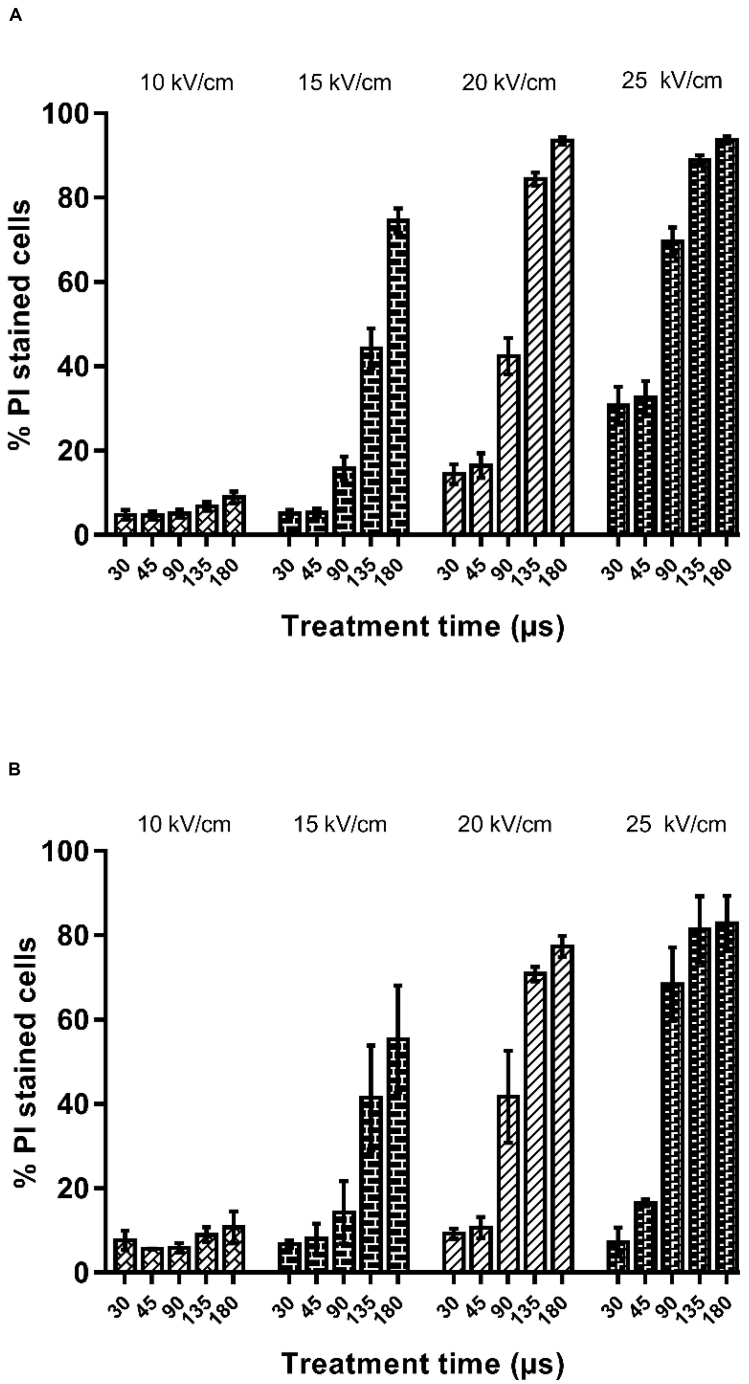

FIGURE A1 | Percentage of propidium iodide uptake by *X. dendrorhous* CECT 11028 **(A)** and *X. dendrorhous* ATCC 74219 **(B)** after PEF treatments with different electric field strength and treatment time.

frontiers in Bioengineering and Biotechnology

ORIGINAL RESEARCH
published: 04 September 2020
doi: 10.3389/fbioe.2020.551272

Pulsed Electric Fields-Assisted Extraction of Valuable Compounds From Arthrospira Platensis: Effect of Pulse Polarity and Mild Heating

Daniele Carullo[1], Gianpiero Pataro[1], Francesco Donsì[1] and Giovanna Ferrari[1,2]*

[1] Department of Industrial Engineering, University of Salerno, Fisciano, Italy, [2] ProdAl Scarl – University of Salerno, Fisciano, Italy

OPEN ACCESS

Edited by:
Eugene Vorobiev, University of Technology of Compiègne, France

Reviewed by:
Nikolai I. Lebovka, Institute of Biocolloidal Chemistry (named after F.D. Ovcharenko), Ukraine
Luis Manuel Redondo, Lisbon Higher Institute of Engineering (ISEL), Portugal

***Correspondence:**
Gianpiero Pataro
gpataro@unisa.it

Specialty section:
This article was submitted to Bioprocess Engineering, a section of the journal Frontiers in Bioengineering and Biotechnology

Received: *12 April 2020*
Accepted: *14 August 2020*
Published: *04 September 2020*

Citation:
Carullo D, Pataro G, Donsì F and Ferrari G (2020) Pulsed Electric Fields-Assisted Extraction of Valuable Compounds From Arthrospira Platensis: Effect of Pulse Polarity and Mild Heating. Front. Bioeng. Biotechnol. 8:551272. doi: 10.3389/fbioe.2020.551272

The present study aimed to investigate the effect of the main pulsed electric field (PEF) process parameters on the cell damages of *A. platensis* microalgae and the extractability of valuable compounds [water-soluble proteins (WSP), C-phycocyanin (C-PC), and carbohydrates (CH)]. Aqueous microalgae suspensions (2%, w/w) were PEF-treated at variable field strength (E = 10, 20, 30 kV/cm), total specific energy (W_T = 20, 60, 100 kJ/kg$_{susp}$), and inlet temperature (25, 35, 45°C), with either monopolar or bipolar square wave pulses (5 μs of width, delay time between pulses of opposite polarities = 1, 5, 10, 20 μs), prior to extraction with water at room temperature (25°C) for up to 3 h. High-pressure homogenization (HPH) treatment (P = 150 MPa, 3 passes) was used to achieve complete cell disruption to quantify the total extractable content of target intracellular compounds. Scanning electron microscopy (SEM) and optical microscopy analyses clearly showed that PEF merely electroporated the membranes of algae cell, without damaging the cell structure and forming cell debris. The application of PEF treatment (monopolar pulses, 20 kV/cm and 100 kJ/kg$_{susp}$) at room temperature significantly enhanced the extraction yield of WSP [17.4% dry weight (DW)], CH (10.1% DW), and C-PC (2.1% DW), in comparison with the untreated samples. Bipolar pulses appeared less effective than monopolar pulses and led to extraction yields dependent on the delay time. Additionally, regardless of pulse polarity, a clear synergistic effect of the combined PEF (20 kV/cm and 100 kJ/kg$_{susp}$)-temperature (35°C) treatment was detected, which enabled the extraction of up to 37.4% (w/w) of total WSP, 73.8% of total CH, and 73.7% of total C-PC. Remarkably, the PEF treatment enabled to obtain C-phycocyanin extract with higher purity than that obtained using HPH treatment. The results obtained in this work suggest that the application of PEF combined with mild heating could represent a suitable approach for the efficient recovery of water-soluble compounds microalgal biomass.

Keywords: *Arhtrospira platensis*, pulsed electric fields, pulse polarity, temperature, extraction, water-soluble compounds, energy efficiency

INTRODUCTION

Arthrospira platensis, commonly known as spirulina, is a cyanobacterium widely used for biotechnological applications. It is a multicellular and filamentous blue-green alga with helical shape (trichomes of 50–500 μm in length, and 3–4 μm in width) and represents one of the richest sources of proteins of microbial origin [55–70% dry weight (DW)]; besides, it also contains significant amounts of carbohydrates (13–16% DW), lipids (6–10% DW), vitamins, and minerals (Lupatini et al., 2016). In particular, *A. platensis* is an excellent source of C-phycocyanin (C-PC), a water-soluble pigmented protein, which has gained importance in many applications in the food, cosmetic and pharmaceutical sectors, thanks to its blue color and its therapeutic properties, as well as for its potential use as a fluorescent marker in biomedical research (Fernández-Rojas et al., 2014). In *A. platensis*, C-PC serves as a light-harvesting pigment for the photosynthetic activity of this cyanobacteria, in which it is assembled, along with other phycobiliproteins, in the thylakoid membranes of chloroplast (Martinez et al., 2020), and may represent more than 20% of its dry weight (Martinez et al., 2017).

In general, the recovery of intracellular compounds of interest from algal biomass via conventional solvent extraction techniques is hampered by the presence of the rigid cell wall and membranes, which act as a barrier that greatly limits the penetration of the solvent into the cytoplasm and the diffusion of the solubilized intracellular compounds during the extraction process (Martinez et al., 2020). For these reasons, to recover a substantial amount of valuable compounds, the conventional extraction techniques may require the use of a large amount of solvent, long extraction time and relatively high temperature that may cause losses of labile compounds, as well as lead to the co-extraction of undesirable components (Günerken et al., 2015; Poojary et al., 2016). Moreover, the extraction process is often conducted upon drying of algae biomass, which requires a significant amount of energy and may cause thermal degradation of valuable compounds (Günerken et al., 2015; Golberg et al., 2016). In this regard, it has been reported that the initial amount of C-PC in *A. platensis* decreased by approximately 50% after the drying of the algae biomass (Martinez et al., 2017).

In light of these drawbacks of conventional solvent extraction methods, cell disruption pre-treatment of wet biomass that causes weakening or breakage of cell envelops is required to intensify the extractability of specific intracellular compounds with reduced energy consumption, while preserving or improving the quality (purity) of the extracts (Poojary et al., 2016). Among the cell disruption methods, freeze/thawing cycles, sonication, bead milling, and high-pressure homogenization (HPH) treatments have been widely studied as pre-treatment of either microalgae and cyanobacteria biomasses, due to their ability to induce complete cell disruption, which markedly increases the extraction yield of the components located within the algae cells. However, all these methods cause the non-selective release of intracellular compounds, with the concurrent dispersion of cell debris or other impurities into the extraction medium, hence decreasing the quality of the extracts and complicating the subsequent downstream purification operations (Aouir et al., 2015; Poojary et al., 2016; Martinez et al., 2017; Carullo et al., 2018; Jaeschke et al., 2019).

In this frame, pulsed electric fields (PEF) is considered to be a very promising technology for mild and scalable cell disruption of wet biomass, thus avoiding the need for energy-intensive drying and the consequent losses of labile compounds (Carullo et al., 2018). The technique consists of exposing fresh algae suspensions to repetitive high-intensity electric field pulses of short (of the order of μs) duration that cause the permeabilization of cell membranes by electroporation. This improves the efficiency of the conventional extraction process of valuable compounds from algae biomass, facilitating the penetration of the solvent into the cells and the selective release of intracellular matter (Poojary et al., 2016) without the formation of cell debris (Martinez et al., 2017; Phong et al., 2017; Carullo et al., 2018; Pataro et al., 2019). Recently, several studies have demonstrated the potential of PEF to intensify the extraction yield of target intracellular compounds, such as lipids, pigments, carbohydrates, and proteins, from different microalgae and cyanobacteria (Goettel et al., 2013; Zbinden et al., 2013; Grimi et al., 2014; Luengo et al., 2015; Parniakov et al., 2015a,b; Carullo et al., 2018; Geada et al., 2018; Silve et al., 2018), even though, to date, only a few works focused on *A. platensis* (Aouir et al., 2015; Martinez et al., 2017; Jaeschke et al., 2019).

However, it has been shown that the recovery of substantial amounts of compounds of relatively high molecular weight (e.g., protein) could require the application of intense PEF processing conditions (high field strengths and energy input), especially in the case of "hard-structured" microalgal cells (Postma et al., 2016; Pataro et al., 2019). Therefore, to reduce the operative costs and to maximize the extraction efficiency of high-added-value components, the use of PEF in a hurdle approach has been suggested. For example, several studies have demonstrated that the combination of PEF with moderate heating decreases the critical electric field required to cause electroporation in both microbial and algae cells, thus resulting in additive or synergistic effects in microbial inactivation or extraction of intracellular compounds (Saldaña et al., 2014; Timmermans et al., 2014; Luengo et al., 2015; Postma et al., 2016; Martinez et al., 2017). However, as per the literature survey, only Martinez et al. (2017) described the effect of temperature (10–40°C) on the release of C-PC during PEF treatment of *A. platensis*, using a batch chamber equipped with a temperature control system.

Additionally, the use of bipolar pulses, which appear to be more efficient than monopolar ones, could be also suggested to obtain the required permeabilization effect with less severe processing conditions or to achieve higher efficacy at the same treatment intensity. Nevertheless, very few works have dealt so far with the influence of pulse polarity on the extent of electroporation of biological cell, and only for microbial inactivation purposes (Chang, 1989; Qin et al., 1994; Beveridge et al., 2002; Evrendilek and Zhang, 2005).

This research aimed to assess the potential of the application of PEF, either as a stand-alone treatment or in a hurdle approach with moderate heating, for the intensification of the extraction of valuable compounds from wet *A. platensis* biomass using a continuous flow system. Specifically, the effect of field strength, energy input, pulse polarity, and inlet temperature of the algae biomass to the PEF chamber on the morphology of algae cells, as well as on the extractability of target intracellular compounds (e.g., water-soluble proteins, C-phycocyanin, and carbohydrates), was assessed.

MATERIALS AND METHODS

Cultivation of Microalgae

Biomass of *A. platensis* (PCC 8005) was kindly supplied by ATI Biotech Srl, an algae producer located in Castel Baronia (Avellino, Italy). *A. platensis* was cultivated in open pond systems, in which a maximum biomass concentration of about 0.4% DW was achieved at the end of the exponential growth phase. After harvesting, the biomass was concentrated through a dewatering system consisting of vibrating screen filters, which allowed to increase the biomass concentration up to 12% DW. The microalgae paste was subsequently packed in polyethylene bags and immediately transported in an expanded polystyrene (EPS) box under refrigerated conditions to the laboratory of ProdAl S.c.a.r.l. (University of Salerno, Fisciano, Italy), where it was stored at 4°C until use, within 2 days from the delivery date.

Before processing, the algae paste was diluted with distilled water up to a final concentration (C_x) of 2% DW with an initial conductivity of about 2.7 mS/cm at 25°C (Conductivity-meter HI 9033, Hanna Instrument, Milan, Italy). The biomass concentration was assessed using the method described by Goettel et al. (2013), with the pellet being dried in a circulating air-drying oven for 24 h at 80°C.

Pulsed Electric Fields System

PEF experiments were conducted in a bench-scale continuous flow PEF system previously described in detail by Postma et al. (2016) and Carullo et al. (2018). Briefly, it consisted of a peristaltic pump used to transfer the microalgal suspension through a stainless steel coiled tube submerged into a water heating bath used to control the inlet temperature to the treatment chamber. The latter consisted of two modules, each made of two co-linear treatment chambers, hydraulically connected in series, with an inner radius of 1.5 mm and a gap distance of 4 mm. The treatment chambers were connected to a high voltage pulsed power (20 kV–100 A) generator (Diversified Technology Inc., Bedford, WA, United States) able to deliver either monopolar or bipolar square wave pulses at different pulse width (1–10 μs), delay time between two consecutive pulses of opposite polarities (1–20 μs) and pulse repetition rate (1–1000 Hz). The maximum electric field intensity (E, in kV/cm) and total specific energy input (W_T, in kJ/kg_{susp}) were measured and calculated as reported in Postma et al. (2016). T-thermocouples (Tersid S.r.L, Milan, Italy) were used to measure the product temperature at the inlet and outlet of each module of the PEF chamber. The total residence time of the algae suspension in the PEF plant at each processing temperature was about 25 s.

PEF Treatments

PEF treatments were carried out by pumping algae suspension (2% DW) from a feeding tank under stirring through the treatment chamber at a constant flow rate of 2 L/h. The operative pressure was about 1 bar. In all the experiments, the pulse width was fixed at 5 μs, while the electric field strength (E) and total specific energy input (W_T) were set by varying the applied voltage and the pulse repetition frequency, respectively. The inlet biomass temperature (T_{IN}) to the PEF treatment chamber was set at 25°C unless otherwise specified.

Three different experiments were carried out to investigate the effect of treatment intensity, pulse polarity, and inlet temperature on the cell damage and extraction efficiency of water-soluble compounds such as proteins, carbohydrates, and C-phycocyanins from *A. platensis* cells.

In the first set of experiments, a screening of the main electric parameters, namely field strength (10, 20, and 30 kV/cm) and energy input (20, 60, and 100 kJ/kg_{susp}), on the release of water-soluble compounds was investigated. The specific energy input per pulse (W_p) was equal to 0.95, 3.65, and 8.36 kJ/kg, when the field strength was set at 10, 20, and 30 kV/cm, respectively, and the number of pulses applied ranged between 2 and 105. The results of this first set of experiments were used to define the optimal PEF conditions (E_{OPT}, $W_{T,OPT}$), which enabled the achievement of the highest recovery yields with the minimum treatment severity.

In the second set of experiments, a comparative study was carried out to investigate the effect of pulse polarity on the cell membrane permeabilization and extraction efficiency. Monopolar and bipolar pulses at different delay times (1, 5, 10, and 20 μs) were applied at the optimal field strength (E_{OPT}) and energy input ($W_{T,OPT}$) defined during the first set of experiments. The typical voltage and current waveforms at the treatment chamber, for either monopolar or bipolar pulses at different delay times, are depicted in **Figure 1**.

Finally, the use of PEF treatments (E_{OPT}, $W_{T,OPT}$) applied using either monopolar or bipolar pulses in combination with mild heating treatment, achieved by raising the inlet biomass temperature (T_{IN}) to the treatment chamber up to 25, 35, and 45°C, was investigated to highlight the existence of possible synergistic effects of the combined treatment in the recovery process of intracellular compounds. Temperatures higher than 45°C were not tested in this work to prevent any damage to proteins as well as degradation of C-PC (Chaiklahan et al., 2012).

Under the selected operating conditions, the maximum temperature increase of the samples, detected at the exit of the treatment chamber, never exceeded 10°C.

For the sake of comparison, untreated (control) samples of the same *A. platensis* suspension were pumped through the PEF plant with the heating bath set at 25, 35, or 45°C, but with the PEF generator switched off.

At the exit of the treatment chamber, untreated (control) and PEF treated algae suspensions were immediately collected in plastic tubes and placed in an ice-water bath to be rapidly

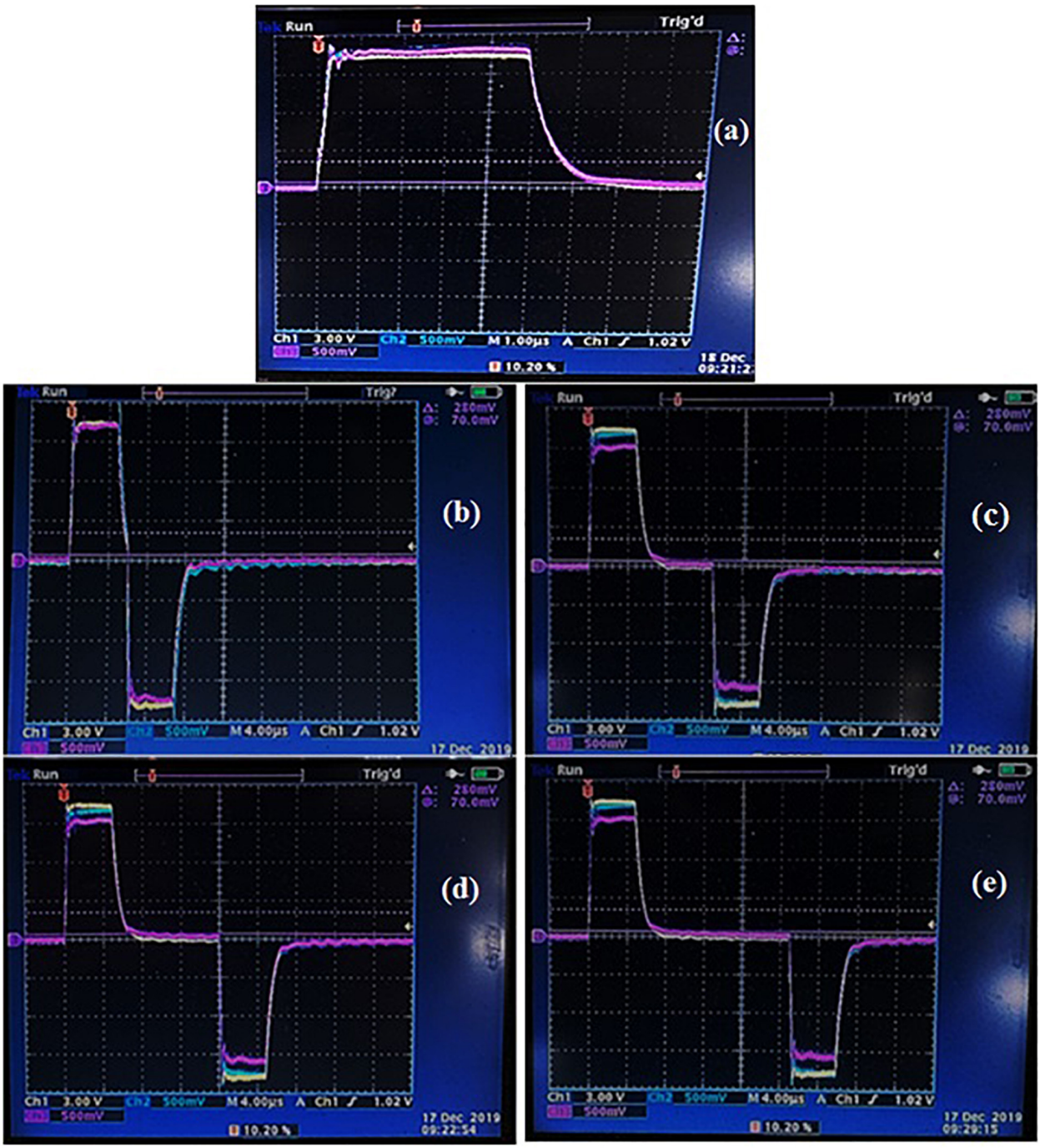

FIGURE 1 | Typical voltage and current waveforms captured at the treatment chamber for either monopolar **(a)** or bipolar pulses at different delay time of 1 µs **(b)**, 5 µs **(c)**, 10 µs **(d)**, and 20 µs **(e)**. Reference color: yellow: voltage waveform; light blue: current waveform at the first module of the treatment chamber; purple: current waveform at the second module of the treatment chamber.

cooled up to a final temperature of 25°C before undergoing to the aqueous extraction process.

Water Extraction

Untreated and PEF treated samples of *A. platensis* suspensions were allowed to stand for 3 h at 25°C under gentle agitation (160 rpm) in an orbital incubator (Model S150, PBI International, Milan, Italy) to allow intracellular components to diffuse out of the cells. Preliminary tests revealed that these conditions were sufficient to achieve significant extraction yields of the target intracellular compounds (data not shown). After this resting time, the cell suspensions were centrifuged for 10 min at 5700 × g

(PK121R model, ALC International, Cologno Monzese, IT) in order to separate the spent pellets from the supernatants. The latter were then transferred to fresh tubes and stored at −20°C until further analysis.

Complete Cell Disruption by HPH Treatment

HPH treatment was used to induce full disruption of *A. platensis* cells to enable the quantification of the total content of target intracellular compounds. HPH treatments were carried out by using an in-house developed laboratory scale high-pressure homogenizer (Carullo et al., 2018). The *A. platensis* suspensions, at the same concentration as for PEF treatment tests (2% DW), were forced to pass through a 100 μm diameter orifice valve (model WS1973, Maximator JET GmbH, Schweinfurt, Germany) upon pressurization through an air-driven Haskel pump (model DXHF-683, EGAR S.r.l., Milan, Italy). According to preliminary tests (data not shown), the full disruption of *A. platensis* cells and, hence, the complete release of intracellular compounds, was achieved at a pressure drop (P) across the orifice of 150 MPa and after three homogenization passes (n_p).

Energy Analysis

To enable the comparison in terms of energy efficiency among the different investigated extraction processes (i.e., PEF, mild heating, combination of PEF and mild heating, and HPH), the energy consumed (EC) to extract 1 kg DW of target intracellular compounds, namely water-soluble proteins (WSP), C-phycocyanin (C-PC) and total carbohydrates (CH), from *A. platensis* cell suspension, was calculated according to Eqs. (1–3).

$$EC_{PEF} = \frac{W_{T,OPT}}{C_x \cdot 3600 \cdot Y_i} \quad (1)$$

$$EC_{HEATING} = \frac{c_P \cdot (T_{IN} - T_0)}{C_x \cdot 3600 \cdot Y_i} \quad (2)$$

$$EC_{HPH} = \frac{P \cdot n_P}{C_x \cdot \eta_{PUMP} \cdot 3600 \cdot \rho_{BIOMASS} \cdot Y_i} \quad (3)$$

where EC is expressed in kWh/kg_{DW}, C_p is the specific heat of the aqueous algae suspensions (∼4.186 kJ/kg), T_0 is the reference temperature (25°C), η_{PUMP} is the overall efficiency of HPH pumping system (0.87) (Carullo et al., 2018), $\rho_{BIOMASS}$ is the density of microalgal suspensions (∼1000 kg/m^3), 3600 is the conversion factor between kJ and kWh, and Y_i is the recovery yield (in kg/kg of DW microalgae) of the interest compounds (i = WSP, C-PC, CH) achieved upon the different extraction processes.

Analytical Methods

Optical Microscopy and Scanning Electron Microscopy (SEM) Analysis

The morphological features and cellular details of untreated (control) and treated (PEF, HPH) algae cells were analyzed by using either optical or Scanning Electron Microscopy (SEM). In the first case, the microscopic images were acquired with an inverted optical microscope (Nikon Eclipse TE2000-S) at 20× magnification. For SEM analysis, pellets derived from the centrifugation of untreated and treated (PEF or HPH) algae suspensions were prepared as described by Carullo et al. (2018) and analyzed in a high-resolution ZEISS HD15 Scanning Electron Microscope (Zeiss, Oberkochen, Germany).

Proteins Analysis

The water-soluble proteins content of supernatants from untreated, PEF, and HPH treated samples was evaluated by using the method of Lowry et al. (1951), with some modifications as described elsewhere (Carullo et al., 2018). Specifically, the reactive system consisted in 0.5 mL of diluted (1/2, v/v in ultra-pure water) Folin-Ciocalteau reactive (Folin and Ciocalteau, 1927), to which 1 mL of fresh sample (supernatant), previously mixed with 5.0 mL of the reactive "C" [50 volumes of reactive "A" (2% Na_2CO_3 + 0.1 N NaOH) + 1 volume of reactive "B" (1/2 volume of 0.5% · $CuSO_4$ $5H_2O$ + 1/2 volume of 1% $KNaC_4H_4O_6$ · $4H_2O$)] (Sigma Aldrich, Milan, Italy) were added. Absorbance was measured at 750 nm against a blank (5 mL reactive "C" + 1 mL deionized water + 0.5 mL Folin-Ciocalteau reactants), 35 min after the start of the chemical reaction, by using a V-650 Spectrophotometer (Jasco Inc., Easton, MD, United States). Bovine serum albumin (BSA) (A7030, Sigma Aldrich, Milan, Italy) was used as a protein standard. The protein yield (Y_{WSP}) was expressed as:

$$Y_{WSP} = \frac{C_{WSP,sup}}{C_{WSP,biomass}} \quad (4)$$

where $C_{WSP,sup}$ is the protein content in the supernatant (% DW), and $C_{WSP,biomass}$ is the total protein content on DW (% DW) achieved upon HPH treatment.

Carbohydrates Analysis

The total carbohydrates concentration of the supernatants was analyzed according to the phenol-sulfuric acid method previously described by DuBois et al. (1956). 0.2 mL of 5% (w/w) phenol and 1 mL of concentrated sulfuric acid (Sigma Aldrich, St. Louis, United States) were added to 0.2 mL of diluted supernatant (Dilution Factor = 5). Samples were then incubated at 35°C for 30 min before reading the absorbance at 490 nm against a blank of 0.2 mL 5% (w/w) phenol, 1 mL concentrated sulfuric acid, and 0.2 mL of deionized water. D-Glucose (G8270, Sigma-Aldrich, Milan, Italy) was used as a standard. The carbohydrate yield (Y_{CH}) was expressed as:

$$Y_{CH} = \frac{C_{CH,sup}}{C_{CH,biomass}} \quad (5)$$

where $C_{CH,sup}$ is the carbohydrates content in the supernatant (% DW) and $C_{CH,biomass}$ is the total carbohydrates content on DW (% DW) achieved upon HPH treatment.

C-Phycocyanin (C-PC) and Purity Ratio

The quantification of C-PC content of the supernatants was performed according to the method of Bennett and Bogorad (1973), which is based on the measurements of absorbance

(A) of the samples at two fixed wavelengths (λ_1 = 615 nm, and λ_2 = 652 nm). The C-phycocyanin concentration (C-PC), expressed as mg/g_{DW} of supernatant, was evaluated according to Eq. (6):

$$C - PC = \frac{(A_{615nm} - 0.474 \cdot A_{652nm})}{5.34 \cdot C_x} \quad (6)$$

The C-PC yield (Y_{C-PC}) was expressed as:

$$Y_{C-PC} = \frac{C_{C-PC,sup}}{C_{C-PC,biomass}} \quad (7)$$

where $C_{C-PC,sup}$ is the C-PC content in the supernatant (% DW), and $C_{C-PC,biomass}$ is the total C-PC content on DW (% DW) achieved upon HPH treatment.

The purity of C-PC extract was monitored spectrophotometrically and calculated by the Eq. (8) (Abelde et al., 1998; Martinez et al., 2017):

$$EP = \frac{A_{615nm}}{A_{280nm}} \quad (8)$$

where EP is the protein extract purity, $A_{615\ nm}$ absorbance represents the maximum absorption of the C-phycocyanin peak, proportional to its concentration in the supernatant, and $A_{280\ nm}$ is the absorbance of the at 280 nm, indicating the total concentration of proteins in the supernatant.

Statistical Analysis

All treatments and analyses were performed in triplicate and the results were reported as mean values ± standard deviations. The statistical analysis was performed with IBM SPSS Statistics 20.0 (SPSS Inc., Chicago, United States) software by means of One-way analysis of variance (ANOVA). Tukey's test was executed at a fixed significance level ($p \leq 0.05$), for the determination of any statistical difference among the untreated and processed samples.

RESULTS AND DISCUSSION

Influence of PEF Treatment Intensity on the Recovery of Water-Soluble Intracellular Compounds

The biomass composition of *A. platensis* used in this study was quantified upon complete cell disruption by HPH treatment (P = 150 MPa; n_P = 3). Results revealed that the extractable content of WSP and CH from *A. platensis* cells was 68.5% DW and 15.8% DW, respectively, which are in line with the total content of proteins (55–70% DW) and carbohydrates (13–20% DW) typically reported for this cyanobacterium (Lupatini et al., 2016). At the same time, it was also found that the total content of C-PC was 5.7% DW, which is consistent with the content found in other works (Martinez et al., 2017; Jaeschke et al., 2019). The results of this study will be presented in terms of extraction yields expressed with respect to this biomass composition according to Eqs. (4–6).

Figure 2 shows the extraction yields of water-soluble proteins (WSP) and carbohydrates (CH) detected in the supernatant of untreated and PEF-treated (monopolar pulses; T_{IN} = 25°C) *A. platensis* cell suspensions at different field strength (10–30 kV/cm) and energy input (20–100 kJ/kg_{susp}), after 3 h of extraction in water.

Results show that a small leakage of water-soluble compounds from untreated algae cells occurred during the extraction step, leading to final yields of proteins and carbohydrates in the aqueous supernatant of 2.2 and 14.8%, respectively. This leakage of intracellular compounds may be ascribed to either a concentration gradient across the intact cell membranes or to spontaneous cell lysis (Carullo et al., 2018).

The exposure of *A. platensis* cell suspensions to an external electric field that caused the electroporation of cytoplasmatic membranes, thus facilitating the mass transfer of intracellular compounds toward the external medium, markedly enhanced the extraction efficiency up to 12.7-fold for WSP and 4.6-fold for CH, as compared with untreated samples. However, significant differences ($p \leq 0.05$) between untreated and PEF-treated samples were detected only when energy input greater than 20 kJ/kg_{susp} were delivered to the algae suspension, independently of the field strength applied. This observation confirms the results obtained by other scientists on the electroporation of bacteria and microalgae (Garcia et al., 2007; Luengo et al., 2015; Martinez et al., 2017; Carullo et al., 2018; Jaeschke et al., 2019), indicating the key role played by the energy input, besides the electric field strength applied, in determining the degree of cell membrane permeabilization required to intensify the extractability of target intracellular compounds.

Moreover, it is worth noting that, among the PEF-treated samples, the applied field strength was likely high enough to induce the electroporation of the algae cells so that its effect appeared less important than that of the energy input within the investigated range, which is in agreement with previous findings (Pataro et al., 2017, 2019; 't Lam et al., 2017a; Carullo et al., 2018). In particular, significant differences ($p \leq 0.05$) in the content of both intracellular compounds were detected when PEF treatments were carried out at different energy inputs, regardless of the field strength applied. As an example, when the energy input was increased from 60 to 100 kJ/kg_{susp} at 20 kV/cm, the content of proteins and carbohydrates in the supernatant increased by 2.7 and 2.2 times, respectively. In contrast, when PEF treatments were carried out at different field strengths, significant ($p \leq 0.05$) increase in the content of both proteins and carbohydrates was detected only when the field strength was increased from 10 to 20 kV/cm and for a fixed energy input of 100 kJ/kg_{susp}. At a fixed energy input of 60 kJ/kg_{susp}, instead, a significant ($p \leq 0.05$) increase was observed only for proteins when the field strength was increased from 10 to 30 kV/cm.

From the results of **Figure 2**, it can be concluded that a field strength of 20 kV/cm and an energy input of 100 kJ/kg_{susp} were sufficient to significantly intensify the extractability of proteins and carbohydrates from *A. platensis* cells, leading to extraction yields of 25.4 and 64.1% of biomass WSP and CH content, respectively.

The positive impact of PEF pre-treatment on the extraction of valuable intracellular compounds from *A. platensis* cell suspensions was also previously observed by other scientists

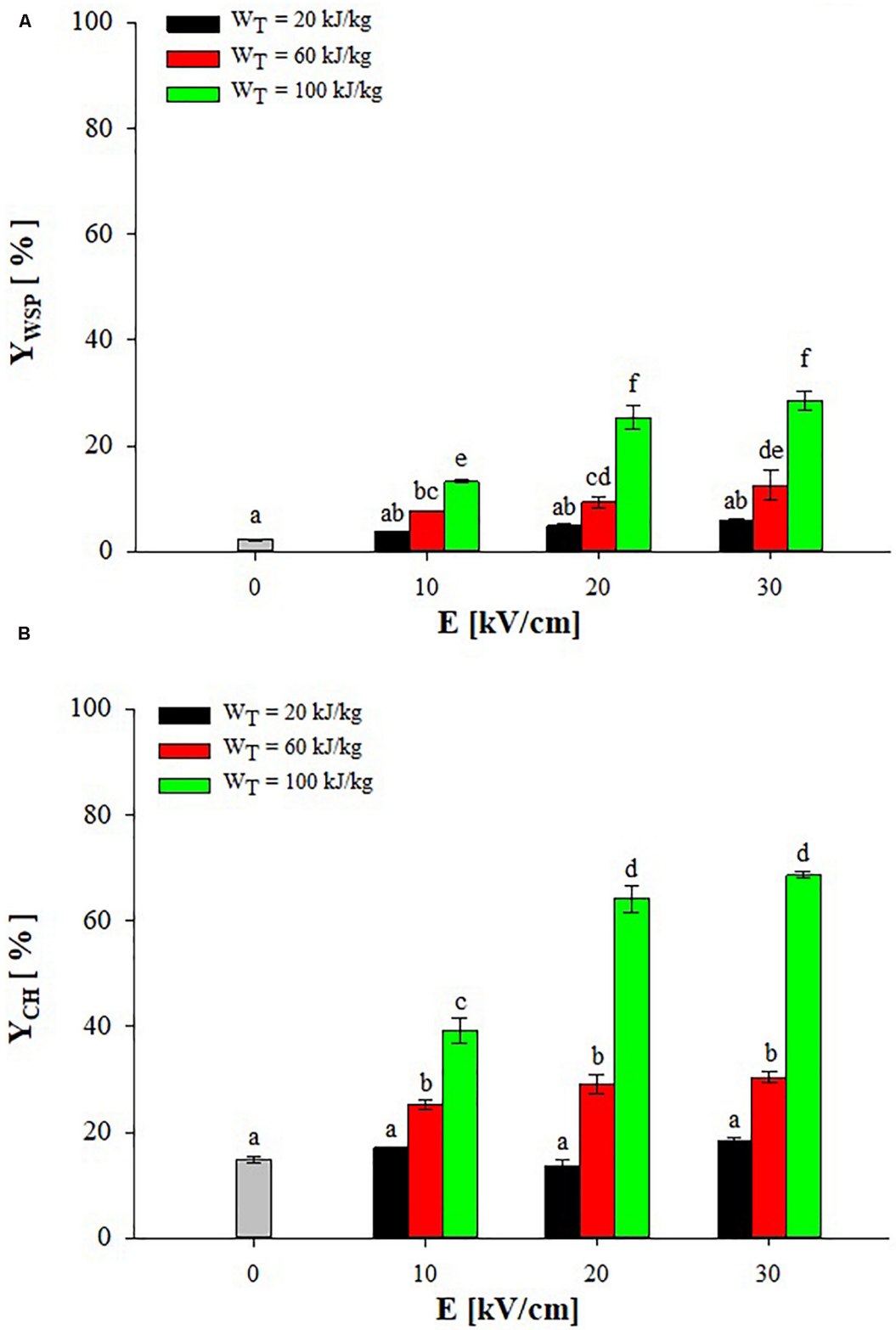

FIGURE 2 | Extraction yield of water-soluble proteins **(A)** and carbohydrates **(B)** in the supernatant of untreated (0 kV/cm) and PEF (T_{IN} = 25°C) treated *A. platensis* suspension 3 h after treatment as a function of the field strength and for different energy input. The yields were calculated considering 100% extraction yield upon the HPH treatment (P = 150 MPa, n_P = 3). Different letters above the bars indicate significant differences among the mean values of the samples ($p \leq 0.05$).

(Aouir et al., 2015; Martinez et al., 2017; Jaeschke et al., 2019), even though, to date, only Jaeschke et al. (2019) focused on PEF-assisted extraction of total proteins, while no work was addressed to the extractability of carbohydrates from this cyanobacteria. However, these authors found a lower amount in WSP (4.84% DW biomass) as compared with that detected in the present work (17.4% DW biomass), despite the algae suspension was subjected to similar energy input (56–122 kJ/kg_{susp}) but at higher field strength (40 kV/cm) than those used in our work. The differences in PEF equipment, experimental conditions, algae strain, and cultivation techniques could contribute to explain these different results.

Moreover, in agreement with previous research (Goettel et al., 2013; Postma et al., 2016; Pataro et al., 2017; 't Lam et al., 2017a; Carullo et al., 2018), results of the present work seem to highlight the capacity of PEF to efficiently release small components, such as CH and WSP of small molecular weight, while most proteins, which are likely larger and more bounded to intracellular structure, remained entrapped into cells after PEF treatment. This may be explained considering that, in comparison with HPH, PEF is a mild disruption technology able to simply permeabilize the cell membranes (Carullo et al., 2018), without affecting the rigid outer cell wall of most algae cells ('t Lam et al., 2017b), thus limiting the mass transfer of some intracellular compounds.

In this line, differences in cell wall composition could in part also explain the higher extraction yields of protein (17.1% DW) achieved in this work after aqueous extraction of PEF-treated *A. platensis* cells (**Figure 2**), in comparison to those (1–13% DW) detected by other scientists for different microalgae species, such as *Chlorella vulgaris*, *Auxenochlorella protothecoides*, *Neochloris oleoabundans*, *C. reinhardtii* (Goettel et al., 2013; Postma et al., 2016; Pataro et al., 2017; 't Lam et al., 2017a,b; Carullo et al., 2018). It is known that *A. platensis* has a relatively fragile cell wall, composed mainly of murein (peptidoglycan) without any cellulose (Lu et al., 2006; Safi et al., 2014), while the other microalgae cited above have a more robust cell wall, mainly composed of cellulose and hemicelluloses, which would explain the lower protein extraction yield in these cases (Lu et al., 2006; Safi et al., 2015; Jaeschke et al., 2019).

According to the results shown so far, further investigations aimed at studying the influence of pulse polarity and mild heating on the extraction efficiency of valuable compounds from *A. platensis* cell suspensions were carried out with the PEF conditions set at 20 kV/cm and 100 kJ/kg_{susp}.

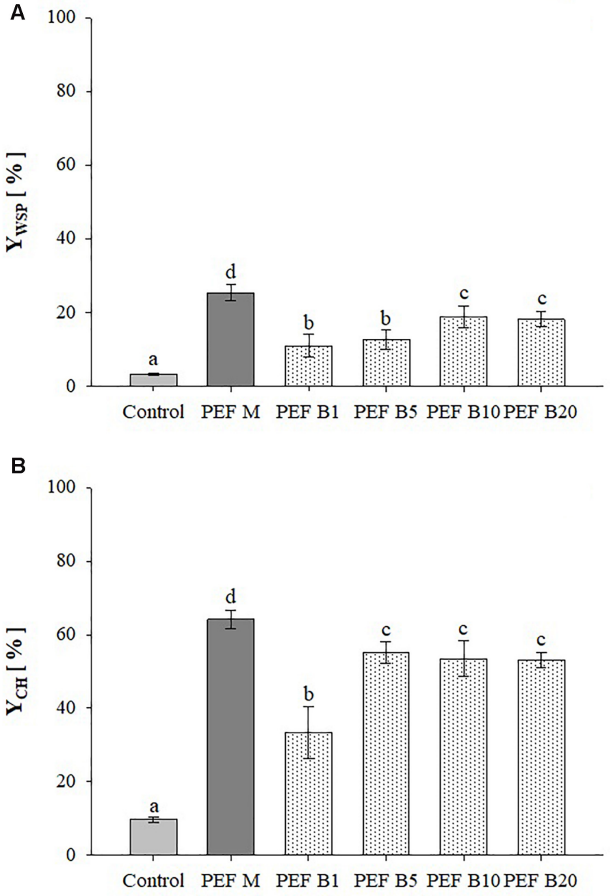

FIGURE 3 | Extraction yield of water-soluble proteins **(A)** and carbohydrates **(B)** in the supernatant of untreated (Control) and PEF-treated (E = 20 kV/cm; W_T = 100 kJ/kg_{susp}; T_{IN} = 25°C) *A. platensis* suspensions with either monopolar (M) or bipolar (B) pulses at variable delay time (1, 5, 10, and 20 μs). The yields were calculated considering 100% extraction yield upon the HPH treatment (P = 150 MPa, n_P = 3). Different letters above the bars indicate significant differences among the mean values ($p \leq 0.05$).

Effect of Pulse Polarity on the Recovery of Water-Soluble Compounds and Cell Morphology

Figure 3 shows the extraction yields of WSP and CH detected in aqueous extracts obtained from untreated and PEF treated *A. platensis* cell suspensions at constant treatment intensity (E = 20 kV/cm; W_T = 100 kJ/kg_{susp}) and inlet temperature (T_{IN} = 25°C), using either monopolar pulses or bipolar pulses at variable delay times (1–20 μs). The results show that, regardless of the delay time, bipolar pulses significantly ($p \leq 0.05$) increased the content of WSP and CH in the extracts, as compared with untreated samples. Interestingly, changing in pulse delaying times resulted in different extraction yields of the intracellular compounds of interest, showing the existence of a threshold delay time above which no additional positive effect was detected. In particular, significant differences ($p \leq 0.05$) were observed only when the delay time was increased from 5 to 10 μs for proteins and from 1 to 5 μs for carbohydrates, which led to a maximum recovery yield of 18.8 and 55.2%, respectively.

To the best of our knowledge, the literature data lack sufficient information on the effect of bipolar pulses at different delay times on the extractability of valuable intracellular compounds from algae cells. However, when looking into microbial inactivation, Evrendilek and Zhang (2005) reported that changing pulse delaying times within the range 3–1430 μs resulted in different inactivation levels of *E. coli* O157:H7 inoculated in either apple juice or skim milk. In particular, the authors found that 20 μs

was the most effective delay-time value within the investigated range, which appears somehow consistent with results achieved in the present study. The authors concluded that most probably, there was not enough time to charge capacitors of their pulse generator after each discharging when the duration of pulse delay time was really short (3–5 μs). On the other hand, as the delay time between pulses of opposite polarities was lengthened up to 1430 μs, the time interval between two pulses of opposite polarity was so long that adversely affected the efficacy of the treatment. This explanation could not justify our results due to the narrower range of delay time investigated and to the fact that the same voltage value was measured across the electrodes of the treatment chamber when bipolar pulses of different delaying times were delivered (data not shown).

As it is shown in **Figure 3**, the extracts obtained for the application of bipolar pulses showed significantly ($p \leq 0.05$) lower yields of intracellular compounds of interest, as compared to the samples treated with monopolar pulses, being the extraction efficiency decreased by 1.4-fold for proteins and 1.2-fold for carbohydrates.

Only a few authors have investigated the comparative effect of mono ad bipolar pulses on the extent of cell membrane permeabilization of biological cells, but focusing only on microbial inactivation and obtaining controversial results. For example, Chang (1989) and Qin et al. (1994) found that bipolar pulses provided a more efficient inactivation of microorganisms in liquid foods, as compared to monopolar pulses. To explain these results the authors proposed that the alternating stress induced by bipolar pulses results in structural fatigue of the membrane, which thereby enhances its susceptibility to electrical breakdown. In contrast with these findings, Beveridge et al. (2002) observed that bipolar pulses did not provide superior inactivation levels of different bacterial cells compared with monopolar pulses. In another study, Evrendilek and Zhang (2005) found that there was no significant difference ($p > 0.05$) between mono and bipolar pulses on the inactivation of bacterial cells inoculated into apple juice, while bipolar pulses resulted significantly more efficient than their monopolar counterpart for the inactivation of the same bacteria in skim milk. In agreement with Qin et al. (1994), the authors explained this different behavior as due to the deposition of milk proteins on the electrode surface (fouling effect) when monopolar pulses were applied, which caused several problems such as distortion of the electric field within the treatment zone, thus lowering the PEF performance.

In the case of the results of **Figure 3**, the lower extractability of water-soluble molecules from *A. platensis* cells measured for bipolar pulses than for monopolar ones applied at the same intensity could be explained in term of the slightly lower efficacy in opening the pores at the cellular membrane level of the bipolar pulses. In particular, this explanation can be supported by the previously observed polarization behavior of the cell membranes when exposed to pulses of different polarity and delay time (Beveridge et al., 2002). In this regard, it can be hypothesized that when monopolar pulses of sufficient width and amplitude, such as those used in this work, are applied, a cumulative build-up of charges across the cell membrane occurs, and when the transmembrane potential threshold is exceeded, the membrane becomes electroporated, exhibiting increased permeability. On the other hand, when polarities switch in the bipolar pulses, an effect of residual polarization, due to the so-called cancelation or healing mechanism (Beveridge et al., 2002; Sweeney et al., 2016), may occur that would decrease the probability of membrane permeabilization. In such a case, it has been proposed that the polarization effect induced by the previous pulse would first have to be neutralized before reverse polarization of the membrane can occur when the second pulse of opposite polarity is applied. This effect could cause an incomplete charging of cell membranes, leading to the formation of a smaller number of pores or pores of smaller size in the cell membrane than those induced by monopolar pulses of the same intensity, lowering the extractability of intracellular compounds. However, such cancelation effect could be partially mitigated at the expense of either higher applied voltages or by increasing the time elapsing between two consecutive pulses of opposite polarity (Sweeney et al., 2016), as if they were delivered independently, which is consistent with results presented in **Figure 3**.

The results of **Figure 3** are also corroborated by the micrographs presented in **Figure 4**, which clearly show the different impact of HPH treatments and PEF treatments of different pulse polarity on the morphology of *A. platensis* cells. From the micrographs of **Figure 4A** it is possible to notice that, as expected, HPH caused the complete disruption of *A. platensis* cells and the formation of cell debris, which was consistent with the results of **Figure 3**. The application of a PEF treatment with monopolar pulses (PEF M) caused only the partial separation of trichomes that form the characteristic cylindrical filaments of *A. platensis*, and preserved the overall structure of the cells, avoiding the formation of cells debris. It is also worth noting that PEF M treatment induced the formation of colored spots surrounding the algae cells (red arrows), likely due to the leakage of intracellular matter into the extraction medium, which can be attributed to the formation of pores in the cell membranes of the algae cells. Similarly, Martinez et al. (2017) observed that, while a highly intensive cell disruption method, such as bead milling, caused the complete breakage of the *A. platensis* cells, PEF treatments carried out using monopolar pulses led only to a partial fragmentation of cells in trichomes, with no visible effects on the whole structure of the algae, but with a clear release of intracellular matter.

In contrast, the application of bipolar pulses (PEF B) evidenced a lower release of intracellular matters and a lower separation of cells in trichomes than monopolar pulses, thus revealing a lower capability of inducing electroporation phenomena, which is consistent with the results illustrated in **Figure 3**.

The results of **Figure 4A** are also supported by the corresponding SEM images shown in **Figure 4B**. The surface of untreated *A. platensis* cells appeared regular and smooth. Interestingly, the application of PEF with either monopolar (PEF M) or bipolar (PEF B) pulses led to an increase of surface roughness and the formation of cracks and depressions on the surface of the cells, more evident for the samples treated with monopolar pulses, which could be ascribed to the mentioned

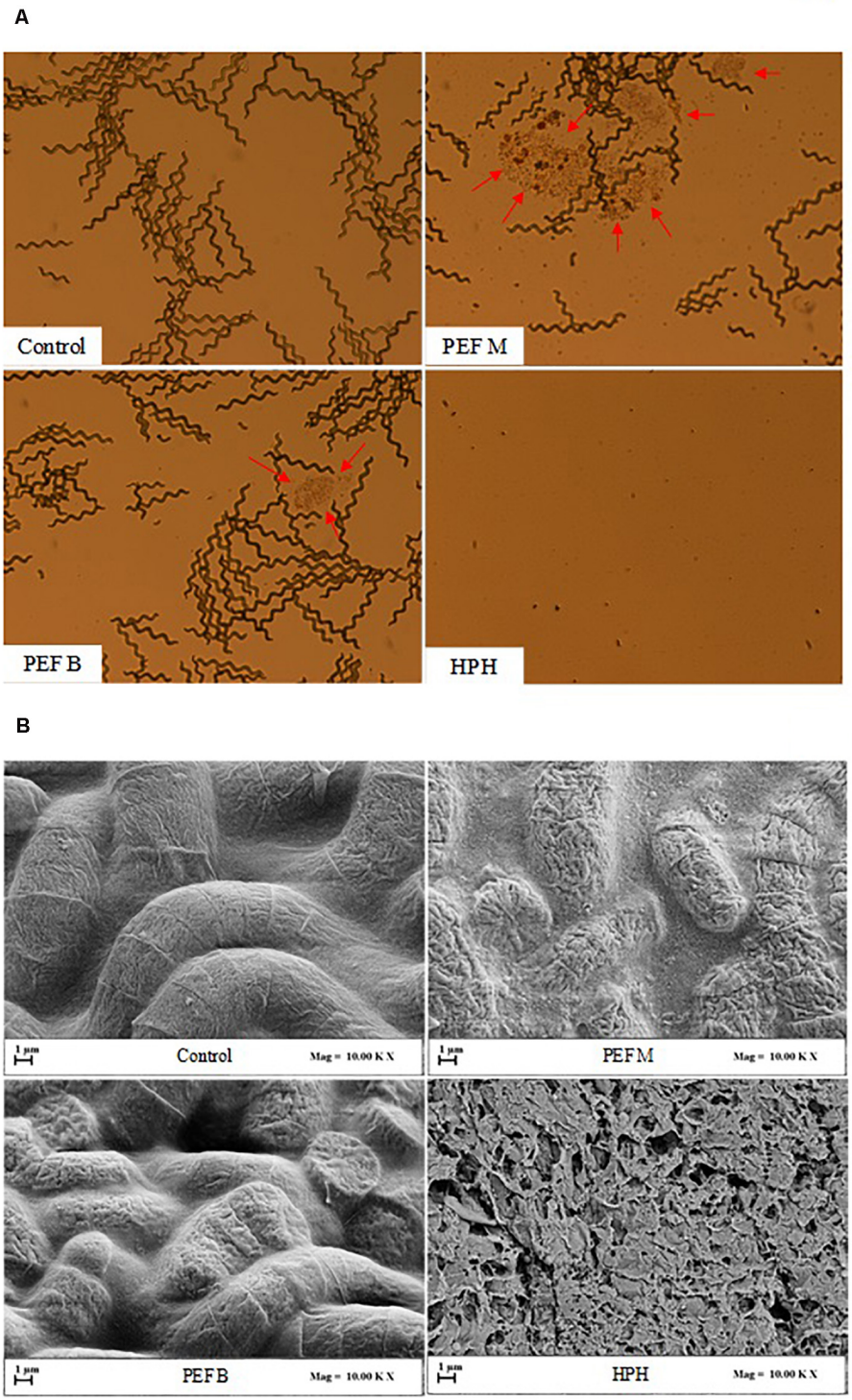

FIGURE 4 | Optical microscopy (20× magnification) **(A)** and scanning electron microscopy (SEM) **(B)** of *A. platensis* cells, before (Control) and after PEF (E = 20 kV/cm; W_T = 100 kJ/kg$_{susp}$; T_{IN} = 25°C) using either monopolar (PEF M) or bipolar (PEF B) pulses, and HPH (P = 150 MPa; n_P = 3) treatment. Red arrows indicate release of intracellular material.

more intense electroporation phenomena and subsequent more abundant leakage of intracellular compounds. Similar findings were previously reported by Han et al. (2019), who observed an increase in surface roughness of *C. pyrenoidosa* cells after the electroporation effect induced upon the application of PEF treatment at 20 kV/cm. On the other hand, in agreement with

the results of a previous research carried out on *C. vulgaris* microalgae (Carullo et al., 2018), the results of **Figure 4B** show that HPH treatment led to the formation of a large amount of cell debris, reflecting its capability of inducing full cell disruption (**Figure 2**).

Effect of Combined PEF-Temperature Treatment on the Extractability of Water-Soluble Compounds

Processing temperature during PEF treatment, through the interaction with the electrical parameters, may influence the extent of membrane electroporation and the subsequent extraction of intracellular compounds from PEF-treated biomass. Therefore, the potential of PEF in a hurdle approach with mild heating was investigated to furtherly intensify the recovery yield of water-soluble compounds.

Figure 5 shows the extraction yields of WSP, CH, and C-PC as well as the C-PC purity for untreated and PEF-treated (E = 20 kV/cm, W_T = 100 kJ/kg$_{susp}$) *A. platensis* cell suspensions, using either monopolar and bipolar pulses, after mildly pre-heating the algae biomass at temperatures from 25 to 45°C.

The results show that only a small fraction of the total content of WSP (Y_{WSP} < 1.1%), CH (Y_{CH} < 5.2%), and C-PC (Y_{C-PC} < 2.5%) was released in the supernatant of the algae suspensions at a processing temperature between 25 and 45°C when no PEF treatment was applied. This suggests that no cell structural damage was induced by either pumping of *A. platensis* cell suspensions through the PEF plant or by mild heating. This is also corroborated by the findings of Jaeschke et al. (2019), who observed that pumping alone or thermal treatment at 42°C for 15 min of *A. platensis* cell suspensions were not sufficient to induce damages in the cell envelope and to extract appreciable amounts of WSP and C-PC, even after 6 h of incubation.

However, when PEF pre-treatments of different polarity were applied at processing temperature between 25 and 45°C, the amount of WSP (**Figure 5A**), CH (**Figure 5B**), and C-PC (**Figure 5C**) significantly ($p \leq 0.05$) increased, as compared with untreated samples, in a manner dependent on pulse polarity, temperature and type of compounds to be extracted. In particular, the capability of PEF treatment at room temperature to induce cell membrane permeabilization, and the subsequent intensification of the extractability of WSP (25.4% for PEF

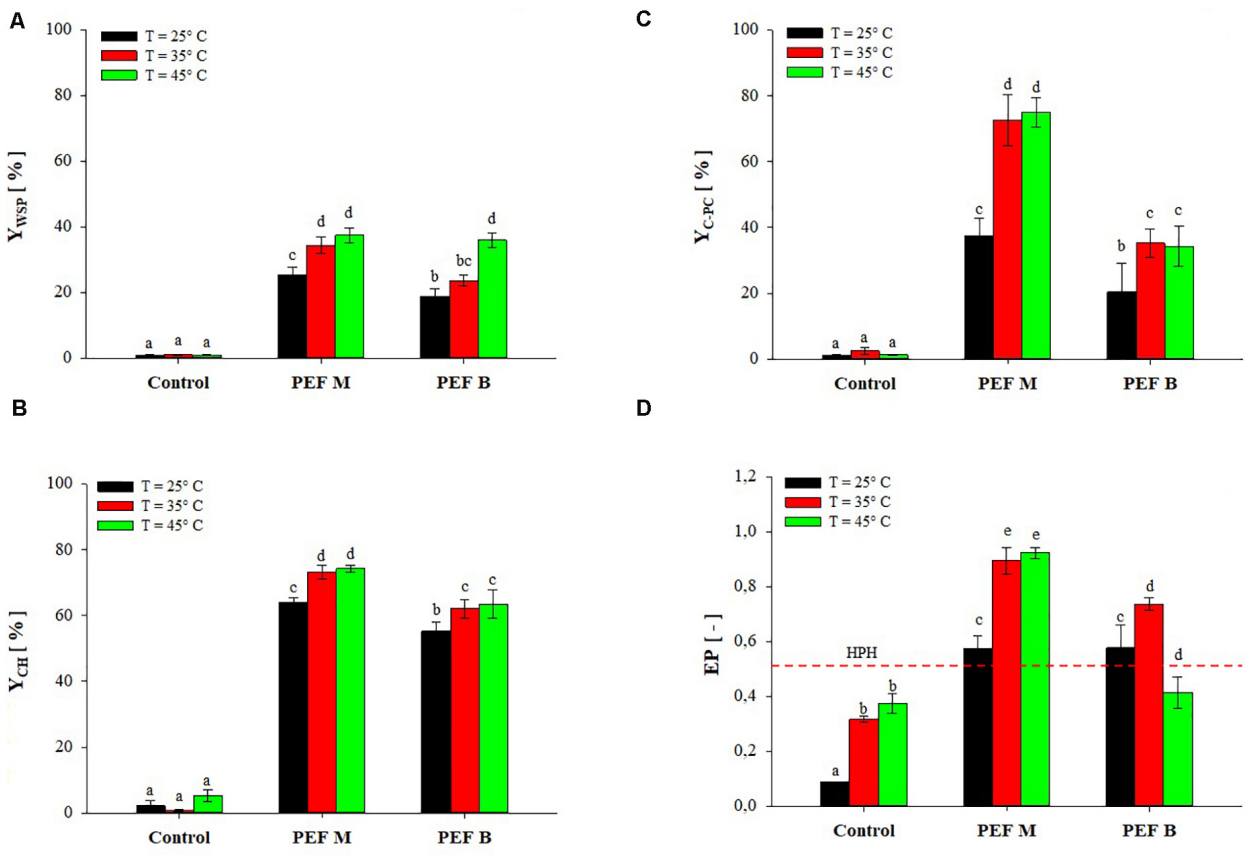

FIGURE 5 | Extraction yield of water-soluble proteins **(A)**, carbohydrates **(B)**, and C-PC **(C)**, and protein purity **(D)** of extracts obtained from untreated (Control) and PEF-treated (E = 20 kV/cm; W_T = 100 kJ/kg$_{susp}$) *A. platensis* suspensions with either monopolar (M) or bipolar (B) pulses (10 μs pulse delay time), as a function of the inlet processing temperature The yields were calculated considering 100% extraction yield upon the HPH treatment (P = 150 MPa, n_P = 3). Different letters above the bars indicate significant differences among the mean values ($p \leq 0.05$).

M, 18.8% for PEF B) and CH (64.1% for PEF M, 55.2% for PEF B), has been also previously shown in **Figures 2**, **3**. Coherently with these findings, the results of **Figure 5C** show that the application of PEF treatment at room temperature also caused a significant ($p \leq 0.05$) improvement in the release of C-PC, as compared with the untreated samples, leading to an extraction yield of 37.4% for monopolar pulses and 20.4% for bipolar pulses.

However, when the processing temperature was raised to 35°C, a clear synergistic effect of the combined treatment was detected for monopolar pulses, leading to an increase in WSP, CH, and C-PC yields up to 34.4, 73.1, and 72.5%, respectively. At this processing temperature, a slight synergistic effect was also observed when bipolar pulses were applied which, however, still appeared less effective than monopolar pulses, leading to extraction yields of 23.7, 62.0, and 35.2% for WSP, CH, and C-PC, respectively.

Further increases of the processing temperature up to 45°C appeared to contribute to a significant ($p \leq 0.05$) increase in the extraction yield, but only for WSP and when bipolar pulses were applied. It is worth noting that, in this latter case, the extraction yield of WSP increased up to 36.0%, a level comparable to that detected in samples treated with monopolar pulses (37.4%) at the same temperature.

The observed increase in the release of intracellular compounds with increasing of the inlet processing temperature up to 45°C during PEF treatment, was likely due to the interaction between field strength and temperature rather than further cellular damages induced by excessive heating of the samples. This is corroborated by the fact that the maximum sample temperature measured at the exit of the PEF chamber was about 51°C, which was measured under the most intensive treatment conditions (30 kV/cm, 100 kJ/kg) for an inlet temperature of 45°C. Additionally, the suspension was maintained at this temperature for only 2–3 s before being collected in plastic tubes and immediately placed in a water-ice bath.

The positive impact of the combined PEF-heat treatment on the extraction of valuable compounds from algae cell suspensions was previously observed by few other scientists, even though, to date, no previous works dealt with the use of bipolar pulses. For example, Postma et al. (2016) studied the effect of PEF treatment (17.1 kV/cm; 100 kJ/kg_{susp}) combined with mild heating (25–65°C) on the extractability of valuable compounds from *C. vulgaris* cells suspensions. They observed only a slight positive interaction between PEF and temperature on the recovery of WSP when the temperature was increased in the range 25–45°C, leading to a maximum extraction yield of 4.4%. The analysis of the carbohydrates in the supernatant, instead, revealed the existence of a clear synergistic effect of the combined treatment, but only when the processing temperature was increased from 45 to 55°C, leading to an increase in carbohydrates yield from 25 to 39% of total biomass carbohydrate content. With regard to the extraction of pigments, Luengo et al. (2015) found that an increase of the temperature of PEF treatment (25 kV/cm, 150 μs) of *C. vulgaris* from 10 to 40°C increased the concentration of lutein in the extracts from 451 to 753 $\mu g/g_{DW}$. Similarly, Martinez et al. (2017) found that the increment of the processing temperature from 10 to 40°C during PEF treatment (25 kV/cm, 150 μs) of *A. platensis* cells suspensions remarkably increased the extraction yield of C-phycocyanin up to a maximum value of 16.0% DW.

Interestingly, in all these works it was stated that mild heating of algae suspension contributes not only to enhance the diffusivity and solubility of intracellular compounds in water but also to make the lipid bilayer of the cell membrane more susceptible for breakdown under the PEF treatment (Timmermans et al., 2014; Luengo et al., 2015; Postma et al., 2016; Martinez et al., 2017). This would also explain the synergistic effect of the combined PEF-heat treatment on the extractability of water-soluble compounds observed in the present work.

However, although the hurdle approach revealed a positive interaction between electric field and moderate temperatures, the results of **Figure 5** show that the maximum amount of the target compounds released after the combined treatment still remained lower than that achieved with the benchmark HPH process. This is somehow consistent with the findings previously reported by other scientists. For example, when comparing the extraction yield of water-soluble compounds achieved by the combined PEF-heat treatment of microalgae with those obtained after complete cell disruption by bead milling, Postma et al. (2016) estimated that about 10% of the total content of WSP was extracted from *C. vulgaris* cells, whereas Martinez et al. (2017) calculated a 70% of the total content of C-PC from *A. platensis* cells. This suggests that the combination of PEF with mild heating treatment is effective in the selective release of CH, C-PC, and WSP of small molecular weight compounds, while the extraction of larger compounds more bounded to intracellular structure, would require the application of more effective cell disruption techniques than PEF, such as bead milling or HPH (Postma et al., 2016; Martinez et al., 2017; Pataro et al., 2017; Carullo et al., 2018). In this latter case, however, higher recovery yields would likely be achieved at expenses of lower purity of the extracts. This is clearly shown by the results presented in **Figure 5D**, which highlights that, regardless of the processing temperature and pulse polarity, the purity of the C-PC extract from *A. platensis* cells suspensions upon the application of PEF pre-treatment was always higher (0.71–0.89) than that estimated for the extracts obtained after treating the cells with HPH (0.53), which is consistent with the finding of Martinez et al. (2017). Interestingly, since a C-PC purity of 0.7 is required for food-grade products (Vernès et al., 2015), the C-PC extract obtained after PEF treatment could potentially be used for food application without the need for further refining stages (Rito-Palomares et al., 2001).

Energy Efficiency Analysis

After demonstrating that PEF treatment (20 kV/cm, 100 kJ/kg_{susp}), especially when using monopolar pulses combined with moderate heating (35°C), is effective for promoting the selective extraction of water-soluble compounds from *A. platensis* cells suspensions, in the last step of this work we also evaluated its feasibility in terms of energy consumption.

Results of **Table 1** highlight the comparison among the different cell disruption techniques investigated (PEF M and PEF B at processing temperature of 25 or 35°C, mild heating at 35°C, combined PEF (mono or bipolar)-heating (35°C), and HPH) in terms of the energy consumed to extract 1 kg of the target water-soluble compounds (WSP, CH, C-PC) from *A. platensis* cells. Overall, the estimated energy consumptions show that PEF is more efficient than HPH in a manner dependent on the type of compounds to be extracted and processing conditions applied. In particular, PEF M applied at room temperature enabled the recovery of either CH and C-PC at comparable yields with HPH, but with higher purity and significantly lower energy consumption, with the perspective of facilitating purification operations in downstream processes. In the case of WSP, instead, PEF M at room temperature showed only a slightly higher energy efficiency than HPH, likely due to the limited capacity of the simply electroporated cells to release a significant amount of large molecular-weight proteins in comparison with the cells completely disintegrated by HPH treatment. As expected, the lower extraction yields of WSP and C-PC achieved upon the application of PEF B at room temperature than PEF M, required higher energy consumption for the recovery of these water-soluble compounds. In comparison with HPH, PEF B was more energetically efficient only in the case of CH recovery.

The mild heating of the algae suspension at 35°C without any PEF treatment scarcely affected the release of the target water-soluble compounds, requiring the highest expenditures of energy. Interestingly, the combined PEF M-temperature treatment required comparable energy consumptions per unit mass of WSP and CH to those required by PEF M at room temperature, while showing a significantly lower energy consumption for the recovery of C-PC. These results can be explained by the synergistic effect of the combined treatment on the extractability of intracellular compounds. A similar trend was observed when PEF B was combined with moderate heating, which appeared more energetically efficient than HPH for the recovery of only CH and C-PC.

TABLE 1 | Specific energy consumptions (EC, in kWh/kg_{DW}) of the different cell disruption techniques for the recovery of a unit mass of target compounds (WSP, water-soluble proteins; C-PC, C-phycocyanin; CHO, carbohydrates) from *A. platensis* microalgae suspensions.

Disruption method	Specific energy consumption (kWh/kg_{DW})		
	WSP	C-PC	CH
PEF M (T_{IN} = 25°C)	8.1	65.7	13.7
PEF B (T_{IN} = 25°C)	10.8	120.1	15.9
Mild heating (T_{IN} = 35°C)	79.6	401.3	443.9
Mild heating (T_{IN} = 35°C) + PEF M	8.4	47.9	17.1
Mild heating (T_{IN} = 35°C) + PEF B	12.1	100.1	20.1
HPH	10.5	110.5	53.7

PEF M and PEF B indicate the PEF treatment (20 kV/cm, 100 kJ/kg) with mono and bipolar pulses (delay time = 10 μs), respectively. HPH treatment conditions: P = 150 MPa; n_P = 3.

These results are consistent with findings previously reported by other scientists when comparing PEF and HPH in terms of energy consumed to extracts water-soluble compounds, even though from different algae cells and focusing only on monopolar pulses during treatment at room temperature. For example, when Grimi et al. (2014) and Carullo et al. (2018) compared PEF and HPH in terms of the energy consumed to extract 1 kg of carbohydrates or proteins from *Nannochloropsis* spp. and *C. vulgaris* microalgae, they found that PEF was slightly less energetically efficient than HPH for the recovery of WSP, while showed lower energy consumption than HPH for the recovery of CH.

Further studies are required to comparatively investigate the effect of PEF and HPH on microalgae strain characterized by different cell envelops, as well as processing biomass with higher solid concentrations than the diluted suspension used in this work, since those parameters could significantly affect the energy efficiency of both PEF and HPH treatment (Goettel et al., 2013; Yap et al., 2015).

CONCLUSION

Results obtained in this study have demonstrated the potential of PEF technology to intensify the selective release of water-soluble compounds (WSP, CH, C-PC) from *A. platensis* cell suspensions.

The extraction efficiency of intracellular compounds by PEF treatment depended on electrical parameters such as electric field strength, energy input, pulse polarity, and delay time between pulses of opposite polarity. The application of bipolar pulses resulted to be less effective in the permeabilization of the membranes of algae cells and the subsequent recovery of the target intracellular compounds than the usage of monopolar pulses, at least in the range of operative conditions investigated in this work. However, the optimization of the time delay between two consecutive pulses of opposite polarity appeared crucial to increase the probability of membrane permeabilization and the extraction efficiency of bipolar pulses. Therefore, further studies are needed in order to better elucidate the effect of bipolar pulses and the role played by the delay time and pulse width on the algae cell permeabilization. Improving the efficacy of bipolar pulses in the electroporation process could be very interesting, since its use will enable to drastically limit the occurrence of undesired electrochemical reactions (e.g., corrosion, electrolysis) at the electrode interface when monopolar pulses are applied (Pataro and Ferrari, 2020).

Interestingly, the use of PEF in a hurdle approach with mild heating of the biomass at 35°C remarkably enhanced the extractability of intracellular compounds showing a clear synergistic effect, regardless of the pulse polarity. In comparisons with the highly disruptive effect of HPH treatment, PEF enabled the selective release of low molecular weight WSP, CH and especially the recovery of high purity (>0.7) C-PC extract, lowering the energy consumption and without the formation of cell debris, which might facilitate the subsequent downstream purification operations.

DATA AVAILABILITY STATEMENT

All datasets generated for this study are included in the article/supplementary material.

AUTHOR CONTRIBUTIONS

GP and GF contributed to the conception and design of the study. DC was in charge of performing the chemical and statistical analysis and wrote the first draft of the manuscript. GP, FD, and DC performed the experiments. GF supervised the study. All authors contributed to manuscript revision, read and approved the submitted version.

ACKNOWLEDGMENTS

We wish to thank the ATI Biotech Company for providing *A. platensis* biomass and Dr. Mariarosa Scognamiglio for her invaluable help with SEM analyses.

REFERENCES

Abelde, J., Betancourt, L., Torres, E., Cid, A., and Barwell, C. (1998). Purification and characterization of phycocyanin from the marine cyanobacteriums *Synechococcus* sp. IO9201. *Plant Sci.* 136, 109–120. doi: 10.1016/S0168-9452(98)00113-117

Aouir, A., Amiali, M., Kirilova-Gachovska, T., Benchabane, A., and Bitam, A. (2015). "The effect of pulsed electric field (PEF) and ultrasound (US) technologies on the extraction of phycopiliproteins from *Arthrospira platensis*," in *Proceedings of the Canada International Humanitarian Technology Conference*, Ottawa, ON.

Bennett, A., and Bogorad, L. (1973). Complementary chromatic adaptation in a filamentous blue-green alga. *J. Cell Biol.* 58, 419–435. doi: 10.1083/jcb.58.2.419

Beveridge, J. R., MacGregor, S. J., Marsili, L., Anderson, J. G., Rowan, N. J., and Farish, O. (2002). Comparison of the effectiveness of biphase and monophase rectangular pulses for the inactivation of micro-organisms using pulsed electric fields. *IEEE Trans. Plasma Sci.* 30, 1525–1531. doi: 10.1109/tps.2002.804204

Carullo, D., Abera, B. D., Casazza, A. A., Donsì, F., Perego, P., Ferrari, G., et al. (2018). Effect of pulsed electric fields and high pressure homogenisation on the acqueous extraction of intracellular compounds from the microalgae *Chlorella vulgaris*. *Algal Res.* 31, 60–69. doi: 10.1016/j.algal.2018.01.017

Chaiklahan, R., Chirasuwan, N., and Bunnag, B. (2012). Stability of phycocyanin extracted from Spirulina sp.: influence of temperature, pH and preservatives. *Process Biochem.* 47, 659–664. doi: 10.1016/j.procbio.2012.01.010

Chang, D. C. (1989). Cell poration and cell fusion using an oscillating electric field. *Biophys. J.* 56, 641–652. doi: 10.1016/S0006-3495(89)82711-82710

DuBois, M., Gilles, K. A., Hamilton, J. K., Rebers, P. A., and Smith, F. (1956). Colorimetric method for determination of sugars and related substances. *Anal. Chem.* 28, 350–356. doi: 10.1021/ac60111a017

Evrendilek, G. A., and Zhang, Q. (2005). Effects of pulse polarity and pulse delaying time on pulsed electric fields-induced pasteurization of *E. coli* O157:H7. *J. Food Eng.* 68, 271–276. doi: 10.1016/j.jfoodeng.2004.06.001

Fernández-Rojas, B., Hernández-Juárez, J., and Pedraza-Chaverri, J. (2014). Nutraceutical properties of phycocyanin. *J. Funct. Foods* 11, 375–392. doi: 10.1016/j.jff.2014.10.011

Folin, O., and Ciocalteau, V. (1927). On tyrosine and tryptophane determinations in proteins. *J. Biol. Chem.* 73, 627–650.

Garcia, D., Gomez, N., Mañas, P., Raso, J., and Pagan, R. (2007). Pulsed electric fields cause bacterial envelopes permeabilization depending on the treatment intensity, the treatment medium pH and the microorganism investigated. *Int. J. Food Microbiol.* 113, 219–227. doi: 10.1016/j.ijfoodmicro.2006.07.007

Geada, P., Rodriguez, R., Loureiro, L., Pereira, R., Fernandez, B., Teixeira, J. A., et al. (2018). Electrotechnologies applied to microalgal biotechnology-applications, techniques and future trends. *Renew. Sust. Environ. Rev.* 94, 656–668. doi: 10.1016/j.rser.2018.06.059

Goettel, M., Eing, C., Gusbeth, C., Straessner, R., and Frey, W. (2013). Pulsed electric field assisted extraction of intracellular valuables from microalgae. *Algal Res.* 2, 401–408. doi: 10.1016/j.algal.2013.07.004

Golberg, A., Sack, M., Teissie, J., Pataro, G., Pliquett, U., Saulis, G., et al. (2016). Energy-efficient biomass processing with pulsed electric fields for bioeconomy and sustainable development. *Biotechnol. Biofuels* 9, 1–22. doi: 10.1201/9780429133459-1

Grimi, N., Dubois, A., Marchal, L., Jubeau, S., Lebovka, N. I., and Vorobiev, E. (2014). Selective extraction from microalgae *Nannochloropsis* sp. using different methods of cell disruption. *Bioresour. Technol.* 153, 254–259. doi: 10.1016/j.biortech.2013.12.011

Günerken, E., D'Hondt, E., Eppink, M. H. M., Garcia-Gonzales, L., Elst, K., and Wijffels, R. H. (2015). Cell disruption for microalgae biorefineries. *Biotechnol. Adv.* 33, 243–260. doi: 10.1016/j.biotechadv.2015.01.008

Han, S.-F., Jin, W., Yang, Q., Abomohra, A. E.-F., Zhou, X., Tu, R., et al. (2019). Application of pulse electric field pretreatment for enhancing lipid extraction from *Chlorella pyrenoidosa* grown in wastewater. *Renew. Environ.* 133, 233–239. doi: 10.1016/j.renene.2018.10.034

Jaeschke, D. P., Domeneghini Mercali, G., Ferreira Marczak, L. D., Müller, G., Frey, W., and Gusbeth, C. (2019). Extraction of valuable compounds from *Arthrospira platensis* using pulsed electric field treatment. *Bioresour. Technol.* 283, 207–212. doi: 10.1016/j.biortech.2019.03.035

Lowry, O. H., Rosebrough, N. J., Farr, A. L., and Randall, R. J. (1951). Protein measurement with the Folin phenol reagent. *J. Biol. Chem.* 193, 265–275.

Lu, H. K., Hsieh, C. C., Hsu, J. J., Yang, Y. K., and Chou, H. N. (2006). Preventive effects of *Spirulina platensis* on skeletal muscle damage under exercise-induced oxidative stress. *Eur. J. Appl. Physiol.* 98, 220–226. doi: 10.1007/s00421-006-0263-260

Luengo, E., Martı nez, J. M., Bordetas, A., Alvarez, I., and Raso, J. (2015). Influence of the treatment medium temperature on lutein extraction assisted by pulsed electric fields from *Chlorella vulgaris*. *Innov. Food Sci. Emerg. Technol.* 29, 15–22. doi: 10.1016/j.ifset.2015.02.012

Lupatini, A. L., Colla, L. M., Canan, C., and Colla, E. (2016). Potential application of microalgae *Spirulina platensis* as a protein source. *J. Sci. Food Agric.* 97, 724–732. doi: 10.1002/jsfa.7987

Martinez, J. M., Delso, C., Alvarez, I., and Raso, J. (2020). Pulsed electric field-assisted extraction of valuable compounds from microorganisms. *Compr. Rev. Food Sci. Food Saf.* 19, 530–552. doi: 10.1111/1541-4337.12512

Martinez, J. M., Luengo, E., Saldana, G., Alvarez, I., and Raso, J. (2017). C-phycocyanin extraction assisted by pulsed electric field from *Artrosphira platensis*. *Food Res. Int.* 99, 1042–1047. doi: 10.1016/j.foodres.2016.09.029

Parniakov, O., Barba, F. J., Grimi, N., Marchal, L., Jubeau, S., Lebovka, N., et al. (2015a). Pulsed electric field and pH assisted selective extraction of intracellular components from microalgae *Nannochloropsis*. *Algal Res.* 8, 128–134. doi: 10.1016/j.algal.2015.01.014

Parniakov, O., Barba, F. J., Grimi, N., Marchal, L., Jubeau, S., Lebovka, N., et al. (2015b). Pulsed electric field assisted extraction of nutritionally valuable compounds from microalgae *Nannochloropsis* spp. using the binary mixture of organic solvents and water. *Innov. Food Sci. Emerg. Technol.* 27, 79–85. doi: 10.1016/j.ifset.2014.11.002

Pataro, G., Carullo, D., and Ferrari, G. (2019). PEF-assisted supercritical CO_2 extraction of pigments, from microalgae *Nannochloropsis oceanica* in a continuous flow system. *Chem. Eng. Trans.* 74, 97–102. doi: 10.3303/CET1974017

Pataro, G., and Ferrari, G. (2020). "Limitations of pulsed electric field utilization in food industry," in *Pulsed Electric Field to Obtain Healthier and Sustainable Food for Tomorrow*, eds F. Barba, O. Parniakov, and A. Wiktor (London: Academic Press), 283–310. doi: 10.1016/b978-0-12-816402-0.00013-6

Pataro, G., Goettel, M., Straessner, R., Gusbeth, C., Ferrari, G., and Frey, W. (2017). Effect of PEF treatment on extraction of valuable compounds from Microalgae *C. vulgaris*. *Chem. Eng. Trans.* 57, 67–72. doi: 10.3303/CET1757012

Phong, W. N., Show, P. L., Ling, T. C., Juan, J. C., Ng, E.-P., Chang, J.-S., et al. (2017). Mild cell disruption methods for bio-functional proteins recovery from microalgae-recent developments and future perspectives. *Algal Res.* 31, 506–516. doi: 10.1016/j.algal.2017.04.005

Poojary, M. M., Barba, F. J., Aliakbarian, B., Donsì, F., Pataro, G., Dias, D. A., et al. (2016). Innovative alternative technologies to extract carotenoids from microalgae and seaweeds. *Mar. Drugs* 14, 214. doi: 10.3390/md14110214

Postma, P. R., Pataro, G., Capitoli, M., Barbosa, M. J., Wijffels, R. H., Eppink, M. H. M., et al. (2016). Selective extraction of entracellular components from the microalga *Chlorella Vulgaris* by combined pulsed electric field-temperature treatments. *Bioresour. Technol.* 203, 80–88. doi: 10.1016/j.biortech.2015.12.012

Qin, B. L., Zhang, Q., Swanson, B. G., and Pedrow, P. D. (1994). Inactivation of microorganism by different pulsed electric fields of different voltage waveforms. *IEEE T. Ind. App.* 1, 1047–1057. doi: 10.1109/94.368658

Rito-Palomares, M., Nunez, M., and Amador, D. (2001). Practical application of aqueous two-phase systems for the development of a prototype process for c-phycocyanin recovery from *Spirulina maxima*. *J. Chem. Technol. Biotechnol.* 76, 1273–1280. doi: 10.1002/jctb.507

Safi, C., Charton, M., Ursu, A. V., Laroche, C., Zebib, B., Pontalier, P.-Y., et al. (2014). Release of hydro-soluble microalgal proteins using mechanical and chemical treatments. *Algal Res.* 3, 55–60. doi: 10.1016/j.algal.2013.11.017

Safi, C., Frances, C., Ursu, A. V., Laroche, C., Pouzet, C., Vaca-Garcia, C., et al. (2015). Understanding the effect of cell disruption methods on the diffusion of *Chlorella vulgaris* proteins and pigments in the aqueous phase. *Algal Res.* 8, 61–68. doi: 10.1016/j.algal.2015.01.002

Saldaña, G., Álvarez, I., Condón, S., and Raso, J. (2014). Microbiological aspects related to the feasibility of PEF technology for food pasteurization. *Crit. Rev. Food Sci. Nutr.* 54, 1415–1426. doi: 10.1080/10408398.2011.638995

Silve, A., Papachristou, I., Wustner, R., Strabner, R., Schirmer, M., Leber, K., et al. (2018). Extraction of lipids from wet microalga *Auxenochlorella protothecoides* using pulsed electric field treatment and ethanol-hexane blends. *Algal Res.* 29, 212–222. doi: 10.1016/j.algal.2017.11.016

Sweeney, D. C., Reberšek, M., Dermol, J., Rems, L., Miklavčič, D., and Davalos, R. V. (2016). Quantification of cell membrane permeability induced bymonopolar and high-frequency bipolar bursts of electrical pulses. *Biochim. Biophys. Acta* 1858, 2689–2698. doi: 10.1016/j.bbamem.2016.06.024

Timmermans, R. A. H., Nierop Groot, M. N., Nederhoff, A. L., van Boekel, M. A. J. S., Matser, A. M., and Mastwijk, H. C. (2014). Pulsed electric field processing of different fruit juices: impact of pH and temperature on inactivation of spoilage and pathogenic micro-organisms. *Int. J. Food Microbiol.* 173, 105–111. doi: 10.1016/j.ijfoodmicro.2013.12.022

Vernès, L., Granvillain, P., Chemat, F., and Vian, M. (2015). Phycocyanin from Arthrospira platensis. Production, extraction and analysis. *Curr. Biotechnol.* 4. doi: 10.2174/2211550104666151006002418

Yap, B. H. J., Dumsday, G. J., Scales, P. J., and Martin, G. J. O. (2015). Energy evaluation of algal cell disruption by high pressure homogenization. *Bioresour. Technol.* 184, 280–285. doi: 10.1016/j.biortech.2014.11.049

Zbinden, M. D. A., Sturm, B. S., Nord, R. D., Carey, W. J., Moore, D., Shinogle, H., et al. (2013). Pulsed electric field (PEF) as an intensification pretreatment for greener solvent lipid extraction from microalgae. *Biotechnol. Bioeng.* 110, 1605–1615. doi: 10.1002/bit.24829

't Lam, G. P., Postma, P. R., Fernandes, D. A., Timmermans, R. A. H., Vermue, M. H., Barbosa, M. J., et al. (2017a). Pulsed electric field for protein release of the microalgae *Chlorella vulgaris* and Neochloris oleoabundans. *Algal Res.* 24, 181–187. doi: 10.1016/j.algal.2017.03.024

't Lam, G. P., van der Kolk, J. A., Chordia, A., Marian, H., Vermuë, M. H., Olivieri, G., et al. (2017b). Mild and selective protein release of cell wall deficient microalgae with pulsed electric field. *ACS Sustainable Chem. Eng.* 5, 6046–6053. doi: 10.1021/acssuschemeng.7b00892

Conflict of Interest: The authors declare that the research was conducted in the absence of any commercial or financial relationships that could be construed as a potential conflict of interest.

Copyright © 2020 Carullo, Pataro, Donsì and Ferrari. This is an open-access article distributed under the terms of the Creative Commons Attribution License (CC BY). The use, distribution or reproduction in other forums is permitted, provided the original author(s) and the copyright owner(s) are credited and that the original publication in this journal is cited, in accordance with accepted academic practice. No use, distribution or reproduction is permitted which does not comply with these terms.

frontiers in Bioengineering and Biotechnology

ORIGINAL RESEARCH
published: 08 September 2020
doi: 10.3389/fbioe.2020.543187

Evaluation and Optimization of Protein Extraction From *E. coli* by Electroporation

*Saša Haberl Meglič[1], Nika Janež[2,3], Matjaž Peterka[2], Karel Flisar[1], Tadej Kotnik[1] and Damijan Miklavčič[1]**

[1] Faculty of Electrical Engineering, University of Ljubljana, Ljubljana, Slovenia, [2] Centre of Excellence for Biosensors, Instrumentation and Process Control, Centre for Biotechnology, Ajdovščina, Slovenia, [3] Department of Biotechnology, Jožef Stefan Institute, Ljubljana, Slovenia

Growing diversity of protein-based technologies dictates further development of bio manufacturing to lower the cost of production and maximize yields. Intracellularly expressed recombinant proteins must be extracted from production host prior to purification. Use of electroporation to obtain proteins from bacteria and yeasts has been demonstrated in several studies for different modes of operation and formats. Here we tested various protocols for protein extraction from *Escherichia coli* by means of electroporation. The tested protocols were compared to established extraction methods of ultrasonication and glass-bead milling in terms of protein yields and content of impurities such as host cell DNA and endotoxins in the lysate. Protein extraction yield was maximal when exponentially growing bacteria were treated at 37°C, regardless of the electroporation mode of operation (batch or flow). We were unable to eliminate co-extraction of host DNA and endotoxins, but with 8 × 1 ms, 5 kV/cm, 1 Hz pulses they were minimized. Yields with optimized electroporation (up to 86 g protein/kg dry weight) were inferior to those in ultrasonication (up to 144 g protein/kg dry weight) and glass-bead milling (up to 280 g protein/kg dry weight). Nevertheless, electroporation largely avoids cell lysis and disintegration with which the extract is a mix of extracted proteins with debris of the bacterial envelope and bacterial DNA, which necessitates further purification.

Keywords: protein extraction, *E. coli*, electroporation, glass–bead milling, ultrasonication, host DNA, endotoxin

OPEN ACCESS

Edited by:
Lucia Gardossi, University of Trieste, Italy

Reviewed by:
Evangelia Chronopoulou, Agricultural University of Athens, Greece
Alexandra Marisa Targovnik, University of Buenos Aires, Argentina

***Correspondence:**
Damijan Miklavčič
damijan.miklavcic@fe.uni-lj.si

Specialty section:
This article was submitted to Industrial Biotechnology, a section of the journal Frontiers in Bioengineering and Biotechnology

Received: *16 March 2020*
Accepted: *20 August 2020*
Published: *08 September 2020*

Citation:
Haberl Meglič S, Janež N, Peterka M, Flisar K, Kotnik T and Miklavčič D (2020) Evaluation and Optimization of Protein Extraction From E. coli by Electroporation. Front. Bioeng. Biotechnol. 8:543187. doi: 10.3389/fbioe.2020.543187

INTRODUCTION

In the bio manufacturing of intracellular proteins, host cell envelope disruption is required to release the target recombinant proteins into the medium. The resulting lysate contains target proteins as well as impurities from host cells and growth medium which are then removed by purification. The type of extraction method affects the co-extraction of host cell components i.e., impurities, which is especially important in the production of protein therapeutics. Methods to open cell envelope and extract proteins are divided into mechanical and non-mechanical (Tan and Yiap, 2009). Mechanical methods like bead milling, high pressure homogenization, ultrasonication, cause cell lysis. Non-mechanical methods, chemical or enzymatic, are gentler, causing limited changes in cell envelope permeability resulting in outflow of intracellular content, but still have drawbacks, including expensive and often toxic chemicals, with their pharmaceutical production restricted by regulatory bodies.

Escherichia coli and other bacteria used as production hosts have the advantage of fast and easy cultivation as well as high recombinant protein production yields (Assenberg et al., 2013). Key microbial cell impurities affecting product's safety and efficiency are endotoxins (lipooligosaccharides), host cell DNA and host cell proteins. Endotoxins are a potent pyrogenic compound causing strong immunogenic response in mammals and must be reduced to concentration below 5 EU/kg/hr according to European Pharmacopoeia[1]. Host cell DNA contributes to increased viscosity of lysate resulting from cell disruption, impedes purification processes, and carries potential risk for human health (Stone et al., 2018). Host cell proteins, produced by the host to sustain normal cell functions, may be immunogenic, toxic or active in human bodies, and if they possess proteolytic activity, they may cause degradation of the recombinant protein (Goey et al., 2018).

Protein extraction by means of electroporation has been implemented to date in batch and flow modes of operation, as well as on microchips to assist protein research (Shiina et al., 2004; Matos et al., 2013; Flisar et al., 2014; Haberl Meglic et al., 2015). The extraction mechanism is based on induction of changes in cell envelope permeability due to exposure to sufficiently strong electric pulses (Kotnik et al., 2010). The choice of electric pulse parameters depends on the desired effect on bacteria, where a suitable choice of amplitude, duration and number of electric pulses delivered is of key importance (Kotnik et al., 2015). Longer electric pulses with lower amplitudes have been demonstrated to give rise to higher protein yields without severely compromising cell viability, and are therefore considered optimal for protein extraction (Haberl Meglic et al., 2015). Even though electroporation can also result in loss of cell viability, the damage is in general more limited than in chemical cell lysis, which is advantageous for extraction, as impurities are not as extensively co-extracted. For Gram-negative bacteria, electroporation efficiency was found to depend on the inherent properties of bacterial cell envelope and differs on a species and strain level (Wirth et al., 1989). Inner membrane integrity depends on culture medium, cultivation mode, growth rate and growth phase (Chou, 2007). These host envelope properties were also found to affect cell's susceptibility to electric pulses and protein extraction efficiency (Coustets et al., 2015; Haberl Meglic et al., 2015). Protein extraction by means of electroporation was found to increase enzyme activity and production yields in fed-batch processes compared to traditional extraction methods (Shiina et al., 2004; Coustets et al., 2015).

Here, we optimized extraction temperature and bacterial growth phase to maximize protein yield and survival of bacteria treated with electroporation. We further evaluated and compared extractions by electroporation with two established methods ultrasonication and glass-bead milling in terms of protein yield and co-extraction of impurities. Additionally, we compared electroporation in batch and continuous flow mode. This mode of operation has gained importance in protein manufacturing for the production of new products, labile biologics and those with uncertain demand (Hernandez, 2017).

[1]https://www.edqm.eu/en/european-pharmacopoeia-ph-eur-9th-edition

MATERIALS AND METHODS

Bacterial Strains and Cultivation

Two ***E. coli*** TOP10 (K12 derivative) variants were used in this study: the kanamycin-resistant TOP10 pEGFP-N1 and the ampicillin-resistant TOP10 pUC19-hMGFP (both from Clontech Laboratories Inc., Mountain View, CA, United States). Strains were grown in LB medium (Sigma-Aldrich Chemie GmbH, Schnelldorf, Germany) supplemented by 50 μg/ml kanamycin (Carl ROTH Gmbh, Germany) for TOP10 pEGFP-N1 or 100 μg/ml ampicillin (Sigma-Aldrich Chemie GmbH) for TOP10 pUC19-hMGFP. Bacteria for extraction were prepared by shake flask cultivation at 37°C, 200 rpm. Based on the pre-determined growth curve (Haberl-Meglič et al., 2016), bacteria were harvested at appropriate growth phase by centrifugation (4,248 × **g**, 30 min, 4°C) and resuspended to OD600 2.1 corresponding to about 10^9 colony forming units per milliliter (CFU/ml).

Escherichia coli TOP10 pEGFP-N1 strain was used for: (i) optimizing electroporation protocol (to assess the effect of bacterial growth phase and pre-/post-pulse incubation temperature) (see **Figures 1**, **2**); (ii) assessing scalability of electroporation (continuous flow electroporation extraction) (see **Figures 1**, **2**); (iii) assessing the effect of different treatments on total protein extraction and co-extraction of unwanted compounds (endotoxins, host DNA) (see **Figures 3–5**); and (iv) assessing bacterial morphology after different treatments (see **Figure 6**).

Escherichia coli TOP10 pUC19-hMGFP strain carries GFP protein which was chosen as model target protein, because its fluorophore gives stable signal in various media due to its tight and stable structure. Therefore, this strain was used only to show the difference in extraction of model target protein by different methods (electroporation, ultrasonication, and glass-bead milling) (see **Figure 7**).

Assessing the Effect of Bacterial Growth Phase and Pre-/Post-Pulse Incubation Temperature on Protein Extraction by Means of Batch or Flow Continuous Electroporation Treatment

Bacterial culture TOP10 pEGFP-N1 was in first set of experiments grown to early exponential phase (5 h) or stationary growth phase (10 h), harvested as described above (see section "Bacterial Strains and Cultivation") and chilled to 4°C for 30 min before the electric pulse application. After the treatment, bacterial suspension was again chilled to 4°C for 1 h.

In second set of experiments bacterial culture TOP10 pEGFP-N1 was grown to early exponential phase (5 h), harvested as described above (see section "Bacterial Strains and Cultivation") and aliquoted for following parallel experiments. Each aliquot was incubated at a different temperature (4, 22, 37, 45°C) for 30 min prior to electroporation.

After the incubation, bacteria were exposed to batch or flow continuous electroporation treatment and then again incubated at a different temperature (4, 22, 37, 45°C) for 1 h.

In batch electroporation treatment, 140 μl of bacterial suspension was placed between stainless steel plate electrodes (1 mm gap) and electroporated by a square wave electric pulse generator HVP – VG (IGEA s.r.l., Italy) using 8 rectangular pulses with duration of 1 ms, electric field strength 5 kV/cm, and repetition frequency 1 Hz. These electroporation parameters were used as they were previously found efficient for protein extraction (Haberl Meglic et al., 2015).

In flow continuous electroporation treatment, laboratory scale flow system with square wave prototype pulse generator and treatment chamber (**Supplementary Figure 1**) was used. Flow treatment chamber has a cross section area of 2.5 × 2.0 mm and is 10 cm long, with an inter electrode gap (stainless steel electrodes) of 2.5 mm (**Supplementary Figure 1**). Bacteria were subjected to a train of 8 rectangular pulses with duration of 1 ms, electric field strength 5 kV/cm (500 V) and repetition frequency 10 Hz. The flow velocity through the chamber was adjusted as to expose each bacterial cell to eight electrical pulses as in batch extraction experiments – 50 ml of bacterial suspension was loaded into the flow treatment chamber at 37.5 ml/min using a peristaltic pump. The lysate was analyzed after a single passage through the continuous flow cell. Prior to the treatment, the tubing and the continuous flow treatment chamber were flushed with 70 % ethanol and sterile distilled water. Extraction by flow system was compared to batch extraction to evaluate effect of the growth phase and of the pre- and post-pulse temperature on extraction outcome.

Treatment was repeated at least twice on separate occasions using fresh bacterial suspensions until adequate lysate volume was obtained. Electric field strength was estimated as $E = U/d$, where U denotes applied voltage and d inter-electrode distance.

As control, we used bacterial suspensions that were not subjected to electroporation but were otherwise treated in the same way as experimental samples.

Assessing the Effect of Electroporation Parameters, Ultrasonication and Glass-Bead Milling

Bacterial culture TOP10 pEGFP-N1 was grown to early exponential phase (5 h), harvested as described in see section "Bacterial Strains and Cultivation" and incubated for 30 min at 37°C prior the extraction.

Extraction by means of electroporation was carried out in batch system, using following electroporation parameters: (i) a train of 8 rectangular pulses of 100 μs, electric field strength 20 kV/cm (2000 V) and repetition frequency 1 kHz, (ii) a train of 8 rectangular pulses of 1 ms, 5 kV/cm (500 V) 1 Hz, and (iii) a train of 32 rectangular pulses of 100 μs, 20 kV/cm (2000 V), 1 Hz.

The energy input was calculated using the formula below, where U is applied voltage, I electric current, n number of applied pulses, T pulse duration and V sample volume. The results are presented in **Table 1**.

$$W = \frac{U \cdot I \cdot n \cdot T}{V}$$

TABLE 1 | Calculated energy input delivered by each set of pulse parameters in batch extraction of proteins from *E. coli*.

Operation mode	Electroporation pulse parameters	Energy input (kJ/L)
Batch	8 × 100 μs, 20 kV/cm, 1 kHz	65
	8 × 1 ms, 5 kV/cm, 1 Hz	37
	32 × 100 μs, 20 kV/cm, 1 Hz	379
Continuous	8 × 1 ms, 5 kV/cm, 10 Hz	37

Extraction by means of ultrasonication was performed with Ultrasonic homogenizer 4710 (Cole Parmer Instrument Co, Vernon Hills, IL, United States). 3 ml of bacterial suspension was sonicated three times for 20 s at 90 W amplitude and 25 Hz frequency. Samples were kept on ice while sonicated to prevent heating.

Extraction by means of glass-bead milling was carried out by mixing 1.2 ml of bacterial suspension and 0.1 mm glass-beads at approximate ratio 1:1. Homogenization was performed for 5 min at 2850 rpm using bead beater Digital Disruptor Genie (Scientific Industries Inc., Bohemia, NY, United States).

The bacterial suspension was after all treatments incubated for 1 h at 37°C. As control, we used bacterial suspensions that were not subjected to extraction methods but were otherwise treated in the same way as experimental samples.

Assessing Total and Target (GFP) Proteins

Total protein extraction was determined with assay based on the Bradford Reagent (Sigma-Aldrich Chemie GmbH, Germany) (BSA) and was performed according to the manufacturer's recommendations. This reagent is suitable for 1–10 μg/ml micro assays. Calibration curve was prepared from serial dilutions of bovine serum albumin of known concentration. Samples for total protein quantification were sterile filtered through a 0.22 μm filter (Millex-GV; Millipore Corporation, Billerica, MA, United States) immediately after the post-treatment incubation. Final concentration of extracted proteins in the sample was determined after the protein concentration in the control was subtracted from the initial protein concentration in the sample. Protein concentration was expressed as grams of protein per kilogram of dry weight (abbreviated in the Results as g protein/kg dw).

Samples for GFP quantification were clarified after the post-treatment incubation by centrifugation 7155 × *g*, 5 min, 4°C. The supernatants were collected, and pellets were gently re-suspended in the sterile distilled water. Fluorescence was measured in the pellets and supernatants immediately after extraction. Detection of GFP was carried out on spectrofluorometer (Tecan infinite M200, Tecan, Austria) at excitation wavelength 490 nm and emission wavelength 520 nm. Concentration of GFP was estimated from the calibration curve, and as a standard, purified GFP of known concentration was used. Limit of detection was estimated at 17 μg GFP/ml and limit of quantification 22 μg GFP/ml.

Bacterial Viability Assessment

Immediately after the post-treatment incubation, serial dilution of 50 μl sample aliquots in 0.9% NaCl was made. One hundred microliters of each dilution were plated onto the LB agar supplemented by suitable antibiotic (see section "Bacterial Strains and Cultivation") and incubated for 24 h at 37°C. From the bacterial counts' CFU/ml were calculated. The bacterial cell number reduction was expressed as log (N/N_0), where N represents the number of CFU/ml in treated sample and N_0 the number of CFU/ml in the control sample.

Assessing Host Cell DNA Extraction After Different Treatments

Host cell DNA was quantified by real time quantitative PCR (qPCR) analysis based on amplification of 16 rRNA gene developed by external service provider NIB (Ljubljana, Slovenia). As reference material, purified and restricted *E. coli* DH5α DSM 6897 genomic DNA was used, since both bacteria belong to the same species and have the same number of rRNA copies in their genome (Durfee et al., 2008; Anton and Raleigh, 2016). Samples for qPCR analysis were sterile filtered through a 0.22 μm filter immediately after the post-treatment incubation and kept at −20°C until analysis.

Assessing Endotoxin Extraction After Different Treatments

Endotoxin content was measured using chromogenic limulus amoebocyte assay (LAL assay) by external service provider Jafral d.o.o. (Ljubljana, Slovenia). Samples for LAL assay were sterile filtered through a 0.22 μm filter immediately after the post-treatment incubation and kept at 4°C until analysis.

Assessing Bacterial Morphology After Different Treatments

Morphology of bacteria after different treatment methods was assessed by transmission electron microscopy – TEM (Philips CM 100, Philips Electronics, Amsterdam, Netherlands). The cells were applied to Formvar/carboned 400-mesh copper grids immediately after the treatment without post incubation and were negatively stained by 1% uranyl acetate.

Statistical Analysis

Experiments were repeated three or more times, on different days to prove repeatability. Results were evaluated using an unpaired t-test analysis (SigmaPlot 11.0, Systat Software, Richmond, CA, United States) and were considered as statistically different at $p < 0.05$.

RESULTS

Effect of Bacterial Growth Phase, Pre- and Post-Treatment Temperature on Protein Extraction by Means of Batch or Flow Continuous Electroporation Treatment

Bacterial growth phase strongly affects bacterial metabolism as well as the ratio of protein to lipid content in the membrane, which also affects the efficiency of electroporation (Haberl-Meglič et al., 2016). Therefore, we firstly assessed the effect of bacterial growth phase on protein extraction by means of electroporation in batch and flow continuous system (**Figure 1**). The highest protein yield was obtained from bacteria in exponential growth

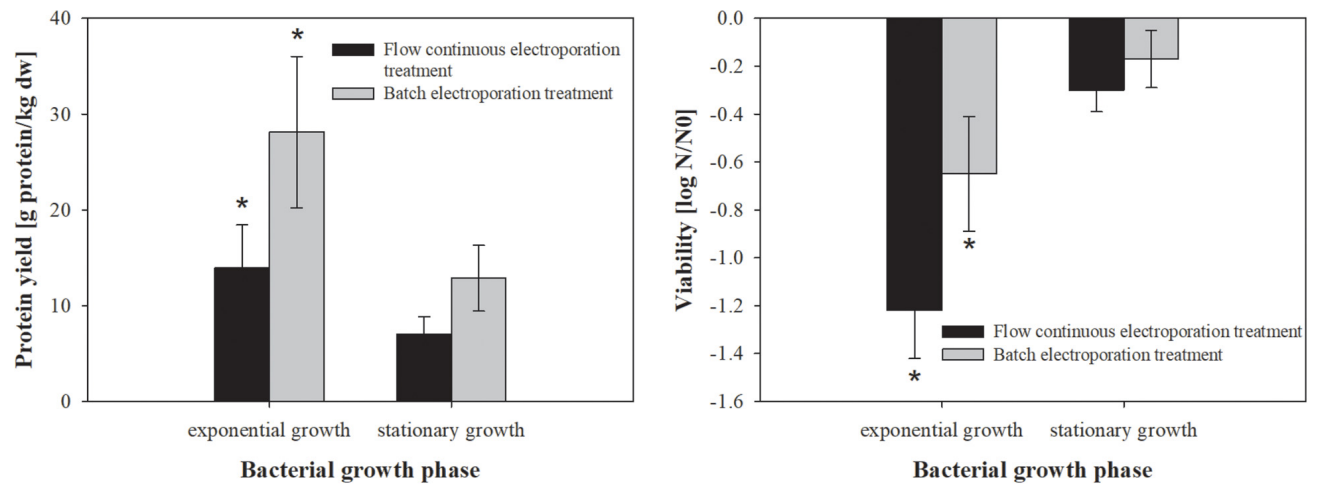

FIGURE 1 | The effect of bacterial growth phase on protein extraction **(left)** and bacterial viability **(right)**. Bacterial cells (*E. coli* TOP10 pEGFP-N1) were grown to exponential (5 h growth time; treated mass of cells was 2.968×10^{-7} kg dw) and stationary (10 h growth time; treated mass of cells was 9.38×10^{-7} kg dw) growth phase, incubated for 30 min at 4°C and exposed to two different electroporation treatments: (black column) flow continuous electroporation treatment where each bacterial cell was subjected to eight pulses with 5 kV/cm of electric field strength, 1 ms pulse duration and 10 Hz of repetition frequency; (gray column) batch electroporation treatment where eight pulses were applied with 5 kV/cm of electric field strength, 1 ms pulse duration and 1 Hz of repetition frequency. After the treatment bacterial cells were incubated for 1 h at 4°C. Values represent means (all tests were performed in triplicate) and error bars are determined from standard deviation. Asterisk (*) represents statistically significant ($p < 0.05$) difference versus stationary growth phase.

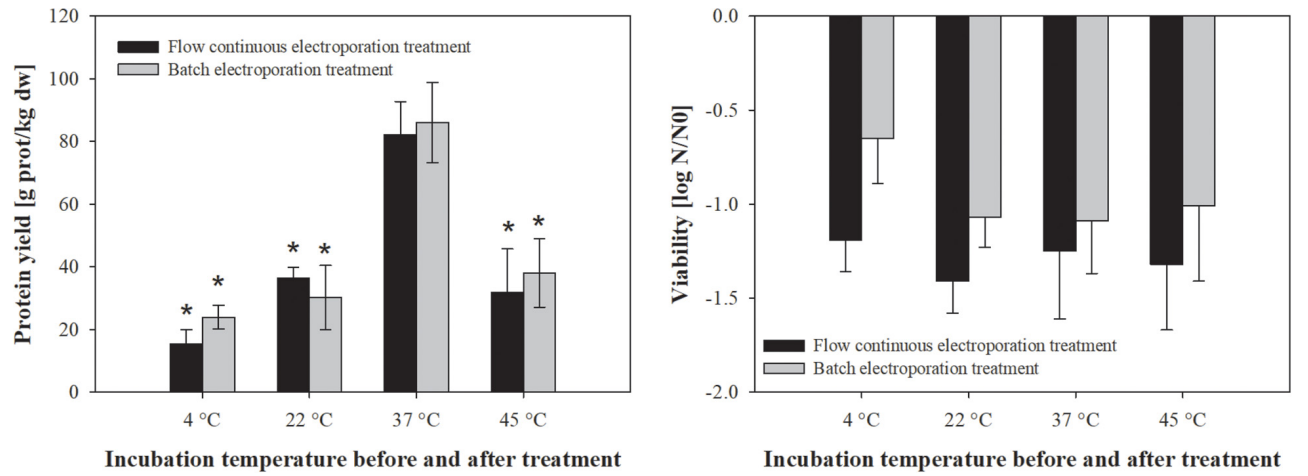

FIGURE 2 | The effect of incubation temperature before and after treatment on protein extraction **(left)** and bacterial viability **(right)**. Bacterial cells (*E. coli* TOP10 pEGFP-N1) in exponential growth phase were incubated before (30 min) and after treatment (1 h) at different temperatures (4, 22, 37, and 45°C) and exposed to two different electroporation treatments: (black column) flow continuous electroporation treatment where each bacterial cell was subjected to eight pulses with 5 kV/cm of electric field strength, 1 ms pulse duration and 10 Hz of repetition frequency; (gray column) batch electroporation treatment where eight pulses were applied with 5 kV/cm of electric field strength, 1 ms pulse duration and 1 Hz of repetition frequency. Treated mass of cells was 2.532×10^{-7} kg dw. Values represent means (all tests were performed in triplicate) and error bars are determined from standard deviation. Asterisk (*) represents statistically significant ($p < 0.05$) difference versus incubation temperature at 37°C.

phase (14 ± 4.4 g prot/kg dw), compared to stationary phase (7 ± 1.8 g prot/kg dw), but the stationary growth phase exhibited lower viability loss (**Figure 1**). There was no statistically significant difference in protein extraction or viability loss between flow continuous and batch electroporation treatment for either bacterial growth phase.

Based on our results bacterial cells were most susceptible to electric pulses (more proteins were extracted) in earlier stages of growth (exponential growth phase).

Temperature has a significant effect on cell membrane structure and by that on permeabilization of the cell membrane. Thus, we secondly assessed the effect of different incubation temperatures on protein extraction by means of electroporation in batch and flow continuous system (**Figure 2**). The increase in pre- and post-pulse temperature resulted in improved protein yield, with the highest protein concentration obtained at 37°C (82 ± 10.6 g prot/kg dw), followed by 22°C (36.4 ± 3.4 g prot/kg dw), 45°C (31.8 ± 13.9 g prot/kg dw) and 4°C (15.3 ± 4.6 g prot/kg dw) for batch and flow continuous electroporation treatment (**Figure 2**). There was no statistically significant effect of different incubation temperatures on viability when bacterial cells were electroporated (**Figure 2**).

Our results show that the higher amount of extracted proteins can be achieved when bacterial cells are electroporated in exponential growth phase (**Figure 1**) and incubated at 37°C (**Figure 2**). Therefore all the following experiments were performed at these conditions.

The efficiency of extraction by means of electroporation did not differ when performed in batch or flow continuous treatment mode, thus scaling up for protein extraction seems achievable.

Comparison of Extraction of Proteins by Means of Electroporation, Ultrasonication and Glass-Bead Milling

Our motivation in this part of the study was to compare extraction by means of electroporation with two most widely used methods for protein extraction. Moreover, different electroporation parameters (electric field strength, pulse duration, pulse amplitude, and repetition frequency) strongly affect the magnitude of membrane permeabilization and by that also extraction yield. Therefore, three different electroporation protocols were tested. The lysates obtained from *E. coli* TOP10 pEGFP-N1 by the different extraction methods were compared in terms of total protein content, bacterial viability after the treatment (**Figure 3**), and co-extracted undesired molecules in lysate (host cell DNA-**Figure 4** and endotoxins-**Figure 5**). Here, total protein content was used to describe overall protein yield and to observe differences between proteins extracted by tested extraction methods, although this parameter commonly reflects proteinaceous impurities in the protein therapeutics. Bacteria *E. coli* TOP10 pEGFP-N1 were harvested at early exponential phase (5 h) and incubated for 30 min at 37°C prior treatment.

The highest total protein yield was obtained by ultrasonication (144.4 ± 2.6 g prot/kg dw) followed by electroporation protocol 8 × 100 μs, 20 kV/cm, 1 kHz (137.9 ± 45.6 g prot/kg dw), glass-bead milling (131.6 ± 9.5 g prot/kg dw), and electroporation protocols 32 × 100 μs, 20 kV/cm, 1 Hz (92.6 ± 22.9 g prot/kg dw), 8 × 1 ms, 5 kV/cm, 1 Hz (29.2 ± 5.4 g prot/kg dw) (**Figure 3**, left). Considering the protein concentration in the electroporated lysates, we obtained 50 ± 12% proteins by 100 μs electric pulses

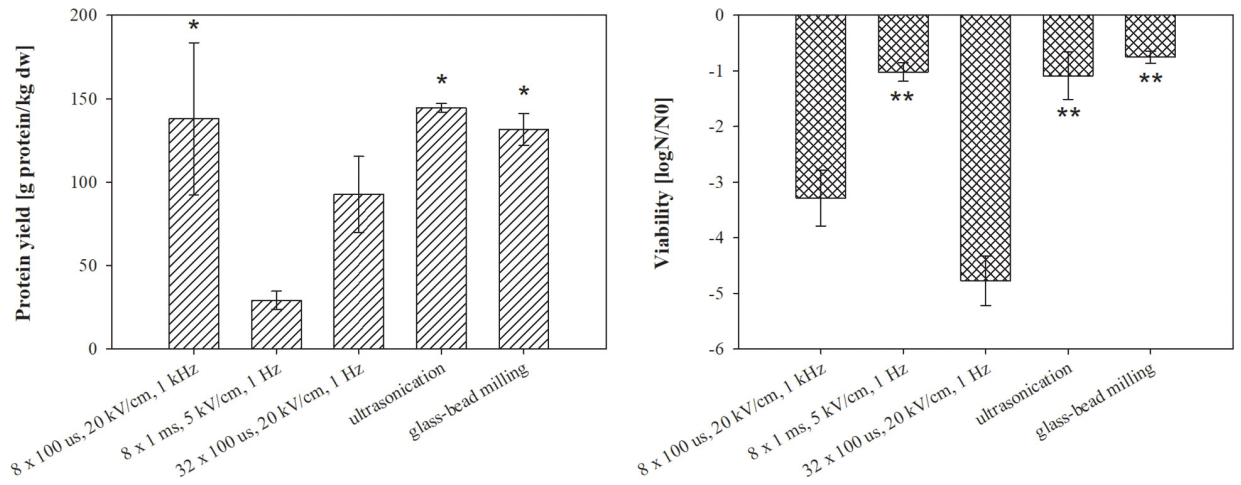

FIGURE 3 | The effect of different treatments on protein extraction **(left)** and bacterial viability **(right)**. Bacterial cells (*E. coli* TOP10 pEGFP-N1) in exponential growth phase were incubated before and after treatment at 37°C and exposed to three different treatments: batch electroporation treatments, ultrasonication and glass-bead milling. Treated mass of cells was 2.422×10^{-7} kg dw. Values represent means (all tests were performed in triplicate) and error bars are determined from standard deviation. Asterisk (*) represents statistically significant ($p < 0.05$) difference versus electroporation protocols 8 × 1 ms, 5 kV/cm, 1 Hz and 32 × 100 μs, 20 kV/cm, 1 Hz. Two asterisk (**) represents statistically significant ($p < 0.05$) difference versus electroporation protocols 8 × 100 μs, 20 kV/cm 1 kHz and 32 × 100 μs, 20 kV/cm, 1 Hz.

and 12 ± 6% with pulse parameter 8 × 1 ms, 5 kV/cm, 1 Hz. Protein yields and viability of extraction replicates varied, but the measurement trends were clear.

As it can be seen in **Figure 3-left**, electroporation can be effectively used for protein extraction; moreover, different electroporation parameters affect the protein yield. As expected, electroporation protocol 32 × 100 μs, 20 kV/cm, 1 Hz most strongly affected bacterial viability (**Figure 3-right**) due to higher energy input (379 kJ/L) (Novickij et al., 2018). Nevertheless protein yields were lower compared to electroporation protocol where lower energy of the pulses was applied – 65 kJ/L (8 × 100 μs, 20 kV/cm, 1 kHz), which suggests that the risen temperature during the treatment possibly damaged proteins. With electroporation protocol 8 × 100 μs, 20 kV/cm, 1 kHz, a similar amount of proteins as with two standard protein extraction methods (ultrasonication, glass-bead milling) was obtained.

The viability loss of treated bacteria was lower after glass-bead milling, electroporation protocol of 8 × 1 ms, 5 kV/cm, 1 Hz, and ultrasonication (**Figure 3-right**). Since we predicted that bacterial viability was associated with the release of unwanted molecules, we checked the amount of extracted host DNA and endotoxins. The bacterial viability loss was, however, not congruent with the measured concentration of host cell DNA. The highest concentration of host cell DNA was detected in the lysates obtained by glass-bead milling (336.34 ± 74.73 ng/μl) and ultrasonication (214.34 ± 13.35 ng/μl), more than ten times higher as in lysates obtained by means of electroporation protocols 32 × 100 μs, 20 kV/cm, 1 Hz (23.36 ± 0.66 ng/μl) and 8 × 100 μs, 20 kV/cm, 1 kHz (19.33 ± 1.65 ng/μl) (**Figure 4**).

The lowest concentration of co-extracted host cell DNA, below 2 ng/μl (1.28 ± 0.73 ng/μl), was obtained with pulse parameters 8 × 1 ms, 5 kV/cm, 1 Hz (**Figure 4**). Our results implies that selection of appropriate electroporation protocol is important in order to avoid also co-extraction of unwanted host DNA.

Endotoxins are considered contaminants in lysate and were co-extracted at elevated levels by all tested extraction methods (**Figure 5**). The highest amount of endotoxins was extracted with ultrasonication (274167 ± 76977 EU/ml), followed by electroporation protocols 8 × 100 μs, 20 kV/cm, 1 kHz (168537 ± 56659 EU/ml), 32 × 100 μs, 20 kV/cm, 1 Hz (166485 ± 30772 EU/ml), 8 × 1 ms, 5 kV/cm, 1 Hz (107401 ± 15669 EU/ml) and glass-bead milling (78808 ± 19775 EU/ml). Biological replicate measurements fluctuated and masked the trends in the endotoxin level of co-extraction in this study. The post-pulse incubation at 37°C did not affect the co-extraction of endotoxins, and neither did the growth in the media with or without antibiotic (data not shown).

TEM was used to assess the effect of the methods on bacterial morphology. Irrespective of extraction method, we observed that treated bacteria have an enlarged periplasmic space, which indicates that outer membrane was interrupted (**Figure 6**). Cell debris was evident after electroporation protocol of 32 × 100 μs, 20 kV/cm, 1 Hz, as well as after glass–bead milling and ultrasonication (**Figures 6B,E,F**), which implies that these methods for protein extraction are the most destructive for the bacteria. Additionally, bacterial ghost-like structures and elongated bacterium-like structures were present in all analyzed lysates. The effect of electric pulses on bacterial morphology is similar among tested parameters, but the extent of damage differs, with the protocol of 8 × 1 ms, 5 kV/cm, 1 Hz causing the mildest effect (**Figure 6D**).

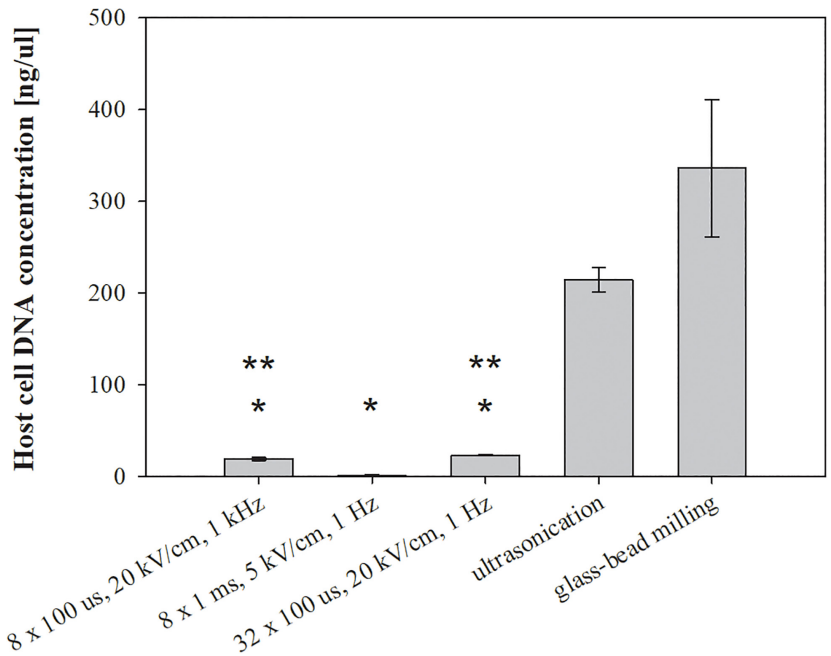

FIGURE 4 | The effect of different treatments on host DNA leakage. Bacterial cells (*E. coli* TOP10 pEGFP-N1) in exponential growth phase were incubated before and after treatment at 37°C and exposed to three different treatments: batch electroporation treatments, ultrasonication and glass-bead milling. Treated mass of cells was 2.072×10^{-7} kg dw. Values represent means (all tests were performed in triplicate) and error bars are determined from standard deviation. Asterisk (*) represents statistically significant ($p < 0.05$) difference versus ultrasonication or glass-bead milling. Two asterisk (**) represent statistically significant ($p < 0.05$) difference versus electroporation protocol 8 × 1 ms, 5 kV/cm, 1 Hz.

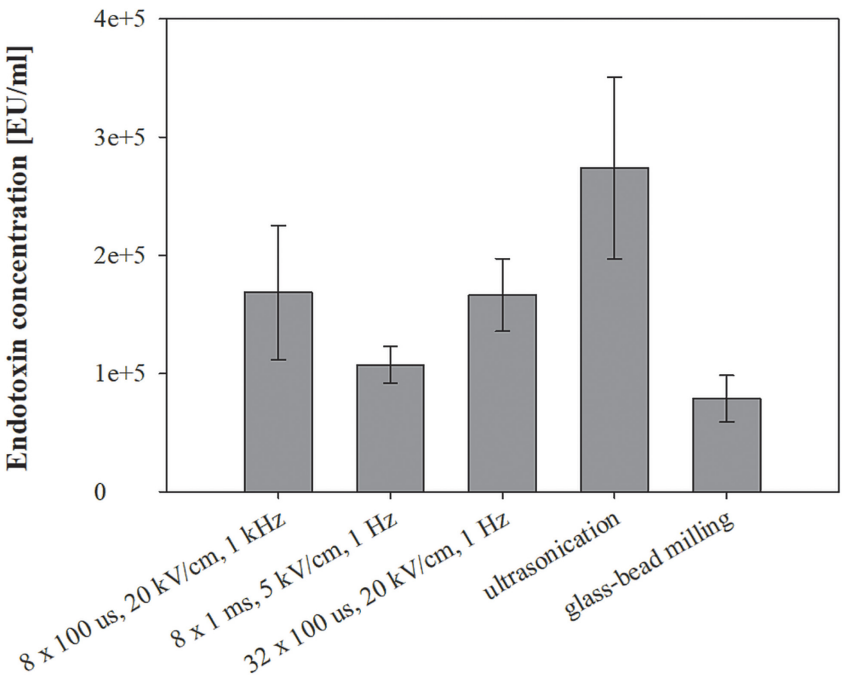

FIGURE 5 | The effect of different treatments on endotoxin leakage. Bacterial cells (*E. coli* TOP10 pEGFP-N1) in exponential growth phase were incubated before and after treatment at 37°C and exposed to three different treatments: batch electroporation treatments, ultrasonication and glass-bead milling. Endotoxin Units (EU) is a measure of the activity of endotoxin and one EU is approximately equivalent to 100 pg of *E. coli* lipopolysaccharide – the amount present in approximately 105 bacteria. Treated mass of cells was 2.498×10^{-7} kg dw. Values represent means (all tests were performed in triplicate) and error bars are determined from standard deviation.

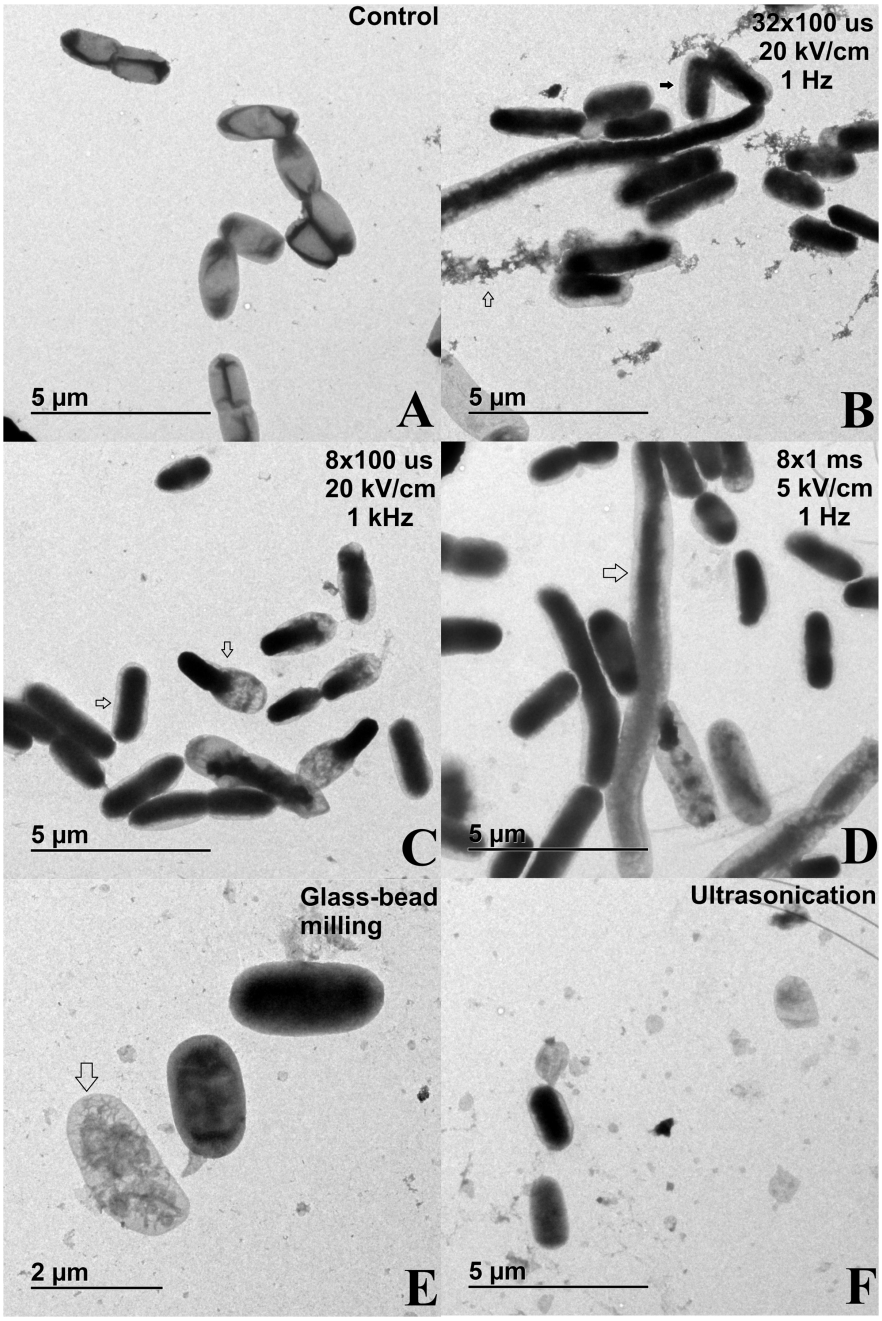

FIGURE 6 | TEM images of bacterial cells (*E. coli* TOP10 pEGFP-N1) subjected to different treatment: **(A)** control sample – bacterial suspensions of *E. coli* TOP10 pEGFP-N1 that were not subjected to extraction methods but were otherwise treated in the same way as experimental samples; **(B)** electric pulses 32 × 100 µs, 20 kV/cm, 1 Hz; **(C)** electric pulses 8 × 100 µs, 20 kV/cm, 1 kHz; **(D)** electric pulses 8 × 1 ms, 5 kV/cm, 1 Hz; **(E)** glass–bead milling; **(F)** ultrasonication. Bacterial cells in exponential growth phase were incubated before and after treatment at 37°C.

Extraction of GFP by Electric Pulses, Glass-Bead Milling and Ultrasonication

The above tested extraction methods were further utilized to extract specific protein (GFP) from *E. coli* TOP10 pUC19-hMGFP. We have chosen this bacteria, since it is constitutively expressing GFP. The viability and level of impurities for this bacteria did not differ from the above presented measurements, thus validating them (data not shown). The highest concentration of GFP was measured in the lysates obtained by glass-bead milling (24 ± 3.96 µg/ml), and the second highest by ultrasonication (19.65 ± 1.91 µg/ml) (**Figure 7**). Although the amount of extracted GFP was with electroporation protocols lower compared to glass-bead

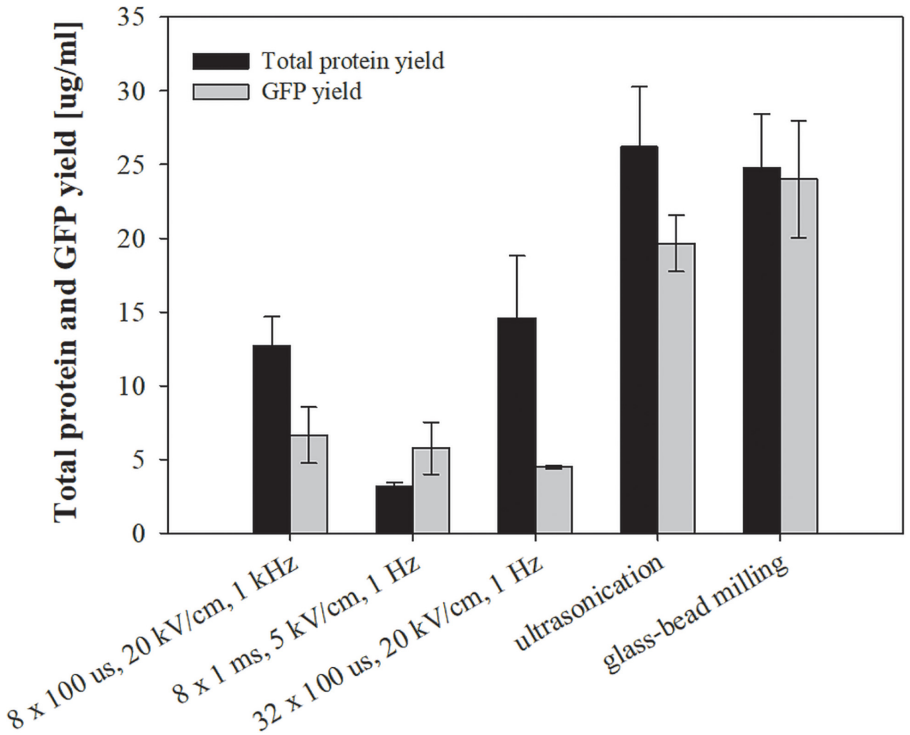

FIGURE 7 | The effect of different treatments on total protein and specific (GFP) protein extraction. Bacterial cells *E. coli* TOP10 pUC19-hMGFP in exponential growth phase were incubated before and after treatment at 37°C and exposed to three different treatments: batch electroporation treatments, ultrasonication and glass–bead milling. Values represent means (all tests were performed in triplicate) and error bars are determined from standard deviation.

milling or ultrasonication, selectivity for GFP extraction was observed with the protocol of 8 × 1 ms, 5 kV/cm, 1 Hz, where GFP concentration remained as high as with other two parameters, while total protein content was notably lower (see **Figure 7**).

DISCUSSION

Protein extraction from *E. coli* by electroporation is based on transient permeabilization of cell envelope, allowing the outflow of cytoplasmic content to the medium without causing cell disintegration. Based on our previous work (Haberl Meglic et al., 2015) we focused here on optimization of the extraction protocol and evaluation of protein extraction by electroporation in comparison to glass-bead milling and ultrasonication as two established methods that generally lead to total cell disintegration. Superior protein yield was obtained from bacteria in exponential growth phase regardless of the electroporation mode of operation (batch, flow) (**Figure 1**). Inner membrane of Gram-negative bacteria in exponential growth phase is known to be more permeable than in stationary phase, probably causing increased susceptibility to heat, antimicrobial agents and electric pulses (Coustets et al., 2015; Pletnev et al., 2015; **Figure 1**). It was also previously shown that exponential and stationary bacteria also significantly differ in their resting membrane potential values (Bot and Prodan, 2010). Membrane fluidity (viscosity) is also almost instantly affected by large fluctuations in environmental temperature, since cooling causes lipids to pack closely together and increases membrane rigidity, while heating causes the opposite effects (Mika et al., 2016). This apparently causes the electropermeabilized membrane to reseal slower at lower temperatures, thus prolonging the leakage of the intracellular content into the medium (Xie and Tsong, 1992). However, we observed that higher pre- and post-treatment temperatures are favorable for extraction of proteins regardless of the electroporation mode of operation (batch, flow), possibly due to higher membrane viscosity facilitating the permeabilization or hindering the resealing (**Figure 2**). Protein extraction yield and viability fluctuations among the extraction replicates can be attributed to large heterogeneity among bacteria in terms of membrane viscosity and other physical parameters of the bacteria observed elsewhere (Mika et al., 2016). The efficiency of extraction by means of electroporation did not differ significantly when performed in batch or continuous mode of operation, thus demonstrating its flexibility. As electroporation has been successfully used in an industrial pilot unit to pasteurize liquid foodstuff, scaling up in protein production seems feasible and viable (Picart-Palmade et al., 2019).

Using electroporation pulses differing in length, repetition frequency and amplitude, we achieved substantial differences in overall protein yield rather than a selective extraction of group of proteins with similar physical-chemical properties (**Figures 3**, **7**). Absolute values of protein concentration in

this study may be underestimated, because the lysates contain a wide variety of proteins with different dye responses, in contrast to the protein standard (BSA) – used for determining protein concentration (see section "Assessing Total and Target (GFP) Proteins") – that has stable and unusually large dye response. Thus, lower signals may be falsely interpreted as lower concentrations. We observed also that GFP yield, estimated from fluorescence measurements, dropped when bacterial culture was treated by pulse parameter where higher energy was applied – 32 × 100 μs, 20 kV/cm, 1 Hz (**Figure 7**). Loss of fluorescence in tight structure of GFP is usually associated with denaturation that could be due to Joule heating.

Cell debris indicating cell envelope disintegration was notable after the glass–bead milling and ultrasonication as expected (**Figures 6E,F**), while after electroporation the highest amount of host cell DNA was co-extracted with 32 × 100 μs, 20 kV/cm, 1 Hz (**Figure 4**). The host cell DNA level in the lysates obtained by ultrasonication and glass-bead milling was likely overestimated, as viability loss is caused by lysis, and consequently host DNA is released. But viability was incongruent with released DNA, probably due to DNA fragmentation upon release to the medium and its accessibility to DNA polymerase in qPCR assay, resulting in concentration overestimation. Irrespective of the extraction method, the treated bacteria had an enlarged periplasmic space, which could also be a consequence of post-osmotic stress (**Figure 6**). Additionally, bacteria were resuspended in sterile distilled water, which enhances the stress and hinders cell recovery after the treatment. Modifications of electroporation medium could be important in bacterial survival, as it was shown before that by changing medium pH or supplementing it with reagents, both the electroporation efficiency and the host cell survival were improved (Garcia et al., 2007; Coustets et al., 2015). Beside changes in inner membrane permeability discussed above, outer membrane was often interrupted at one of the poles, thus enabling physical separation of cell wall and inner membrane, resulting in ghost like structures (**Figure 6**). The importance of these structures remains unknown in the context of extraction, but they have applications in other biotechnical fields (Langemann et al., 2010). The elongated bacterium-like structures were also observed, and these cannot be attributed to sample preparation, neither could they arise from growth, as bacteria were analyzed immediately after the extraction and prior to incubation. These structures suggest that bacterial fusion is happening during exposure to external electric field, as already observed but never examined in detail (Tyurin et al., 1997). We hypothesize that the observed cell wall ruptures at the poles may facilitate bacterial fusion by exposing the parts of the cell envelope that were reported to enable fusion of bacterial protoplasts (Gokhale et al., 1993). Bacterial fusion was historically used as a method to transfer genetic material between bacteria, and fusion by electric pulses has been suggested as a mechanism of horizontal gene transfer during early evolution when other mechanisms for such transfer did not yet exist or were still evolving (Kotnik, 2013).

Endotoxins were co-extracted in elevated concentrations regardless of the extraction method and independently from the cultivation with antibiotics (**Figure 5**). However, the lowest amount of endotoxins was obtained with glass-bead milling. Growing bacteria are known to constantly release endotoxins into the environment both *in vivo* and *in vitro*. This shedding is enhanced when bacterial culture is exposed to antibiotics, but the cells survive even when deprived of 40% of the lipopolysaccharide (LPS) layer – also known as lipoglycan layer or endotoxin layer (Marvin et al., 1989; Crosby et al., 1994). Since extraction mechanisms differ among tested methods, the endotoxins may be released into the medium in various physical-chemical forms, thus differently exposing the biologically active moiety. Namely, endotoxin is a large molecule consisting of a lipid A and polysaccharides (inner and outer core, and O-antigen). It has been shown that free endotoxins shed into the medium enhance the exposure of lipid A, which consequently results in stronger activation of LAL assay (assay for determining endotoxin levels in our study) components than purified endotoxin used as standard (Mattsby-Baltzer et al., 1991). This leads to interpretation of stronger signals as higher endotoxin concentrations, and absolute endotoxin content can thus be determined only by additional chemical analysis.

Total protein content, co-extraction of host cell DNA and endotoxins, and viability loss during electroporation of *E. coli* K12 carrying two different types of plasmids (pEGFP-N1 cloning vector vs. pUC19-hMGFP expression plasmid) were consistent (data not shown). Although recombinant protein yields (GFP) obtained with electroporation are not superior to ultrasonication or glass-bead milling, to certain degree, selectivity for GFP extraction was observed with the protocol of 8 × 1 ms, 5 kV/cm, 1 Hz, where GFP concentration remained as high as with other two electroporation parameters, while total protein content was notably lower (**Figure 7**). Energy consumption using the electroporation protocol of 32 × 100 μs, 20 kV/cm, 1 Hz was ten times larger than for 8 × 100 μs, 20 kV/cm, 1 kHz (**Table 1**). In terms of energy input, the most efficient extraction of total proteins was obtained by 8 × 100 μs, 20 kV/cm, 1 kHz and the highest GFP yield was for 8 × 1 ms, 5 kV/cm, 1 Hz.

In general, though total protein yields obtained by electroporation are not superior to ultrasonication or glass-bead milling, electroporation could be advantageous in the production of proteins where overexpressed native proteins challenge the host cell with toxicity or metabolic burden, as demonstrated in fed-batch production of α-amylase (Shiina et al., 2004). Extraction by means of electroporation was superior in terms of ratio between target protein and contaminating host protein. Furthermore, it was shown to largely avoid cell lysis and disintegration with which the extract is a mix of extracted proteins with debris of the bacterial envelope and bacterial DNA, which necessitates further purification. We expect that reduction of contaminants achieved by extraction by means of electroporation could lower the number of purification steps in the downstream process and decrease its costs.

We have also shown that the efficiency of extraction by means of electroporation is comparable in both electroporation systems (batch and flow through system), thus demonstrating feasible scale-up. Based on the successful application of electroporation in the food industry (Picart-Palmade et al., 2019), electroporation could be, owing to its flexibility and scalability, suitable for large scale protein production. The key benefit of electroporation is that is a non-heating technology with moderate energy consumption, thereby preventing unwanted effects of heat on final product. Furthermore, it can be implemented in any continuous production line (as sole technique or combined with other techniques) where thousands liters per hour are treated. Nevertheless, there are still some drawbacks and limitations, for instance high cost of the equipment, too high medium conductivity disables usage of electroporation, and optimization of the parameters are still needed (Martinez et al., 2020).

DATA AVAILABILITY STATEMENT

All datasets generated for this study are included in the article/**Supplementary Material.**

AUTHOR CONTRIBUTIONS

SHM and NJ drafted the manuscript, conceptualized the study, and conducted experiments. KF conducted experiments and developed the generator of electric pulses. DM and MP conceptualized the study and supervised the experimental work. DM and TK critically revised the manuscript, and improved the work with important intellectual content. All authors read and approved the submitted manuscript.

FUNDING

This study was funded by the Slovenian Research Agency grant J7-6783 and P2-0249. The work was performed in the infrastructure center MRIC at University of Ljubljana (I0-0022).

ACKNOWLEDGMENTS

We thank Dr. Magda Tušek Žnidarič for interpretation of electron microscope micrographs and Dr. Tatjana Simčič for lending Ultrasonic homogenizer.

SUPPLEMENTARY MATERIAL

The Supplementary Material for this article can be found online at: https://www.frontiersin.org/articles/10.3389/fbioe.2020.543187/full#supplementary-material

FIGURE S1 | Flow treatment chamber used for continuous flow extraction by means of electroporation.

REFERENCES

Anton, B. P., and Raleigh, E. A. (2016). Complete genome sequence of NEB 5-alpha, a derivative of *Escherichia coli* K-12 DH5 alpha. *Microbiol. Resour. Ann.* 4:e01245-16.

Assenberg, R., Wan, P. T., Geisse, S., and Mayr, L. M. (2013). Advances in recombinant protein expression for use in pharmaceutical research. *Curr. Opin. Struct. Biol.* 23, 393–402. doi: 10.1016/j.sbi.2013.03.008

Bot, C. T., and Prodan, C. (2010). Quantifying the membrane potential during *E. coli* growth stages. *Biophys. Chem.* 146, 133–137. doi: 10.1016/j.bpc.2009.11.005

Chou, C. P. (2007). Engineering cell physiology to enhance recombinant protein production in *Escherichia coli*. *Appl. Microbiol. Biotechnol.* 76, 521–532. doi: 10.1007/s00253-007-1039-0

Coustets, M., Ganeva, V., Galutzov, B., and Teissie, J. (2015). Millisecond duration pulses for flow-through electro-induced protein extraction from *E-coli* and associated eradication. *Bioelectrochemistry* 103, 82–91. doi: 10.1016/j.bioelechem.2014.08.008

Crosby, H., Bion, J., Penn, C., and Elliott, T. (1994). Antibiotic-induced release of endotoxin from bacteria in-vitro. *J. Med. Microbiol.* 40, 23–30. doi: 10.1099/00222615-40-1-23

Durfee, T., Nelson, R., Baldwin, S., Plunkett, G., Burland, V., Mau, B., et al. (2008). The complete genome sequence of *Escherichia coli* DH10B: Insights into the biology of a laboratory workhorse. *J. Bacteriol.* 190, 2597–2606. doi: 10.1128/jb.01695-07

Flisar, K., Haberl Meglic, S., Morelj, J., Golob, J., and Miklavcic, D. (2014). Testing a prototype pulse generator for a continuous flow system and its use for *E. coli* inactivation and microalgae lipid extraction. *Bioelectrochemistry* 100, 44–51. doi: 10.1016/j.bioelechem.2014.03.008

Garcia, D., Gomez, N., Manas, P., Raso, J., and Pagan, R. (2007). Pulsed electric fields cause bacterial envelopes permeabilization depending on the treatment intensity, the treatment medium pH and the microorganism investigated. *Int. J. Food Microbiol.* 113, 219–227. doi: 10.1016/j.ijfoodmicro.2006.07.007

Goey, C. H., Alhuthali, S., and Kontoravdi, C. (2018). Host cell protein removal from biopharmaceutical preparations: towards the implementation of quality by design. *Biotechnol. Adv.* 36, 1223–1237. doi: 10.1016/j.biotechadv.2018.03.021

Gokhale, D. V., Puntambekar, U. S., and Deobagkar, D. N. (1993). Protoplast fusion: a tool for intergeneric gene transfer in bacteria. *Biotechnol. Adv.* 11, 199–217. doi: 10.1016/0734-9750(93)90041-k

Haberl Meglic, S., Marolt, T., and Miklavcic, D. (2015). Protein extraction by means of electroporation from *E. coli* with preserved viability. *J. Membr. Biol.* 248, 893–901. doi: 10.1007/s00232-015-9824-7

Haberl-Meglič, S., Levičnik, E., Luengo, E., Raso, J., and Miklavčič, D. (2016). The effect of temperature and bacterial growth phase on protein extraction by means of electroporation. *Bioelectrochemistry* 112, 77–82. doi: 10.1016/j.bioelechem.2016.08.002

Hernandez, R. (2017). *Integrated Continuous Manufacturing of Biologics: Trends in the Field*. Boston: BioProcess International.

Kotnik, T. (2013). Lightning-triggered electroporation and electrofusion as possible contributors to natural horizontal gene transfer. *Phys. Life Rev.* 10, 351–370. doi: 10.1016/j.plrev.2013.05.001

Kotnik, T., Frey, W., Sack, M., Haberl Meglic, S., Peterka, M., and Miklavcic, D. (2015). Electroporation-based applications in biotechnology. *Trends Biotechnol.* 33, 480–488. doi: 10.1016/j.tibtech.2015.06.002

Kotnik, T., Pucihar, G., and Miklavcic, D. (2010). Induced transmembrane voltage and its correlation with electroporation-mediated molecular transport. *J. Membr. Biol.* 236, 3–13. doi: 10.1007/s00232-010-9279-9

Langemann, T., Koller, V. J., Muhammad, A., Kudela, P., Mayr, U. B., and Lubitz, W. (2010). The Bacterial Ghost platform system: production and applications. *Bioeng. Bugs* 1, 326–336. doi: 10.4161/bbug.1.5.12540

Martinez, J. M., Delso, C., Alvarez, I., and Raso, J. (2020). Pulsed electric field-assisted extraction of valuable compounds from microorganisms. *Compr. Rev. Food. Sci. Food Saf.* 19, 1–23. doi: 10.1007/978-3-319-26779-1_160-1

Marvin, H. J., ter Beest, M. B., and Witholt, B. (1989). Release of outer membrane fragments from wild-type *Escherichia coli* and from several *E. coli* lipopolysaccharide mutants by EDTA and heat shock treatments. *J. Bacteriol.* 171, 5262–5267. doi: 10.1128/jb.171.10.5262-5267.1989

Matos, T., Senkbeil, S., Mendonca, A., Queiroz, J. A., Kutter, J. P., and Bulow, L. (2013). Nucleic acid and protein extraction from electropermeabilized *E. coli* cells on a microfluidic chip. *Analyst* 138, 7347–7353. doi: 10.1039/c3an01576a

Mattsby-Baltzer, I., Lindgren, K., Lindholm, B., and Edebo, L. (1991). Endotoxin shedding by enterobacteria: free and cell-bound endotoxin differ in Limulus activity. *Infect. Immun.* 59, 689–695. doi: 10.1128/iai.59.2.689-695.1991

Mika, J. T., Thompson, A. J., Dent, M. R., Brooks, N. J., Michiels, J., Hofkens, J., et al. (2016). Measuring the viscosity of the *Escherichia coil* plasma membrane using molecular rotors. *Biophys. J.* 111, 1528–1540. doi: 10.1016/j.bpj.2016.08.020

Novickij, V., Svediene, J., Paskevicius, A., Markovskaja, S., Lastauskiene, E., Zinkeviciene, A., et al. (2018). Induction of different sensitization patterns of MRSA to antibiotics using electroporation. *Molecules* 23:1799. doi: 10.3390/molecules23071799

Picart-Palmade, L., Cunault, C., Chevalier-Lucia, D., Belleville, M. P., and Marchesseau, S. (2019). Potentialities and limits of some non-thermal technologies to improve sustainability of food processing. *Front. Nutr.* 5:130. doi: 10.3389/fnut.2018.00130

Pletnev, P., Osterman, I., Sergiev, P., Bogdanov, A., and Dontsova, O. (2015). Survival guide: *Escherichia coli* in the stationary phase. *Acta Nat.* 7, 22–33. doi: 10.32607/20758251-2015-7-4-22-33

Shiina, S., Ohshima, T., and Sato, M. (2004). Extracellular release of recombinant alpha-amylase from *Escherichia coli* using pulsed electric field. *Biotechnol. Prog.* 20, 1528–1533. doi: 10.1021/bp049760u

Stone, M. C., Borman, J., Ferreira, G., and Robbins, P. D. (2018). Effects of pH, conductivity, host cell protein, and DNA size distribution on DNA clearance in anion exchange chromatography media. *Biotechnol. Prog.* 34, 141–149. doi: 10.1002/btpr.2556

Tan, S. C., and Yiap, B. C. (2009). DNA, RNA, and protein extraction: the past and the present. *J. Biomed. Biotechnol.* 2009:574398.

Tyurin, M. V., Doroshenko, V. G., and Oparina, N. Y. (1997). Electrofusion of *Escherichia coli* cells. *Membr. Cell Biol.* 11, 121–129.

Wirth, R., Friesenegger, A., and Fiedler, S. (1989). Transformation of various species of gram-negative bacteria belonging to. *Mol. Gen. Genet.* 216, 175–177. doi: 10.1007/bf00332248

Xie, T. D., and Tsong, T. Y. (1992). Study of mechanisms of electric field-induced DNA transfection. III. Electric parameters and other conditions for effective transfection. *Biophys. J.* 63, 28–34. doi: 10.1016/s0006-3495(92)81580-1

Conflict of Interest: The authors declare that the research was conducted in the absence of any commercial or financial relationships that could be construed as a potential conflict of interest.

Copyright © 2020 Haberl Meglič, Janež, Peterka, Flisar, Kotnik and Miklavčič. This is an open-access article distributed under the terms of the Creative Commons Attribution License (CC BY). The use, distribution or reproduction in other forums is permitted, provided the original author(s) and the copyright owner(s) are credited and that the original publication in this journal is cited, in accordance with accepted academic practice. No use, distribution or reproduction is permitted which does not comply with these terms.

frontiers in Bioengineering and Biotechnology

ORIGINAL RESEARCH
published: 22 September 2020
doi: 10.3389/fbioe.2020.552261

Confocal Microscopy Improves 3D Microdosimetry Applied to Nanoporation Experiments Targeting Endoplasmic Reticulum

Annalisa De Angelis[1,2†], Agnese Denzi[1†], Caterina Merla[3], Frank M. Andre[4], Lluis M. Mir[4], Francesca Apollonio[1,2] and Micaela Liberti[1,2]*

[1] Inter University Center for the Study of Electromagnetic Fields and Biological Systems (ICEmB) at Department of Electronic Engineering and Telecommunications (DIET), University of Rome "La Sapienza", Rome, Italy, [2] Center for Life Nano Science@Sapienza, Istituto Italiano di Tecnologia, Rome, Italy, [3] National Italian Agency for Energy, New Technologies and Sustainable Economic Development – Department of Sustainability (ENEA, SSPT) – Division of Health Protection Technologies, Rome, Italy, [4] Université Paris-Saclay, Institut Gustave Roussy, CNRS, Metabolic and Systemic Aspects of Oncogenesis, Villejuif, France

In the last years, microdosimetric numerical models of cells including intracellular compartments have been proposed, aiming to investigate the poration induced by the application of nanosecond pulsed electric fields (nsPEFs). A limitation of such models was the extremely approximate cell and organelle shapes, leading to an incorrect estimation of the electric field or transmembrane potential distribution in the studied domain. In order to obtain a reliable model of *in vitro* experiments and a one-to-one comparison between experimental and simulated results, here, a realistic model of 12 human mesenchymal stem cells was built starting from their optical microscopy images where different cell compartments were highlighted. The microdosimetric analysis of the cells group was quantified in terms of electric field and transmembrane potentials (TMPs) induced by an externally applied 10-ns trapezoidal pulse with rise and fall times of 2 ns, with amplitudes ranging from 2 to 30 MV/m. The obtained results showed that the plasma and endoplasmic reticulum (ER) membrane of each cell respond in a different way to the same electric field amplitude, depending on differences in shape, size, and position of the single cell with respect to the applied electric field direction. Therefore, also the threshold for an efficient electroporation is highly different from cell to cell. This difference was quantitatively estimated through the cumulative distribution function of the pore density for the plasma and ER membrane of each cell, representing the probability that a certain percentage of membrane has reached a specific value of pore density. By comparing the dose-response curves resulted from the simulations and those from the experimental study of De Menorval et al. (2016), we found a very good matching of results for plasma and ER membrane when 2% of the porated area is considered sufficient for permeabilizing the membrane. This result is worth of noting as it highlights the possibility to effectively predict the behavior of a cell (or of a population of cells) exposed to nsPEFs. Therefore, the microdosimetric realistic model described here could represent a valid tool in setting up more efficient and controlled electroporation protocols.

Keywords: confocal fluorescence microscopy, microdosimetry, electroporation, electropermeabilization, nanosecond pulses, nanoporation experiments, endoplasmic reticulum, realistically shaped cell models

OPEN ACCESS

Edited by:
Saša Haberl Meglič, University of Ljubljana, Slovenia

Reviewed by:
Quanshun Li, Jilin University, China
Stefania Romeo, National Research Council (CNR), Italy

****Correspondence:***
Micaela Liberti
micaela.liberti@uniroma1.it

† These authors have contributed equally to this work

Specialty section:
This article was submitted to Bioprocess Engineering, a section of the journal Frontiers in Bioengineering and Biotechnology

Received: *15 April 2020*
Accepted: *24 August 2020*
Published: *22 September 2020*

Citation:
De Angelis A, Denzi A, Merla C, Andre FM, Mir LM, Apollonio F and Liberti M (2020) Confocal Microscopy Improves 3D Microdosimetry Applied to Nanoporation Experiments Targeting Endoplasmic Reticulum. Front. Bioeng. Biotechnol. 8:552261. doi: 10.3389/fbioe.2020.552261

INTRODUCTION

Microdosimetry has gained a crucial role in the study of the electromagnetic field interaction with the biological matter. It offers the possibility to quantitatively evaluate local electromagnetic quantities induced by the application of an external electric field such as the electric fields local amplitude, the current densities and the local values of the induced transmembrane potential (TMP) differences. Such *in silico* precise descriptions allow a deeper understanding of the relationships between the applied electric field amplitudes and the biological effects experimentally observed (Apollonio et al., 2013; Merla et al., 2019). Moreover, following a scheme of infinite loop between "dry" and "wet" experiments (Kitano, 2002), used here as synonymous of *in silico* and *in vitro or in vivo* experiments, respectively, a microdosimetric model could represent a validation tool for the hypothesis formulated on the basis of the experimental observations (experiment-driven approach). Or, on the contrary, microdosimetry could provide predictions on the effects of the electromagnetic stimulation to be successively tested by *in vitro* and *in vivo* studies (model-driven approach). Indeed, the "infinite loop concept," introduced by Kitano and further elaborated by the authors in Denzi et al. (2017; **Figure 1**), represents the possibility to get knowledge by a continuous exchange of information between numerical and experimental studies in which the outcomes from the first could be used as starting point of the second and *vice versa*. In the case of the experiment-driven approach as the former described above the need to reproduce real cellular and subcellular structure emerged as a crucial point, due to the dependence of the electric field induced in the cell on real irregular shapes (Denzi et al., 2016). Final purpose is to elucidate the physical and biological responses when relating the experimental exposure conditions to the observed effects.

Recently, different 2D numerical models of cell including intracellular compartments have been proposed in order to study the electroporation phenomenon induced by short pulsed electric fields on biological cells. These cell models were based on the transport lattice approach (Gowrishankar et al., 2006; Esser et al., 2010) or on meshed transport network (Smith et al., 2006; Zaklit et al., 2017). A limitation of such models relies in the shape approximation of the cell and organelles that can imply unreliability of the estimated spatial distribution of the electric field, of the transmembrane voltage, and of the pore density. Moreover, most of these models consider a single isolated cell that cannot be fully representative of a cell mixture, since, in the most of *in vitro* studies, researchers deal with populations of cells in suspension or in monolayers (Kotnik et al., 2010). Hence, in order to obtain a reliable model of *in vitro* experiments and a one-to-one comparison between experimental and microdosimetric results, it is necessary to build up an accurate model starting from the real geometrical and topological details of the cells used in the experiments (Pucihar et al., 2006, 2008; Towhidi et al., 2008; Kotnik et al., 2010). Indeed, it has been shown that the maximum TMP, computed for realistically shaped cells, can differ (by up to 30%) from models using simplified geometries (Pucihar et al., 2006). Towhidi et al. (2008), considered a population of irregularly shaped cells, and showed how the effects of local membrane curvature could lead to large variability (up to 100%) in the TMP determination. Further, it has been shown that it is harder to electroporate cells in a cluster due to the presence of multiple cell boundaries close each other and, in some cases, randomly oriented (Pavlin et al., 2002; Pucihar et al., 2007; Joshi et al., 2008; Kotnik et al., 2010). In Denzi et al. (2016) starting from microscopy images, we reconstructed a realistic 2D model of five human neuroblastoma cells with nucleus, considering their real shape, density and packaging, and applying pulses of different duration (100 μs, 60 ns, and 1 ns). In that study we confirmed the importance to take into account the real experimental conditions, and the duration (spectral content) of the applied pulse to understand the different responses. Indeed, generally speaking, microsecond electric pulses with amplitude of few kV/m (e.g., like those used in electrochemotherapy) are able to permeabilize the plasma membrane and, thus, can be used to favor the uptake of drugs and non-permeant molecules in the cell interior (Cadossi et al., 2014). nsPEFs with higher amplitude of the order of MV/m, due to their higher frequency content, are able to permeabilize also the subcellular membranes (such as mitochondria and ER) (De Menorval et al., 2016; Kulbacka, 2017). Poration of cellular and subcellular membranes has been widely used as a biotechnological tool for incorporating various molecules (genes, DNA, RNA, proteins, drugs, antibodies, and fluorescence probes) into many different kinds of cells (bacteria, yeast, plant, and mammalian cells). Hence, in the last years the study of the interaction between nanosecond electric pulses and cells with organelles like ER, have gained increasing interest. Some papers report experimental results showing that nanosecond pulses are able to induce intracellular calcium release from ER (Vernier et al., 2003; Joshi et al., 2007; Scarlett et al., 2009; Semenov et al., 2013; De Menorval et al., 2016). Calcium regulates a number of cell signaling, including cell apoptosis, enzyme activation, gene transcription, neurotransmitter release, and muscle contraction (Berridge et al., 2003; Sun et al., 2007; Frandsen et al., 2012; Petecchia et al., 2015). In particular, De Menorval et al. (2016) experimentally showed that a single pulse of 10 ns and few tens of MV/m is able to modulate the intracellular calcium release in a population of human mesenchymal stem cells (MSCs), by mimicking the spontaneous oscillations of Ca^{2+} ions in the cytosol. For a fully controlled modulation of the calcium release, it is important to exactly relate the gradient in Ca^{2+} concentration with the electric stimulation parameters (amplitude, duration and shape). This could be feasible using a model of the entire experimental poration set up as realistic as possible.

In the present work, we implemented a 3D model of the same cells used in the experimental work (De Menorval et al., 2016) reconstructed from cell images obtained with confocal microscopy. The aim is to demonstrate the importance of an accurate 3D realistic model of cells and subcellular organelles morphologies in relating the exposure condition to the electroporation phenomenon. Our novel model may be applied as a predictive tool for a better control of the experimental exposure settings.

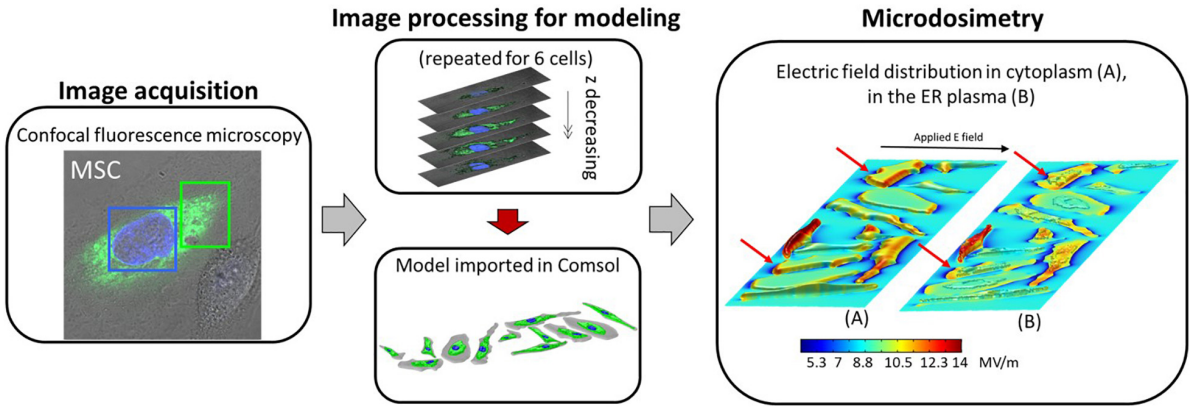

FIGURE 1 | Block scheme of the microdosimetric modeling enhanced by confocal fluorescence microscopy, from the microscopy image acquisition to the microdosimetric analysis. The six reconstructed cells were doubled and randomly placed to form the cell mixtures. In the last block "Microdosimetry," the electric field distribution over the entire domain for one of the four investigated cell mixtures, at the time corresponding to the end of the pulse plateau (t = 10 ns) is shown, highlighting the electric field induced in **(A)** the cytoplasm, and **(B)** the ER plasm.

First the method used to reconstruct the real shape of the cells will be described. Then, the implementation of the electromagnetic model will be detailed. Finally, a comparison between the experimental results and those from the simulation will be presented and discussed, in terms of the percentage of porated cells induced by increasing intensity of the applied electric field, with a major focus on the electric quantities that determine such effects.

MATERIALS AND METHODS

In order to reconstruct the realistic geometry representative of the real biological target we followed a procedure similar to the one of Denzi et al. (2016), Hanna et al. (2017). We employed the cell images provided by a confocal fluorescence microscope (Leica TCS SPE, Germany, 63×, 1.30 NA oil), that allows to visualize the different cell compartments treated with a specific fluorescent dye. Green dye (pcDNA-D1ER, excitation and emission at 480 and 535 nm, respectively) was used for the ER and a blue marker (Hoechst 33342, excitation and emission at 405 and 486 nm, respectively) for the cell nuclei. The images were taken without electronic zooming. Twenty-three slices were taken each time to produce stacks of cell images with a z distance of 0.8 μm between them. More details of the technique are reported in Hanna et al. (2017). Each slice recorded at different depths was processed as follows with a custom MATLAB^{TM} (v. 2016) automated routine: the RGB microscopy images were converted and normalized using double precision in order to improve the intensity contrast between the image pixels. Then, considering a color channel at a time, the converted images were elaborated through segmentation, clusterization (with the threshold values reported in Hanna et al., 2017) and edge extraction as detailed in Denzi et al. (2016) and shown in **Supplementary Figure S1** of Supplementary. Finally, each region (cytoplasm, ER, and nucleus) was extruded for a thickness corresponding to the step of the microscopy procedure (z-stack of 0.8 μm), smoothed and harmonized. Then a STL file, in which all the information about the 3D model were stored, was extracted. The obtained 3D STL file of the cell can be directly imported in the used simulation software Comsol Multiphysics (v. 5.3). In **Figure 1**, a summary scheme of the used procedure and the resulted geometric model imported in Comsol Multiphysics are reported for six different mesenchymal stem cells (Hanna et al., 2017), then duplicated and placed in random position in order to obtain a mixture of 12 cells (an example is show in **Figure 1** "Model imported in Comsol"). The procedure has been repeated four times in order to obtain four different mixtures of 12 cells. A more detailed scheme of the image processing and 3D cell reconstruction is reported in **Supplementary Figure S1**.

A numerical model was realized based on the dielectric properties of the cell as reported in **Table 1** (Denzi et al., 2016). A parallelepiped box was used to represent the extracellular medium surrounding the cells. The right side of the box was set to the ground and the left one was excited by a single 10-ns trapezoidal pulse and variable amplitudes. The problem for the described geometry was solved in the Electric Currents mode of the AC/DC module of Comsol (Time Dependent Study). In this module, the voltage at each point is evaluated by the following equation:

$$-\nabla\left(\sigma_i \nabla V\right) - \varepsilon_0 \varepsilon_r \nabla\left(\frac{\partial\left(\nabla V\right)}{\partial t}\right) = 0 \qquad (1)$$

TABLE 1 | Electrical permittivity and conductivity of the cell compartments (Denzi et al., 2016).

Compartment	ε_S	σ (S/m)
Membranes (Plasmatic and ER)	11.7	s(TMP)
Nucleus membrane	11.7	8.3×10^{-5}
Plasmas	67	0.3
Extracellular medium	72	1.4

Where σ_i and e_r are the electrical conductivity and the relative permittivity of the specific compartment under study (extracellular medium, membranes, cytoplasm, ER plasm and nucleoplasm) and e_0 is the permittivity of the vacuum and t the time. The gradient of the voltage ∇V represents the TMP, the difference between the membrane internal and external voltage.

For all internal boundaries, continuity conditions were set. Moreover, in order to take into account the membrane conduction and the displacement currents, the *Contact Impedance condition:*

$$n \cdot J_1 = \frac{1}{d_s}\left(\sigma_m + \varepsilon_0 \varepsilon_m \frac{d}{dt}\right)(V_1 - V_2)\,, \tag{2}$$

was imposed to the plasma, ER and nuclear membranes, instead of considering them as physical domains. This choice is justified by the fact that we were not interested here in the events occurring inside the membrane, avoiding the problem of generating a mesh of very small elements for the membrane interior (Pucihar et al., 2007, 2008). The pore formation dynamics were studied through the asymptotic model proposed by DeBruin and Krassowska (1999), implemented in the model using the Boundary ODEs (ordinary differential equations) and DAEs (differential-algebraic equations) application of the Mathematics module:

$$\frac{dN}{dt} = \alpha e^{\left(\frac{TMP}{V_{ep}}\right)^2}\left(1 - \frac{N}{N_0} e^{-q\left(\frac{TMP}{V_{ep}}\right)^2}\right) \tag{3}$$

N is the density of the pores forming per second and per m^2 across the membrane. The other parameters are specified in **Table 2**. The pore creation determines an increase in the membrane conductivity, as further conducting pathways opened, increasing the current density flow across the membrane. For considering this event, the following formula was used:

$$\sigma_m = \sigma_{m0} + \sigma_{ep} \tag{4}$$

adding to the unporated membrane conductivity σ_{m0}, the term σ_{ep} representing the changes in the conductivity of the membrane due to the pores formation, as in Mercadal et al. (2016).

$$\sigma_{ep} = N\frac{2\pi r_p^2 \sigma_p h}{\pi r_p + 2h} \tag{5}$$

TABLE 2 | Parameters used in the asymptotic equation of the pore formation (DeBruin and Krassowska, 1999).

Parameter	Value	Description
σ_{m0}	1.1×10^{-7} (S/m)	Initial conductivity
r_p	0.76 (nm)	Pore radius
α	10^9	Electroporation parameter
q	2.46	Electroporation constant
h	5 (nm)	Membrane thickness
N_0	1.5×10^9 (m^{-2})	Equilibrium pore density
V_{ep}	258 (mV)	Characteristic voltage of electroporation

$$\sigma_p = \frac{\sigma_e - \sigma_i}{ln\left(\frac{\sigma_e}{\sigma_i}\right)} \tag{6}$$

All the parameters not defined above are reported in **Table 2**.

In the present study, the same range of electric field used in De Menorval et al. (2016) from 0 to 36 MV/m was simulated. More specifically, a time domain study was performed simulating single trapezoidal 10-ns long pulses (2 ns rise and fall times) at 2.7, 6, 8.8, 10, 13, 16.2, 21, 25.2, 27, 36 MV/m, the same tested field amplitudes of the experimental study (De Menorval et al., 2016). Four different simulations have been performed, remixing the 12 cells in different positions and orientations with respect to the electric field direction, investigating a total of forty-eight cells.

RESULTS

In the last block of the schematic diagram in **Figure 1** the electric field distribution over the entire domain for one of the four investigated cell mixtures is shown, at the time corresponding to the end of the pulse plateau (t = 10 ns). In panel (a), we report the extracellular electric field in 2D at a given quote together with the 3D representation of the induced electric field in the cytoplasm. In a similar way, in panel (b) we reported a 2D slice plot with the external and cytoplasmic electric field distribution together with the 3D electric field distribution on the ER plasma. The electric field penetrates the cells since the first instants of the pulse application and easily arises because of the displacement current associated with the distributed capacitance of the plasma membrane (**Supplementary Figure S2**). When the pulse is at the end of its plateau, the electric field within the cell is higher probably due to the pore conduction that becomes more important than passive displacement currents (Gowrishankar et al., 2006). Moreover, as the irregular shape of the plasma and ER membrane causes changes in the intensity and directions of the electric field similarly to what discussed in Denzi et al. (2016), the intracellular field is distributed non-uniformly. In some cells of the mixture, the electric field penetrates more easily than in others, in particular the cells exposing a larger area of membrane resulted in the higher amount of internal electric field. By comparing the duplicated cells (as those indicated by the red flashes in **Figures 1A,B**), one can notice that the internal field is very different. As the size and the shape are the same in this case, these results suggest that the position occupied by the cell in the chamber (i.e., the presence of the surrounding cells) and the orientation of the normal to the membranes with respect to the applied electric field direction, also affects the cell response/behavior. The external electric field experienced by each cell is strongly affected by the cell placement. Indeed, where the cells are more packed, the electric field presents local variations in terms of direction and intensity due to the interfering cells.

This heterogeneity in the cell response well reflects the non-uniform TMP induction on the opposite sides of the membranes (**Figures 2A–C**). The TMP is generally considered a valid indicator of the electroporation occurrence. Experimental studies report different electroporation thresholds ranging from 0.2 and

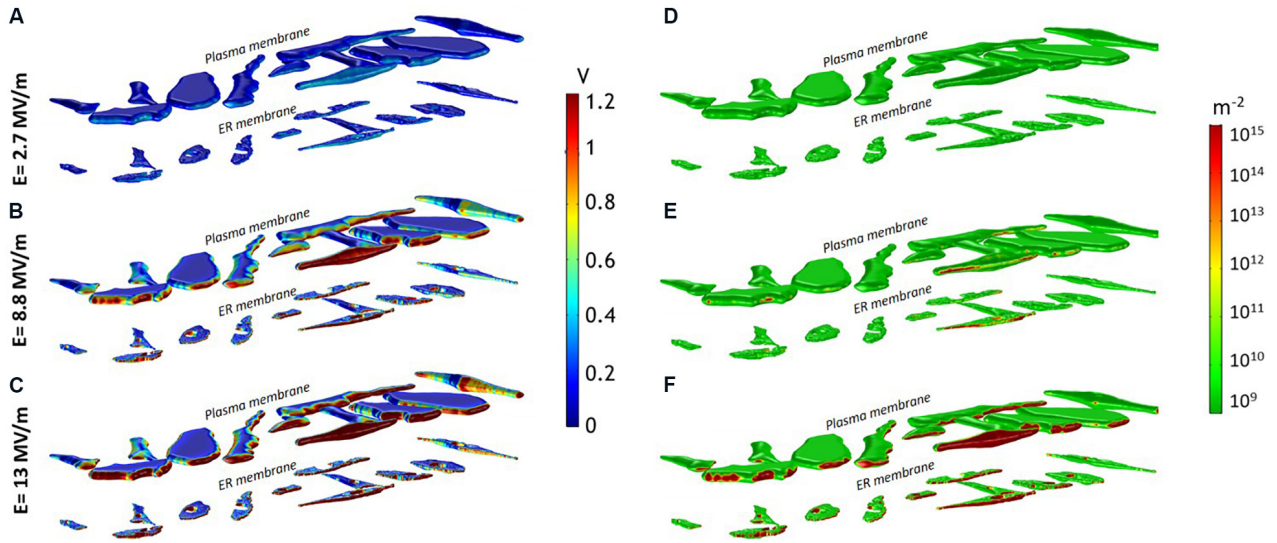

FIGURE 2 | (A–C) Induced TMP and **(D–F)** pore density spatial distribution on the entire investigated domain (12 cells) at 10 ns for an applied pulse amplitude of **(A,D)** 2.7 MV/m, **(B,E)** 8.8 MV/m, **(C,F)** 13 MV/m.

1 V (Denzi et al., 2016), depending on cell type and experimental conditions (Merla et al., 2017). Here, a TMP > 1 V has been considered as the threshold value for the onset of the pore formation in the membranes. In **Figures 2A–C** the spatial map of the TMP induced at the end of the pulse plateau (t = 10 ns) by three increasing electric field intensities, (A) E_1 = 2.7 MV/m, (B) E_2 = 8.8 MV/m and (C) E_3 = 13 MV/m is shown. For each field condition, the upper row reports the TMP on the plasma membrane and the lower row the TMP on the ER membrane. At 2.7 MV/m, no cell experienced a TMP >1 V (**Figure 2A**). At 8.8 MV/m, the red patches of the plasma and ER membranes are those where the TMP is above the threshold value of 1 V (**Figure 2B**). As evident, the induced TMP does not reproduce the typical symmetry of the regularly shaped cells, presenting strong local variations on the membrane of the same cell and from cell to cell. The extremely folded membrane experiences different TMP due to the fact that the cosine law in the Schwan's equation (Foster and Schwan, 1986) loses its validity in irregular structures as reported also in Pucihar et al. (2006), Denzi et al. (2016) and Hanna et al. (2017). At 13 MV/m more extensive patches of plasma and ER membrane experienced a TMP >1 V in all the cells (**Figure 2C**).

In a more quantitative manner, we can derive the TMP trend during the stimulation period on the plasma and ER membranes of the same cell. The induced TMP averaged on the plasma membrane (**Supplementary Figure S3**) was higher than but very close to that on ER membranes for all the applied electric fields, confirming that a 10-ns electric pulse is potentially able to partially porate the ER with electric field values slightly greater than the ones needed to porate the plasma membrane. This result is clearly related to the high frequency content of the short pulse, mainly associated to the fast rise and fall times (2 ns).

In **Figures 2D–F** is reported the spatial distribution of the pore density over the same cell mixture and for the same three electric fields considered in **Figures 2A–C**. As evident from a qualitative inspection, some portions of the plasma and ER membranes showed a more important electroporation than others (significant pore density $\geq 10^{14}$). Indeed, in good accordance with the experimental results and with the simulated TMP maps, a single 10-ns pulse of 2.7 MV/m was insufficient to electroporate the plasma and the ER membranes in all the cells (**Figure 2D**). The plasma membrane of some more responsive cells starts to be porated at 6 MV/m (not shown), while for porating the ER membrane an electric field of at least 8.8 MV/m was necessary (**Figure 2E**), confirming that slightly lower amplitudes of nsPEF are needed to permeabilize the plasma membrane than those required for the ER membranes. At 13 MV/m both plasma and ER membranes of most of the cells were efficiently porated (**Figure 2F**). Interestingly, once the threshold for the ER electroporation is reached (at electric field > 9 MV/m), pore density could be even higher than that of the plasma membrane as showed in **Supplementary Figure S4**. Here, the maximum density of pores reached at each applied electric field intensity is reported for two selected cells, representative of the general cell behavior. This result is in accordance with the experimental observation that nsPEF <9 MV/m induced a modest peak of intracellular calcium, only due to the poration of the plasma membrane, while for amplitudes higher than 9 MV/m, when both plasma and ER membrane were permeabilized, a more important and sharp increase of the calcium concentration was recorded (De Menorval et al., 2016).

Supplementary Figure S5 reports an example of the cumulative distribution function directly estimated from the simulations, it represents the probability that a certain percentage of membrane has reached a value less than or equal to a specific pore density. The curves in **Figure 3** were derived from the ones in **Supplementary Figure S5** as their complementary

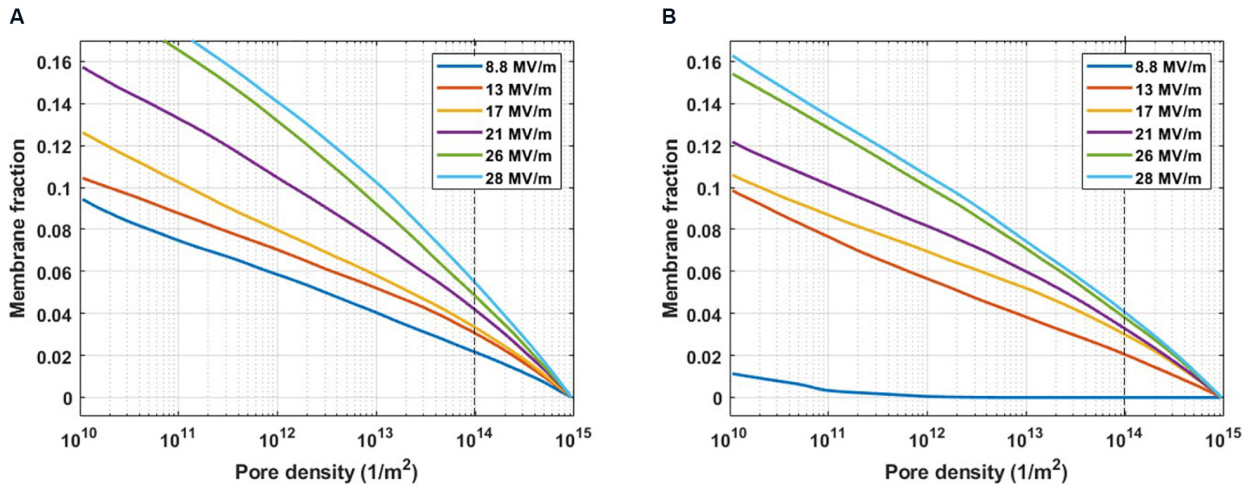

FIGURE 3 | Pore density histogram on a single cell evaluated for the complementary cumulative distribution function. The fraction of the PM **(A)** and ER **(B)** membrane where the pore density reached at least the value indicated on the x-axis, at increasing electric field amplitudes from 8.8 to 28 MV/m. The dashed line indicates the threshold value for a significant density of the pore (10^{14} m^{-2}).

cumulative distribution function (known also as reliability function; Ebeling, 2010).

Figure 3 represents the cumulative fraction of the plasma (**Figure 3A**) and ER (**Figure 3B**) membranes which has reached a density of the pores of at least the value reported in the x-axis, induced by increasing electric field amplitude (from 8.8 to 28 MV/m), at the end of the simulation (t = 10 ns). In particular, in the case of the cell reported in **Figure 3**, when an electric field of 8.8 MV/m is applied, a fraction of the plasma membrane equal to 0.02 is significantly porated (pore density $\geq 10^{14}$) (**Figure 3A**). In order to observe a comparable percentage in the ER membrane, a pulse amplitude of at least 13 MV/m becomes necessary (**Figure 3B**). Increasing amplitudes of the applied electric field result in increasing fractions of porated plasma and ER membranes patches, as expected. Then, the response of the cell mixture to the electric stimulation was quantified in terms of percentage of the porated cells in function of the applied electric field amplitudes. This percentage was evaluated, for each electric field intensity, as the ratio between the number of cells that, at the end of the stimulation (t = 12 ns), have reached the same fraction of porated membrane, according to **Figure 3**, and the total number of cells. The dose-response curves obtained considering different fractions of porated membrane, ranging from 0.01 to 0.05 overlapped to the experimental curve, are reported in **Supplementary Figure S6**. As in the experimental study where De Menorval et al. (2016) used two different extracellular conditions (in the presence and in the absence of external Ca^{2+}), the poration of the plasma membranes (**Supplementary Figure S6A**) and the ER membranes (**Supplementary Figure S6B**) were investigated separately. A very good matching between the simulated and the experimental results was found when a fraction of the porated membrane of both the plasma and the ER equal to 0.02 is considered sufficient for permeabilizing the membrane (**Figure 4**). Here, the solid lines represent the average of the percentages resulted from the four simulations, reported as scattered points (small circles) in the same figure. A pulse amplitude of 7 MV/m is needed to efficiently porate the plasma membrane of about 10% of the cells in the mixture. 13 MV/m induced poration in 50% of the plasma membranes, while 17 MV/m is required to porate the plasma membrane in 100% of the cells (**Figure 4A**). Concerning the ER membranes poration (**Figure 4B**), an applied electric field of 9 MV/m was required for the onset of the poration (10% of the cells); while at 26 MV/m the ER membrane was extensively porated in 100% of the cells. These results, obtained in 3D realistic model, reconstructed from real images, are in good accordance with those obtained experimentally, investigating a number of cells (i.e., 48 in simulations vs. around the double in experiments).

DISCUSSION

nsPEFs induce the transient permeabilization of the cell membranes with an extent that depends on the nsPEF parameters (amplitude, duration, number, and repetition rate in case of a pulse train). However, the model has highlighted strong differences in the responses of each cell in the mixture when the same nsPEF was applied. This is because the position of the cell, the proximity of other cells as well as its orientation with respect to the electric field direction have an important impact on the cell response to the stimulation. As shown, not all the cells in the mixture experiment the same electric field amplitude, as the presence of other cells could mask the external field. In the part of the exposure chamber where the cells are more isolated, a higher electric field penetrates the cell and the ER. Indeed, due to the high frequency content of a 10-ns pulse with fast rise and fall times, the membrane becomes more conductive, allowing the subcellular electric field to fast

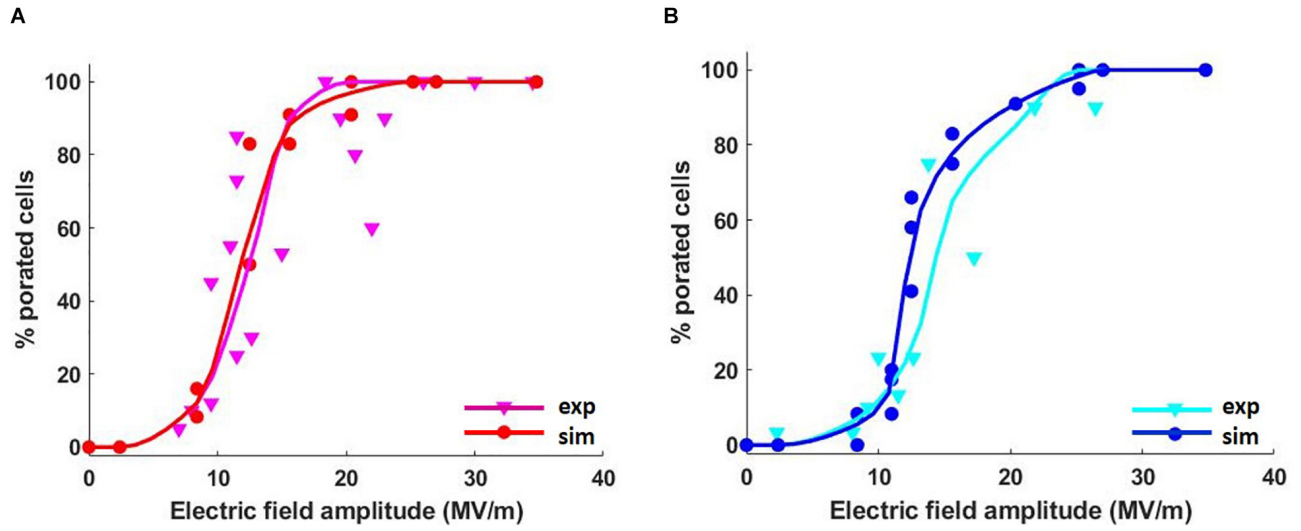

FIGURE 4 | Average percentage of the cells with porated **(A)** plasma and **(B)** ER membranes in four different mixtures as a function of the applied electric field. The red and blue curves represent the average simulated data interpolation, while the magenta and the cyan curves are the interpolation of the average experimental data. Cubic Spline Interpolation was used for both the simulated and the experimental data.

increase. Another important aspect highlighted by the simulation concerns the possibility to estimate the total amount of the cellular and subcellular membranes experiencing an electric field able to porate them, and the degree of the poration. The general trend of a cell in the mixture reveals that a single 10-ns PEF is able to porate both the ER and plasma membrane with field intensities slightly different. In particular, the amplitude of the electric field necessary to porate the plasma membrane is moderately lower than that necessary to permeabilize the reticulum membrane as experimentally observed in Semenov et al. (2013), De Menorval et al. (2016).

Note-worthy, our realistic model is able to relate the percentage of the cellular and subcellular porated membrane to the applied electric field amplitude (and, presumably, to other PEF parameters like duration, rise and fall times, repetition rate). In our specific case, a fraction of 0.02 of porated membrane has resulted sufficient for permeabilizing the membrane at a detectable fluorescence intensity, proportional to the intracellular calcium concentration increase. Higher fractions of porated membrane would allow higher cytosolic calcium concentration. In that way, the presented model could be used to correctly set the PEF parameters for manipulating the calcium concentration on demand, and to control the related biological processes. Moreover, the extremely good accordance between the experimental curve of the cells presenting an observable calcium peak and the simulated dose-response curve when considering a porated membrane fraction of 0.02, suggests that this value could represent the minimum percentage of membrane that has to be porated in order to obtain an efficient effect in the experimental counterpart. Although we cannot completely replicate the experimental condition, like for example, the cell concentration in the pulsed sample, or their adhesion on the cover slip, the obtained results highlight the effectiveness of our numerical model in predicting the real response of a cell population to nsPEFs.

CONCLUSION

A 3D realistic model of six human mesenchymal stem cells with ER and nucleus was built starting from their optical confocal microscopy images where different cell compartments were highlighted (Hanna et al., 2017). Confocal florescence microscopy has enabled the possibility to build such realistic 3D models from real images of 12 cells. Each reconstructed cell geometry was imported in Comsol Multiphysics (v. 5.3), duplicated and put in random positions as to obtain a mixture of 12 cells. The microdosimetric analysis of the group of cells was quantified in terms of electric field and TMPs induced by an externally applied 10-ns trapezoidal pulse with rise and fall times of 2 ns, with amplitudes ranging from 2 to 36 MV/m as to simulate the same electric field used in the experimental work of (De Menorval et al., 2016). Then, the cell-by-cell pore density estimation from the simulation was used to evaluate the percentage of electroporated cells as a function of the applied electric field intensity. The comparison between the simulated dose-response curves with those obtained experimentally by De Menorval et al. (2016) displayed a very good matching of results for plasma and ER membrane when a fraction of 0.02 of the porated membrane is considered sufficient for permeabilizing the membrane. The simulation has highlighted that plasma and ER membrane of each cell responds in a different way to the same electric field amplitude. As a consequence, also the threshold for an efficient electroporation is highly different from cell to cell. Indeed, some portions of the cell and ER membranes showed a more important electroporation than others, coherently

with the TMP estimation, due to their extremely irregular and folded structure. The non-uniformity in the induced electric field distributions was due to the differences in shape, size, and position of each cell and its orientation with respect to the applied electric field direction. The relevance of this study lays in the possibility to effectively predict the behavior of a cell (or of a population of cells) exposed to a nsPEF with specific parameters. Therefore, the microdosimetric realistic 3D model described in this study, could represent a valid tool in setting up a more efficient and controlled electroporation protocol.

DATA AVAILABILITY STATEMENT

All datasets generated for this study are included in the article/**Supplementary Material**.

AUTHOR CONTRIBUTIONS

ADA performed the simulation, analyzed and elaborated the data, and wrote the manuscript. AD built the 3D model of the cell used in this study and reviewed the manuscript. CM contributed to the analysis and understanding of data and reviewed the manuscript. FMA and LM are the authors of the previous experimental work related to this article, provided the confocal microscopy images used for modeling the cells and reviewed the manuscript. FA and ML are the PI of this research study. All authors contributed to the article and approved the submitted version.

FUNDING

The authors acknowledge the funding of their research by the CNRS, Université Paris-Saclay and Gustave Roussy.

SUPPLEMENTARY MATERIAL

The Supplementary Material for this article can be found online at: https://www.frontiersin.org/articles/10.3389/fbioe.2020.552261/full#supplementary-material

REFERENCES

Apollonio, F., Liberti, M., Paffi, A., Merla, C., Marracino, P., Denzi, A., et al. (2013). Feasibility for microwaves energy to affect biological systems via nonthermal mechanisms: a systematic approach. *IEEE Trans. Microwave Theor. Tech.* 61, 2031–2045. doi: 10.1109/TMTT.2013.2250298

Berridge, M. J., Bootman, M. D., and Roderick, H. L. (2003). Calcium signalling: dynamics, homeostasis and remodelling. *Nat. Rev. Mol. Cell Biol.* 4, 517–529. doi: 10.1038/nrm1155

Cadossi, R., Ronchetti, M., and Cadossi, M. (2014). Locally enhanced chemotherapy by electroporation: clinical experiences and perspective of use of electrochemotherapy. *Future Oncol.* 10, 877–890. doi: 10.2217/fon.13.235

De Menorval, M. A., Andre, F. M., Silve, A., Dalmay, C., Français, O., Le Pioufle, B., et al. (2016). Electric pulses: a flexible tool to manipulate cytosolic calcium concentrations and generate spontaneous-like calcium oscillations in mesenchymal stem cells. *Sci. Rep.* 6:32331. doi: 10.1038/srep32331

DeBruin, K. A., and Krassowska, W. (1999). Modeling electroporation in a single cell. I. Effects of field strength and rest potential. *Biophys. J.* 77, 1213–1224. doi: 10.1016/S0006-3495(99)76973-0

Denzi, A., Camera, F., Merla, C., Benassi, B., Consales, C., Paffi, A., et al. (2016). A microdosimetric study of electropulsation on multiple realistically shaped cells: effect of neighbours. *J. Membr. Biol.* 249, 691–701. doi: 10.1007/s00232-016-9912-3

Denzi, A., Della Valle, E., Esposito, G., Mir, L. M., Apollonio, F., and Liberti, M. (2017). Technological and theoretical aspects for testing electroporation on liposomes. *BioMed. Res. Int.* 2017:5092704. doi: 10.1155/2017/5092704

Ebeling, C. (2010). *An Introduction to Reliability and Maintainability Engineering*, 2nd Edn. Long Grove, IL: Waveland Press.

Esser, A. T., Smith, K. C., Gowrishankar, T. R., Vasilkoskl, Z., and Weaver, J. C. (2010). Mechanisms for the intracellular manipulation of organelles by conventional electroporation. *Biophys. J.* 98, 2506–2514. doi: 10.1016/j.bpj.2010.02.035

Foster, K. R., and Schwan, H. P. (1986). *Handbook of Biological Effects of Electromagnetic Fields*. Boca Raton, FL: CRC Press.

Frandsen, S. K., Gissel, S. H., Hojman, P., Tramm, T., Eriksen, J., and Gehl, J. (2012). Direct therapeutic applications of calcium electroporation to effectively induce tumor necrosis. *Cancer Res.* 72, 1336–1341. doi: 10.1158/0008-5472.CAN-11-3782

Gowrishankar, T. R., Esser, A. T., Vasilkoskl, Z., Smith, K. C., and Weaver, J. C. (2006). Microdosimetry for conventional and supra-electroporation in cells with organelles. *Biochem. Biophys. Res. Commun.* 341, 1266–1276. doi: 10.1016/j.bbrc.2006.01.094

Hanna, H., Denzi, A., Liberti, M., André, F. M., and Mir, L. M. (2017). Electropermeabilization of inner and outer cell membranes with microsecond pulsed electric fields: quantitative study with calcium ions. *Sci. Rep.* 7:13079. doi: 10.1038/s41598-017-12960-w

Joshi, R. P., Mishra, A., and Schoenbach, K. H. (2008). Model assessment of cell membrane breakdown in clusters and tissues under high-intensity electric pulsing. *IEEE Trans. Plasma Sci.* 36(4 Pt 3), 1680–1688. doi: 10.1109/TPS.2008.917307

Joshi, R. P., Nguyen, A., Sridhara, V., Hu, Q., Nuccitelli, R., Beebe, S. J., et al. (2007). Simulations of intracellular calcium release dynamics in response to a high-intensity, ultrashort electric pulse. *Phys. Rev. E Stat. Nonlinear Soft Matter Phys.* 75:041920. doi: 10.1103/PhysRevE.75.041920

Kitano, H. (2002). Computational systems biology. *Nature* 420, 206–210. doi: 10.1038/nature01254

Kotnik, T., Pucihar, G., and Miklavčič, D. (2010). Induced transmembrane voltage and its correlation with electroporation- mediated molecular transport. *J. Membr. Biol.* 236, 3–13. doi: 10.1007/s00232-010-9279-9

Kulbacka, J. (2017). *Transport Across Natural and Modified Biological Membranes and Its Implications in Physiology and Therapy*, Vol. 227. New York, NY: Springer International Publishing. doi: 10.1007/978-3-319-56895-9

Mercadal, B., Vernier, P. T., and Ivorra, A. (2016). Dependence of electroporation detection threshold on cell radius: an explanation to observations non compatible with Schwan's equation model. *J. Membr. Biol.* 249, 663–676. doi: 10.1007/s00232-016-9907-0

Merla, C., Liberti, M., Consales, C., Denzi, A., Apollonio, F., Marino, C., et al. (2019). Evidences of plasma membrane-mediated ROS generation upon ELF exposure in neuroblastoma cells supported by a computational multiscale approach. *Biochim. Biophys. Acta Biomembr.* 1861, 1446–1457. doi: 10.1016/j.bbamem.2019.06.005

Merla, C., Pakhomov, A. G., Semenov, I., and Vernier, P. T. (2017). Frequency spectrum of induced transmembrane potential and permeabilization efficacy of bipolar electric pulses. *Biochim. Biophys. Acta Biomembr.* 1859, 1282–1290. doi: 10.1016/j.bbamem.2017.04.014

Pavlin, M., Slivnik, T., and Miklavčič, D. (2002). Effective conductivity of cell suspensions. *IEEE Trans. Biomed. Eng.* 49, 77–80. doi: 10.1109/10.972843

Petecchia, L., Sbrana, F., Utzeri, R., Vercellino, M., Usai, C., Visai, L., et al. (2015). Electro-magnetic field promotes osteogenic differentiation of BM-HMSCs through a selective action on Ca 2+-related mechanisms. *Sci. Rep.* 5:13856. doi: 10.1038/srep13856

Pucihar, G., Kotnik, T., Miklavčič, D., and Teissié, J. (2008). Kinetics of transmembrane transport of small molecules into electropermeabilized cells. *Biophys. J.* 95, 2837–2848. doi: 10.1529/biophysj.108.135541

Pucihar, G., Kotnik, T., Teissié, J., and Miklavčič, D. (2007). Electropermeabilization of dense cell suspensions. *Eur. Biophys. J.* 36, 173–185. doi: 10.1007/s00249-006-0115-1

Pucihar, G., Kotnik, T., Valič, B., and Miklavčič, D. (2006). Numerical determination of transmembrane voltage induced on irregularly shaped cells. *Ann. Biomed. Eng.* 34, 642–652. doi: 10.1007/s10439-005-9076-2

Scarlett, S. S., White, J. A., Blackmore, P. F., Schoenbach, K. H., and Kolb, J. F. (2009). Regulation of intracellular calcium concentration by nanosecond pulsed electric fields. *Biochim. Biophys. Acta Biomembr.* 1788, 1168–1175. doi: 10.1016/j.bbamem.2009.02.006

Semenov, I., Xiao, S., Pakhomova, O. N., and Pakhomov, A. G. (2013). Recruitment of the intracellular Ca2+ by ultrashort electric stimuli: the impact of pulse duration. *Cell Calc.* 54, 145–150. doi: 10.1016/j.ceca.2013.05.008

Smith, K. C., Gowrishankar, T. R., Esser, A. T., Stewart, D. A., and Weaver, J. C. (2006). The spatially distributed dynamic transmembrane voltage of cells and organelles due to 10 Ns pulses: meshed transport networks. *IEEE Trans. Plasma Sci.* 34, 1394–1404. doi: 10.1109/TPS.2006.878436

Sun, S., Liu, Y., Lipsky, S., and Cho, M. (2007). Physical manipulation of calcium oscillations facilitates osteodifferentiation of human mesenchymal stem cells. *FASEB J.* 21, 1472–1480. doi: 10.1096/fj.06-7153com

Towhidi, L., Kotnik, T., Pucihar, G., Firoozabadi, S. M. P., Mozdarani, H., and Miklavčič, D. (2008). Variability of the minimal transmembrane voltage resulting in detectable membrane electroporation. *Electromagn. Biol. Med.* 27, 372–385. doi: 10.1080/15368370802394644

Vernier, P. T., Sun, Y., Marcu, L., Salemi, S., Craft, C. M., and Gundersen, M. A. (2003). Calcium bursts induced by nanosecond electric pulses. *Biochem. Biophys. Res. Commun.* 310, 286–295. doi: 10.1016/j.bbrc.2003.08.140

Zaklit, J., Craviso, G. L., Leblanc, N., Yang, L., Vernier, P. T., and Chatterjee, I. (2017). Adrenal chromaffin cells exposed to 5-Ns pulses require higher electric fields to porate intracellular membranes than the plasma membrane: an experimental and modeling study. *J. Membr. Biol.* 250, 535–552. doi: 10.1007/s00232-017-9983-9

Conflict of Interest: The authors declare that the research was conducted in the absence of any commercial or financial relationships that could be construed as a potential conflict of interest.

Copyright © 2020 De Angelis, Denzi, Merla, Andre, Mir, Apollonio and Liberti. This is an open-access article distributed under the terms of the Creative Commons Attribution License (CC BY). The use, distribution or reproduction in other forums is permitted, provided the original author(s) and the copyright owner(s) are credited and that the original publication in this journal is cited, in accordance with accepted academic practice. No use, distribution or reproduction is permitted which does not comply with these terms.

frontiers in Bioengineering and Biotechnology

ORIGINAL RESEARCH
published: 03 December 2020
doi: 10.3389/fbioe.2020.552357

AC Pulsed Field Ablation Is Feasible and Safe in Atrial and Ventricular Settings: A Proof-of-Concept Chronic Animal Study

Guido Caluori[1,2,3], Eva Odehnalova[1], Tomasz Jadczyk[1,4], Martin Pesl[1,5,6], Iveta Pavlova[7], Lucia Valikova[8], Steffen Holzinger[9], Veronika Novotna[1,10], Vladimir Rotrekl[1,5], Ales Hampl[1,11], Michal Crha[8], Dalibor Cervinka[10] and Zdenek Starek[1,6]**

[1] International Clinical Research Center, St. Anne's University Hospital Brno, Brno, Czechia, [2] IHU LIRYC, Electrophysiology and Heart Modeling Institute, Fondation Bordeaux Université, Pessac, France, [3] Univ. Bordeaux, INSERM, UMR 1045, Cardiothoracic Research Center of Bordeaux, Pessac, France, [4] Department of Cardiology and Structural Heart Diseases, Medical University of Silesia, Katowice, Poland, [5] Department of Biology, Faculty of Medicine, Masaryk University, Brno, Czechia, [6] First Department of Internal Medicine-Cardioangiology, St. Anne's University Hospital, Masaryk University, Brno, Czechia, [7] Institute of Scientific Instruments of the Czech Academy of Sciences, Brno, Czechia, [8] Faculty of Veterinary Medicine, University of Veterinary and Pharmaceutical Sciences, Brno, Czechia, [9] R&D EP Systems & Sensors, BIOTRONIK SE & Co., KG, Berlin, Germany, [10] Department of Power Electrical and Electronic Engineering, Faculty of Electrical Engineering and Communication, Brno University of Technology, Brno, Czechia, [11] Department of Histology and Embryology, Faculty of Medicine, Masaryk University, Brno, Czechia

Introduction: Pulsed field ablation (PFA) exploits the delivery of short high-voltage shocks to induce cells death via irreversible electroporation. The therapy offers a potential paradigm shift for catheter ablation of cardiac arrhythmia. We designed an AC-burst generator and therapeutic strategy, based on the existing knowledge between efficacy and safety among different pulses. We performed a proof-of-concept chronic animal trial to test the feasibility and safety of our method and technology.

Methods: We employed 6 female swine – weight 53.75 ± 4.77 kg – in this study. With fluoroscopic and electroanatomical mapping assistance, we performed ECG-gated AC-PFA in the following settings: in the left atrium with a decapolar loop catheter with electrodes connected in bipolar fashion; across the interventricular septum applying energy between the distal electrodes of two tip catheters. After procedure and 4-week follow-up, the animals were euthanized, and the hearts were inspected for tissue changes and characterized. We perform finite element method simulation of our AC-PFA scenarios to corroborate our method and better interpret our findings.

Results: We applied square, 50% duty cycle, AC bursts of 100 μs duration, 100 kHz internal frequency, 900 V for 60 pulses in the atrium and 1500 V for 120 pulses in the septum. The inter-burst interval was determined by the native heart rhythm – 69 ± 9 bpm. Acute changes in the atrial and ventricular electrograms were immediately visible at the sites of AC-PFA – signals were elongated and reduced in amplitude ($p < 0.0001$) and tissue impedance dropped ($p = 0.011$). No adverse event (e.g., esophageal temperature rises or gas bubble streams) was observed – while twitching was avoided by addition of electrosurgical return electrodes.

OPEN ACCESS

Edited by:
Saša Haberl Meglič,
University of Ljubljana, Slovenia

Reviewed by:
Damijan Miklavčič,
University of Ljubljana, Slovenia
Luke Hong Lu Zhao,
The University of Sydney, Australia, in collaboration with reviewer DM
Anna Bulysheva,
Old Dominion University, United States

***Correspondence:**
Guido Caluori
guido.caluori@ihu-liryc.fr;
guido.cal87@gmail.com
Zdenek Starek
ice.icrc@gmail.com;
zdenek.starek@fnusa.cz

Specialty section:
This article was submitted to Bioprocess Engineering, a section of the journal Frontiers in Bioengineering and Biotechnology

Received: 15 April 2020
Accepted: 09 November 2020
Published: 03 December 2020

Citation:
Caluori G, Odehnalova E, Jadczyk T, Pesl M, Pavlova I, Valikova L, Holzinger S, Novotna V, Rotrekl V, Hampl A, Crha M, Cervinka D and Starek Z (2020) AC Pulsed Field Ablation Is Feasible and Safe in Atrial and Ventricular Settings: A Proof-of-Concept Chronic Animal Study. Front. Bioeng. Biotechnol. 8:552357. doi: 10.3389/fbioe.2020.552357

The implemented numerical simulations confirmed the non-thermal nature of our AC-PFA and provided specific information on the estimated treated area and need of pulse trains. The postmortem chest inspection showed no peripheral damage, but epicardial and endocardial discolorations at sites of ablation. T1-weighted scans revealed specific tissue changes in atria and ventricles, confirmed to be fibrotic scars via trichrome staining. We found isolated, transmural and continuous scars. A surviving cardiomyocyte core was visible in basal ventricular lesions.

Conclusion: We proved that our method and technology of AC-PFA is feasible and safe for atrial and ventricular myocardial ablation, supporting their systematic investigation into effectiveness evaluation for the treatment of cardiac arrhythmia. Further optimization, with energy titration or longer follow-up, is required for a robust atrial and ventricular AC-PFA.

Keywords: pulsed field ablation, irreversible electroporation (IRE), radiofrequency ablation, atrial fibrillation, ventricular arrhythmia (VA), preclinical cardiology

INTRODUCTION

Pulsed field ablation (PFA) is a recent method for interventional treatment of cardiac arrhythmia. It exploits the localized application of short – nano/microseconds - high-voltage electric fields to induce irreversible electroporation, a prolonged state or pore-induced permeability that triggers non-necrotic deaths (Davalos et al., 2005), in the proximal tissue (Wittkampf et al., 2018; Wojtaszczyk et al., 2018; Sugrue et al., 2019) with high selectivity (Miklavčič, 2018) and without strict need of contact (Ramirez et al., 2020). These characteristics make the method an excellent candidate to avoid thermal collateral damages observed with radiofrequency and cryo-balloon ablation, among which phrenic/vagal nerve injury/palsy, atrio-esophageal fistula, pulmonary vein stenosis and thrombus formation (Sugrue et al., 2018; Wojtaszczyk et al., 2018).

Different tissues present different sensitivities to irreversible electroporation, with the striated muscle (including myocardium) proven the most susceptible one (Wittkampf et al., 2018), for reasons still not fully understood. This peculiar sensitivity prompted researchers and physicians to perfect a selective ablation of heart muscle using pulsed irreversible electroporation. Several short-term animal studies have proven how PFA does not affect the coronary vasculature, the local innervation, and the adjacent structures (e.g., esophagus and lungs) (Sugrue et al., 2019). A first in-human trial for paroxysmal atrial fibrillation ablation via pulmonary vein isolation has delivered promising results, with a 12-month Kaplan-Meier estimate of freedom from arrhythmia of 87.4 $\pm$ 5.6%, outperforming in the medium term the mentioned radiofrequency (RF) and cryo-balloon studies (Reddy et al., 2019).

Notwithstanding these promising reports, several open issues call for more investigation and optimization. There is no consensus on which pulse shape and dynamics possess the best tradeoff between efficacy and safety. Pulsed electric field energy can be delivered according to different parameters: Shape of the voltage pulse, predominantly DC/AC square; voltage level and current compliance; number of pulses; interpulse distance (Wojtaszczyk et al., 2018).

DC monophasic pulses are historically the most employed for electroporation of cell suspensions, but they can lead to potentially painful nerve and muscle capture (Mercadal et al., 2017), arcing, metallic release in solution (Meir and Rubinsky, 2014), and bubble stream formation, also due to electrolysis without arcing (van Es et al., 2019a). These issues require a careful control of DC pulses delivery and avoid direct galvanic coupling between electrodes and tissue. AC biphasic pulses or bursts can help to prevent these issues (Wojtaszczyk et al., 2018), although they impose a lower equivalent electric field on the tissue, and they are more subjected to electrode surface heating due to skin-effect. Asymmetrical AC has been introduced, proved feasible and effective in animal studies (Stewart et al., 2019) and clinical trials (Reddy et al., 2018). Both symmetrical and asymmetrical AC pulses have been proved to ablate ventricular myocardium in an epicardial porcine model with customized applicators (van Es et al., 2019b). From this evidence, symmetrical AC bursts of sufficient duration do not suffer from "cancelation effect", where the effect of the first phase of the pulse is canceled by the second phase (Polajžer et al., 2020). Therefore, AC bursts are a suitable PFA waveform yet to be tested in endocardial settings with commercial catheters.

The voltage level is determinant to impose a sufficiently high electric field across the tissue – hundreds of Vcm^{-1}. The available catheter technology and cardiac anatomy require pulse generators to provide at least units of kV. Current compliance, typically in tens of A, is determined by the quality of tissue/electrode contact and the number of electrode pairs to excite in parallel: this determines the design of the pulse generator components with respect to the application. Multiple pulse delivery is preferable to keep a longer state of enhanced permeability to favor irreversible electroporation-related processes, although it might lead to heating and overtreatment (Garcia et al., 2014). Interpulse distance, especially

Abbreviations: AC, alternating current; DC, direct current; PFA, pulsed field ablation; RF, radiofrequency.

in cardiac applications, is conditioned by synchronization with the ventricular effective refractory period – an approach a.k.a. ECG-gating – not to elicit potentially lethal arrhythmias (Arena et al., 2011).

Given this set of knowledge, we have designed a pulse delivery strategy for PFA with a purely AC square burst, timed by ECG-gating. In our developed generator, a transformer-based design provides excellent insulation between the power line and the electrodes applied in the patients' heart. We have envisioned two uses of our pulse generator: Parallel energy delivery through a circular catheter for pulmonary vein isolation; two-catheter energy delivery across the ventricular septum to test ventricular arrhythmia ablation. We have tested our implemented technology and design of PFA on a chronic swine model.

MATERIALS AND METHODS

Animal Preparation

The animal experiments were approved by the ethic commission of the University of Veterinary and Pharmaceutical Sciences in Brno. We used 6 female swine – weight 53.75 ± 4.77 kg, 6 months old. One animal was used in a pilot procedure primarily to identify the: maximum voltage applicable in each setting; the optimal circular catheter size, in terms of navigation and multiple application in the left atrium. All the operators and the supporting staff were protected from X-ray radiation during procedures, and potentially dangerous chemicals were handled according to safety norms.

Anesthesia and preparation were performed accordingly to previously published studies (Soucek et al., 2020). Briefly, the animals were generally anesthetized and kept under mechanical ventilation with 1.5% isoflurane. We shaved the chest and groin, where we applied limb and precordial ECG electrodes. Two venous and two arterial access were obtained on the groins using 8F introducers. Blood pressure was monitored via one arterial access on the groin. Electroanatomical mapping patches (CARTO, Biosense Webster, Irvine, CA, United States) were placed on the back and the chest according manufacturer instructions. One electrosurgical return electrode was placed, to avoid muscle twitching, on the lower back and connected to the grounding pole of the AC-PFA generator.

Amiodarone (5 mg/kg) was administered to prevent ventricular fibrillation. Heparin (10000 Units) was administered in bolus after introducers and catheters insertion and was continued with half the initial dose every hour.

Mapping and Ablation

A 6F diagnostic quadripolar catheter (Inquiry™, Abbott, Chicago, IL, United States) was inserted in the right ventricle for monitoring and subsequently act as reference electrode in ventricular ablation. We obtained a left atrial access via transseptal puncture assisted with an ultrasound catheter (AcuNav™, Biosense Webster). On the left side we used a steerable sheath (Agilis™, Abbott) to insert and guide a 7F decapolar circular catheter (AFocus II™, Abbott) or an 8F force-sensing, 4 mm tip ablation catheter (Thermocool® Smarttouch®, Biosense Webster). We obtained anatomical and voltage mapping with the ablation catheter, with irrigation 2 ml/min and contact force > 5 g.

We performed PFA in the left atrium aiming at the following locations: right and left pulmonary vein ostia; lateral, anterior and anteroseptal walls. In the ventricular compartment, we ablated the following locations: apical and basal interventricular septum with AC bursts; anterolateral wall with radiofrequency energy – 30 W, 20 s, 30 ml/min – provided by a commercial generator (Smartablate™, Biosense Webster). A custom ECG-gating circuit controlled the AC-burst delivery by detecting the over-threshold voltage of the QRS complex on lead III of the surface ECG. The pulses were delivered in sinus rhythm, with heart rate measured of 69 ± 9 bpm. Each AC burst had a square shape, duty cycle 50%, duration of 100 μs and internal high frequency 100 kHz (i.e., ten oscillations per burst).

The AC-PFA generator (registered at the Czech Industry Propriety Office, utility model no. 33133; Czech patent 308415 approved 28/07/2020) was connected to the common ground. Using a custom-made switchbox (**Supplementary Figure 1A**), we connected the odd number electrodes of the circular catheter to the generator line pole while the even numbers to the neutral pole; this allowed us to have consecutive and shifting anode-cathode pairs across the loop (**Figure 1A**). We used the same box to connect the ablation catheter distal electrode to the line pole and the diagnostic catheter one to the neutral pole. A detailed schematic of the relevant electrical circuits present in the operating room is presented in **Figure 1B**. Electrode contact before ablation was overall verified via fluoroscopy and catheter positions on the electroanatomical maps.

For safety reasons, we used a 3-probe esophageal temperature probe set behind the animal's heart to measure eventual temperature spikes during atrial applications. We also employed intracardiac echo to observe an eventual bubble streaming flowing out of the aortic valve.

After the procedure, the animals were awakened, underwent antibiotic and analgesic therapy, and recovered for 4 weeks. In two animals, we repeated the electroanatomical maps to monitor eventual changes in the voltage amplitude of the treated tissue. All the animals were eventually euthanized by overdose of T61 anesthetic and they underwent pathological inspection and characterization of tissue changes.

Tissue Inspection, Magnetic Resonance Imaging and Histopathology

After euthanasia, we opened the chest cavity to inspect the heart status and the eventual peripheral damages. The organ was excised and inspected, before perfusion fixation in 10% formaldehyde. The organs were fixed for at least 1 week prior to magnetic resonance imaging.

The samples were scanned as a whole and then divided in atria and ventricles. To provide a control for the tissue changes in the atria, a non-ablated left atrium was excised and scanned from an age-matched animal involved in a parallel trial on ventricular ablation. Before scanning, the samples were rinsed

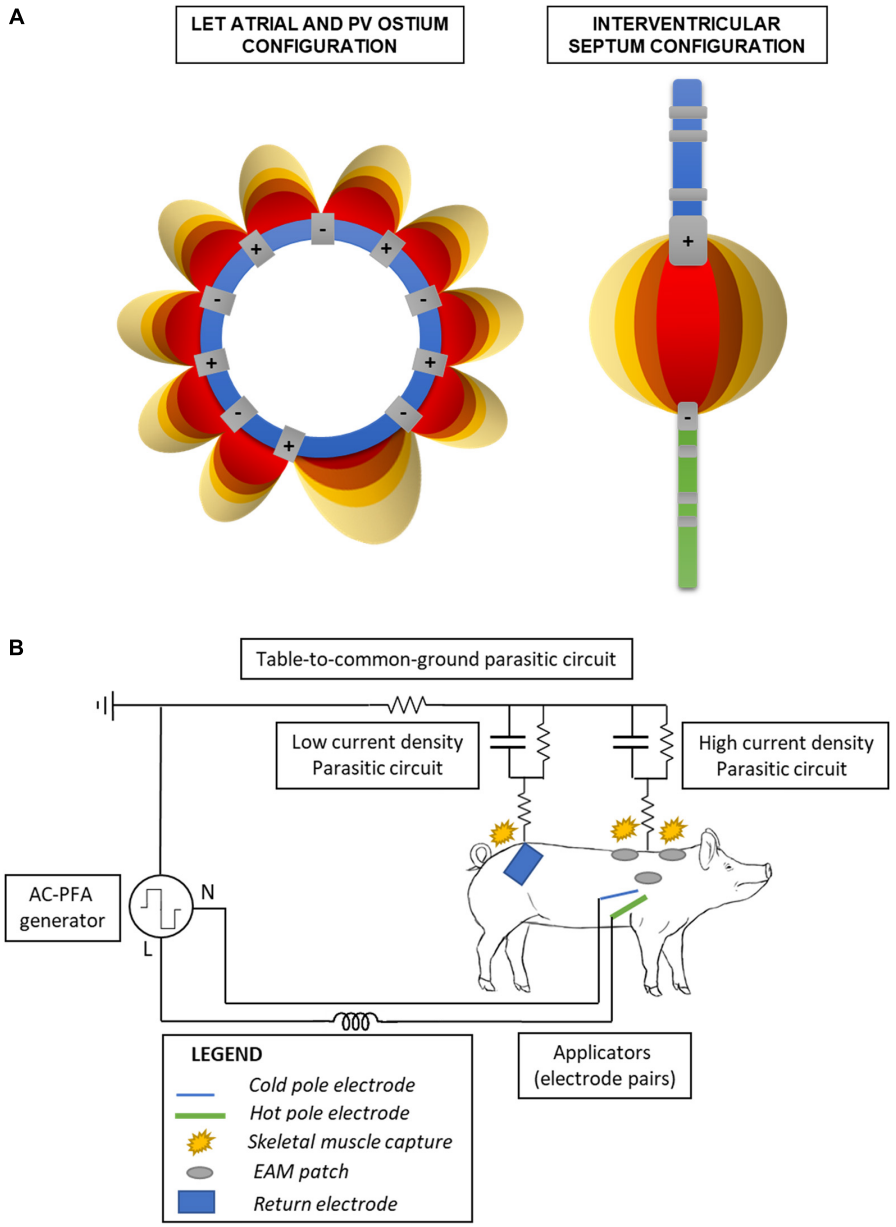

FIGURE 1 | Schematic of the electronics configuration. **(A)** Bipolar catheter electrodes pairings in the atrial and ventricular configuration. The electric fields internal to the loop (left) are not shown for clarity of the figure. **(B)** Simplified schematic of the electric circuits formed in the operating table, when employing the ventricular configuration. Parasitic circuits are present through the table to the common ground, and the return electrode favors a low impedance/current density pathway on the lower back avoiding capture of the upper limbs into muscle twitching.

with physiological salt solution (0.9% w/v NaCl), to remove all formaldehyde residues, and placed in a saline-filled jar. Air bubbles inside the samples were carefully removed to avoid imaging artifacts.

We scanned the samples with a 9.4T magnetic resonance system (Bruker BioSpec 94/30USR), equipped with volume coil 1H 198/154 mm, as previously described (Jež et al., 2019) with few modifications. The methods are detailed in the Supplements. Briefly, T2-weighted images were obtained in axial, sagittal and coronal direction using a TurboRARE sequence. T1-weighted images were obtained from the atria parts in axial direction only using a T1-FLASH sequence. The scans covered the whole sample volumes with a slice thickness of 1mm, no gap between slices and up to 512 × 512 pixel resolution. The scientist performing the scans was aware of the protocol name and pig number, but not aware of the specific treatment received. The scans were converted into DICOM series, segmented for volumetric calculations and rendered using ITK Snap (Yushkevich et al., 2006). The images were analyzed by a researcher with 4-year experience in RF ablation lesion

evaluation. The image analysis was not blinded because of the presence of a single treatment group and control. The percentage amount of non-myocardial atrial tissue, estimating the amount of native and ablation-derived non-muscular tissue, was calculated as:

$$V^i_{\%} = \frac{V^i_{tot} - V^i_{not\_myo}}{V^i_{tot}} \quad (1)$$

Where V^i_{tot} is the volume of the specimen i = 1–5, and $V^i_{not\_myo}$ is the volume of tissue presenting a T1 different from the myocardial one, in the i^{th} specimen. The final ablated volume was estimated with the formula:

$$V^{i^*}_{\%} = V^i_{\%} - V^0_{\%} \quad (2)$$

Where $V^0_{\%}$ is the percentage of non-myocardium present in an age-matched non-ablated atrium. As further individual-specific estimator, we have calculated the ratio between the ablated volume in an individual atrium, and the cylindrical volume obtained by extruding the loop catheter along the thickest section of the atrial wall. After scanning, selected atria and ventricles were sliced, paraffin-embedded and stained with hematoxylin/eosin or trichrome staining for histopathological examination. We digitized the tissue slides with a TissueFAX system (TissueGnostics GmbH, Wien, Austria), 600 × 600 μm field of view and 200x magnification. The expert technician confirming the presence of fibrosis was blinded about the different treatments producing the lesions and was only aware on the animal number and the original location (left atrium or interventricular septum). The linear dimensions of the detected fibrosis -width and depth - were measured in ImageJ (Rueden et al., 2017) after image calibration. Again, the image analysis was not blinded because of univocal origin of the fibrotic lesions, with RF used as control for qualitative tissue changes and not size.

Finite Element Method AC-PFA Numerical Simulations

To validate our ablation design, we performed finite element simulations in COMSOL Multiphysics 5.5. The blood flow is simulated by a static simulation of laminar flow solving the Navier-Stokes equations. The result of this static simulation is then inserted in a dynamics simulation using the electric currents interface of the AC/DC module coupled to the bioheat transfer interface of the heat transfer module. The single AC-burst had the same aforementioned features used *in vivo*.

We implemented two models for the left atrium scenarios: ablation across a pulmonary vein ostium, with diameter ranging 12–14 mm; ablation of the atrial wall, free of trabecule. To simulate the ventricular scenarios, we considered the two catheters across a 15 mm myocardium barrier in 3 configurations: perfect alignment; 10 mm alignment offset; 45° relative tilting; a combination of the previous two. The complete set of simulated geometries are shown in **Supplementary Figure 3A–F**. The simulated geometries were meshed by a free tetrahedral method.

The biophysical parameters for myocardium and blood are taken from the literature and are listed in **Supplementary Table 1**. All other material properties of the catheter (Pt electrodes and Nylon as insulator material) are taken from the COMSOL database.

Statistical Evaluation

The continuous variables are represented as mean ± standard deviation. Confirmation of normal distribution, statistical tests and graphs are obtained in GraphPad Prism 8 or Matlab. For comparisons between two groups we employed the paired Student's t-test with Welch's correction when necessary. For comparisons among multiple groups we employed the Kruskal-Wallis test with Dunn's *post hoc* correction. A p-value inferior to 0.05 was considered significant.

RESULTS

Ablation Procedure and Safety

The pilot animal died of complications due to transseptal puncture and did not complete the follow-up. The remaining five animals underwent the programmed AC-PFA protocol. The ECG-gating circuit timed the AC-bursts delivery in the effective refractory period of the QT interval, with delays ranging 50–75 ms (**Supplementary Figure 1B**). The voltage level was maximized, limited by the 12 A current compliance of our AC-PFA generator, to V_{atria} = 900 V and $V_{ventricle}$ = 1500 V. An example of the pulse shape is visible in **Supplementary Figure 1C**.

We successfully maneuvered toward the pulmonary vein ostia, atrial walls and interventricular septum (**Figure 2A–C**). Not all planned ablations were possible in all the animals due to different atrial size, difficulty in outlining the pulmonary veins, or timing. We applied 60-burst trains in the atrium and 120-burst ones across the interventricular septum, accounting for differences in the tissue volume to be treated. The esophageal probe did not show temperature increase during applications; the intracardiac echography did not detect a gas bubble stream formation; we observed occasional twitching of the upped limbs during atrial applications, in absence or bad contact of the return electrode (**Supplementary Video 1**).

After each AC-burst train application, we monitored significant changes in the intracardiac electrograms (**Figure 1D** for atria and **Figure 1E** for ventricles). We quantified differences in electrograms duration – elongated after ablation - and amplitude – decreased after ablation - of the atrial and ventricular electrograms. Occasionally, the ventricular electrogram had an only positive shape, with no changes on the surface ECG. These results are detailed in **Table 1**. We measured the impedance changes upon ablation, finding a significant decrease (-31.75 ± 13.92 Ω @100 Hz, p = 0.011).

At the end of procedure, no charring or clots were observed on the catheter surface (**Supplementary Figure 2A**). We noticed in the first and second animal burned areas in correspondence of the mapping electrodes on the back (**Supplementary Figure 2B,C**). The burnt regions healed in a week, causing no visible discomfort to the animals. This collateral damage was

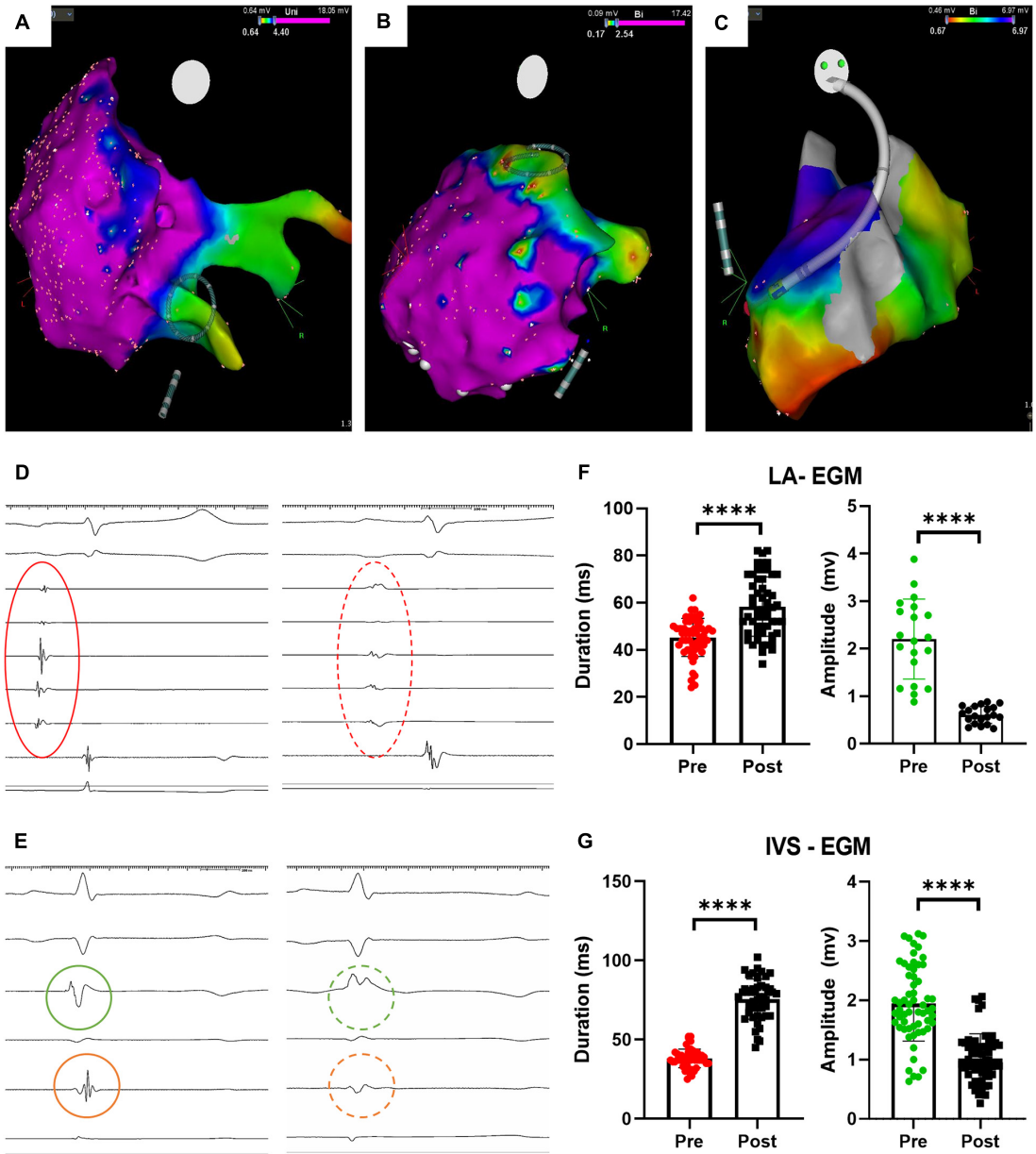

FIGURE 2 | Procedural imaging and electrophysiological results. **(A)** Circular catheter positioning before pulmonary vein ostium ablation; **(B)** Circular catheter positioning before atrial wall ablation; **(C)** catheter positioning across the interventricular septum before ablation; **(D)** atrial electrograms before (red continuous circle) and after (red dashed circle) ablation; **(E)** ventricular electrograms before (green, on left ventricle, and orange, on right ventricle, continuous circle) and after (dashed circles) ablation; **(F)** atrial electrograms changes upon ablation (****$p < 0.0001$); **(G)** ventricular electrograms changes upon ablation (****$p < 0.0001$). LA = left atrium; IVS = interventricular septum, EGM = electrogram.

TABLE 1 | Electrophysiological parameters changes upon ablation.

Application	EGM amplitude pre-ablation (mV)	EGM amplitude post-ablation (mV)	EGM duration pre-ablation (ms)	EGM duration post-ablation (ms)	*p*-value
Left atrium	2.20 ± 0.84	0.61 ± 0.18	45.29 ± 8.1	58.38 ± 12.61	<0.0001
Interventricular septum	1.95 ± 0.63	1.02 ± 0.41	38.20 ± 5.894	75.62 ± 12.70	<0.0001

avoided in the next animals by placing one return electrodes on their back, thus increasing the surface for dissipation of parasitic currents.

AC-PFA Numerical Simulations

We performed atrial and ventricular simulations imposing a voltage level of 900V and 1500V, respectively, as these were the maximum voltage levels imposable *in vivo*. The single AC-burst had the same duration and high frequency features of the one used *in vivo*. We used a static flow simulation of the atrial wall applications with a circular catheter as a worst-case scenario to simulate temperature rise in tissue. Upon the delivery of an AC burst, the simulation showed a temperature spike which followed an exponential decay. We fitted the simulated curves and found the following parameters: amplitude peak A_{blood} = 19°C and A_{tissue} = 7.6°C; decay constant τ_{blood} = 2.91 ms and one τ_{tissue} = 9.22 ms. Due to the considered interpulse interval of 800 ms – as determined by a resting 75 bpm sinus rhythm – we concluded that the temperature rise, and other physical parameters, can be studied with a single AC burst.

We then tested, on the same model, the effect of the convective cooling effect of parallel blood flow: the blood temperature peak dropped from 56.5°C (no flow) to 47.5°C (0.08 ms^{-1} and above). A two-fold velocity increase above 0.08 ms^{-1} determined a 1% temperature decrease. We concluded that, in conditions of normal flow, where the pulmonary venous velocity is approximately double in late diastole (0.16 ± 0.09 ms^{-1}) (Meijburg et al., 1992), the AC-burst we use does not drive a temperature increase sufficient to elicit a thermal ablation (Haines, 1993; Dewhirst et al., 2003).

The electrothermal simulations of the atrial (**Figure 3A**) and ventricular (**Figure 3B**) ablations show the electric field sharply decreasing from the electrode surface. An electric field with enough strength to elicit irreversible electroporation in muscle (above 400 Vcm^{-1}) (Èoroviæ et al., 2010; Kaminska et al., 2012) is present in a 3 mm radius ca. from the electrode surface. This radius decreases to approximately 1.85 mm in the space between the electrodes (**Figure 3C**). In the ventricular model, in conditions of perfect alignment, the effective electric field radius was 5 mm from the electrode surfaces. This radius was slightly affected by the inspected alignment errors: we estimated an 8.8% coefficient of variation. The average electric field strength decreased significantly when the electrode pairs were misaligned and tilted (p = 0.044, **Figure 3D**). The untreated region was wider when the two electrodes were misaligned, irrespective of tilting – from 4 mm without misalignment to 8 mm ca (**Supplementary Table 2**).

The current density in all the models was higher in the blood pool, showing an asymmetric profile in the catheters' cross sections (**Figures 3C,D**). Correspondingly with the different electrode size, in the ventricular models the current density was higher at the diagnostic distal electrode. The temperature at the tissue-electrode interface was slightly over 40°C. In the ventricular models, this was higher at the diagnostic distal electrode interface. Some notable results from the simulations are shown in **Table 2**.

Tissue Changes

In two animals, we performed a follow-up electroanatomical mapping: we observed, both in the left atrium and ventricle, an increased area of low voltage, consistent with tissue remodeling after myocardial ablation. An example is shown in **Supplementary Figures 3A,B**. After euthanasia, the chest cavity inspections did not show visible collateral damage on the lungs, esophagus, or pericardium. After excision, the left atrium was closely examined: epicardial discoloration was noticed, in one case in full circular shape (**Figure 4A**); endocardial discoloration was reported close to the pulmonary vein ostia (**Figure 4B**).

The *ex vivo* magnetic resonance imaging showed localized tissue discoloration and darkened areas in the expected ablation targets. We scanned and segmented an age-matched untreated left atrium to confirm that atrial changes are not due to the physiological presence of epicardial fat or proximity of the mitral anulus (**Supplementary Figures 5A–F**). In the ventricular scans we observed two types of tissue changes: septal morphological changes, accompanied by discoloration, and left anterolateral darkening (**Supplementary Figures 6A–E**). Based on position and appearance, we measured the lesions dimensions and assigned the septal discolorations and darkening to AC-PFA, and the anterior-lateral darkening to RF ablations. The manual atrial segmentation (**Supplementary Figures 7A,B** and **Supplementary Video 2**) allowed us to estimate the amount of tissue affected in correspondence with the expected position of the loop catheter. A consistent part of the posterior wall in correspondence of the pulmonary veins presented the mentioned tissue changes, as well as localized areas in the lateral and anterior wall (**Figure 4C**), not observed in the control atrium (**Figure 4D**). The volumetric ratio of the non-myocardial tissue was 20.25 ± 4.40% for AC-PFA treated atria (N = 5, n = 40 slices/heart), versus 9.225 ± 6.175% in the healthy control (calculated across n = 40 slices), with p = 0.005 with one-sample t-test. After subtraction of the control non-myocardial tissue volume, the percentage of tissue volume ablated was 11.03 ± 4.41% (N = 5). Individual comparisons were also significant with respect to the control atrium (**Table 3**). The atrium-specific volume estimator showed that the ablated volume is 1.412 ± 0.672 times (N = 5) the internal volumetric reference. We could not confirm atrial tissue changes transmurality from T1-weighted MRI alone. For anatomical reference, the measured thickness across the atria myocardium is 5.85 ± 2.11 mm, with decreasing thickness on the posterior wall. On the few lesions that were isolated, the width was 22.98 ± 2.49 mm and the depth 5.41 ± 0.52 mm – superior to the numerically predicted effective electric field radius, probably as an effect of multiple pulses.

Via trichrome staining we confirmed that the darkened areas of corresponded to post-ablation fibrosis: we observed circular continuous lesions near the pulmonary vein ostia, and transmural lesions from smooth to trabeculated zones, in one heart (**Figure 4E**); the atrial control presented only connective tissue coloration in correspondence of the endocardial and epicardial lining (**Figure 4F**).

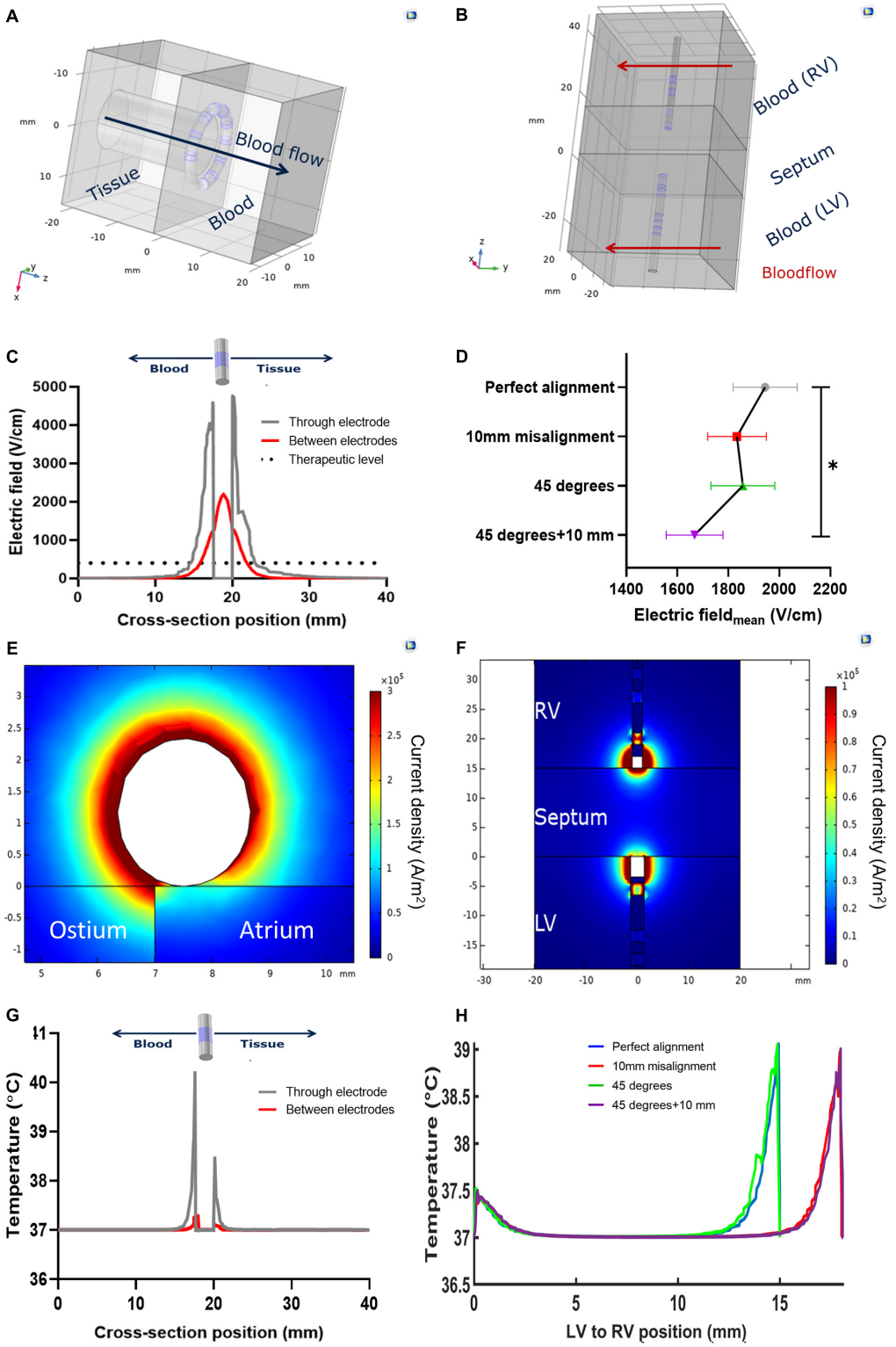

FIGURE 3 | Models and notable results of numerical simulations. **(A)** Geometry of the pulmonary vein ostium ablation; **(B)** Geometry of the interventricular septum ablation, with perfect alignment; **(C)** Electric field variation across the circular catheter used in the left atrium; **(D)** Average electric field across the interventricular septum, with respect to the relative linear misalignment or angular tilting (*$p < 0.05$); **(E)** current density profile in pulmonary vein ostium ablation; **(F)** current density profile in the interventricular septum ablation in perfect alignment; **(G)** Temperature profile across the circular catheter used in the left atrium; **(H)** temperature profile across the interventricular septum upon ablation, with respect to the relative linear misalignment or angular tilting.

TABLE 2 | Notable results of the electrothermal simulations.

Model	Voltage applied (V)	Electric field max (kV/cm)	Electric field mean (V/cm)	Current density mean (kA/m^2)	Current density max (kA/m^2)	Temperature max at the interface ($^\circ$C)
Atrial wall	900	5.19	0.95	47.32	361.52	40.11
Pulmonary vein ostium	900	2.19	0.48	40.37	317.55	40.19
Interventricular septum	1500	4.84	1.97	56.01	127.57	39.13

In the ventricles, transmural lesion across the septum could be found at the apical region, whereas isolated opposing lesions were observed as a result of application in more basal locations (**Figure 5B** and **Supplementary Video 3**). For reference, the measured septum thickness is 15.21 $\pm$ 4.27 mm, increasing toward the base. The lesions linear depth was 5.99 $\pm$ 0.75 mm, and the width 6.37 $\pm$ 0.62 mm, compatible with the numerically predicted effective radius, despite of misalignment and most probably due to multiple applications.

The trichrome staining confirmed that the observed discolorations were area of undergoing fibrosis, with mixed borders. A remarkable tissue shrinking was observed on transmural lesions (**Figure 5C**). Interestingly, isolated AC-burst ablation lesions could present a core of intact cardiomyocytes (**Figure 5D**). The core presents with jagged borders and fibrotic infiltration. No difference could be observed qualitatively between histology of RF lesion and AC-PFA ones (**Supplementary Figures 7C,D**).

DISCUSSION

PFA holds the promise to positively disrupt the field of catheter ablation of arrhythmia. This is due to its remarkable differences with respect to RF ablation, specifically: non-thermal nature; tissue specificity; cardiac muscle sensitivity; higher flexibility, speed and versatility. With its benefits, PFA comes with specific safety issues.

In our study, during the AC-PFA applications, we did not estimate a temperature increase able to produce damage. We have validated the non-thermal nature of our AC-burst with electrothermal simulations, finding that temperature increases in tissues are below the thermal damage threshold (Kolandaivelu et al., 2010) and were mitigated in the first tens of milliseconds – $4\tau_{tissue}$ = 36.88 ms – after energy delivery. This result is particularly important for atrial applications, were loop catheters with close electrodes imposed electric fields ten times the therapeutic threshold, without the need of irrigation. Accordingly, we did not observe the following issues: temperature increase in the esophagus during atrial applications; charring or clotting on the non-irrigated catheters; lesions on the esophagus during chest inspection. Our findings concur with dedicated animal studies that investigated how PFA does not cause esophageal damage upon direct or endovascularly proximal applications (Neven et al., 2017; Koruth et al., 2020).

Tissue specificity was not an investigative target or our study; nevertheless, we did obtain contained lesions and no observable peripheral damage to the pericardium, esophagus, or lungs. This feature of PFA was extensively investigated in animal models, specifically for coronary vessels (Neven et al., 2014), phrenic nerves (van Driel et al., 2015), and pulmonary veins (van Driel et al., 2014; Witt et al., 2018).

Cardiac muscle sensitivity has been demonstrated in several *in vitro*, *in vivo* (Sugrue et al., 2019), and in pilot clinical studies (Reddy et al., 2018). It represents, with tissue selectivity, the cornerstone of the potential success of PFA in clinical trials. We observed, in atria and ventricles, and efficient ablation by acute changes in electrograms amplitude and shapes, as reported in similar studies (DeSimone et al., 2014; Stewart et al., 2019). Ventricular potential changes in terms of and hyper/depolarization of the baseline were reported in studies characterizing unwanted electroporation during defibrillation (Nikolski and Efimov, 2005). We also report a significant elongation of local electrograms, which has the direct consequence to change the local refractory period of the tissue - although not clearly whether in the absolute or relative refractoriness, nevertheless without elicited atrial or ventricular arrhythmia in presence of amiodarone. After 4 weeks, we observed transmural scars formation both at the atria and the ventricular level. To our best knowledge, we are the first to report the use of purely AC bursts in the left atrium, and particularly in the ventricular endocardium with commercial catheters. A study similar to the one we presented compares the use of symmetrical and asymmetrical – which deeper lesions - biphasic high frequency pulses; several differences exist, among which the use an epicardial unipolar (electrode vs patch) approach (van Es et al., 2019b). We also provide a first use of 9.4T MRI to estimate the tissue changes 4 weeks after non-thermal cardiac ablation. Interestingly, the absence of clear transmural T1 contrast did not implicate the absence of transmural lesions. T1 signal in PFA lesions – which derive from a non-necrotic fibrosis - might be regionally and globally different from RFA ones, and more similar to myocardial signal. Also, due to the spatial gradient of the electric field, the lesion maturation state can differ between endocardial, midmyocardial, and epicardial layers after 4 weeks. Until anatomical contrast-enhanced MRI methods are validated, only histopathology can confirm the extent of chronic lesions after PFA.

The occasional surviving cardiomyocyte core appears preferentially oriented perpendicularly to the cutting plane. It is intriguing to think that the reason of such muscular residual derives from the changing relative angle between the electric field and the cardiac fibers across the septum (Buckberg, 2006). Previous studies demonstrated that in mouse skeletal muscle and ventricular cardiomyocytes the fiber orientation determines different electroporation and irreversible damage levels (Èoroviæ et al., 2010), especially at our employed scale (Semenov et al., 2018). Atrial lesions did

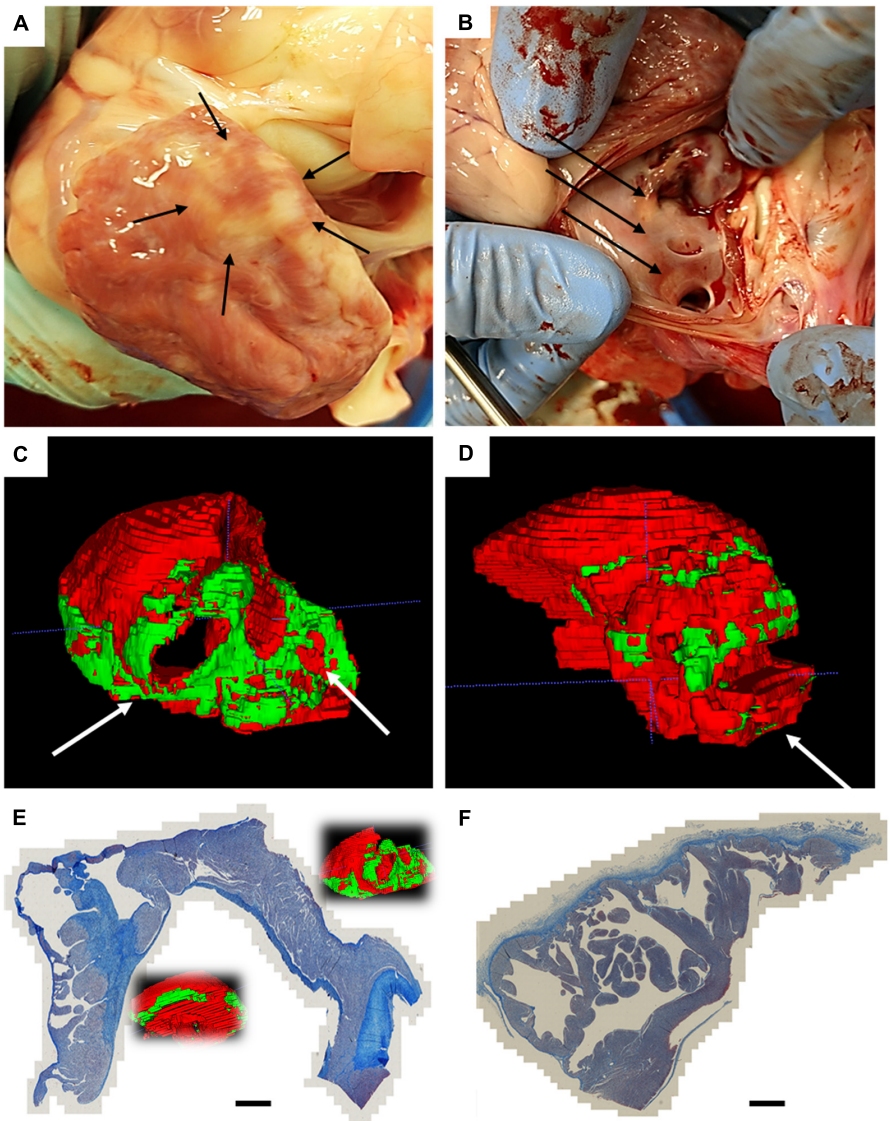

FIGURE 4 | Atrial findings at the end of follow-up. **(A)** Epicardial circular discoloration observed on the left atrium; **(B)** diffuse endocardial discoloration in proximity of the pulmonary veins; **(C)** Posterior view of the 3D rendering of the manual segmentation of normal myocardium (red) and non-myocardial tissue (green), with white arrows pointing at pulmonary vein ostia; **(D)** Posterior view of the 3D rendering of an age-matched non-ablated control, segmented with same criteria; **(E)** trichrome staining of left atrium which underwent AC pulsed electric field ablation, showing circular continuous and transmural lesions; **(F)** trichrome staining of age-matched non-ablated control. Scalebar is 3 mm.

TABLE 3 | Volumetric ratio of the non-myocardial tissue as calculated from manual segmentation of the 9.4T MRI atrial scans.

	AC-PFA#1	AC-PFA#2	AC-PFA#3	AC-PFA#4	AC-PFA#5	CTL
			Non-myocardial volume percentage			
Mean ± SD (%)	70.34 ± 21.98	78.49 ± 16.41	81.77 ± 12.17	82.71 ± 11.36	82.61 ± 12.40	90.77 ± 6.164
***p*-value vs. CTL**	<0.0001	0.0010	0.0075	0.0100	0.0158	NA

not present a different T1 signal or surviving cardiomyocytes in the observed area, but animal studies on intact rabbit hearts hinted that the atria might be more susceptible to electroporation (Fedorov et al., 2008). It is also possible that AC-PFA lesions might take more time to mature, compared to RF ones, due to the non-necrotic scar formation (Reddy et al., 2018).

Flexibility of PFA is demonstrated by the similar efficacy reported with the plethora of pulse features presented in the literature. New pulses or previously unreported applications

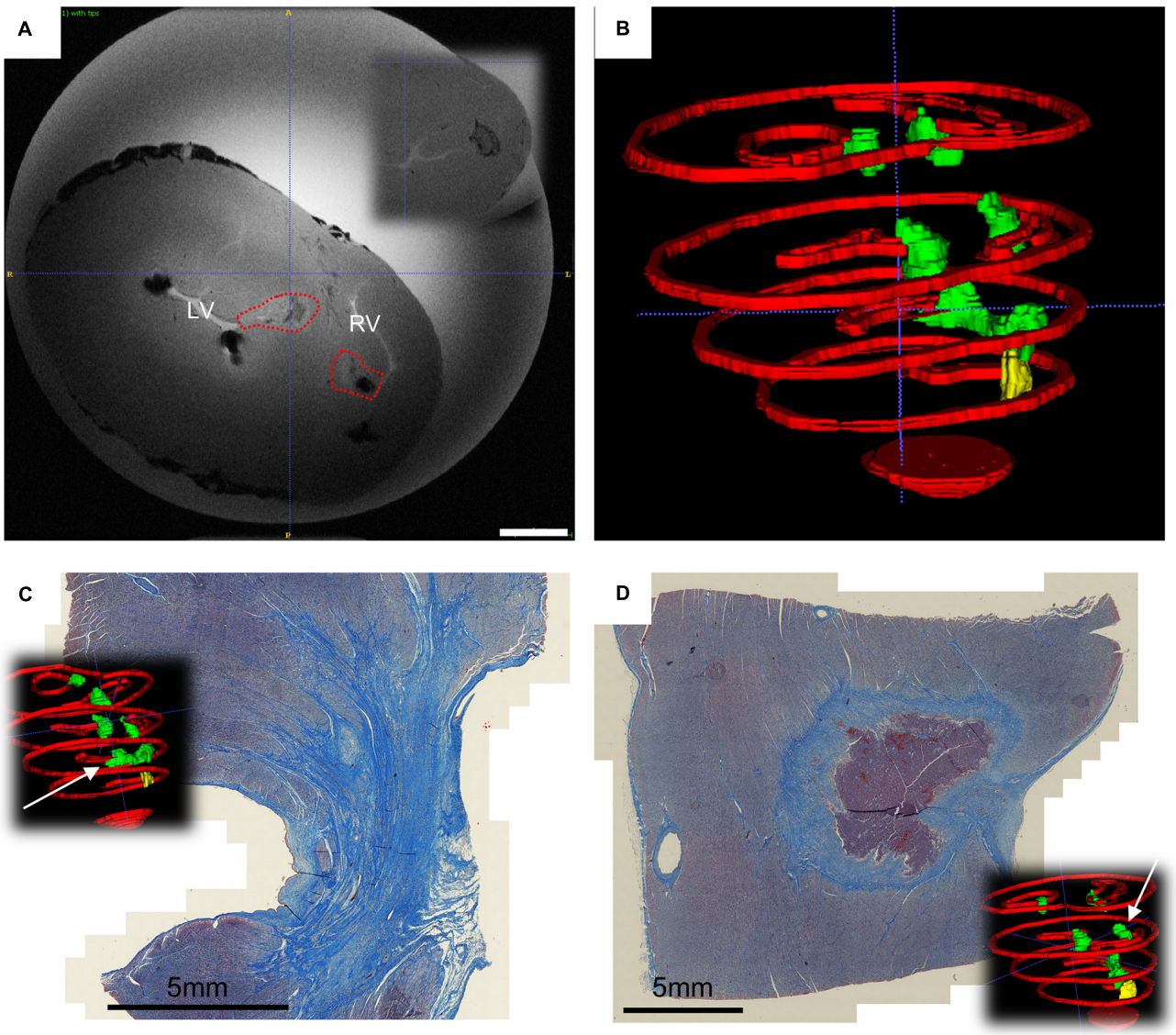

FIGURE 5 | Ventricular findings at the end of follow-up. **(A)** *Ex vivo* T1 axial scans with highlighted changes identified with AC pulsed field ablation lesions (red dotted lines) – in the inset it is visible a control RF ablation lesion. Scale bar is 10 mm; **(B)** Posterior view of the 3D rendering of ventricular myocardial perimeter (red), AC pulsed field ablation lesions (green) and RF ablation lesions (yellow); **(C)** trichrome staining of apical transmural lesions across the interventricular septum; **(D)** trichrome staining of basal isolated AC pulsed electric field ablation lesion, with intact core of cardiomyocytes.

need to be nevertheless accurately validated, primarily for feasibility and safety, as we presented for symmetrical AC-bursts in this work. Therapies are deliverable from the epicardium or endocardium, in unipolar and bipolar mode. Due to our generator compliance, and in order to prove the efficacy of AC-bursts in a relevant setting, we focused on the endocardial bipolar application. This approach guarantees a tight control on the imposable electric field.

The ablative treatment, with appropriate energy delivery and contact, can be delivered in one shock, but multiple shocks can produce irreversible electroporation effects even at subthreshold levels (Golberg and Rubinsky, 2010; Garcia et al., 2014). Our applications time was below 2 minutes overall and we opted for a multiple AC burst train which proved beneficial in the ventricular settings, were the simulations shows that the area below threshold is expectedly very much dependent on catheter relative placement.

We have presented how PFA methods, and in particular AC-PFA, can readily benefit from the existing catheter technologies: we employed commercially available catheters, in particular non-irrigated diagnostic circular ones, with good efficacy. Other groups, or companies, have presented their own dedicated catheter design (DeSimone et al., 2014; Neven et al., 2014; Reddy et al., 2018; Stewart et al., 2019), which is usually matched with a specific or proprietary PFA generator. The acquired experience within the bioengineering and medical communities led to the

overcoming of the initial issues with DC-PFA, such as arching, barotrauma and arrhythmia induction (Guandalini et al., 2019).

Short term safety is related to the effective ECG-gating to synchronize the PFA with the absolute refractory period. Failure to synchronize can potentially trigger lethal (Deodhar et al., 2011). Some PFA generators, like the NanoKnife (Angiodynamics) use an AccuSync R wave trigger (AccuSync MRC) that times the delivery after 50 ms from detection (Bertacchini et al., 2007). Our AC-PFA generator presents a similar lag, with maximum observed delay of 75 ms: this timing is suitable for energy delivery in the safe region of QT intervals ranges (Caluori et al., 2019; Colunga et al., 2019), without myocardial premature excitation. Interestingly, when an occasional synchronization failure occurred, due to ambient electronic noise on ECG leads, the AC-busts delivered on the T-wave did not elicit premature ventricular contractions. This might be due to the high frequency nature of the pulse. Overall, with adequate placement of a return electrode, we did not observe involuntary muscle twitching, but we reported occasional occurrence during single atrial applications.

Long-term safety is an open issue and might be related to electrolytic bubble formation upon DC-PFA applications. This can cause gas microemboli with consequent coronary occlusion, stroke or silent cerebral events. To our best knowledge, there is no systematic characterization of this phenomenon for therapies employing DC-PFA, with a notable exception for LifePak9 DC-pulses which are characterized *in vitro* (van Es et al., 2019a). In our experience, DC pulse trains of microseconds can also produce gas bubble stream (**Supplementary Video 4**). Therefore, we adopted an AC-burst delivery, which avoids or minimized this issue. Consequently, we did not observe gas bubble stream across the aortic valve, during a trial or ventricular application.

The study presents several limitations: (i) no energy titration was considered, and the generator settings were tuned to the maximum voltage available (ii) the follow-up was limited to 4 weeks and the scarring process (especially in the interventricular septum) might have been interrupted prematurely (iii) the employed circular catheter was selected by diameter for easy maneuverability, and not optimized to obtain an homogeneous electric field – aiming to create a continuous circular scar - along the pulmonary vein ostium (iv) part of the analysis is not blinded for lack of multiple grouping v) only one selected heart was used to fully characterize myocardial changes via both MRI and histology, compelling future works on AC_PFA with systematic histological quantification to test effectiveness and the anatomical relationship between MRI tissue pattern and ablation fibrosis.

CONCLUSION

We proved in this chronic animal study that AC-PFA is feasible and safe to induce electrical changes and selectively ablate atrial and ventricular myocardium, with no acute or short-term notable adverse effects. The results support further preclinical investigation of the proposed AC-PFA method with the purpose of atrial and ventricular therapies. The encouraging data on the presence of transmural lesions call for the systematic quantification of lesion formation and features – to estimate effectiveness – and titration of voltage/pulse number combination. For the first time, we proved the feasibility of AC-PFA in ventricular endocardial approaches, although the presence of survived cardiomyocytes constitutes an important warning, needing further characterization and dedicated optimization before therapeutic use.

DATA AVAILABILITY STATEMENT

The raw data supporting the conclusions of this article will be made available by the authors, without undue reservation.

ETHICS STATEMENT

The animal study was reviewed and approved by University of Veterinary and Pharmaceutical Sciences, Brno.

AUTHOR CONTRIBUTIONS

GC designed the study, co-designed the AC pulse generator, supervised the experiments, performed the analysis, interpreted the results, and drafted the manuscript. EO was responsible of the animal protocols, care and samples handling. TJ, MP, and LV assisted in the animal experiments. IP was responsible for the *ex vivo* magnetic resonance imaging. SH designed and performed the numerical simulations. VN and DC co-designed, fabricated and tested the AC pulse generator, and supervised the technical aspect of the animal experiments. VR, AH, and MC secured the use of histological and veterinary facilities. ZS secured funding, approved the animal protocols, the experimental design, and performed the ablation procedures. All authors participated in the manuscript revision.

FUNDING

The animal experiments, tissue analysis and MRI scans in this work were funded by the Ministry of Education, Youth and Sport of the Czech Republic (CZ.02.1.01/0.0/0.0/16_019/0000868 [ENOCH], LM2015062 [Czech-BioImaging], LQ1605 [FNUSA-ICRC from the National Program of Sustainability II] and CZ.1.05/1.1.00/02.0123 [OP VaVpI]). The presented technology and device development was funded by the Technology Agency of the Czech Republic [TG02010048 from the GAMA-H program] and the Brno University of Technology [FEKT-S-20-6379].

ACKNOWLEDGMENTS

The authors would like to thank Mrs. Katarina Marečková for her technical help in the immunohistochemical preparation of the samples, Mrs. Martina Jeřábková, Mr. Kamil Jaeger, MV Dr. Iva Trojanová, Ph.D., and MV Dr. Petr Raušer, Ph.D. for their technical support in animal care

and handling during the experiments. The DC-PFA generator mentioned and discussed in **Supplementary Video 2** was gently lent by MUDr. Tomáš Andrašina, Ph.D. This research work was carried out in the Centre for Research and Utilization of Renewable Energy (CVVOZE).

SUPPLEMENTARY MATERIAL

The Supplementary Material for this article can be found online at: https://www.frontiersin.org/articles/10.3389/fbioe.2020.552357/full#supplementary-material

REFERENCES

Arena, C. B., Sano, M. B., Rossmeisl, J. H., Caldwell, J. L., Garcia, P. A., Rylander, M. N., et al. (2011). High-frequency irreversible electroporation (H-Fire) for non-thermal ablation without muscle contraction. *Biomed.* Eng. 10: 102. doi: 10.1186/1475-925X-10-102

Bertacchini, C., Margotti, P. M., Bergamini, E., Lodi, A., Ronchetti, M., and Cadossi, R. (2007). Design of an irreversible electroporation system for clinical use. *Technol. Cancer Res. Treat.* 6, 313–320. doi: 10.1177/153303460700600408

Buckberg, G. D. (2006). The ventricular septum: the lion of right ventricular function, and its impact on right ventricular restoration. *Eur. J. Cardiothorac. Surg.* 29, S272–S278. doi: 10.1016/j.ejcts.2006.02.011

Caluori, G., Wojtaszczyk, A., Yasin, O., Pesl, M., Wolf, J., Belaskova, S., et al. (2019). Comparing the incidence of ventricular arrhythmias during epicardial ablation in swine versus canine models. *Pac. Clin. Electrophysiol.* 42, 862–867. doi: 10.1111/pace.13698

Colunga, S., Padrón, R., García-Iglesias, D., Rubín, J. M., Pérez, D., Del Valle, R., et al. (2019). The QT interval dynamic in a human experimental model of controlled heart rate and QRS widening. *J. Clin. Med.* 8:jcm8091417. doi: 10.3390/jcm8091417

Èoroviæ, S., Županiè, A., Kranjc, S., Al Sakere, B., Leroy-Willig, A., Mir, L. M., et al. (2010). The influence of skeletal muscle anisotropy on electroporation: in vivo study and numerical modeling. *Med. Biol. Eng. Comput.* 48, 637–648. doi: 10.1007/s11517-010-0614-611

Davalos, R. V., Mir, L. M., and Rubinsky, B. (2005). Tissue ablation with irreversible electroporation. *Ann. Biomed. Eng.* 33:223. doi: 10.1007/s10439-005-8981-8988

Deodhar, A., Dickfeld, T., Single, G. W., Hamilton, W. C., Thornton, R. H., Sofocleous, C. T., et al. (2011). Irreversible electroporation near the heart: ventricular arrhythmias can be prevented with ECG synchronization. *Am. J. Roentgenol.* 196, W330–W335. doi: 10.2214/AJR.10.4490

DeSimone, C. V., Ebrille, E., Syed, F. F., Mikell, S. B., Suddendorf, S. H., Wahnschaffe, D., et al. (2014). Novel balloon catheter device with pacing, ablating, electroporation, and drug-eluting capabilities for atrial fibrillation treatment–preliminary efficacy and safety studies in a canine model. *Transl. Res.* 164, 508–514. doi: 10.1016/j.trsl.2014.07.002

Dewhirst, M. W., Viglianti, B. L., Lora-Michiels, M., Hoopes, P. J., and Hanson, M. (2003). Thermal dose requirement for tissue effect: experimental and clinical findings. *Proc. SPIE Int. Soc. Opt. Eng.* 4954:37. doi: 10.1117/12.476637

Fedorov, V. V., Kostecki, G., Hemphill, M., and Efimov, I. R. (2008). Atria are more susceptible to electroporation than ventricles: implications for atrial stunning, shock-induced arrhythmia and defibrillation failure. *Heart Rhythm.* 5, 593–604. doi: 10.1016/j.hrthm.2008.01.026

Garcia, P. A., Davalos, R. V., and Miklavcic, D. (2014). A numerical investigation of the electric and thermal cell kill distributions in electroporation-based therapies in tissue. *PLoS One* 9:e103083. doi: 10.1371/journal.pone.0103083

Golberg, A., and Rubinsky, B. (2010). A statistical model for multidimensional irreversible electroporation cell death in tissue. *Biomed. Eng.* 9:13. doi: 10.1186/1475-925X-9-13

Guandalini, G. S., Liang, J. J., and Marchlinski, F. E. (2019). Ventricular tachycardia ablation: past, present, and future perspectives. *JACC Clin. Electrophysiol.* 5, 1363–1383. doi: 10.1016/j.jacep.2019.09.015

Haines, D. E. (1993). The biophysics of radiofrequency catheter ablation in the heart: the importance of temperature monitoring. *Pac. Clin. Electrophysiol.* 16, 586–591. doi: 10.1111/j.1540-8159.1993.tb01630.x

Jež, J., Caluori, G., Jadczyk, T., Lehar, F., Pešl, M., Kulík, T., et al. (2019). Remotely navigated ablations in ventricle myocardium result in acute lesion size comparable to force-sensing manual navigation. *Circ. Arrhythm. Electrophysiol.* 12:e007644. doi: 10.1161/CIRCEP.119.007644

Kaminska, I., Kotulska, M., Stecka, A., Saczko, J., Drag-Zalesinska, M., Wysocka, T., et al. (2012). Electroporation-induced changes in normal immature rat myoblasts (H9C2). *Gen. Physiol. Biophys.* 31, 19–25. doi: 10.4149/gpb_2012_003

Kolandaivelu, A., Zviman, M. M., Castro, V., Lardo, A. C., Berger, R. D., and Halperin, H. R. (2010). Noninvasive assessment of tissue heating during cardiac radiofrequency ablation using MRI thermography. *Circ. Arrhythm. Electrophysiol.* 3, 521–529. doi: 10.1161/CIRCEP.110.942433

Koruth, J. S., Kuroki, K., Kawamura, I., Brose, R., Viswanathan, R., Buck, E. D., et al. (2020). Pulsed field ablation versus radiofrequency ablation. *Circ. Arrhythm. Electrophysiol.* 13:e008303. doi: 10.1161/CIRCEP.119.008303

Meijburg, H. W. J., Visser, C. A., Westerhof, P. W., Kasteleyn, I., van der Tweel, I., and Robles de Medina, E. O. (1992). Normal pulmonary venous flow characteristics as assessed by transesophageal pulsed doppler echocardiography. *J. Am. Soc. Echocardiogr.* 5, 588–597. doi: 10.1016/S0894-7317(14)80324-80326

Meir, A., and Rubinsky, B. (2014). Alternating electric field capacitively coupled micro-electroporation. *RSC Adv.* 4, 54603–54613. doi: 10.1039/C4RA09054C

Mercadal, B., Arena, C. B., Davalos, R. V., and Ivorra, A. (2017). Avoiding nerve stimulation in irreversible electroporation: a numerical modeling study. *Phys. Med. Biol.* 62, 8060–8079. doi: 10.1088/1361-6560/aa8c53

Miklavčič, D. (2018). Cardiac ablation by electroporation. *J. Am. Coll. Cardiol. EP* 4, 1481–1482. doi: 10.1016/j.jacep.2018.09.014

Neven, K., van Driel, V., van Wessel, H., van Es, R., du Pré, B., Doevendans, P. A., et al. (2014). Safety and feasibility of closed chest epicardial catheter ablation using electroporation. *Circ. Arrhythm. Electrophysiol.* 7, 913–919. doi: 10.1161/CIRCEP.114.001607

Neven, K., van Es, R., van Driel, V., van Wessel, H., Fidder, H., Vink, A., et al. (2017). Acute and long-term effects of full-power electroporation ablation directly on the porcine esophagus. *Circ. Arrhythm. Electrophysiol.* 10:e004672. doi: 10.1161/CIRCEP.116.004672

Nikolski, V. P., and Efimov, I. R. (2005). Electroporation of the heart. *Europace* 7, S146–S154. doi: 10.1016/j.eupc.2005.04.011

Polajžer, T., Dermol-Èerne, J., Reberšek, M., O'Connor, R., and Miklavèiè, D. (2020). Cancellation effect is present in high-frequency reversible and irreversible electroporation. *Bioelectrochemistry* 132:107442. doi: 10.1016/j.bioelechem.2019.107442

Ramirez, F. D., Reddy, V. Y., Viswanathan, R., Hocini, M., and Jaïs, P. (2020). Emerging technologies for pulmonary vein isolation. *Circ. Res.* 127, 170–183. doi: 10.1161/CIRCRESAHA.120.316402

Reddy, V. Y., Koruth, J., Jais, P., Petru, J., Timko, F., Skalsky, I., et al. (2018). Ablation of atrial fibrillation with pulsed electric fields: an ultra-rapid, tissue-selective modality for cardiac ablation. *JACC Clin. Electrophysiol.* 4, 987–995. doi: 10.1016/j.jacep.2018.04.005

Reddy, V. Y., Neuzil, P., Koruth, J. S., Petru, J., Funosako, M., Cochet, H., et al. (2019). Pulsed field ablation for pulmonary vein isolation in atrial fibrillation. *J. Am. Coll. Cardiol.* 74, 315–326. doi: 10.1016/j.jacc.2019.04.021

Rueden, C. T., Schindelin, J., Hiner, M. C., DeZonia, B. E., Walter, A. E., Arena, E. T., et al. (2017). ImageJ2: imageJ for the next generation of scientific image data. *BMC Bioinform.* 18:529. doi: 10.1186/s12859-017-1934-z

Semenov, I., Grigoryev, S., Neuber, J. U., Zemlin, C. W., Pakhomova, O. N., Casciola, M., et al. (2018). Excitation and injury of adult ventricular cardiomyocytes by nano- to millisecond electric shocks. *Sci. Rep.* 8:8233. doi: 10.1038/s41598-018-26521-26522

Soucek, F., Caluori, G., Lehar, F., Jez, J., Pesl, M., Wolf, J., et al. (2020). Bipolar ablation with contact force-sensing of swine ventricles shows improved acute lesion features compared to sequential unipolar ablation. *J. Cardiovasc. Electrophysiol.* 31, 1128–1136. doi: 10.1111/jce.14407

Stewart, M. T., Haines, D. E., Verma, A., Kirchhof, N., Barka, N., Grassl, E., et al. (2019). Intracardiac pulsed field ablation: proof of

feasibility in a chronic porcine model. *Heart Rhythm.* 16, 754–764. doi: 10.1016/j.hrthm.2018.10.030

Sugrue, A., Maor, E., Ivorra, A., Vaidya, V., Witt, C., Kapa, S., et al. (2018). Irreversible electroporation for the treatment of cardiac arrhythmias. *Expert Rev. Cardiovasc. Therapy* 16, 349–360. doi: 10.1080/14779072.2018.1459185

Sugrue, A., Vaidya, V., Witt, C., DeSimone, C. V., Yasin, O., Maor, E., et al. (2019). Irreversible electroporation for catheter-based cardiac ablation: a systematic review of the preclinical experience. *J. Intervent. Cardiac. Electrophysiol.* 55, 251–265. doi: 10.1007/s10840-019-00574-573

van Driel, V. J. H. M., Neven, K., van Wessel, H., Vink, A., Doevendans, P. A. F. M., and Wittkampf, F. H. M. (2015). Low vulnerability of the right phrenic nerve to electroporation ablation. *Heart Rhythm.* 12, 1838–1844. doi: 10.1016/j.hrthm.2015.05.012

van Driel, V. J. H. M., Neven, K. G. E. J., van Wessel, H., du Pré, B. C., Vink, A., Doevendans, P. A. F. M., et al. (2014). Pulmonary vein stenosis after catheter ablation: electroporation versus radiofrequency. *Circ. Arrhythm. Electrophysiol.* 7, 734–738. doi: 10.1161/CIRCEP.113.001111

van Es, R., Groen, M. H. A., Stehouwer, M., Doevendans, P. A., Wittkampf, F. H. M., and Neven, K. (2019a). In vitro analysis of the origin and characteristics of gaseous microemboli during catheter electroporation ablation. *J. Cardiovasc. Electrophysiol.* 30, 2071–2079. doi: 10.1111/jce.14091

van Es, R., Konings, M. K., Du Pré, B. C., Neven, K., van Wessel, H., van Driel, V. J. H. M., et al. (2019b). High-frequency irreversible electroporation for cardiac ablation using an asymmetrical waveform. *Biomed. Eng.* 18:75. doi: 10.1186/s12938-019-0693-697

Witt, C. M., Sugrue, A., Padmanabhan, D., Vaidya, V., Gruba, S., Rohl, J., et al. (2018). Intrapulmonary vein ablation without Stenosis: a novel balloon-based direct current electroporation approach. *J. Am. Heart Assoc.* 7:e009575. doi: 10.1161/JAHA.118.009575

Wittkampf, F. H. M., van Es, R., and Neven, K. (2018). Electroporation and its relevance for cardiac catheter ablation. *JACC Clin. Electrophysiol.* 4, 977–986. doi: 10.1016/j.jacep.2018.06.005

Wojtaszczyk, A., Caluori, G., Pešl, M., Melajova, K., and Stárek, Z. (2018). Irreversible electroporation ablation for atrial fibrillation. *J. Cardiovasc. Electrophysiol.* 29, 643–651. doi: 10.1111/jce.13454

Yushkevich, P. A., Piven, J., Hazlett, H. C., Smith, R. G., Ho, S., Gee, J. C., et al. (2006). User-guided 3D active contour segmentation of anatomical structures: significantly improved efficiency and reliability. *Neuroimage* 31, 1116–1128. doi: 10.1016/j.neuroimage.2006.01.015

Conflict of Interest: SH was employed by BIOTRONIK SE & Co. KG.

The remaining authors declare that the research was conducted in the absence of any commercial or financial relationships that could be construed as a potential conflict of interest.

Copyright © 2020 Caluori, Odehnalova, Jadczyk, Pesl, Pavlova, Valikova, Holzinger, Novotna, Rotrekl, Hampl, Crha, Cervinka and Starek. This is an open-access article distributed under the terms of the Creative Commons Attribution License (CC BY). The use, distribution or reproduction in other forums is permitted, provided the original author(s) and the copyright owner(s) are credited and that the original publication in this journal is cited, in accordance with accepted academic practice. No use, distribution or reproduction is permitted which does not comply with these terms.

frontiers in Bioengineering and Biotechnology

ORIGINAL RESEARCH
published: 15 December 2020
doi: 10.3389/fbioe.2020.552335

Extraction of Proteins and Other Intracellular Bioactive Compounds From Baker's Yeasts by Pulsed Electric Field Treatment

Valentina Ganeva, Boyana Angelova, Bojidar Galutzov, Vasilij Goltsev and Miroslava Zhiponova*

Biological Faculty, Sofia University "St. Kl. Ohridski", Sofia, Bulgaria

Yeasts are rich source of proteins, antioxidants, vitamins, and other bioactive compounds. The main drawback in their utilization as valuable ingredients in functional foods and dietary supplements production is the thick, indigestible cell wall, as well as the high nucleic acid content. In this study, we evaluated the feasibility of pulsed electric field (PEF) treatment as an alternative method for extraction of proteins and other bioactive intracellular compounds from yeasts. Baker's yeast water suspensions with different concentration (12.5–85 g dry cell weight per liter) were treated with monopolar rectangular pulses using a continuous flow system. The PEF energy required to achieve irreversible electropermeabilization was significantly reduced with the increase of the biomass concentration. Upon incubation of the permeabilized cells in water, only relatively small intracellular compounds were released. Release of 90% of the free amino acids and low molecular UV absorbing compounds, 80% of the glutathione, and ∼40% of the total phenol content was achieved about 2 h after pulsation and incubation of the suspensions at room temperature. At these conditions, the macromolecules (proteins and nucleic acids) were retained largely inside. Efficient protein release (∼90% from the total soluble protein) occurred only after dilution and incubation of the permeabilized cells in buffer with pH 8–9. Protein concentrates obtained by ultrafiltration (10 kDa cut off) had lower nucleic acid content (protein/nucleic acid ratio ∼100/4.5) in comparison with cell lysates obtained by mechanical disintegration. The obtained results allowed to conclude that PEF treatment can be used as an efficient alternative approach for production of yeast extracts with different composition, suitable for application in food, cosmetics and pharmaceutical industries.

Keywords: pulsed electric field treatment, flow system, baker's yeast, extraction, protein, bioactive compounds

OPEN ACCESS

Edited by:
Eugene Vorobiev, University of Technology Compiegne, France

Reviewed by:
Gianpiero Pataro, University of Salerno, Italy
Mohamed Koubaa, École Supérieure de Chimie Organique et Minérale, France

****Correspondence:***
Valentina Ganeva
valentinaganeva@abv.bg;
vganeva@biofac.uni-sofia.bg

Specialty section:
This article was submitted to Bioprocess Engineering, a section of the journal Frontiers in Bioengineering and Biotechnology

Received: *15 April 2020*
Accepted: *23 November 2020*
Published: *15 December 2020*

Citation:
Ganeva V, Angelova B, Galutzov B, Goltsev V and Zhiponova M (2020) Extraction of Proteins and Other Intracellular Bioactive Compounds From Baker's Yeasts by Pulsed Electric Field Treatment. Front. Bioeng. Biotechnol. 8:552335. doi: 10.3389/fbioe.2020.552335

INTRODUCTION

Baker's yeast is currently the most distributed commercial yeast worldwide. It consists of one or several selected strains of *Saccharomyces cerevisiae*, which are able to develop very fast and give high biomass quantities. The primary raw material utilized for their cultivation is molasses, a by-product of the refining of sugar beets and sugar cane, which makes their production on industrial scale very cost effective (Pérez-Torrado et al., 2015).

Besides its principal use as a leavening agent in baking and in other traditional fermentation processes, such as wine and beer making, *S. cerevisiae* which has GRAS (Generally recognized for safe) status has found a variety of applications in agriculture, food, cosmetics, and pharmaceutical industries (Pérez-Torrado et al., 2015; Żymańczyk-Duda et al., 2017).

Yeast are a rich source of proteins with a high level of many of the essential amino acids. *S. cerevisiae* is among the most widely used microorganisms for production of Single Cell Protein for animal feed and human diet (Halász and Lásztity, 1991; Bekatorou et al., 2006). Due to its high content of vitamins, minerals, antioxidants, and other bioactive compounds, the yeast biomass is used in different preparations as health supplements and natural flavor compounds for food industry and as additives for the cosmetic industry (Abbas, 2006).

Today, *S. cerevisiae* is one of the main microorganisms for fermentative production of glutathione for food and pharmaceutical industries (Li et al., 2004). The yeast is also an important source of β-glucans, many industrial enzymes and metabolites (Żymańczyk-Duda et al., 2017).

The yeast biomass can be used in different ways—as whole cells after inactivation by heating (inactive dry yeast), as autolysates and hydrolysates, or after extraction, fractionation, and purification of the valuable intracellular compounds (Halász and Lásztity, 1991; Bekatorou et al., 2006).

S. cerevisiae, in the form of inactivated whole cells, is used nowadays mainly as a protein supplement in animal feeding. Despite the high content of protein and other bioactive substances, there are two main factors, which restrict the use of whole cells in a human diet. The yeast has a very rigid, indigestible cell wall, which decreases the bioavailability of the intracellular compounds and can provoke allergies and gastrointestinal disorders (Kinsella and Shetty, 1978). The other serious limitation is the high nucleic acid (NA) content, which for yeast is in the range of 10–15% on dry cell bases (Halász and Lásztity, 1991; Nasseri et al., 2011). Human body lacks the enzyme uricase meaning that purine metabolism leads to the production of uric acid in humans. Overproduction of uric acid plays an emerging role in many human diseases (Maiuolo et al., 2016). Therefore, the utilization of yeast protein for human consumption requires destruction of the cell wall and significant reduction of the NA contents.

S. cerevisiae is the main starting material for production of yeast extracts with different composition. Currently at the industrial level there are two main methods for production of yeast extracts: (a) by autolysis, i.e. digestion of the cell wall components and the intracellular macromolecules by endogenous enzymes, a process which can be further optimized by addition of exogenous enzymes and chemical treatment; (b) by mechanical disintegration (Halász and Lásztity, 1991; Nasseri et al., 2011; Jacob et al., 2019). Yeast autolysates are used mainly as a component of microbial culture media while in the food industry they are added as a flavoring agent in many foods at 0.5–2% content. Mechanical disintegration is applied as a first step for production of polysaccharides (β-glucan) from yeast and is also the main method for extraction of proteins, antioxidants and other soluble intracellular products from yeast (Middelberg, 2012; Bzduhcha-Wróbel et al., 2014). Despite being routinely applied in biotechnology, mechanical disintegration leads to non-selective release of the product, increase in the viscosity, and micronization of the cell debris, which complicates the liquid–solid separation and the following downstream processing (Balasundaram et al., 2009). On the other hand, when the yeast derived compounds are intended for use in the food, cosmetics or pharmaceutical industry, multiple steps of purification are needed in order to obtain an odorless, tasteless, and colorless product which furthermore does not contain potentially harmful substances. In this case, a more selective and mild extraction procedure can simplify the production process and make it less expensive and time consuming.

During the last few years many data have been accumulated on the application of pulsed electric field (PEF) treatment as an alternative, non-thermal method for extraction of bioactive compounds from microorganisms and plant tissues (Lebovka et al., 2005; Golberg et al., 2016; Postma et al., 2016). The electrical treatment provokes plasma membrane permeabilization known as electropermeabilization or electroporation, which is associated with the induction of an additional transmembrane potential (Rols and Teissie, 1990; Weaver and Chizmadzhev, 1996). Depending on the electrical parameters, the cell characteristics (size, age, and shape), the pulsing media composition etc., the loss of the membrane integrity can be reversible or irreversible. The electropermeabilization is associated with a leakage of many soluble intracellular compounds. The extraction efficiency depends on the fraction of the irreversibly permeabilized cells and in case of macromolecules such as proteins and NA can vary greatly in dependence of the cell wall structure and the conditions of the post-pulse incubation (Ganeva et al., 2003; Shynkaryk et al., 2009; Liu et al., 2012; Goettel et al., 2013; Coustets et al., 2015).

It has been shown recently, that irreversible electropermeabilization by using a continuous flow system followed by an incubation of the cells in buffer with a pH 7–7.5 led to massive release of native intracellular enzymes from different yeast species (Ganeva et al., 2003, 2014). At these conditions, a release of about 40–50% from the total soluble protein was observed, depending on the species and cell growth phase.

In the present study, we evaluated the feasibility of PEF treatment applied in a flow mode as an alternative method for extraction of protein and low molecular weight biologically active compounds from fresh baker's yeast.

MATERIALS AND METHODS

Materials

2,2′-bis(3-ethylbenzthiazoline-6-sulfonic acid) diammonium salt (ABTS) and dithiothreitol (DTT) were purchased from GERBU (Germany). Propidium iodide (PI), lyticase, reduced L-glutathione and glass beads were purchased from Sigma-Aldrich (Germany), other chemicals were bought from AppliChem (Germany).

Yeast Strain

The experiments were performed with commercial fresh baker's yeast (VIVO, Lesaffre Magyarország). The cells were washed once, resuspended in distilled water and incubated for 1 h. Next, the suspension was centrifuged, and the cells were diluted in distilled water to final concentrations corresponding to 12.5–85 g dry cell weight per liter (gDCW L^{-1}). The suspensions conductivity was adjusted to 150 ± 5 μS cm^{-1} with 0.2 M KCl.

Pulsed Electric Field (PEF) Treatment

The electric field treatment in a continuous-flow chamber was performed with a generator of monopolar rectangular pulses (2300V-10A), a Hydropuls mini specially fabricated GBS-Elektronik (Germany). The pulse duration and frequency were regulated by an arbitrary waveform generator RIGOL DG1012 (China). The chambers (0.3 and 0.5 mL volume) have two parallel stainless steel electrodes that are 0.3 and, respectively, 0.4 cm apart, specially manufactured by MEHEL (Bulgaria). The PEF treatment was performed at flow rates of 9, 27, and 130 mL min^{-1}, controlled by a peristaltic pump. During the passage through the chamber, the cells received a train of pulses with a duration of 0.8 or 0.5 ms and electric field strength range of 2.5–5.5 kV cm^{-1} (**Table 1**). The total treatment time (t) was defined as the number of pulses (n) multiplied by the single pulse duration (τ):

$$t = n \cdot \tau \quad (1)$$

All pulsing parameters were monitored online with an Instek GDS 2064 oscilloscope (Taiwan). Schematic representation of the experimental setup used for PEF treatment is included as **Supplementary Material 1**.

The specific treatment energy per liter of cell suspension (W_{sus}, kJ L^{-1}) was then calculated by dividing the average power associated to the train of pulses (P_{avg}, W) by the flow rate [Φ (L s^{-1})] (Lindgren et al., 2002):

$$W_{sus} = \frac{P_{avg}}{\Phi} = \frac{U \cdot I \cdot \tau \cdot f}{\Phi} \quad (2)$$

where U is the applied voltage (V), I is the current (A), τ is the single pulse duration (s), and f is the pulse frequency (Hz).

The inlet temperature of the suspensions was 23–24°C. The outlet temperature was registered by a K-type thermocouple connected to a digital thermometer, and the sensor was attached to the end of the tubing. After pulsation, the suspensions were incubated at room temperature or alternatively were diluted in potassium phosphate buffer (PPB) to final concentration of 167 mM and incubated at room temperature. Samples were taken at various times after pulsation and centrifuged for 2 min at 10,750×g in an Eppendorf centrifuge or for 10 min at 2,000×g (ROTINA 380). The supernatants were kept at 4°C until further analysis.

TABLE 1 | PEF treatment conditions.

Pulsing chamber (mL)	Flow rate (mL min^{-1})	Pulse number	Pulse duration (ms)	Pulse freqency (Hz)	Cell concentration (gDCW L^{-1})
0.3	9	15	0.8	7.5	12.5–85
0.5	27	19	0.5	17.1	66
	130	19	0.5	82.3	66

Determination of Irreversible Electropermeabilization

The membrane permeabilization was assayed by loading the cells with PI. To determine the fraction of cells with irreversibly permeabilized membranes, 5 μL of 0.5 mM solution of PI in distilled water were added to 50 μL cell suspension 1 h after pulsation of the cells. The number of fluorescent cells was counted under an epifluorescent microscope (L3201 LED, Microscopesmall, China). The permeabilization was expressed as a percentage of the number of fluorescent cells relative to the total cell number.

Preparation of the Cell Lysate

At first, 1 mL water suspension of control, untreated cell was mixed with an equal volume of glass beads (diameter 0.42–0.6 mm, Sigma) and vortexed 8 times for 1 min each, with 15 s pause intervals with ice incubation, respectively. The resulting lysate was centrifuged at 10,750×g for 5 min, and the supernatant was kept at 4°C until used for amino acid, total antioxidant activity, glutathione and total phenol content analyses.

Secondly, control yeast cells diluted in PPB to the same concentration as electrically treated cells, were mixed with an equal volume of glass beads and vortexed 8 times for 1 min each, with 30 s pause intervals with ice incubation, respectively.

This procedure led to about 99% cell lysis, as determined by counting the cells in a Thoma chamber.

Lyticase Test

To detect electroinduced changes in the cell wall porosity, pulsed and untreated, control cell suspensions were diluted in PPB pH 7.5 (167 mM final concentration) to 10 mgDCW mL^{-1}. To this suspension, lyticase was added to final concentration of 60 U mL^{-1} and the suspensions were incubated at 30°C. At different intervals, samples were added to 1,000 μL of distilled water, and the optical density (OD) at 660 nm was determined. A decrease of the OD directly reflects the degree of cell lysis. OD values measured at different intervals after enzyme addition were expressed as percentages and were plotted against time. The OD of the sample before enzyme addition was 100%.

Determination of the Release of UV Absorbing Substances From Electropermeabilized Cells

Cell suspensions (66 gDCW L^{-1}) were treated at a flow rate of 27 mL min^{-1} in pulsing chamber with 0.5 mL volume with 19 pulses of 0.5 ms duration (total treatment time of 9.5 ms). The field strength was set at 3 kV cm^{-1}. Samples of 0.5 mL were taken at various times after pulsation and centrifuged for 2 min at 10,750×g in an Eppendorf centrifuge. Next, 20 μL of the supernatants were mixed with 980 μL distilled water

and the absorbance at 260 nm was read by using UV/VIS spectrophometer BOECO.

Analytical Methods

Total protein content was determined according to Bradford (1976) with bovine serum albumin as a standard. Free amino acids were determined with Ninhydrin method according to Lamoolphak et al. (2006) with leucine as a standard, the total purine content was determined according to Loring et al. (1952) and the NA according to Spirin (1958). The alcohol dehydrogenase activity (ADH) was determined according to Scopes et al. (1981).

Total antioxidant activity was determined by TEAC (Trolox equivalent antioxidant capacity) assay as described by Pellegrini et al. (2003) with slight modifications. The $ABTS^+$ stock solution (7 mM aqueous solution of ABTS with 2.45 mM potassium persulfate) was diluted with 50 mM PPB, pH 7 to the absorbance of 0.70 ± 0.02 at 734 nm. The samples (10 μL) of fivefold diluted water extracts were mixed with 990 μL of working solution. The decrease of the absorbance at 734 nm was measured after 15 min. The Trolox standard curve was determined in the range of 0.1–15 μM. The data are expressed as mg Trolox Equivalent per gram of cell dry weight—mgTE $gDCW^{-1}$.

The reduced form of glutathione (GSH) was determined by the colorimetric method with 5,5′-dithiobis-(2-nitrobenzoic acid), DTNB according to Rahman et al. (2006) with modifications. Briefly, 20 μL of 0.4% solution of DTNB in 0.1 M PPB pH 7.5, 5 mM EDTA were added to 960 μL of the same buffer. Afterward, 20 μL samples (supernatant of electrically treated and control cell suspensions, soluble fraction of the cell lysate obtained after mechanical disintegration) were added and the suspensions were incubated for 2–10 min at room temperature. The absorbance at 412 nm in triplicates was measured and the concentration of GSH was obtained from a standard curve using reduced L-glutathione.

The total phenolic content was determined according to Singleton et al. (1999) with modifications. Test samples contained 0.1 mL supernatant of electrically treated and control cell suspensions or cell lysate, 1.5 mL Folin-Ciocalteau reagent (previously diluted 10 times in distilled water), 1.4 mL 7.5% Na_2CO_3. The samples were incubated at dark, at room temperature for 30 min. The absorbance was measured at 765 nm by spectrophotometer Shimadzu UV 1800. Standard curve, made with known concentrations of gallic acid (GA), was used to calculate the quantity of phenolic compounds as gallic acid equivalents per fresh weight (mg gallic acid g^{-1} FW).

The yeast biomass was measured as dry weight using an infrared moisture analyzer method according to Li and Mira de Orduña (2010).

Statistics

The results from three to six independent experiments are shown as a mean value ± SD. The Student *t*-test was applied for statistical evaluation. Differences were considered significant if $P < 0.05$.

RESULTS AND DISCUSSION

Electroinduced Extraction of Protein

Influence of Medium pH on the Protein Release Efficiency

As shown earlier with other yeast systems, significant release of intracellular proteins occurs only under electrical conditions leading to irreversible plasma membrane damage, i.e., irreversible electropermeabilization (Ganeva et al., 2003, 2015).

In this study, to obtain a suitable combination of electrical parameters, the suspensions with a biomass concentration corresponding to 37.5 gDCW L^{-1} were subjected to 15 pulses of 0.8 ms duration with 7.5 Hz frequency at a flow rate of 9 mL min^{-1}. The electrical treatment was performed in a continuous flow chamber with a volume of 0.3 mL. Optimization of the electropulsation protocol was performed by varying the field strength in the range of 2–4 kV cm^{-1}. The degree of irreversible permeabilization was determined by loading the cells with PI.

We found that irreversible permeabilization of 99–100% of the cells is reached at 3.3 kV cm^{-1}. Therefore, to evaluate the effect of the pH on the protein release efficiency, the cells were permeabilized at this field strength. After electrical treatment, the cell suspensions were diluted in potassium phosphate buffer (PPB) with pH 5–9 to final cell concentration of 12.5 gDCW L^{-1} (final buffer concentration 167 mM). DTT was added to a final concentration of 2 mM and the suspensions were incubated for 16 h at room temperature (24°C). Next, the cells were removed by centrifugation and the protein concentration in the supernatant of pulsed cells was determined as described in section "Materials and Methods."

According to Sergeev et al. (1984), the pH of the medium has a significant impact on the protein extractability from mechanically disintegrated yeast cells. In their study, the lowest extraction efficiency (30% from total) was observed at pH 4–5, while maximal yield was reached in a medium with a pH 8.5–12 when the yield increase reaches an approximate plateau above pH 9.

In our hands, maximal yield of soluble protein after mechanical disintegration of the cells was reached at pH 8.5–8.75. Therefore, in order to estimate the protein release efficiency, we set as 100% the protein released from cells disintegrated in PPB with pH 8.5 containing 2 mM DTT which was 199 ± 8 mg $gDCW^{-1}$.

As shown in **Figure 1**, more substantial protein release occurred at pH above 6. The maximal yield (88 ± 9%), was obtained by incubation in a buffer with pH 8.5–9. The protein release from permeabilized cells incubated in water was about 2% from the total protein. The protein release from control cells incubated for 16 h in 167 mM PPB pH 8.5 with 2 mM DTT was 1.75 ± 0.2%. Taking into account these results, we concluded, that it is rather the pH then the ionic strength, which so strongly affects the efflux of intracellular proteins.

In yeast, the cytoplasmic buffering capacity is determined mainly by inorganic phosphate (Poznanski et al., 2013). The

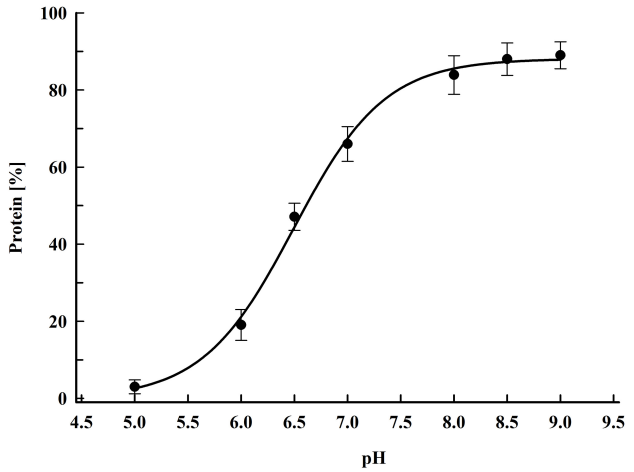

FIGURE 1 | Influence of pH on protein release efficiency from electropermeabilized cells. Electrical conditions: field strength 3.3 kV cm^{-1}, 15 pulses of 0.8 ms duration, pulse frequency 7.5 Hz, flow rate 9 mL min^{-1}. After PEF treatment, the cells were diluted in PPB, containing 2 mM DTT and incubated for 16 h at room temperature. 100% corresponds to the total protein in the cell lysate. The values represent the mean ± SD of five different experiments.

electroinduced loss of plasma membrane integrity results in a very fast release of ions into the medium (Ganeva et al., 2003; Pavlin et al., 2007). Here we confirmed that after electrical treatment, leading to irreversible permeabilization, the conductivity of undiluted yeast suspension reached stable value of 1.5 ± 0.2 mS cm^{-1} within 10 min. The pH of cell suspension with the same concentration was 4.3–4.5 before treatment, and within 10–15 min after treatment reached values of about 5.5.

The isoelectric point for most of the cytoplasmic proteins in yeast is in the range of 4.5–6 (Schwartz et al., 2001). The cytoplasmic pH varies depending on the growth phase and nutrient starvation. For cells in exponential growth phase, cytoplasmic pH is 7–7.2 (Valli et al., 2005; Orij et al., 2009). The yeast cells respond to nutrient starvation by arresting growth and entering stationary phase, which is associated with many morphological and physiological changes. One of them is the decrease of cytoplasmic pH to 5.7–5.8 (Orij et al., 2009). Recent evidence showed that this acidification led to interaction of many soluble proteins with each other and reversible formation of assemblies and filaments, which triggers the transition of the cytoplasm from fluid—to a solid-like state (Narayanaswamy et al., 2009; Munder et al., 2016).

Because of the fast equilibration of ions between the cytosol and the medium after membrane permeabilization, it could be suggested that the incubation of irreversibly permeabilized cells in water contributes additionally to cytoplasmic proteins association and formation of different kinds of aggregates, which occurs naturally in stationary phase cells.

The yeast cell wall is an elastic, layered structure with a thickness of 100–200 nm (Klis et al., 2006). The outer mannoprotein layer limits the permeability of the wall for macromolecules and confers a negative charge to the cell surface. With the transition to stationary growth phase, the cell wall becomes thicker and less porous (Valentin et al., 1987; de Nobel et al., 1990).

Although the electrical treatment has some influence on the cell wall porosity it does not lead to yeast cells lysis (Ganeva et al., 2003, 2014). Therefore, the low extraction efficiency in water and in buffer with pH 5–6 could be attributed to the aggregation of the soluble cytoplasmic proteins, which prevents their diffusion through the wall.

Other groups working with spent brewer's yeast and dry wine yeast (Liu et al., 2012, 2013) also observed a low protein extractability (2.78–4%) from electropermeabilized cells diluted in water. Their results, as well as data obtained in this study, are in discrepancy with the data reported earlier by Monch and Stute (2002) according to which, PEF treatment in a batch mode led to 30% release of proteins from baker's yeast diluted in water. As no information is given about what is accepted in their study for 100% protein, the observed discrepancy could be due to differences in the protocol used for cell disruption and protein extraction (i.e., underestimation of the total protein content), or to the different methods used for protein quantification.

Influence of Cell Concentration

An important factor that can significantly modulate the effect of PEF on membrane integrity is the cell concentration. Recently, while studying the electroextraction of cytoplasmic enzymes from yeast, we found that there is no change of the electrical treatment efficiency at least up to cell concentration of 50 gDCW L^{-1}, and also that the increase of the cell concentration led to reduction of the optimal field strength. We assumed that this effect is due to the strong conductivity increase during treatment of denser suspensions (Ganeva et al., 2003).

Here, we explore in more details the influence of the cell concentration on the efficiency of protein release. The suspensions used in these experiments had a biomass concentration corresponding to 12.5, 25, 37.5, 50, 66, 70, and 85 gDCW L^{-1}. The pulsing chamber and the treatment conditions were the same as in the previous experiment. The only parameter varied to optimize the protein liberation was the electric field strength. After treatment, the cells were diluted in PPB pH 8.75 to final concentrations between 12.5 and 17 gDCW L^{-1}, DTT was added to a final concentration of 2 mM and the suspensions were incubated for 16 h at room temperature.

Figure 2 shows the dependence of the protein release on the field strength for five different concentrations. The maximal protein yield was between 86 and 91% from the total. This was achieved at field strengths where more (over 98%) of the cells were irreversibly permeabilized as detected by PI labeling. Treatment of the cells at field strength above the optimal led to a strong decrease in the protein extractability. A similar dependence on the field strength was observed for all tested concentrations. The specific treatment energy per liter of cell suspension (W_{sus}) at optimal electrical conditions was in the range of 100–140 kJ L^{-1}.

The reported in the literature data about the influence of cell concentration on PEF treatment efficiency are contradictory. This could be due to the different cell types utilized in these studies—mammalian cells or microorganisms (yeast, algae),

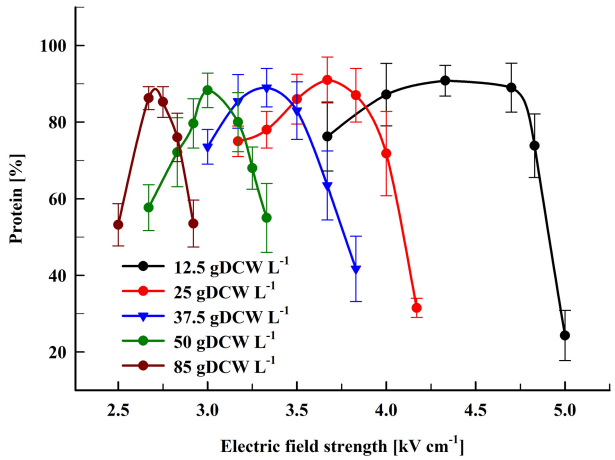

FIGURE 2 | Influence of the field strength on the protein release efficiency. Cell suspensions with biomass concentration corresponding to 12.5–85 gDCW L^{-1} were treated with 15 pulses of 0.8 ms duration, frequency 7.5 Hz, flow rate 9 mL min^{-1}. After PEF treatment, the cells were diluted in PPB pH 8.75 and incubated for 16 h at room temperature. 100% corresponds to the total protein in the cell lysate. The values represent the mean ± SD of three to six different experiments.

the differences in conductivity of the electropermeabilization media, the different mode of PEF treatment—batch treatment, or treatment by using a continuous-flow chambers (Gášková et al., 1996; Álvarez et al., 2000; El Zakhem et al., 2006; Pucihar et al., 2007; Goettel et al., 2013).

The data we present here showed that there is no significant change of PEF efficiency at least up to yeast biomass concentration of 85 gDCW L^{-1}. On the other hand, the increase of the concentration led to a significant reduction of the optimal field strength.

Studying the extraction of different intracellular components from algae, Goettel et al. (2013) found, that the PEF efficiency is not affected even at biomass concentrations of 167 gDCW L^{-1}. The authors reported a significant reduction of the PEF-demand energy (MJ $kgDCW^{-1}$) with the increase of the biomass concentration.

In our experiments, the increase of the yeast cell concentration from 12.5 to 85 gDCW L^{-1} resulted in PEF energy reduction from 10.5 to about 1.56 MJ $kgDCW^{-1}$. Despite the applied different electrical conditions to induce irreversible permeabilization—i.e., moderate field strength (2.5–5 kV cm^{-1}) and series of relatively long (0.8 ms) pulses, the PEF-demand energy required for maximal protein recovery from yeast was close to the one reported about algae suspensions with similar concentration. Based on the results obtained by Goettel et al. (2013), it seems possible to increase further the yeast biomass without changing the PEF treatment efficiency.

Upscaling of the PEF Treatment Protocol: Temperature Effect on the Protein Release Efficiency

PEF treatment in a flow mode can be easily scaled up by preserving the same extraction efficiency. For example, an increase in the flow rate can be obtained by using pulsing chambers with larger volumes and by pulse frequency increase.

Here, we performed experiments on protein extraction by using a chamber with a volume of 0.5 mL. Firstly, the cell suspension (66 gDCW L^{-1}) was treated at flow rate of 27 mL min^{-1}. During their passage through the chamber the cells received 19 pulses (pulse frequency 17.1 Hz) of 0.5 ms duration which corresponds to a total treatment time of 9.5 ms. After electrical treatment, the suspensions were diluted in PPB containing DTT and then incubated at room temperature for 16 h. At these conditions, maximal protein release (87.8 ± 3%) was obtained at field strength of about 3 kV cm^{-1} (**Figure 3**). The specific treatment energy per liter of cell suspension (W_{sus}) was 120 kJ L^{-1}. As already shown (**Figure 2**), treatment at higher field strengths led to a significant reduction in the protein yield.

Next, we studied the protein extraction efficiency at higher flow rate—130 mL min^{-1}. To assure that the cells receive the same pulse number (19 pulses, total treatment time of 9.5 ms), the pulse frequency was increased to 82.3 Hz and the PEF treatment optimization was performed only by varying the electric field strength. The permeabilized cells were diluted and incubated at room temperature as already described. We found that at this flow rate the same extraction efficiency is reached at field strength in the range of 2.75–2.88 kV cm^{-1} (**Supplementary Material 2**). At 3 kV cm^{-1} the protein yield started to decrease and at 3.16 kV cm^{-1} the difference between the protein yields obtained at 27 and 130 mL min^{-1} became statistically significant ($P < 0.01$).

Although the PEF treatment is considered as a non-thermal method, it is associated with a temperature rise due to Joule heating. This effect could be significant when dense cell suspensions are treated under conditions leading to irreversible permeabilization, such as in our experiments. The observed phenomenon is consequence from the strong

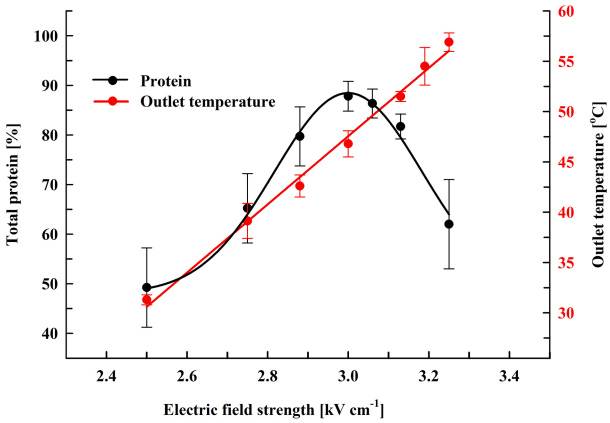

FIGURE 3 | Influence of field strength on protein release efficiency and outlet temperature. Electrical conditions: 19 pulses of 0.5 ms duration, pulse frequency 17.1 Hz, flow rate 27 mL min^{-1}. After PEF treatment, the cells were diluted threefold in 250 mM PPB pH 8.75 containing 2 mM DTT and incubated for 16 h at room temperature. 100% corresponds to the total protein in the cell lysate. The values represent the mean ± SD of five different experiments.

increase in conductivity during pulse application because of an instantaneous release of intracellular ions. We measured the outlet temperature at the different field strengths applied. At a flow rate of 27 mL min^{-1}, in our system the residence time of the cells inside the treatment chamber was about 1.1 s and the outlet temperature was registered about 4 s after the cells received 19 pulses with 0.5 ms duration. We found that the outlet temperature reached a maximal value about 20 s after the start of the pulsation and then remained stable despite the lack of cooling system. As shown in **Figure 3**, at field strengths leading to maximal protein yields, the outlet temperature was in the range of 46–49°C.

Treatment of the suspensions at about 3.13 kV cm^{-1} (outlet temperatures over 50°C) led to a significant ($P < 0.01$) decrease in the protein release and at about 3.25 kV cm^{-1} (outlet temperature of 56–58°C) the yield dropped to 62 ± 9%. We assumed that the decrease observed might be a result of temperature-induced change in the conformation of the cell wall mannoproteins. Changes in the conformation of the soluble intracellular proteins could further complicate their diffusion through the wall.

Yeast susceptibility to lytic enzymes is a routine approach used to reveal changes in the structure of the outer mannoprotein layer of the yeast cell wall under influence of different factors (de Nobel et al., 2000; Simões et al., 2003; Ganeva et al., 2014). We compared the sensitivity to lytic enzyme of control cells and cells treated at two different field strengths: 3 and 3.25 kV cm^{-1}. As illustrated in **Figure 4**, at optimal field strength there is a significant increase of cell sensitivity to lytic enzyme, while treatment at higher field strength led to a statistically significant reversal of the effect and respective decrease of the cell sensitivity to lyticase.

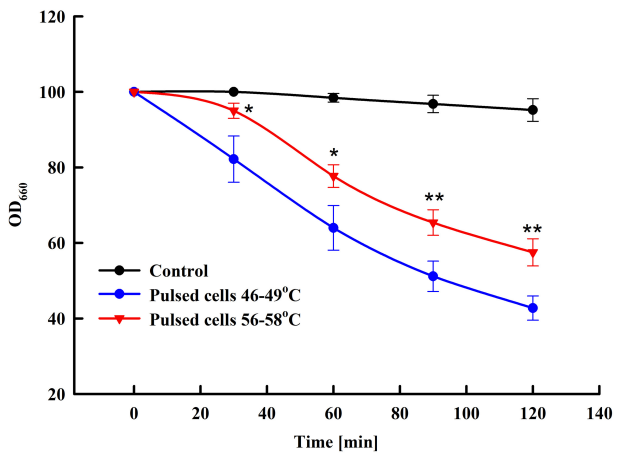

FIGURE 4 | Influence of PEF treatment on lyticase sensitivity of baker's yeast. Electrical conditions: 19 pulses of 0.5 ms duration, pulse frequency 17.1 Hz, flow rate 27 mL min^{-1}, field strength 3 kV cm^{-1} (outlet temperature 46–49°C) and 3.25 kV cm^{-1} (outlet temperature 56–58°C). Electrically treated and control cells were diluted in PPB pH 7.5, lyticase was added to final concentration 60 U mL^{-1} and the cells were incubated at 30°C. The values represent the mean ± SD of three different experiments. *$P < 0.05$; **$P < 0.01$.

To check for temperature-induced changes in the conformation of the soluble proteins, we compared the activity of the enzyme alcohol dehydrogenase (ADH) in the lysates prepared from control cells and cells treated at two different field strengths—3 kV cm^{-1} (outlet temperature 49°C) and 3.25 kV cm^{-1} (outlet temperature 57–58°C). We found that cell treatment at 3 kV cm^{-1} (optimal conditions for total protein extraction) did not affect the ADH activity. On other hand, ADH activity of cells pulsed at 3.25 kV cm^{-1} was 20 ± 1.8% lower than this of the control, untreated cells. It has to be pointed out that in our experiments the temperature of the collected samples incubated at room temperature decreased very fast and in a few minutes (3–5 min) after electrical treatment it reached values of 40–45°C.

Based on the results from the lyticase test and ADH activity measurement, we concluded that at electrical conditions leading to maximal protein extraction, no significant protein denaturation takes place. However, these results also showed that under certain electrical conditions the temperature rise, which occurred during pulse application, could provoke some conformational changes in both, the cell wall mannoproteins and the soluble proteins, causing reduced diffusion efficiency through the cell wall.

There are numerous data obtained with different cell types indicating that the temperature of the samples (cell suspension or tissue) during pulse application influences electropermeabilization. Experiments with algae, mammalian cells and animal tissues demonstrated that electrical treatment at physiological temperatures is more efficient than treatment of samples chilled to 4–5°C (Coster and Zimmermann, 1975; Gallo et al., 2002; Kandušer et al., 2008).

There is also evidence, that moderate preheating of the samples improves electropermeabilization and lowers the energy consumption. Synergism between thermal and electric field effect has been observed for PEF microorganism inactivation (Wouters et al., 1999; Heinz et al., 2003; Amiali et al., 2007) and electrically induced extraction of intracellular compounds from plant tissues and algae (Lebovka et al., 2005; Postma et al., 2016). One of the possible reasons for these effects seems to be the temperature-induced increase of membrane fluidity, which facilitates the electroinduced loss of plasma membrane integrity (Kandušer et al., 2008).

In our experiments, the inlet temperature was about 24°C and the temperature rise of the suspensions at optimal electrical conditions was 22–25°C. Since we do not control the temperature during the pulsation, it is difficult to separate the contribution of the PEF effect and the thermal effect, but it seems highly probable, that the temperature increase during pulse application facilitates electropermeabilization. On the other hand, as mentioned above, higher temperature increase has an inverse effect on the protein release, which could be explained by temperature-induced changes in the conformation of the cell wall mannoproteins and the cytoplasmic proteins.

Recently, working with the thermotolerant yeast *Hansenula polymorpha*, we obtained maximal protein extraction at electrical conditions where outlet temperatures of 59–60°C had been reached (Ganeva et al., 2018). It could be assumed that the effect

of the temperature on the protein release efficiency depends on the system particularity—the cell wall composition and structure, the plasma membrane composition, the thermostability of the soluble proteins.

In our experiments, high protein yield was achieved by incubation of the pulsed cells at room temperature, which in terms of performance is simple and cost-effective. On the other hand, the prolonged incubation (16 h) carries some risks of bacterial contamination. We evaluated the protein release rate and found that main release (68.6 ± 5.4%) occurred during the first 5 h of post-pulse incubation (**Figure 5**). The thiol compound, which increases cell wall porosity by reducing the disulfide bonds between the cell wall mannoproteins (Zlotnik et al., 1984), significantly enhanced the yield. As diffusion is a temperature-dependent process, we tried to accelerate the protein release by incubation of the cells at a higher temperature, as done earlier for the extraction of intracellular proteins (Ganeva et al., 2003, 2018). The increase of the temperature from 24 to 30°C had some impact on the rate and efficiency of protein release mainly during the first several hours, however, the maximal yield reached after 14–16 h of incubation at these two temperature was rather similar. These results led to the conclusion that the incubation of the permeabilized cells can be performed at room temperature without significant decrease of the protein yield.

Nucleic Acid Content of the Extracts

Once the proteins are extracted, they have to be concentrated and purified to remove the undesired or potentially harmful substances coming from the cells or introduced during extraction (Middelberg, 2012). Ultrafiltration is a commonly employed method for protein concentration, buffer exchange and purification in the biotechnology industry (van Reis and Zydney, 2007). That is why we applied this technique to concentrate the proteins released from the permeabilized cells. The electrical treatment and the conditions of post-pulse incubation are as described in the text to **Figure 3**. After 16 h of incubation at room temperature the cells were removed by centrifugation and the supernatants obtained were subjected to ultrafiltration at 10 kDa.

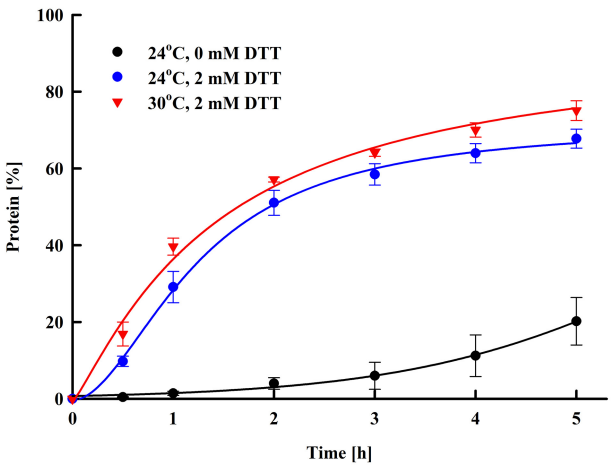

FIGURE 5 | Electroinduced release of total protein at various periods after PEF treatment. Electrical conditions: 19 pulses of 0.5 ms duration, pulse frequency 17.1 Hz, flow rate 27 mL min^{-1}, field strength 3 kV cm^{-1}. After PEF treatment, the cells were diluted in 250 mM PPB pH 8.75 with or w/o 2 mM DTT and incubated at room temperature or at 30°C. 100% corresponds to the total protein in the cell lysate. The values represent the mean ± SD of three different experiments.

Next, after appropriate dilution the protein and NA content in the retentates were determined. The percentage decrease of the protein content after ultrafiltration was 3 ± 0.2%, which most probably was due to some protein retention by the membrane as we did not detect protein in the eluate. This result suggests that at the applied conditions (alkaline pH, room temperature) no significant proteolytic degradation occurred despite of the prolonged time of incubation. On the other hand, the protein/NA ratio in the concentrated supernatants was 100/5.6 ± 0.9.

As shown in **Figure 5**, the permeabilized cells diluted in buffer without DTT released only about 1.6–2.2% protein during the first 1–1.5 h incubation. Therefore, we evaluated also the amount of released NA by using a different protocol for post-pulse incubation. In these experiments a pretreatment step was introduced, where after electrical treatment, the cells were diluted in PPB without DTT and incubated for 1.5 h. Afterward, the supernatant was removed, the cells were diluted in PPB with DTT and incubated as described above. We found that this pretreatment of the cells led to an additional decrease of the protein/NA ration −100/4.5 ± 0.3.

The main limiting factor for utilization of yeast biomass as a protein source in human diet is the high NA content, because in human, the purine nucleotides are metabolized to uric acid. Reduction of the purine content of yeast has been studied extensively for the past few years and different methods based on chemical or enzymatic treatment have been developed (Halász and Lásztity, 1991; Nasseri et al., 2011). Although they allow production of protein concentrates with low NA and nucleotides content, several problems associated with their application exist. Chemical processing, often applied in combination with heating, can result in alteration of the amino acid profile, to formation of potentially toxic products, such as lysinoalanine and to denaturation, which decreases the nutritive properties of the proteins (Shetty and Kinsella, 1979; Halász and Lásztity, 1991; Nasseri et al., 2011). The enzymatic methods based on the utilization of exogenous nucleases are limited because of the cost of the catalyst, while NA reduction by autolytic degradation is often performed under conditions where protein hydrolysis also occurs (Trevelyan, 1976).

According to the literature, the protein/NA ratio for the lysates obtained by mechanical disintegration of *S. cerevisiae* is in the range of 100/12–100/25 (Shetty and Kinsella, 1979; Halász and Lásztity, 1991). The lower NA content in the protein concentrates obtained after PEF treatment can be explained by the fact, that about 80% of the yeast RNA is ribosomal (Waldron and Lacroute, 1975; Warner, 1999) and is part of large nucleoprotein complexes, which generally cannot be released from the permeabilized cells. As there is no cell lysis, the DNA is also retained inside, and the NA released after plasma membrane permeabilization are most probably mainly tRNAs and mRNAs.

Depending on the yeast type and growth conditions, the protein content of the fresh baker's yeast ranges between 40.8 and 58% of the dry cell matter (Bekatorou et al., 2006). According to Kinsella (1987) only 40% from the total protein in yeast is soluble (cytoplasmic) protein, the other part consists of ribosomal protein (40%) and cell wall protein (20%). The protein yield we obtained after disruption of the cells with glass beads was 199 mg $gDCW^{-1}$, which corresponds approximately to the average content of soluble protein in baker's yeast.

The data presented in this study demonstrated that the PEF treatment applied in flow mode, followed by incubation of the electropermeabilized yeast cells in a buffer with alkaline pH, resulted in a highly efficient extraction of the intracellular soluble protein with low content of NA. The protein yield of 170–180 mg $gDCW^{-1}$ is lower than that obtained by high pressure homogenization (Sergeev et al., 1984; Jacob et al., 2019). On the other hand, PEF treatment is a milder technique, which does not provoke protein denaturation when used with the appropriate combination of electrical parameters. The release of intracellular compounds, including proteins, is a result of plasma membrane permeabilization and there is no cell fragmentation, which allows separation of the cells by microfiltration or low speed centrifugation. The release of the proteins is a slow process, but the incubation of the permeabilized cells in alkaline pH buffer and temperatures of 24–30°C seems to prevent the protein hydrolysis. There are data indicating that electrical treatment performed in a batch and continuous mode caused accelerated yeast autolysis. It has to be pointed out that in these studies the treated cells were incubated for several days at 18–26°C (Martinez et al., 2016; Maza et al., 2020) or several hours at 40–60°C and pH 6.6 (Monch and Stute, 2002).

The results from our study demonstrated the principal possibility for utilization of PEF treatment for production of protein concentrates with low NA content, thus suitable for human consumption. The proteins were not modified due to thermal or chemical treatment during the extraction process. The reduction of the NA content did not require additional chemical or enzymatic treatment, while the concentration by ultrafiltration also allowed the removal of the nucleotides liberated during post pulse incubation. We do not exclude, that some changes of post-pulse incubation, as well as utilization of membranes with a cutoff higher than 10 kDa could lead to further reduction of the NA without substantial loss of proteins.

Since the treated cells become more sensitive to lytic enzymes (Ganeva et al., 2014, 2018) and to mechanical disintegration (Shynkaryk et al., 2009), the residual biomass after removal of the protein, could be further processed to induce autolysis (Monch and Stute, 2002; Maza et al., 2020) or it could be disintegrated by high pressure homogenization for recovery of additional valuable compounds—amino acids, nucleotides, proteins, and polysaccharides.

Electroinduced Extraction of Low Molecular Compounds

As shown in this study, incubation of the electropermeabilized baker's yeast in water led to very poor protein release, which is most probably a result of protein aggregation and retention by the cell wall. These incubation conditions, however, do not prevent the diffusion of small water-soluble substances through the yeast cell wall (Monch and Stute, 2002; Shynkaryk et al., 2009).

We evaluated the rate and efficiency of liberation of different intracellular compounds—free amino acids, antioxidants and nucleotides, from irreversibly permeabilized cells. In these experiments, we applied the electrical conditions, which we found as optimal for protein extraction (**Figure 3**). Cell suspensions (66 $gDCW\ L^{-1}$) with conductivity of 150 $\mu S\ cm^{-1}$ were treated at a flow rate of 27 mL min^{-1} in pulsing chamber with 0.5 mL volume with 19 pulses of 0.5 ms duration (total treatment time of 9.5 ms). The field strength was set at 3 kV cm^{-1}. After pulsation, the suspensions were incubated without dilution at room temperature. Samples were taken at defined time intervals, the cells were removed by centrifugation and the supernatants were analyzed for the different substances. As 100% was set the content of the analyzed compound in the soluble fraction obtained after mechanical disintegration of suspensions from control untreated cells with the same concentration.

As shown in **Figure 6**, about 70% of the free amino acids were released 15 min after electrical treatment. Afterward, the amino acids leakage continued slowly and at 4 h after pulsation the yield reached 90–95% from total content corresponding to 51.8 ± 8.6 mg amino acids $gDCW^{-1}$. Taking into account that the free amino acids are distributed between the cytosol and the vacuole (Kitamoto et al., 1988), it could be hypothesized that there is also a change in the vacuolar membrane's integrity. Vacuoles in stationary phase cells are large organelles, which occupy most of the intracellular space, and it is possible that in part of the cells the loss of vacuolar membrane integrity is a direct effect of the electrical treatment (i.e., electropermeabilization). However, given that the release of the free amino acids, which are small molecules, continues for several hours, it is possible that the subsequent vacuolar rupture is caused by osmotic imbalance.

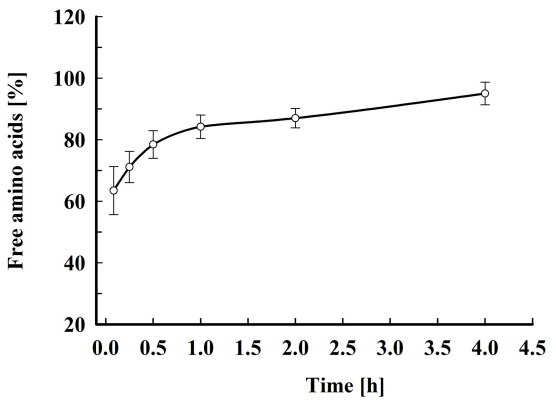

FIGURE 6 | Electroinduced release of free amino acids at various periods after PEF treatment. Electrical conditions: as described in **Figure 3**. After PEF treatment, the cell suspensions were incubated at room temperature without dilution. 100% corresponds to the free amino acid content in the cell lysate. The values represent the mean ± SD of five different experiments.

Yeast antioxidant potential is determined by different soluble and insoluble cell components (Santiago and Mori, 1993; Jaehrig et al., 2008). According to Santiago and Mori (1993), 85–90% of the free radical scavenging activity of the soluble fraction obtained after mechanical cell disruption is due to thermostable compounds with molecular mass under 10 kDa. Yeast have different low molecular compounds with antioxidant properties but one of the most important antioxidants in the cell is glutathione. *S. cerevisiae* and *Candida utilis* are currently used for industrial production of glutathione, which has found application in pharmaceutics, as an additive for the production of functional foods and as a natural antioxidant for preservation of food quality (Li et al., 2004). To assess the applicability of PEF treatment for extraction of antioxidants from yeast we determined the total antioxidant activity, the glutathione and the total phenolic metabolites released from the cells, at different time intervals after pulsation. As in previous experiments, the cell suspensions were incubated at room temperature without dilutions.

The total antioxidant activity in the lysate and in the supernatants obtained 2 h after PEF treatment was determined by estimating the ABTS radical-scavenging activity. As shown in **Figure 7**, the permeabilized cells released 78 ± 4.6% of the total antioxidant activity corresponding to 19.65 ± 1.5 mgTE $gDCW^{-1}$. The antioxidant activity of the permeate obtained after ultrafiltration of the supernatants at 10 kDa was 68.3 ± 3.5% which brought us to the conclusion that the antioxidant activity released after electrical treatment and incubation of the cells in water is mainly due to low molecular compounds.

We evaluated the glutathione liberation, as well. The release of this cytosol tripeptide was almost instantaneous—10 min after pulsation 78 ± 6% from the total content corresponding to 9.6 ± 0.5 mg $gDCW^{-1}$ was detected in the supernatant of the permeabilized cells. Further incubation (up to 4 h after pulsation) did not improved the yield.

As illustrated in **Figure 8**, permeabilized cells released about 41% of their total phenolic content 1 h after pulsation. Prolonged incubation did not significantly improve the yield. This lower extraction efficiency could be due to specificities in their intracellular location and/or interaction with other cellular components such as cell wall (Mohamed et al., 2018).

As shown in **Figure 9**, there is very rapid release from the electropermeabilized cells of substances absorbing at 260 nm. Maximal absorbance was observed about 60 min after electrical treatment. No further changes were registered even after prolonged (up to 20 h) incubation of the electropermeabilized cells at room temperature. Therefore, we assumed that the absorbance was mainly due to leakage of nucleotides, nucleosides, cofactors, and other low molecular weight compounds. We measured the absorbance of the permeate obtained after ultrafiltration of the supernatants at 10 kDa cut off and found only 7.2 ± 1% decrease which supported our assumptions. In addition, we measured the absorbance of the permeate obtained after ultrafiltration of the soluble part of the lysate and found that the electropermeabilized cells incubated in water release about 92% from the low molecular UV absorbing substances present in the cell. These data led us to conclude that when the permeabilized cells are incubated in water, RNA is generally retained inside, as shown for proteins. On the other hand, it seems that at the used incubation conditions yeast RNAses have very low (or even no) activity, otherwise we should have registered an increase in the absorption at 260 nm over time.

We also determined the total purine content of the supernatants obtained after electrical treatment and incubation of the cell suspension for 4 h at room temperature. The obtained value, calculated by gram dry biomass, was 2.13 ± 0.4 mg $gDCW^{-1}$, which is significantly lower than the purine content of the whole cell (Kaneko et al., 2014).

The data presented here demonstrated that incubation of permeabilized cells in water led to liberation mainly of relatively

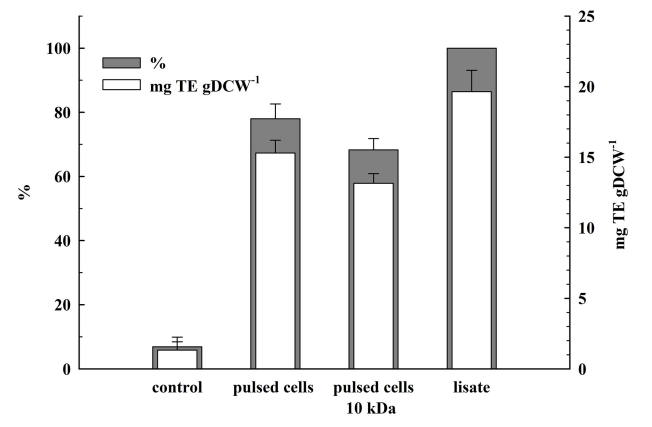

FIGURE 7 | Release of total antioxidant activity from electrically treated and control cells. Electrical conditions: as described in **Figure 3**. Control and electrically treated cells were incubated at room temperature for 2 h without dilution. 100% corresponds to the total antioxidant activity in the cell lysate. The values represent the mean ± SD of three different experiments.

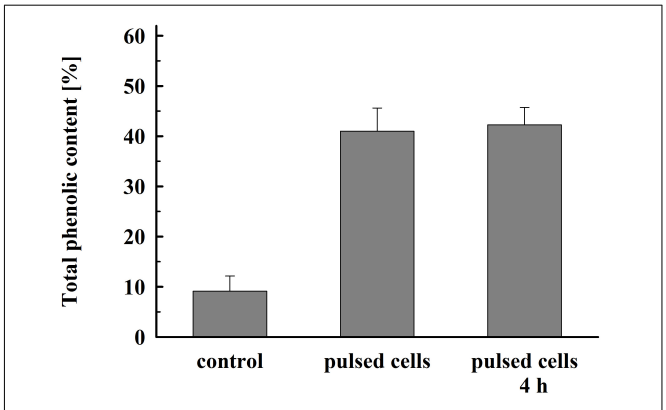

FIGURE 8 | Total phenolic content released from electrically treated and control cells. Electrical conditions: as described in **Figure 3**. Control cell were incubated for 4 h, electrically treated cells were incubated for 1 h and, respectively, 4 h. 100% corresponds to the total phenolic content in the cell lysate. The values represent the mean ± SD of four different experiments.

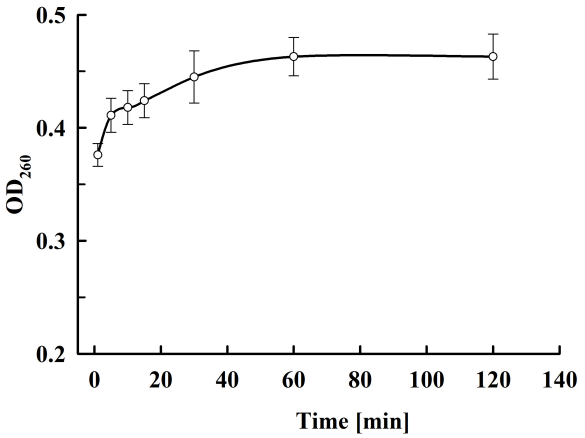

FIGURE 9 | Release of UV absorbing substances at various periods after PEF treatment. Electrical conditions: as described in **Figure 3**. The values represent the mean ± SD of four different experiments.

low molecular compounds. At these incubation conditions, the soluble proteins and NA were largely retained inside. On the other hand, water extracts contained most (about 80%) of the total antioxidant activity and glutathione content of the cells. The cell suspensions used in this study were relatively dense—approximately 260 g fresh weight L^{-1}. It is possible that the yield could be improved by re-extraction with water or by additional dilution.

It seems highly probable that other bioactive compounds localized in the cytosol, for example water soluble B-complex vitamins and small peptides, could be released with similar efficiency. The release of the low molecular compounds is fast, and there is no need for incubation at high temperature, or addition of chemicals (salt, solvents) or enzymes.

Our data demonstrate that the amino acid content of the studied extracts is significantly lower than what is reported for the autolysates (Jacob et al., 2019). This could be explained by the observation that PEF treatment itself does not provoke protein degradation and the following incubation of the permeabilized cells in water does not cause significant protein hydrolysis. Most importantly, it seems that at these conditions, there is also no NA degradation and, as a result, electropermeabilization led to leakage mainly of the free nucleotides present in the cells.

The main limitation for using whole yeast as a source of vitamins, antioxidants and other biologically active substances in human diet is the high NA content. The same problem exists with the utilization of autolysates (often indicated as yeast extracts) as a food additive, because they have practically the same purine content as intact cells. The water extracts obtained after PEF treatment have a very low level of purine nucleotides in comparison to whole cells. Thus, it is possible that after appropriate concentration they could be utilized for health supplements in human diet or as a source of glutathione for preservation of different food from oxidative damage without the risk of undesirable purine content increase.

PEF treatment by using continuous-flow chambers has all the prerequisites to be developed as an alternative method for extraction of glutathione and other low molecular compounds from yeast. The technique is suitable for large-scale biomass processing. Irreversible permeabilization of water suspensions with high biomass content can be achieved after a single pass through the pulsing chamber and the treatment can be performed at room temperature without using cooling system. After appropriate time of incubation, the pulsed cells, which have been demonstrated to have a strong tendency to aggregate (Shynkaryk et al., 2009), can be easily separated from the supernatants containing the low molecular bioactive compounds. Then these cells, which practically retain most of the macromolecules—proteins, polysaccharides, and NA, can be further processed for recovery of these valuable compounds or simply dried and distributed as an animal feed or fertilizers.

CONCLUSION

The present study demonstrated that the PEF treatment applied in flow mode, followed by incubation of the electropermeabilized yeast cells in a buffer with alkaline pH, results in highly efficient extraction of the intracellular soluble proteins. At electrical conditions leading to maximal protein extraction, no significant protein denaturation takes place. The PEF energy needed to achieve irreversible electropermeabilization was significantly reduced with the increase of the biomass concentration. The protein release is a slow process, but the incubation at alkaline pH and room temperature seems to prevent the protein hydrolysis. The protein concentrates obtained by ultrafiltration had lower NA content in comparison to the cell lysates obtained by mechanical disintegration, most probably due to the retention of part of the NA (ribosomal RNA and DNA) inside the cells. The possibility for utilization of PEF treatment in a continuous flow mode for production of protein concentrates suitable for human consumption is suggested.

Incubation of permeabilized yeast cells in water led to leakage mainly of relatively low molecular compounds. The water extracts contain most of the total antioxidant activity, glutathione and phenolic compounds present in the cell, and in same time had a very low level of purine nucleotides in comparison to whole cells. These specificities in their composition make the yeast water extracts suitable for utilization as supplements representing a source of natural antioxidants for health purposes and in the food industry.

DATA AVAILABILITY STATEMENT

The original contributions presented in the study are included in the article/**Supplementary Materials**, further inquiries can be directed to the corresponding author.

AUTHOR CONTRIBUTIONS

VGa and BG designed the study. VGa, BA, and MZ contributed to data acquisition and read and approved the final version of the manuscript. VGa, BG, and VGo performed the data analysis and data interpretation. VGa wrote the manuscript. All authors contributed to the article and approved the submitted version.

FUNDING

This research received funding from the European Union Seventh Framework Programme (FP7/2012-2017) under grant agreement n° 312004.

SUPPLEMENTARY MATERIAL

The Supplementary Material for this article can be found online at: https://www.frontiersin.org/articles/10.3389/fbioe.2020.552335/full#supplementary-material

Supplementary Material 1 | Schematic representation of the experimental setup used for PEF treatment.

Supplementary Material 2 | Influence of field strength on protein release efficiency. Electrical conditions: 19 pulses of 0.5 ms duration, flow rate 27 mL min^{-1} (pulse frequency 17.1), flow rate 130 mL min^{-1} 82.3 Hz. Hz, flow rate. After PEF treatment, the cells were diluted threefold in 250 mM PPB pH 8.75 containing 2 mM DTT and incubated for 16 h at room temperature. 100% corresponds to the total protein in the cell lysate. The values represent the mean ± SD of four different experiments (**$P < 0.01$).

REFERENCES

Abbas, C. A. (2006). "Production of antioxidants, aromas, colours, flavours, and vitamins by yeasts," in *Yeasts in Food and Beverages*, eds A. Querol and G. Fleet (Berlin: Springer), 285–334. doi: 10.1007/978-3-540-28398-0_10

Álvarez, I., Raso, J., Palop, A., and Sala, F. J. (2000). Influence of different factors on the inactivation of *Salmonella* senftenberg by pulsed electric fields. *Int. J. Food Microbiol.* 55, 143–146. doi: 10.1016/s0168-1605(00)00173-2

Amiali, M., Ngadi, M. O., Smith, J. P., and Raghavan, G. S. V. (2007). Synergistic effect of temperature and pulsed electric field on inactivation of *Escherichia coli* O157:H7 and *Salmonella enteritidis* in liquid egg yolk. *J. Food Eng.* 79, 689–694. doi: 10.1016/j.jfoodeng.2006.02.029

Balasundaram, B., Harrison, S., and Bracewell, G. B. (2009). Advances in product release strategies and impact on bioprocess design. *Trends Biotechnol.* 27, 477–485. doi: 10.1016/j.tibtech.2009.04.004

Bekatorou, A., Psarianus, C., and Koutinas, A. A. (2006). Production of food grade yeasts. *Food Technol. Biotechnol.* 44, 407–415.

Bradford, M. M. (1976). A rapid and sensitive method for the quantitation of microgram quantities of protein utilizing the principle of protein-dye binding. *Anal. Biochem.* 72, 248–254. doi: 10.1006/abio.1976.9999

Bzduhcha-Wróbel, A., Blażejak, S., Kawarska, A., Stasiak-Różańska, L., Gientka, I., and Majewska, E. (2014). Evaluation of the efficiency of different disruption methods on yeast cell wall preparation for β-glucan isolation. *Molecules* 19, 20941–20961. doi: 10.3390/molecules191220941

Coster, H. G., and Zimmermann, U. (1975). The mechanism of electrical breakdown in the membranes of Valonia utricularis. *J. Membr. Biol.* 22, 73–90. doi: 10.1007/bf01868164

Coustets, M., Joubert-Durigneux, V., Herault, J., Schoefs, B., Blanckaert, V., Garnier, J.-P., et al. (2015). Optimization of protein electroextraction from microalgae by a flow process. *Bioelectrochemistry* 103, 74–81. doi: 10.1016/j.bioelechem.2014.08.022

de Nobel, H., Ruiz, C., Martin, H., Morris, W., Brul, S., Molina, M., et al. (2000). Cell wall perturbation in yeast results in dual phosphorylation of the Slt2/Mpk1 MAP kinase and in an Slt2-mediated increase in FKS2-lacZ expression, glucanase resistance and thermotolerance. *Mcrobiology* 146, 2121–2132. doi: 10.1099/00221287-146-9-2121

de Nobel, J. G., Klis, F. M., Priem, J., Munnik, T., and van den Ende, H. (1990). The glucanase-soluble mannoproteins limit cell wall porosity in *Saccharomyces cerevisiae*. *Yeast* 6, 491–499. doi: 10.1002/yea.320060606

El Zakhem, H., Lanoisellé, J. L., Lebovka, N. I., Nonus, M., and Vorobiev, E. (2006). Behavior of yeast cells in aqueous suspension affected by pulsed electric field. *J. Colloid Interface Sci.* 300, 553–563. doi: 10.1016/j.jcis.2006.04.055

Gallo, S. A., Sen, A., Hensen, M. L., and Hui, S. W. (2002). Temperature-dependent electrical and ultrastructural characterizations of porcine skin upon electroporation. *Biophys. J.* 82, 109–119. doi: 10.1016/S0006-3495(02)75378-2

Ganeva, V., Galutzov, B., Angelova, B., and Suckow, M. (2018). Electroinduced extraction of human ferritin heavy chain expressed in Hansenula polymorpha. *Appl. Biochem. Biotechnol.* 184, 1286–1307. doi: 10.1007/s12010-017-2627-9

Ganeva, V., Galutzov, B., and Teissie, J. (2003). High yield electroextraction of proteins from yeast by a flow process. *Anal. Biochem.* 315, 77–84. doi: 10.1016/s0003-2697(02)00699-1

Ganeva, V., Galutzov, B., and Teissie, J. (2014). Evidence that pulsed electric field treatment enhances the cell wall porosity of yeast cells. *Appl. Biochem. Biotechnol.* 172, 1540–1552. doi: 10.1007/s12010-013-0628-x

Ganeva, V., Stefanova, D., Angelova, B., Galutzov, B., Velasco, I., and Arevalo-Rodrigez, M. (2015). Electroinduced release of recombinant β-galactosidase from *Saccharomyces cerevisiae*. *J. Biotechnol.* 211, 12–19. doi: 10.1016/j.jbiotec.2015.06.418

Gášková, D., Sigler, K., Janderová, B., and Plášek, J. (1996). Effect of high-voltage electric pulses on yeast cells: factors influencing the killing efficiency. *Bioelectrochem. Bioenerget.* 39, 195–202. doi: 10.1016/0302-4598(95)01892-1

Goettel, M., Eing, C., Gsubeth, C., Straessner, R., and Frey, W. (2013). Pulsed electric field assisted extraction of intracellular valuables from microalgae. *Algal Res.* 2, 401–408. doi: 10.1016/j.algal.2013.07.004

Golberg, A., Sack, M., Teissie, J., Pataro, G., Pliquett, U., Saulis, G., et al. (2016). Energy-efficient biomass processing with pulsed electric fields for bioeconomy and sustainable development. *Biotechnol. Biofuels.* 9:94. doi: 10.1186/s13068-016-0508-z

Halász, A., and Lásztity, R. (1991). *Use of Yeast Biomass in Food Production*. Boca Raton, FL: CRC Press, 127–135.

Heinz, V., Toepfl, S., and Knorr, D. (2003). Impact of temperature on lethality and energy efficiency of apple juice pasteurization by pulsed electric fields treatment. *Innov. Food Sci Emerg. Technol.* 4, 167–175. doi: 10.1016/S1466-8564(03)00017-1

Jacob, F. F., Striegel, L., Rychlik, M., Hutzler, M., and Methner, F.-J. (2019). Yeast extract production using yeast from beer manufacture:influence of industrially applicable disruption methods on selected groups with biotechnological relevance. *Eur. Food Res. Technol.* 245, 1169–1182. doi: 10.1007/s00217-019-03237-9

Jaehrig, S. C., Rohn, S., Kroh, L. W., Wildenauer, F., Lisdat, F., Fleischer, L. G., et al. (2008). Antioxidative activity of (1-3, (1-6)-β-D-glucan from Saccharomyces cerevisiae grown on different media. *LWT Food Sci. Technol.* 41, 868–877. doi: 10.1016/j.lwt.2007.06.004

Kandušer, M., Šentjurc, M., and Miklavčič, D. (2008). The temperature effect during pulse application on cell membrane fluidity and permeabilization. *Bioelectrochemistry* 74, 52–57. doi: 10.1016/j.bioelechem.2008.04.012

Kaneko, K., Aoyagi, Y., Fukuuchi, T., Inasawa, K., and Yamaoka, N. (2014). Total purine and purine base content of common foodstuffs for facilitating nutritional therapy for gout and hyperuricemia. *Biol. Pharm. Bull.* 37, 709–721. doi: 10.1248/bpb.b13-00967

Kinsella, J. E. (1987). "Funcional properties from yeast nucleoprotein for food uses. Methods for isolation," in *Food Biochemistry*, ed. D. Knorr (New York, NY: Marcel Dekker), 363–391.

Kinsella, J. E., and Shetty, K. J. (1978). Yeast proteins: Recovery, nutritional and functional properties. *Adv. Exp. Med. Biol.* 105, 797–825. doi: 10.1007/978-1-4684-3366-1_38

Kitamoto, K., Yoshizawa, K., Ohsumi, Y., and Anraku, Y. (1988). Dynamic aspects of vacuolar and cytosolic amino acid pool of *Saccharomyces cerevisiae*. *J. Bacteriol.* 170, 2683–2686. doi: 10.1128/jb.170.6.2683-2686.1988

Klis, F. M., Boorsma, A., and De Groot, P. W. (2006). Cell wall construction in Saccharomyces cerevisiae. *Yeast* 23, 185–202.

Lamoolphak, W., Goto, M., Sasaki, M., Suphantharika, M., Muangnapoh, C., Prommuag, C. et al. (2006). Hydrothermal decomposition of yeast cells for production of proteins and amino acids. *J. Hazard. Mater.* 137, 1643–1648. doi: 10.1016/j.jhazmat.2006.05.029

Lebovka, N. I., Praporscic, I., Ghnimi, S., and Vorobiev, E. (2005). Temperature enhanced electroporation under the pulsed electrical field treatment of food tissue. *J. Food Eng.* 69, 177–184. doi: 10.1016/j.jfoodeng.2004.08.037

Li, E., and Mira de Orduña, R. A. (2010). A rapid method for the determination of microbial biomass by dry weight using a moisture analyser with an infrared heating source and an analytical balance. *Lett. Appl. Microbiol.* 50, 283–288. doi: 10.1111/j.1472-765X.2009.02789.x

Li, Y., Wei, G., and Chen, J. (2004). Glutathione: a review on biotechnological production. *Appl. Microbiol. Biotechnol.* 66, 233–241. doi: 10.1007/s00253-004-1751-y

Lindgren, M., Aronsson, K., Galt, S., and Ohlsson, T. (2002). Simulation of the temperature increase in pulsed electric field (PEF) continuous flow treatment chambers. *Innov. food sci. emerg. Technol.* 3, 233–245. doi: 10.1016/S1466-8564(02)00044-9

Liu, D., Lebovka, N. I., and Vorobiev, E. (2013). Impact of electric pulse treatment on selective extraction of intracellular compounds from *Saccharomyces cerevisiae* yeasts. *Food Bioproc. Tech.* 6, 576–584. doi: 10.1007/s11947-011-0703-7

Liu, M., Zhnag, M., Lin, S., Lui, J., Yang, Y., and Jin, Y. (2012). Optimization of extraction parameters for protein from beer waste brewing yeast treated by pulsed electric fields (PEF). *African J. Microbiol. Res.* 6, 4739–4746. doi: 10.5897/AJMR12.117

Loring, H. S., Fairley, J. L., Bortner, H. W., and Seagran, H. L. (1952). A spectrophotometric method for the analysis of the purine and pyrimidine components of ribonucleic acid. *J. Biol. Chem.* 197, 809–821.

Maiuolo, J., Oppedisano, F., Gratteri, S., Muscoli, C., and Mollace, V. (2016). Regulation of uric acid metabolism and excretion. *Int. J. Cardiol.* 213, 8–14. doi: 10.1016/j.ijcard.2015.08.109

Martinez, J. M., Gebrian, G., Alvarez, I., and Raso, J. (2016). Release of mannoproteins during *Saccharomyces cerevisiae* autolysis induced by pulsed electric field. *Front. Microbiol.* 7:1435. doi: 10.3389/fmicb.2016.01435

Maza, M. A., Delso, C., Álvarez, I., Raso, J., and Martínez, J. M. (2020). Effect of pulsed electric fields on mannoproteins release from *Saccharomyces cerevisiae* during the aging on lees of Caladoc red wine. *LWT* 118:108788. doi: 10.1016/j.lwt.2019.108788

Middelberg, A. P. J. (2012). "Releasing biopharmaceutical products from cells," in *Biopharmaceutical Production Technology*, ed. G. Subramanian (Hoboken, NJ: John Wiley & Sons), 79–105. doi: 10.1002/9783527653096.ch3

Mohamed, Z., Ridha, M. O., Eddine, L. S., and Rebiai, A. (2018). Phenolic content, antioxidant and antibacterial activities of peel extract from Punica Granatum L. *Res. J. Chem. Environ.* 22, 9–15.

Monch, S., and Stute, R. (2002). *Process for production yeast extracts*. US 2002/0081357 A1.

Munder, M. C., Midtvedt, D., Franzmann, T., Nüske, E., Otto, O., Herbig, M., et al. (2016). A pH-driven transition of the cytoplasm from a fluid- to a solid-like state promotes entry into dormancy. *eLife* 5, e09347. doi: 10.7554/eLife.09347

Narayanaswamy, R., Levy, M., Tsechansky, M., Stovall, G. M., O'Connell, J. D., Mirrielees, J., et al. (2009). Widespread reorganization of metabolic enzymes into reversible assemblies upon nutrient starvation. *Proc. Natl. Acad. Sci. U S A.* 106, 10147–10152. doi: 10.1073/pnas.0812771106

Nasseri, A. T., Rasoul-Amini, S., Morowvat, M. H., and Younes, G. (2011). Single cell protein: production and process. *American J. Food Sci.* 6, 103–116. doi: 10.3923/ajft.2011.103.116

Orij, R., Postmus, J., Ter Beek, A., Brul, S., and Smits, G. J. (2009). In vivo measurement of cytosolic and mitochondrial pH using a pH-sensitive GFP derivative in *Saccharomyces cerevisiae* reveals a relation between intracellular pH and growth. *Microbiology* 155, 268–278. doi: 10.1099/mic.0.022038-0

Pavlin, M., Leben, V., and Miklavčič, D. (2007). Electroporation in dense cell suspension-theoretical and experimental analysis of ion diffusion and cell permeabilization. *Biochem. Biophys. Acta* 1770, 12–23. doi: 10.1016/j.bbagen.2006.06.014

Pellegrini, N., Serafini, M., Colombi, B., Del Rio, D., Salvatore, S., Bianchi, M., et al. (2003). Total antioxidant capacity of plant foods, beverages and oils consumed in Italy assessed by three different in vitro assays. *J. Nutr.* 133, 2812–2819. doi: 10.1093/jn/133.9.2812

Pérez-Torrado, R., Gamero, E., Gómez-Pastor, R., Garre, E., Aranda, A., and Matallana, E. (2015). Yeast biomass, an optimized product with myriad applications in the food industry. *Trends Food Sci.Technol.* 46, 167–175. doi: 10.1016/j.tifs.2015.10.008

Postma, P. R., Pataro, G., Capitoli, M., Barbosa, M. J., Wijffels, R. H., Eppink, M. H., et al. (2016). Selective extraction of intracellular components from the microalga *Chlorella vulgaris* by combined pulsed electric field-temperature treatment. *Bioresour. Technolol.* 203, 80–88. doi: 10.1016/j.biortech.2015.12.012

Poznanski, J., Szczesny, P., Ruszczynska, K., Zielenkiewicz, P., and Paczek, L. (2013). Proteins contribute insignificant to the intrinsic buffering capacity of yeast cytoplasm. *Biochem. Biophys. Res. Commun.* 430, 741–744. doi: 10.1016/j.bbrc.2012.11.079

Pucihar, G., Kotnik, T., Teissié, J., and Miklavcic, D. (2007). Electropermeabilization of dense cell suspensions. *Eur. Biophys. J.* 36, 173–185. doi: 10.1007/s00249-006-0115-1

Rahman, I., Kode, A., and Biswas, S. K. (2006). Assay for quantitative determination of glutathione and glutathione disulfide levels using enzymatic recycling method. *Nat. Protoc.* 1, 3159–3165. doi: 10.1038/nprot.2006.378

Rols, M. P., and Teissie, J. (1990). Electropermeabilisation of mammalian cells. Quantitative analysis of the phenomenon. *Biophys. J.* 58, 1089–1098. doi: 10.1016/S0006-3495(90)82451-6

Santiago, L. A. and Mori, A. (1993). Antioxidant defenses of baker's yeast against free radicals and lipid peroxides in rat brain. *Arch. Biochem. Biophys.* 306, 16–21. doi: 10.1006/abbi.1993.1474

Schwartz, R., Ting, C. S., and King, J. (2001). Whole proteome pI values correlate with subcellular localizations of proteins for organisms within the three domains of life. *Genome Res.* 11, 703–709. doi: 10.1101/gr.158701

Scopes, R. K., Griffits-Smith, K., and Millar, D. G. (1981). Rapid purification of yeast alcohol dehydrogenase. *Anal. Biochem.* 118, 284–285. doi: 10.1016/0003-2697(81)90583-2

Sergeev, V. A., Solosenko, V. M., Besrukov, M. G., and Saporovskaja, M. B. (1984). Vergleichscharakteristik von isolaten der gesamteiweisse der Hefe in Abhängigkeit von den bedingungen ihrer abscheidung. *Acta Biotechnol.* 4, 105–115. doi: 10.1002/abio.370040204

Shetty, K. J., and Kinsella, J. E. (1979). Preparation of yeast protein isolate with low nucleic acid by succinylation. *J. Food Sci.* 44, 633–638. doi: 10.1111/j.1365-2621.1979.tb08464.x

Shynkaryk, M. V., Lebovka, N. I., Lannoisellé, J.-L., Nonus, M., Bedel-Clotour, C., and Vorobiev, E. (2009). Electrically-assisted extraction of bio-products using high pressure disruption of yeast cells (*Saccharomyces cerevisiae*). *J. Food Engineer.* 92, 189–195. doi: 10.1016/j.jfoodeng.2008.10.041

Simões, T., Teixeira, M. C., Fernandes, A. R., and Sá-Correia, I. (2003). Adaptation of *Saccharomyces cerevisiae* to the herbicide 2,4-dichlorophenoxyacetic acid, mediated by Msn2p- and Msn4p-regulated genes: Important role of SPI1. *Appl. Environ. Microbiol.* 69, 4019–4028. doi: 10.1128/AEM.69.7.4019-4028.2003

Singleton, V. L., Orthofer, R., and Lamuela-Raventós, R. M. (1999). Analysis of total phenols and other oxidation substrates and antioxidants by means of folin–ciocalteu reagent. *Methods Enzymol.* 299, 152–178. doi: 10.1016/S0076-6879(99)99017-1

Spirin, A. S. (1958). Spectrophotometric determination of total nucleic acids. *Biokhim* 23, 656–662.

Trevelyan, W. E. (1976). Autolytic methods for the reduction of the purine content of baker's yeast, a form of single-cell protein. *J. Sci. Food Agric.* 27, 753–762. doi: 10.1002/jsfa.2740270809

Valentin, E., Herrero, E., Rico, H., Miragall, F., and Sentandreu, R. (1987). Cell wall mannoproteins during the population growth phases in *Saccharomyces cerevisiae*. *Arch. Microbiol.* 148, 88–94. doi: 10.1007/BF00425354

Valli, M., Sauer, M., Branduardi, P., Borth, N., Porro, D., and Mattanovich, D. (2005). Intracellular pH distribution in *Saccharomyces cerevisiae* cell population, analyzed by flow cytometry. *Appl. Environ. Microbiol.* 71, 1515–1521. doi: 10.1128/AEM.71.3.1515-1521.2005

van Reis, R., and Zydney, A. (2007). Bioprocess membrane technology. *J. Membr. Sci.* 297, 16–50. doi: 10.1016/j.memsci.2007.02.045

Waldron, C., and Lacroute, F. (1975). Effect of growth rate on the amounts of ribosomal and transfer ribonucleic acids in yeast. *J. Bacteriol.* 122, 855–865. doi: 10.1128/jb.122.3.855-865.1975

Warner, J. R. (1999). The economics of ribosome biosynthesis in yeast. *Trends Biochem. Sci.* 22, 437–440. doi: 10.1016/s0968-0004(99)01460-7

Weaver, J. C., and Chizmadzhev, Y. A. (1996). Theory of electroporation: A review. *Bioelectrochem. Bioenerg.* 41, 135–160. doi: 10.1016/S0302-4598(96)05062-3

Wouters, P. C., Dutreux, N., Smelt, J. P., and Lelieveld, H. L. (1999). Effects of pulsed electric fields on inactivation kinetics of *Listeria innocua*. *Appl. Environ. Microbiol.* 65, 5364–5371. doi: 10.1128/AEM.65.12.5364-5371.1999

Zlotnik, H., Fernandez, M. P., Bowers, B., and Cabib, E. (1984). Saccharomyces cerevisiae mannoproteins form an external layer that determinates wall porosity. *J. Bacteriol.* 159, 1018–1026. doi: 10.1128/jb.159.3.1018-1026.1984

Żymańczyk-Duda, E., Brzezińska-Rodak, M., Klimek-Ochab, M., Duda, M., and Zerka, A. (2017). Yeast as a versatile tool in biotechnology. *Yeast Ind. Appl.* 1, 3–40. doi: 10.5772/intechopen.70130

Conflict of Interest: The authors declare that the research was conducted in the absence of any commercial or financial relationships that could be construed as a potential conflict of interest.

Copyright © 2020 Ganeva, Angelova, Galutzov, Goltsev and Zhiponova. This is an open-access article distributed under the terms of the Creative Commons Attribution License (CC BY). The use, distribution or reproduction in other forums is permitted, provided the original author(s) and the copyright owner(s) are credited and that the original publication in this journal is cited, in accordance with accepted academic practice. No use, distribution or reproduction is permitted which does not comply with these terms.

Advantages of publishing in Frontiers

OPEN ACCESS
Articles are free to read for greatest visibility and readership

FAST PUBLICATION
Around 90 days from submission to decision

HIGH QUALITY PEER-REVIEW
Rigorous, collaborative, and constructive peer-review

TRANSPARENT PEER-REVIEW
Editors and reviewers acknowledged by name on published articles

Frontiers
Avenue du Tribunal-Fédéral 34
1005 Lausanne | Switzerland

Visit us: www.frontiersin.org
Contact us: frontiersin.org/about/contact

REPRODUCIBILITY OF RESEARCH
Support open data and methods to enhance research reproducibility

DIGITAL PUBLISHING
Articles designed for optimal readership across devices

FOLLOW US
@frontiersin

IMPACT METRICS
Advanced article metrics track visibility across digital media

EXTENSIVE PROMOTION
Marketing and promotion of impactful research

LOOP RESEARCH NETWORK
Our network increases your article's readership